Characterization of neutron radiation fields: applications in scanning proton radiotherapy

Miguel Ángel Caballero Pacheco

Characterization of neutron radiation fields: applications in scanning proton radiotherapy

Miguel Ángel Caballero Pacheco

PhD Thesis

Universitat Autònoma de Barcelona
Departament de Física
Programa de doctorat en Física

Supervisor:
Dr. Carles Domingo Miralles

2023

The research work performed during the elaboration of this Ph.D. Thesis has been partially financed by the Spanish "Ministerio de Ciencia e Innovación" under projects PGC2018-093836-B-C22 and PID2021-128346NB-C21.

Many experimental results presented and analysed in this work have been obtained from measurement campaigns organized at different research centers, all of whom I thank:

- *MAASTRO Clinic, Maastricht, Netherlands. Irradiation campaign at the Mevion proton radiotherapy facility, organized by the WG9 (radiation dosimetry in radiotherapy) of EURADOS (the European Radiation Dosimetry Group).*
- *CERF (CERN-EU high-energy Reference Field) at CERN, Switzerland.*
- *ALBA-CELLS Synchroton, Cerdanyola del Vallès, Spain.*
- *ENEA Frascati, Italy. Irradiation at the HOTNES thermal neutron source.*

I thank EURADOS for the Young Scientist Grant 2020 to the proposal "Methodology on out-of-field doses in proton radiotherapy", that financed a 2 months research stay at SCK-CEN. Also to UAB for the research mobility grant financing a 3 months research stay at LNF-INFN.

Contents

Agradecimientos

Este trabajo va dedicado a mi familia y amigos.

De mi madre, **Pepi Pacheco Amaya** (La Pepi), destaca su poder de intuición y una armadura la cual frecuentemente olvidamos que protege un corazón. De mi padre, **José Antonio Caballero Ruiz**, destaca el sentido de la disciplina y la responsabilidad. De mi hermano, **José Antonio Caballero Pacheco**, destaca el sentido de la responsabilidad por el trabajo bien hecho y la independencia frente a opiniones externas. Por insistencia vamos a poner también a mi cuñada, de **María Tombilla Sanromán** me gustaría destacar su actitud crítica y la capacidad de ver una situación desde varios puntos de vista.

Me gustaría dedicar esta tesis a una gran amiga, **Andrea Herrera González**, la cual se encuentra en estos momentos, y ya durante demasiados años, en una batalla. Por sus virtudes, y en especial, por su sentido del humor y por su fortaleza, ella es un espejo en la que me veo reflejado. Está claro que estas palabras no van a ayudarte a avanzar en la batalla, pero que sepas que siempre me acuerdo de ti y que estoy, como siempre, a tú disposición.

Mis amigos de toda la vida, de **Borja Labrador Reina** destaca su carácter humilde y tranquilo. Básicamente, sé que tengo otro hermano en caso de que necesitara cualquier cosa. **Laia Lorenzo Venzal** es imparable en general. De **Berta Lopez Soler** vamos a destacar su carácter humilde y alegre (excepto cuando la hacemos enfadar a propósito). **Omar Mingorance Pajares**, **Marta Valls Peralbo**, **Maria Sánchez Camacho**, **Paula Fontrodona Serra**, **Sergi Parra Barnes**, **Núria Nogueras Segura**, **Paula Serra González** destacan, esencialmente, su carácter amable y sencillo. Las virtudes que todos ellos tienen en común es que tienen un gran sentido del humor y obertura de mente.

No olvidemos al exiliado **Nícolas Blanco van Bergen** y hermano **Facundo Blanco van Bergen**.

Las virtudes que yo pueda poseer provienen, en parte, debido a todos los mencionados y a lo que sigo aprendiendo de ellos.

Tengo suerte de conocer estas almas donde uno puede reposar y donde se puede hablar de todo con humildad, en libertad y con humor. La verdad es que me gustaría veros muchísimo más, pero de sobra conocéis mis circunstancias. Sinceramente creo que todo va a mejorar en un futuro próximo y realmente espero que no nos dejemos de reunir y de alquilar cuantas casas rurales hagan falta. Creo sinceramente que nos lo pasamos muy bien juntos.

Rodéate de buenos y tú lo parecerás.
Rodéate de sabios y algo en ti se quedará.

Abstract

This work presents the techniques and methodologies employed by the Universitat Autònoma de Barcelona (UAB) radiation research group in neutron spectrometry and neutron dosimetry topics as well as their application in different situations. Up to four techniques are used by the group: a neutron dosimeter based on the plastic Poly Allyl Diglycol Carbonate (PADC) used as etched track detector, a Bonner Sphere System (BSS) using a ^{3}He proportional counter as a thermal neutron detector, a BSS using gold foils as a thermal neutron detector and Monte Carlo (MC) simulations employing MCNP executables.

In particular, experimental characterization and measurements of the neutron field were performed in three different particle accelerators: in a proton radiotherapy centre using the Mevion S250i Hyperscan single-room delivery system, in ALBA electron synchrotron, and in the CERN-EU high-energy Reference Field (CERF) facility. Measurements of the neutron component in proton radiotherapy were done when the particle beam scanning technique was used and the measurements took place in points outside of the therapeutic proton field but inside of phantoms (water tank phantom and child anthropomorphic phantom). Spectrometric measurements in air around the anthropomorphic phantom were also obtained. MC simulations were heavily used in order to improve the neutron dose assessment, according to the presented methodologies. An approximation to model the energy degraders used in proton radiotherapy is presented as well.

Due to the increasing interest in the impact of mixed radiation fields in the total response of a radiation detector, an equation is proposed to deal with mixed radiation fields when a radiation detector has a main sensitivity to a specific type of particle but it has, unavoidably, a residual response to other particles of the field. Energy dependence on the response is included in the mentioned equation.

On the other hand, as neutron quality factors are needed in order to provide the neutron dose equivalent (for instance in proton radiotherapy out-of-field neutron doses) and it turns out that they are lacking in an explicit way in the energy range from 25 to 10^4 MeV, a methodology to compute them is presented and a recommendation in that energy range is given. Secondary results of this work are the energy distribution characterization of the neutrons in the HOmogeneous Thermal NEutron Source (HOTNES) design found in ENEA-Frascati facility and the use of MC simulations to study the impact of moist soils on the energy distribution of the neutron fluence near ground.

Total out-of-field doses in proton radiotherapy treatments with Mevion S250i Hyperscan single-room delivery system are lower in comparison with total out-of-field doses in photon treatments. However, the design of the facility and the delivery system used in proton radiotherapy treatments (under the particle beam scanning technique) are critical in the production of secondary radiation and, in particular, in the production of neutrons.

In combination with the results from other works, for anthropomorphic paediatric 5 years old phantom at a distance of 12 cm from the isocenter, a total out-of-field dose (per therapeutic Gy) of ~ 7000 μSv Gy^{-1} is found for photon treatments, while in particle beam scanning proton radiotherapy treatments, a total out-of-field dose of ~ 300 μSv Gy^{-1} is found in Mevion S250i Hyperscan single-room delivery system and ~ 100 μSv Gy^{-1} is found in IBA multiple-room delivery system. Economical aspects in the construction of a proton radiotherapy centre are important and ALARA principle should be properly interpreted.

Chapter 1

Introduction and objectives

Among the common radiations, neutrons have always been regarded as the most difficult to detect. One of the reasons is that neutrons have no net charge and can only be detected via nuclear reactions, so that heavy secondary charged products can be registered. Charged particles are produced from a neutron field, using neutron converters. While gamma rays also do not have a net charge, their interactions are traditionally covered by atomic reactions (*i.e.,* interactions with atomic electrons) through the three well-known atomic processes: the photoelectric effect, compton scattering and pair production, whose theoretical bases are well understood in the energy range for the traditional uses of that radiation. On the other hand, neutron cross sections with matter are often based on empirical data that are often inadequate to cover the desired energy range. Another factor that makes neutron detection difficult is that neutron radiation can span over 12 decades in energy (from 10^{-9} to 10^{3} MeV) compared to approximately 4 decades for traditional gamma rays (about 10 keV to 100 MeV). To further complicate the detection of neutrons, energy distributions of the neutron fluence in the thermal region are influenced by the molecular structure, while in the high-energy region, many reaction channels are possible and existing nuclear interaction models are not fully well known. Due to the difficulties in fully understanding the neutron transport in the mentioned energy range, neutron detection remains very much an empirical science [IAEA, 2020].

Due to the intrinsic properties of neutrons, they are a powerful probe of the matter and they can be used to face actual scientific and societal problems in the areas of energy, transport, communications, computing technology, environment and health care. More specifically, through the study of the neutrons and their different kind of interactions and physical principles in a material, applications can be defined under the frame of: neutron scattering and spectroscopy (solid state physics and chemistry, metallurgy, soft matter, magnetism, geophysics and oil industry, soil moisture studies [IAEA, 2017], etc), neutron imaging (qualification of pyrotechnics for propulsion and explosives in space and aerospace systems, presence of nuclear elements, quality control in car, aviation and building industry, non-destructive examination of nuclear fuel and its shield, geology, plants, archeology, metallurgy, etc), nuclear physics (measurement of cross sections in nuclear astrophysics and nuclear structure, etc), activation (inspection of bridges weakened by salt ingress by investigating the chlorine content in concrete bridges and structures, forensic science, art, archaeology, homeland security, etc), irradiation (neutron irradiation damage in materials, radiobiology, radioisotope production, silicon doping, neutron resistance tests of structural materials, etc), reactor physics, Boron Neutron Capture Therapy (BNCT) and metrology (test and calibration of reference detectors, qualification of dosimetry equipment, etc)

[IAEA, 2021].

In this work, in particular, we have been working in the frame of metrology (according to the classification before) where neutrons contribute to an undesired out-of-field dose equivalent in particle beam scanning (PBS) proton radiotherapy treatments [ICRU, 2007] which is the application in that most of our experimental measurements have been carried out.

In this work, experimental measurements on neutrons have been carried out using three different techniques: using a neutron radiation detector based on Poly Allyl Diglycol Carbonate (PADC) or CR-39, using an active Bonner Sphere System (BSS) whose thermal neutron detector is an ^{3}He proportional tube and using a passive BSS whose thermal neutron detector is a gold foil which is activated by neutrons.

In addition to the experimental techniques, Monte Carlo (MC) simulations were used to complement the experimental work.

Radiation is a well-documented risk factor for cancer induction in virtually any tissue as shown through atomic bomb studies, accidental and occupational exposures, and medically exposed individuals. Different organs show different susceptibilities to radiation-induced cancer per Sv of dose equivalent, and this susceptibility varies with age and, to a lesser extent, sex. Children are several times more sensitive to radiation-induced cancer than adults and also depending on the particular organ [Kry et al., 2017].

Radiation is a clear risk factor for second cancers, but it is only one of many etiologic bases. Roughly 10 % of long-term survivors develop a second cancer; however, only a fraction of these second cancers are attributable to radiation treatment. Age, genetics, and environmental factors also contribute to the risk of developing a second cancer. Recent studies in adults show that of the 10 % of patients who developed a second cancer, 8 % of those were attributable to the actual radiation exposure from radiotherapy. That is to say, slightly less than 1 % of long-term survivors developed a second cancer from their radiotherapy. However, radiation appears to be a larger risk factor for pediatric patients and further quantification is required [Kry et al., 2017].

It was found that 12 % of second cancers occurred within the treated volume, 66 % occurred at the periphery of the treated volume (within 5 cm of the field edge), and 22 % occurred more than 5 cm away from the treated volume, although the study was not limited to radiation-induced second cancers [Kry et al., 2017].

The ALARA principle (exposure and the likelihood of exposure being as low as reasonably achievable) is defined in order to *reasonably* protect the public and environment, economic and social factors being taken into account [IAEA, 2018]. According to IAEA [2018], this means that the level of protection would be the best possible under the prevailing circumstances, and will thus not necessarily be the option with the lowest risk or dose. In order to understand better the *reasonable* concept in the definition of the ALARA principle, and in particular, when ALARA is applied in out-of-field doses when radiation treatments are being carried out, research in aspects of radiation protection and radiobiology should be fostered.

The radiation protection measurements done by Universitat Autònoma de Barcelona (UAB) and, in particular, through its collaboration with the Working Group 9: Radiation dosimetry in radiotherapy of the European Radiation Dosimetry Group (EURADOS-WG9) are relevant due to the fact that out-of-field doses cannot be computed with commercial treatment planning systems because they are not commissioned for *small* doses

(thought to be less than 1 % in respect to the target dose) and do not explicitly fully take into account the particle type and energy distribution of secondary radiation (which at the same time would increase computational times) [Paganetti, 2019]. Treatment planning systems become dramatically inaccurate outside the treatment field, necessitating a measurement or some other means of assessing the dose [Kry et al., 2017]. Therefore, measurements and MC simulations for out-of-field doses in-phantom or out-of-phantom is a task that can be done, in particular, by public institutions.

Among other results, in this work out-of-field neutron dose equivalents using experimental methods complemented by Monte Carlo simulations have been obtained so that, in the end, out-of-field neutron dose equivalent conversion coefficients (from therapeutic Gy to out-of-field mSv) are provided in Mevion S250i Hyperscan single-room environment under different parameters and experimental settings when the particle beam scanning proton radiotherapy modality is used.

It is well known that neutron radiation detectors must discriminate the signal coming from photons and the signal coming from neutrons in order to not overestimate the neutron reported dose. This thought can be extended at least in the case of passive systems, as it has been reported that mixed radiation fields can have an impact in the reported doses [Stolarczyk et al., 2018] which, in the end, will influence the total dose equivalent since radiation weighting factors and quality factors can depend on the particle type and their energy.

Summarising, the main objective of the work related to this Ph.D. Thesis is to determine dose equivalents (ambient and in-phantom) in proton radiotherapy with UAB methodologies. During the realization of this work, two issues were encountered: energy distributions of the neutron fluence can extend beyond 20 MeV (where neutron quality factors are explicitly missing) and radiation fields can actually be complicated mixed radiation fields. In order to tackle these problems, a methodology to compute neutron quality factors was designed and an equation to be used in mixed radiation fields was proposed. While elaborating this work, there was the opportunity of participating in other experiments or simulations for other projects, different from proton accelerators for radiotherapy, where contributions were made.

The manuscript is organized as follows: in Chapter 2 a brief summary is presented on how neutrons appear in particle accelerators and once these neutrons appear, how they can interact with matter. Chapter 3 introduces briefly the whole spectrum of quantities used to characterize a radiation field, dose equivalent definitions are expanded, and how neutron produces radiobiological damage is summarized. In Chapter 4 we describe the concept of calibration and we describe the detector systems used by UAB to characterize neutron fields. In Chapter 5 the main important concepts and procedures when using MC simulations as a complementary tool are presented. A very simple approximation to model energy degraders is highlighted and in spite of being a first approximation, it has delivered useful MC results. In this chapter it is also introduced how neutron-producing elements in PBS proton radiotherapy facilities are modelled (in the frame of this work). In Chapter 6 an equation to deal with mixed radiation fields is presented. The proposed equation simply links the calibration information to all particle types and energies from a given detector (*i.e.,* one has to know how a detector responds to any particle with any energy) with the probabilities of a given particle of a given energy to reach the boundaries of the detector. In other words, this mathematical equation express the fact that each particle type with a specific energy will produce *partial* responses on the detector so that the total interaction with the whole mixed radiation field will give rise to the total signal *stored* by the detector. In Chapter 7 we present the explicit results found in real neutron

fields during the realization of this work. The chapter is subdivided into three sections: Section 7.1 summarises the results obtained in the experiments performed in scanning proton radiotherapy facilities, which constitute the mainstream of this Ph.D. Thesis work; Section 7.2 abridges the results from MC calculations of the neutron quality factor, $Q(E)$, in a wide energy range; and finally, Section 7.3 presents the experimental and MC results for other applications both in similar and different neutron energy ranges than in the case of proton radiotherapy. Finally, conclusions and perspectives are included in Chapter 8.

Chapter 2

Neutron physics

The aim of this chapter is to make a brief and general introduction to the nuclear reactions that result, in their final state, in neutrons. Plenty of books and works exist today which perform an introduction to nuclear reactions and their associated kinematic relationships (*e.g.,* Baldin et al. [1961]). Regarding on the important details learnt by the kinematic equations, these will be highlighted in the text when needed.

Is important to notice that not all relevant physics of nuclear reactions is contained in the kinematic relationships. In the end, and taking into account all the complexity involved in nuclear reactions from both the theoretical side and the experimental side, it is important to focus our attention on the insights that can be learnt from cross section quantities and their associated differential distributions. This is the vision followed in this chapter and in this work, in general.

However, by analysing the actual knowledge (numerical values) of cross sections and their associated differential distributions, it turns out that experimental cross section data [EXFOR, 2022] and even evaluated cross section type quantities [ENDF, 2022] are scarce. This is specially the case in high energy regimes so that Monte Carlo (MC) simulation codes have to rely on nuclear models at these energies.

All together, it is important to consider MC simulations as a complementary tool rather than a independent tool from experimental measurements. A degree of benchmarking and validation must always exist between MC simulations and experimental measurements. This is specially relevant when MC simulations are intended to be used as independent tool [Kry et al., 2017], specially in higher energy regimes.

Neutrons discovered by Chadwick [1932] are particles constituted by three charged quarks, one positive charged quark u ($q_{\mathrm{u}} = \frac{2}{3}q_{\mathrm{e}^-}$) and two negative charged quarks d ($q_{\mathrm{d}} = -\frac{1}{3}q_{\mathrm{e}^-}$) where q_{e^-} is the electrical charge of the electron. The spatial distribution of the quarks inside the neutron produces a spatial charge density, $\rho(r, \theta, \varphi)$, related to that shown in Figure 2.1.

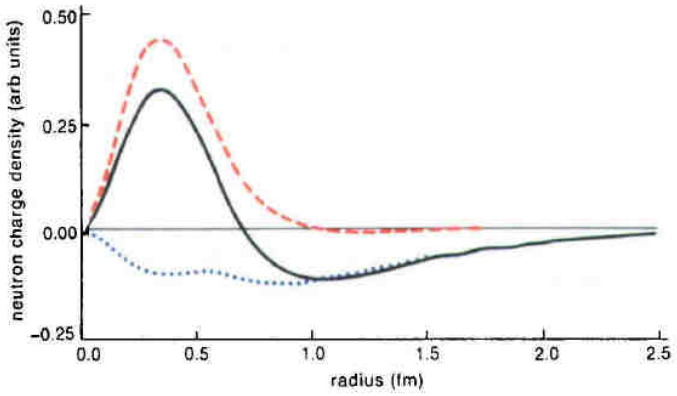

Figure 2.1: Spatial charge density of a neutron is shown in black. From Górski et al. [1992] and Brand et al. [1996].

However, in integrating this spatial charge density in the volume of the neutron, V_{ne}, we obtain that the net charge of the neutron, q_{ne}, is

$$q_{\mathrm{ne}} = \int_{V_{\mathrm{ne}}} \rho(r, \theta, \varphi)\, \mathrm{d}V_{\mathrm{ne}} = 0. \tag{2.1}$$

Moreover, due to the currents of the quarks inside the neutron, a neutron magnetic moment in the sense and direction of the also generated neutron magnetic field arise. We can imagine this situation as each quark forming circular closed currents inside the neutron and generating each of them a quark magnetic moment so that the addition of these three contributions give rise to the actual neutron magnetic moment.

So, when a neutron is travelling in a material it is seeing the distribution of nuclei and the distribution of electronic magnetization and the reason is that the magnetic moment of the neutron interacts with the magnetic moment of the atomic electrons or the magnetic field produced by the atomic electrons [Kittel, 2005]. The cross section for the neutron-electron interactions can be even of the same order of magnitude than that of the neutron-nuclear interaction [Kittel, 2005], [Bacon, 1966], [Halpern et al., 1938], [Lynn, 2012], [Pynn, n.d.], [Zaliznyak et al., 2015]. Although magnetic scattering can have relevance, it does not produce a transformation of the neutron into another particle in the final state and it is only of relevance for thermal neutrons as their associated De Broglie wavelength can span up to several atoms according to the classification of the matter and neutrons shown in Tables 2.1 and 2.2, respectively.

Table 2.1: Lengths in matter

Scale	Length
Molecular or inter-atomic distances	$>$ Å
Atomic	$\sim$ Å
Nuclear	$\sim$ fm
Nucleon	$<$ fm

Particles are, at the same, waves. Specifically, a free particle in space is a wave packet so, actually, particles are dislocalized in space forming a probability wave or a cloud whose shape is precisely related to the wave function shown in Figure 2.2, which is also related

Table 2.2: Neutron classification in energies and neutron interactions with the matter

Neutron classification	$E_{\mathrm{MIN.}}$	$E_{\mathrm{MAX.}}$	λ_{DB}	Comment on the interaction
Thermal neutrons	-	1 eV	$\lambda_{\mathrm{DB}} > 0.29$ Å	Interaction with whole molecules
Epithermal neutrons	1 eV	0.1 MeV	0.29 Å $> \lambda_{\mathrm{DB}} > 90.44$ fm	Main interactions with the atomic nucleus
Fast neutrons	0.1 MeV	10 MeV	90.44 fm $> \lambda_{\mathrm{DB}} > 9.02$ fm	
High energy neutrons	10 MeV	-	$\lambda_{\mathrm{DB}} < 9.02$ fm	Main interactions with nucleons

to the De Broglie wavelength

$$\lambda_{\mathrm{DB}} = \frac{\mathrm{h}}{|\boldsymbol{p}|} = \frac{\mathrm{h}}{\sqrt{\left(\frac{E}{\mathrm{c}}\right)^2 + 2mE}}, \tag{2.2}$$

where $\mathrm{h} = 4.1356$ eV $\cdot$ s is the Planck constant, $|\boldsymbol{p}|$ is the linear momentum associated to the free particle, E is the kinetic energy of the particle, m is the mass of the particle (for a neutron $m_{\mathrm{ne}} = 939.5654$ MeV c^{-2}) and $\mathrm{c} = 2.9979 \times 10^8$ m s^{-1} is the velocity of light. The total energy of the free particle E_{T} is, therefore,

$$E_{\mathrm{T}} = E + m\mathrm{c}^2 = \sqrt{(|\boldsymbol{p}|\mathrm{c})^2 + (m\mathrm{c}^2)^2}. \tag{2.3}$$

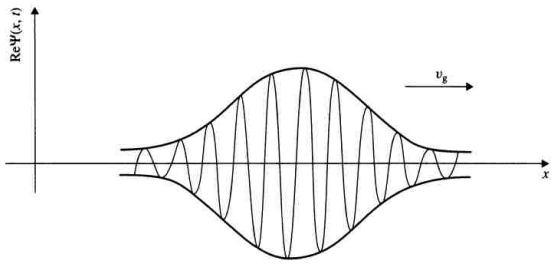

Figure 2.2: The function Re($\Psi(x,t)$) for a wave packet of a free particle propagating along the x-axis, with a group velocity. From Bransden et al. [2000].

Qualitatively speaking, one can interpret that the width of a wavepacket (of the wavefunction), Figure 2.2, is proportional to the De Broglie wavelength, Equation (2.2), and therefore the degree of dislocalization of the incident particle and the extension of its range of interaction with its surroundings can be qualitative assessed in terms of λ_{DB}.

Therefore, while higher values of λ_{DB} about the order of the length of a molecule mean that the wavefunction of the incident particle is interacting with whole molecules, smaller values about the order of the length of the nucleon mean that the interaction may take place with individual nucleons. For instance, thermal neutrons, with kinetic energies of the order of 10^{-9} MeV, and therefore with values of $\lambda_{\mathrm{DB}} = 9.04$ Å, have an interaction in a molecular level, so their transport has to include molecular and binding effects (target particles cannot be considered as free atoms). However, for high energy neutrons (with $E = 120$ MeV and $\lambda_{\mathrm{DB}} = 2.53$ fm) the interaction will be preferentially with the atomic nucleus or even with individual nucleons.

2.1 Cross sections

Any nuclear interaction i can be characterized by an equation like

$$\mathrm{a} + \mathrm{X} \rightarrow \mathrm{Y} + \mathrm{b}, \tag{2.4}$$

where a is the projectile, X is the target, Y is a reaction product and b is the ejectile, reaction product or outgoing particle. Equation (2.4) can be written simply as X(a,b)Y or (a,b).

A nuclear interaction i can be described by its cross section,

$$\sigma_i \quad \text{or} \quad \sigma\left(\mathrm{X(a,b)Y}\right), \tag{2.5}$$

which is related to the probability of the nuclear reaction i to take place. It has the dimension of an area (unit cm^2 or barn $\equiv 10^{-24}$ cm^2). In particular, the cross section depends not only on the reaction type, but also on the energy of the projectile and usually it will be written as $\sigma_i(E)$.

Usually we are interested in the energy and angular distributions of the outgoing particles coming from a nuclear reaction i, *i.e.,* particle b from Equation (2.4), and for that reason the differential cross section is defined. We can define the following differential cross section

$$\frac{\mathrm{d}^2\sigma_i}{\mathrm{d}E_\mathrm{b}\,\mathrm{d}\Omega_\mathrm{b}}, \tag{2.6}$$

so that the quantity $\mathrm{d}^2\sigma_i$ is related to the probability of having reaction i and having as a result an outgoing particle within an energy between E_b and $E_\mathrm{b} + \mathrm{d}E_\mathrm{b}$ and a solid angle between Ω_b and $\Omega_\mathrm{b} + \mathrm{d}\Omega_\mathrm{b}$. Actually, differential cross section, Equation (2.6), depends on the energy of the projectile and ejectile and the solid angle subtended by the ejectile, so Equation (2.6) can be written as $\frac{\mathrm{d}^2\sigma_i}{\mathrm{d}E_\mathrm{b}\,\mathrm{d}\Omega_\mathrm{b}}(E, E_\mathrm{b}, \Omega_\mathrm{b})$.

Along this work we will be using 2D plots and when plotting $\frac{\mathrm{d}^2\sigma_i}{\mathrm{d}E_\mathrm{b}\,\mathrm{d}\Omega_\mathrm{b}}(E, E_\mathrm{b}, \Omega_\mathrm{b})$, we will have to fix 2 variables, which will usually be E and Ω_b, so we can have an idea about the probability of having nuclear reactions giving, as a result, an energy distribution of E_b. Figure (2.3) is an example in which the energy distribution of the outgoing neutrons from reaction ^{12}C(p,xn)Y (p = proton) (according to the evaluated data ENDF/HE-VI) is exposed.

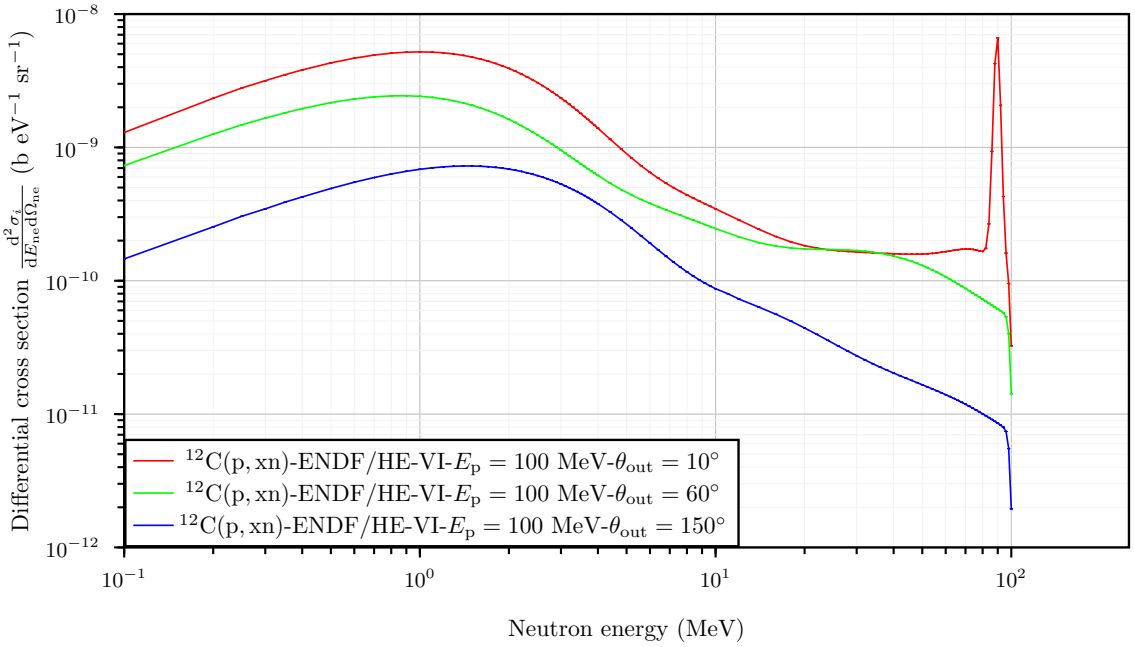

Figure 2.3: Energy distribution of the neutrons generated through reactions $^{12}C(p,xn)Y$. Evaluated data taken from ENDF [2022].

2.2 Neutron production caused by incident photons

In electron accelerators, the neutron production is dominated by the interaction of the electron induced bremsstrahlung photons with matter rather than by the direct interaction between the electrons and matter [International Atomic Energy Agency, 1979].

The radiation yield is the quantity that describes how much of the kinetic energy of the electrons is transformed into photon energy inside of a material. If one electron of initial kinetic energy $T_{el}^{(1)}$ is stopped in a material, its radiation yield is calculated as [Berger et al., 1964]

$$Y(T_{el}^{(1)}) = \frac{1}{T_{el}^{(1)}} \int_0^{T_{el}^{(1)}} \frac{S_{rad}(T)}{S_{el}(T) + S_{nuc}(T) + S_{rad}(T)} \, dT, \tag{2.7}$$

where the quantity $S_i(T)$ is the stopping power of an electron with kinetic energy T and for the physical process i (see Section 3.2). If the material is characterized by an atomic number Z, Equation (2.7) can be approximated by the following expression [Turner, 2007] [Koch et al., 1959]

$$Y(T_{el}^{(1)}, Z) = \frac{E_{ph}^{(N)}}{T_{el}^{(1)}} = \frac{6 \times 10^{-4} \, Z \, T_{el}^{(1)}}{1 + 6 \times 10^{-4} \, Z \, T_{el}^{(1)}}, \tag{2.8}$$

where $E_{ph}^{(N)}$ is the total energy brought by N photons.

Figure 2.4 presents the radiation yielding for different materials for electrons with energy up to 100 MeV.

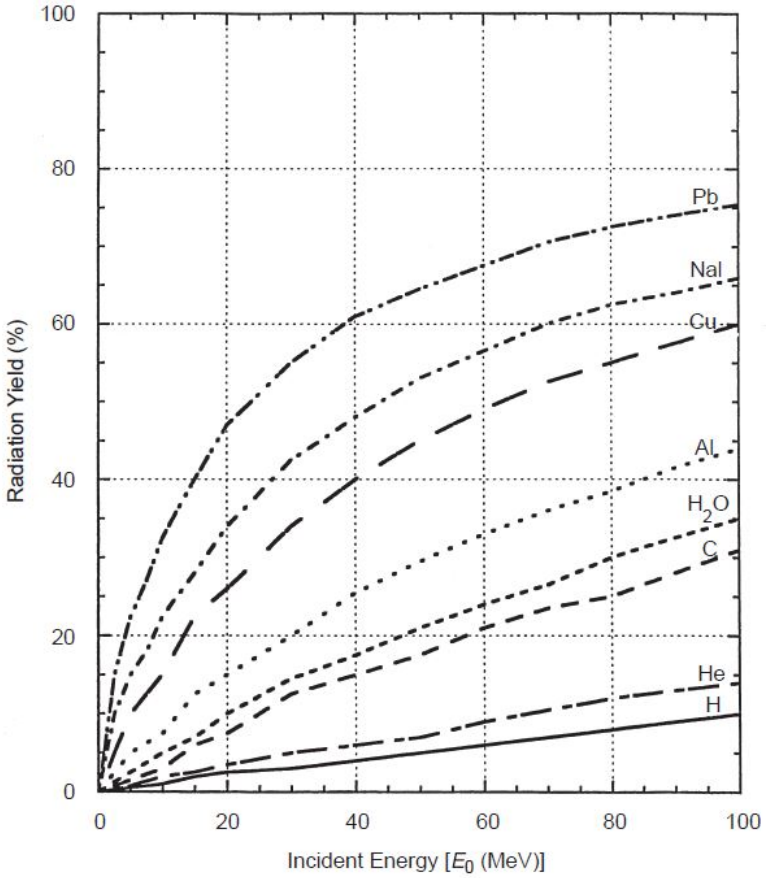

Figure 2.4: Radiation yield induced by incident electrons of energy E_0 in different materials. From NCRP [2003].

For each nucleus, there is a low-energy threshold for the incident photon, E_{th}, in which neutron production can be possible. These thresholds can be seen in the cross section plots in Figure 2.5. In the work of Di Fulvio et al. [2013] non-negligible neutron doses were measured in 6 MV X-ray treatment.

Photons can interact with matter producing photo-nuclear or photo-fission nuclear reactions leading to the production of angular and energy distributions of outgoing neutrons. This is mainly done through three different processes [International Atomic Energy Agency, 1979]:

1. The giant photonuclear resonance, between photon energies from E_{th} to ~ 30 MeV.
2. The quasi-deuteron effect, between photon energies from ~ 30 MeV to ~ 300 MeV.
3. The photopion production, for photon energies greater than ~ 300 MeV.

Currently, there are few measurements of the energy and angular distributions of secondary particles emitted in photonuclear reactions and, in addition, most of the existing measurements are for bremsstrahlung photon sources (see, *e.g.,* Jones et al. [1953], Price [1954], Reinhardt et al. [1962], Kashual et al. [1968], Shin et al. [1970], Alsmiller et al. [1970]), rather than of for monoenergetic sources as required for a complete cross section evaluation.

Usually, Monte Carlo (MC) simulations of the radiation transport largely depends upon nuclear model calculations to estimate emission spectra. These calculated spectra are

consistently obtained from the calculated cross sections for various channels *i.e.,* $(\gamma, 1n)$, $(\gamma, 2n)$, etc, and they can be validated through comparisons with measured values [Chadwick et al., 2003].

Typically, evaluated cross section data for photoneutron production have the shape shown in Figure 2.5, and it is thought that the dependency in the whole photon energy range should be that shown in Figure 2.6. The theoretical dependency shown in Figure 2.6 is taken into account in the nuclear models implemented in the MC codes [Chadwick et al., 2003].

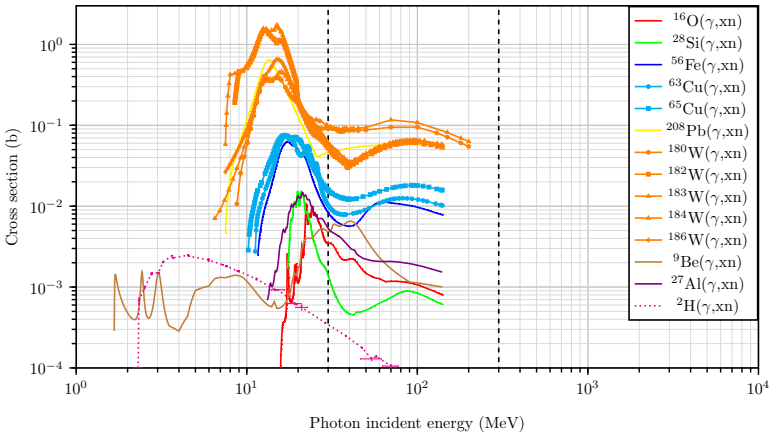

Figure 2.5: Photoneutron cross section per nucleus for incident photons. The vertical dashed lines split the three physical processes that produce photoneutrons (see text). From Kishida et al. [2005].

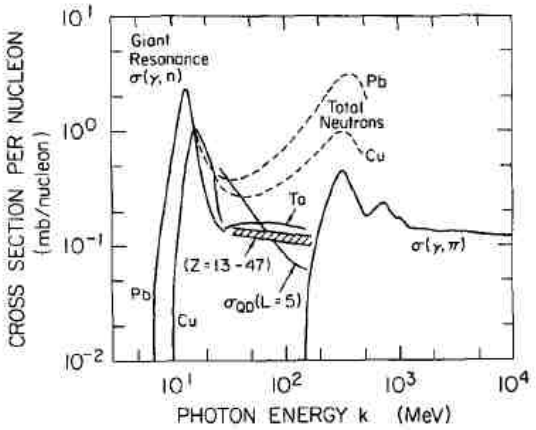

Figure 2.6: Photoneutron cross section per nucleon for incident photons. From International Atomic Energy Agency [1979].

In the region of the giant photonuclear resonance ($30\,\mathrm{MeV} > E > E_{\mathrm{th}}$), the photon wavelength is comparable to the size of the nucleus, so that photoabsorption proceeds primarily through a collective excitation of the nucleus, where the neutron and proton distributions undergo a bulk oscillation against each other [Chadwick et al., 1994]. There is some degree of anisotropy neutron emission following a dipole shape (peaking at 90° in respect to the direction of the incident photon) which is more important in heavy elements than in light elements [Chadwick et al., 2003] [Price, 1954] and is more important for neutrons with higher energies than those of lower energies as can be deduced from Figures 2.7, 2.8 and 2.9.

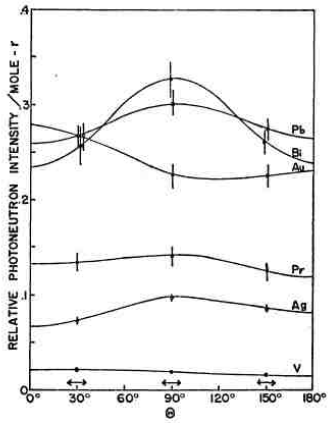

Figure 2.7: Angular distribution of photoneutrons created by 22 MeV bremsstrahlung photons incident on different materials. Neutrons detected by a moderated neutron detector sensitive to neutrons with energy higher than 10^{-7} MeV. From Price [1954].

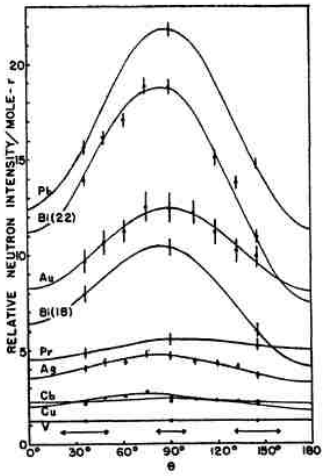

Figure 2.8: Angular distribution of photoneutrons created by 22 MeV bremsstrahlung photons incident on different materials. Neutrons detected by a threshold detector based on $^{27}Al(n,p)$ cross section with a threshold of 1.95 MeV. Therefore a configuration sensitive to neutrons with energy higher than 1.95 MeV. From Price [1954].

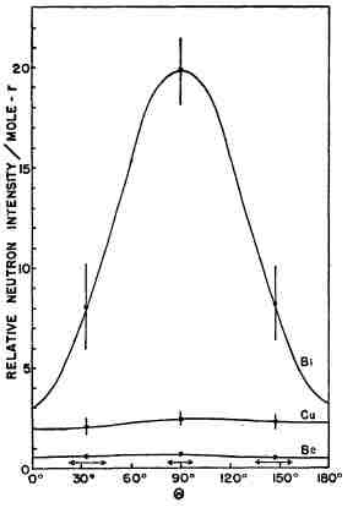

Figure 2.9: Angular distribution of photoneutrons created by 22 MeV bremsstrahlung photons incident on different materials. Neutrons detected by a threshold detector based on $^{28}Si(n,p)$ cross section with a threshold of 2.69 MeV. Therefore a configuration sensitive to neutrons with energy higher than 2.69 MeV. From Price [1954].

In the work of Price [1954] is also proved, through the use of an *epithermal neutron detector*, that neutrons of energy up to 0.13 MeV are emitted isotropically. Assuming isotropy, the unit energy distribution of the neutron fluence of the photoneutrons generated by the giant photonuclear resonance process is similar to the unit energy distribution of the neutron fluence of fission neutrons, both processes being well approximated using some of the following analytical expressions [International Atomic Energy Agency, 1979] [NCRP, 2003] [Vorobyev et al., 2011] [Bedogni et al., 2007]

$$\frac{1}{\Phi}\frac{\mathrm{d}\Phi(E)}{\mathrm{d}E} = \frac{\mathrm{d}\varphi(E)}{\mathrm{d}E} = \varphi_E(E) \tag{2.9}$$

$$\varphi_{E,\mathrm{FIS.}}(E) = \left(\frac{E}{T_{\mathrm{FIS.}}^2}\right)\mathrm{e}^{-\frac{E}{T_{\mathrm{FIS.}}}}, \tag{2.10}$$

$$\varphi_{E,\mathrm{MAX.}}(E) = \left(\frac{2}{\sqrt{\pi}}\right)\left(\sqrt{\frac{E}{T_{\mathrm{MAX.}}^3}}\right)\mathrm{e}^{-\frac{E}{T_{\mathrm{MAX.}}}}, \tag{2.11}$$

$$\varphi_{E,\alpha,\beta}(E) = N_{\alpha,\beta}\cdot E^{\alpha}\mathrm{e}^{-\frac{E}{\beta}}, \tag{2.12}$$

$$\varphi_{E,\mathrm{GAU.}}(E) = N_{\mathrm{GAU.}}\cdot \mathrm{e}^{-\frac{(E-\bar{E})^2}{2\sigma^2}}. \tag{2.13}$$

where $E > 0$ is the kinetic energy of the neutron and

$$T_i = k_{\mathrm{B}}\cdot t, \tag{2.14}$$

is an associated *temperature* in the fitted analytical distribution for the physical process i. It can be shown that T_i is actually the most probable kinetic energy of the encountered neutrons modelled with the Maxwell–Boltzmann distribution [Tipler et al., 2008]. $k_{\mathrm{B}} = 8.6173 \times 10^{-11}$ MeV K^{-1} is the Boltzmann constant and t is the temperature in units of Kelvin. N_i is the normalization constant associated with the fitted analytical distribution i so that

$$\int_0^\infty \varphi_{E,i}(E)\mathrm{d}E = 1. \tag{2.15}$$

Using Equation (2.15) it can be proved that

$$N_{\mathrm{GAU.}} = \frac{1}{\sqrt{\frac{\pi}{2}}\left(\mathrm{erf}\left(\frac{\bar{E}}{\sqrt{2}\sigma}\right)+1\right)\sigma}, \tag{2.16}$$

$$N_{\alpha,\beta} = \frac{1}{\beta^{\alpha+1}\Gamma(\alpha+1)}. \tag{2.17}$$

Where $\mathrm{erf}(x)$ is the error function and $\Gamma(x)$ is the gamma function.

Examples of distribution Equations (2.10), (2.11), (2.12) and (2.13) are graphically shown in Figure (2.10).

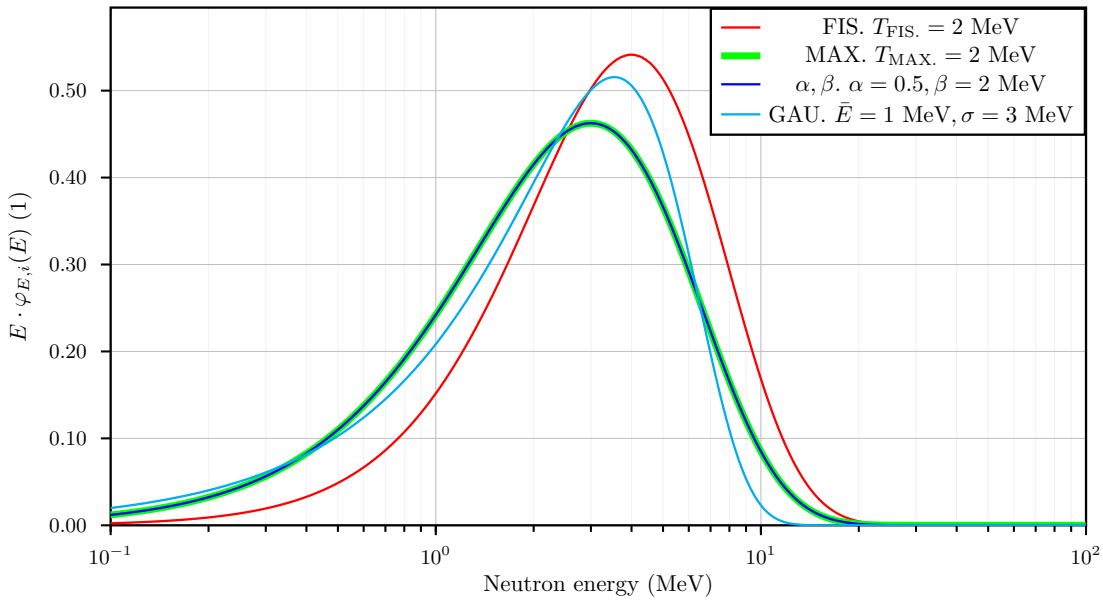

Figure 2.10: Lethargy representation (see Appendix C) of the unit energy distributions of the neutron fluence using Equations (2.10), (2.11), (2.12) *and* (2.13).

In the region of the quasi-deuteron effect ($300\,\mathrm{MeV} > E > 30\,\mathrm{MeV}$), the photon wavelength becomes smaller so that the interaction will take place with nuclear substructures rather than with the nucleus as a whole. In this energy range the dominant photoabsorption occurs primarily with neutron-proton pairs (quasideuterons) [Chadwick et al., 1994]. A two step model which considers the primary photoabsorption occurring via neutron-proton pairs, followed by a mechanism of fission-evaporation competition for the excited residual nucleus is usually employed [Terranova et al., 1998]. There is also a moderately degree of anisotropy in the neutron emission but this time slightly in the forward direction, see Figure 2.11. In addition, the degree of anisotropy depends on the energy of the emitted neutron as can be deduced by Figure 2.12 [Levinger, 1951]. As can be seen in Figures 2.5 and 2.6, the cross-section for this mechanism is about an order of magnitude below than

the giant photonuclear resonance process.

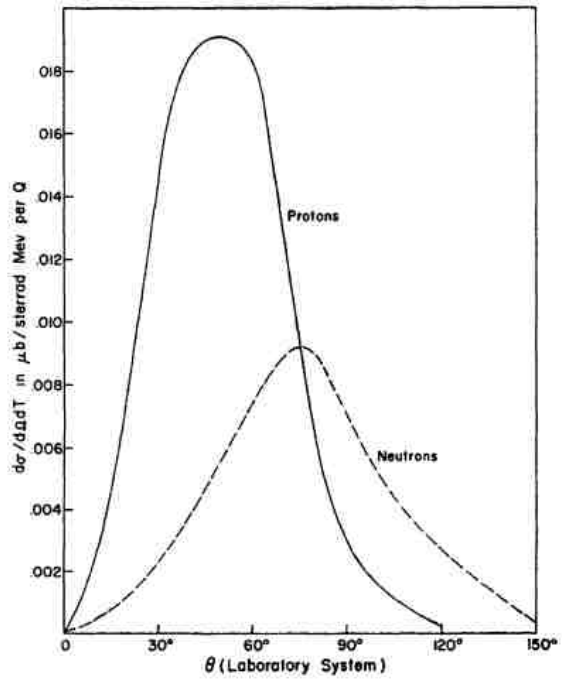

Figure 2.11: Theoretical differential cross section for photoneutron production per deuteron target in the quasi-deuteron model to obtain protons and neutrons with a kinetic energy of 100 MeV for an enough energetic incident photon spectrum. From Levinger [1951].

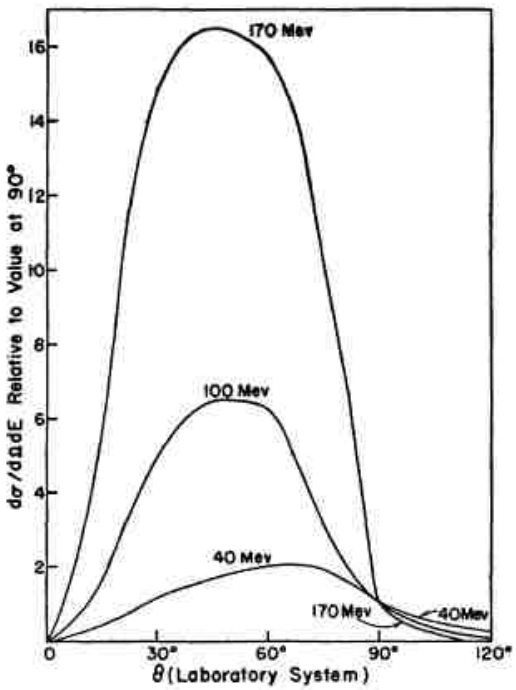

Figure 2.12: Theoretical differential cross section for photoproton production per deuteron target in the quasi-deuteron model to obtain protons with the indicated proton kinetic energies for an enough energetic incident photon spectra. From Levinger [1951].

Proofs that the proposed quasi-deuteron model and experiments are in agreement can be found, mostly for photoprotons, in Whitehead et al. [1958] and Gabriel et al. [1958].

When the two previous process are considered together with the interaction of the local generated photonucleons with the rest of the nucleus (pre-equilibrium and equilibrium stages [Chadwick et al., 1994]), it can be obtained the differential cross section shown in Figure 2.13 using the GNASH code [Chadwick et al., 1994]. Figure 2.13 shows that, in the end, neutrons with energies up to 10 MeV are emitted isotropically while neutrons with higher energies have a tendency to be emitted in the forward direction.

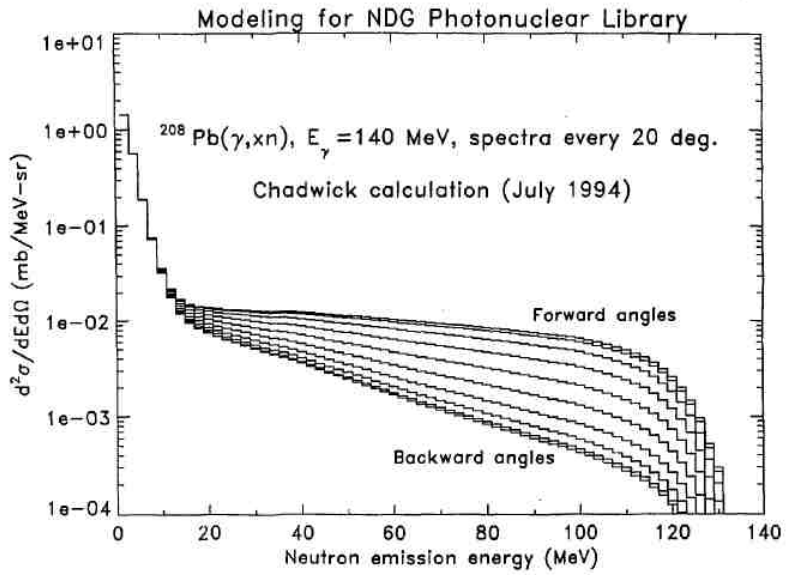

Figure 2.13: Theorical differential cross section for photoneutron production for mono-energetic photons of energy 150 MeV for Pb. From Chadwick et al. [1994].

In the region in which the photopion production is dominant ($E > 300\,\mathrm{MeV}$), the photon wavelength becomes even smaller so that the interaction will take place, in general, with single nucleons. Therefore, in this energy regime, the substructure of the nucleon is relevant [Rachen, 1996] [Armstrong et al., 1972]. The particular reactions that have neutrons in the final state are [Armstrong et al., 1972]

$$\gamma + \mathrm{p} \rightarrow \mathrm{n} + \pi^{+}, \tag{2.18}$$

$$\gamma + \mathrm{n} \rightarrow \mathrm{n} + \pi^{0}, \tag{2.19}$$

$$\gamma + \mathrm{d} \rightarrow \mathrm{n} + \pi^{0} + \mathrm{n}_{\mathrm{spectator}}, \tag{2.20}$$

$$\gamma + \mathrm{d} \rightarrow \mathrm{n} + \pi^{0} + \mathrm{p}_{\mathrm{spectator}}, \tag{2.21}$$

$$\gamma + \mathrm{n} \rightarrow \mathrm{n} + \mathrm{p}. \tag{2.22}$$

Figure 2.14 shows the total inelastic photonuclear cross section including the photopion production regime as a function of the incident photon energy.

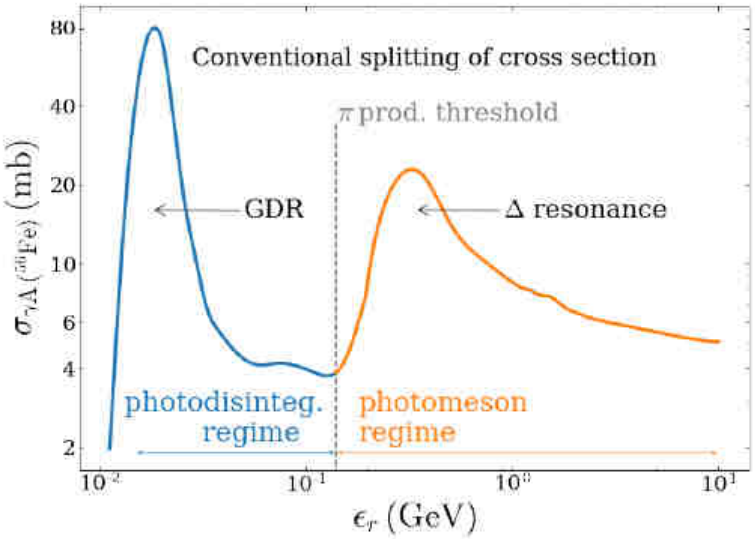

Figure 2.14: Total inelastic photonuclear cross section for ^{56}Fe as a function of photon energy. The convention of distinguishing two regions based on the photon energy is represented with a change of the color. The photodisintegration portion (in blue) refers to photon energies below the photopion production threshold (∼ 140 MeV), and the the photomeson portion (in orange) refers to photon energies above the photopion production threshold. From Morejon et al. [2019].

The conclusion of the previous exposed physics is that when a photoabsorption mechanism (through some of the three previous interactions) takes place and the resulting energy is partially or totally shared with the rest of the nucleus (pre-equilibrium or equilibrium stage [Chadwick et al., 2003]), it turns out that the angular distribution of neutrons is not isotropic and therefore this fact has to be taken into account in designing irradiation campaigns dedicated to neutron detection. Moreover, experimental data in angular distributions of outgoing neutrons is scarce and this has, as a consequence, that nuclear models are implemented in the MC codes and therefore MC simulations have only a degree of reliability.

2.3 Neutron production caused by incident hadrons

Besides low-energy nuclear reactions, we can classify the reactions induced by hadrons leading to neutrons in the final state as follows

- Spontaneous fission, as a physical process not induced by any incident particle.
- Induced fission with low-energy incident hadrons.
- Induced fission with high-energy incident hadrons and photons.
- Spallation processes.

2.3.1 Spontaneous fission

Spontaneous fission of a nucleus takes place in its ground state due to quantum tunnelling arising from the Coulomb repulsion of the protons inside the nucleus [Naik et al., 2021].

A perfect example of a nuclide undergoing spontaneous fission is ^{252}Cf, which is, in addition, a neutron calibration source [ISO-8529-1:2021, 2021]. From evaluation Brown et al. [2018] it is seen that, given a radioactive activity A, only 3.0920 ± 0.0080 % (branching ratio) of the times ^{252}Cf is undergoing spontaneous fission while a 96.9080 ± 0.0080 % of the times ^{252}Cf undergoes alpha decay. Therefore, the spontaneous fission activity would be $0.03920 \cdot A$.

During the fission process there is emission of, at least, fission products, neutrons and photons other than those emitted by an excited state of the daughter ^{248}Cm from ^{252}Cf when the latter decays to the former via alpha decay.

Regarding the fission products coming from ^{252}Cf, there is an A (mass number) and Z (atomic number) distribution of these fission products. An A distribution of the spontaneous fission products from ^{252}Cf is shown in Figure 2.15. In the papers the most probable Z for a given A is also found. The fact that an A and Z distribution of the fission products exists means that the number of emitted neutrons is also following a probability distribution and therefore the quantity: average neutron multiplicity, $\overline{\nu}_{\mathrm{ne}}$, is defined.

Usually, in the spontaneous fission of ^{252}Cf ($A_{\mathrm{M}} = 252$), there is the emission of a light mass particle ($A_{\mathrm{L}} = 86-127$)(and short-lived fission product) and the emission of a heavy mass particle ($A_{\mathrm{H}} = 127-162$)(and long-lived fission product) plus neutrons, photons and additional radiation coming from further radioactive decay of daughter nuclei. Therefore, it is also defined the average light mass, $\overline{A}_{\mathrm{L}}$, the average heavy mass, $\overline{A}_{\mathrm{H}}$, and the average photon multiplicity, $\overline{\nu}_{\mathrm{ph}}$. Finally, the cumulative fission yield, Y_{C}, is defined as the total number of atoms of a specific nuclide produced (directly and via decay of precursors) in 100 fission reactions.

In the work of Naik et al. [2021] are obtained, for the spontaneous fission of ^{252}Cf, the values $\overline{A}_{\mathrm{L}} = 106.13 \pm 0.03$, $\overline{A}_{\mathrm{H}} = 142.02 \pm 0.04$ and $\overline{\nu}_{\mathrm{ne}} = 3.848 \pm 0.052$.

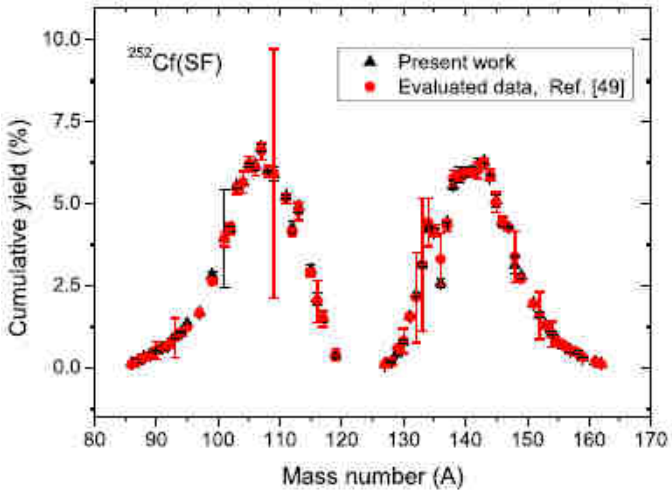

Figure 2.15: Comparison of experimental cumulative yields of fission products in the ^{252}Cf(SF) reaction from work Naik et al. [2021] and the evaluated data from ENDF/B-VIII.0 Brown et al. [2018]. Figure from Naik et al. [2021].

The energy distribution of the emitted neutrons during the spontaneous fission process of ^{252}Cf is shown in Figure 2.16, while the energy distribution of the emitted neutrons together with the energy distribution of the emitted photons (due to the fission process) is shown in Figure 2.17. Physical fission processes tend to be isotropic but in reality, when

^{252}Cf is encapsulated or geometrically distributed in some shape, anisotropies can exist and they need to be evaluated (see ISO-8529-1:2021 [2021]).

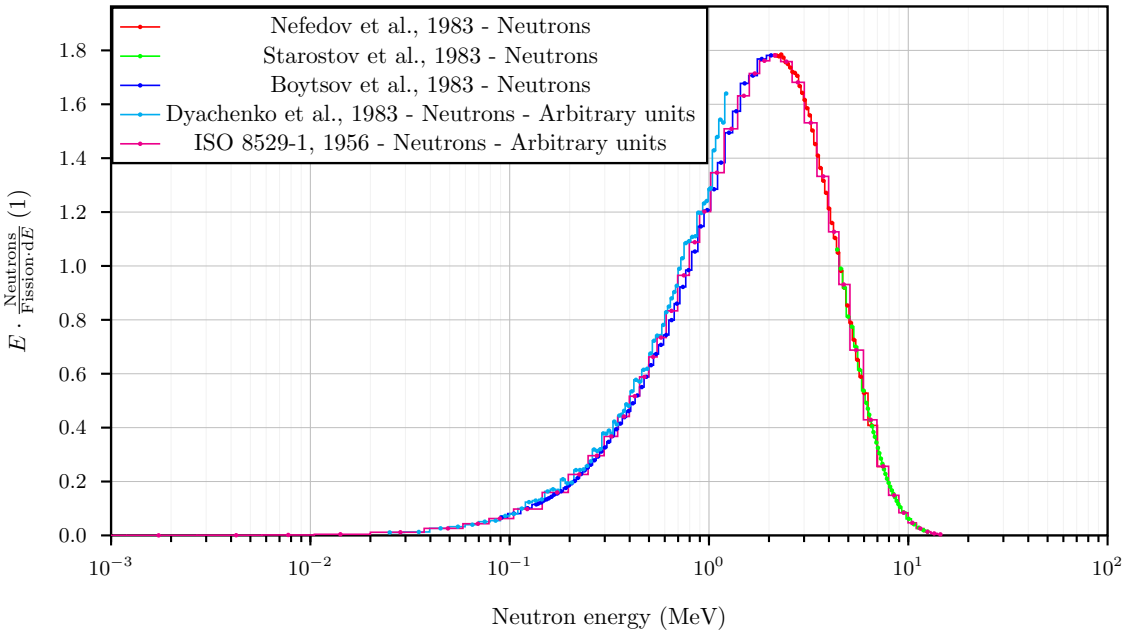

Figure 2.16: Energy distribution of the outgoing neutrons from ^{252}Cf source. From works Nefedov et al. [1984], Starostov et al. [1984], Boytsov et al. [1984], Lajtai et al. [1990] and ISO-8529-1:2021 [2021].

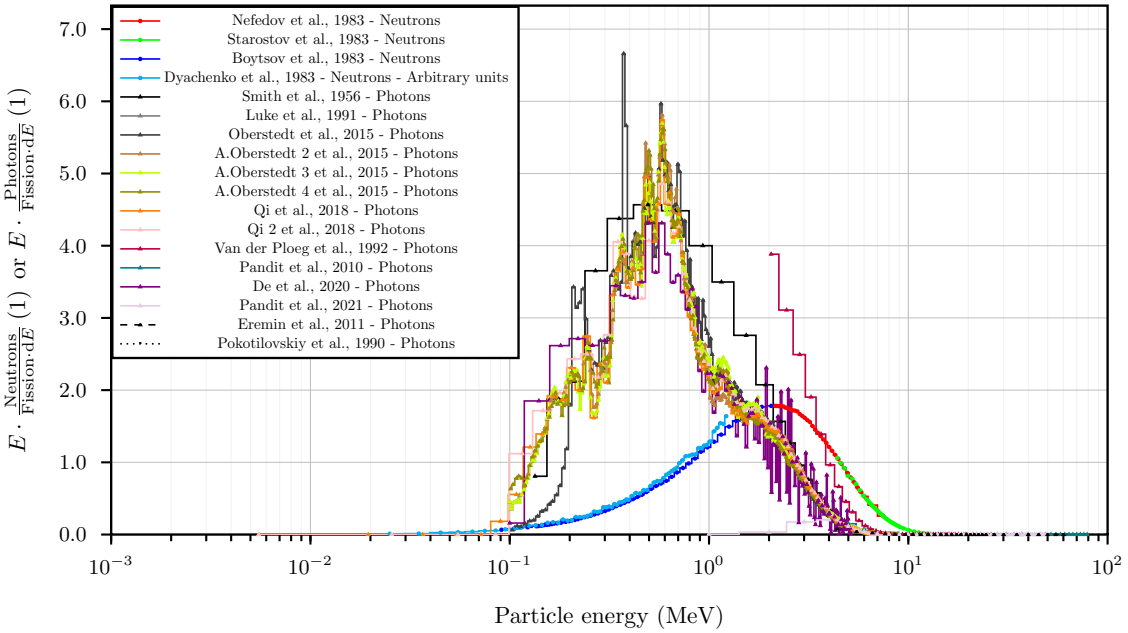

Figure 2.17: Energy distribution of the outgoing fission neutrons and photons from ^{252}Cf source. From works Smith et al. [1956], Luke et al. [1991], Oberstedt et al. [2015], Qi et al. [2018], Ploeg et al. [1992], Pandit et al. [2010], De et al. [2020], Pandit et al. [2021] and EREMIN et al. [2010].

The decays different from the mentioned spontaneous fission (alpha, beta and gamma decay) will produce a distribution of daughters which can be in their fundamental or excited state so finally giving rise to a distribution of emitted particles with an energy distribution. Examples of these distributions are found in Figures 2.18 and 2.19 for the

decay $^{252}\mathrm{Cf} \rightarrow {}^{248}\mathrm{Cm}^{i} + \alpha^{i}$ and $^{248}\mathrm{Cm} \rightarrow {}^{244}\mathrm{Pu}^{i} + \alpha^{i}$, where i is a reminder that daughters can be in an excited state.

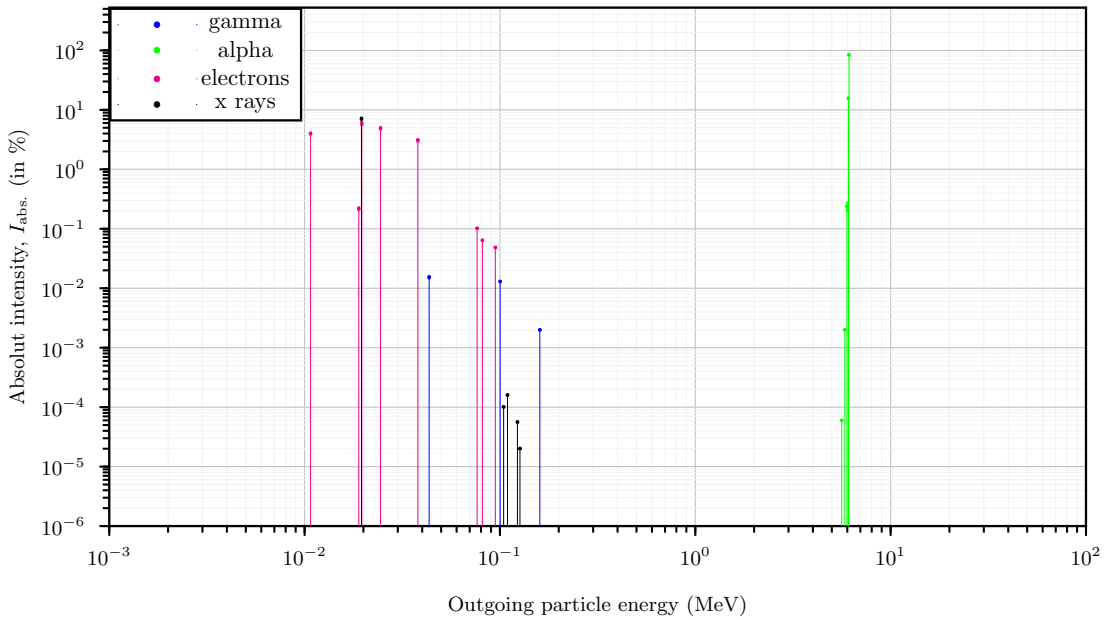

Figure 2.18: Energy distribution of the outgoing particles from decay $^{252}Cf \rightarrow {}^{248}Cm^{i} + \alpha^{i}$. From ENDF [2022].

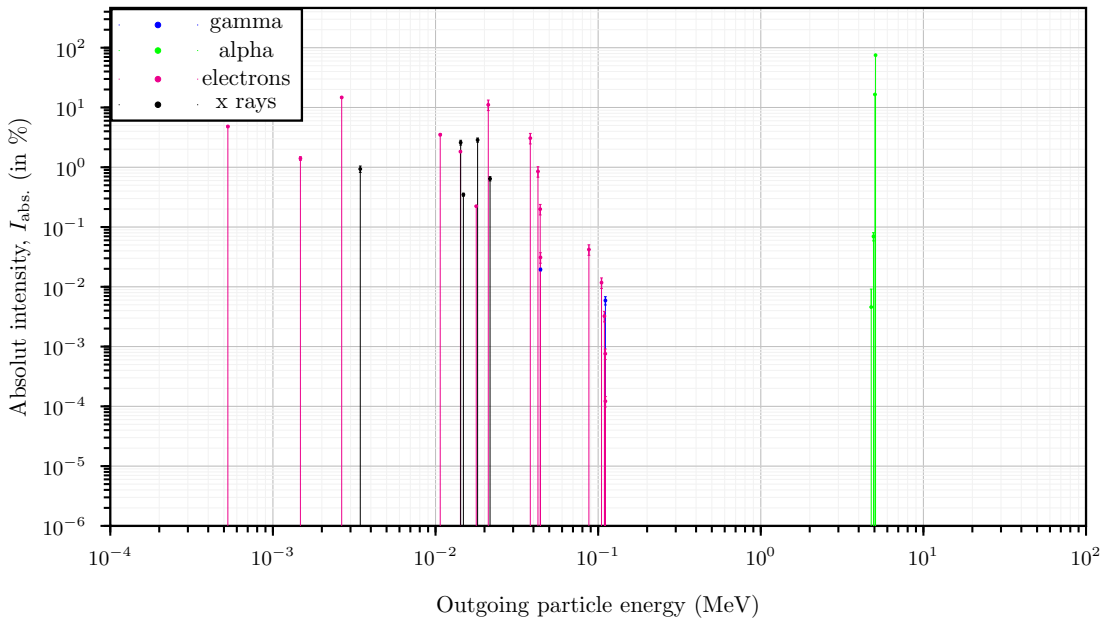

Figure 2.19: Energy distribution of the outgoing particles from decay $^{248}Cm \rightarrow {}^{244}Pu^{i} + \alpha^{i}$. From ENDF [2022].

^{252}Cf could be classified as belonging to the Thorium Series (as an integer n is found in equalling $4n = 252$) [Krane, 1987] so one could trace the distribution of daughters and emitted radiation by studying each decay in the mentioned series.

Because of their range, it is obvious that fission fragments and alpha particles will not reach a radiation detector that is going to be calibrated to the neutrons from a ^{252}Cf

source. Nevertheless, the photon and electron components could give rise to signal pulses in the detector. This fact may affect the calculation of the calibration coefficient to neutrons. To proceed correctly, the non-neutron signal has to be processed and filtered by an appropriate software managing the radiation detector.

Spontaneous fission decay mode usually does not compete successfully with other type of decays, like α decay. In the case of ^{238}U is seen that the probability of having a spontaneous fission is 5.45×10^{-5} % (branching ratio) while α decay has a branching ratio of essentially 100 %. Spontaneous fission decay mode does not become an important decay process until we get to nuclei of mass 250 an above [Krane, 1987]. However, for not so heavy nuclei, the situation is different if we have an initial particle interacting with the nucleus in the initial state. Induced fission could take place and a compound nucleus or excited state could be produced.

Detailed explanation can be found in Krane [1987].

2.3.2 Induced fission with low-energy incident neutrons

The absorption by a nucleus of a relatively small amount of energy, such as from a low-energy neutron or photon, leads to an intermediate state due to the kinetic energy of the incident particle and its binding energy. A compound nucleus or excited state is generated, whose energy is at or above the coulomb barrier (which is the energetic barrier to be overcome in order to the fission process be observable), so that induced fission competes successfully with the other modes of decay of the compound nucleus. If the intermediate state is below the barrier, other decay modes, including re-emission of the absorbed particle may dominate. For some nuclei, absorption of thermal neutrons may be sufficient to push them over the barrier, while for others, fast (MeV) neutrons may be required [Krane, 1987] [Filges et al., 2009] [Naik et al., 2021].

Therefore, while spontaneous fission can be seen from nuclei with mass numbers from 250, induced fission is seen from mass numbers of 232 from thorium ($Z = 90$) [Krane, 1987].

Low energy induced fission is the main physical process in conventional nuclear power plants, that is to say, when the moderated low-energy neutron induces fission in typical fissile materials such as ^{233}U, ^{235}U, ^{239}Pu and ^{241}Pu [Krane, 1987].

Energy induced fission can be also used to develop a neutron radiation detector based on Solid State Nuclear Track Detectors since fission fragments can produce etchable tracks, as seen in the work of Baumgartner et al. [1966].

Usually, the experimental induced fission energy distribution of the neutron fluence resulting from a fissile material is compared with theoretical energy distributions to better understand the fission process itself as well as to make extrapolations when needed [Lajtai et al., 1985]. These distributions are precisely distribution Equations (2.10), (2.11), (2.12) and (2.13).

Figure 2.20 shows the neutron induced fission cross sections from cold to high energy incident neutrons for different nuclei which are used as fuel in conventional nuclear power plants or as a neutron converters.

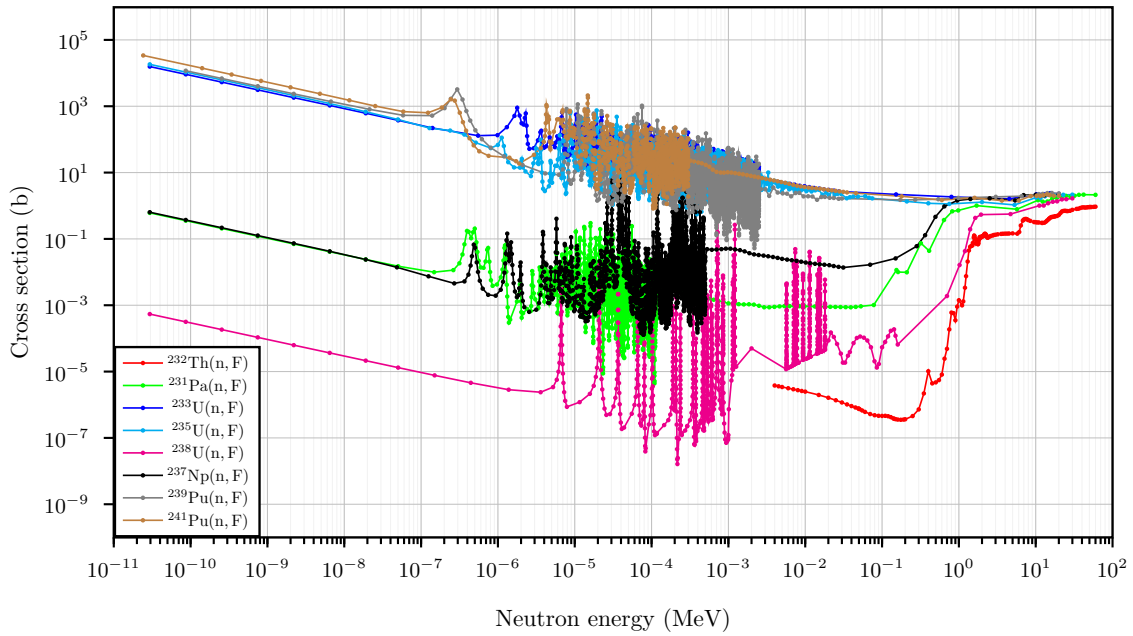

Figure 2.20: Neutron induced fission cross sections for ^{232}Th, ^{231}Pa, ^{233}U, ^{235}U, ^{238}U, ^{237}Np, ^{239}Pu, ^{241}Pu. From ENDF [2022].

2.3.3 Induced fission with high-energy incident hadrons and photons

As can be seen from Figure (2.20), induced fission for incident photons not only happens for thermal ($E \lesssim 1$ eV) or epithermal (1 eV $\lesssim E < 0.1$ MeV) neutrons but it can also occur for fast (0.1 MeV $< E <$ 10 MeV) and even high energy ($E >$ 10 MeV) neutrons.

Other high-energy incident hadrons, like protons, or photons can also induce fission, see cross sections from Figure (2.21).

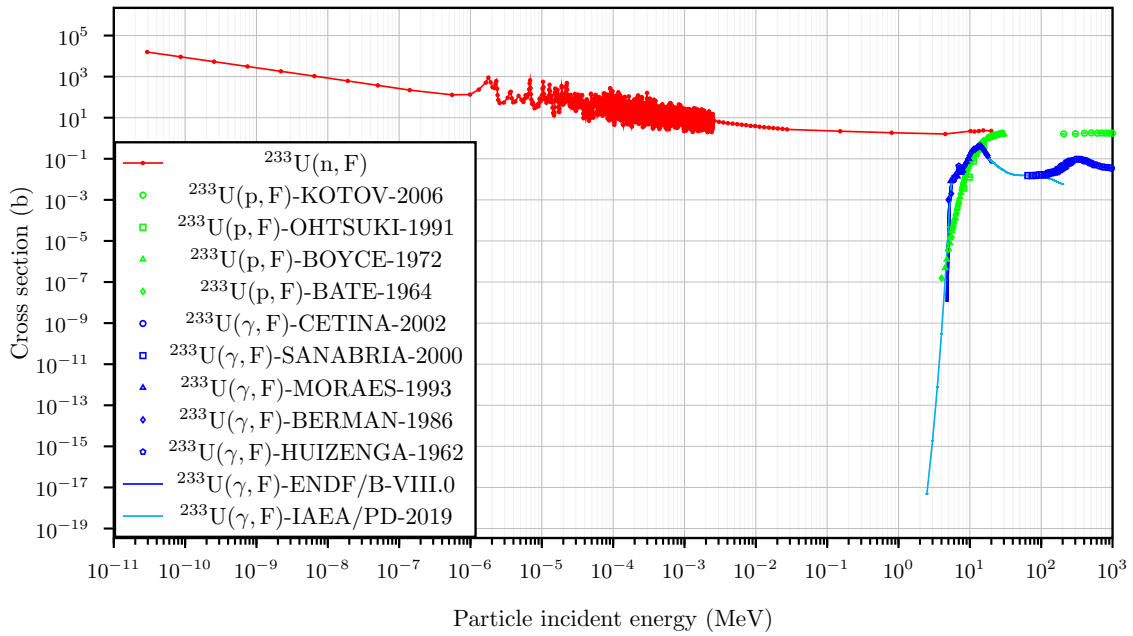

Figure 2.21: Evaluated and experimental high-energy protons and photons induced fission cross section. From ENDF [2022] and EXFOR [2022].

Induced fission with fast neutrons is a key principle in fast neutron reactors [*Status of Fast Reactor Research and Technology Development* 2013].

2.3.4 Spallation processes

A spallation reaction is a combination of different nuclear reactions observed in astrophysics, cosmic ray physics, geophysics, radiotherapy, radiobiology, and at all applications together with accelerators. Spallation refers to inelastic nuclear reactions that occur when particles with enough kinetic energy, for example, protons, neutrons, pions (or hadrons in general), interact with an atomic nucleus producing rich and abundant radiation of many different particles such as neutrons, protons, pions, muons, electrons, photons, charged particles, and neutrinos [Filges et al., 2009].

The spallation reaction can be seen as a combination of the following nuclear reactions:

1. A combination of two body collisions between the incident particle and nucleons or also known as intranuclear cascade.
2. High-energy induced fission and/or collective distribution of the incident energy over the target nucleus.
3. *Evaporation*-decay processes.

Each nuclear process will generate characteristic energy and angular distributions of the particle fluences.

Intranuclear cascade is understood as two body collisions because the associated wavelength of the incident particle is shorter than the size of the nucleus and, in general terms, it can be thought that the incident particle can effectively see each nucleon. Moreover, the stricken nucleon will not have enough time to distribute the energy received over the whole nucleus in a first stage. Anyway, there will be some energy transfer from this stricken nucleon to the whole nucleus. From the previous argument, it is understood that intranuclear cascades do not form a compound nucleus. The result of the intranuclear cascades are the ejection of nucleons or small groups of nucleons, which usually have directional angular distributions and high energies (up to the energy of the incident particle producing the intranuclear cascade).

Some of the stricken nucleons could induce high-energy fission instead of leaving the nucleus, producing different energy and angular distributions of the emitted radiation.

On the other hand, from the sum of the transfers of the already ejected nucleons or group of nucleons to the whole nucleus, the nucleus can reach a very high excited state which can decay with the emission of fast or evaporation neutrons, protons, alpha particles, light heavy ions, etc. After the evaporation, the resulting nucleus may still be radioactive and may emit additional radiation.

Figure 2.22 presents a comparison between the produced unit energy distribution of the neutron fluence generated by thermal induced fission and the produced unit energy distribution of the neutron fluence generated by a spallation target.

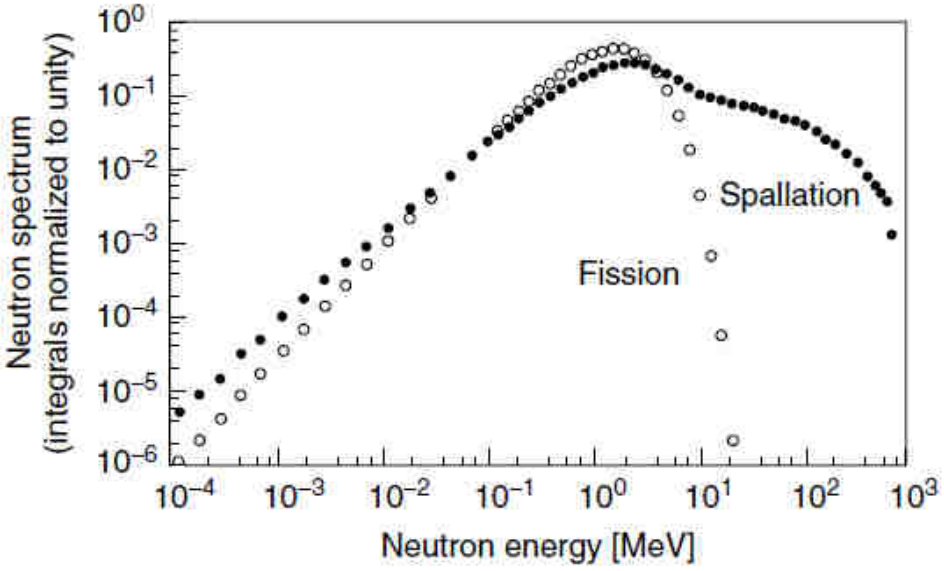

Figure 2.22: Spallation neutron energy distribution compared to a typical neutron energy distribution from thermal neutron fission of ^{235}U. The spallation energy distribution is measured at 90° from a finite 10 cm diameter by 30 cm long tungsten target bombarded by 800 MeV protons. From Filges et al. [2009].

On one hand, energy distribution of the neutron fluence originated from fission or evaporation processes tends to be isotropic and a physical peak appears around 1-10 MeV. On the other hand, the energy distribution of the neutron fluence created by spallation reactions, besides of containing the evaporation or fast peak, contains also a high-energy peak whose center is highly angular dependent and it will also contain a tail extending up to the energy of the incident particle. The high energy peak or intranuclear cascade neutrons are angular dependent but forwardly emitted.

The epithermal and thermal part of the energy distribution of the neutron fluence are dependent on the geometrical setting of materials around the measuring point rather than directly dependant on the previous introduced physics. A brief summary of the physics governing the thermal and epithermal neutrons is given in Section 2.4.

Although there is no clear separation of spallation from the lower energy nuclear reactions (an energy threshold), one type may merge into the other as the energy of the incident particle increases [Filges et al., 2009] and is natural to accept that reactions of the kind (p,xn + etc) or (n,xn + etc) are coming from spallation reactions. Keep in mind that fission induced reactions are limited to heavy nuclei.

The relevant spallation cross sections (p,xn + etc) in tissue are summarised in Figures E.1, E.3, E.4 and E.5 from Appendix E. In Figure E.1 we find the cross section for (p,xn + etc) processes in the most abundant isotopes in human tissue while in Figures E.3 and E.5 we find the energy distribution of the generated neutrons. Finally in Figure E.4 we see the anisotropy of the generated neutron field for incident protons of energy 160 MeV incident on ^{12}C.

2.4 Neutron interactions with matter

Once neutrons have been produced, interaction with detectors and biological matter takes place. Specific reactions will be highlighted, in general, in Chapter 4.

Neutrons, as photons, have no net charge which make them highly penetrating in matter. Figure 2.23 shows the total nuclear cross section for incident neutrons and the total atomic cross section for incident photons for elements hydrogen, carbon, oxygen and silicon so a first idea of the penetrability of each kind of radiation can be inferred. For instance, for Oxygen, it is concluded that neutrons with energies below than 0.2 MeV are more penetrating than photons, however neutrons with energies higher than 0.2 MeV are a little less penetrating than photons. Neutrons can be totally invisible to a general detector of common size [Knoll, 2010].

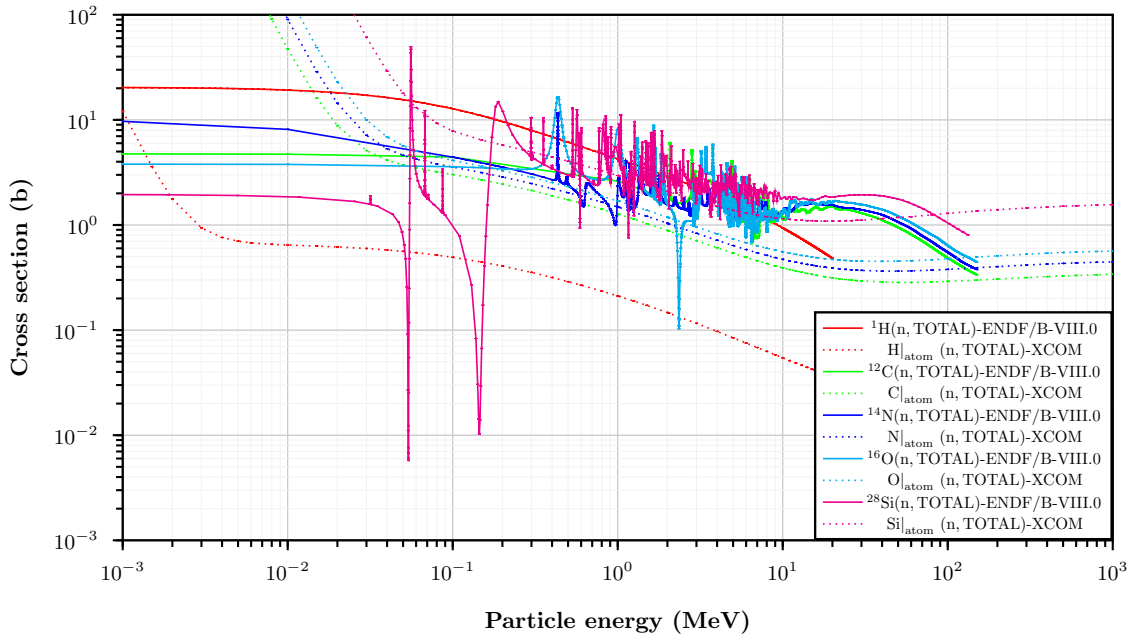

Figure 2.23: Photon and neutron cross section for HCNO materials and Si. Solid lines correspond to nuclear processes while dotted lines correspond to atomic processes. Data taken from ENDF [2022] and Berger et al. [2022].

A difference between neutrons and photons is that the former interact with matter producing heavy particles. While the latter produce electrons. Therefore, neutrons are a very important source of radiobiological damage.

Neutron interactions can be classified as:

- Elastic interactions.
- Inelastic interactions.
  - Inelastic interactions leading to a neutron in the final state.
    - Interactions in which the energy transferred to the nucleus does not produce fission nor spallation (*i.e.*, only an excitation of the nucleus).
    - Fission reactions.
    - Spallation reactions.

- Inelastic interactions with no neutrons is in the final state.
  - Radiative capture.
  - Non-Radiative capture.

Elastic interactions

Is the case in which there are no nuclear transformations and the initial total kinetic energy of the system is conserved *i.e.,* there is only kinetic energy transference between the particles.

From the kinematics of these reactions (application of the total energy conservation and total linear momentum, see *e.g.,* Turner [2007] or Caswell et al. [1980]) is learnt that in case that the projectile and the target have identical masses, the kinetic energy transference is maximized. Moreover, in the particular case that the recoil target follows the same initial direction of the projectile, the kinetic energy transference is an absolute maximum and in this situation the kinetic energy of the recoil target is the same as the kinetic energy brought by the projectile. This is the reason why neutrons are effectively moderated materials with high contain of hydrogen as well as by the fact that elastic cross section $\sigma_{^1\mathrm{H(n,EL)}^1\mathrm{H}}(E)$ (EL stands for elastic reaction) has a high value, see Figure 2.24.

Another relevant fact is that experimentally, for neutron energies up to about 10 MeV, is observed that neutrons and protons are deflected isotropically in the center-of-mass coordinate system [Turner, 2007]. The average kinetic energy transferred to the proton (average kinetic energy of the proton or average kinetic energy lost by the incident neutron) is the half of the kinetic energy brought by the incident neutron [Turner, 2007].

There exists the so called thermal region in which the kinetic energy of the neutron in ambient temperature (20 °C = 293.15 K) is probable to be found around the value $T_0 = 2.5262 \times 10^{-8}$ MeV = 0.0253 eV (using Equation (2.14)). This happens because the concept of temperature in air is directly translated to the motion of the atoms in air according to statistical physics. In consequence, there is a low kinetic energy threshold (depending on the temperature of the air of a room) in which a thermal neutron will never be found since these low energy neutrons are constantly interacting elastically with the atoms found in air until they are captured or they decay. Therefore, the Maxwell–Boltzmann kinetic energy distribution, Equation (2.11), which is applied for gases, is describing at the same time the kinetic energy of thermal atoms in air as well as the kinetic energy of the thermal neutrons in equilibrium.

Inelastic interactions

Inelastic interactions are those interactions in which there can be nuclear transformations and the initial total kinetic energy of the system is not conserved because there are internal processes in the target nucleus. An overview of kinematic formulas can be found in Caswell et al. [1980].

As sometimes, in experiments, we are forced to use holders or additional elements to support the detectors system, we should make sure that the materials introduced perturb as less as possible the neutron field to be measured. For neutron energies below 1 keV, ideally these elements should be made of Al as its total neutron cross section is lower in comparison, for instance, to plastics which essentially contain H, C, N and O elements, as shown in Figure 2.25.

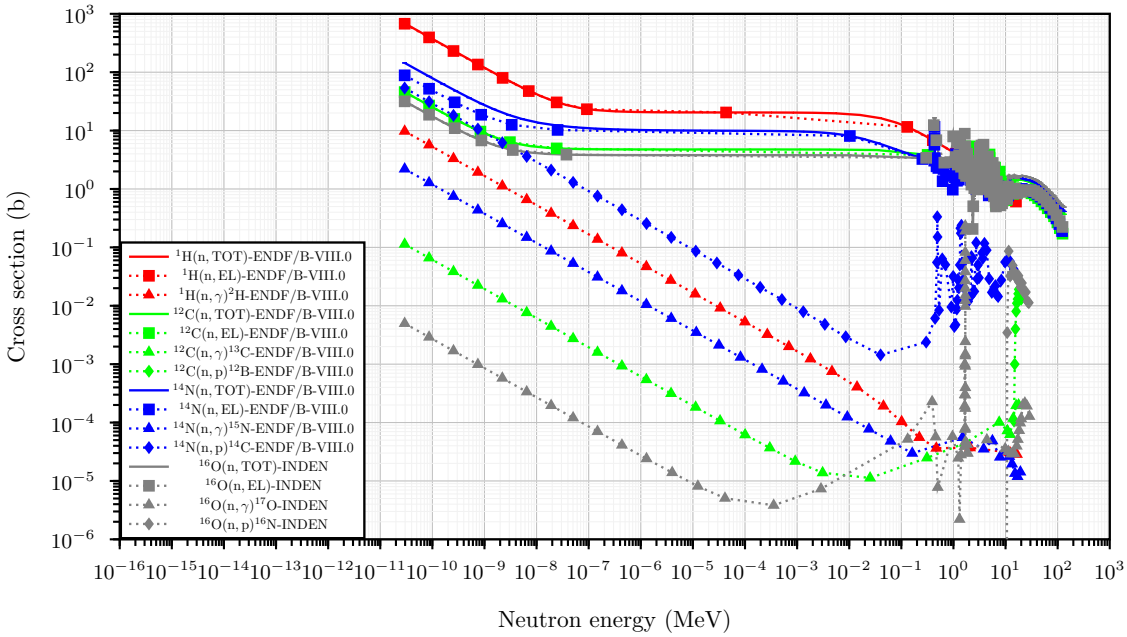

Figure 2.24: Neutron cross sections for HCNO materials. From ENDF [2022].

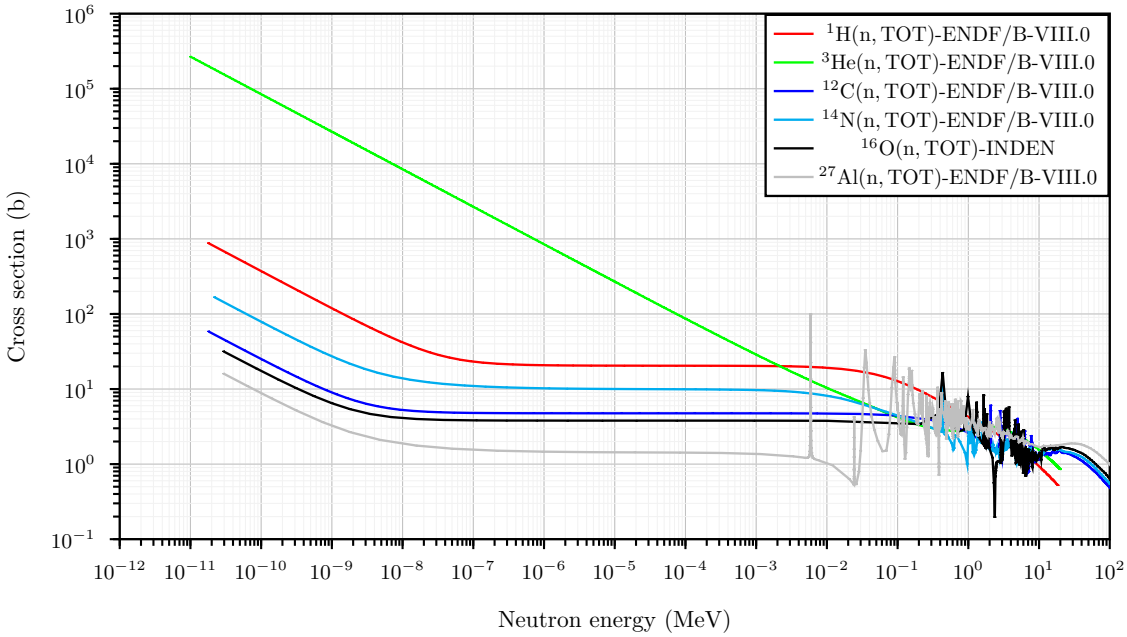

Figure 2.25: Total neutron cross sections for ^{3}He, ^{1}H, ^{12}C, ^{14}N, ^{16}O and ^{27}Al. From ENDF [2022].

Chapter 3

Characterization of radiation fields

The aim of this chapter is to present the quantities defined in the actual radiological protection system most useful for the objectives of this work.

The quantities introduced in this chapter rely directly on national or international bodies as the International Commission on Radiation Units (ICRU), International Commission on Radiological Protection (ICRP), International Atomic Energy Agency (IAEA), National Council on Radiation Protection and Measurements (NCRP), International Organization for Standardization (ISO) [ISO-8529-1:2021, 2021] [ISO-8529-2:2000, 2000] [ISO-8529-3:1998, 1998].

As we will see in Chapter 4, radiation detectors can be experimentally calibrated to any physical quantity or also be calibrated to any protection or operational quantity but keeping in mind that those last quantities, in general, are computed by applying physical-to-dose conversion coefficients obtained through Monte Carlo simulations in the very specific conditions in which the dose quantity is defined. See, for instance, ICRU [1998].

3.1 Quantities used to characterize a radiation field

Unless otherwise specified, hereinafter all the following quantities are non-stochastic or averaged quantities.

3.1.1 Physical quantities

Fluence

Fluence, Φ, is computed over a sphere of volume $\mathrm{d}V$ and cross sectional area $\mathrm{d}a$ as the quotient between the number of particles crossing the sphere, $\mathrm{d}N$ and $\mathrm{d}a$, therefore

$$\Phi = \frac{\mathrm{d}N}{\mathrm{d}a}. \tag{3.1}$$

It can be applied to both neutral and charged particles. In case of need, a subscript will appear to discriminate between different type of particles.

Energy distribution of the fluence or spectrum

Energy distribution of the fluence, $\Phi_E(E)$, describes the fluence of particles with energies between E and $E + \mathrm{d}E$, $\mathrm{d}\Phi(E)$, as

$$\Phi_E(E) = \frac{\mathrm{d}\Phi(E)}{\mathrm{d}E}, \tag{3.2}$$

therefore $\mathrm{d}\Phi(E) = \Phi_E(E)\,\mathrm{d}E$. Fluence is obtained through

$$\Phi = \int_E \mathrm{d}\Phi(E) = \int_E \Phi_E(E)\,\mathrm{d}E. \tag{3.3}$$

Unit energy distribution of the fluence or unit spectrum

Unit energy distribution of the fluence, $\varphi_E(E)$, can be interpreted as the probability density function of having a particle with energies between E and $E + \mathrm{d}E$ in the radiation field and is defined as

$$\varphi_E(E) = \frac{\Phi_E(E)}{\Phi}. \tag{3.4}$$

The probability of a particle with energies between E and $E + \mathrm{d}E$ in the radiation field is then $\varphi_E(E)\mathrm{d}E$. Using Equation (3.2) in Equation (3.4) we obtain

$$\varphi_E(E) = \frac{\left[\frac{\mathrm{d}\Phi(E)}{\mathrm{d}E}\right]}{\Phi}, \tag{3.5}$$

$$\varphi_E(E)\mathrm{d}E = \frac{\mathrm{d}\Phi(E)}{\Phi}. \tag{3.6}$$

And, as any probability density function, it is normalized to 1,

$$\int_E \varphi_E(E)\mathrm{d}E = \int_E \frac{\mathrm{d}\Phi(E)}{\Phi} = \frac{1}{\Phi}\int_E \mathrm{d}\Phi(E) = \frac{\Phi}{\Phi} = 1. \tag{3.7}$$

Energy-angular distribution of the fluence

Energy-angular distribution of the fluence, $\Phi_{E,\Omega}(E, \Omega)$, describes the fluence of particles with energies between E and $E + \mathrm{d}E$ with an angular direction or solid angle between Ω and $\Omega + \mathrm{d}\Omega$, $\mathrm{d}^2\Phi(E, \Omega)$, as

$$\Phi_{E,\Omega}(E, \Omega) = \frac{\mathrm{d}^2\Phi(E, \Omega)}{\mathrm{d}E\mathrm{d}\Omega}, \tag{3.8}$$

therefore $\mathrm{d}^2\Phi(E, \Omega) = \Phi_{E,\Omega}(E, \Omega)\,\mathrm{d}E\mathrm{d}\Omega$. By definition, it is accomplished that

$$\Phi_E(E) = \int_\Omega \Phi_{E,\Omega}(E, \Omega)\mathrm{d}\Omega. \tag{3.9}$$

Therefore, fluence can be obtained through the next manipulations

$$\Phi = \int_E \int_\Omega \mathrm{d}^2\Phi(E, \Omega) = \int_E \left[\int_\Omega \Phi_{E,\Omega}(E, \Omega)\mathrm{d}\Omega\right] \mathrm{d}E = \int_E \Phi_E(E)\mathrm{d}E. \tag{3.10}$$

Kerma (Kinetic Energy Released per MAss)

Kerma, K, is defined in a volume as the ratio between the mean sum of the initial kinetic energies of all charged particles liberated by uncharged particles, $\mathrm{d}E_{\mathrm{tr}}$, and the mass $\mathrm{d}m$ of the material in the volume (see also Equation (3.103))

$$K = \frac{\mathrm{d}E_{\mathrm{tr}}}{\mathrm{d}m}. \tag{3.11}$$

Kerma is only defined for neutral particles. In case of need, a subscript will appear to discriminate between different type of neutral particles. The energy expended to overcome the binding energies, usually a relatively small component, is by definition, not included. It can be proved that kerma can be written as [ICRU, 2011]

$$K = \int_E E\,\Phi_E(E) \left[\frac{\mu_{\mathrm{tr}}(E)}{\rho}\right] \mathrm{d}E, \tag{3.12}$$

where $\left[\frac{\mu_{\mathrm{tr}}(E)}{\rho}\right]$ is the mass energy-transfer coefficients.

Mono-energetic fluence-to-kerma conversion coefficients

Mono-energetic fluence-to-kerma conversion coefficients, $k_\Phi(E)$, are theoretically computed in Caswell et al. [1980] and Chadwick et al. [1999] and are defined as

$$k_\Phi(E) = \frac{\mathrm{d}K(E)}{\mathrm{d}\,\Phi(E)}. \tag{3.13}$$

It can be proved that mono-energetic fluence-to-kerma conversion coefficients can be written as [ICRU, 2011]

$$k_\Phi(E) = E \left[\frac{\mu_{\mathrm{tr}}(E)}{\rho}\right]. \tag{3.14}$$

And therefore, Kerma, K, can also be computed as

$$K = \int_E \mathrm{d}K(E) = \int_E k_\Phi(E)\mathrm{d}\,\Phi(E) = \int_E k_\Phi(E)\,\Phi_E(E)\,\mathrm{d}E. \tag{3.15}$$

In case of need, a subscript will appear to discriminate between different type of neutral particles. Mono-energetic fluence-to-kerma conversion coefficients depend on the material.

Figure 3.1 shows the fluence-to-kerma conversion coefficients for neutrons in ICRU tissue, which has a composition specified in Section 3.1.5. They are computed according to the weight of H, C, N and O in tissue, as done by Siebert et al. [1995].

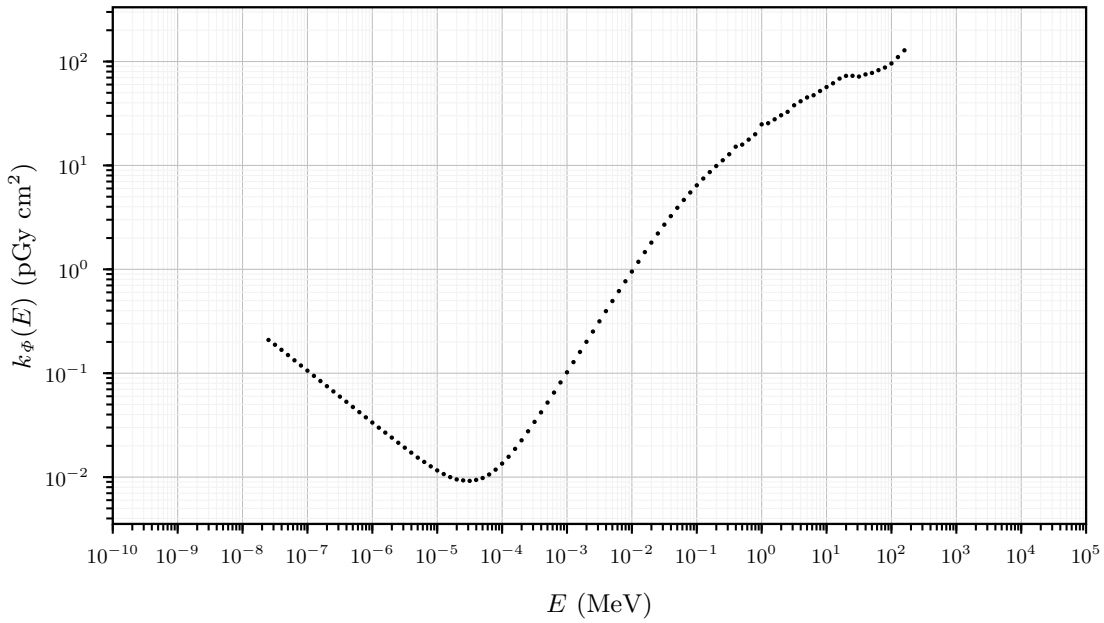

Figure 3.1: Fluence-to-kerma conversion coefficients for neutrons in ICRU tissue based on Chadwick et al. [1999] and Siebert et al. [1995].

Similarly to Figure 3.1, in Figure 3.2 the fluence-to-kerma conversion coefficients for photons and neutrons in ICRU tissue and water is found.

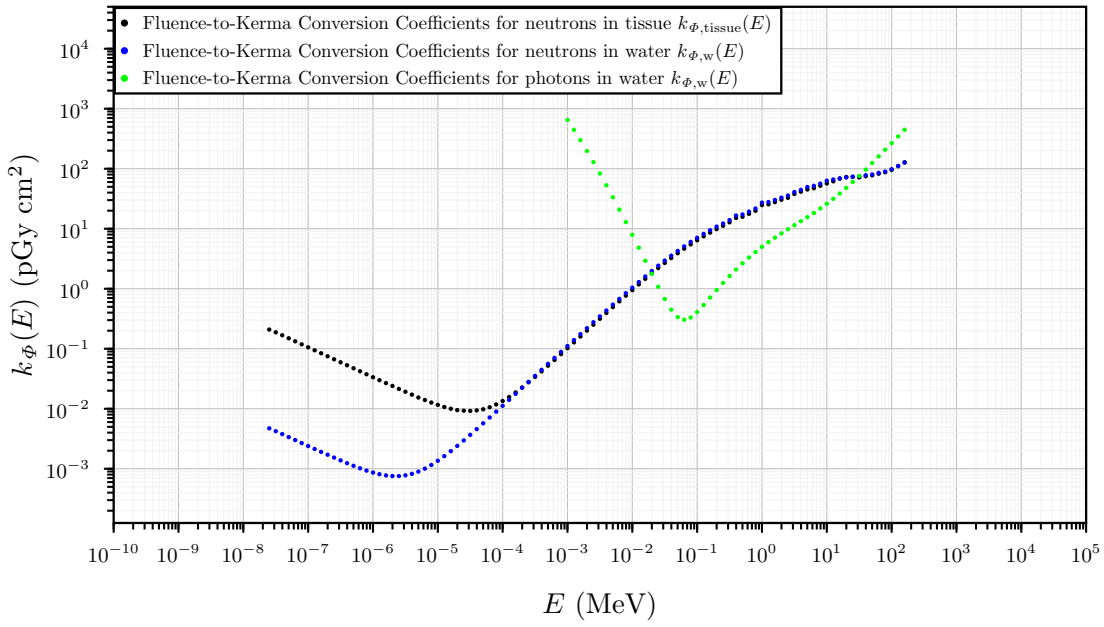

Figure 3.2: Fluence-to-kerma conversion coefficients for photons and neutrons in ICRU tissue and water based on Chadwick et al. [1999], Siebert et al. [1995] and Higgins et al. [1992].

Absorbed dose

Absorbed dose, D, is defined in a volume as the quotient between the mean energy im-

parted by the radiation, $\mathrm{d}\bar{\epsilon}$, and the mass of the volume, $\mathrm{d}m$, [ICRU, 2011]

$$D = \frac{\mathrm{d}\bar{\epsilon}}{\mathrm{d}m}. \tag{3.16}$$

The associated stochastic quantity to absorbed dose is the specific energy, z, whose probability density function is $f(z)$. Specific energy is defined as

$$z = \frac{\epsilon}{m}. \tag{3.17}$$

To appropriately work with the concept of absorbed dose in a certain volume $\mathrm{d}V$ small but not very small (strong fluctuations in z) it has to be accomplished that $\overline{z} = \int_z z f(z) \mathrm{d}z$ is similar to D and the associated variance to $f(z)$ should be small (low fluctuations in z). For more details see ICRU report ICRU [1983].

Energy and LET distribution of the absorbed dose

Energy distribution of the absorbed dose, $D_E(E)$, describes the absorbed dose contributed by particles with energies between E and $E + \mathrm{d}E$, $\mathrm{d}D(E)$, as

$$D_E(E) = \frac{\mathrm{d}D(E)}{\mathrm{d}E}, \tag{3.18}$$

therefore $\mathrm{d}D(E) = D_E(E)\,\mathrm{d}E$. Absorbed dose is obtained through

$$D = \int_E \mathrm{d}D(E) = \int_E D_E(E)\,\mathrm{d}E. \tag{3.19}$$

If instead of working with energy E we work in LET L (see Section 3.2) we can do the change $E \leftrightarrow L$ so previous expression will remain as, for the LET distribution of the absorbed dose

$$D_L(L) = \frac{\mathrm{d}D(L)}{\mathrm{d}L}, \tag{3.20}$$

and for the absorbed dose

$$D = \int_L \mathrm{d}D(L) = \int_L D_L(L)\,\mathrm{d}L. \tag{3.21}$$

Unit energy or unit LET distribution of the absorbed dose

Unit energy distribution of the absorbed dose, $d_E(E)$, can be interpreted as the probability density function of all particles (of one type) with energies between E and $E + \mathrm{d}E$ in a radiation field and to contribute to the absorbed dose, D, and is defined as

$$d_E(E) = \frac{D_E(E)}{D}. \tag{3.22}$$

The probability of all particles (of one type) with energies between E and $E + \mathrm{d}E$ in a radiation field and contribute to absorbed dose, D, is $d_E(E)\mathrm{d}E$ and using Equation (3.18) in Equation (3.22) we obtain

$$d_E(E) = \frac{\left[\frac{\mathrm{d}D(E)}{\mathrm{d}E}\right]}{D}, \tag{3.23}$$

$$d_E(E)\mathrm{d}E = \frac{\mathrm{d}D(E)}{D}. \tag{3.24}$$

And, as any probability density function, it is normalized to 1,

$$\int_E d_E(E)\mathrm{d}E = \int_E \frac{\mathrm{d}D(E)}{D} = \frac{1}{D}\int_E \mathrm{d}D(E) = \frac{D}{D} = 1. \tag{3.25}$$

If instead of working with energy E we work in LET L we can do the change $E \leftrightarrow L$ so previous expression will remain as, for the unit LET distribution of the absorbed dose in form of probability density function

$$d_L(L) = \frac{D_L(L)}{D}, \tag{3.26}$$

and, for the unit LET distribution of the absorbed dose in form of probability, as

$$d_L(L)\mathrm{d}L = \frac{\mathrm{d}D(L)}{D}. \tag{3.27}$$

3.1.2 Radiobiological damage unification factors

3.1.2.1 Relative Biological Effectiveness (RBE)

The Relative Biological Effectiveness, RBE, which is the relative biological damage or relative effect of ionizing radiation is dependent, at least, on:

- the reference radiation in which the RBE is defined,
- the type of radiation and its energy E, that is related with the density of ionisations per unit path length of the ionising particles or Linear Energy Transfer (LET). One has to take into account that in the experimental system in which the biological effects are evaluated (to compute the RBE) we will have, generally, an energy distribution of the fluence for the incident radiation.
- the absorbed dose,
- the absorbed dose rate,
- fractionation of the absorbed dose,
- range of the secondary particles,
- the specific biologic effect or biologic endpoint under study,
- cells, tissues or organs in which the effect is being assessed,
- the spatial distribution of the energy imparted or distribution of hits in the cell.

For an introduction on the topic, see ICRP [2003] and references therein.

In this work we justify the dependence of RBE on the quality of the radiation through the next argument. Let us suppose a certain volume $\mathrm{d}V$, one proton with a track of length $\mathrm{d}l$ will transfer a certain energy $\mathrm{d}E$ which is equivalent to several tracks of electrons with a similar length $\mathrm{d}l$ that, even contributing in the sum, to the same energy $\mathrm{d}E$, while

the electrons have shared the total energy in different tracks, the proton has focused all the transferred energy in one track, therefore highly damaging the biological elements in this track and increasing more effectively the probability of the appearance of a biological negative effect in this elemental volume dV.

Other fact to be considered is that, in a single cell, for an specific energy E, not only LET L is important but it is also relevant if the particle is capable of depositing that energy in the dimensions of the cell or in its nucleus.

Therefore, RBE is a function of many variables.

At this point we define the RBE for a radiation beam (of a certain quality) as the absorbed dose that this beam has to contribute in order to produce the same biological effect as the absorbed dose of the radiation of reference. This is expressed as

$$\mathrm{RBE} = \mathrm{RBE}\left(\text{Radiation-Quality}, D, \dot{D}, \text{Endpoint}, \text{Reference}, ...\right) = \left.\frac{D_{\text{Reference}}}{D}\right|_{\text{Same effect}}. \quad (3.28)$$

Where the reference low-LET radiation is commonly 250 $\mathrm{kV_p}$ X-rays or ^{60}Co γ-rays since these irradiations are usually available everywhere [Joiner et al., 2009] and paragraph 115 from ICRP [2007b].

Therefore RBE can be obtained in a range of doses. What is more interesting is the RBE at low doses or doses which are found in clinics or radiation protection. RBE increases to a maximum value $\mathrm{RBE_M}$ in decreasing the dose and the dose rate, see paragraph (114) and (B 75) in ICRP [2007b]. Therefore RBE computed at low doses is called $\mathrm{RBE_M}$.

$$\mathrm{RBE_M} = \mathrm{RBE}\left\{\text{Low doses}\right\}. \quad (3.29)$$

Tables 3.1, 3.2, 3.3, 3.4 show different values of RBE for neutrons, photons, electrons, alphas, and protons.

Table 3.1: RBE for neutrons following fission spectrum, Table D-1 from ICRU [1986].

Biologic endpoint	Neutron dose (Gy)	Approx. RBE	Approx. RBE (0.01 Gy, low γ ray dose rate as reference)
Cytogenetic, human and mouse	0.05	15-25[a]	15-25
Mutation (HGPRT)	0.1	10[b]	30
Transformation	0.025	35[c]-70[d]	35
Tumor induction:			
Mice	0.1	40	100
Rats	0.001	100	50
Life shortening:			
Single irradiation	0.05	20	30[e]-15[f]
Fractionated	0.2	20	60[e]-30[f]

[a] One estimate, RBE 45
[b] Heavy ions vs. acute X or γ rays.
[c] Low dose rate γ rays.
[d] Fractionated γ rays.
[e] Argonne National Laboratory (ANL) published.
[f] Estimated by author from ANL published.

Table 3.2: RBE_M for neutrons following fission spectrum (or optimum energy[a]) with fractionated γ rays[b], Table D-4 from ICRU [1986].

Biologic endpoint	RBE_M
Tumor induction	3-200
Life shortening	15-45
Transformation	35-70
Cytogenic studies	40-50
Genetic endpoints in mammalian systems	10-45
Other endpoints	
Lens opacification	25-200
Micronucleus assay	6-60
Testes weight loss	5-20

[a] *Optimum energy* is the most biologically effective energy
[b] Implied where not actually measured

Table 3.3: RBE for different types of radiation using Co-60 γ rays as reference for the endpoint: chromosome aberrations in human lymphocytes, adapted Table D-2 from ICRU [1986].

Radiation type and quality	RBE
15 MeV electrons	0.35
15 MeV electrons (pulsed)	0.57
Co-60 γ rays	1
250 KV X rays	3.03
14.7 MeV neutrons	16.7
Cyclotron neutrons ($\overline{E} = 7.6$ MeV)	38.2
^{252}Cf neutrons ($\overline{E} = 2.13$ MeV)	46.4
Fission neutrons ($\overline{E} = 0.7$ MeV)	53.1
Alpha particles 5.15 MeV (^{239}Pu)	23.9
Alpha particles 4.9 MeV (^{242}Cm)	18.2

Proton RBE values from Paganetti [2014] are found in Table 3.4. They, of course, depend on the averaged LET and the absorbed dose delivered. Indeed finding maximum values of RBE, RBE_M, at low doses.

Table 3.4: Proton RBE values for clonogenic cell survival from Paganetti [2014].

Proton RBE values
1-2

In order to benefit from the extensive experience from photon treatments, proton radiotherapy prescriptions are based on the absorbed dose for photons divided by the proper

RBE value. This is called Gy[RBE]. RBE for protons relative to high energy photons is accepted to be 1.1, see Paganetti [2014], therefore

$$\text{RBE} = \frac{D_{\text{ph-reference}}}{D_{\text{pr}}} = 1.1. \tag{3.30}$$

So a prescription of 2 Gy of photons will correspond to a proton dose of 2Gy[RBE] or 1.8 Gy (*i.e.,* proton dose of 2Gy[RBE] ≡ proton dose of 1.8 Gy), indeed

$$D_{\text{pr}} = \frac{D_{\text{ph-prescription}}}{\text{RBE}} = 1.8 \text{ Gy}. \tag{3.31}$$

Proton absorbed dose 1.8 Gy is also called physical absorbed dose. Unless other thing is written explicitly all proton absorbed doses in Chapter 7 will be understood as Gy[RBE].

3.1.2.2 Quality factor for charged particles

Quality factor function for a mono-LET charged particle at a point tissue, $Q(L)$, is defined in tissue as a function of the unrestricted Linear Energy Transfer (LET), L_∞, in water. Hereinafter we will write L instead if L_∞ but we will be referring to the latter. $Q(L)$ is derived from RBE_M. $Q(L)$ was first introduced in ICRP [2007a]. The actual $Q(L)$ dependence was defined in ICRP [1991] based on ICRU [1986], and is presented in Table 3.5 and Figure 3.3.

Table 3.5: $Q(L)$ relationships defined in ICRP [1991].

Unrestricted LET, L, in water (KeV μm^{-1})	$Q(L)$
< 10	1
$10 - 100$	$0.32L - 2.2$
> 100	$\frac{300}{\sqrt{L}}$

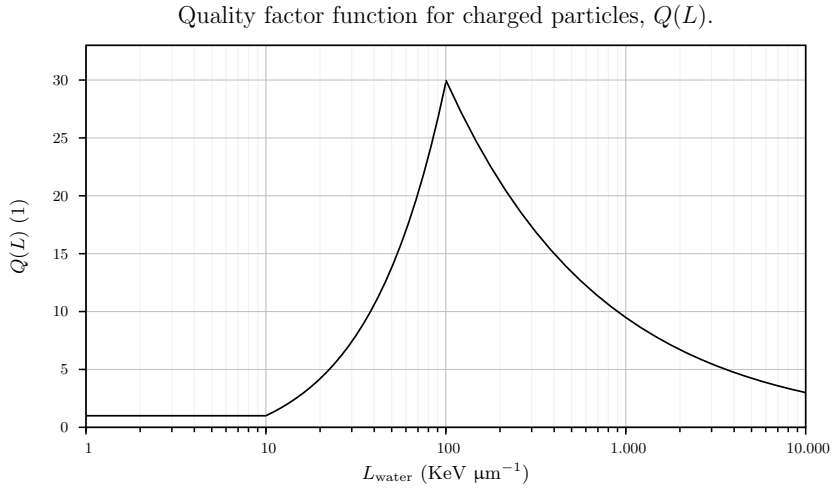

Figure 3.3: The quality factor proposed in ICRU report 40 [ICRU, 1986] and in ICRP 60 [ICRP, 1991].

3.1.2.3 Quality factor for neutral particles

Quality factor is primarily defined for charged particles. Anyway one can define quality factors for any particle as contemplated in ICRU report 40 [ICRU, 1986] and in ICRP 60 [ICRP, 1991]. In particular this can be done for neutral particles and the procedure is to do a computation over the secondary induced charged particles. In fact, this is what is done for neutrons in the works of Leuthold et al. [1992] and Siebert et al. [1995]. For neutrons, quality factor is symbolized as simply $Q(E)$ or, if needed, $Q_{\mathrm{ne}}(E_{\mathrm{ne}})$. In Section 3.1.4.2, the definition of the quality factor for neutrons is expanded.

In Figure 3.4 the quality factor for neutral particles coming from the work of Siebert et al. [1995] in the energy range between 10^{-9} MeV and 19.5 MeV is shown.

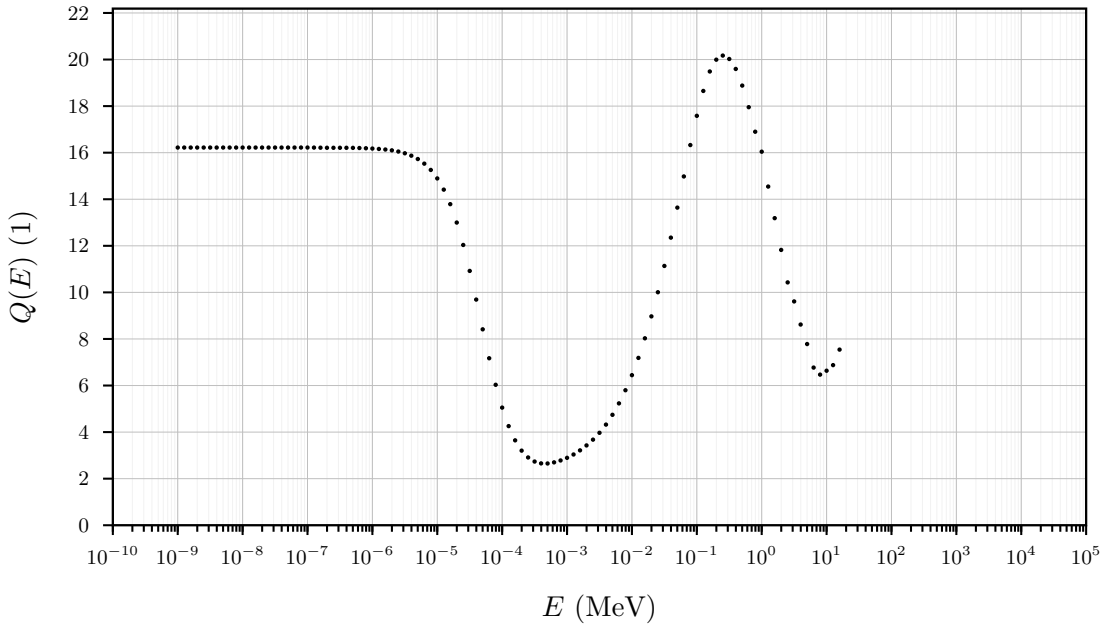

Figure 3.4: Neutron quality factors. From Siebert et al. [1995].

Quality factor for neutrons only take into account the local damage produced by neutrons (through the produced secondary charged particles) considering that secondary charged particles will be stopped in a *small* ICRU tissue *i.e.,* it does not take into account the photons reaching this *small* ICRU tissue. See Section 3.1.4.2.

3.1.2.4 Radiation weighting factor w_R

We consider ICRP report 103 [ICRP, 2007b] for the definitions of w_R. ICRP report 92 [ICRP, 2003] investigates the concept of w_R. w_R is derived from $\mathrm{RBE_M}$ and fixed values are assigned to it. In Section 3.1.4.2, the general definition of quality factor is expanded.

Table 3.6: Recommended radiation weighting factors, w_R [ICRP, 2007b].

Radiation type	w_R
Photons	1
Electrons and muons	1
Protons and charged pions	2
Alpha particles, fission fragments, heavy ions	20
Neutrons	A continuous function of neutron energy

3.1.3 Protection quantities

Mean absorbed dose in organ

An organ of total mass m_{T} is constituted by elementary masses, dm, so

$$m_{\mathrm{T}} = \int_{m_{\mathrm{T}}} \mathrm{d}m. \tag{3.32}$$

The mean energy imparted to the whole organ, $\bar{\epsilon}$, is the sum of the mean energy imparted differentials

$$\bar{\epsilon} = \int_{m_{\mathrm{T}}} \mathrm{d}\bar{\epsilon}. \tag{3.33}$$

The mean absorbed dose in an organ is defined as

$$D_{\mathrm{T}} = \frac{\bar{\epsilon}}{m_{\mathrm{T}}} = \frac{1}{m_{\mathrm{T}}} \int_{m_{\mathrm{T}}} \mathrm{d}\bar{\epsilon}. \tag{3.34}$$

Equivalent dose

The protection quantities are used to specify exposure limits to ensure that the occurrence of stochastic health effects is kept below unacceptable levels and that tissue reactions are avoided [ICRP, 2007b]. The definition of the protection quantities is based on the average absorbed dose, $D_{T,R}$ in the volume of a specified organ or tissue T (see Table 3.7), due to radiation of type R (see Table 3.6). The radiation R is given by the type and energy of radiation either incident on the body or emitted by radionuclides residing within it. The protection quantity equivalent dose in an organ or tissue, H_T, is then defined by

$$H_T = \sum_R w_R D_{T,R}, \tag{3.35}$$

where w_R is the radiation weighting factor for radiation R. The sum is performed over all types of radiations involved. The SI unit of equivalent dose is J kg^{-1} and has the special name sievert (Sv).

Effective dose

Effective dose, E, is defined as [ICRP, 2007b]

$$E = \sum_T w_T H_T. \tag{3.36}$$

Where w_T is the tissue weighting factor to represent the relative contribution of that tissue or organ to the total health detriment resulting from uniform irradiation of the body [ICRP, 2007b]. It is weighted such that

$$\sum_T w_T = 1. \tag{3.37}$$

Table 3.7: Recommended tissue weighting factors, w_T, from Table 3 of ICRP [2007b].

Tissue	w_T	$\sum_T w_T$
Bone-marrow (red), Colon, Lung, Stomach, Breast, Remainder tissues*	0.12	0.72
Gonads	0.08	0.08
Bladder, Oesophagus, Liver, Thyroid	0.04	0.16
Bone surface, Brain, Salivary glands, Skin	0.01	0.04
	Total	1.00

* Remainder tissues: Adrenals, Extrathoracic (ET) region, Gall bladder, Heart, Kidneys, Lymphatic nodes, Muscle, Oral mucosa, Pancreas, Prostate, Small intestine, Spleen, Thymus, Uterus/Cervix.

3.1.4 The dose equivalent

3.1.4.1 The dose equivalent produced by charged particles

The dose equivalent, H, is introduced in order to take into account the radiobiological damage of the different types of radiations in mixed radiation fields. To do so, this quantity uses the quality factor for a mono-LET charged particle at a point tissue.

The absorbed dose contributed by all charged particles of type i having a LET, L, between L and $L + \mathrm{d}L$ is

$$\mathrm{d}D_i(L). \tag{3.38}$$

The absorbed dose contributed by all charged particles of type i is then

$$D_i = \int_L \mathrm{d}D_i(L). \tag{3.39}$$

The absorbed dose contributed by all charged particles, in the mixed radiation field, is

$$D = \sum_i D_i \tag{3.40}$$

The dose equivalent contributed by all charged particles of type i having a LET, L, between L and $L + \mathrm{d}L$ is

$$\mathrm{d}H_i(L) = Q(L)\mathrm{d}D_i(L). \tag{3.41}$$

The dose equivalent contributed by all charged particles of type i is

$$H_i = \int_L \mathrm{d}H_i(L) = \int_L Q(L)\mathrm{d}D_i(L). \tag{3.42}$$

The dose equivalent contributed by all charged particles, in the mixed radiation field, is

$$H = \sum_i H_i = \sum_i \int_L \mathrm{d}H_i(L) = \sum_i \int_L Q(L)\mathrm{d}D_i(L). \tag{3.43}$$

We can also introduce the LET distribution of the absorbed dose for particles of type i through Equation (3.20), $\mathrm{d}D_i(L) = D_{L,i}(L)\mathrm{d}L$, or we can also introduce the unit LET distribution of the absorbed dose for particles of type i through Equation (3.27), $\mathrm{d}D_i(L) = D_i\, d_{L,i}(L)\,\mathrm{d}L$ so our final expressions for the dose equivalent in mixed radiation fields can be expressed as

$$H = \sum_i \int_L Q(L)\mathrm{d}D_i(L) \tag{3.44}$$

$$= \sum_i \int_L Q(L)D_{L,i}(L)\mathrm{d}L \tag{3.45}$$

$$= \sum_i \int_L Q(L)D_i\, d_{L,i}(L)\,\mathrm{d}L = \sum_i D_i \int_L Q(L)d_{L,i}(L)\,\mathrm{d}L \tag{3.46}$$

3.1.4.2 The dose equivalent produced by neutral particles

According to ICRP publication 60 [ICRP, 1991], ICRP publication 116 [ICRP, 2010] and the works of Siebert et al. [1995] and Leuthold et al. [1992], one can express the quality factor for any particle as

$$Q = \frac{1}{D}\int_L Q(L)D_L(L)\mathrm{d}L \tag{3.47}$$

$$= \frac{1}{D}\int_L Q(L)\mathrm{d}D(L). \tag{3.48}$$

Where it is understood that $\mathrm{d}D(L)$ is the absorbed dose of all type of secondary charged particles which have a LET between $L + \mathrm{d}L$ and D is the total absorbed dose contributed by all charged particles. So, it is verified that

$$\mathrm{d}D(L) = \sum_i \mathrm{d}D_i(L), \tag{3.49}$$

and

$$D = \sum_i D_i, \tag{3.50}$$

where i is the the type of charged particle and

$$D_i = \int_L \mathrm{d}D_i(L). \tag{3.51}$$

If we introduce Equation (3.49) and Equation (3.50) in Equation (3.48) we obtain

$$Q = \frac{1}{\left[\sum_i D_i\right]} \int_L Q(L) \left[\sum_i \mathrm{d}D_i(L)\right], \tag{3.52}$$

$$= \frac{1}{\left[\sum_i D_i\right]} \sum_i \int_L Q(L)\mathrm{d}D_i(L). \tag{3.53}$$

We have to remember that LET, L, unifies the different types of charged particles, *i.e.,* two different type of particles with the same L have different energies E_1 and E_2. Despite the previous fact, we usually work using the frame of energies instead of LETs. For this reason, let us expand the Equation (3.53) to be used in energies and for incident neutrons of energy E_{ne}. In this way, the quality factor for neutrons, Q_{ne}, is

$$Q_{\mathrm{ne}}(E_{\mathrm{ne}}) = \frac{1}{\left[\sum_i D_i\right]} \sum_i \int_L Q(L)\mathrm{d}D_i(L), \tag{3.54}$$

$$= \frac{1}{\left[\sum_i D_i\right]} \left[\int_{E_{\mathrm{pr}}} Q(E_{\mathrm{pr}})\mathrm{d}D_{\mathrm{pr}}(E_{\mathrm{pr}}) + \int_{E_{\mathrm{de}}} Q(E_{\mathrm{de}})\mathrm{d}D_{\mathrm{de}}(E_{\mathrm{de}}) + \cdots\right], \tag{3.55}$$

$$= \frac{\int_{E_{\mathrm{pr}}} Q(E_{\mathrm{pr}})\mathrm{d}D_{\mathrm{pr}}(E_{\mathrm{pr}}) + \int_{E_{\mathrm{de}}} Q(E_{\mathrm{de}})\mathrm{d}D_{\mathrm{de}}(E_{\mathrm{de}}) + \int_{E_{\mathrm{tr}}} Q(E_{\mathrm{tr}})\mathrm{d}D_{\mathrm{tr}}(E_{\mathrm{tr}}) + \cdots}{D_{\mathrm{pr}} + D_{\mathrm{de}} + D_{\mathrm{tr}} + D_{\mathrm{he}} + D_{\mathrm{al}} + D_{\mathrm{hi}} + \cdots}, \tag{3.56}$$

$$= \frac{H_{\mathrm{pr}} + H_{\mathrm{de}} + H_{\mathrm{tr}} + H_{\mathrm{he}} + H_{\mathrm{al}} + H_{\mathrm{hi}} + \cdots}{D_{\mathrm{pr}} + D_{\mathrm{de}} + D_{\mathrm{tr}} + D_{\mathrm{he}} + D_{\mathrm{al}} + D_{\mathrm{hi}} + \cdots}. \tag{3.57}$$

Where $i = \mathrm{pr}, \mathrm{de}, \mathrm{tr}, \mathrm{he}, \mathrm{al}, \mathrm{hi}, ...$ is the particle identification for protons, deuterons, tritons, helions, alphas and heavy ions, respectively.

Therefore, once the $Q_{\mathrm{ne}}(E_{\mathrm{ne}})$ are established, the neutron dose equivalent can be computed, for instance, through the same reasoning of Equations (3.41) and (3.42). Indeed, if we name $\mathrm{d}H_{\mathrm{ne}}(E_{\mathrm{ne}})$ as the dose equivalent differential contributed by neutrons with energies between E_{ne} and $E_{\mathrm{ne}} + \mathrm{d}E_{\mathrm{ne}}$ we see that

$$\mathrm{d}H_{\mathrm{ne}}(E_{\mathrm{ne}}) = Q_{\mathrm{ne}}(E_{\mathrm{ne}})\mathrm{d}D_{\mathrm{ne}}(E_{\mathrm{ne}}). \tag{3.58}$$

For neutrons, usually the kerma approximation is used, this consists in working with kerma instead of absorbed dose, so the kerma approximation consists in

$$\mathrm{d}D_{\mathrm{ne}}(E_{\mathrm{ne}}) \simeq \mathrm{d}K_{\mathrm{ne}}(E_{\mathrm{ne}}). \tag{3.59}$$

The kerma approximation is valid when the situation of electronic equilibrium is reached. If now we use Equation (3.59) in Equation (3.41) we obtain

$$\mathrm{d}H_{\mathrm{ne}}(E_{\mathrm{ne}}) = Q_{\mathrm{ne}}(E_{\mathrm{ne}})\mathrm{d}K_{\mathrm{ne}}(E_{\mathrm{ne}}), \tag{3.60}$$

and we can introduce fluence-to-kerma conversion coefficients for neutrons, $k_{\Phi,\mathrm{ne}}(E_{\mathrm{ne}})$,

Equation (3.13). So

$$\mathrm{d}H_{\mathrm{ne}}(E_{\mathrm{ne}}) = Q_{\mathrm{ne}}(E_{\mathrm{ne}})k_{\Phi,\mathrm{ne}}(E_{\mathrm{ne}})\mathrm{d}\Phi_{\mathrm{ne}}(E_{\mathrm{ne}}) \tag{3.61}$$

$$= Q_{\mathrm{ne}}(E_{\mathrm{ne}})k_{\Phi,\mathrm{ne}}(E_{\mathrm{ne}})\,\Phi_{E_{\mathrm{ne}}}(E_{\mathrm{ne}})\mathrm{d}E_{\mathrm{ne}}. \tag{3.62}$$

Therefore neutron dose equivalent is computed as

$$H_{\mathrm{ne}} = \int_{E_{\mathrm{ne}}} \mathrm{d}H_{\mathrm{ne}}(E_{\mathrm{ne}}) \tag{3.63}$$

$$= \int_{E_{\mathrm{ne}}} Q_{\mathrm{ne}}(E_{\mathrm{ne}})k_{\Phi,\mathrm{ne}}(E_{\mathrm{ne}})\,\Phi_{E_{\mathrm{ne}}}(E_{\mathrm{ne}})\mathrm{d}E_{\mathrm{ne}}. \tag{3.64}$$

The conversion coefficient $Q_{\mathrm{ne}}(E_{\mathrm{ne}})k_{\Phi,\mathrm{ne}}(E_{\mathrm{ne}}) \equiv Q(E)k_{\Phi,\mathrm{ne}}(E)$ is therefore the fluence-to-dose equivalent (in kerma approximation) conversion coefficient for neutrons in ICRU tissue. It is shown in Figure (3.5). Of course it is the product between numerical values from Figure (3.4) and Figure (3.1).

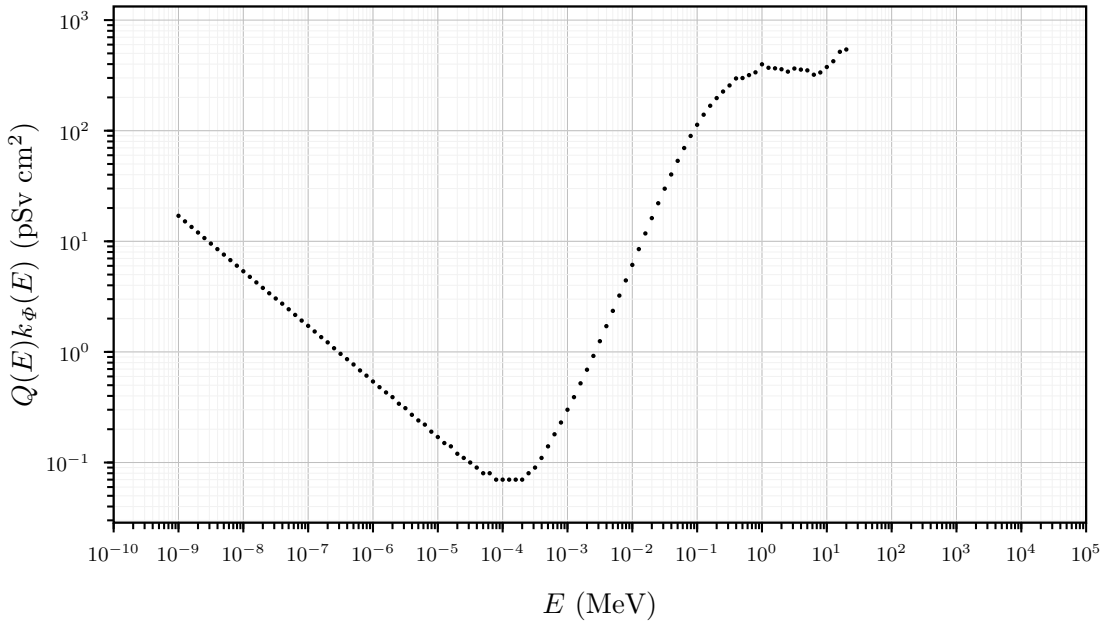

Figure 3.5: Fluence-to-dose equivalent (in kerma approximation) conversion coefficient for neutrons in ICRU tissue. From Siebert et al. [1995].

3.1.4.3 The total dose equivalent produced in mixed radiation fields

Even though the total dose equivalent can be computed through Equation (3.43) and considering that a mixed radiation field is, in the end, constituted by only charged particles, from the point of view of detector measurements and some methodologies that we suggest in Chapter 6, it is interesting to try to separate the contributions of the field in *local* neutrons, *local* photons and charged particles (which its origin is not from the *local* neutrons or *local* photons).

Some of these charged particles will be created from other charged particles or *non-local* neutrons or *non-local* photons. The situation and the notion of *locality* or *non-locality* is shown in Figure 3.6. From the Monte Carlo simulations point of view, we can find

problems in double scoring as will be commented in Chapter 5.

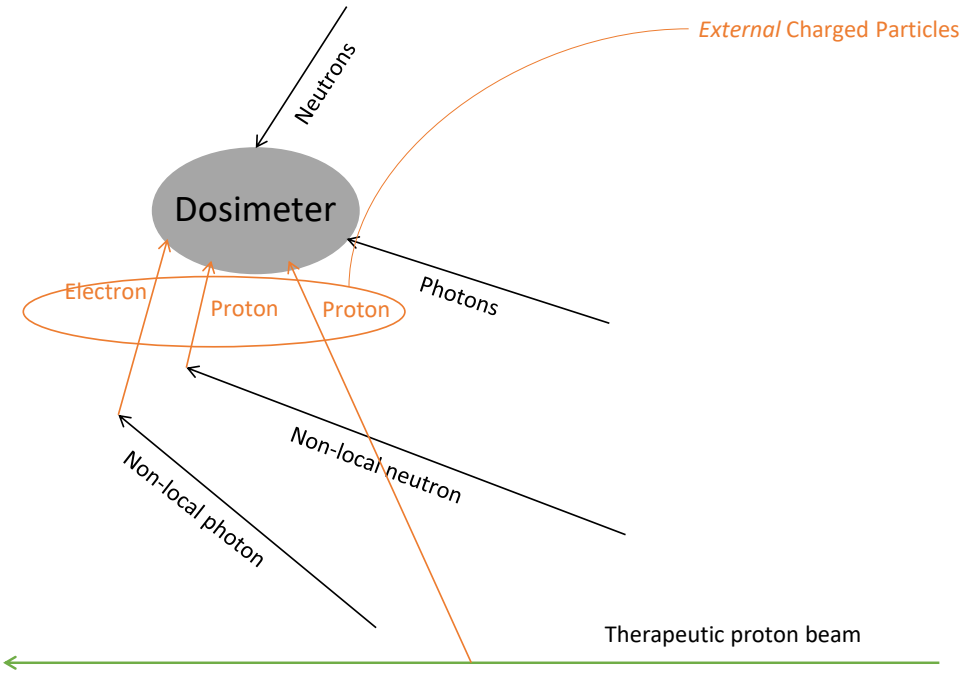

Figure 3.6: Mixed radiation field situation where the notions of locality or non-locality are shown.

So, the total dose equivalent produced by a mixed radiation field constituted by local neutrons, local photons and charged particles is

$$H = H_{\mathrm{ne}} + H_{\mathrm{ph}} + H_{\mathrm{ch}} \tag{3.65}$$

$$= \int_{E_{\mathrm{ne}}} Q_{\mathrm{ne}}(E_{\mathrm{ne}}) k_{\Phi,\mathrm{ne}}(E_{\mathrm{ne}})\, \Phi_{E_{\mathrm{ne}}}(E_{\mathrm{ne}}) \mathrm{d}E_{\mathrm{ne}} + \int_{E_{\mathrm{ph}}} Q_{\mathrm{ph}}(E_{\mathrm{ph}}) k_{\Phi,\mathrm{ph}}(E_{\mathrm{ph}})\, \Phi_{E_{\mathrm{ph}}}(E_{\mathrm{ph}}) \mathrm{d}E_{\mathrm{ph}}$$

$$+ \sum_i \int_L Q(L) \mathrm{d}D_i(L). \tag{3.66}$$

If we introduce that $Q_{\mathrm{ph}}(E_{\mathrm{ph}}) = 1$, the unit energy distribution of the fluence for photons and neutrons and define $Q(E_{\mathrm{ne}}) \equiv Q_{\mathrm{ne}}(E_{\mathrm{ne}})$, taking into account Equation (3.6), and the unit LET distribution of the dose, Equation (3.27), we obtain

$$H = \Phi_{\mathrm{ne}} \int_{E_{\mathrm{ne}}} Q(E_{\mathrm{ne}}) k_{\Phi,\mathrm{ne}}(E_{\mathrm{ne}}) \varphi_{E_{\mathrm{ne}}}(E_{\mathrm{ne}}) \mathrm{d}E_{\mathrm{ne}} + \Phi_{\mathrm{ph}} \int_{E_{\mathrm{ph}}} k_{\Phi,\mathrm{ph}}(E_{\mathrm{ph}}) \varphi_{E_{\mathrm{ph}}}(E_{\mathrm{ph}}) \mathrm{d}E_{\mathrm{ph}}$$

$$+ \sum_i D_i \int_L Q(L) d_{L,i}(L) \mathrm{d}L. \tag{3.67}$$

The term $\mathrm{d}D_i(L)$ can also be obtained through cema approximation (see ICRU [2011]) as

$$\mathrm{d}D_i(E_i) = \Phi_{E_i,i}(E_i) \left[\frac{S_{\mathrm{mat},i}(E_i)}{\rho_{\mathrm{mat}}}\right] \mathrm{d}E_i \tag{3.68}$$

$$= \Phi_i\, \varphi_{E_i,i}(E_i) \left[\frac{S_{\mathrm{mat},i}(E_i)}{\rho_{\mathrm{mat}}}\right] \mathrm{d}E_i. \tag{3.69}$$

Where ρ_{mat} is the mass density of the material and $S_{\text{mat},i}(E_i)$ is the stopping power for the particle type i with energy E_i when travels through the particular material. If we substitute Equation (3.69) in the last term of Equation (3.67), we can write

$$H = \Phi_{\text{ne}} \int_{E_{\text{ne}}} Q_{\text{ne}}(E_{\text{ne}}) k_{\Phi,\text{ne}}(E_{\text{ne}}) \varphi_{E_{\text{ne}}}(E_{\text{ne}}) \mathrm{d}E_{\text{ne}} + \Phi_{\text{ph}} \int_{E_{\text{ph}}} k_{\Phi,\text{ph}}(E_{\text{ph}}) \varphi_{E_{\text{ph}}}(E_{\text{ph}}) \mathrm{d}E_{\text{ph}} + \sum_i \Phi_i \int_{E_i} Q(E_i) \varphi_{E_i,i}(E_i) \left[\frac{S_{\text{mat},i}(E_i)}{\rho_{\text{mat}}} \right] \mathrm{d}E_i. \tag{3.70}$$

3.1.5 Operational quantities

ICRU tissue

According to ICRU report 44 [ICRU, 1989], average soft tissue has a mass density of 1 g cm^{-3} and an elemental composition of 10.1 % H, 11.1 % C, 2.6 % N and 76.2 % by weight (mass) fraction. In this work, the term ICRU tissue is understood as that material having the previous characteristics.

ICRU sphere

According to ICRU report 44 [ICRU, 1989], the ICRU sphere has a diameter of 30 cm, and is made of ICRU tissue.

ICRU slab

According to ICRU report 47 [ICRU, 1992], an ICRU slab is made of ICRU tissue an has dimensions of 30 cm × 30 cm × 15 cm.

Expanded field

If in an infinitesimal point there is an energy-angular distribution of the fluence, $\Phi_{E,\Omega}(E, \Omega)$, the expanded field consists in assuming that we will have the same energy-angular distribution of the fluence not only in the point but also in a general volume V. See Figure 3.7. In other words, there will be uniformity or constancy of this energy-angular distribution along any $\mathrm{d}V$ possibly build inside of V.

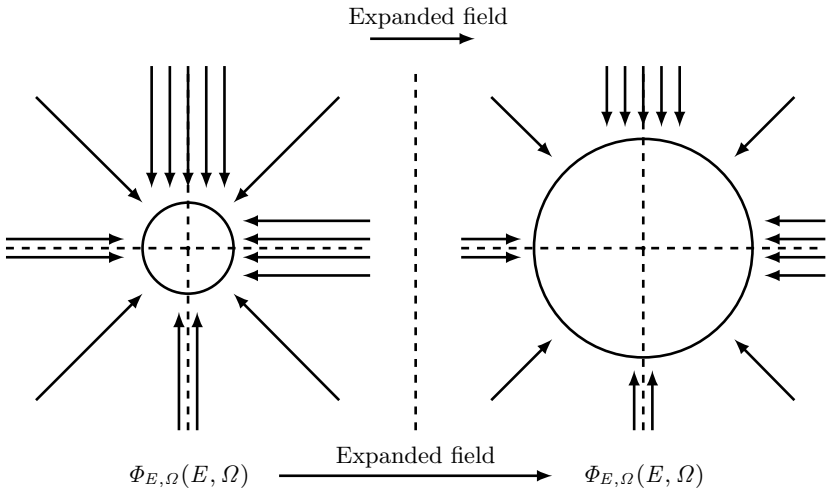

Figure 3.7: Definition of expanding the field. The features of the field (number of arrows coming from different directions) are kept constant even expanding the field accordingly to the new volume.

Defined quantities can use the concept of expanded field in their definitions just to be capable of defining a calibration coefficient for some particular radiation detector which occupies a certain volume V. It is important to keep in mind that if a detector has a volume V, this detector will not be able of informing about the field in smaller volumes $\mathrm{d}V$ inside of the volume V (space resolution). In any case, and according to the size limitations of the detector and the definition of expanded field, the features of the field in a sub-volume $\mathrm{d}V$ are, usually, assumed to be the same as the field described in V. If it turns out that the radiation field is highly non-uniform inside the volume V occupied by the detector, this means that this detector is *too big* to characterize the field. Of course we can work in approximations even if we know (or we do not know) if the field is very heterogeneous in the volume of the detector.

Aligned field

If in an infinitesimal or volumic point there is a general energy-angular distribution of the fluence, $\Phi_{E,\Omega}(E,\Omega)$, the aligned field consists in doing, as Equation (3.9),

$$\Phi_E(E) = \int_{\Omega} \Phi_{E,\Omega}(E,\Omega)\mathrm{d}\Omega. \tag{3.71}$$

And assume that the whole energy distribution of the fluence is impinging from one particular direction Ω_0. See Figure 3.8.

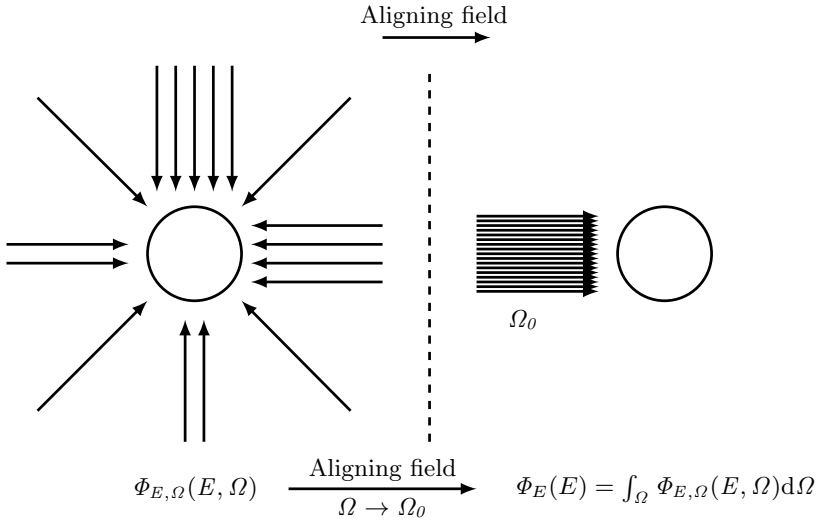

Figure 3.8: Definition of the alignment of the field. Note that there are the same number of arrows in the left and the right plot.

If it turns out that the field is intrinsically aligned in a direction Ω_0, this means

$$\Phi_{E,\Omega}(E,\Omega) = \Phi_E(E)\delta(\Omega - \Omega_0), \tag{3.72}$$

where $\delta(\Omega - \Omega_0)$ is the dirac delta function and therefore

$$\int_\Omega f(E,\Omega)\,\Phi_{E,\Omega}(E,\Omega)\mathrm{d}\Omega = \int_\Omega f(E,\Omega)\,\Phi_E(E)\delta(\Omega - \Omega_0)\mathrm{d}\Omega = f(E,\Omega_0)\,\Phi_E(E). \tag{3.73}$$

Where $f(E,\Omega_0)$ is any function depending on E and Ω, for instance the response of a radiation detector or the value of some conversion coefficient with angle dependence. If needed, the notation can be more specific in regards to the angle of incidence of the incoming particles.

Some quantities are defined using the concept of aligned field and therefore for using that dosimetric quantity in a calibration coefficient it has to be proved that the radiation detector is isotropic. In the case of non-isotropic devices such isotropic assuming definitions should not be used.

Expanded and aligned field

Is a combination between expanding and aligning the field.

Ambient dose equivalent

According to [ICRU, 1998], ambient dose equivalent, $H^*(d)$, at a point in a radiation field is the dose equivalent that would be produced by the corresponding expanded and aligned field in the ICRU sphere at a depth, d, on the radius opposing the direction of the aligned field. This point is characterized by letter P. The recommended value of d is 10 mm for penetrating radiation and 0.07 mm for low-penetrating radiation. See how point P is defined and how $H^*(d)$ is computed in Figures 3.9, 3.10 and 3.11.

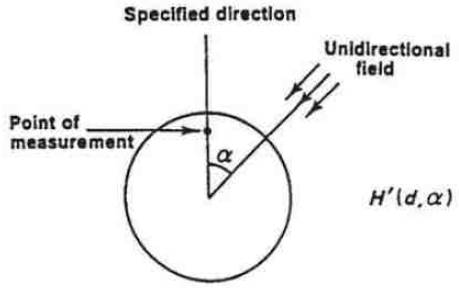

Figure 3.9: Notice how point P (point of measurement) is defined. It turns out that $H'(d, \alpha = 0°) = H'(d) = H^*(d)$. From ICRU [1998].

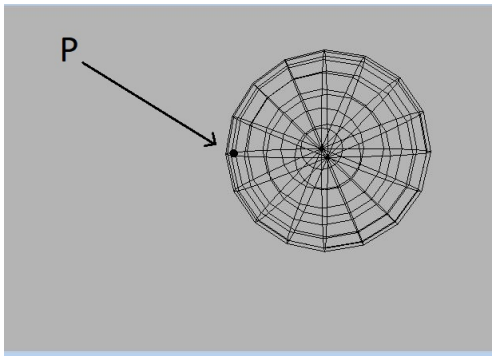

Figure 3.10: ICRU sphere. In this representation, point P is a little black sphere near the big sphere surface.

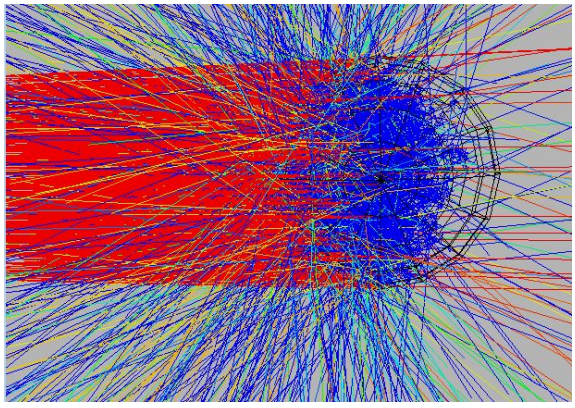

Figure 3.11: Mono-energetic neutron beam incident on the ICRU sphere. In this irradiation and geometry we execute the definition of ambient dose equivalent. Color represents the energy of the neutrons. Notice that the energy distribution reaching the sphere is different from that of the point P.

By applying the previous definition one can compute the fluence-to-ambient dose equivalent conversion coefficients for a particle of type i with energy between E and $E + \mathrm{d}E$, $h^*_{\Phi,i}(10, E)$. This is done using MC simulations. Let us suppose, by MC simulations, that we irradiate the ICRU sphere with a beam which illuminates (or expands into) the whole cross sectional area of the ICRU sphere (see Figures 3.9, 3.10 and 3.11). This incident beam is characterized by $\mathrm{d}\Phi_i(E)$. Therefore fluence-to-ambient dose equivalent conversion coefficient is primarily defined as

$$h^*_{\Phi,i}(10, E) = \left[\frac{\mathrm{d}H^*_i(10, E)}{\mathrm{d}\Phi_i(E)}\right]. \tag{3.74}$$

Moreover if we develop the previous definition, Equation (3.74), we can write for any charged or neutral particle that

$$h^*_{\Phi,i}(10, E) = \frac{\mathrm{d}H^*_i(10, E)}{\mathrm{d}\Phi_i(E)} = \frac{1}{\mathrm{d}\Phi_i(E)} \underbrace{(\mathrm{d}H_i)}_{\text{in P}} = \frac{1}{\mathrm{d}\Phi_i(E)} \underbrace{\left(\int_{E'} Q(E')\mathrm{d}D'_i(E')\right)}_{\text{in P}}. \tag{3.75}$$

Where $'$ reminds us that one thing is the radiation field reaching the point P and another thing is the radiation field in which the ICRU sphere is being irradiated. For a neutral

particle (neu) such as neutrons and fotons one can, additionally, write

$$h^*_{\Phi,\mathrm{neu}}(10,E) = \frac{\mathrm{d}H^*_{\mathrm{neu}}(10,E)}{\mathrm{d}\,\Phi_{\mathrm{neu}}(E)} = \frac{1}{\mathrm{d}\,\Phi_{\mathrm{neu}}(E)} \underbrace{(\mathrm{d}H_i)}_{\text{in P}} \simeq \tag{3.76}$$

$$\simeq \tfrac{1}{\mathrm{d}\,\Phi_{\mathrm{neu}}(E)} \underbrace{\left(\int_{E'} Q_{\mathrm{ph}}(E') k_{\Phi,\mathrm{ph}}(E')\, \Phi'_{E',\mathrm{ph}}(E')\mathrm{d}E' + \int_{E'} Q_{\mathrm{ne}}(E') k_{\Phi,\mathrm{ne}}(E')\, \Phi'_{E',\mathrm{ne}}(E')\mathrm{d}E' + \mathrm{Crossing} \right)}_{\text{in P}} \simeq \tag{3.77}$$

$$\simeq \frac{1}{\mathrm{d}\,\Phi_{\mathrm{neu}}(E)} \underbrace{\left(K'_{\mathrm{ph}} + \int_{E'} Q_{\mathrm{ne}}(E') k_{\Phi,\mathrm{ne}}(E')\, \Phi'_{E',\mathrm{ne}}(E')\mathrm{d}E' + \mathrm{Crossing} \right)}_{\text{in P}} \simeq \tag{3.78}$$

$$\simeq \frac{1}{\mathrm{d}\,\Phi_{\mathrm{neu}}(E)} \underbrace{\left(K'_{\mathrm{ph}} + \int_{E'} Q_{\mathrm{ne}}(E') k_{\Phi,\mathrm{ne}}(E')\, \Phi'_{E',\mathrm{ne}}(E')\mathrm{d}E' \right)}_{\text{in P}}. \tag{3.79}$$

Where the term "Crossing" refers to charged particles crossing the volume defined in point P and contributing to the dose equivalent. It can be proved that their contribution is negligible in front of the other contributions.

$\mathrm{d}H^*_i(10,E)$ is then the dose equivalent contributed in point P, precisely, by the incident particles of type i and energy between E and $E + \mathrm{d}E$.

Once the coefficient $h^*_{\Phi,i}(10,E)$ is known, in practise is used, according to its own definition, Equation (3.74), so that the ambient dose equivalent, $H^*_i(10)$, is found as

$$H^*_i(10) = \int_E \mathrm{d}H^*_i(10,E) = \int_E h^*_{\Phi,i}(10,E)\mathrm{d}\,\Phi_i(E) = \int_E h^*_{\Phi,i}(10,E)\,\Phi_{E,i}(E)\mathrm{d}E. \tag{3.80}$$

Figure 3.12 shows the fluence-to-ambient dose equivalent conversion coefficient for neutrons in ICRU tissue, $h^*_{\Phi,i}(10,E)$, Equation (3.74), and its comparison with the fluence-to-dose equivalent (in kerma approximation) for neutrons in ICRU tissue, $Q_{\mathrm{ne}}(E)k_{\Phi,\mathrm{ne}}(E)$, Equations (3.54) and (3.13) (product of Figures 3.1 and 3.4). Actually, $Q_{\mathrm{ne}}(E)k_{\Phi,\mathrm{ne}}(E)$ are used for the computation of $h^*_{\Phi,i}(10,E)$. While the first ones are broadly accepted in the range between 10^{-9} MeV and 10^4 MeV through the works of, for example, ICRU [1998], Siebert et al. [1995] and Pelliccioni [2000] the latter are only well documented (to the author knowledge) up to 20 MeV in the case of $Q_{\mathrm{ne}}(E)$ [Siebert et al., 1995] and up to 150 MeV in the case of $k_{\Phi,\mathrm{ne}}(E)$ [Caswell et al., 1980] [Chadwick et al., 1999].

As shown in Figure 3.12 the difference between the conversion coefficients is that fluence-to-ambient dose equivalent conversion coefficients take into account the dose produced by photons simply by definition.

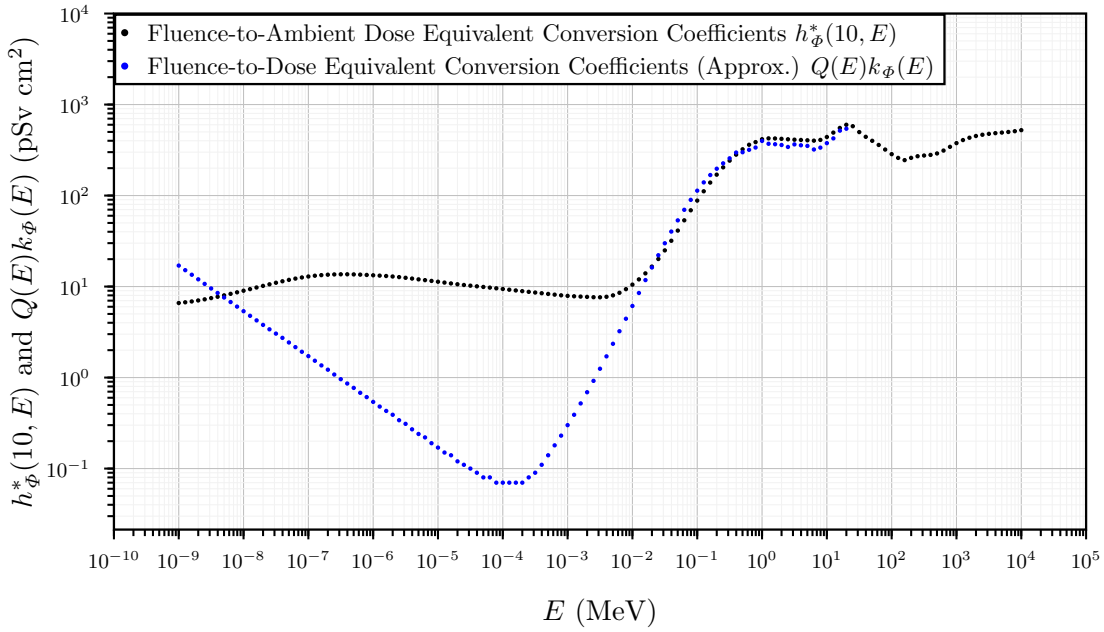

Figure 3.12: Fluence-to-ambient dose equivalent conversion coefficient for neutrons in ICRU tissue and its comparison with the fluence-to-dose equivalent (in kerma approximation) for neutrons in ICRU tissue.

Directional dose equivalent

According to ICRU [1998], directional dose equivalent, $H'(d,\Omega)$, at a point in a radiation field is the dose equivalent that would be produced by the corresponding expanded field in the ICRU sphere at depth, d, on a specified radius. The direction can be specified in terms of the angle, α, between the specified radius and the radius opposing the incident field, characterized by the direction Ω. The recommended value of d is 10 mm for penetrating radiation and 0.07 mm for low-penetrating radiation. It is verified that $H'(d,\alpha=0°) = H'(d) = H^*(d)$.

Personal dose equivalent

According to ICRU [1998], personal dose equivalent is defined in a phantom including the ICRU sphere and the ICRU slab but also in anthropomorphic phantoms. It is defined as the dose equivalent in these bodies in a certain depth inside of the phantom.

3.2 Related quantities

Stopping power

Charged particles lose their energy in a material through different processes [ICRU, 1984], [ICRU, 1993] [Durrani et al., 1987]:

1. Inelastic coulomb interactions-collisions between an incident charged particle of energy E and bound atomic electrons of the medium resulting in ionization and excitation. This process is taken into account through the *electronic stopping power* $S_{\text{el}}(E)$. The binding energy of the atomic electrons is included.

2. Elastic coulomb interactions-collisions between an incident charged particle of energy E and the whole atom, which can result in the ejection of the target atoms from lattice sites or from molecular chains. This process is taken into account through *nuclear stopping power* $S_{\mathrm{nuc}}(E)$.

3. Emission of radiation in form or photons, bremsstrahlung radiation, due to the interaction between the incident charged particle of energy E and the electric field generated by the atomic nucleus and the atomic electrons. This process is taken into account through *radiative stopping power* $S_{\mathrm{rad}}(E)$. The bremsstrahlung radiation will not be deposited locally.

4. Excitation through vibrations and rotations of the molecules. These processes can be disregarded if the charged incident particle has an energy above the threshold energy to produce electronic excitation.

5. Inelastic nuclear interactions, but such processes are not usually described by a stopping power [ICRU, 2011].

Total stopping power or simply stopping power is the mean energy lost (defined positive), $\mathrm{d}\tilde{E} > 0$, per unit pathlength, $\mathrm{d}l$, due to any of the three first kind of interactions described above so it is written as

$$S(E) = \frac{\mathrm{d}\tilde{E}}{\mathrm{d}l} = S_{\mathrm{el}}(E) + S_{\mathrm{nuc}}(E) + S_{\mathrm{rad}}(E). \tag{3.81}$$

In the electronic stopping power, secondary electrons may hold any energy between 0 and the maximum possible energy according to conservation laws and binding energies.

Stopping power is always defined positive because is understood as the mean energy *transferred-lost* to matter (*i.e.,* $\mathrm{d}\tilde{E} > 0$). However, from the point of view of a travelling particle of initial energy E_{i}, when it travels a distance $\mathrm{d}l$ it will have now an energy $E_{\mathrm{f}} < E_{\mathrm{i}}$ so that

$$E_{\mathrm{f}} = E_{\mathrm{i}} - \mathrm{d}\tilde{E}, \tag{3.82}$$

$$\underbrace{(E_{\mathrm{f}} - E_{\mathrm{i}})}_{<0} = \underbrace{\mathrm{d}E}_{<0} = -\underbrace{\left(\mathrm{d}\tilde{E}\right)}_{>0}, \tag{3.83}$$

$$\mathrm{d}E = -\mathrm{d}\tilde{E}. \tag{3.84}$$

In conclusion

$$S(E) = \frac{\mathrm{d}\tilde{E}}{\mathrm{d}l} = -\frac{\mathrm{d}E}{\mathrm{d}l} > 0. \tag{3.85}$$

$$\mathrm{d}\tilde{E} = S(E)\mathrm{d}l > 0 \quad \text{the mean energy transferred to the matter is a positive quantity.} \tag{3.86}$$

$$\mathrm{d}E = -S(E)\mathrm{d}l < 0 \quad \text{indeed, the mean energy of the particle decreases in each interaction.} \tag{3.87}$$

Values of stopping power for electrons, protons or helium ions according to the methods described in ICRU [1984] and ICRU [1993] can be found in the databases ESTAR, PSTAR, and ASTAR [Berger et al., 1993]. Stopping-power and range tables can be calculated for electrons in any user-specified material and for protons and helium ions in 74 materials.

Another way to obtain the stopping power is to use the group of programs of SRIM (the Stopping and Range of Ions in Matter) [Ziegler et al., 1985].

Restricted collisional stopping power

A fraction of the energy lost in ionizing collisions is converted to kinetic energy of secondary electrons (inelastic coulomb interactions between the incident charged particle and bound atomic electrons) and they will excite and ionize the matter some distance away from the primary particle track. Therefore the *restricted collisional stopping power* for charged particles of a given type and energy E travelling in a material is the quotient of $\mathrm{d}E_{\mathrm{el}}$ by $\mathrm{d}l$, where $\mathrm{d}l$ is the distance traversed by the particle and $\mathrm{d}E_{\mathrm{el}}$ is the mean energy lost due to electronic interactions with kinetic energies of the secondary electrons less than some specified value Δ. It is written as:

$$S_{\mathrm{el}}(E)|_{\Delta} = \left.\frac{\mathrm{d}E}{\mathrm{d}l}\right|_{\mathrm{el},\Delta}. \tag{3.88}$$

Therefore, in the restricted collisional stopping power, we are interested in the energy deposited by the secondary electrons with any energy between 0 and less than Δ. In the actual definition (due to the work of Kellerer et al. [1992]) it is included the energy deposited due to the fact of overcoming the binding energy of the electrons.

Linear Energy Transfer (LET)

According to the actual definition, it is the same as the restricted collision stopping power. The symbol L_{Δ} is used.

A related stochastic quantity to LET is the linear energy, y, whose probability density function is $f(y)$. Linear energy is defined as

$$y = \frac{\epsilon_{\mathrm{s}}}{\bar{l}}, \tag{3.89}$$

where ϵ_{s} is the energy imparted in a given volume by a single energy-deposition event and $\bar{l}$ is the mean chord length of that volume. Under approximations the mean value $\overline{y} = \int_y y f(y)\mathrm{d}y$ is similar to LET. For more details see ICRU [1983].

Unrestricted Linear Energy Transfer

Corresponds to the situation in which the secondary electrons can have any energy with the only restriction of conservation laws. Therefore, unrestricted linear energy transfer, symbolised as L_{∞}, is equal to $S_{\mathrm{el}}(E)$, so

$$L_{\infty} \equiv L = S_{\mathrm{el}}(E) = \left.\frac{\mathrm{d}E}{\mathrm{d}l}\right|_{\mathrm{el}}. \tag{3.90}$$

Cema (Converted Energy per MAss)

The cema, C, for ionizing charged particles, is the quotient of $\mathrm{d}E_{\mathrm{el}}$ by $\mathrm{d}m$, where $\mathrm{d}E_{\mathrm{el}}$ is the mean energy lost in electronic interactions in a mass $\mathrm{d}m$ of a material by the charged particles, except secondary electrons, incident on $\mathrm{d}m$, thus

$$C = \frac{\mathrm{d}E_{\mathrm{el}}}{\mathrm{d}m}. \tag{3.91}$$

The energy lost by charged particles in electronic interactions includes the energy expended to overcome the binding energy and the initial kinetic energy of the liberated electrons, referred to as secondary electrons. It can be proved that cema can be written as [ICRU,

2011]

$$C = \int_E \Phi_E(E) \left[\frac{S(E)}{\rho}\right] \mathrm{d}E. \tag{3.92}$$

According to the definition of cema, the energy distribution of the fluence in Equation (3.92) does not include the contribution of secondary electrons, but the contributions of all other charged particles, such as secondary protons, alpha particles, tritons, and ions produced in nuclear interactions, are included in the respective individual cema.

Number of reactions

By definition of the reaction cross section, the number of nuclear reactions that are originated, $\mathrm{d}N_{\mathrm{Reactions}}(E)$, by incident particles of energy E characterized by an energy distribution of the fluence, $\mathrm{d}\,\Phi(E)$, and with a interaction probability related to cross section, $\sigma(E)$, are [Krane, 1987]

$$\mathrm{d}N_{\mathrm{Reactions}}(E) = N_{\mathrm{Targets}} \cdot \sigma(E) \cdot \mathrm{d}\,\Phi(E), \tag{3.93}$$

where N_{Target} are the number of targets illuminated by the incident radiation field $\mathrm{d}\,\Phi(E)$.

3.2.1 Conversion coefficients between different physical quantities

Sometimes it is pertinent to express one quantity in terms of another different quantity, in other words, to use a first quantity-to-second quantity conversion coefficient (or factor) for some particle in some material. This is useful when we want to express, for instance, a calibration coefficient for some detector in terms of a different physical quantity (fluence, kerma in some material, absorbed dose in some material) or different material.

In the actual radiation protection system, the energy integrated physical quantities are Equations (3.6), (3.12) and (3.92) and can be written as:

$$\Phi_i = \int_E \mathrm{d}\,\Phi_i(E) = \Phi_i \cdot \int_E \varphi_{E,i}(E)\,\mathrm{d}E = \Phi_i, \tag{3.94}$$

$$K_{i\to\mathrm{mat}} = \int_E \mathrm{d}K_{i\to\mathrm{mat}}(E) = \Phi_i \cdot \int_E \varphi_{E,i}(E) \underbrace{E\left[\frac{\mu_{i,\mathrm{tr,mat}}(E)}{\rho_{\mathrm{mat}}}\right]}_{k_{\Phi,i,\mathrm{mat}}(E)} \mathrm{d}E, \tag{3.95}$$

$$D_{i\to\mathrm{mat}} = \int_E \mathrm{d}D_{i\to\mathrm{mat}}(E) = \Phi_i \cdot \int_E \varphi_{E,i}(E) \left[\frac{S_{i,\mathrm{mat}}(E)}{\rho_{\mathrm{mat}}}\right] \mathrm{d}E. \tag{3.96}$$

Equation (3.94) can be used for both, neutral and charged particles while Equation (3.95) can be used only for neutral particles and Equation (3.96) can be only used for charged particles.

For instance, let us suppose that we encounter a mono-energetic field of photons in some calibration facility and the facility provide us with the quantity kerma in air for these mono-energetic photons. In the case that we are interested in the kerma in water for these mono-energetic photons we have to define the conversion factor:

$$\left[\frac{\mathrm{d}K_{\mathrm{ph}\to\mathrm{w}}(E)}{\mathrm{d}K_{\mathrm{ph}\to\mathrm{air}}(E)}\right] = \left[\frac{\Phi_{\mathrm{ph}} \cdot \varphi_{E,\mathrm{ph}}(E)\, k_{\Phi,\mathrm{ph,w}}(E)\,\mathrm{d}E}{\Phi_{\mathrm{ph}} \cdot \varphi_{E,\mathrm{ph}}(E)\, k_{\Phi,\mathrm{ph,air}}(E)\,\mathrm{d}E}\right] = \left[\frac{k_{\Phi,\mathrm{ph,w}}(E)}{k_{\Phi,\mathrm{ph,air}}(E)}\right]. \tag{3.97}$$

If the mono-energetic field approximation is not appropriate, we can deal with the whole

energy distribution of the fluence so that:

$$\left[\frac{K_{\mathrm{ph}\to\mathrm{w}}}{K_{\mathrm{ph}\to\mathrm{air}}}\right] = \left[\frac{\Phi_{\mathrm{ph}}\cdot\int\limits_{E}\varphi_{E,\mathrm{ph}}(E)\,k_{\Phi,\mathrm{ph,w}}(E)\mathrm{d}E}{\Phi_{\mathrm{ph}}\cdot\int\limits_{E}\varphi_{E,\mathrm{ph}}(E)\,k_{\Phi,\mathrm{ph,air}}(E)\mathrm{d}E}\right] = \left[\frac{\int\limits_{E}\varphi_{E,\mathrm{ph}}(E)\,k_{\Phi,\mathrm{ph,w}}(E)\mathrm{d}E}{\int\limits_{E}\varphi_{E,\mathrm{ph}}(E)\,k_{\Phi,\mathrm{ph,air}}(E)\mathrm{d}E}\right]. \tag{3.98}$$

And similarly for other types of conversion coefficients.

Of course, it is satisfied that

$$\left[\frac{\mathrm{d}K_{i\to\mathrm{mat}}(E)}{\mathrm{d}\,\Phi_i(E)}\right] = \left[\frac{\Phi_i\cdot\varphi_{E,i}(E)\,k_{\Phi,i,\mathrm{mat}}(E)\,\mathrm{d}E}{\Phi_i\cdot\varphi_{E,i}(E)\,\mathrm{d}E}\right] = k_{\Phi,i,\mathrm{mat}}(E), \tag{3.99}$$

which is Equation (3.13).

And is also satisfied that:

$$\left[\frac{\mathrm{d}D_{i\to\mathrm{mat}}(E)}{\mathrm{d}\,\Phi_i(E)}\right] = \left[\frac{\Phi_i\cdot\varphi_{E,i}(E)\left[\frac{S_{i,\mathrm{mat}}(E)}{\rho_{\mathrm{mat}}}\right]\mathrm{d}E}{\Phi_i\cdot\varphi_{E,i}(E)\,\mathrm{d}E}\right] = \left[\frac{S_{i,\mathrm{mat}}(E)}{\rho_{\mathrm{mat}}}\right]. \tag{3.100}$$

Therefore it is clear that according to Equation (3.100), in cema approximation, the massic stopping power or unrestricted LET is actually the fluence-to-absorbed dose conversion coefficient (in some material) for charged particles.

3.3 Neutron induced charged particles and radiobiological damage

The main references to understand the assignment of neutron dose equivalent type quantities and their implications are Caswell et al. [1980], Chadwick et al. [1999], Siebert et al. [1995] and references therein.

To understand the neutron radiobiological damage produced by neutrons due to the induction of secondary charged particles in tissue is necessary to understand how monoenergetic fluence-to-kerma conversion coefficients for neutrons are computed. From Equations (3.13), (3.14) and from Caswell et al. [1980] we can write

$$k_{\Phi}(E) = \frac{\mathrm{d}K(E)}{\mathrm{d}\,\Phi(E)} \tag{3.101}$$

$$= E\left[\frac{\mu_{\mathrm{tr}}(E)}{\rho}\right] \tag{3.102}$$

$$= \sum_{j}\left[\frac{n_j^{\mathrm{T}}}{\rho}\right]\sum_{i}\overline{E}_{i,j}^{\mathrm{tr}}\;\sigma_{i,j}(E). \tag{3.103}$$

Where the index j identifies the element or nuclide, i identifies the type of nuclear reaction, n_j^{T} is the number of nuclei-targets of the jth element or nuclide per cm^3, ρ is the mass density (g per cm^3) and $\overline{E}_{i,j}^{\mathrm{tr}}$ is the average amount of energy transferred to kinetic energy of charged particles in a collision whose cross section is $\sigma_{i,j}(E)$. The fundamental way to compute kerma coefficients is, therefore, using Equation (3.103).

By studying references Chadwick et al. [1999], Caswell et al. [1980] and ICRP [2010]

the elements or isotopes relevant for the radiobiological damage of neutrons in ICRU tissue which depends on the incident energy of the neutron are understood. According to Section 3.1.5, ICRU tissue is constituted by 10.1 % H, 11.1 % C, 2.6 % N and 76.2 % O by weight fraction so the relationship between the elemental kerma coefficients, $k_{\Phi,i}(E)$, defined for each element or most abundant isotope, and the ICRU tissue kerma coefficients is

$$k_{\Phi,\mathrm{ICRU}}(E) = 0.101 \cdot k_{\Phi,^{1}\mathrm{H}}(E) + 0.111 \cdot k_{\Phi,^{12}\mathrm{C}}(E) + 0.026 \cdot k_{\Phi,^{14}\mathrm{N}}(E) + 0.762 \cdot k_{\Phi,^{16}\mathrm{O}}(E). \tag{3.104}$$

Figure 3.13 shows the elemental fluence-to-kerma conversion coefficients for neutrons, $k_{\Phi,^{1}\mathrm{H}}(E)$, $k_{\Phi,^{12}\mathrm{C}}(E)$, $k_{\Phi,^{14}\mathrm{N}}(E)$ and $k_{\Phi,^{16}\mathrm{O}}(E)$. From Figure 3.13 is learnt that a material constituted only by ^{1}H would receive a lot of energy or damage because of the recoil of ^{1}H (or protons) when neutrons are incident. We can also extract some details about the physics involved in the mentioned isotopes, we could say that the physics regarding the production of secondary particles is similar for ^{12}C, ^{14}N and ^{16}O in the energy range from 0.1 and 150 MeV. It is also learnt that for energies lower than 0.01 MeV we see that ^{14}N fluence-to-kerma conversion coefficients for neutrons have high values, due to the reaction ^{14}N(n,p)^{14}C. Finally, it can be proven that for ^{12}C and ^{16}O and for incident neutrons of energy lower than 30 MeV, the total elemental kerma coefficients of these isotopes is dominated by the production of alpha particles [Chadwick et al., 1999]. However, this fact will not be relevant when we analyse the ICRU tissue kerma coefficients because the presence of ^{1}H (and its recoil protons) and the presence of ^{14}N (and its proton production due to ^{14}N(n,p)^{14}C) will be dominant over the damage produced by the mentioned alpha particles.

In Figure 3.14 the ICRU fluence-to-kerma conversion coefficients for neutrons, $k_{\Phi,\mathrm{ICRU}}(E)$, Equation (3.104), as well as the weighted contributions from the right side of Equation (3.104) is shown. Some conclusions can be extracted from Figure 3.14:

1. For neutron energies up to 4×10^{-5} MeV, ICRU fluence-to-kerma conversion coefficients for neutrons are dominated by the presence of ^{14}N and its proton production due to ^{14}N(n,p)^{14}C.

2. For neutron energies from 4×10^{-5} MeV to 70 MeV, ICRU fluence-to-kerma conversion coefficients for neutrons are dominated by the presence of ^{1}H and its proton production due to the recoil of ^{1}H itself.

3. For neutron energies from 70 MeV to 150 MeV, ICRU fluence-to-kerma conversion coefficients for neutrons are dominated by the presence of ^{16}O and its proton production.

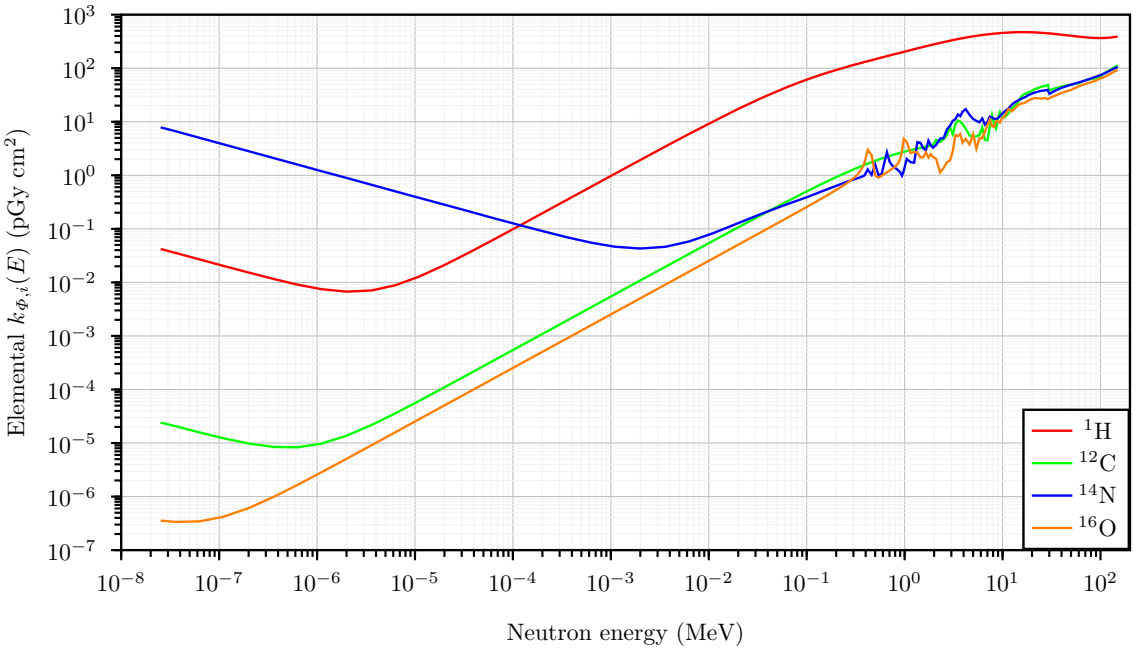

Figure 3.13: Fluence-to-kerma conversion coefficients for neutrons in elemental tissue. Data from Caswell et al. [1980] and Chadwick et al. [1999].

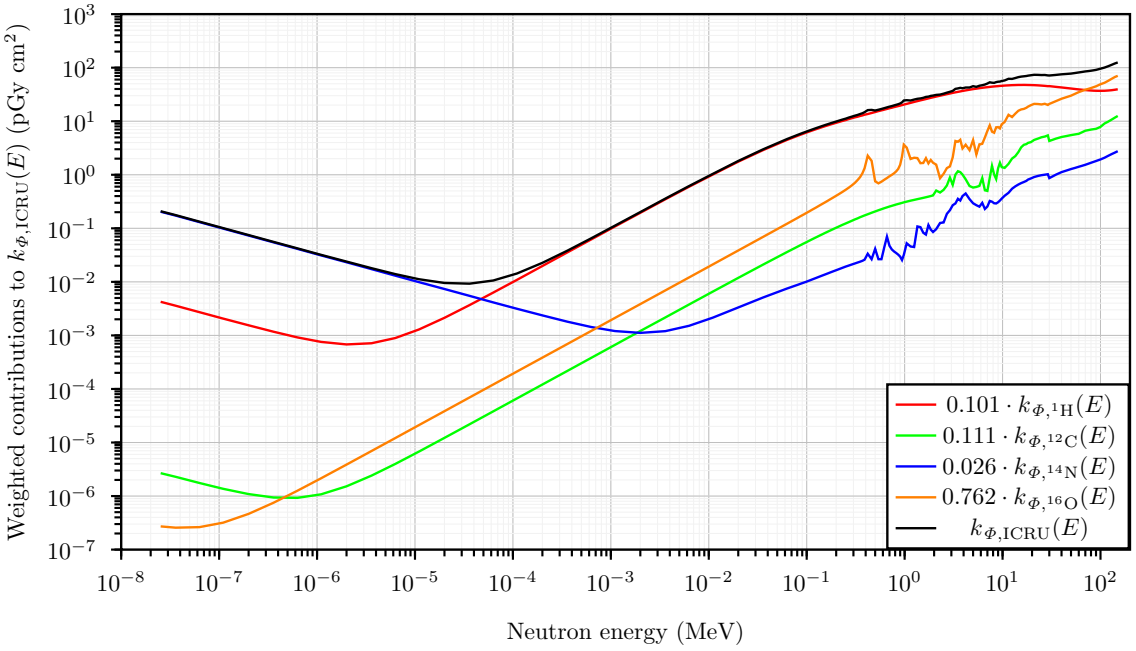

Figure 3.14: Fluence-to-kerma conversion coefficients for neutrons in ICRU tissue. Data from Caswell et al. [1980] and Chadwick et al. [1999].

Figure 3.15 shows the calculated percentage kerma due to protons, alpha particles, non-elastic recoils, and elastic recoils in ICRU tissue. Above 30 MeV we can state that proton production from all isotopes contained in ICRU tissue (^{1}H, ^{12}C, ^{14}N, ^{16}O) are the dominant contribution for producing radiobiological damage. For energies below 30 MeV, as we explained before, for ^{12}C and ^{16}O, the elemental kerma coefficients of these isotopes is dominated by the production of alpha particles but the presence of ^{1}H and ^{14}N produce such quantity of protons so that this alpha contribution is actually not dominant.

Figure 3.16 can be seen as an extension of Figure 3.15 considering that photons are not taken into account in the computation of the ICRU fluence-to-kerma conversion coefficients for neutrons. The notions of local damage and not local damage as well as the differences between the fluence-to-dose equivalent in ICRU tissue, $Q(E)k_{\Phi}(E)$ (Section 3.1.4.2) and the fluence-to-ambient dose equivalent, $h^*_{\Phi}(10, E)$ (Section 3.1.5) can be better understood studying Figures 3.15, 3.16 and 3.12 regarding the neutron and the photon contribution to the radiobiological damage.

Figure 3.16 is precisely, and according to ICRP [2010], "*the relative absorbed dose contribution of secondary charged particles in the whole body of the male voxel phantom in ISO geometry as a function of incident neutron energy. For neutrons with incident energies up to ∼ 10 keV, secondary photons contribute the major fraction of the absorbed dose deep within the body, and ∼ 90 % of the absorbed dose comes from 2.2 MeV photons emitted during neutron capture by hydrogen. As photons deposit their energy via electrons and positrons, the photon contribution is classified in Fig. 4.17 under 'Electron/Positron'. The rest of the absorbed dose (∼ 10 %) originates from the* $^{14}N(n,p)^{14}C$ *reaction; protons and 14C recoil nuclei deposit their energy and are classified into 'Proton' and 'Nucleus', respectively. Photons contribute 90 % of the absorbed dose from irradiation by thermal- and epithermal neutrons; at neutron energies above 10 keV, the contribution to absorbed dose from photons falls sharply and is less than 20 % at 1 MeV. At energies above ∼ 1 keV, the energy deposited by recoil protons from elastic scattering with hydrogen becomes important, while at energies above a few MeV, the production of charged particles by nuclear reactions becomes an increasingly important mechanism for the deposition of incident neutron energy. As the incident energy of the neutrons increases, various secondary particles emitted in inelastic nuclear reactions play an important part in the distribution of absorbed dose to internal organs.*"

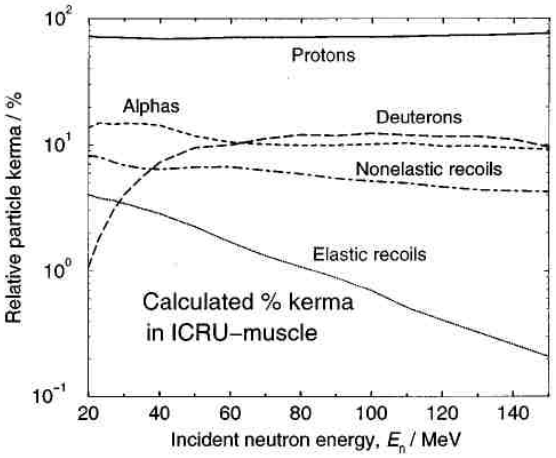

Figure 3.15: Percentage kerma due to protons, alpha particles, non-elastic recoils, and elastic recoils in ICRU tissue. Note that the n-p kerma coefficient was classed under "protons" and not "elastic recoils". From Chadwick et al. [1999].

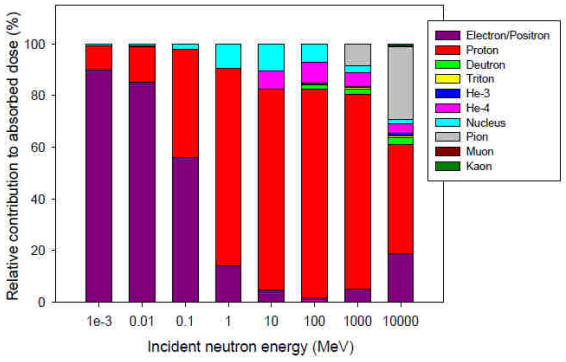

Figure 3.16: The relative absorbed dose contribution of secondary charged particles in the whole body of the male voxel phantom in ISO geometry as a function of incident neutron energy. From ICRP [2010].

Chapter 4

Principles, procedures and calibrations in radiation detectors

The *response*, *reading*, *signal* or *counts* of a radiation detector to a specific and well known radiation environment (*i.e.,* in a calibration or reference facility) is described by a *calibration coefficient* or *sensitivity coefficient*, or a *response function*. A calibration coefficient is easier to obtain in comparison with the response function as the former can be obtained even for complicated mixed radiation fields while the latter is usually viewed as that mathematical fit function that collects the mono-energetic responses of the detector for one type of particle reaching the detector from a specific direction. Both quantities have the same units and can be exchanged in some very particular situations. Of course is technically more difficult to obtain or to know the response function of one detector than a calibration coefficient since, by definition, to know the first one is required to do a great number of irradiations and MC simulations.

The response of a detector is quantified according to the nature of the detector. A good general description of the several detector systems that exist today and related techniques can be found in Knoll [2010].

Some examples of responses are the following:

1. The number of nuclear, atomic or molecular reactions in the detector system that can be translated in electrical pulses of equal amplitude such as in a geiger tube or electrical pulses of different amplitudes and shapes. For instance, detectors based on scintillator [Birks, 1964] + PhotoMultiplier Tube (PMT) [McKeever, 1983], detectors based on ^{3}He gas in proportional counters (as in this work) and semiconductor diode detectors [Bedogni et al., 2015].

2. The number of tracks in a Solid State Nuclear Track Detector (SSNTD) or track-etch detector [Fleischer et al., 1975] [Durrani et al., 1987]. For instance, the tracks quantified in a Poly Allyl Diglycol Carbonate (PADC) layer after an electrochemical etching procedure [Domingo et al., 2013].

3. The number of excitations in a Luminescence Dosimeter (LD), which is quantified by measuring the desexcitations reactions quantified using a PMT. For instance, ThermoLuminescence Dosimeter (TLD) and RadioPhotoLuminescence dosimeter (RPL).

4. The activation rate in a foil of adequate material, quantified from the rate of desexcitation reactions measured using a scintillator and a PMT. For instance, detectors

based on the activation of gold plates [Amgarou et al., 2009].

Electronic detectors (those which originate electrical signals at the time of the measurement) are, using a suitable electronic chain, capable of producing a Pulse Height Distribution (PHD). The regions of the interest (ROIs) of the PHD can be properly integrated so that a single number would constitute the response of this electronic detector to the radiation field.

According to how the previous radiation detectors are used, we can build different detector systems that can be classified as mono-channel, few-channel or multi-channel detector systems. Electronic detectors with the PHD capability are intrinsically multi-channel detector although they can be converted to a single-channel detector according to the previous paragraph by using ROIs. ^{3}He proportional counters are (once integrated properly the PHD) mono-channel detectors but if they are considered thermal neutron detectors and they are used as the central detector in a Bonner Sphere System (BSS) [Bramblett et al., 1960] the whole system will be transformed in a few-channel detector system.

4.1 Procedures in detectors in general

Radiation detectors are calibrated in a situation (*the calibration case*) which may not be the same as the real, experimental or unknown situation (*the real case*) in which they are going to be used in the future. Figures 4.1, 4.2 and 4.3 show the unit energy distribution of the neutron fluence in different calibration cases. Energy distributions of the neutron fluence in real cases may significantly differ from the *calibration cases*, as found in results of this work (Chapter 7).

The *quality* of a radiation field is determined only by the *shape* of the energy distribution of the fluence *i.e.,* it is determined by the unit energy distribution of the fluence, $\varphi_E(E)$, Equation (3.4).

The *quality* and *quantity* of a radiation field is determined by the energy distribution of the fluence, $\Phi_E(E)$, Equation (3.2).

For linear detectors, the importance relies in the fact that the *quality* of the radiation may be different in the real case in comparison to the calibration case. For non-linear detectors, not only the changes in the *quality* of the radiation are important but also the changes in the *quantity* of radiation.

4.1.1 Calibration coefficients

For any detector we can define a calibration coefficient (in terms of some quantity as fluence or dose) under a general but well known situation. To not complicate and overcharge more the notation, we now are going to consider that in calibration facilities, parasitic contributions from undesired particles are not relevant. Let us then irradiate our device in a poly-energetic radiation field containing only particles of type j and characterized by the total fluence of particles of type j, Φ_j. In that case, the calibration coefficient (in terms of fluence) can be written as

$$R_{\Phi_j} = \left[\frac{R_{j,\text{Calibration}}}{\Phi_{j,\text{Calibration}}}\right], \tag{4.1}$$

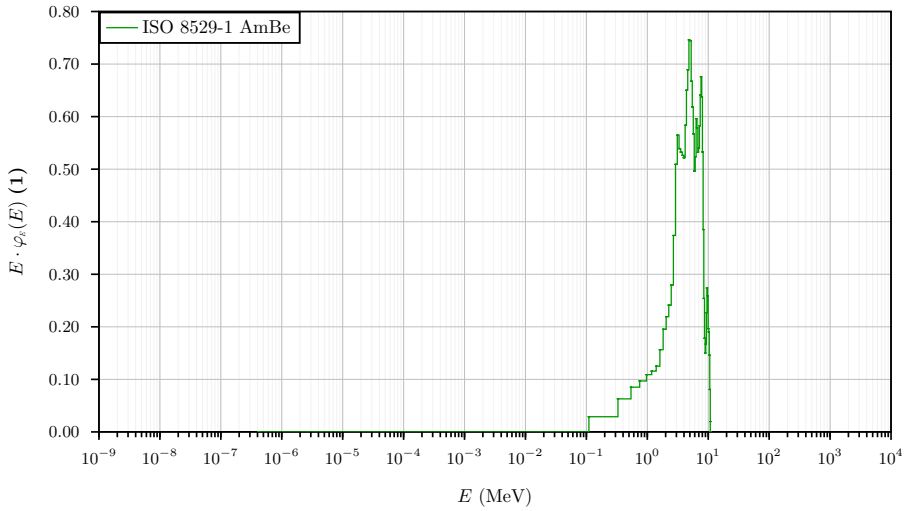

Figure 4.1: Representation of the unit energy distribution of the neutron fluence from an Am-Be source provided by the ISO 8529-1 [ISO-8529-1:2021, 2021].

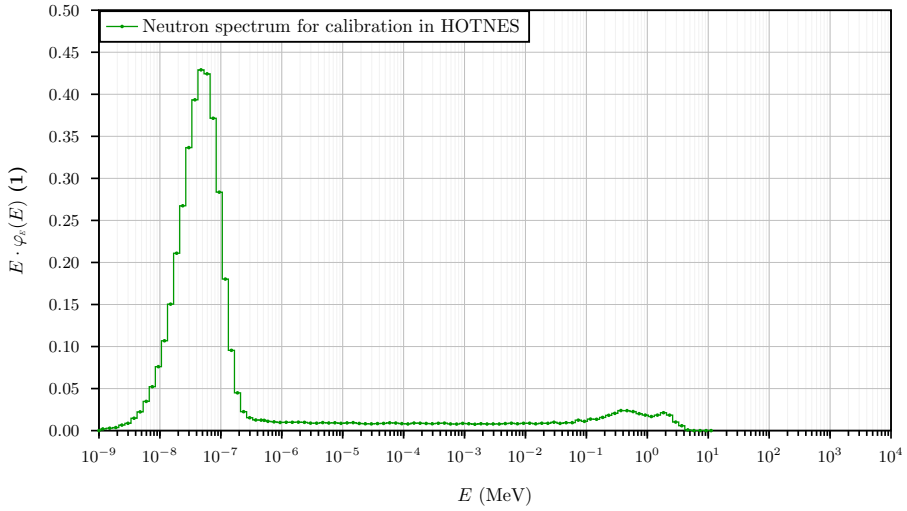

Figure 4.2: Representation of the unit energy distribution of the neutron fluence from the facility HOTNES [Bedogni et al., 2017].

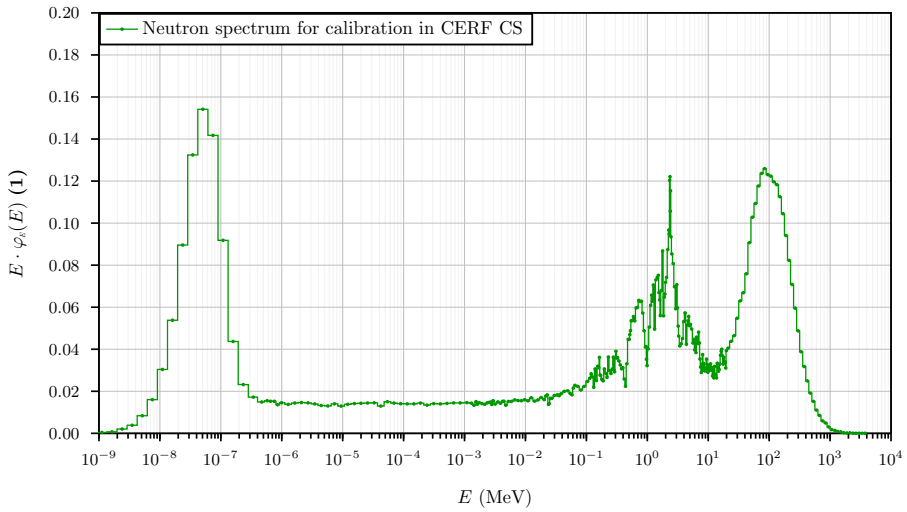

Figure 4.3: Representation of the unit energy distribution of the neutron fluence from the facility CERF [Mitaroff et al., 2002], [Pozzi et al., 2020].

where $R_{j,\text{Calibration}}$ is the response of the detector in the calibration situation and $\Phi_{j,\text{Calibration}}$ is the total fluence of particles of type j in this calibration situation.

We could also define a calibration coefficient in terms of the ambient dose equivalent and that would be written as

$$R_{H_j^*(10)} = \left[\frac{R_{j,\text{Calibration}}}{H^*_{j,\text{Calibration}}(10)}\right]. \tag{4.2}$$

If the specific device is linear, this means that the term R_{Φ_j} is a constant when we change the *quantity* of radiation reaching the detector. In other words, when we double, triple, etc the fluence, the response also, doubles, triples, etc. This enable us to write

$$R_{\Phi_j} = \left[\frac{R_{j,\text{Calibration}}}{\Phi_{j,\text{Calibration}}}\right] = \frac{R_{j,\text{Experiment}}}{\Phi_{j,\text{Experiment}}}. \tag{4.3}$$

Where $R_{j,\text{Experiment}} \equiv R_j$ is the response or reading of the detector in the, a priori, unknown or real situation and $\Phi_{j,\text{Experiment}} \equiv \Phi_j$ is the unknown or real quantity which characterizes the radiation field that we wish to obtain through the good use of a calibration coefficient. So, if we measure R_j in a real case (and we decide that a particular calibration coefficient, R_{Φ_j}, is good for this situation) we will find the experimental fluence, through Equation (4.3), as

$$\Phi_j = \frac{R_j}{\left[\frac{R_{j,\text{Calibration}}}{\Phi_{j,\text{Calibration}}}\right]} = \frac{R_j}{R_{\Phi_j}}. \tag{4.4}$$

The subscript j can be unnecessary when the context is clear *i.e.,* when is clear that we work in mono-particle radiation fields.

4.1.2 Response function

The response of some channel of some detector or the response of a detector to mono-energetic particles of type j with energy E is written as

$$\mathrm{d}R_j(E). \tag{4.5}$$

Let us suppose that in the point where we placed the detector there is a fluence of mono-energetic particles of type j and with energy E that we denote as

$$\mathrm{d}\Phi_j(E). \tag{4.6}$$

The response function (in terms of the fluence) or the fluence-to-response conversion coefficient of a detector to mono-energetic particles of type j with energy E is defined as

$$R_{\Phi_j}(E) = \left[\frac{\mathrm{d}R_j(E)}{\mathrm{d}\Phi_j(E)}\right]. \tag{4.7}$$

Now if the response function (in terms of fluence), Equation (4.7), is known for a detector, the total response due to the presence of a poly-energetic radiation field of particles of

type j and characterized by an energy distribution of the fluence $\mathrm{d}\Phi_j(E)$ is then

$$R_j = \int_E \mathrm{d}R_j(E) = \int_E R_{\Phi_j}(E)\mathrm{d}\Phi_j(E) = \int_E R_{\Phi_j}(E)\,\Phi_{E,j}(E)\mathrm{d}E = \Phi_j \int_E R_{\Phi_j}(E)\varphi_{E,j}(E)\mathrm{d}E. \quad (4.8)$$

Where we have used Equation (3.2) and Equation (3.4).

So, it is clear that through Equation (4.8) we can compute, at least formally, the total response of a detector characterized by the response function $R_{\Phi_j}(E)$ and immersed in an experimental radiation field characterized by $\Phi_{E,j}(E)$.

One application of Equation (4.8) is to find an *ad-hoc* and *better* calibration coefficient that the ones defined in Equation (4.1), as long as we know the response function of the detector and as long as we know the unit energy distribution of the neutron fluence in which the detector is going to be immersed during the measurement. From Equation (4.8) and observing Equation (4.1) we can isolate so that

$$\left[\frac{R_{j,\mathrm{Calibration}}}{\Phi_{j,\mathrm{Calibration}}}\right]_{\text{BSS or MC}} = \int_E R_{\Phi_j}(E)\varphi_{E,j}(E)\mathrm{d}E = \langle R_{\Phi_j}\rangle. \quad (4.9)$$

Remember that $\varphi_{E,j}(E)$ can be understood as a probability density function. Subscripts BSS or MC appear in Equation (4.9) because, usually, the unit energy distribution of the fluence is found by experimental measurements using a BSS or by MC simulations.

Calibration coefficients obtained from Equation (4.9) can be *better* than those obtained in some reference facilities as we are taking into account the energy dependence of the response of our detector to the *exact* radiation field in which the detector is going to be used. In other words, not all energies have the same *efficiency* in inducing a response in the detector.

By substituting Equation (4.9) in Equation (4.4) is then obtained

$$\Phi_j = \frac{R_j}{\left[\frac{R_{j,\mathrm{Calibration}}}{\Phi_{j,\mathrm{Calibration}}}\right]} = \frac{R_j}{R_{\Phi_j}} = \frac{R_j}{\left[\int_E R_{\Phi_j}(E)\varphi_{E,j}(E)\mathrm{d}E\right]}. \quad (4.10)$$

At this point, it is convenient to distinguish between two situations in the conventional methods to calibrate a detector.

1. We have a device A in which we wish to perform radiation measurements, but we do not know its response function to the particles of the radiation field. A calibration coefficient can be always calculated following Equation (4.1). Equation (4.4) can then be used for determining the variable characterizing the unknown field from the measured R_j.

2. We have a device A in which we wish to perform radiation measurements for which we know its response function to the particles of the field. In this case, the variable characterizing the unknown field may be obtained directly from Equation (4.10) and experimental measurement R_j. In this situation, the unit energy distribution of the neutron fluence, $\varphi_{E,j}(E)$, must be known by some means, usually from a reference spectrometer measurement or from MC simulations. This second situation is also described in ISO-8529-3:1998 [1998].

Similar Equations to (4.9) and (4.10) can be obtained if we are interested to obtain a dose equivalent quantity instead of the particle fluence. For instance, ambient dose equivalent contributed by particles of type j is

$$H_j^*(10) = \int_E h_{\Phi_j}^*(10,E)\,\Phi_{E,j}(E)\mathrm{d}E = \Phi_j \int_E h_{\Phi_j}^*(10,E)\varphi_{E,j}(E)\mathrm{d}E, \tag{4.11}$$

where $h_{\Phi_j}^*(10,E)$ are the fluence-to-ambient neutron dose equivalent conversion coefficients introduced in Section 3.1.5, Equations (3.74) and (3.80). By dividing Equation (4.8) and Equation (4.11) we obtain

$$\left[\frac{R_{j,\text{Calibration}}}{H^*_{j,\text{Calibration}}(10)}\right]_{\text{BSS or MC}} = \left[\frac{\Phi_j \int_E R_{\Phi_j}(E)\varphi_{E,j}(E)\mathrm{d}E}{\Phi_j \int_E h^*_{\Phi_j}(10,E)\varphi_{E,j}(E)\mathrm{d}E}\right] = \left[\frac{\int_E R_{\Phi_j}(E)\varphi_{E,j}(E)\mathrm{d}E}{\int_E h^*_{\Phi_j}(10,E)\varphi_{E,j}(E)\mathrm{d}E}\right] \tag{4.12}$$

and, by analogy to Equation (4.4), we obtain

$$H_j^*(10) = \frac{R_j}{\left[\frac{R_{j,\text{Calibration}}}{H^*_{j,\text{Calibration}}(10)}\right]} = \frac{R_j}{R_{H_j^*(10)}}. \tag{4.13}$$

If we now substitute Equation (4.12) in Equation (4.13) we obtain

$$H_j^*(10) = \frac{R_j}{R_{H_j^*(10)}} = \frac{R_j}{\left[\frac{\int_E R_{\Phi_j}(E)\varphi_{E,j}(E)\mathrm{d}E}{\int_E h^*_{\Phi_j}(10,E)\varphi_{E,j}(E)\mathrm{d}E}\right]}. \tag{4.14}$$

Therefore if one is interested in obtaining the ambient dose equivalent contributed by particles j using a detector characterized by a known response function (in terms of fluence), $R_{\Phi_j}(E)$, and in a place where exists a unit energy distribution of the fluence of particles j, $\varphi_{E,j}(E)$, one can do an experimental measurement with the mentioned device, obtaining R_j and finally apply Equation (4.14).

There are some subtleties in the definition of calibration coefficients and response functions that have to be highlighted now:

1. Calibration coefficients and response functions can be defined in terms of physical quantities (Φ, D_k and K_k) (where k is the material), operational quantities (as, for instance, $H^*(10)$) or protection quantities. Notice that physical quantities depend on the material except for the particle fluence, Φ.

2. Calibration coefficients and response functions are defined so that the physical, operational or protection quantities used in Equations like (4.1) and (4.7) are those provided by the calibration facility and their numerical values are obtained in the absence of the detector to be calibrated. In other words, when we describe the radiation field using our detector, we describe the un-perturbed field.

3. The response generated in a detector is due to an *internal* radiation field, $\mathrm{d}\Phi^{\text{in}}(E)$, which is different from the *external* radiation field, $\mathrm{d}\Phi(E)$, reaching the boundaries of the detector, see a representation of the situation in Figure 4.4. Is important to notice that we always want to describe the external radiation field reaching the boundaries of the detector or the un-perturbed field even when the internal radiation

field is the responsible for generating the response $\mathrm{d}R(E)$ in the detector in the particular situation. For these reasons, previous point 2 must be followed. It is well clear then that Equations like (4.1) and (4.7) will be always defined in the sense $R_{\Phi}(E) = \left[\frac{\mathrm{d}R(E)}{\mathrm{d}\Phi(E)}\right]$ and never defined as $R_{\Phi}(E) = \left[\frac{\mathrm{d}R(E)}{\mathrm{d}\Phi^{\mathrm{in}}(E)}\right]$.

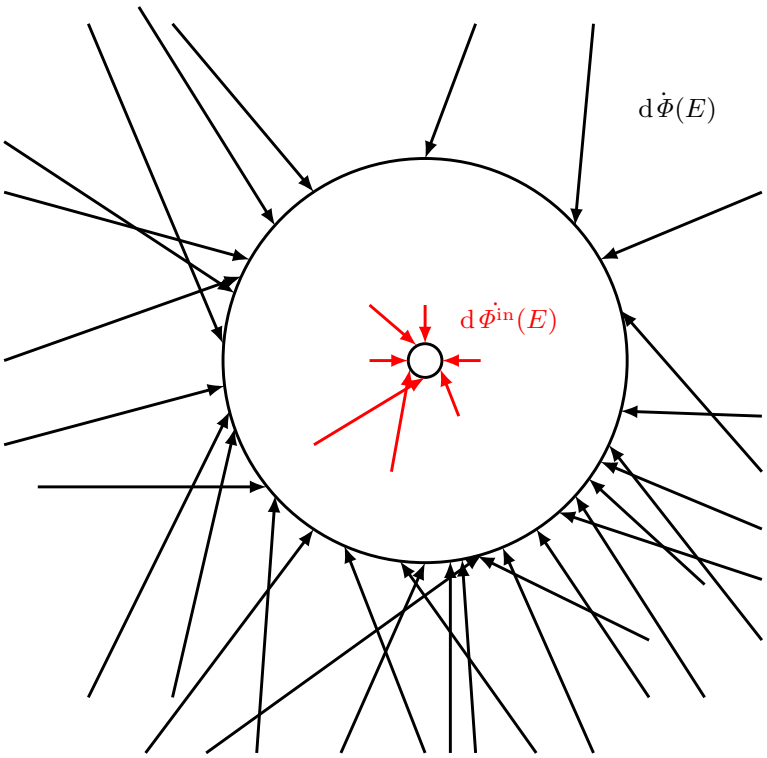

Figure 4.4: The inner volume would be the active volume of a detector or the active volume of a detector configuration. The energy distribution of the fluence reaching the active volume is the internal radiation field, $d\Phi^{in}(E)$. This internal radiation field is actually the reponsible of generating the response of the detector, however, we are interested in describing the external radiation field, $d\Phi(E)$, when employing this detector.

4.1.3 Evaluation of the response function

It is expected that the reading R of a given detector provides information of the unperturbed external field $\Phi_E(E)$ so its response function $R_{\Phi}(E)$ relates R with $\Phi_E(E)$.

Nevertheless, when calculating the response function $R_{\Phi}(E)$ for a detector, for instance, from MC simulations, one has to consider the physical effects produced by the non-active region of the detector. The response of a detector R is actually produced in the active region whose dimensions can be a fraction of the total dimensions of the detector. Therefore, the external radiation field to be measured, $\Phi_E(E)$, will be affected by the non-active region of the detector giving rise to $\Phi_E^{\mathrm{in}}(E)$ in the active region. The situation is represented in Figure 4.4.

In other words, response functions $R_{\Phi}(E)$ will always provide information of the unperturbed external field $\Phi_E(E)$ while the response of the detector R is actually produced by $\Phi_E^{\mathrm{in}}(E)$ (related with the external field $\Phi_E(E)$).

Recalling Equation (3.93). The response of a detector l using $\mathrm{d}\Phi^{\mathrm{in}}(E)$ can be then written

as

$$\mathrm{d}R_l(E) \equiv \mathrm{d}N_{l,\mathrm{Reactions}}(E) = N_{l,\mathrm{Targets}} \cdot \sigma_l(E) \cdot \mathrm{d}\,\Phi^{\mathrm{in}}(E). \tag{4.15}$$

Where $N_{l,\mathrm{Targets}}$ is the number of target isotopes of the detector type l that through a nuclear reaction characterized by $\sigma_l(E)$ and given the presence of $\mathrm{d}\,\Phi^{\mathrm{in}}(E)$ give rise to a response in the detector.

For thermal neutron detectors based on ^{3}He, the nuclear reaction responsible for generating the response is $^3\mathrm{He(n,p)}^3\mathrm{H}$ $\left(\sigma_l(E) \equiv \sigma_{^3\mathrm{He(n,p)}^3\mathrm{H}}(E)\right)$ (where p stands for proton) so $N_{l,\mathrm{Targets}} \equiv N_{^3\mathrm{He,Targets}}$ and the number of targets are the number of ^{3}He isotopes.

For thermal neutron detectors based on the activation of gold isotopes ^{197}Au, the nuclear reaction responsible for generating the response is $^{197}\mathrm{Au(n,}\gamma)^{198}\mathrm{Au}$ $\left(\sigma_l(E) \equiv \sigma_{^{197}\mathrm{Au(n,}\gamma)^{198}\mathrm{Au}}(E)\right)$ so $N_{l,\mathrm{Targets}} \equiv N_{^{197}\mathrm{Au,Targets}}$ and the number of targets are the number of ^{197}Au isotopes.

For thermal neutron detectors based on ^{6}Li, the nuclear reaction responsible for generating the response is $^6\mathrm{Li(n,}\alpha)^3\mathrm{H}$ $\left(\sigma_l(E) \equiv \sigma_{^6\mathrm{Li(n,}\alpha)^3\mathrm{H}}(E)\right)$ so $N_{l,\mathrm{Targets}} \equiv N_{^6\mathrm{Li,Targets}}$ and the number of targets are the number of ^{6}Li isotopes.

The complete response generated by the whole energy distribution of the particle fluence in the detector l would be the integral of Equation (4.15) so that

$$R_l = \int_E \mathrm{d}R_l(E) = N_{l,\mathrm{Targets}} \cdot \int_E \sigma_l(E) \cdot \mathrm{d}\,\Phi^{\mathrm{in}}(E) = N_{l,\mathrm{Targets}} \cdot \int_E \sigma_l(E) \cdot \Phi_E^{\mathrm{in}}(E)\mathrm{d}E. \tag{4.16}$$

As response functions and calibration coefficients are defined in the way

$$R_{l,\Phi}(E) = \left[\frac{\mathrm{d}R_l(E)}{\mathrm{d}\,\Phi(E)}\right] \neq \left[\frac{\mathrm{d}R_l(E)}{\mathrm{d}\,\Phi^{\mathrm{in}}(E)}\right] \tag{4.17}$$

we can also write

$$R_l = \int_E R_{l,\Phi}(E)\mathrm{d}\,\Phi(E) = \int_E R_{l,\Phi}(E)\,\Phi_E(E)\mathrm{d}E = \Phi \cdot \int_E R_{l,\Phi}(E)\varphi_E(E)\mathrm{d}E. \tag{4.18}$$

Notice how Equation (4.16) depends on the internal radiation field, $\Phi_E^{\mathrm{in}}(E)$, and how Equation (4.18) depends on the external radiation field, $\Phi_E(E)$.

The response function (in terms of fluence) of a device l with isotropic response to neutrons of energy E is computed by MC simulations by externally irradiating the whole face of the modelled device to a mono-energetic neutron field, by computing the response with Equation (4.16) and finally by applying Equation (4.17). This is the procedure that will be followed in Section 5.3.

Finally, the MC simulations of the response function have to be experimentally validated and properly corrected through the factor f, as explained in Appendix D.

4.2 Specific procedures for thermoluminescence detectors

Without taking into account the particularities of each kind of luminescence detector we can establish in this section the notation used in this work when dealing with these type

of detectors, this section can be seen as an introduction to *basic* equations for TLD that will be expanded in Chapter 6. Of course the general idea behind of the basic equations introduced in the previous section is also true for luminescence detectors, or any radiation detector.

The analogy between Equation (4.1) and the equation used in thermoluminescence detectors for particles of type j is

$$\eta_{D_{\mathrm{w},j}} = \frac{\left[\frac{S_{j,\mathrm{Calibration}}}{D_{\mathrm{w},j,\mathrm{Calibration}}}\right]}{\left[\frac{S_{\mathrm{Co\text{-}60}}}{D_{\mathrm{Co\text{-}60}}}\right]} \quad \longleftrightarrow \quad R_{\Phi_j} = \left[\frac{R_{j,\mathrm{Calibration}}}{\Phi_{j,\mathrm{Calibration}}}\right]. \tag{4.19}$$

Where $\eta_{D_{\mathrm{w},j}}$ is known as the relative luminescence efficiency and $\left[\frac{S_{\mathrm{Co\text{-}60}}}{D_{\mathrm{Co\text{-}60}}}\right]$ is described at the end of this section.

The analogy between Equation (4.4) and the equation used in thermoluminescence detectors for particles of type j is

$$D_{\mathrm{w},j} = \frac{\left[\frac{S_j}{\eta_{D_{\mathrm{w},j}}}\right]}{\left[\frac{S_{\mathrm{Co\text{-}60}}}{D_{\mathrm{Co\text{-}60}}}\right]} \quad \longleftrightarrow \quad \Phi_j = \frac{R_j}{\left[\frac{R_{j,\mathrm{Calibration}}}{\Phi_{j,\mathrm{Calibration}}}\right]} = \frac{R_j}{R_{\Phi_j}}. \tag{4.20}$$

The analogy between Equation (4.7) and the equation used in thermoluminescence detectors for particles of type j is

$$\eta_{D_{\mathrm{w},j}}(E) = \frac{\left[\frac{\mathrm{d}S_j(E)}{\mathrm{d}D_{\mathrm{w},j}(E)}\right]}{\left[\frac{S_{\mathrm{Co\text{-}60}}}{D_{\mathrm{Co\text{-}60}}}\right]} \quad \longleftrightarrow \quad R_{\Phi_j}(E) = \left[\frac{\mathrm{d}R_j(E)}{\mathrm{d}\Phi_j(E)}\right]. \tag{4.21}$$

The equation equivalent to Equation (4.8) can be found using Equation (4.21) so that

$$\frac{S_j}{\left[\frac{S_{\mathrm{Co\text{-}60}}}{D_{\mathrm{Co\text{-}60}}}\right]} = \frac{\int\limits_E \mathrm{d}S_j(E)}{\left[\frac{S_{\mathrm{Co\text{-}60}}}{D_{\mathrm{Co\text{-}60}}}\right]} = \int\limits_E \eta_{D_{\mathrm{w},j}}(E)\,\mathrm{d}D_{\mathrm{w},j}(E) = D_{\mathrm{w},j}\int\limits_E \eta_{D_{\mathrm{w},j}}(E) d_{E,\mathrm{w},j}(E)\mathrm{d}E. \tag{4.22}$$

The term $\frac{S_j}{\left[\frac{S_{\mathrm{Co\text{-}60}}}{D_{\mathrm{Co\text{-}60}}}\right]}$ is also known as ^{60}Co gamma equivalent absorbed dose in water so that $\frac{S_j}{\left[\frac{S_{\mathrm{Co\text{-}60}}}{D_{\mathrm{Co\text{-}60}}}\right]} \equiv D_{\mathrm{w},j,^{60}\mathrm{Co\text{-}eq}}$.

Therefore the analogy between Equation (4.8) and the equation used in thermoluminescence detectors for particles of type j is

$$D_{\mathrm{w},j,^{60}\mathrm{Co\text{-}eq}} \equiv \frac{S_j}{\left[\frac{S_{\mathrm{Co\text{-}60}}}{D_{\mathrm{Co\text{-}60}}}\right]} = D_{\mathrm{w},j}\int\limits_E \eta_{D_{\mathrm{w},j}}(E) d_{E,\mathrm{w},j}(E)\mathrm{d}E \quad \longleftrightarrow \quad R_j = \Phi_j \int\limits_E R_{\Phi_j}(E)\varphi_{E,j}(E)\mathrm{d}E. \tag{4.23}$$

From Equation (4.23) we can derive an analogy with Equation (4.10) so that

$$D_{\mathrm{w},j} = \frac{\left[\frac{S_j}{\int\limits_E \eta_{D_{\mathrm{w},j}}(E) d_{E,\mathrm{w},j}(E)\mathrm{d}E}\right]}{\left[\frac{S_{\mathrm{Co\text{-}60}}}{D_{\mathrm{Co\text{-}60}}}\right]} = \frac{D_{\mathrm{w},j,^{60}\mathrm{Co\text{-}eq}}}{\int\limits_E \eta_{D_{\mathrm{w},j}}(E) d_{E,\mathrm{w},j}(E)\mathrm{d}E} \quad \longleftrightarrow \quad \Phi_j = \frac{R_j}{\int\limits_E R_{\Phi_j}(E)\varphi_{E,j}(E)\mathrm{d}E}. \tag{4.24}$$

In the field of thermoluminescence detectors, in order to guarantee that all the steps in preparing, using and reading the detectors are kept uniform in time, a *pair* of TLDs are always related in the sense that while one of the TLDs is irradiated in the real situation, the other one is irradiated in the reference irradiation which is usually the Co-60 field. This fact is manifested in the equations through the term $\left[\frac{S_{\text{Co-60}}}{D_{\text{Co-60}}}\right]$.

4.3 Definition of an operational dosimeter

In the frame of this work the following definitions are understood.

Uncertainty

Due to the lack of a total knowledge of the calibration radiation field and features of the radiation detector (such as its response to different incident energies or angular dependencies in the response), quantities cannot be expressed with a single numerical value but in a range values so that the previous lack of complete knowledge is taking into accout.

Neutron radiation detector

Device that responds to a neutron field.

Operational neutron radiation dosimeter

An operational neutron radiation dosimeter is defined as that neutron radiation detector capable of measuring a dose equivalent (personal dose equivalent, ambient dose equivalent, etc) produced by a neutron field spanning from an energy E_1 to an energy E_2 with a relative uncertainty lower than 50 %. Such dosimeter should be able to provide a numerical value in a *reasonable* length of time.

The previous definition of operational neutron radiation dosimeter is derived from European Commission, Directorate-General for Energy and Transport et al. [2009] where it is stated:

- *In the workplace, where the energy spectrum and orientation of the radiation field are generally not well known, the uncertainties in a measurement made with an individual dosimeter will be significantly greater. Non-uniformity and uncertain orientation of the radiation field will introduce errors in the use of standard models.*
- *In most cases, an overall uncertainty of one standard deviation of 30 % should be acceptable. The error of instruments may substantially exceed this limit at some radiation energies and for certain angles of incidence, but conform to it when they occur in a radiation field with a broad energy spectrum and broad angular distribution.*
- *For a measurement of the operational quantity $H_p(10)$ for a single field component for a quantity value equal to or greater than 1 mSv (annual dose limit for E for members of the public) in proportion to the wear period, the combined standard uncertainty should be less than 30 % for photon electron workplace fields and less than 50 % for neutron fields.*
- *From considerations of the response characteristics of neutron personal dosimeters in current use and from the results of intercomparisons, there are certainly difficulties meeting 30 % combined standard uncertainty for doses to the whole body from neutrons. Even with a relaxation of the criterion to 50%, it is not possible with*

any current design of dosimeter to meet the criterion over the full range of neutron energies possibly present in the workplace. However, there are generally only small contributions to total dose for those neutron energies for which there are greatest difficulties. In practice, therefore, a combined standard uncertainty of 50 % should be achievable for single measurements in actual workplace fields.

To carry out and apply the definition of operational neutron radiation dosimeter to a neutron radiation detector (candidate to be an operational neutron radiation dosimeter in an energy range) one should follow the next procedure:

1. Experimentally and reasonably prove that the particular neutron radiation detector responds to the neutron fields in the energy range from E_1 and E_2 and to know calibration coefficients in terms of dose or the response function in terms of dose in that energy range. In particular to know or estimate the calibration coefficient, $k(E)$, in E_1, $k(E_1)$ and in E_2, $k(E_2)$.
2. To choose a value for a new calibration coefficient, k_{new}, that will be valid in the energy range from E_1 to E_2 so it is verified that $\frac{|k_{\text{new}}-k(E_1)|}{k_{\text{new}}} \leq 0.5$, $\frac{|k_{\text{new}}-k(E_2)|}{k_{\text{new}}} \leq 0.5$ and in general $\frac{|k_{\text{new}}-k(E)|}{k_{\text{new}}} \leq 0.5$ for $E_1 < E < E_2$.
3. Once the previous point is proved we can state that the neutron radiation detector is in fact an operational neutron radiation dosimeter in the energy range from E_1 to E_2.

4.3.1 The ideal operational dosimeter

Besides other features, an ideal operational radiation dosimeter characterized by a response function in terms of fluence to a particle type j would be that radiation detector whose response function in terms of fluence is proportional (or can be considered proportional) to some fluence-to-dose conversion coefficient with the same proportional coefficient in each incident particle energy E, *i.e.*, $R_{\Phi_j}(E) = k \cdot h_{\Phi_j}(E)$, so that Equation (4.8) yields

$$R_j = \Phi_j \int_E R_{\Phi_j}(E)\varphi_{E,j}(E)\mathrm{d}E = k \cdot \Phi_j \int_E h_{\Phi_j}(E)\varphi_{E,j}(E)\mathrm{d}E. \tag{4.25}$$

On the other hand, a dose quantity, H_j, with its fluence-to-dose conversion coefficients, $h_{\Phi_j}(E)$, can be written of course as

$$H_j = \Phi_j \int_E h_{\Phi_j}(E)\varphi_{E,j}(E)\mathrm{d}E. \tag{4.26}$$

In non-ideal conditions, the calibration coefficient for the dosimeter immersed in a real field characterized by $\varphi_{E,j}(E)$ can be written as

$$\left[\frac{R_j}{H_j}\right] = \left[\frac{\Phi_j \int_E R_{\Phi_j}(E)\varphi_{E,j}(E)\mathrm{d}E}{\Phi_j \int_E h_{\Phi_j}(E)\varphi_{E,j}(E)\mathrm{d}E}\right] = \left[\frac{\int_E R_{\Phi_j}(E)\varphi_{E,j}(E)\mathrm{d}E}{\int_E h_{\Phi_j}(E)\varphi_{E,j}(E)\mathrm{d}E}\right]. \tag{4.27}$$

But in this non-ideal situation we need to know the unit energy distribution of the fluence for particle of type j in order to compute the calibration coefficient (4.27). However in

the ideal condition, $R_{\Phi_j}(E) = k \cdot h_{\Phi_j}(E)$, Equation (4.27) results in

$$\left[\frac{R_j}{H_j}\right] = \left[\frac{\Phi_j \int\limits_E R_{\Phi_j}(E)\varphi_{E,j}(E)\mathrm{d}E}{\Phi_j \int\limits_E h_{\Phi_j}(E)\varphi_{E,j}(E)\mathrm{d}E}\right] = \left[\frac{k \cdot \Phi_j \int\limits_E h_{\Phi_j}(E)\varphi_{E,j}(E)\mathrm{d}E}{\Phi_j \int\limits_E h_{\Phi_j}(E)\varphi_{E,j}(E)\mathrm{d}E}\right] = k, \tag{4.28}$$

which means that the calibration coefficient for this ideal operational dosimeter does not depend on the unit energy distribution of the fluence or, in other words, that the calibration coefficient k from Equation (4.28) is universal and valid for any $\varphi_{E,j}(E)$ as long as $R_{\Phi_j}(E) = k \cdot h_{\Phi_j}(E)$ holds. Actually what we did in the previous Section 4.3 is to assume that $\left[\frac{R_j}{H_j}\right]$ is approximately constant, in other words, to say that is constant under relative differences lower than 50 %.

4.4 Neutron dosimetry based on solid state nuclear track detectors

The departure point of the method known as Solid State Nuclear Track Detection (SSNTD) can be traced back to 1958 with the work of Young [1958], although there were several other posterior authors which also realised about the phenomenon in an independent way like Silk et al. [1959]. More details can be seen in Fleischer et al. [1975] and Durrani et al. [1987].

The radiation detectors that can be classified as Solid State Nuclear Track Detectors are those which [Guo et al., 2020]:

- Record tracks of heavy charged particles ($Z \geqslant 1$).
- Are essentially solids.

So, for instance, nuclear emulsions are SSNTD [Guo et al., 2020]. However in this work when we refer to SSNTD we mean those detectors in which some kind of chemical etching is used.

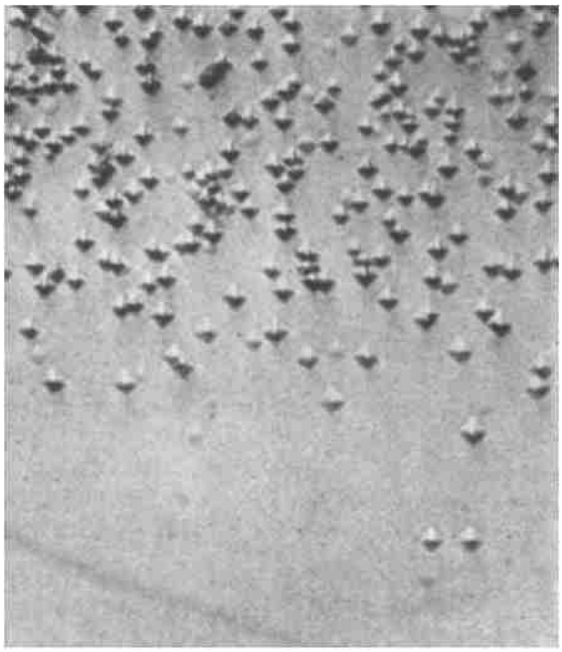

Figure 4.5: Conventional microscopy. 8 min. etch. (magnification × 640). From Young [1958].

Figure 4.6: Electron microscopy. 1 min. etch. (magnification × 13300). From Young [1958].

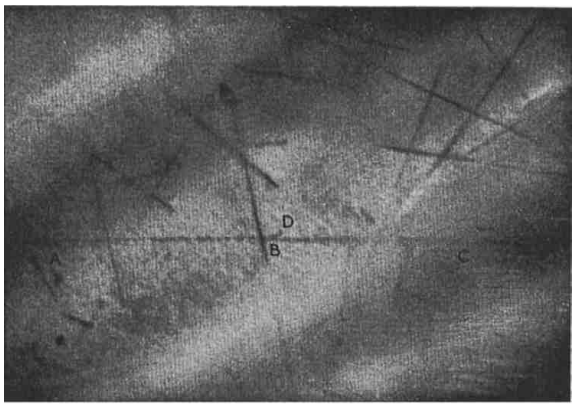

Figure 4.7: Fission tracks in mica crystals. No etching procedure was used. Silks et al., noted that tracks had a diameter less than 300 Å and some of them had a length superior to 4 µm. *There is a fission fragment travelling in the path AB and undergoing a slight deflection at B to proceed along BC. The particle performing the way BD is possibly an atom of mica crystal displaced by an elastic-Rutherford-type collision [Durrani et al., 1987] [Silk et al., 1959].*

In general, early studies on SSNTD were already noticing the following features in etchable tracks, they were:

1. Produced only by heavily ionizing particles.
2. Stable even when subjected to light or high doses of photons and electrons.
3. Produced only in electrical insulators (like in polymeric materials) or poor semiconductors.

Previous properties 1 and 2 make the SSNTD method very interesting as we can discriminate heavy charged particles (also protons) from photons and electrons. Property 3 means

that the materials can be simple and cheap.

As it can be derived from the previous properties 1 and 2, a threshold must exist in each material related to the stopping power or the density of ionizations produced by a charged particle, which has to be overcome in order to the damage produced by the ionizing radiation be significant and be capable to be enhanced by the etching procedure.

The damage produced by the radiation is, in crystals, translated as the production of defects which correspond to ion displacements *i.e.,* the creation of vacancies-interstitial ion pairs while in the case of polymers, this damage is translated as broken molecular-chemical bonds. In Figure 4.8 the chemical structure of the monomer Allyl Diglycol Carbonate (ADC) which has the formula $C_{12}H_{18}O_7$ is shown.

The origins of the ADC are in 1940, when the company Pittsburgh Plate Glass Company owned a subsidiary company called Columbia Southern Chemical Company where a research team was assigned the responsibility for investigating clear resins. They called this project "Columbia Resins" [Burneni, 1997]. They found that the 39th formula or compound offered unique characteristics. For this reason the ADC monomer can be also called, as a brand name, as CR-39. It is very common to use the name CR-39 for the Poly Allyl Diglycol Carbonate (PADC) (once the polymerization of the ADC monomers has been performed) which is the final form of a radiation detector based on this polymer.

The damage produced by the irradiation in the polymers SSNTDs is represented in Figure 4.9. The annealing process at elevated temperatures after an etchable track is formed occurs because broken molecular chains (and in particular the tail of these chains) may rejoin.

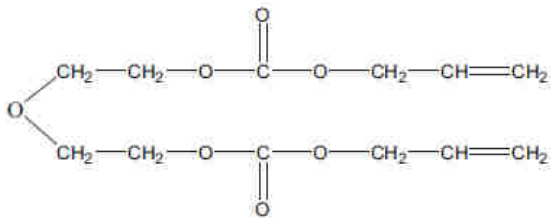

Figure 4.8: Chemical structure of the monomer Allyl Diglycol Carbonate (ADC) which has the formula $C_{12}H_{18}O_7$. From Guo et al. [2020].

The physics of track formation as well as the related criteria for track formation are still not fully understood [Durrani et al., 1987] [Guo et al., 2020].

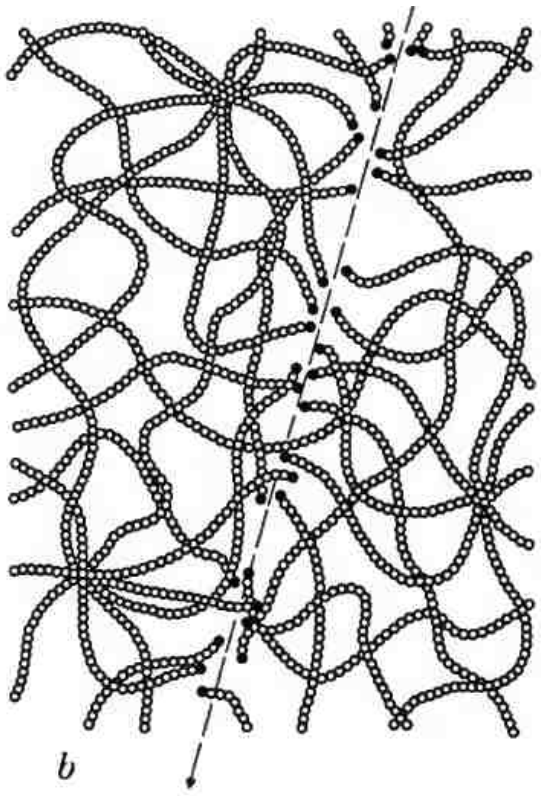

Figure 4.9: Damage in plastics is translated as the break of molecular bonds. If the latent damage is annealed, there will be the recombination of the ends of the molecular chains. Figure taken from [Fleischer et al., 1975].

Currently exist different models for both the physics of track formation processes and the criteria to know if a latent track can be created and can be quantified in the specific material. For a better review of the physics of track formation and related criteria see Durrani et al. [1987], Guo et al. [2020] and Bolzonella et al. [2021].

For materials with a crystal structure, one accepted model is the ion-explosion spike model [Fleischer et al., 1965].

In summary, from this model it is justified that:

- The finding of tracks only in materials of low hole mobility is consistent with the requirement that the ionization created by a passing charged particle must exist long enough to allow ions to seek out interstitial positions. In other words, if recombination time (between the removed electron and the produced positive ion) is too short, the latent damage would not have enough time to be produced.
- According to the reasoning of Fleischer et al. [1965], the diameter of the tracks are compatible with the fact that atomic displacements are not the main responsible for the track creation.
- The measured critical energy loss threshold (energy loss per unit distance required to form a track, according to a certain model that will be explained later) generally increase monotonically with the lattice bonding forces calculated from the model.

In the case of high polymers, molecular chains are broken in receiving 2 eV (as a result of excited electrons [Fleischer et al., 1965]) which is much less than the energy required

to ionize an atom (at least 5-17 eV [Guo et al., 2020]), for this reason, in the case of high polymers the ion-explosion spike model is not so relevant. The fact of breaking locally the bonds means that molecular weight decreases thus accelerating the chemical attack in the locality [Fleischer et al., 1965]. Theoretically, for plastics, the incident charged particles are also capable of producing displaced atoms.

The previous chain breaking mechanism in high polymers justifies that:

- Light particles such as alphas and protons can be efficiently detected using high polymers as simple bond breaking would give a sufficient number of reactive sites to enhance the etching rate locally.

There are studies inquiring in the transformations of the chemical bonds in materials using infrared absorption spectroscopy and ultraviolet and visible spectroscopy, see Guo et al. [2020] and references therein, and Lounis-Mokrani et al. [2003].

Two relatively accepted criteria for a track to be created and chemically etchable are:

- The critical energy loss rate criterion [Fleischer et al., 1964].
- The primary ionization rate criterion [Fleischer et al., 1967].

The former proposes that a track is formed when the stopping power or energy loss rate $\left(\frac{\mathrm{d}E}{\mathrm{d}x}\right)$ exceeds some critical value $\left(\frac{\mathrm{d}E}{\mathrm{d}x}\right)_{\mathrm{Crit.}}$. Although this first criterion was already rejected by Fleischer [Fleischer et al., 1967], in favour to the primary ionization rate criterion, the critical energy loss rate criterion is still used as approximation.

The primary ionization rate criterion, which is directly related to the ion-explosion spike model, proposes that the formation of etchable tracks is related to the number of primary ionizations produced close to the ion path rather than the energy loss rate.

As Young already noticed in his work [Young, 1958], the chemical etchants used are capable of degrading the damaged regions at a higher rate than the undamaged material and therefore the damaged region is able to grow and be enhanced forming a hole. As the undamaged material is also removed from the chemical attack, if the rate of attack into the damaged region is not high enough, it happens that the damaged region is not capable to grow and be quantified. The rate of chemical attack along the track is termed the *track etching velocity*, V_{T}, while the rate of chemical attack in undamaged regions is termed *bulk etching velocity*, V_{B}. Figure 4.10 displays the chemically etched track formation process along the path of an incident charged particle.

Bulk etching velocity, V_{B}, depends on:

- The material. And for a specific material it can depends on the crystallographic orientation (in crystals) or the thickness of the removed surface (in polymers).
- The temperature.
- The etchants.
- The concentration of the etchants.
- Etching experimental set-up (geometry of the etching chambers).

Track etching velocity, V_{T}, depends on:

- The same parameters in which depends the bulk etching velocity, V_{B}.
- The kinetic energy, mass and charge of the track forming particle or amount of damage located in the track.

The fact that the track etching velocity and range depends on the track forming particle (kinetic energy, mass and charge) means that the shape and features of the spots revealed in the etching process will provide information, precisely, about the track forming particle and this is actually what is really important in those research groups which use the SSNTD method and the chemical etching procedure in the field of radiation dosimetry [Jadrníčková et al., 2008].

In CE procedures, we can summarise the track-spot formation process in the following way, see Figure 4.10.

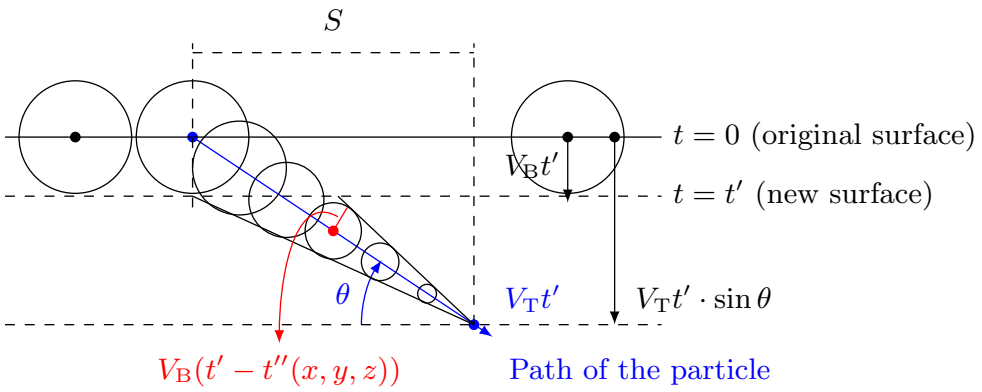

Figure 4.10: 2D slice representation of the path followed by a particle and the effect of the chemical attack in the latent damage and undamaged regions. In this representation the damaged region is only the path of the particle or the blue line. This corresponds to a general situation of a particle entering the detector with an angle θ in respect to the surface. A particle with a more tangential (to the surface) incidence below the critical angle θ_c (see text) will produce latent damage but it will not etchable due to the rate, V_B, in which the undamaged surfaces are removed. S would be the projected surface of the spot-track measured by standard microscopy in the CE method.

As can be deduced from Figure 4.10 and from the previous discussion, the condition for a track to be able to grow is that the perpendicular projection of the track etching velocity ($V_{\mathrm{T}} \cdot \sin\theta$) to be greater than the bulk etching velocity (V_{B}), therefore a limit situation occurs if the angles of incidence θ (in respect to the surface of the material) are smaller so that a situation like

$$V_{\mathrm{T}} \cdot \sin\theta_{\mathrm{c}} = V_{\mathrm{B}} \rightarrow \sin\theta_{\mathrm{c}} = \frac{V_{\mathrm{B}}}{V_{\mathrm{T}}}, \tag{4.29}$$

is reached. Therefore, particles entering to the material with angles smaller than θ_{c} cannot be calculated. From this fact we can already predict that the response function of these type of detectors will be angle dependent and its response will not be, of course, isotropic. As we can see from Equation (4.29), if the attack to the undamaged regions is very slow in comparison to the attack in the damaged regions ($V_{\mathrm{B}} << V_{\mathrm{T}}$) we obtain critical angles approaching to $\theta_{\mathrm{c}} \rightarrow 0$ and therefore we would have a detector with a good wide response to different entrance angles.

In the firsts attempts to try to understand how the shape of the track is formed it is assumed that V_T is a constant (assumed in the drawings of Figure 4.10 and the consequence of that approximation is to obtain very peaked cone shapes. The reality is that, in general, the track etching velocity increases with the ionization rate [Fleischer et al., 1975] or, as an approximation, with the energy loss rate. This fact changes slightly the peaked cone shape, the changes can be understood by the motorboat analogy [Fleischer et al., 1975] *i.e.,* by the trail left by a motorboat and how this trail changes when the motorboat slows down or accelerates. When the motorboat holds a constant velocity, the trail is a peaked cone, however in the case that it slows down, the trail left behind approaches to the motorboat so the shape of the trail is rounded outwards. On the other hand, when the motorboat (the track etching velocity) accelerates, the motorboat is capable of leaving farther the trail produced seconds before. These effects can be seen in Figure 4.11.

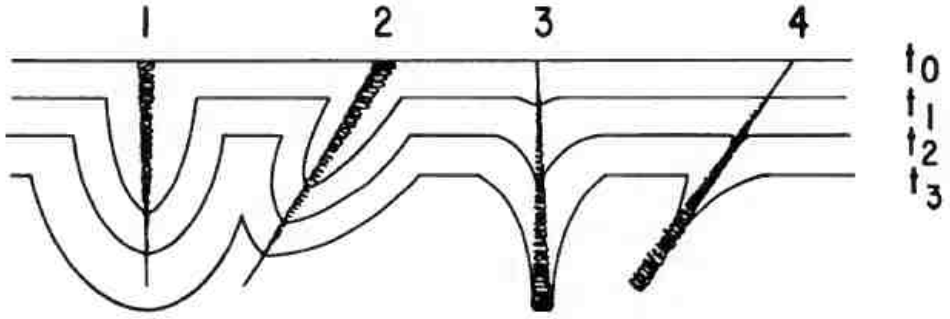

Figure 4.11: In subfigures 1 and 2 we see that the track etching velocity decreases which means that the energy loss rate is decreasing (notice the shape of the produced cone, black solid lines). The opposite behaviour is seen in subfigures 3 and 4. From Fleischer et al. [1975].

Therefore, the shape of the chemical etched track depends on the energy loss rate of a charged particle or, in other words, the shape of the etched track depends on the kinetic energy of a charged particle.

In CE procedures, in order to measure the surface projection of the etched tracks-spots is necessary to use a standard (high magnification) optical microscope and proceed with the study of the tracks. There are technical developings that design procedures which perform an automatic evaluation using the CE method, for more details see Durrani et al. [1987].

ElectroChemical Etching (ECE) enlarges the tracks to sizes in the order of $\sim 100\,\mu m$ so the counting of the tracks is easier as only low magnification is required, thus allowing observation by naked eye, slide projector or a document scanner. The method was first suggested by Tommasino around 1970 [Tommasino, 1970] [Tommasino et al., 1973]. In its simplest form, the ECE method consists in to place a plastic detector to be etched in contact with a suitable etchant (as NaOH or KOH) and under the presence of an alternating electric field.

What happens in the ECE method is that the conducting etchant begins to form a conducting cone along the track and as it is known by electrostatics, when a conductor has a sharp point or a corner, in the vicinity of these points high electric fields are achieved so that oscillations of this field can produce dielectric breakdowns in each track tip [Tipler et al., 2008] [Durrani et al., 1987]. The electric field lines produced in the tip of the cone are represented in the Figure 4.12. The dielectric breakdown in the plastic produces a spot with the shape of a tree as shown in Figures 4.13 and 4.14.

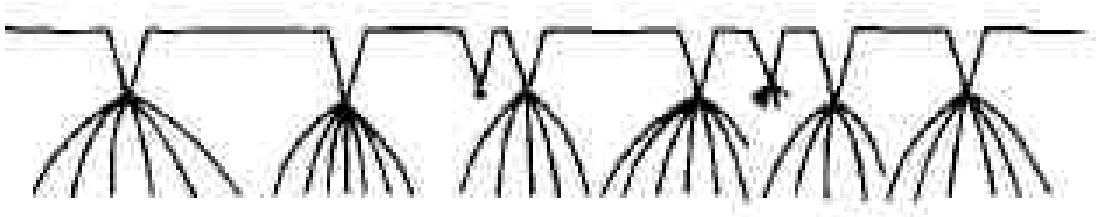

Figure 4.12: Some of the tracks will not develop a tree as the electric field from others cone tips are interfering. From Al-Najjar et al. [1979].

Figure 4.13: Lateral view of the developed trees of the tracks in the ECE method. From Al-Najjar et al. [1979].

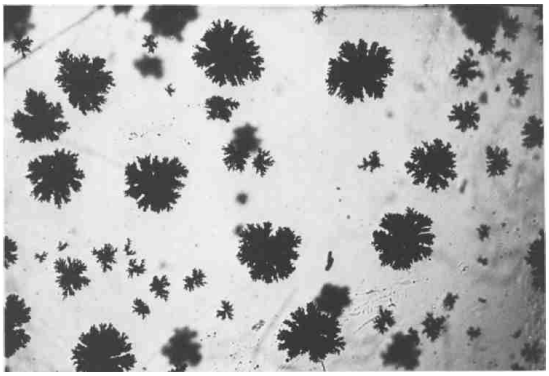

Figure 4.14: Top view of the ECE track spots from a CR-39. Some of the ECE spots have failed to develop fully because of local electrical shielding effects. From Durrani et al. [1987].

The set of ECE etching conditions are defined by the following parameters:

- The electric field strength.
- The frequency of the electric field.
- The waveform used for the electric field.
- The temperature.
- The etchants.
- The concentration of the etchants.
- Number of ECE steps and their duration time in the whole ECE process.
- Etching experimental set-up (electrodes position, etc).

Is important to keep in mind that the response function of a detector in which the ECE method is used is going to depend on the previous parameters.

The effects of using different combination of the ECE etching conditions are studied, for instance, in the works of Tommasino et al. [1973], Somogyi [1977], Al-Najjar et al. [1979], Durrani et al. [1980], Sohrabi [1981], Green et al. [1982] and Hashemi-Nezhad et al. [1982]. Some destacable remarks of these studies are the following:

- In unexposed foils using higher and higher field-strengths during the ECE process an increasing number of discharge spots is observed. These spots can be usually

attributed to defects or scratches in the foils. In order to avoid this effect it is advisable to apply field-strengths as low as possible. A pre-etching procedure could be used to round surface imperfections and reduce the chance of these defects to develop a spot-tree.

- In general, spot diameter increases when increasing the electric field strength, the frequency, the temperature and the etching time.
- Spot diameter is constant in a range of radiation fluences but then starts to decrease in increasing more the fluence. The reason is that the local electric field around a track is modified by the distribution of the electric field over the area of the surrounding tracks, see Figure 4.12.
- Following the reasoning of the previous point, as the local electric field can be decreased by the interaction of the surrounding electric fields thus decreasing the chance of developing a spot-tree in that latent track, this could mean that at certain point, increasing the radiation fluence is not translated to a proportional increase in the spots and therefore the consequence of this fact is the loss of linearity in the response function or calibration coefficient. In case that a detector shows a non-linear behaviour (for instance to neutron fluence) one can simply find calibration coefficients for different neutron fluences and use them properly. See Figure 4.15 [Hankins et al., 1986].
- There exists an etchant molarity which maximises the etch rate ratio $\frac{V_T}{V_B}$, so the ECE procedure can be time accelerated.

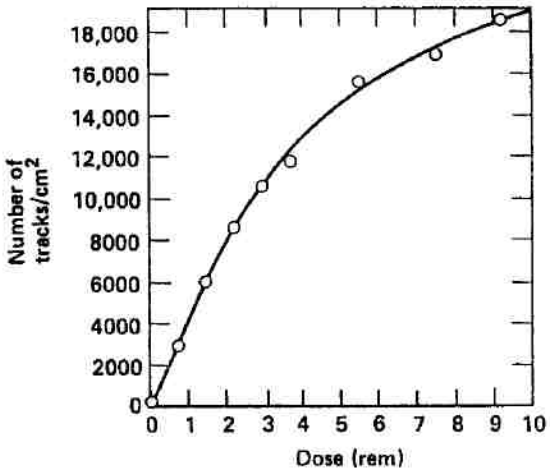

Figure 4.15: Track density in foils of CR-39 after being irradiated to diferent doses of neutrons coming from a bare ^{252}Cf source. A non-linear behaviour can be seen around 2 rem. See details in text. From Hankins et al. [1986].

A difference between CE and ECE procedures to be kept in mind is the one visually exhibited in the work of Tommasino et al. [1984], Figure 4.16. If an ECE tree has the opportunity to begin a sufficiently peaked cone generated by the enhanced chemical attack through the latent track, this tree is unstoppable and is not lost by using longer etching times.

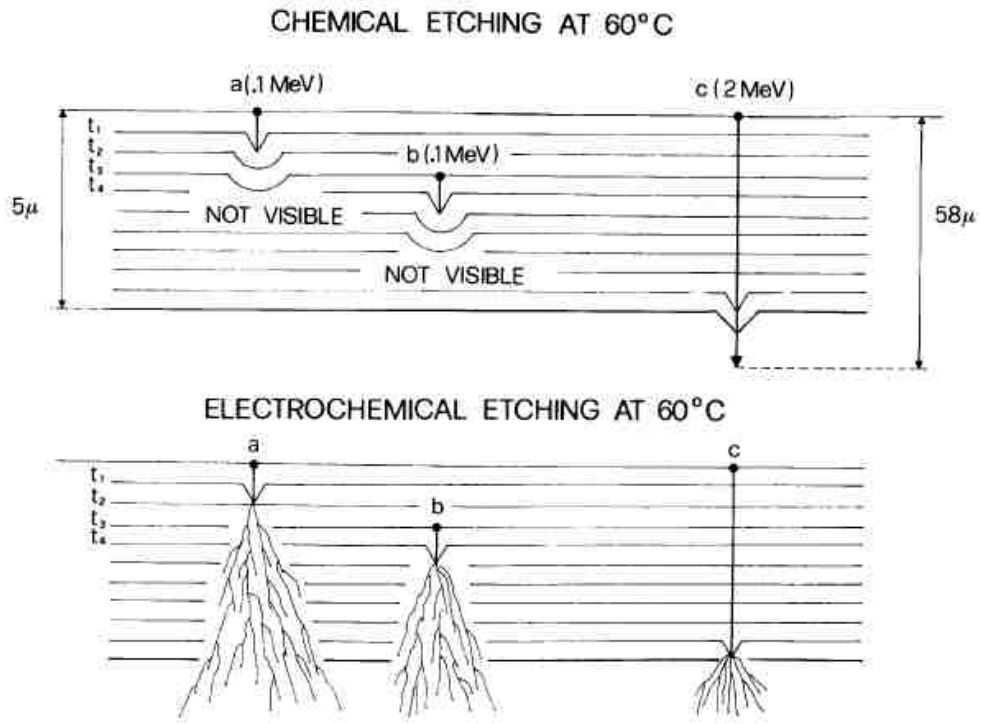

Figure 4.16: Differences in the final track shape when using different etching times in using CE and ECE procedires.

Neutron dosimetry with SSNTD and fissile materials was, for the first time, described in the work of Walker et al. [1963]. In this work there was no an explicit experiment involved, but it was theoretically described how a neutron dosimeter could be built. It basically consists in placing a SSNTD in contact with a sheet of fissile material so when a neutron induces a fission reaction, the fission fragments create latent tracks in the SSNTD and therefore the previous methods or other equivalent procedures to etch tracks can be applied. They also propose to use Cadmium in order to separate the thermal neutron component and the non-thermal neutron component. Finally they also explain some limitations of the method in the sense than enough energetic photons can cause fission and therefore there could be a contamination on reading the neutron component in mixed radiation fields. In the work of Baumgartner et al. [1966], taking advantage of the energetic dependence of the fission cross sections of ^{237}Np, ^{235}U and ^{238}U and the radiative capture cross section of Cd, is used Lexan polycarbonate as SSNTD with CE procedures to etch the tracks. The disadvantages of the dosimeters using the fission fragment damage principle is the intrinsic radioactivity of the fissile radiators. Moreover, the use of radioactive material for personnel dosimetry can be prohibited in facilities either by regulation or by management policy [Griffith et al., 1979].

4.4.1 Background on dosimetry with PADC and etching procedures

In the work of Cartwright et al. [1978] it was realised that the monomer Allyl Diglycol Carbonate (ADC) ($C_{12}H_{18}O_7$) or CR-39, or the polymerization of the ADC monomers which gives place to the Poly Allyl Diglycol Carbonate (PADC) [Burneni, 1997], could reach a threshold sensitivity as low as $\frac{Z}{\beta} = 10$ which means that the PADC was capable (with a CE process) to detect, for instance, 1 MeV protons and 6 MeV alphas. Moreover it was noticed that PADC was very homogeneous so the etched surfaces of the PADC were

very smooth and without scratches in comparison with Lexan.

The work of Cassou et al. [1978] introduced the idea of using radiators or converters in front of the PADC to produce recoil protons (as well as carbon recoils) through the neutron interactions.

In the work of Al-Najjar et al. [1979], neutrons with energies, E, of 0.5, 1.0 and 1.5 MeV were shoot to 450 µm thick foils of CR-39 (supplied by Pershore Mouldings Limited, Pershore, England), no converters were used. The whole ECE procedure was the following: First, a CE procedure with 30 % in weight fraction of KOH at 60 °C for 5.5 h. Second, an ECE procedure with 15 % KOH + 45 % H_2O + 40 % C_2H_5OH (weight fractions) at 60 °C for 3 h with an electric field strength of 15 kV cm^{-1} at 40 kHz. In this work is concluded that neutron events are detected by the CR-39 through the recoil tracks produced by H, C and O.

In the work of Gomaa et al. [1980], neutrons coming from Am-Be impinge in different configurations of CR-39 (using neutron converters) which have a dimension of 15 × 10 × 0.67 mm^3 with a neutron fluence of 2.27 × 10^8 n cm^{-2}. Only a CE procedure was employed, 6.25 N NaOH was used at 70 °C during 1 h. The results of the work are shown in Table 4.1.

Table 4.1: Calibration coefficients for different CR-39 configurations. See etching parameters in text. From Gomaa et al. [1980].

Configuration	$R_{\Phi_{\mathrm{ne,CE}}}$ (tracks neutron^{-1})
Uncovered	1.94×10^{-4}
Teflon	1.82×10^{-4}
Polyethylene	2.24×10^{-4}
Plastic	2.1×10^{-4}

In this work it was concluded that the main response of the detector was due to neutrons interacting with the detector itself and not due to neutron interaction with the detector covering material.

In the work of Benton et al. [1981], Am-Be neutrons were shoot to foils of CR-39 of 1 cm^2 of area using different set of converters: 0.4 mm of Al, 0.4 mm of Al + 0.025 mm of Be, 0.4 mm of Al + 0.005 mm of Au and 0.4 mm Al + 1 mm of polyethylene, in one of the faces of the CR-39. A CE procedure was employed using 6.25 NaOH at 70 °C for 15.5 h. In Table 4.2 the results of this work are shown.

Table 4.2: Calibration coefficients for different configurations of CR-39. See etching parameters in text. From Benton et al. [1981].

Type of converter	$R_{H_{\mathrm{ne,CE}}}$ (tracks cm^{-2} mrem^{-1})
Al only	3.8
Al + 0.025 mm of Be	3.7
Al + 0.005 mm of Au	2.9
Al + 1 mm of polyethylene	22.7

It was concluded that the main response of the CR-39 used in different configurations is due to neutrons interacting with the polyethylene converter rather than due to the interaction of the neutrons with the CR-39 itself.

In the work of Gammage et al. [1982], fission neutrons were shoot to foils of CR-39 (supplied by American Acrylics and Plastics, Inc., Stratford, Co., USA) of 630 µm of thickness with a protection of 60 µm polyethylene film using a bare CR-39 and one covered by 1 mm thick polyethylene layer. The whole ECE procedure was the following: First, a CE procedure with 9 N KOH at 60 °C for 3 h. Second, an ECE procedure with the same etchant at 25 °C for 4 h with an electric field strength of 20 kV cm^{-1} at a frequency of 1.3 kHz. Results are shown in Table 4.3.

Table 4.3: Calibration coefficients for different CR-39 configurations and etching conditions. See etching parameters in text. From Gammage et al. [1982].

Configuration	$R_{H_{\mathrm{ne}},k}$ (tracks cm^{-2} mrem^{-1})	
	ECE	CE+ECE
CR-39 + 1 mm polyethylene	54	1325
CR-39	42	517

In this work, it is shown that the CR-39 response to neutrons is essentially due to the neutron interaction with the CR-39 material itself in case of using an ECE procedure alone while the main response to the neutron field in case of using a CE + ECE procedures is due to the configuration constituted by the CR-39 + 1 mm polyethylene. In any case, there is an increase of the response in the CR-39 layer when using the 1 mm polyethylene converter.

The work of Tommasino et al. [1984] shows a response function of a CR-39 in terms of equivalent doses, $R_{H_{\mathrm{n}}}(E)$, from 0.02 MeV to 20 MeV when using a CE + ECE procedure (detectors etched electrochemically at 24 °C with an electric field strength of 30 kV cm^{-1} at a frequency of 2 kHz after 5 hours pre-etch at 60 °C) which is plotted in Figure 4.17 as open circles, and the response function when using an ECE process is used alone (5 hours at 60 °C with an electric field strength of 30 kV cm^{-1} at a frequency of 2 kHz) which is plotted in Figure 4.17 as closed circles.

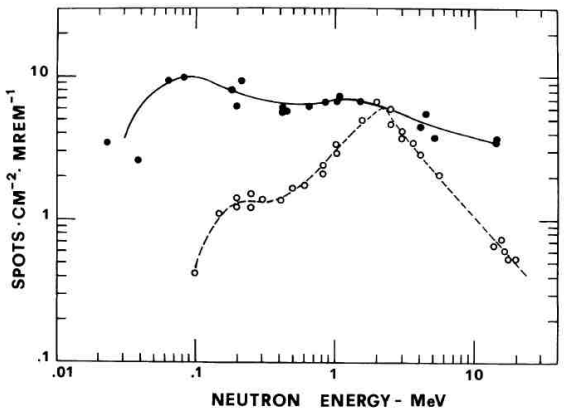

Figure 4.17: Response function in terms of equivalent doses of a CR-39. See etching parameters in text. From Tommasino et al. [1984].

In the work of Hankins et al. [1986] a three step ECE procedure was performed, as summarised in Table 4.4. They characterized their CR-39 system obtaining a response function in terms of equivalent doses, $R_{H_n}(E)$, from 0.05 MeV to 10 MeV, which is shown in Figure 4.18.

Table 4.4: ECE parameters. A post-etch of 15 minutes that makes the tracks rounder is also used. From Hankins et al. [1986].

Etch	Normality of KOH	6.5
	High voltage	3000 V
	Frequency	60 Hz
	Temperature	60°C
	Etch time	5 hr
Blow-up	High voltage	2700 V
	Frequency	2 kHz
	Temperature	60°C
	Time	~ 30 min

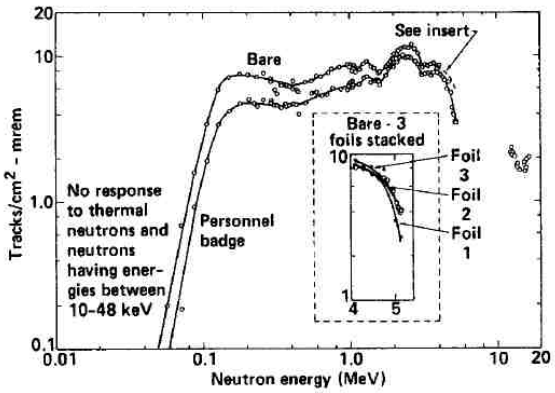

Figure 4.18: Response function in terms of equivalent doses of a CR-39. See etching parameters in text. From Hankins et al. [1986].

4.4.2 Neutron dosimeter developed by UAB

In the late 80's the response of ElectroChemically Etched (ECE) CR-39 track detector was first investigated at UAB [Fernández et al., 1988]. This was the beginning of future developments of neutron dosimeters using a CR-39 layer plus converters. The process of characterizing the whole neutron dosimeter or configuration (the CR-39 + converters) could be done following two approaches. The first approach would be to separate the problem in two steps, so that one should:

1. Characterize the CR-39 layer to proton fields and optimize the set of ECE conditions.
2. Characterize the proton fields emerging from the converters and generated by neutron fields.

The second approach is to simply:

- Characterize the CR-39 + converters to neutron fields.

At the time of developing a detector it can be interesting to separate the contributions and therefore, to follow the first approach so the whole dosimeter or configuration as well as the ECE parameters are well optimized. Once the detector configuration is assumed to be optimized one can obtain calibration coefficients simply by following the second approach.

The relevant published works describing the process of optimization of the PADC-based UAB neutron dosimeter which give rise to the actual standard configuration, are, essentially: Fernández et al. [1988], Fernández et al. [1991], Fernández et al. [1992], Fernández et al. [1996], Bouassoule et al. [1999], García et al. [2005] and Domingo et al. [2013].

Later, we are going to highlight some aspects of these works which are still nowadays relevant to our group. In previous works, for the CR-39 layers alone, the response function to protons (in terms of the proton fluence) is also called the proton efficiency.

Some quantities of interest are the angle of incidence of the radiation, θ, and the so-called critical angle for proton registration at a given energy, $\mu(E)$, which is defined as that where the proton response of the CR-39 is 0.5 tracks proton^{-1}. Both angles are defined in respect to the perpendicular direction of the CR-39 surface.

Figure 4.19 shows the critical angle for proton registration as a function of the proton energy, while Figure 4.20 presents the response function to protons as a function of the proton energy and incidence angle, $R^{\mathrm{CR39}}_{\Phi_{\mathrm{pr}}}(E,\theta)$ [Fernández et al., 1988] [Fernández et al., 1991] [Fernández et al., 1992] [Fernández et al., 1996].

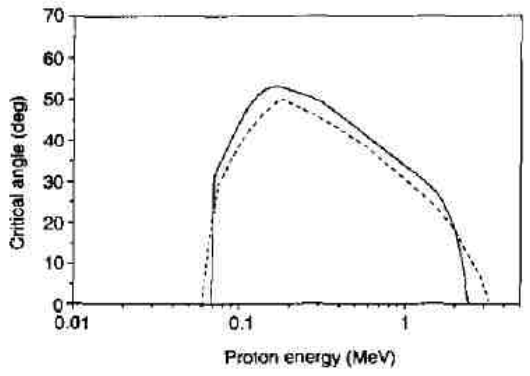

Figure 4.19: Critical angle as a function of the proton energy for 500 µm *thick layer of PADC (manufactured by Pershore Mouldings LTD). ECE conditions are using 6 N KOH solution at 60 °C with three steps: 20 kV cm^{-1} RMS at 50 Hz for 5 h, 20 kV cm^{-1} RMS at 2 kHz for 1 h and 15 min post-etching. With a total removed layer around* 4 µm. *Solid line is the result of the work from Fernández et al. [1996] while doted line is the result obtained in works Cross et al. [1986] and Cross et al. [1987].*

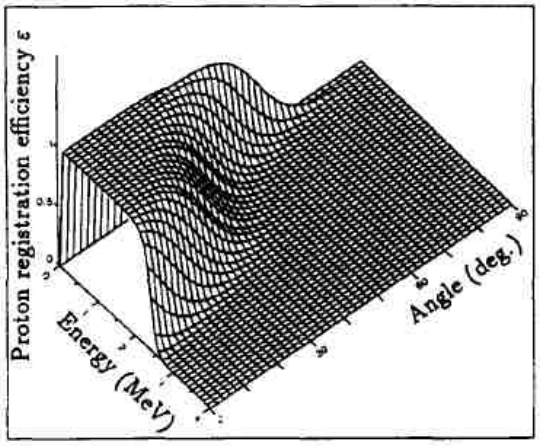

Figure 4.20: Response function to protons as a function of the proton energy and incidence angle for 250 µm *thick layer of PADC (manufactured by Pershore Mouldings LTD). ECE conditions are using 6.5 N KOH solution at 60 °C with three steps: 30 kV cm^{-1} RMS at 50 Hz for 2.5 h, 30 kV cm^{-1} RMS at 2 kHz for 1 h and 15 min post-etching. With a total removed layer around* 3.25 µm. *From Fernández et al. [1991].*

In the works cited in the previous paragraph a semiempirical fit was made to find the response function to protons as a function of the proton energy and incidence angle,

$R_{\Phi_{\rm pr}}^{\rm CR39}(E,\theta)$, which was analytically approximated as

$$R_{\Phi_{\rm pr}}^{\rm CR39}(E,\theta) = \frac{1}{1+{\rm e}^{\frac{\theta-\mu(E)}{\tau}}}, \tag{4.30}$$

with (4.31)

$$\tau = 5.1466 \tag{4.32}$$

$$\mu(E) = \begin{cases} 159923E^6 - 193450E^5 + 61491.8E^4 + 9713.55E^3 - 9045.39E^2 + 1681.61E - 46.86 & \text{if } E < 0.2859 \text{ MeV} \\ -10.44E^3 + 38.24E^2 - 58.07E + 63.92 & \text{if } E \geq 0.2859 \text{ MeV} \end{cases} \tag{4.33}$$

On the other hand, it is also interesting to show here the response function to neutrons in terms of the neutron dose equivalent for different configurations of CR-39 + converters and different ECE conditions. In the works of Fernández et al. [1992] (configuration of CR39 + polyethylene) and Fernández et al. [1996] (configuration of CR39 + makrofol ED + polyethylene) is derived an experimental response function of a CR-39 configuration and under a certain set of ECE conditions and for a perpendicular incidence of the radiation, the shapes of such response functions are shown in Figures 4.21 and 4.22 respectively.

The aim of including the makrofol layer in the detector configuration is to flatten the response function.

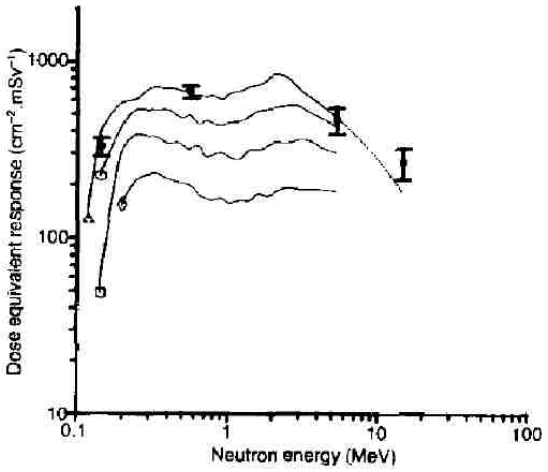

Figure 4.21: Response function to neutrons for 250 µm *thick layer of PADC (manufactured by Pershore Mouldings LTD) + polyethylene. ECE conditions are using 6 N KOH solution at 60 °C with three steps: 20 kV cm^{-1} RMS at 50 Hz for 2.5 h, 20 kV cm^{-1} RMS at 2 kHz for 1 h and 15 min post-etching. With a total removed layer around* 3.5 µm. *Solid lines correspond to a MC model. Angles of incidence:* $\Delta = 0°$, $\circ = 30°$, $\square = 45°$ *and* $\diamondsuit = 60°$. *From Fernández et al. [1992].*

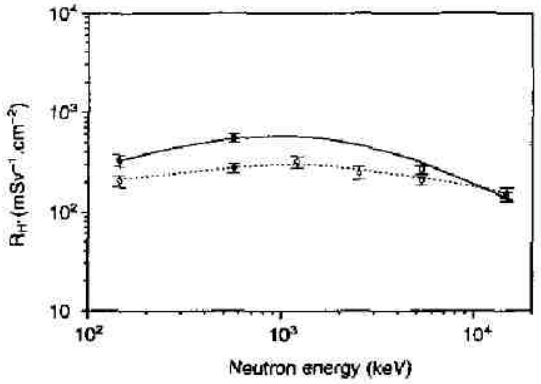

Figure 4.22: Lower points correspond to the response function to neutrons for 500 µm *thick layer of PADC (manufactured by Pershore Mouldings LTD) +* 300 µm *thick layer of makrofol ED + 3 mm thick layer of polyethylene (both converters manufactured by Bayer AG). ECE conditions are using 6 N KOH solution at 60 °C with three steps: 20 kV cm^{-1} RMS at 50 Hz for 5 h, 20 kV cm^{-1} RMS at 2 kHz for 1 h and 15 min post-etching. With a total removed layer around* 4 µm. *Higher points correspond to a configuration without makrofol ED converter. The lines correspond to evaluations. From Fernández et al. [1996].*

In the work of Bouassoule et al. [1999] the objective was to make the configuration of the radiation detector sensitive to thermal neutrons. For doing that, 3 mm of air after the makrofol layer in order to benefit from the reaction ^{14}N(n,p)^{14}C was used. In the cited work it was also studied if using a PMMA (known also as methacrylate or lucite) as a holder was having some significant effect in respect to the configurations studied in previous work. UAB developed neutron dosimeter has superficial dimensions of $\sim$ 6 cm

$\times$ 6 cm where we can fit 9 CR-39 (plus converters) of superficial dimensions of $\sim$ 2 cm $\times$ 2 cm and for that reason, a holder is needed.

The commented configurations were irradiated in neutron fields containing the thermal component (SIGMA facility [Chartier et al., 1995] [Lacoste et al., 2004a]) where it was seen that the response of configuration with 3 mm of air is generated in a 40 % from the thermal component and in a 60 % from the fast component [Bouassoule et al., 1999].

It was experimentally found that for the SIGMA source, the calibration coefficient to neutrons in terms of neutron dose equivalent was (110 ± 15) cm^{-2} mSv^{-1} for configuration without 3 mm of air and (130 ± 25) cm^{-2} mSv^{-1} for configuration with 3 mm of air. The difference is produced because configuration with air is sensitive to the neutron thermal component of SIGMA.

It can also be concluded that the fact of incorporating the holder of PMMA does not alter the neutron response.

In order to increase even more the sensitivity of the radiation detector to thermal neutrons and to make the dosimeter more compact, in the work of García et al. [2005] two configurations of CR-39 were studied and irradiated with neutron sources with one of them substituting a 6 mm thick air layer by a 100 µm thick polyamide nylon 6 (manufactured by Goodfellow) layer. Figure 4.23 shows a representation of the two configurations and the thickness of each layer.

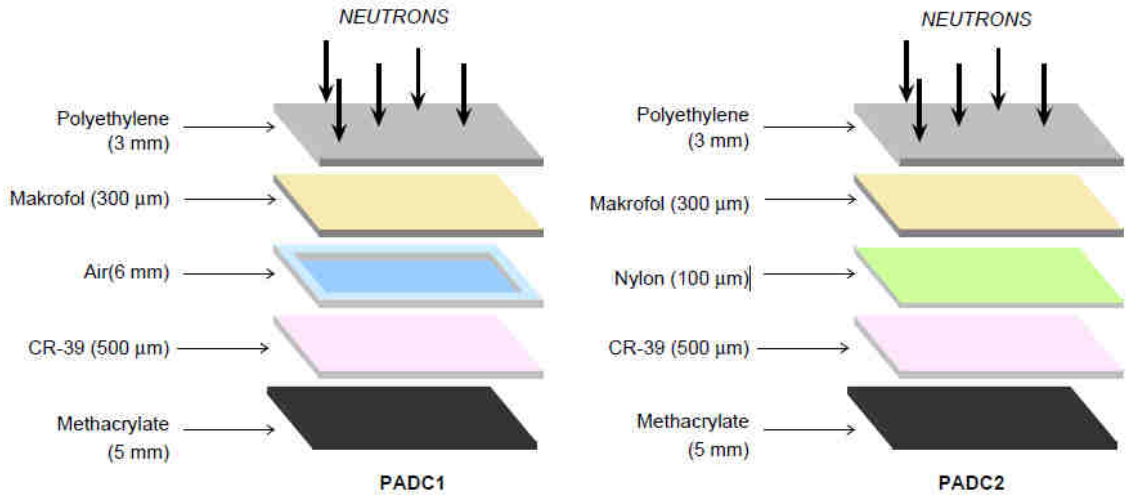

Figure 4.23: Arrangement of the configuration 1 and 2. From García et al. [2005].

In Table 4.5 we find the calibration coefficients to neutrons for the different neutron sources and also for different angular incidence. The ECE conditions were the same as in Bouassoule et al. [1999]. Table 4.5 shows that calibration coefficients of configuration 2 increase, at least, a 28 % in respect to the configuration 1. In the case of SIGMA (in which the presence of thermal neutrons is relevant) the relative increase is 114 %. These results are somehow expected as the nylon thickness (100 µm) is equivalent to an air layer of 15 mm which is a little more than twice the air thickness used in the work.

In the work of Domingo et al. [2013] a response function for this last configuration (right configuration from Figure 4.23) was obtained in the energy range from 10^{-7} MeV to 20 MeV in terms of neutron fluence, Φ_{ne}, and in terms of the personal dose equivalent for perpendicular direction, $H_{\mathrm{p}}(10, 0°)$. The experimental information used to estimate the

Table 4.5: Experimental calibration coefficients to neutrons in different conditions in terms of neutron dose equivalent. From García et al. [2005].

Neutron source	θ (°)	Experimental average response (cm^{-2} mSv^{-1})		Experimental ratio $\frac{R(\theta)}{R(0)}$	
		Configuration 1	Configuration 2	Configuration 1	Configuration 2
Am-Be	0	350 ± 46	449 ± 28	1.00 ± 0.13	1.00 ± 0.05
	30			0.87 ± 0.11	0.76 ± 0.07
	60			0.32 ± 0.05	0.36 ± 0.07
^{252}Cf	0	443 ± 63	570 ± 58	1.00 ± 0.20	1.00 ± 0.14
	30			0.68 ± 0.14	0.73 ± 0.10
	60			0.28 ± 0.06	0.36 ± 0.06
^{252}Cf+D_2O+Cd	0	354 ± 30	485 ± 29	1.00 ± 0.14	1.00 ± 0.08
	30			0.71 ± 0.09	0.80 ± 0.06
	60			0.34 ± 0.08	0.35 ± 0.05
^{252}Cf+D_2O	0	390 ± 38	499 ± 22	1.00 ± 0.14	1.00 ± 0.06
	30			0.74 ± 0.09	0.70 ± 0.07
	60			0.33 ± 0.08	0.32 ± 0.04
SIGMA	0	276 ± 33	592 ± 46	-	-

response function was that in the work of Domingo et al. [2009].

In Table 4.6 we show the experimental calibration coefficients in terms of neutron fluence, $R_{\Phi_{\mathrm{ne}}}$, and in terms of the personal dose equivalent for perpendicular direction, $R_{H_{\mathrm{p}}(10,0^{\circ})}$, used to estimate the response function of the UAB standard dosimeter for the neutron fields coming from the different sources listed.

Table 4.6: Experimental calibration coefficients to neutrons in different neutron radiations. From Domingo et al. [2009].

Neutron source	$\overline{E}_{\Phi}$ (MeV)	Calibration coefficient $R_{\Phi_{\mathrm{ne}}}$ (tracks $\mathrm{neutron}^{-1}$)	Calibration coefficient $R_{H_{\mathrm{p}}(10,0^{\circ})}$ (cm^{-2} mSv^{-1})
SIGMA	0.079	$(1.42 \pm 0.06) \times 10^{-5}$	575 ± 26
T(p,n)^{3}He	0.27	$(4.79 \pm 0.84) \times 10^{-5}$	245 ± 43
^{252}Cf+D_2O	0.539	$(5.17 \pm 0.23) \times 10^{-5}$	575 ± 23
^{252}Cf+D_2O+Cd	0.539	$(5.55 \pm 0.27) \times 10^{-5}$	499 ± 24
T(p,n)^{3}He	0.66	$(1.21 \pm 0.16) \times 10^{-4}$	336 ± 50
^{252}Cf	2.13	$(2.01 \pm 0.13) \times 10^{-4}$	591 ± 39
D(d,n)^{3}He	7.77	$(1.15 \pm 0.21) \times 10^{-4}$	276 ± 51
T(d,n)^{4}He	11.45	$(9.31 \pm 0.16) \times 10^{-5}$	203 ± 41

From the methodology described in Domingo et al. [2013] a response function to neutrons in terms of neutron fluence, $R_{\Phi_{\mathrm{ne}}}(E)$, and in terms of the personal dose equivalent for perpendicular direction, $R_{H_{\mathrm{p}}(10,0^{\circ})}(E)$, are obtained. They are shown in Figures 4.24 and 4.25 respectively.

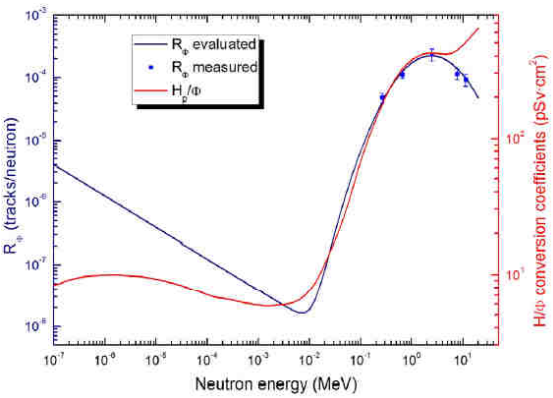

Figure 4.24: Response function to neutrons in terms of neutron fluence is shown in the blue solid line. Some experimental calibration coefficients from Table 4.6 are shown in the fast region. In solid red line we find the fluence-to-personal dose equivalent for perpendicular incidence conversion coefficients for neutrons $\left[\frac{H_p(10,0^\circ)}{\Phi_{ne}}\right]$. *From Domingo et al. [2013].*

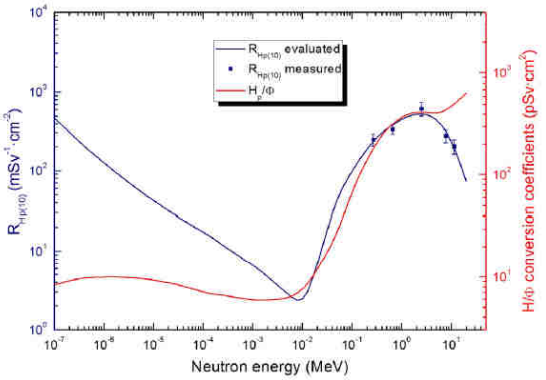

Figure 4.25: Response function to neutrons in terms of personal dose equivalent for perpendicular incidence is shown in the blue solid line. Some experimental calibration coefficients from Table 4.6 are shown in the fast region. In solid red line we find the fluence-to-personal dose equivalent for perpendicular incidence conversion coefficients for neutrons $\left[\frac{H_p(10,0^\circ)}{\Phi_{ne}}\right]$. *From Domingo et al. [2013].*

In order to use the described configuration of the CR-39 as an operational neutron dosimeter one has to take into account the procedures described in Section 4.3. This was precisely done in work Domingo et al. [2013] obtaining as a result that, with a calibration coefficient in terms of personal dose equivalent for perpendicular incidence of 350 cm^{-2} mSv^{-1} it is proved that the PADC 2 configuration (see Figure 4.23) is an operational neutron dosimeter in the energy range from 200 keV to 12 MeV.

The current standard configuration employed by UAB Radiation Physics Group [García-Fusté et al., 2020] is described in Figure 4.26 and Table 4.7 with the ECE conditions specified in Table 4.8. All elements together give rise to the response function to neutrons (in terms of fluence), in units of tracks $\mathrm{neutron}^{-1}$, shown in Figure 4.27. The response of this detector is expressed as the track density, in units of tracks cm^{-2}.

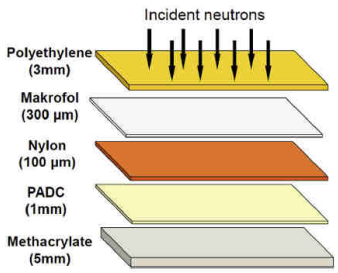

Figure 4.26: Description of the standard neutron dosimeter developed at UAB.

Table 4.7: Description of the standard neutron dosimeter developed at UAB.

Material	Density (g cm^{-3})	Composition	Thickness
Polyethylene	0.94	C_2H_4	3 mm
Makrofol polycarbonate ≡ Lexan	1.2	$C_{16}H_{14}O_3$	300 µm
Nylon type 6	1.14	$C_6H_{11}NO$	100 µm
PADC ≡ CR-39	1.31	$C_{12}H_{18}O_7$	1 mm
Methacrylate ≡ polymethyl methacrylate (PMMA) ≡ Lucite	1.19	$C_5H_8O_2$	5 mm

Table 4.8: Description of the ECE steps currently used at UAB.

Step	Chemical solution	Time	Temperature (°C)	Electric field (kV cm^{-1})	Frequency
1st step	6 M KOH	5 h	60	20	50 Hz
2st step	6 M KOH	1 h	60	20	2 kHz
Post-etching	6 M KOH	15 min	60	-	-

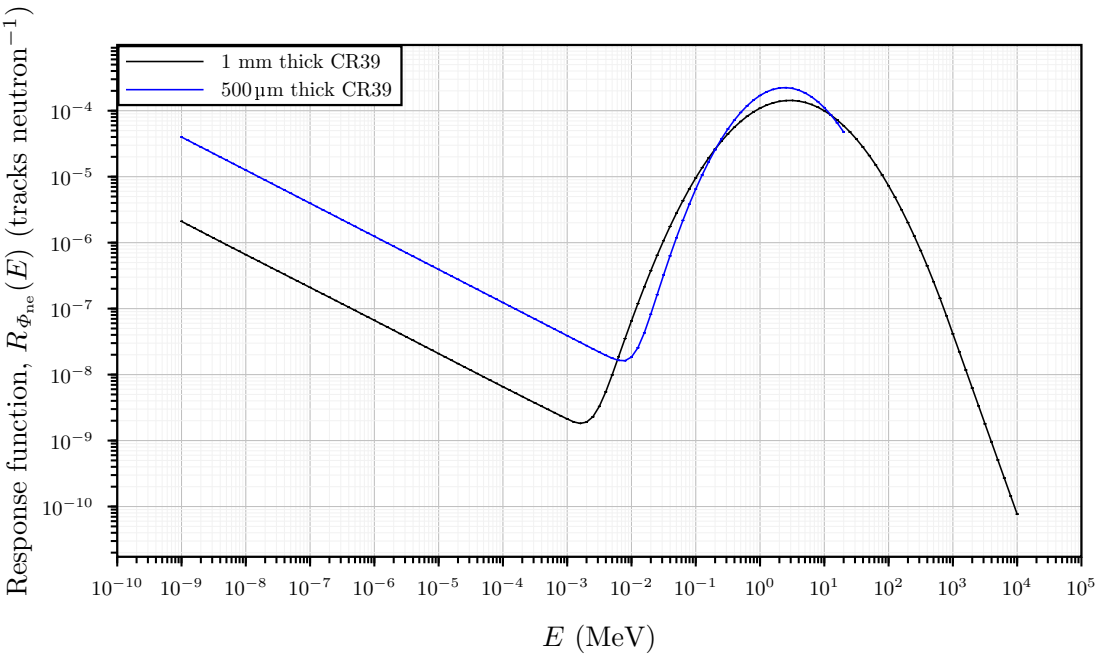

Figure 4.27: Response function when using 500 µm *thick CR-39 in the configuration of the dosimeter (blue line) [Domingo et al., 2013] and when using 1 mm thick CR-39 in the configuration of the dosimeter (black line) [García-Fusté et al., 2020].*

ECE procedures in UAB are carried out in the following way.

Once the UAB neutron dosimeter, see Figure 4.26, has been placed in a neutron field, the PADC layer (which is inside the detector configuration) has to be electrochemically etched. The whole process is carried at a temperature of 60° and is done in a way that PADC layers are inside of an stove. The PADC layers have to be carefully placed so that the irradiated face is in contact with the 6 M KOH dissolution while the not-irradiated face is in contact with a 0.25 M KOH dissolution, the only aim of this low molarity dissolution is to produce an uniform electric field during the ECE process by distributing properly the electrical potential in the region. Up to 20 PADC layers can be simultaneously etched in our LAB, this is achieved with the mounting tower shown in Figures 4.28 and 4.29. For a basic review of chemistry, see Chang et al. [2017].

The elements needed in order to deliver the alternating 2000 V (PADC layer is 0.1 cm thick) first at 50 Hz and after at 2 kHz (according to Table 4.8) are the following. From a computer, a LabView software application is executed in order to control a digital-to-analog converter bought from National Instruments that is capable of producing a peak-to-peak analog alternating voltage. This signal is sent to a Trek model 10/10B-HS high voltage amplifier which amplifies the alternate signal to a potential difference of 2000 V that is finally sent to metallic electrodes which are in permanent contact with the dissolutions. The electric potentials are in proper contact throughout the mounting

tower due to red and black cables so that each PADC layer (up to 20 PADC layers in the whole tower can be simultaneously etched) is under the alternating voltage of 2000 V. The PADC layers properly placed in the mounting tower are inside a stove during the ECE process. An oscilloscope is constantly monitoring the induced current in the PADC layers. An overview of these elements is shown in Figure 4.30.

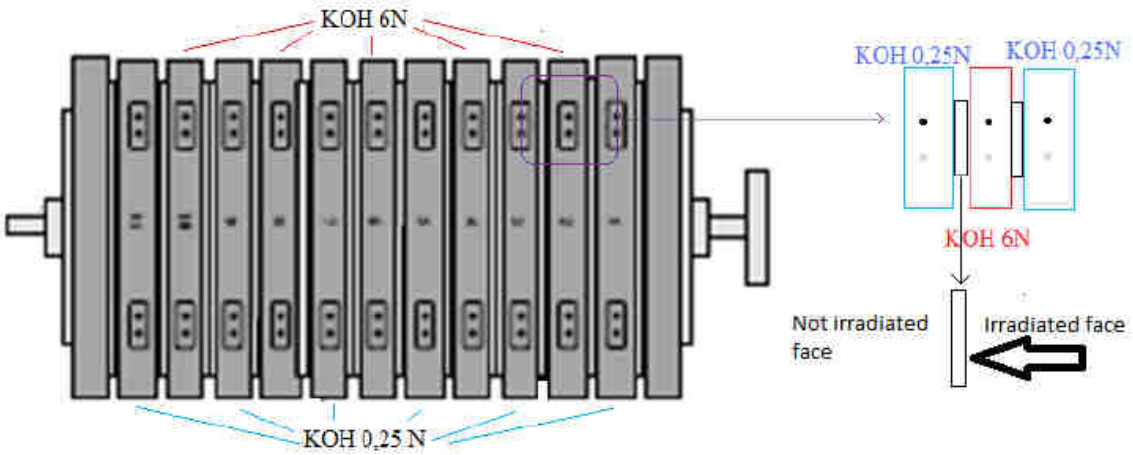

Figure 4.28: Mounting tower and magnified region of the mounting tower. Each PADC layer has its irradiated face which is permanent contact with the 6 M KOH dissolution. During the ECE process each PADC layer is under a alternating potential difference of 2000 V with a frequency according to Table 4.8.

Figure 4.29: In the tiny holes the 0.25 M KOH and 6 M KOH dissolutions are properly introduced so each PADC layer in its irradiated face will meet with the 6 M KOH dissolution. Gray metallic electrodes are in contact with the dissolutions. Black and red cables transport the electric potentials so that each PADC will be under a potential difference.

After following the ECE steps from Table 4.8, in the PADC layer we can quantify and

even see with the naked eye, a track density. An example is shown in Figure 4.31.

Figure 4.30: The elements needed to perform the electrochemical etching are presented.

Figure 4.31: PADC layer once the ECE process has finished.

The PADC layers are then scanned using a commercial high resolution (up to 9600 DPI) scanner so images containing the tracks are obtained and using a home made track counting software [San Pedro Pérez, 2011] or ImageJ [Schneider et al., 2012] or even semi-manual counting. The area scanned is 4 mm × 4 mm and track density is expressed in units of tracks cm^{-2}. See significant examples of how this track density is visualized in a 4 mm × 4 mm surface in Appendix B.

The response of this detector system is precisely the track density.

4.5 Neutron spectrometry based on neutron moderation

A behaviour seen in neutron cross sections in the range from 10^{-11} MeV to 1 MeV is that cross sections increase when decreasing the neutron energy and total neutron cross section is dominated first by the elastic interactions and next by the radiative capture,

see for instance ^{1}H, ^{12}C and ^{16}O in Figure 2.24. However, there are isotopes in which this behaviour is not followed, other interesting reactions are available and relevant and we can take advantage from them.

As we are interested in hunting neutrons, which are particles with no net charge, one should focus in relevant reactions (those with high numerical values in their cross sections) in which charged radiation is found in the final state of the reaction. Some of these relevant reactions are, for instance, ^{3}He(n,p)^{3}H with a Q_0 value of 0.764 MeV or ^{6}Li(n,α)^{3}H with a Q_0 value of 4.78 MeV but one could even benefit from the reaction ^{197}Au(n,γ)^{198}Au and by analysing gamma emission (essentially photons of 0.412 MeV) from the decay of the activated gold foils, as we will see later.

The behaviour of such specific cross sections as well as the total neutron cross section in the mentioned isotopes can be found in Figure 4.32. From Figure 4.32 it can be concluded that the previous reactions are the dominant reactions for the mentioned isotopes. Another fact extracted from Figure 4.32 is that previous reactions are really relevant for thermal neutrons (typically energy distribution of the neutron fluences have a thermal peak centered between 10^{-8} and 10^{-7} MeV according to the temperature of the environment) but they are not so relevant in increasing the neutron energy. In general, for those isotopes showing the previous features, enrichment can be used to build neutron radiation detectors. In the case of ^{3}He, however, as it is a noble gas, no solid compounds can be fabricated and the material must be used in gaseous form.

Of course, if our objective is to describe effectively an unknown neutron radiation field which extends, typically, from 10^{-8} up to 10^{3} MeV, by only using reactions like ^{3}He(n,p)^{3}H we have to do some additional arrangement since, as it can be shown in Figure 4.32, $\sigma_{^{3}\mathrm{He(n,p)}^{3}\mathrm{H}}\left(E = 10^{-7}\ \mathrm{MeV}\right) \sim 10^{3} \cdot \sigma\left(E = 1\ \mathrm{MeV}\right)$.

Therefore, one way to do neutron spectrometry via reactions like ^{3}He(n,p)^{3}H is to consider that this reaction will be, essentially, produced by thermal neutrons (those with $E < 1$ eV) so if one wants to detect neutrons with higher energies one has to moderate (slow down) them first. The pioneers in introducing this technique are considered to be Bramblett, Ewing and Bonner [Bramblett et al., 1960]. In order to be effective in moderating neutrons, hydrogen-containing materials should be employed (as explained previously and also because $\sigma_{^{1}\mathrm{H(n,EL)}^{1}\mathrm{H}}$ is high, see Figure 2.24). A detector configuration can be then constituted by a:

- Thermal neutron detector,
- Moderating material, and additionally,
- Specific materials in order to benefit from particular nuclear reactions.

Of course, by increasing the amount of moderating material in front of the thermal neutron detector, we will be able to count neutrons with higher energies but at the same time, a quantity of neutrons will be lost since they can be absorbed in the moderator itself or they can be deflected by the moderator, so the moderated neutron never reaches the active volume of the detector.

Still an important question remains: given a detector configuration (thermal neutron detector plus moderated material), how many neutrons of energy E we will be able to count ?

This information is contained in the response function of the configuration and each particular configuration (using different sizes of moderator and using different shells) has its

response function. Examples of these response functions can be found in Figures 4.46 and 4.58. The specific and exact definition of response function (as well as its units) has to be given properly for each detector system.

Once a detector system is well characterized, that is to say, when MC simulations of the response function of each detector configuration and experimental validation of such response functions have been performed, one is ready to proceed with measurements with each detector configuration in unknown energy distribution of the neutron fluences and to apply unfolding procedures in order to, precisely, find the unknown energy distribution of the neutron fluence in a point. The unfolding method used by UAB is the FRascati Unfolding Interactive Tool (FRUIT) software (see Bedogni et al. [2007], Bedogni [2006] and Amgarou et al. [2011]).

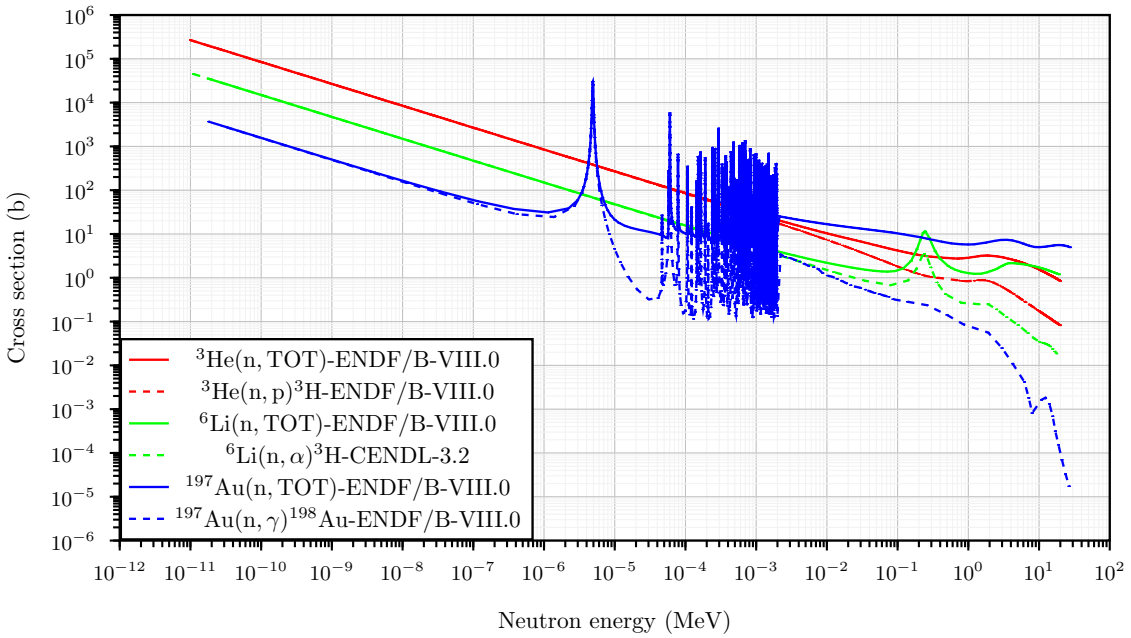

Figure 4.32: Total neutron cross sections and specific cross sections for ^{3}He, ^{6}Li and ^{197}Au. Notice how dominant are the reactions $^{3}He(n,p)^{3}H$, $^{6}Li(n,\alpha)^{3}H$ and $^{197}Au(n,\gamma)^{198}Au$ in comparison with their related total neutron cross sections in the thermal region.

4.5.1 Active neutron spectrometry in UAB

Active neutron spectrometry related to UAB can be traced back to the fundamental works of Bakali [2001], Bouassoule et al. [2001], Muller et al. [2002], Lacoste et al. [2004b] and Bedogni [2006] so only a summary of relevant details will be given in the present work.

Active neutron spectrometry in UAB is carried out by using, as a thermal neutron detector, a cylindrical ^{3}He (99.7 % in isotopic composition) proportional counter of type 0.5NH 1/1KI manufactured by Eurisys Mesures [Eurisys, 1999] with 4.4 cm height and 1 cm diameter. Its active volume is also cylindrical with 1 cm height and 0.9 cm diameter so its active volume is 0.64 cm^{3}. The ^{3}He gas pressure is 8 bar. Figures 4.33 and 4.34 show pictures of the proportional counter and MC model, respectively. The associated electronics is also manufactured by Eurisys Mesures [Eurisys, 1999] and, as a whole, it allows the collection of analogical and digital pulses. The electronics contains an amplifier, pulse shaper and a pulse discriminator. The associated electronics is contained in a metallic box so it is shielded from electromagnetic interactions, as shown in Figure 4.35.

The proportional counter tube is fed by a high voltage (650 V) power supply, 556H model from EG&ORTEC, which can provide voltage to two proportional counter tubes at the same time. The associated electronics to the proportional tube is fed by a home-made low voltage (12 V) power supply.

Analog pulses obtained after amplification and pulse shaper, are sent to a multichannel analyser, in our case to AMPTEK MCA-800, which is connected to a laptop so a pulse height distribution can be obtained. A digital pulse is generated each time that an analog pulse exceeds the discriminator threshold, so that low amplitude pulses due to gamma radiation are filtered. These digital pulses are then sent to the pulse counter NOVELEC E720. The power supplies as well as the NOVELEC E720 and the AMPTEK MCA-800 are already prepared for main supply of conventional 220 V alternate current.

The pulse height distribution obtained by the proportional counter when an AmBe source is used is provided by the manufacturer, see Figure 4.37. Some examples of pulse height distributions obtained experimentally by UAB are those in Figures 4.39 and 4.40. While in Figure 4.39 not relevant low height pulses are present, in Figure 4.40 a very relevant quantity of photons or low height pulses are present even giving rise to pile-up and dead time effects of photons which is an additional source of complexities besides the possible problems of pile-up and dead time effects of neutrons. These effects will affect to the unfolding procedures even to the point that not active spectrometry is feasible. The theoretical pulse height distribution of the proportional counter based on the reaction ^{3}He(n,p)^{3}H is given in Figure 4.38 where the wall effect produced by the secondary charged particles is clearly seen. I performed a very preliminary work in order to inquire about the pulse height distribution generated not only by mono-energetic neutrons but also from other particles such as protons and photons. The MC situation is represented in Figure 4.41. Figure 4.42 shows the pulse height distributions generated in the active region of the ^{3}He proportional counter by different mono-energetic neutron beams. About this paragraph, I would recommend to perform measurements using AmBe conditions to see the *standard* pulse height distributions (in each detector configuration). I would also recommend to promote the mentioned MC work in order to inquire in how a pulse height distribution is, in the end, generated even in a mixed radiation field situation.

Polyethylene (C_2H_4, ρ = 0.920 g cm^{-3}) spheres are used as moderating material and, additionally, spherical shells of Cd, Cu and Pb are also employed in order to benefit from some specific neutron reactions that will be explained later. At this point, it is important to notice that a special tube made by Al (element k in Figure 4.35) surrounds and protects the proportional tube. An special cap made basically of polyethylene but also containing lead (in order to shield partially photons coming, for instance, from radiative captures on the moderating material), peaks the Al tube when a moderating sphere is used. Of course, this special cap is included in the pertinent MC response simulations as shown in the polyethylene and lead materials from the MC model of Figure 4.34.

Currently, UAB uses up to 14 detector configurations plus the bare thermal neutron detector. In Table 4.9 each detector configuration as well as information about the constituting materials is summarised and Figure 4.36 shows the moderating polyethylene spheres and shells needed to form the 14 detector configurations specified in Table 4.9. In Figure 4.43 is shown how a polyethylene sphere and Cd shell is placed. Figure 4.44 presents how polyethylene and Cu shell is used. In the end, the detector configurations containing Cu and Pb are seen as in Figure 4.45 (Cu and Pb shells are in the interior of the configuration) giving rise to a sphere with diameter of 7 ".

Figure 4.33: UAB proportional counter. From Bakali [2001].

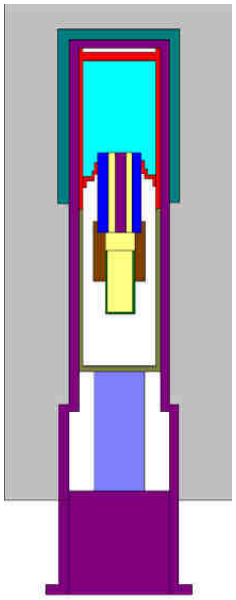

Figure 4.34: 2D MC model of the UAB proportional counter. ■ *≡ polyethylene,* ■ *≡ lead,* ■ *≡ steel,* ■ *≡ copper,* ■ *≡* ^{3}*He,* ■ *≡ ceramic,* ■ *≡ aluminum,* ■ *≡ brass + nickel,* ■ *≡ monel 400,* ■ *≡ air,* ■ *≡ Brass and* ■ *≡* ^{3}*He active volume. See additional details such as densities and isotopic compositions in Bakali [2001].*

Table 4.9: Description of the detector configurations developed at UAB.

Detector configuration number	Short name	Geometrical features
1	2.5 "	Poyethylene sphere of 2.5 " diameter
2	3 "	Poyethylene sphere of 3 " diameter
3	4.2 "	Poyethylene sphere of 4.2 " diameter
4	5 "	Poyethylene sphere of 5 " diameter
5	6 "	Poyethylene sphere of 6 " diameter
6	8 "	Poyethylene sphere of 8 " diameter
7	10 "	Poyethylene sphere of 10 " diameter
8	12 "	Poyethylene sphere of 10 " diameter
9	2.5 " + Cd	Poyethylene sphere of 2.5 " diameter + 1.5 mm thick Cd shell
10	3 " + Cd	Poyethylene sphere of 3 " diameter + 1.5 mm thick Cd shell
11	4.2 " + Cd	Poyethylene sphere of 4.2 " diameter + 1.5 mm thick Cd shell
12	7 "	Poyethylene sphere of 7 " diameter
13	7 " (Cu)	Poyethylene sphere of 4 " diameter + 1 " thick Cu shell + 0.5 " thick polyethylene shell
14	7 " (Pb)	Poyethylene sphere of 4 " diameter + 1 " thick Pb shell + 0.5 " thick polyethylene shell

Figure 4.35: A view of the proportional tube, special Al tube (k) and the metallic box where the associated electronics to the proportional counter is found. High voltage is set through input a. Low voltage is set through input j. Analog pulses are sent through output i. Digital pulses are sent through output h. Pulse tests can be done through output b. Pulse height discriminator is set through entrance c. Voltage of the applied discrimination is measured in d. Gain can be modified e. The configuration of the previous parameters can deleted through entrance f.

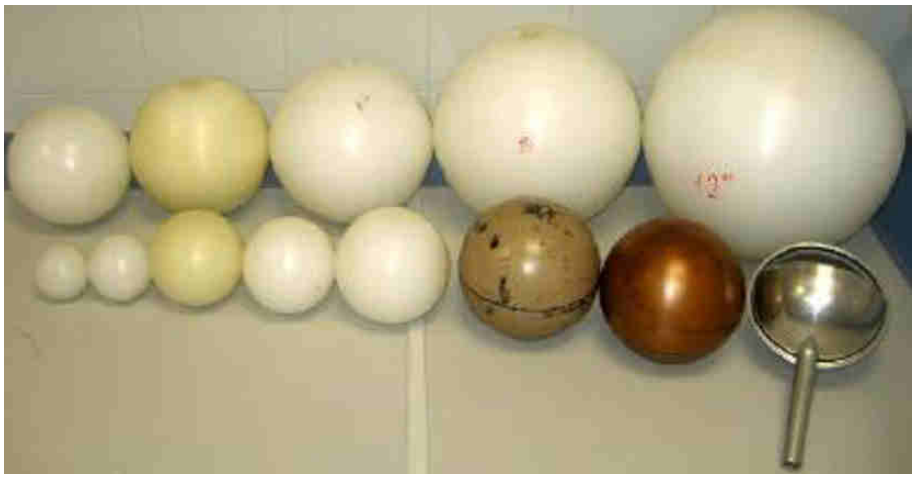

Figure 4.36: Polyethylene spheres, Pb mounted shell, Cu mounted shell and Cd shell.

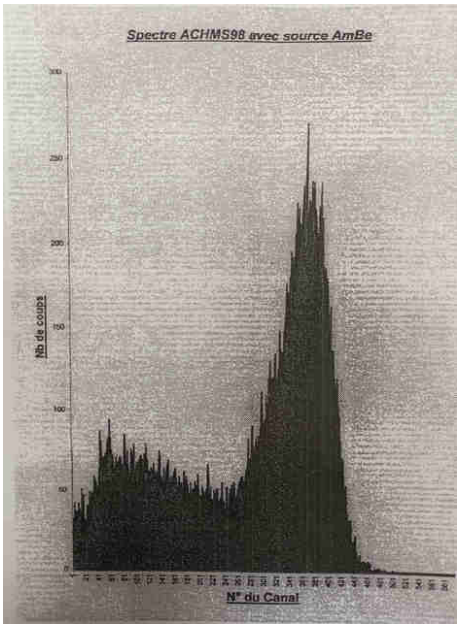

Figure 4.37: Pulse height distribution provided by the manufacturer of the proportional counter Eurisys Mesures [Eurisys, 1999] when an AmBe source is used.

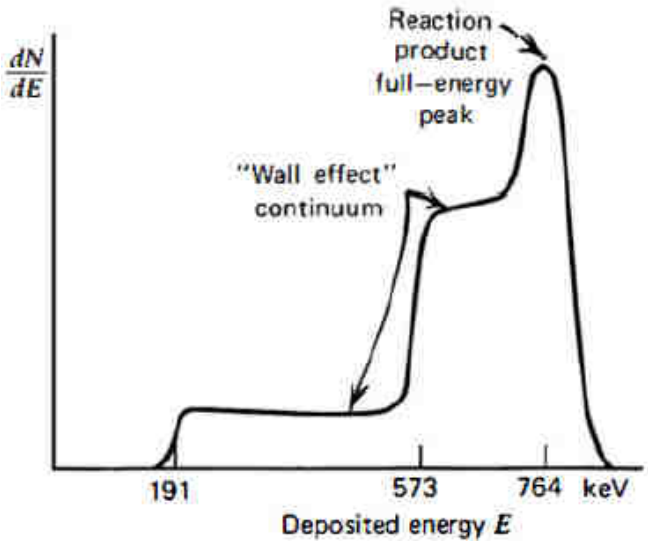

Figure 4.38: Theoretical pulse height distribution, from Knoll [2010].

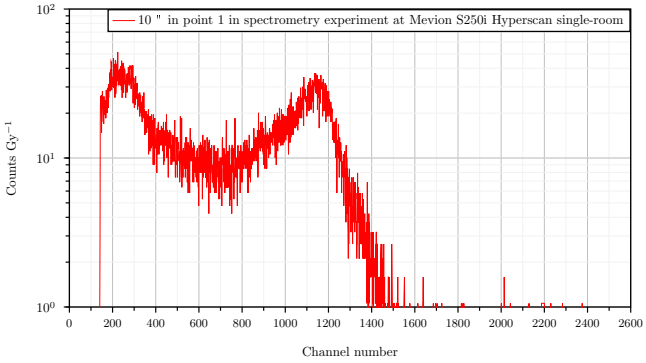

Figure 4.39: Good pulse height distribution obtained in an experimental situation.

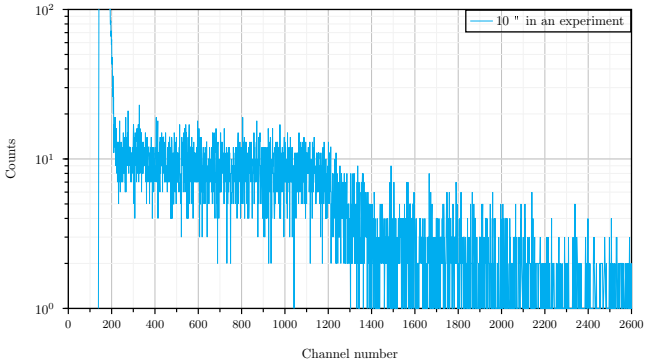

Figure 4.40: Not so good pulse height distribution obtained in an experimental situation.

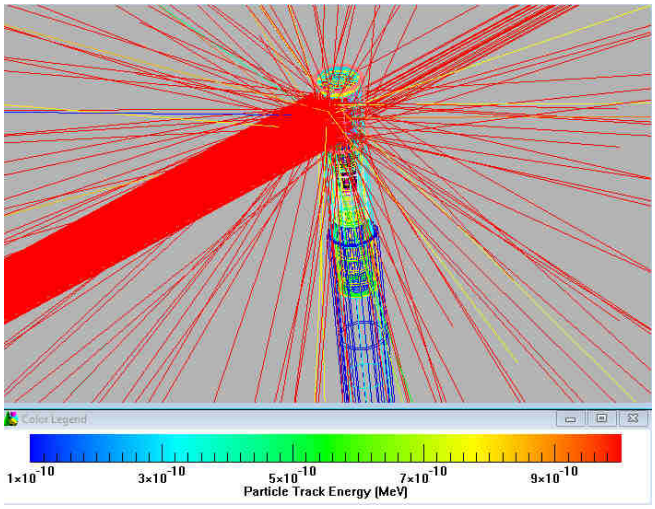

Figure 4.41: MC model to compute the pulse height distribution for different mono-energetic neutrons.

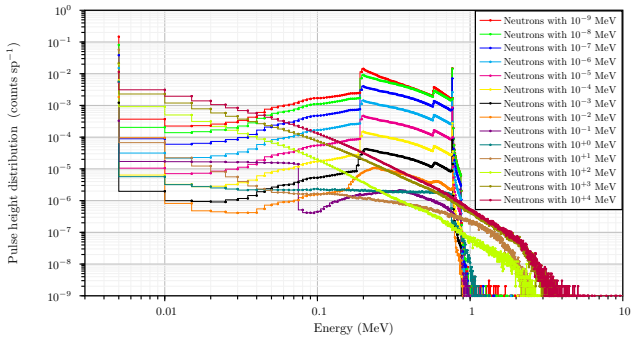

Figure 4.42: Pulse height distribution obtained by MC simulations for different incident mono-energetic neutron beams in the active region of the proportional counter.

Figure 4.43: Situation in which Cd shell is used. Only half of the Cd shell is shown to make the sphere visible. The pertinent moderating sphere will be closed inside the shell.

Figure 4.44: Situation in which the 1 " thick Cu shell will be placed between the 4 " moderating sphere and 0.5 " thick polyethylene shell.

Figure 4.45: Final appearance of a detector configurations 7 " (Cu) and 7 " (Pb).

The response functions to neutrons (in terms of fluence) of the active Bonner Sphere System (BSS) from UAB, in units of cm^2, are shown in Figure 4.46. The response of the active BSS from UAB is simply the number of nuclear reactions induced in the ^{3}He proportional counter. The shape of the response functions is explained by the neutron physics already introduced in this section, that is to say, due to the shape of the cross sections of the materials used.

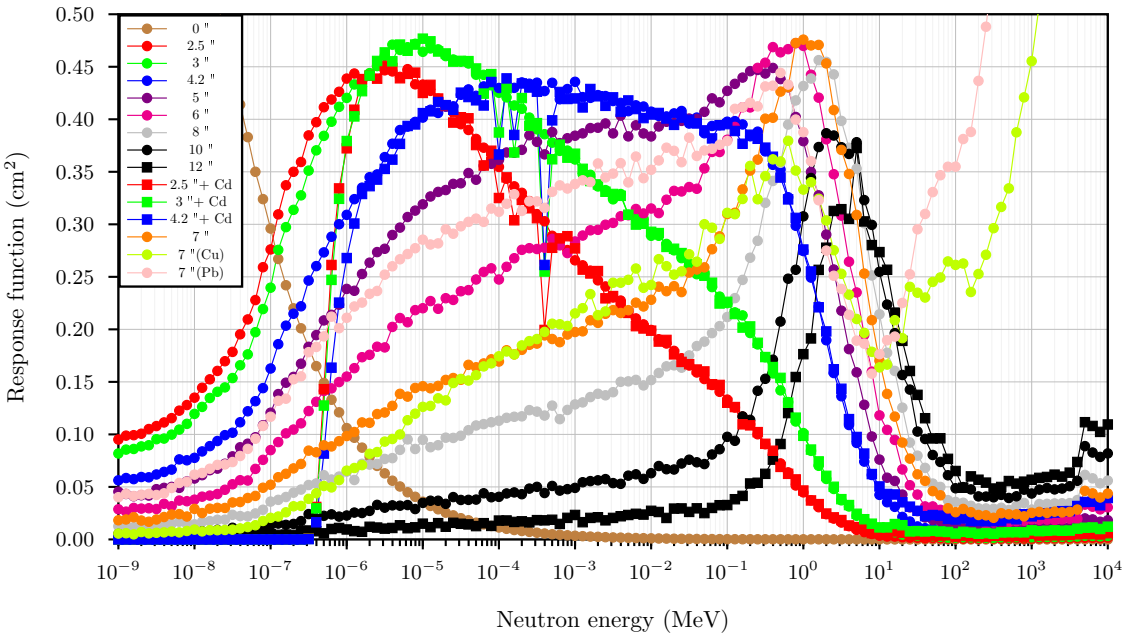

Figure 4.46: Response functions for the active BSS-UAB. Up to 14 detector configurations are used, which are described in Table 4.9. The detector configuration in which only the thermal neutron detector is used (0 ") is also shown.

As we stated previously, by increasing the amount of moderating material in front of the thermal neutron detector, we will be able to count neutrons with higher energies but at the same time, a quantity of neutrons will be lost since they can be absorbed in the moderator itself or they can be deflected by the moderator so the moderated neutron never reaches the active volume of the detector. This fact is explicitly seen, for instance, from the change of the shape of the response functions from the configuration 10 " to 12 " in Figure 4.46.

The detector configurations containing Cd shells exhibit the so-called as the cadmium cutoff [Knoll, 2010] which consists in having no response in the detector configuration for those neutrons with energies lower than 0.5 eV. This can be understood by observing the radiative captures cross sections of Cd. ^{NAT}Cd element contain the *stable* isotopes of ^{114}Cd (28.73 %), ^{112}Cd (24.13 %), ^{111}Cd (12.80 %), ^{110}Cd (12.49 %), ^{113}Cd (12.22 %), ^{116}Cd (7.49 %), ^{106}Cd (1.25 %) and ^{108}Cd (0.89 %). Nuclear cross section depends strongly on the isotope. For instance, in Figure 4.47 we find reactions cross sections for ^{112}Cd, by comparing with H (Figure 2.24) we see that radiative capture in ^{112}Cd is around 5 times the radiative capture in H. However if we examine the radiative capture cross section of ^{NAT}Cd and, in particular, for ^{113}Cd (12.22 %), see Figure 4.48, we see that ^{NAT}Cd, due to the isotope ^{113}Cd (12.22 %), is exhibiting a radiative capture cross section around 10^3 b in respect to, for instance, H. These high values in the radiative capture cross section give rise to the observed cadmium cutoff in the response functions of those detector configurations containing Cd. The detector configurations with Cd shells also express an abrupt valley in the response functions between 10^{-4} and 10^{-3} MeV due to the cross section resonances (see the resonances in Figures 4.47 and 4.48).

The outgoing photons from the radiative capture, for instance in ^{114}Cd (28.73 %) and ^{112}Cd (24.13 %) are shown in Figure 4.49, respectively. Additional information of the outgoing photons for certain elements can be found in Reedy et al. [2002].

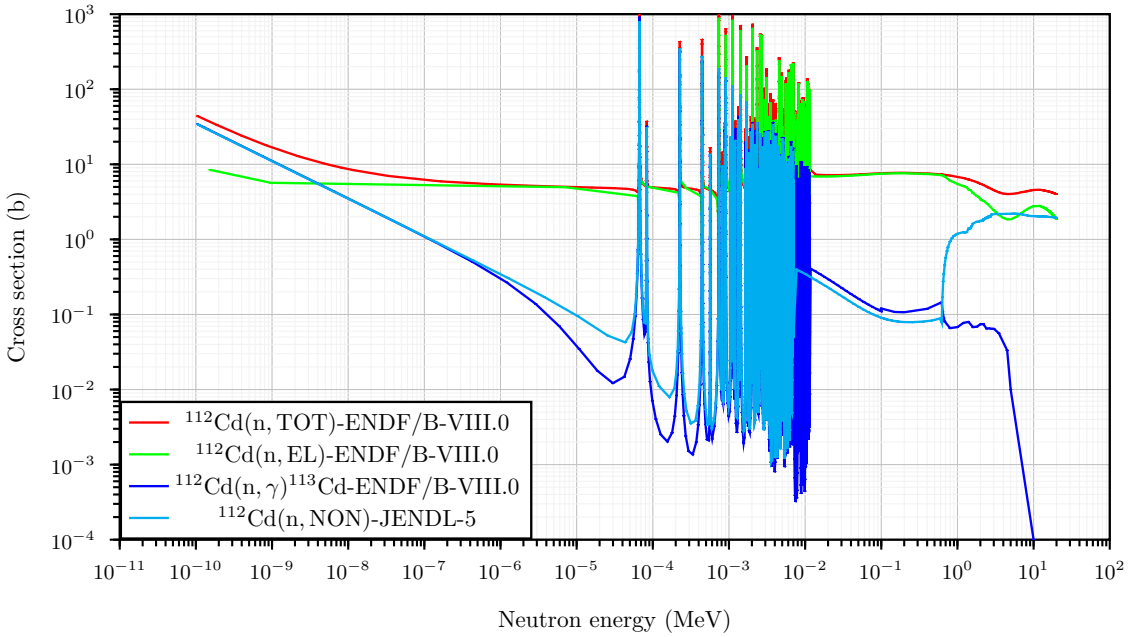

Figure 4.47: Total neutron cross sections and specific cross sections for ^{112}Cd. Notice the dominance of the radiative capture nuclear reaction.

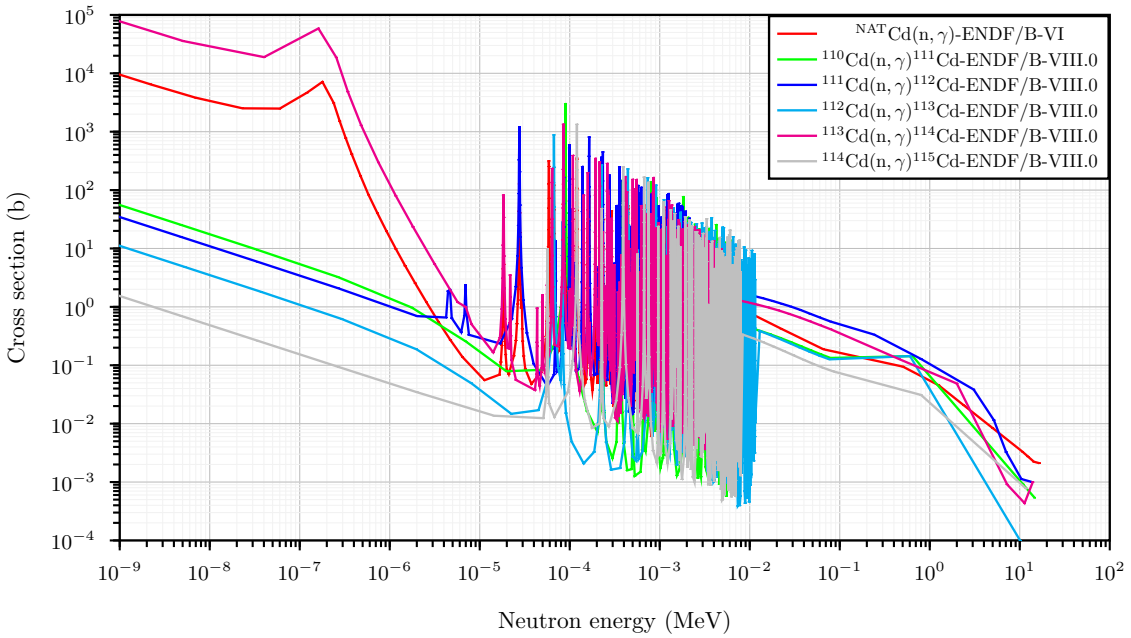

Figure 4.48: Radiative neutron capture cross sections for the Cd element, that is to say, for ^{NAT}Cd and some specific and relevant isotopes. Notice the difference in the cross sections between different isotopes of the same element. Enrichment of materials in specific isotopes can be very relevant.

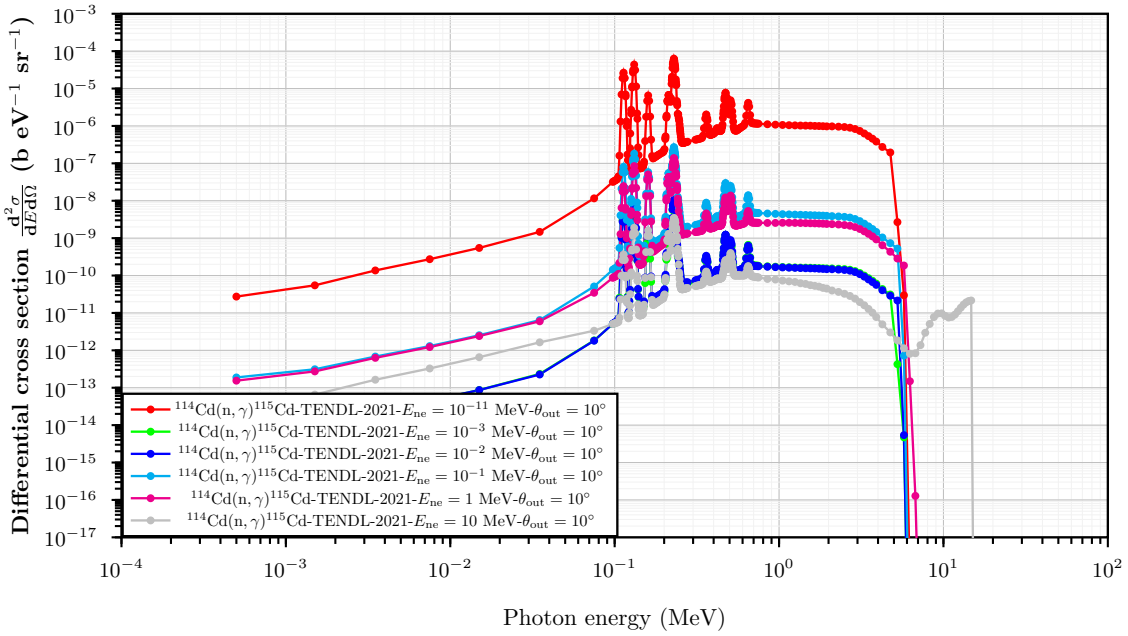

Figure 4.49: Differential cross sections related to the outgoing energy distribution of the photons generated by radiative neutron capture in the dominant isotope ^{114}Cd according to the specific neutron energy in which the reaction is produced and by observing these photons at a fixed outgoing angle of 10°.

The working principles of the high energy spheres (7 " (Cu) and 7 " (Pb)) is to use the spallation reactions (n,xn) available in high energy regimes to produce, from high enery neutrons, fast or epithermal neutrons that can be effectively moderated with a reasonable amount of moderating material. Indeed, these statements can be verified by observing the differential cross section that informs about the outgoing energy distribution of the neutrons after the spallation process, see the case of ^{208}Pb in Figures 4.51 and 4.52.

Response function of the detector configuration of 7 " (Pb) is higher than that from 7 " (Cu) in the energies from 10 MeV because cross sections to have spallation reactions are higher in Pb, as can be verified by observing Figure 4.50.

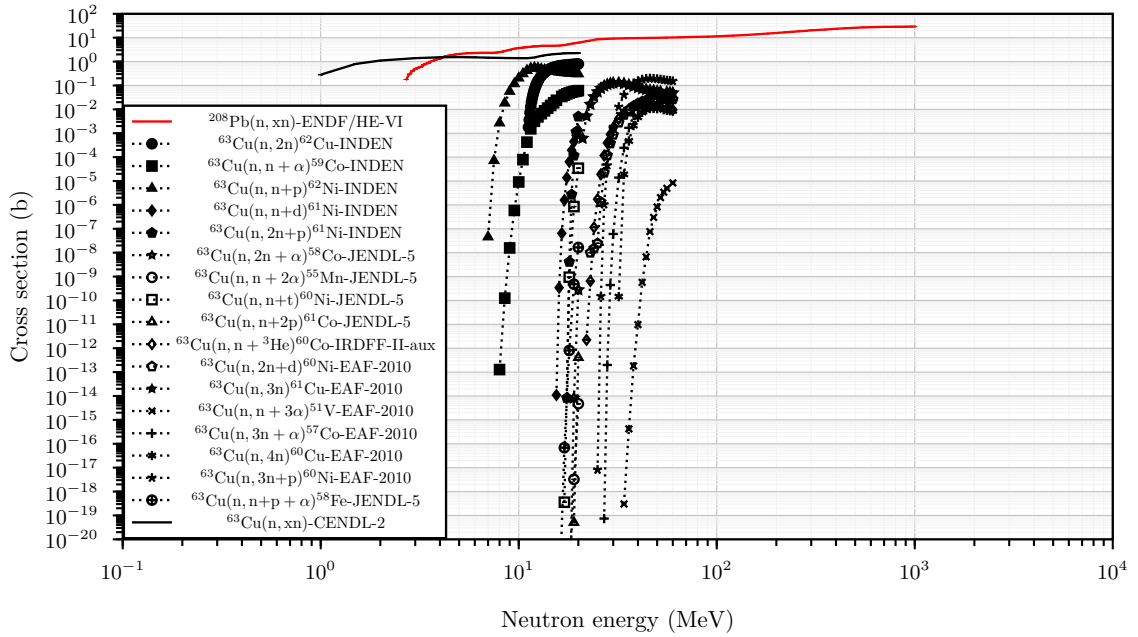

Figure 4.50: Neutron cross section for the production of spallation reactions (n,xn) for ^{208}Pb and and ^{63}Cu. For the case of ^{208}Pb specific spallation reactions are shown. Notice that from around 4 MeV the (n,xn) reactions are more important in ^{208}Pb than in ^{63}Cu.

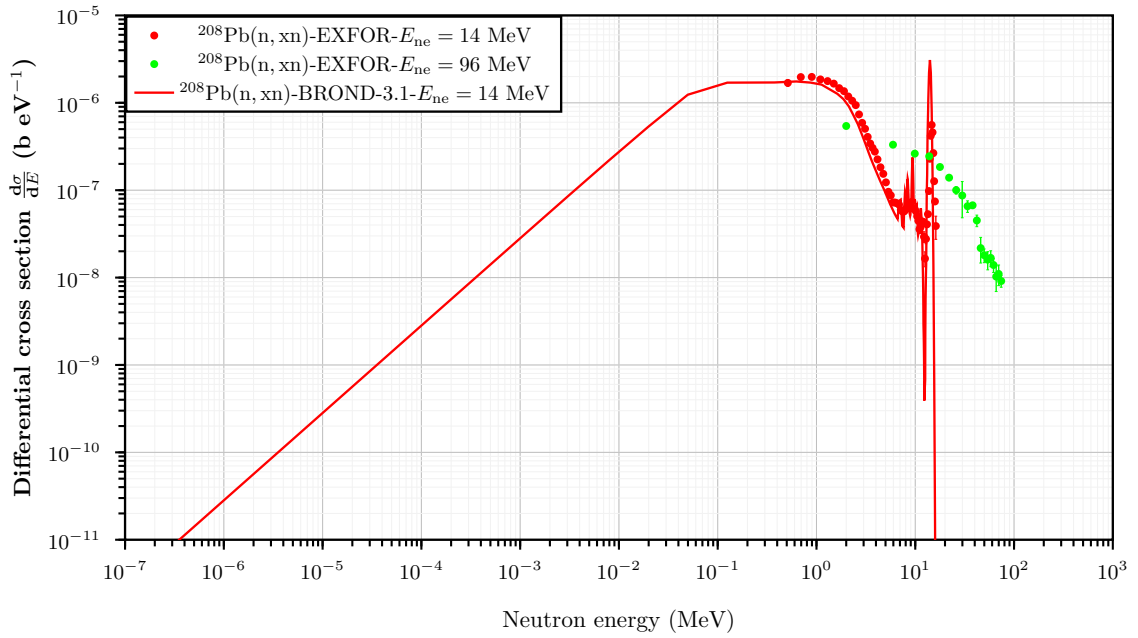

Figure 4.51: Differential cross sections related to the outgoing energy distribution of the neutrons generated by spallation reactions (n,xn) in isotope ^{208}Pb according to the energy of the incident neutrons. In red is shown the case for incident neutrons of energy 14 MeV while in green is shown the case for incident neutrons of energy 96 MeV. See Simakov et al. [1990] and Sagrado García et al. [2011].

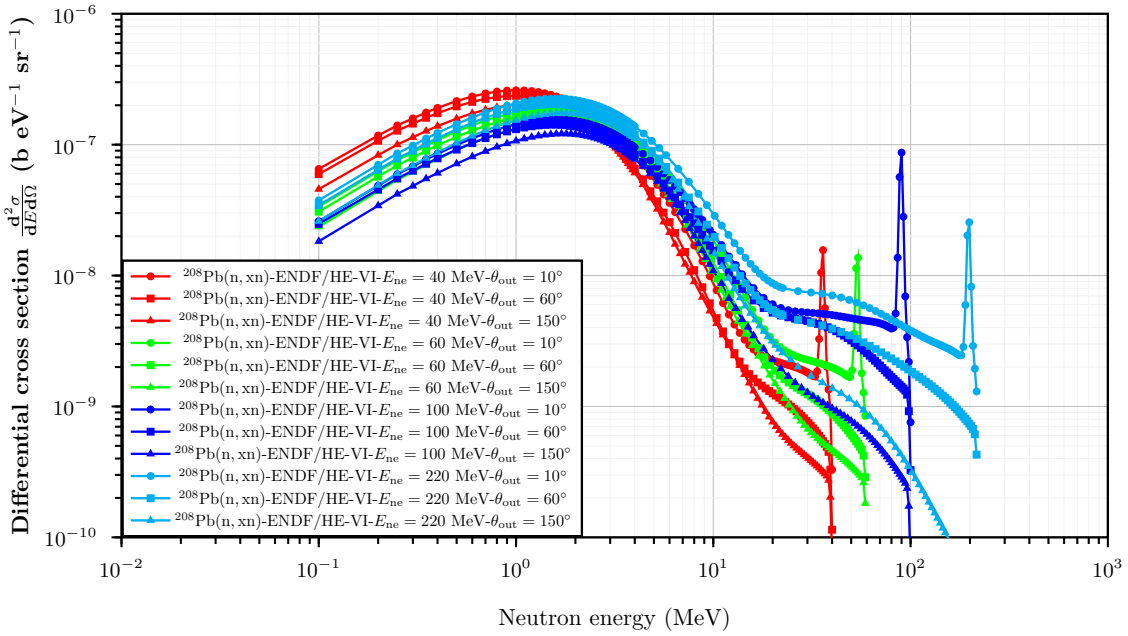

Figure 4.52: Differential cross sections related to the outgoing energy distribution of the neutrons generated by spallation reactions (n,xn) in isotope ^{208}Pb according to the energy of the incident neutrons. See the legend to know the energy of the incident neutrons and the exit angle in which the differential cross section is valid.

One could wonder if other interactions or reactions different from ^{3}He(n,p)^{3}H could contribute to a pulse or count in the proportional counter. This can be analysed from both the MC point of view and the experimental point of view. In Figure 4.53 we see some relevant reaction cross sections for ^{3}He. We see that reaction ^{3}He(n,p)^{3}H is the dominant one for neutron energies below 10^{-2} MeV, however, at neutron energy 10 MeV the dominant reaction is the elastic interaction, followed by ^{3}He(n,p)^{3}H and ^{3}He(n,d)^{2}H. So if, for instance, any neutron of 10 MeV reaches the active volume of the proportional counter of ^{3}He, it could produce a pulse due to the recoil of ^{3}He (elastic interaction), a pulse due to ^{3}He(n,p)^{3}H or a pulse due to ^{3}He(n,d)^{2}H. The previous facts should be included in the MC computation of the response functions.

Photonuclear reactions in ^{3}He are also possible from incident photons of energies over 6 MeV, see cross sections in Figure 4.54. The outgoing energy distributions of charged particles are shown in Figure 4.55.

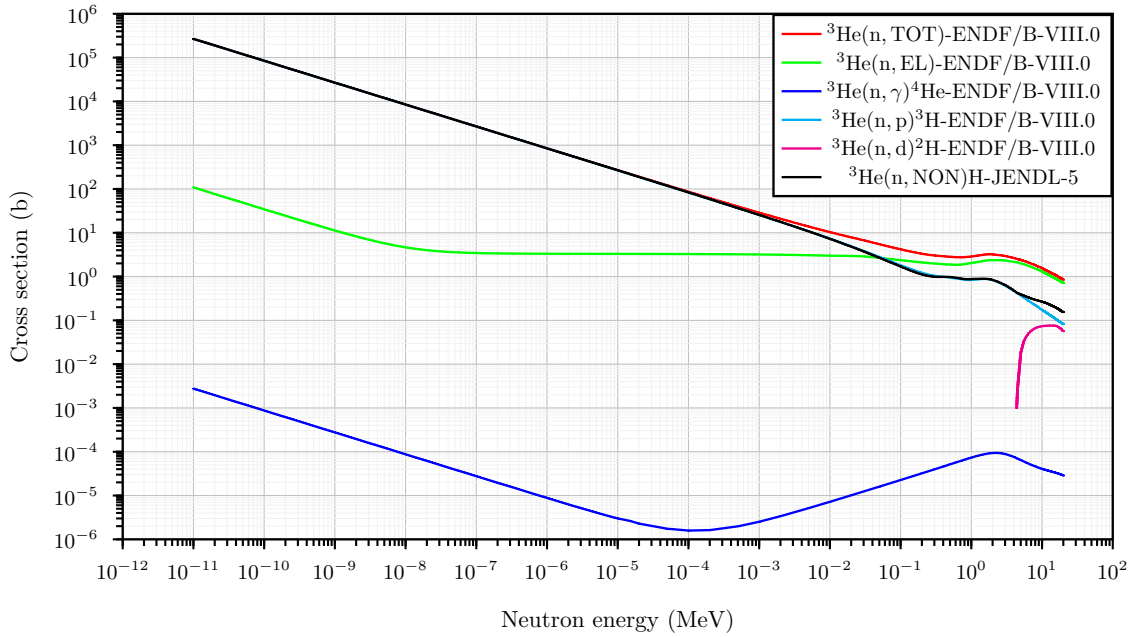

Figure 4.53: Total neutron cross sections and specific cross sections for ^{3}He. Notice how the dominance and importance of the reactions ^{3}He(n,p)^{3}H, ^{3}He(n,EL)^{3}He and ^{3}He(n,d)^{2}H changes according to the energy of the incident neutrons.

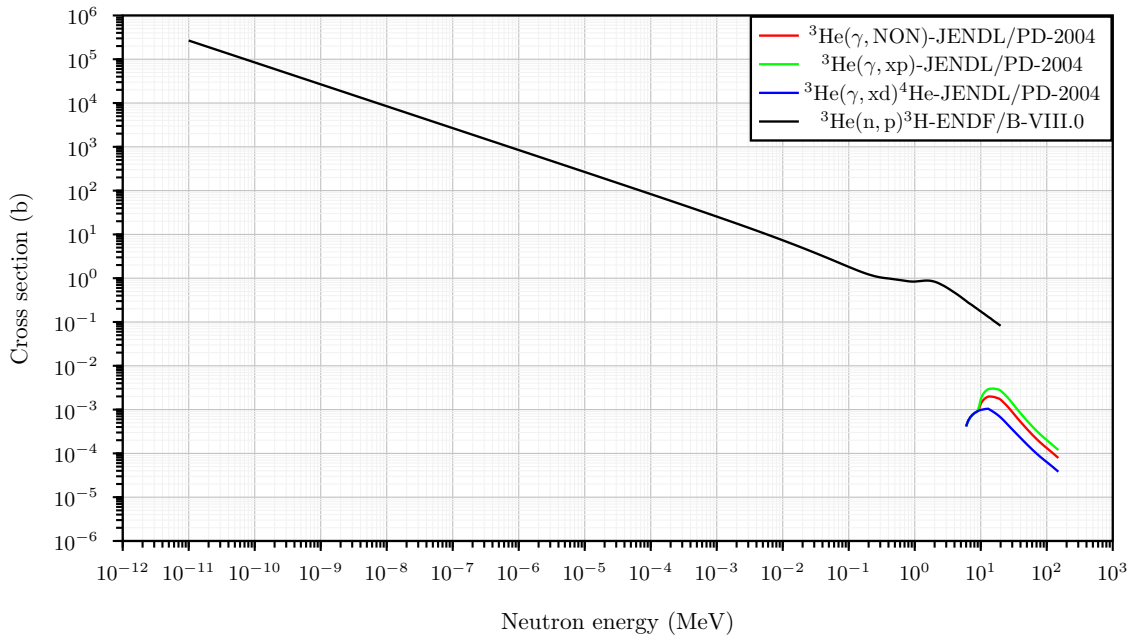

Figure 4.54: Comparison between the main reaction ^{3}He(n,p)^{3}H and the photonuclear reactions in ^{3}He.

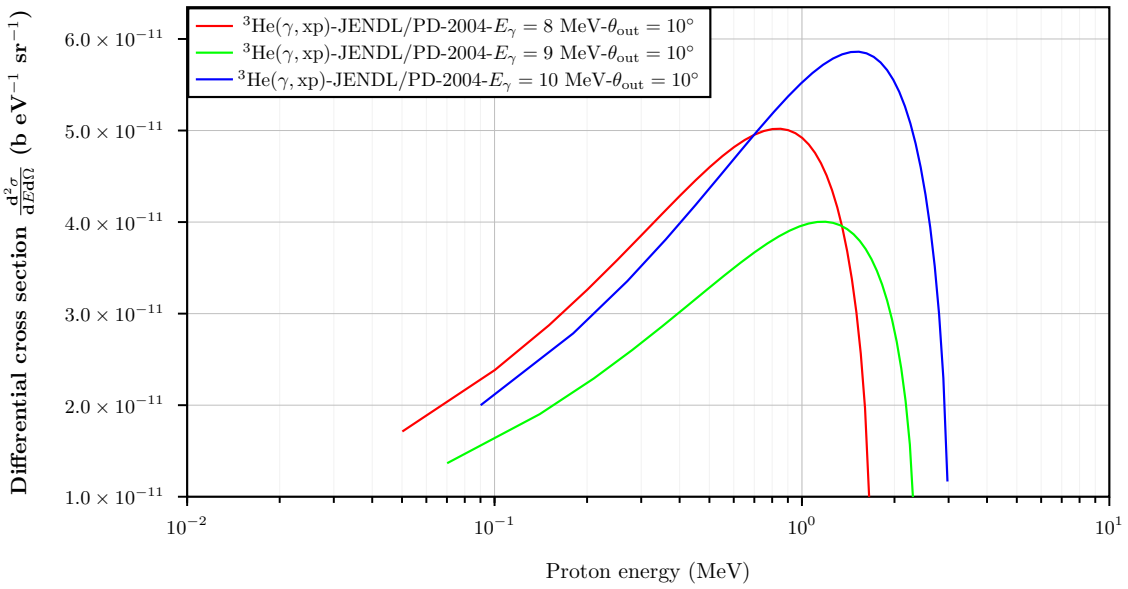

Figure 4.55: Differential cross sections related to the outgoing energy distribution of the charged particles generated by photonuclear reactions in isotope ^{3}He according to the energy of the incident photons. See the legend to know the energy of the incident photons and the exit angle in which the differential cross section is valid.

Probably, the contribution of reactions different from ^{3}He(n,p)^{3}H (^{3}He(n,EL)^{3}He, ^{3}He(n,d)^{2}H and photonuclear reactions in ^{3}He) is not relevant or is covered by experimental uncertainties or the general calibration factor, f (see Appendix D), however, strictly speaking, this should be proved by MC simulations. I would suggest to do a full MC simulation including the previous reactions and to perform a MC simulation of each detector configuration scoring the pulse height distribution in the active volume of the detector.

4.5.2 Passive neutron spectrometry in UAB

Passive neutron spectrometry related to UAB can be traced back to the fundamental works of Amgarou et al. [2007], Fernández et al. [2007], Amgarou et al. [2009], García-Fusté [2010] and Amgarou et al. [2010] so only a summary of relevant details will be given in the present work.

Passive neutron spectrometry at UAB is performed by substituting the thermal neutron detector based on the ^{3}He proportional counter, explained previously, by disc foils of ^{197}Au with a purity of 99.99 %. They are 0.10 mm thick, with a diameter of 15 mm and, in general, with a mass around 350 mg. Each gold disc has a well characterized mass. They were acquired from Goodfellow [GoodFellow, 2023]. The gold foils are introduced in the middle of the detector configurations with an special cap.

As commented previously and as shown in cross sections from Figure 4.32, the tendencies for the nuclear reactions of ^{3}He(n,p)^{3}H and ^{197}Au(n,γ)^{198}Au are very similar in the thermal regions ($E < 1$ eV) (there is one order of magnitude of difference) so from the point of view of nuclear physics, ^{197}Au is a good candidate to be a thermal neutron detector. In general, the main criteria used to choose ^{197}Au as the material to be activated by thermal neutrons are summarised in Amgarou et al. [2007]:

- The induced radioactivity should involve the emission of gamma rays due to their

penetrating nature and to the possibility of performing subsequent photon spectroscopy.

- High values in the thermal neutron radiative capture cross sections and a dependency with neutron kinetic energy so that $\sigma_{(\mathrm{n},\gamma)}(E) \propto \frac{1}{\sqrt{E}}$.
- The decay scheme, in particular, from its ground state, of the radionuclide product should be simple and well-defined.
- The corresponding half-life should be neither too short nor too high. In particular, the ground state of ^{198}Au has a half-life, $T_{\frac{1}{2}}$, of 2.6943(3) days.
- Very high-purity metallic activated samples with one unique stable isotope or at least with a dominating isotopic concentration are often required to avoid interferences.

It is important to notice that the photons measured by the activation of ^{197}Au are not the ones directly coming from the radiative capture, γ_{RC}, that is to say, we are not measuring the photons coming from the process $^{198}\mathrm{Au}^{*} \rightarrow {}^{198}\mathrm{Au} + \gamma_{\mathrm{RC}}$, which takes place during irradiation. We are measuring the 0.412 MeV photons coming from the process $^{198}\mathrm{Hg}^{*} \rightarrow {}^{198}\mathrm{Hg}$ (Stable) $+ \gamma$ where $^{198}\mathrm{Hg}^{*}$ has been produced by the β^{-} decay $^{198}\mathrm{Au} \rightarrow {}^{198}\mathrm{Hg}^{*} + \mathrm{e}^{-} + \bar{\nu}_{\mathrm{e}}$ which has a half-life, $T_{\frac{1}{2}}$, of 2.6943(3) days. See Figure 4.57.

In Tables 4.10 and 4.11 we find the energy and intensities of the gamma and X-ray photon radiations, respectively, due to the β^{-} decay of the ^{198}Au.

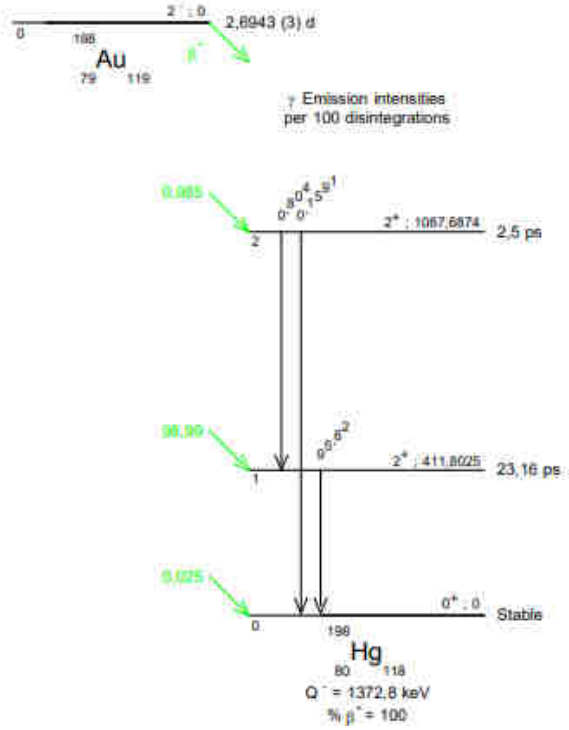

Figure 4.56: β^{-} decay scheme of ^{198}Au (ground state).

Table 4.10: Relevant γ emission energies and intensities associated to β^- from ^{198}Au decay.

Transition	Energy (MeV)	Intensity (photons per 100 disintegrations)
$\gamma_{1,0}(^{198}\mathrm{Hg})$	**0.412**	**95.62**
$\gamma_{2,1}(^{198}\mathrm{Hg})$	0.676	0.804
$\gamma_{2,0}(^{198}\mathrm{Hg})$	1.088	0.159

Table 4.11: Relevant X-Ray emission energies and intensities associated to β^- from ^{198}Au decay.

Transition	Energy (KeV)	Intensity (photons per 100 disintegrations)
L (Hg)	8.7226-14.2672	1.203 (22)
Kα_2 (Hg)	68.895	0.807 (15)
Kα_1 (Hg)	70.82	1.369 (24)
Kβ_3 (Hg)	79.823	
Kβ_1 (Hg)	80.254	0.465(11)
Kβ_5'' (Hg)	80.762	
Kβ_2 (Hg)	82.435	
Kβ_4 (Hg)	82.776	0.136(4)
KO$_{2,3}$ (Hg)	83.028	

It is then clear that the radioactivity induced in ^{197}Au (due to the presence of an energy distribution of the neutron fluence in the location of the gold foil) can be quantified through the measurement of the photons of energy 0.412 MeV, which is the most probable energy emitted as a final consequence of the β^- decay, according to Table 4.10.

By the definition of reaction cross section, the rate in which ^{198}Au isotopes are produced (in the location of the gold foil, that will be usually in the center of a detector configuration) or the number of reactions produced through the radiative capture of the neutron, ^{197}Au(n,γ)^{198}Au, by neutrons of energy E reaching the gold foil, with a fluence rate, $\mathrm{d}\dot{\Phi}^{\mathrm{in}}(E)$, is

$$\mathrm{d}\dot{N}_{^{197}\mathrm{Au}\rightarrow{}^{198}\mathrm{Au}}(E) = N_{\mathrm{Foil}}\cdot\sigma_{^{197}\mathrm{Au}\rightarrow{}^{198}\mathrm{Au}}(E)\cdot\mathrm{d}\dot{\Phi}^{\mathrm{in}}(E), \tag{4.34}$$

where N_{Foil} are the number of targets, ^{197}Au isotopes, illuminated by the neutron field $\mathrm{d}\dot{\Phi}^{\mathrm{in}}(E)$ and $\sigma_{^{197}\mathrm{Au}\rightarrow{}^{198}\mathrm{Au}}(E)\equiv\sigma_{^{197}\mathrm{Au(n,\gamma)}^{198}\mathrm{Au}}(E)$, see Figure 4.32. Is important to insist that $\mathrm{d}\dot{\Phi}^{\mathrm{in}}(E)$ are those neutrons reaching the thermal neutron detector placed inside and in the center of a detector configuration, which are not the neutrons reaching externally the whole detector configuration $\mathrm{d}\dot{\Phi}(E)$ in which the definition of the response function is built (see Section 4.1).

According to the shape and values of $\sigma_{^{197}\mathrm{Au}\rightarrow{}^{198}\mathrm{Au}}(E)$ a whole energy distribution of the neutron fluence reaching the gold foil will be able to produce the reaction ^{197}Au(n,γ)^{198}Au, so actually Equation 4.34 can be integrated so that

$$\begin{aligned}\dot{N}_{^{197}\mathrm{Au}\rightarrow{}^{198}\mathrm{Au}} &= \int_E N_{\mathrm{Foil}}\cdot\sigma_{^{197}\mathrm{Au}\rightarrow{}^{198}\mathrm{Au}}(E)\cdot\mathrm{d}\dot{\Phi}^{\mathrm{in}}(E),\\ &= N_{\mathrm{Foil}}\int_E\sigma_{^{197}\mathrm{Au}\rightarrow{}^{198}\mathrm{Au}}(E)\cdot\dot{\Phi}^{\mathrm{in}}_E(E)\mathrm{d}E.\end{aligned} \tag{4.35}$$

As seen, ^{198}Au isotopes are produced on one hand by the nuclear reaction ^{197}Au(n,γ)^{198}Au but, on the other hand, the decay $^{198}\mathrm{Au}\rightarrow{}^{198}\mathrm{Hg}^*+\mathrm{e}^-+\bar{\nu}_{\mathrm{e}^-}$ exists, giving rise to an equation describing the temporal evolution of the presence of ^{198}Au isotopes in the gold foil

$$\begin{aligned}\frac{\mathrm{d}N_{^{198}\mathrm{Au}}(t)}{\mathrm{d}t} &= +\dot{N}_{^{197}\mathrm{Au}\rightarrow{}^{198}\mathrm{Au}}-\dot{N}_{^{198}\mathrm{Au}\rightarrow{}^{198}\mathrm{Hg}}(t),\\ &= +\dot{N}_{^{197}\mathrm{Au}\rightarrow{}^{198}\mathrm{Au}}-\lambda_{^{198}\mathrm{Au}\rightarrow{}^{198}\mathrm{Hg}}\cdot N_{^{198}\mathrm{Au}}(t).\end{aligned} \tag{4.36}$$

It is important to notice that the temporal dependency, t, is not shown in Equations (4.34) and (4.35) as we are under the approximation that the energy distribution of the neutron fluence $\dot{\Phi}^{\mathrm{in}}_E(E)$ is a time constant during the time in which the gold foil is irradiated. Our detector system has not the capability of seeing differences in time. If the neutron field is actually evolving in time, our final results on the $\dot{\Phi}^{\mathrm{in}}_E(E)$ have to be considered as averaged

results.

The solution for Equation (4.36) is

$$\underbrace{\lambda_{^{198}\mathrm{Au}\rightarrow{}^{198}\mathrm{Hg}}\cdot N_{^{198}\mathrm{Au}}(t)}_{A_{^{198}\mathrm{Au}\rightarrow{}^{198}\mathrm{Hg}}(t)}=\dot{N}_{^{197}\mathrm{Au}\rightarrow{}^{198}\mathrm{Au}}\left(1-\mathrm{e}^{-\lambda_{^{198}\mathrm{Au}\rightarrow{}^{198}\mathrm{Hg}}\cdot t}\right). \tag{4.37}$$

Keep in mind that Equations (4.36) and (4.37) are valid only when the Au foil is being irradiated under an energy distribution of the neutron fluence. This means that time t in Equation (4.37) is understood as the total time elapsed since irradiation started. Therefore, during the irradiation of the Au foil, there will be a net increment of the number of ^{198}Au nuclei (and its related radioactivity measurable with the 0.412 MeV photons) according to Equation (4.37) and its related representation Figure 4.57.

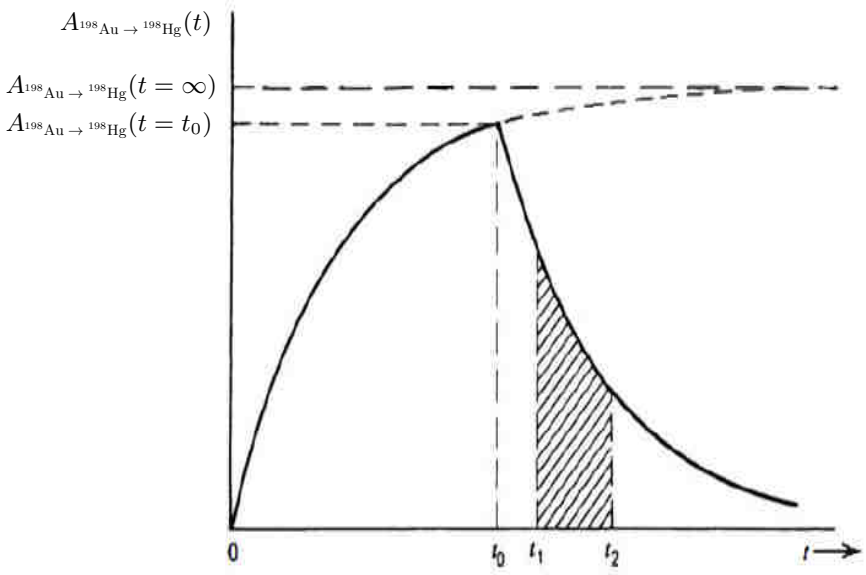

Figure 4.57: The neutron irradiation of the Au foil ($^{197}Au \rightarrow {}^{198}Au$) lasts from $t = 0$ to $t = t_0$. A time $t_1 - t_0$ elapses between the finished neutron irradiation and the beginning of the gamma measurement of the radioactivity induced in the Au foil irradiation. The measurement of the gamma radioactivity ($^{198}Au \rightarrow {}^{198}Hg^* + e^- + \bar{\nu}_{e^-}$, $^{198}Hg^* \rightarrow {}^{198}Hg$ (Stable) $+ \gamma$) lasts a time $t_2 - t_1$. Adapted from Knoll [2010].

From Equation (4.37) can be seen that if the Au foil is irradiated a long time, it is obtained

$$\underbrace{\lambda_{^{198}\mathrm{Au}\rightarrow{}^{198}\mathrm{Hg}}\cdot N_{^{198}\mathrm{Au}}(t=\infty)}_{A_{^{198}\mathrm{Au}\rightarrow{}^{198}\mathrm{Hg}}(t=\infty)}=\dot{N}_{^{197}\mathrm{Au}\rightarrow{}^{198}\mathrm{Au}}\equiv \text{ Saturation activity.} \tag{4.38}$$

Let us now imagine that the gold foil, placed in the center of some detector configuration, is immersed in a neutron field during a total time t_0. The net number of produced ^{198}Au nuclei at that time and its related gamma radioactivity are then $N_{^{198}\mathrm{Au}}(t=t_0)$ and $A_{^{198}\mathrm{Au}\rightarrow{}^{198}\mathrm{Hg}}(t=t_0)$, respectively. So one could find $\dot{N}_{^{197}\mathrm{Au}\rightarrow{}^{198}\mathrm{Au}}$ by Equation (4.37) so that

$$\dot{N}_{^{197}\mathrm{Au}\rightarrow{}^{198}\mathrm{Au}}=\frac{A_{^{198}\mathrm{Au}\rightarrow{}^{198}\mathrm{Hg}}(t=t_0)}{\left(1-\mathrm{e}^{-\lambda_{^{198}\mathrm{Au}\rightarrow{}^{198}\mathrm{Hg}}\cdot t_0}\right)}. \tag{4.39}$$

After the neutron irradiation, when the first term of the right side of the Equation (4.36)

is not present, the solution is the conventional radioactivity decay law. Therefore, the induced radioactivity in the gold foil will decay as

$$A_{^{198}\mathrm{Au}\rightarrow{}^{198}\mathrm{Hg}}(t) = A_{^{198}\mathrm{Au}\rightarrow{}^{198}\mathrm{Hg}}(t=t_0)\cdot \mathrm{e}^{-\lambda_{^{198}\mathrm{Au}\rightarrow{}^{198}\mathrm{Hg}}\cdot(t-t_0)} \qquad (t>t_0). \tag{4.40}$$

The instantaneous activity at t can be ideally measured with photon spectroscopy so that:

$$A_{^{198}\mathrm{Au}\rightarrow{}^{198}\mathrm{Hg}}(t) = \frac{1}{q\cdot\epsilon_{\mathrm{abs}}}\frac{\mathrm{d}C(t)}{\mathrm{d}t}. \tag{4.41}$$

Where $\mathrm{d}C$ are the net counts under the peak corresponding to photons of 0.412 MeV measured by a photon spectrometer. ϵ_{abs} is the absolute efficiency in the conditions in which the measurement (with the photon spectrometer) is done in this work and $q = 0.9562$ takes into account that the radioactivity of the sample produces other gammas different from the one with 0.412 MeV.

By substituting Equation 4.41 in Equation 4.40 and integrating in times from t_1 to t_2 we can find a relationship between $A_{^{198}\mathrm{Au}\rightarrow{}^{198}\mathrm{Hg}}(t=t_0)$ and the measured counts (from t_1 to t_2), C, with the photon spectrometer:

$$A_{^{198}\mathrm{Au}\rightarrow{}^{198}\mathrm{Hg}}(t=t_0) = \frac{\lambda_{^{198}\mathrm{Au}\rightarrow{}^{198}\mathrm{Hg}}\cdot C}{q\,\epsilon_{\mathrm{abs}}\left(\mathrm{e}^{-\lambda_{^{198}\mathrm{Au}\rightarrow{}^{198}\mathrm{Hg}}\cdot(t_1-t_0)}-\mathrm{e}^{-\lambda_{^{198}\mathrm{Au}\rightarrow{}^{198}\mathrm{Hg}}\cdot(t_2-t_0)}\right)}. \tag{4.42}$$

If we substitute Equation (4.42) in Equation (4.39), we find:

$$\dot{N}_{^{197}\mathrm{Au}\rightarrow{}^{198}\mathrm{Au}} = \frac{\lambda_{^{198}\mathrm{Au}\rightarrow{}^{198}\mathrm{Hg}}\cdot C}{q\,\epsilon_{\mathrm{abs}}\left(1-\mathrm{e}^{-\lambda_{^{198}\mathrm{Au}\rightarrow{}^{198}\mathrm{Hg}}\cdot t_0}\right)\left(\mathrm{e}^{-\lambda_{^{198}\mathrm{Au}\rightarrow{}^{198}\mathrm{Hg}}\cdot(t_1-t_0)}-\mathrm{e}^{-\lambda_{^{198}\mathrm{Au}\rightarrow{}^{198}\mathrm{Hg}}\cdot(t_2-t_0)}\right)}. \tag{4.43}$$

By multiplying the numerator and denominator by the quantity $(t_2-t_1)\,\mathrm{e}^{+\lambda_{^{198}\mathrm{Au}\rightarrow{}^{198}\mathrm{Hg}}\cdot(t_1-t_0)}$ in Equation (4.43) we find:

$$\dot{N}_{^{197}\mathrm{Au}\rightarrow{}^{198}\mathrm{Au}} = \frac{(t_2-t_1)\cdot\lambda_{^{198}\mathrm{Au}\rightarrow{}^{198}\mathrm{Hg}}\cdot\dot{C}\cdot\mathrm{e}^{+\lambda_{^{198}\mathrm{Au}\rightarrow{}^{198}\mathrm{Hg}}\cdot(t_1-t_0)}}{q\cdot\epsilon_{\mathrm{abs}}\cdot\left(1-\mathrm{e}^{-\lambda_{^{198}\mathrm{Au}\rightarrow{}^{198}\mathrm{Hg}}\cdot t_0}\right)\cdot\left(1-\mathrm{e}^{-\lambda_{^{198}\mathrm{Au}\rightarrow{}^{198}\mathrm{Hg}}\cdot(t_2-t_1)}\right)}. \tag{4.44}$$

If we divide Equation (4.45) by the mass, m, of the particular gold foil we obtain:

$$\frac{\dot{N}_{^{197}\mathrm{Au}\rightarrow{}^{198}\mathrm{Au}}}{m} = \frac{(t_2-t_1)\cdot\lambda_{^{198}\mathrm{Au}\rightarrow{}^{198}\mathrm{Hg}}\cdot\dot{C}\cdot\mathrm{e}^{+\lambda_{^{198}\mathrm{Au}\rightarrow{}^{198}\mathrm{Hg}}\cdot(t_1-t_0)}}{m\cdot q\cdot\epsilon_{\mathrm{abs}}\cdot\left(1-\mathrm{e}^{-\lambda_{^{198}\mathrm{Au}\rightarrow{}^{198}\mathrm{Hg}}\cdot t_0}\right)\cdot\left(1-\mathrm{e}^{-\lambda_{^{198}\mathrm{Au}\rightarrow{}^{198}\mathrm{Hg}}\cdot(t_2-t_1)}\right)} \equiv A_\infty. \tag{4.45}$$

So that a direct relationship between the count rate $\dot{C}$ and the saturation activity A_∞ is found.

The response functions to neutrons (in terms of fluence rate and mass of the gold foils) of the passive Bonner Sphere System from UAB, in units of $\mathrm{cm}^2\ \mathrm{mg}^{-1}$, are shown in Figure 4.58. The response of this system is $\frac{\dot{N}_{^{197}\mathrm{Au}\rightarrow{}^{198}\mathrm{Au}}}{m} = A_\infty$, with units of $\mathrm{s}^{-1}\ \mathrm{mg}^{-1}$.

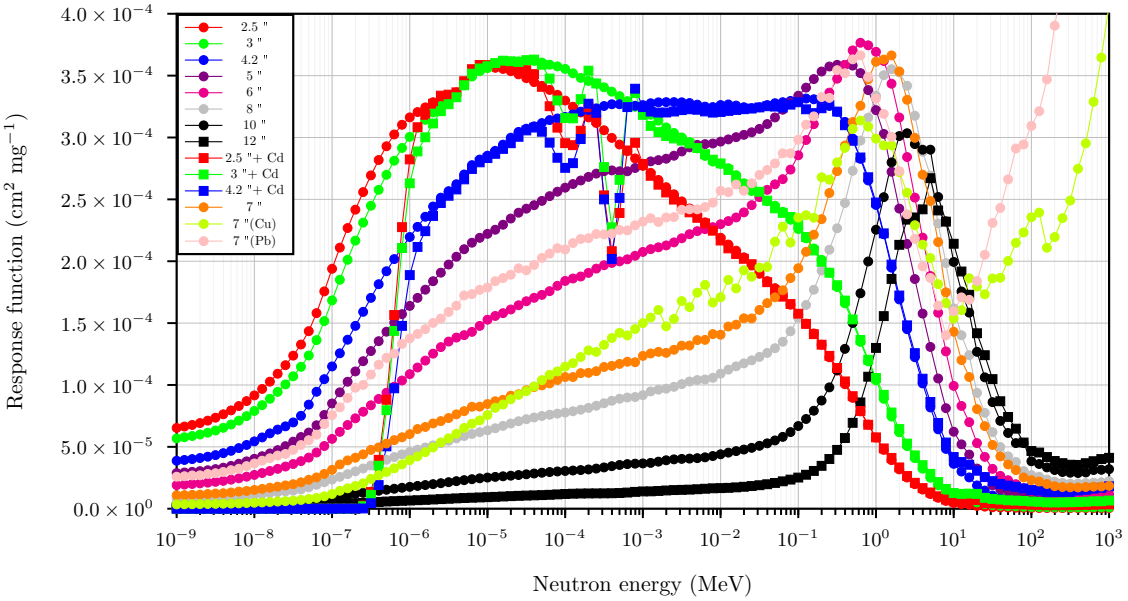

Figure 4.58: Response functions for the passive BSS-UAB. Up to 14 detector configurations are used, which are described in Table 4.9.

The shape of the response functions of the passive BSS, Figure 4.58, and the ones from the active BSS, Figure 4.46, are very similar since the detector configurations, see Table 4.9, are the same with the exception of the thermal neutron detector used. Thus we can say that the shape of these two response functions are dominated by the moderating material and the special shells used rather than by the thermal neutron detector itself. This can be also justified by the fact that cross sections of the main reactions ^{197}Au(n,γ)^{198}Au (passive BSS) and ^{3}He(n,p)^{3}H (active BSS) have the same shape in the thermal region ($E < 1$ eV), see Figure 4.32.

Figure 4.59 shows the cross section for the main reaction ^{197}Au(n,γ)^{198}Au and the reaction ^{197}Au(γ,n)^{196}Au, which is, actually, very dominant in the energy range from around 10 MeV to 20 MeV for mixed radiation fields of photons and neutrons. Notice that σ $_{^{197}\mathrm{Au}(\gamma,\mathrm{n})^{196}\mathrm{Au}}$ (10 MeV $< E <$ 20 MeV) $\gtrsim 10^2 \cdot \sigma$ $_{^{197}\mathrm{Au}(\mathrm{n},\gamma)^{198}\mathrm{Au}}$ (10 MeV $< E <$ 20 MeV). In Figure 4.60 we find the differential cross section of the photoneutron emission due to the process ^{197}Au(γ,n)^{196}Au.

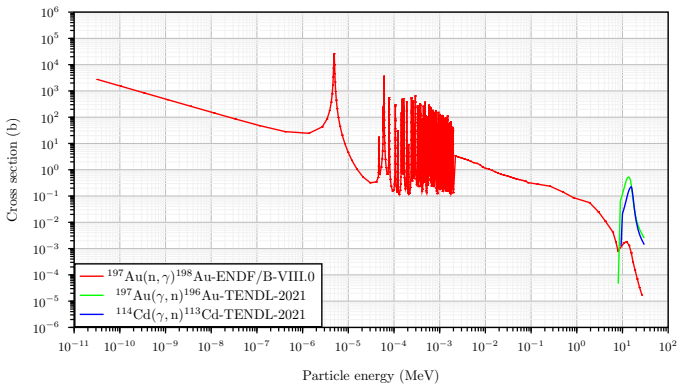

Figure 4.59: Cross section for the reactions $^{197}Au(n,\gamma)^{198}Au$, $^{197}Au(\gamma,n)^{196}Au$ and $^{114}Cd(ph,n)^{113}Cd$.

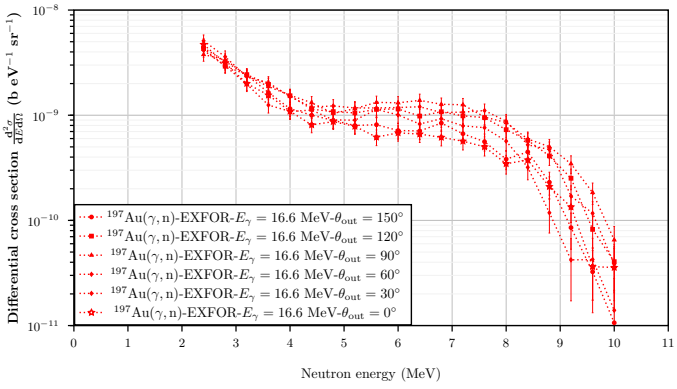

Figure 4.60: Differential cross section related to the energy distribution of the photoneutrons emitted due to the reaction $^{197}Au(\gamma,n)^{196}Au$.

The presence of the isotope ^{196}Au, $T_{\frac{1}{2}} = 6.1669(6)$ d, in the gold foil contributes with gamma emission, see Tables 4.12 and 4.13, due to the decays $^{196}\mathrm{Au} \rightarrow {}^{196}\mathrm{Pt}^* + \mathrm{e}^+ + \nu_\mathrm{e}$ (and electronic capture) with a branch ratio of 93 % and $^{196}\mathrm{Au} \rightarrow {}^{196}\mathrm{Hg}^* + \mathrm{e}^- + \bar{\nu}_\mathrm{e}$ with a branch ratio of 7 %.

Table 4.12: Relevant γ emission energies and intensities associated to EC and β^+ decay (93 %) from ^{196}Au.

Transition	Energy (MeV)	Intensity (photons per 100 disintegrations)
$\gamma(^{196}\mathrm{Pt})$	**0.35573(5)**	**87(3)**
$\gamma(^{196}\mathrm{Pt})$	0.33303(5)	22.9(9)

Table 4.13: Relevant γ emission energies and intensities associated to β^- decay (7 %) from ^{196}Au.

Transition	Energy (MeV)	Intensity (photons per 100 disintegrations)
$\gamma(^{196}\mathrm{Hg})$	0.42610(8)	6.6(3)

Gamma emission associated to ^{196}Au can then contaminate the measurement of the 0.412 MeV photons associated to ^{196}Au. When necessary, a method of peak separation such as a multi-Gaussian fit of the measured pulse height distribution [García-Fusté, 2010] is applied. In the conditions of this work, it has not been necessary to apply this technique. Alternatively, if a high-resolution pure spectrometer is used (like high-purity germanium (HPGe)) the ^{196}Au and ^{198}Au peaks are clearly separated. We used a high-purity germanium (HPGe) [Knoll, 2010] from ENEA-Frascati.

The measured *absolute peak* efficiency for 0.412 MeV photons coming from a point source in the measurement geometry of the HPGe from ENEA-Frascati is 0.00689846 $\left(\epsilon_{\mathrm{abs,Puntual}}(0.412\ \mathrm{MeV}) = \frac{\text{counts under 0.412 MeV peak}}{\text{number total of photons emitted from a puntual source}}\right)$. The *absolute* efficiency (MCNP calculated) for a point source is 0.0069536 $\left(\epsilon_{\mathrm{abs,Puntual}} = \frac{\text{counts}}{\text{number total of photons emitted from a puntual source}}\right)$ while the *absolute* efficiency (MCNP) for our gold foil is 0.094593 $\left(\epsilon_{\mathrm{abs,Disk}} = \frac{\text{counts}}{\text{number total of photons emitted from the gold foil}}\right)$. ϵ_{abs} for Equation (4.41) will then be computed as

$$\epsilon_{\mathrm{abs,Disk}}(0.412\ \mathrm{MeV}) = \epsilon_{\mathrm{abs,Puntual}}(0.412\ \mathrm{MeV}) \cdot \frac{\epsilon_{\mathrm{abs,Disk}}(\mathrm{MCNP})}{\epsilon_{\mathrm{abs,Puntual}}(\mathrm{MCNP})} = 0.09384291. \tag{4.46}$$

In Figure 4.59 we can also notice that photoneutrons from, for example, ^{114}Cd (^{114}Cd(ph,n)^{113}Cd) are also dominant for incident photons with energies in the energy range from 10 MeV to 20 MeV. In the work of Fernández et al. [2007] it was estimated that the contribution of the photon-induced neutrons generated in the Cd shell to the response was less than 5 %.

4.5.3 Spectrometry equations

Each detector configuration i from a detector system of a given spectrometer (the active UAB-BSS or the passive UAB-BSS) has a response function (in terms of fluence) $R_{\Phi,i}(E)$ so that in a unknown neutron field, $\Phi_E(E)$, the response R_i of each detector configuration i, R_i is related with its own response function as (see Equation (4.8))

$$R_i = \int_E R_{\Phi,i}(E)\,\Phi_E(E)\mathrm{d}E \tag{4.47}$$

$$= \Phi \int_E R_{\Phi,i}(E)\varphi_E(E)\mathrm{d}E. \tag{4.48}$$

In the case we use 14 detector configurations there will be 14 Equations (4.48) ($i = 1, ..., 14$). The unfolding procedure (in our case we use software FRUIT described in Bedogni et al. [2007] and Bedogni [2006]) will be capable of providing both the neutron fluence, Φ, and the unit energy distribution of the neutron fluence, $\varphi_E(E)$. Therefore the energy distribution of the neutron fluence, $\Phi_E(E) = \Phi \cdot \varphi_E(E)$, will be completely characterized.

Therefore, assuming that the neutron field, $\Phi_E(E)$, is reasonably constant (if needed we use a detector configuration in a fixed place to monitor the measurement conditions) a neutron spectrometry experiment essentially consists in

1. Placing each detector configuration i in an exact point where the neutron field exists. Each detector configuration must be placed in the point enough time so that its response (nuclear reactions) is statistically significant. In the end, in case we use 14 detector configurations, we will obtain 14 experimental responses $(R_1, ..., R_{14})$.
2. Using unfolding procedures carefully in order to find the best energy distribution of the neutron field, $\Phi_E^{\text{Best}}(E)$, that describes the real neutron field, $\Phi_E(E)$. Essentially, the unfoling procedures consist in assuming physically possible energy distributions of the neutron fluence (also according to the measurement conditions) and to do the necessary changes in the shape of this energy distribution of the neutron fluence so that the experimental responses $(R_1, ..., R_{14})$ are, overall, well reproduced.

Once the energy distribution of the neutron fluence is known, quantities as the neutron ambient dose equivalent, Equation (3.80), can be computed.

4.6 Specific procedures used in this work

4.6.1 Evaluated neutron dose equivalents in tissue with PADC

By Equation (3.64), the neutron dose equivalent in ICRU tissue is

$$H = \int_E Q(E) k_\Phi(E)\, \Phi_E(E) \mathrm{d}E = \Phi \int_E Q(E) k_\Phi(E) \varphi_E(E) \mathrm{d}E \tag{4.49}$$

$$= \left[\frac{R}{\int_E R_\Phi(E) \varphi_E(E) \mathrm{d}E} \right] \int_E Q(E) k_\Phi(E) \varphi_E(E) \mathrm{d}E \tag{4.50}$$

$$= \frac{R}{\left[\frac{\int_E R_\Phi(E) \varphi_E(E) \mathrm{d}E}{\int_E Q(E) k_\Phi(E) \varphi_E(E) \mathrm{d}E} \right]} \tag{4.51}$$

$$= \frac{R}{\left[\frac{R_{\text{Calibration}}}{H_{\text{Calibration}}} \right]_{\text{MC or BSS}}} \sim \frac{R}{\left[\frac{R_{\text{Calibration}}}{H_{\text{Calibration}}} \right]_{\text{AmBe}}}. \tag{4.52}$$

Where we have introduced Equations (3.4) and (4.8), and Equation like (4.12).

The UAB methodology to compute the evaluated neutron dose equivalent in ICRU tissue consists in using Equation (4.51) where R is the experimental track density measure from the standard configuration based on PADC, Figure 4.26, $R_\Phi(E)$ is the response function

(in terms of fluence) of the standard configuration, Figure 4.27, $\varphi_E(E)$ is the unit energy distribution of the neutron fluence obtained by MC simulations ($\varphi_E(E) = \varphi_E^{\text{MC}}(E)$), $Q(E)$ is the neutron quality factor, Figure 3.4, and $k_\Phi(E)$ is the fluence-to-kerma conversion coefficients for neutrons in ICRU tissue, Figure 3.1. The product $Q(E)k_\Phi(E)$ is shown in Figure 3.5.

By using Equation (4.50), it is implicitly assumed that the energy distribution of the neutron fluence or the evaluated energy distribution of the neutron fluence is $\Phi_E(E) \equiv \Phi_E^{\text{EV}}(E) = \Phi^{\text{CR-39}} \cdot \varphi_E^{\text{MC}}(E)$. Where $\Phi^{\text{CR-39}} \equiv \Phi = \frac{R}{\int_E R_\Phi(E)\varphi_E(E)\mathrm{d}E}$. This energy distribution of the neutron fluence is what gives rise to the evaluated neutron dose equivalent Equation (4.50) ($H \equiv H_{\text{ne}}^{\text{EV}}$).

As the product $Q(E)k_\Phi(E)$ is only known from 10^{-9} to 19.5 MeV [Siebert et al., 1995], an approximation has to be made for higher energies. On one hand, $Q(E)$ is known from 10^{-9} to 19.5 MeV [Siebert et al., 1995]. On the other hand, $k_\Phi(E)$ is known from 10^{-5} to 150 MeV [Chadwick et al., 1999]. For the energy range from 19.5 to 150 MeV, $Q(E)$ was taken from United States Nuclear Regulatory Comission [2023] while $k_\Phi(E)$ was taken from Chadwick et al. [1999]. For the energy range from 150 to 400 MeV, $Q(E)$ was also taken from United States Nuclear Regulatory Comission [2023] while $k_\Phi(E)$ was considered constant and equal to the last numerical value provided by Chadwick et al. [1999], *i.e.,* $k_\Phi(E = 150 \text{ MeV}) = 1.25 \times 10^2$ pGy cm^2. Finally, for the energy range from 400 MeV to the required value, $Q(E)$ was also considered constant and equal to the last numerical value provided by United States Nuclear Regulatory Comission [2023], *i.e.,* $Q(E = 400 \text{ MeV}) = 3.5$.

4.6.2 Experimental energy corrections on calibration coefficients

Let us now imagine the situation in which we have a neutron dosimeter whose response function (in terms of fluence) is known, it could be the case if we own a LB 6411 neutron dosimeter from BERTHOLD [Burgkhardt et al., 1997] [BERTHOLD, 2023] whose response function (in terms of fluence) is shown in Figure 4.61

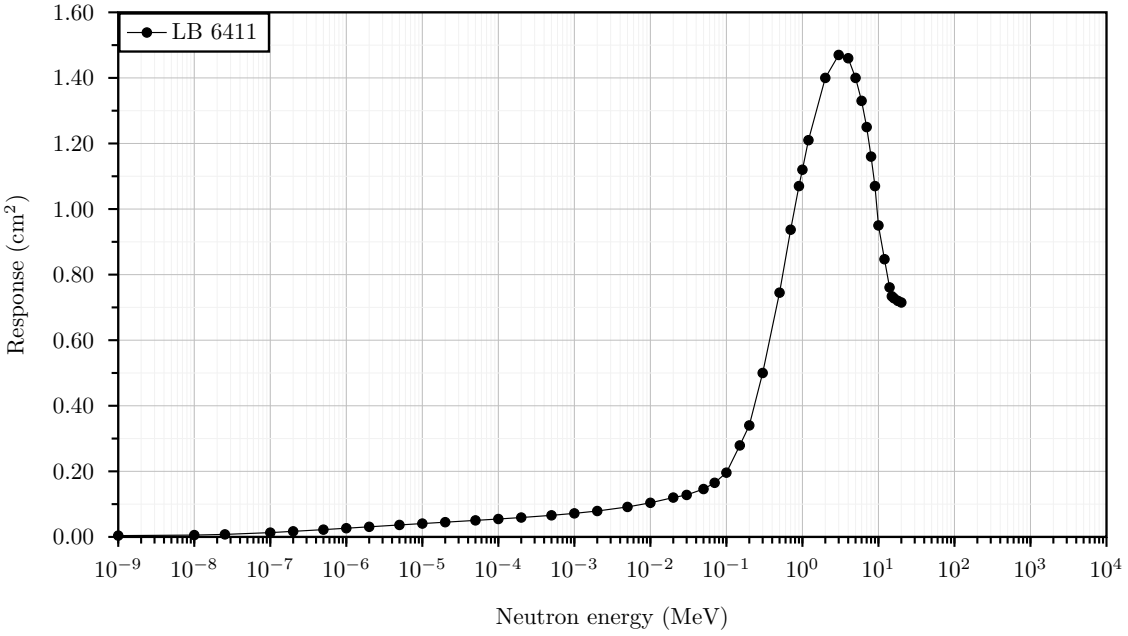

Figure 4.61: Response function of LB 6411 neutron dosimeter (in terms of neutron fluence). From Burgkhardt et al. [1997].

The ambient neutron dose equivalent is computed with Equation (3.80) so that

$$H^*(10) = \int_E h^*_{\Phi}(10,E)\,\Phi_E(E)\mathrm{d}E = \Phi \int_E h^*_{\Phi}(10,E)\varphi_E(E)\mathrm{d}E \tag{4.53}$$

$$= \left[\frac{R}{\int_E R_{\Phi}(E)\varphi_E(E)\mathrm{d}E}\right] \int_E h^*_{\Phi}(10,E)\varphi_E(E)\mathrm{d}E \tag{4.54}$$

$$= \frac{R}{\left[\frac{\int_E R_{\Phi}(E)\varphi_E(E)\mathrm{d}E}{\int_E h^*_{\Phi}(10,E)\varphi_E(E)\mathrm{d}E}\right]} \tag{4.55}$$

$$= \frac{R}{\left[\frac{R_{\mathrm{Calibration}}}{H^*_{\mathrm{Calibration}}(10)}\right]_{\mathrm{BSS}}} \sim \frac{R}{\left[\frac{R_{\mathrm{Calibration}}}{H^*_{\mathrm{Calibration}}(10)}\right]_{\mathrm{AmBe}}}. \tag{4.56}$$

Where we have introduced Equations (3.4), (4.8) and (4.1).

Usually, commercial devices with no spectrometry capability as LB 6411 are calibrated to conventional neutron sources, such as AmBe, and therefore, the calibration coefficient used internally by the device is $\left[\frac{R_{\mathrm{Calibration}}}{H^*_{\mathrm{Calibration}}(10)}\right]_{\mathrm{AmBe}}$, which means that the device is only applicable for neutrons measurements in which the energy distribution of the neutron fluence is similar to the AmBe. This situation is not always fulfilled and therefore, the use of the improved calibration coefficients $\left[\frac{R_{\mathrm{Calibration}}}{H^*_{\mathrm{Calibration}}(10)}\right]_{\mathrm{BSS}} = \left[\frac{\int_E R_{\Phi}(E)\varphi_E(E)\mathrm{d}E}{\int_E h^*_{\Phi}(10,E)\varphi_E(E)\mathrm{d}E}\right]$ will always provide a more accurate assessment of the neutron ambient dose equivalent.

Actually, the situation exposed here is equivalent to the situation explained in Section 4.6.1 (the form of the Equation (4.55) is the same as Equation (4.51)) with the difference that the standard neutron dosimeter developed at UAB is not an isotropic device and therefore, the validity of using the quantity $H^*(10)$ in non-isotropic devices is limited. Even though

the previous limitation is present, in research studies we have used the standard neutron dosimeter developed at UAB as a neutron dosimeter to measure $H^*(10)$, considering an average response for different incident angles.

Some additional difference in respect to Section 4.6.1 is that, here, we would like to stress the importance of obtaining an unit energy distribution of the neutron fluence through the measurement of a BSS rather than by MC simulations, if this is possible (this is not possible inside phantoms with the UAB-BSSs). As a minimum condition, at least in one point of the facility, a validation study should be done between the computed MC unit energy distribution of the neutron fluence and the experimental BSS unit energy distribution of the neutron fluence. Once this validation is done, there is a minimum degree of legitimacy in which one could only rely on MC simulations to obtain the MC unit energy distribution of the neutron fluence in other points of the facility.

By using Equation (4.55), it is implicitly assumed that the energy distribution of the neutron fluence or the evaluated energy distribution of the neutron fluence is $\Phi_E(E) \equiv \Phi_E^{\mathrm{EV}}(E) = \Phi^{\mathrm{LB6411}} \cdot \varphi_E^{\mathrm{MC}}(E)$ or $\Phi_E^{\mathrm{EV}}(E) \equiv \Phi_E(E) = \Phi^{\mathrm{LB6411}} \cdot \varphi_E^{\mathrm{BSS}}(E)$ in case of using a BSS. Where $\Phi = \Phi^{\mathrm{LB6411}} = \frac{R}{\int_E R_\Phi(E)\varphi_E(E)\mathrm{d}E}$. This energy distribution of the neutron fluence is what gives rise to the ambient neutron dose equivalent Equation (4.55), $H^*(10)$.

Chapter 5

Monte Carlo simulation basics and approximations

In this work, the Monte Carlo N-Particle (MCNP) executables from Los Alamos National Laboratory in the versions MCNPX 2.7.0 [Pelowitz, 2011] and MCNP 6.2 [Werner et al., 2017] have been used at a basic user level. The first aim of this chapter is to introduce the necessary connections between the quantities and notations defined in the previous chapters with the scoring tallies used in this work.

5.1 Scoring quantities and connections

A brief description of the most important quantities from the MC point of view, and in particular, when using MCNP is given below.

E Tally Energy

Is the upper bound (in MeV) of the energy bins.

The insights to define a proper energy binning for studying energy distributions of the neutron fluence are explained in Appendix C. It is clear then that if an energy bin is labeled as i, their boundaries are defined by the lower value E_i and the higher value E_{i+1}. By definition of the E Tally Energy, the numerical values appearing in the chart E Tally refer to the upper values E_{i+1} of each energy bin i. As explained in Appendix C, when using logarithmic scale for E, the central value of each bin i is $E = \sqrt{E_i \cdot E_{i+1}}$.

For instance:

$$\text{E4} \quad E_1 \; E_2 \; E_3 \tag{5.1}$$

means that there are 3 energy bins defined for the Tally Card F4 (fluence over a cell-volume tally) with upper boundaries E_1, E_2 and E_3, respectively.

F4 Tally Card type (fluence over a cell-volume tally)

This instruction provides the integrated fluence (energy integrated in a bin i) of some type of particle in a cell or volume.

The units and the equation associated to this tally are exactly:

$$\text{particle} \cdot \text{cm}^{-2} \cdot (\text{source particle})^{-1} \quad \leftrightarrow \quad \text{dF4}_{E_i<E<E_{i+1}} = \frac{\text{d}\,\Phi_{E_i<E<E_{i+1}}}{\text{NPS}}. \tag{5.2}$$

Where NPS is the number of source particles coming out from the radiation source defined in the MC simulation. This number is set by the user in the MCNP input.

Keep in mind that a MC simulation consists in simulating NPS histories and express the FX Tally Card quantities as an average value over these NPS simulated histories. In other words, a MC raw value from the F4 Tally is the fluence contributed by only one source particle. This is the reason why FX Tally Card quantities contain the unit $(\text{source particle})^{-1}$. Unit source particle will be also expressed simply as sp.

If the input of the MC code contains the instruction given in Equation (5.1) and the instruction

$$\text{F4:N} \quad 1, \tag{5.3}$$

that is to say, the fuence of neutrons over the cell-volume labelled as 1. This means that the MCNP output will contain:

$$\text{d}\,\Phi_{0<E<E_1} \quad \text{in the energy bin defined by 0 up to } E_1, \tag{5.4}$$

$$\text{d}\,\Phi_{E_1<E<E_2} \quad \text{in the energy bin defined by } E_1 \text{ up to } E_2, \tag{5.5}$$

$$\text{d}\,\Phi_{E_2<E<E_3} \quad \text{in the energy bin defined by } E_2 \text{ up to } E_3, \tag{5.6}$$

with the fluence in the total bin being

$$\Phi_{\text{Total}} = \text{d}\,\Phi_{0<E<E_1} + \text{d}\,\Phi_{E_1<E<E_2} + \text{d}\,\Phi_{E_2<E<E_3}. \tag{5.7}$$

Due to the instruction Equation (5.3), in which we specify that we are scoring neutrons, the units of Equations from (5.4) to (5.7) are

$$\text{neutron} \cdot \text{cm}^{-2} \cdot (\text{source particle})^{-1}. \tag{5.8}$$

Now, it is clear that the MC energy distribution of the neutron fluence would be built, in the present example, as

$$\Phi_E\left(E = \sqrt{E_1 \cdot E_2}\right) = \frac{\text{d}\,\Phi_{0<E<E_1} + \text{d}\,\Phi_{E_1<E<E_2}}{E_2 - E_1}, \tag{5.9}$$

$$\Phi_E\left(E = \sqrt{E_2 \cdot E_3}\right) = \frac{\text{d}\,\Phi_{E_2<E<E_3}}{E_3 - E_2}. \tag{5.10}$$

Note that the first energy bin is always tricky in the sense that at some point the central value $\sqrt{E_i \cdot E_{i+1}}$ must be defined and at the same time we want to preserve the information of the tally up to value E_1. In the approximation of Equation (5.9) what we do is to consider that all neutrons with energy below that E_1 have actually an energy ranged between E_1 and E_2. In general, the MC energy distribution of the neutron fluence is

$$\Phi_E\left(E = \sqrt{E_i \cdot E_{i+1}}\right) = \frac{\text{d}\,\Phi_{E_i<E<E_{i+1}}}{E_{i+1} - E_i} \sim \frac{\text{d}\,\Phi(E)}{\text{d}E}. \tag{5.11}$$

The units of Equation (5.11) are still $\text{neutron} \cdot \text{cm}^{-2} \cdot (\text{source particle})^{-1}$. The total MC neutron fluence can be written, for instance, as

$$\Phi_{\text{Total}} = \sum_i \text{d}\,\Phi_{E_i<E<E_{i+1}}. \tag{5.12}$$

The MC unit energy distribution of the neutron fluence is therefore,

$$\varphi_E(E) = \frac{\Phi_E(E)}{\Phi_{\text{Total}}} = \frac{1}{\Phi_{\text{Total}}} \frac{\mathrm{d}\Phi_{E_i<E<E_{i+1}}}{E_{i+1}-E_i} \sim \frac{\mathrm{d}\varphi(E)}{\mathrm{d}E}. \tag{5.13}$$

Notice that $\varphi_E(E)$ has units of MeV^{-1}, it can be interpreted as a probability density function so that the value $\varphi_E(E)\,\mathrm{d}E$ has no units and actually it is interpreted as the probability of a neutron to reach the cell 1 (in the example defined by Equation (5.3)) with an energy between E and $E+\mathrm{d}E$.

F6 Tally Card type (energy deposition averaged over a cell-volume or kerma/cema tally)

This instruction provides the energy integrated kerma (for neutral particles) or cema (for charged particles) in a bin i of some type of particle in a cell or volume.

The units and the equation associated to this tally are exactly:

$$\text{MeV}\cdot\text{g}^{-1}\cdot(\text{source particle})^{-1} \quad \leftrightarrow \quad \text{dF6}_{E_i<E<E_{i+1}} = \frac{\mathrm{d}K_{E_i<E<E_{i+1}}}{\text{NPS}}. \tag{5.14}$$

What we explained previously for F4 Tally Card type is also true for F6 Tally Card type if in Equations from 5.4 to 5.11 we replace

$$\Phi_E(E) \leftrightarrow D_E(E), \tag{5.15}$$

$$\varphi_E(E) \leftrightarrow d_E(E). \tag{5.16}$$

In order to study the goodness of any MC simulation in comparison with the experimental situation that it represents, two steps are followed:

1. To choose a reference quantity in a reference point that will connect the MC world and the real world. In other words, we force the MC world to reproduce the real world. This step will result in the *number of source particles needed in my MC simulation in order to reproduce the reference quantity in the reference point from the real world*, N_{sp}. For instance, in proton radiotherapy we know the **therapeutic proton absorbed dose delivered in the isocenter**. The therapeutic proton absorbed dose would be the reference quantity and the isocenter would be the reference point. In this example, first, we would model the situation so we can compute, by MC, **the MC therapeutic proton absorbed dose per source particle delivered in the isocenter**. Then, N_{sp} is computed.

2. As the connection is established, now we can use N_{sp} to compute non-reference quantities in non-reference points coming from the MC world that can be directly confronted with experimental measurements. In other words, we can multiply raw MC results (those with the sp unit dividing), *i.e.,* MCNP tallies, by N_{sp} and these products would be, for instance, **the MC neutron fluence obtained in a non-reference location** or **the MC proton absorbed dose delivered in a non-reference location**. Notice how these results are no longer per source particle.

To clarify better the previous steps, let us suppose that in a proton radiotherapy room, in the reference point, an absorbed dose, $D_{\text{p,EXP}}$ (usually in units of Gy), of 40 Gy of protons are delivered. As the proton radiotherapy room and its proton beam are modelled in the MC geometry, this means that in the same reference point we can compute the

absorbed dose (in kerma approximation) through the tally F6, obtaining $D_{\mathrm{p,Total,MC}}$ (in units of $\mathrm{MeV}\cdot\mathrm{g}^{-1}\cdot(\text{source particle})^{-1}$). Subscript "Total" means that it is proton energy integrated. By multiplying $D_{\mathrm{p,Total,MC}}$ by 1.6022×10^{-10} we express the dose in units of $\mathrm{J}\cdot\mathrm{Kg}^{-1}\cdot(\text{source particle})^{-1}$ *i.e.,* $1.6022\times10^{-10}\cdot D_{\mathrm{p,Total,MC}}$ is in units of $\mathrm{J}\cdot\mathrm{Kg}^{-1}\cdot(\text{source particle})^{-1}$.

Therefore, the question is, how many protons (source particles) we have to shoot in our MC simulation (and using a geometrical model of the reality) in order to reproduce the therapeutic proton absorbed dose used when we were doing our measurements with radiation detectors ? (*number of source particles needed in my MC simulation in order to reproduce the reference quantity in the reference point from the real world*). This question is translated mathematically to

$$D_{\mathrm{p,EXP}} = N_{\mathrm{sp}}\cdot\left(1.6022\times10^{-10}\cdot D_{\mathrm{p,Total,MC}}\right), \tag{5.17}$$

so that

$$N_{\mathrm{sp}} = \frac{D_{\mathrm{p,EXP}}}{1.6022\times10^{-10}\cdot D_{\mathrm{p,Total,MC}}}. \tag{5.18}$$

Definition of radiation sources

By using the instruction SDEF in MCNP, we can define the radiation source of our MC simulation. This radiation source can have variables that follow probability density functions. For instance, a non-point radiation source is no more that a point radiation source whose position is properly sampled in a surface or volume according to a probability density function. Energy distribution of the outgoing particles from the source is also an important variable that can be controlled.

Let us suppose that in our MC input is the SDEF instruction so that

$$\text{SDEF} \quad \ldots \text{ ERG=D1 } \ldots \tag{5.19}$$

This means that the energy distribution of the particles coming from the source follow a probability density function. The sampling is controlled by the instructions SI and SP. SI define the energy ranges, for instance, from E_1 to E_2 ($\Delta E = E_2 - E_1$) in which there is a probability $\mathrm{d}\varphi_j(E=\sqrt{E_1\cdot E_2}) = \varphi_{E,j}(E=\sqrt{E_1\cdot E_2})\Delta E \equiv \mathrm{d}p_{E_1,E_2}$ ($\int_E \mathrm{d}\varphi_j(E) = 1$) of a particle type j to come out from the source with an energy between E_1 and E_2. Following the example defined by Instruction (5.19)

$$\text{SI1 H } E_0\ E_1\ E_2\ E_3\ \ldots \tag{5.20}$$

$$\text{SP1 D 0 } \mathrm{d}p_{E_0,E_1}\ \mathrm{d}p_{E_1,E_2}\ \mathrm{d}p_{E_2,E_3}\ \ldots \tag{5.21}$$

Parameter H means that values E_0 E_1 E_2 E_3 are the upper boundaries of the energy bins while parameter D means that values 0 $\mathrm{d}p_{E_0,E_1}$ $\mathrm{d}p_{E_1,E_2}$ $\mathrm{d}p_{E_2,E_3}$ are bin probabilities, as already introduced.

5.1.1 Normalization for two neutron producing radiation beams

In some experimental measurements in anthropomorphic phantoms, beams were coming from two directions (see for instance Figures 7.11, 7.12 and 7.13 from Chapter 7) so that two MC simulations, one for each incidence direction, were done. As the proton radiotherapy facility informed about the proton absorbed dose delivered from each direction, we can

do the normalization procedure as follows. Let us suppose that one beam is coming from the 140° direction, contributing with an experimental dose in a reference point $D_{\mathrm{p,EXP,140^\circ}}$ and another beam is coming from the 270° direction, contributing with $D_{\mathrm{p,EXP,270^\circ}}$. In each MC simulation, the MC number of protons needed to reproduce the experimental doses are, using Equation (5.18)

$$N_{\mathrm{sp,140^\circ}} = \frac{D_{\mathrm{p,EXP,140^\circ}}}{1.6022 \times 10^{-10} \cdot D_{\mathrm{p,Total,MC,140^\circ}}}, \tag{5.22}$$

$$N_{\mathrm{sp,270^\circ}} = \frac{D_{\mathrm{p,EXP,270^\circ}}}{1.6022 \times 10^{-10} \cdot D_{\mathrm{p,Total,MC,270^\circ}}}, \tag{5.23}$$

so that, during the whole irradiation, or rather during the whole MC irradiation, the differential of fluence accumulated due to the two beams in an energy bin in a cell-volume is

$$\mathrm{d}\Phi(E) = \frac{\mathrm{d}\Phi_{140^\circ}(E)}{N_{\mathrm{sp,140^\circ}}} + \frac{\mathrm{d}\Phi_{270^\circ}(E)}{N_{\mathrm{sp,270^\circ}}}, \tag{5.24}$$

where $\mathrm{d}\Phi_{140^\circ}(E)$ and $\mathrm{d}\Phi_{270^\circ}(E)$ are computed in a cell-volume in their respective MC simulation and have units of neutron $\cdot\, \mathrm{cm}^{-2} \cdot$ (source particle)$^{-1}$ if we are computing the energy distribution of the neutron fluence, while $\mathrm{d}\Phi(E)$ (from Equation 5.24) has already units of neutron $\cdot\, \mathrm{cm}^{-2}$. Of course other relevant equations have also the form of Equation (5.24), for instance, by dividing Equation (5.24) by $\mathrm{d}E$

$$\Phi_E(E) = \frac{\Phi_{E,140^\circ}(E)}{N_{\mathrm{sp,140^\circ}}} + \frac{\mathrm{d}\Phi_{270^\circ}(E)}{N_{\mathrm{sp,270^\circ}}}, \tag{5.25}$$

and integrating in some energy range or the whole energy range, we can also obtain

$$\Phi_{\mathrm{Total}} = \frac{\Phi_{\mathrm{Total,140^\circ}}}{N_{\mathrm{sp,140^\circ}}} + \frac{\Phi_{\mathrm{Total,270^\circ}}}{N_{\mathrm{sp,270^\circ}}}, \tag{5.26}$$

so that the unit energy distribution of the neutron fluence, $\varphi_E(E)$, is simply obtained by dividing Equations (5.25) and (5.26)

$$\varphi_E(E) = \frac{\Phi_E(E)}{\Phi_{\mathrm{Total}}}. \tag{5.27}$$

5.2 Monte Carlo modelling of energy degraders

In Particle Beam Scanning (PBS) proton radiotherapy treatments, the final unit energy distribution of the protons delivered to the patient can be known though the PBS Layer Definition (PLD) file (see Dowdell [2011]). In the information provided by the PLD file the energy degradation process is already taken into account (as we say, the PLD file contains the final unit energy distribution of the protons delivered to the patient) so if we want to try to model the neutron production by the degradation process we have to proceed with some methodology. Although it is true that the energy degrader is far from the radiotherapy room in the usual *multiple-room* solutions (see Figure 7.2) this could be not the case in *single-room* and compact solutions (see, for instance, Figure 7.3).

The approximation taken in this work to model an energy degrader is to consider the PBS (an active or dynamic process with dot beams) as a static one dot with the initial energy being the extraction energy of the proton accelerator. In the case of the Mevion S250i Hyperscan single-room, see Figure 7.3 and Vilches-Freixas et al. [2020], the protons coming

from the accelerator had a fixed energy of 227 MeV. Given the PLD file, we can compute the final average energy of the protons delivered to the patient. The approximation then consists in setting a thickness of the energy degrader so that

$$227 \text{ MeV} \rightarrow \underbrace{\text{Energy degrader}}_{\text{What thickness is needed ?}} \rightarrow \bar{E}_{\text{PLD}}. \tag{5.28}$$

A simple approximation was performed. Under this approximation, the aim is to find, precisely, the thickness of the energy degrader. The energy degrader or range modulator system in the case of Mevion S250i Hyperscan single-room, see Figure 7.3 and Vilches-Freixas et al. [2020], is Lexan ($C_{16}H_{14}O_3$) with mass density 1.2 g cm^{-3}. Approximation Equation (5.28) has been applied in the MC simulations regarding the Mevion S250i Hyperscan single-room in the situations highlighted in Table 5.1, where the obtained lexan thicknesses are also presented.

Table 5.1: Values of the thicknesses for the energy degraders according to approximation Equation (5.28) *and PLD files.*

Experimental situation	Initial energy (MeV)	Final mean energy (MeV)	Thickness of Lexan (cm)
140° proton beam to anthropomorphic phantom (Figure 7.12)	227	93	22.3 cm
270° proton beam to anthropomorphic phantom (Figure 7.11)	227	117	19.4 cm
Proton beam to water tank phantom (Figure 7.10)	227	163	12.04 cm
Proton beam to anthropomorphic phantom (spectrometry) (Figure 7.32)	227	122	18.6 cm

The equation to find the thickness of a certain material, $R\,(E_1 \rightarrow E_2)$, required to have final charged particles with energy E_2 when the charged particles strike the material with energy E_1 is presented in the next section Section 5.2.1.

5.2.1 Charged particle range and material thickness

Stopping power, Equation (3.81), can be written for a particle whose kinetic energy is described by E' as

$$S(E') = -\frac{\mathrm{d}E'}{\mathrm{d}x}(E') \quad \leftrightarrow \quad \mathrm{d}x(E') = -\frac{\mathrm{d}E'}{S(E')}. \tag{5.29}$$

Now if we are interested in computing the distance travelled by a particle with initial kinetic energy $E' = E$ when going from $E' = E$ to $E' = E - \mathrm{d}\tilde{E}'$ ($\Delta x(E')$), the distance travelled by the particle when going from $E' = E - \mathrm{d}\tilde{E}'$ to $E' = E - \mathrm{d}\tilde{E}' - \mathrm{d}\tilde{E}'$ ($\Delta x(E' - \mathrm{d}\tilde{E}')$) and so on, we can write

$$\int_{x(E'=E)=0}^{x(E'=0)=R(E)} \mathrm{d}x(E') = R(E) - 0 = \Delta x(E') + \Delta x(E' - \mathrm{d}\tilde{E}') + \cdots + \underbrace{\Delta x(0)}_{0}. \tag{5.30}$$

Integration limits from left side of Equation (5.30) can be understood as follows. The x coordinate in which the particle has all its kinetic energy ($E' = E$) is $x = 0$. When the particle losses all its kinetic energy ($E' = 0$) it has traveled, precisely, the range distance associated a particle with initial kinetic energy E, $R(E)$.

By combining Equations (5.29) and (5.30) we obtain

$$R(E) = \int_{x(E'=E)=0}^{x(E'=0)=R(E)} \mathrm{d}x(E') = -\int_{E'=E}^{E'=0} \frac{\mathrm{d}E'}{S(E')} = \int_0^E \frac{\mathrm{d}E'}{S(E')}. \tag{5.31}$$

Therefore

$$R(E) \equiv R\left(E_\mathrm{i} = E \rightarrow E_\mathrm{f} = 0\right) \equiv R\left(E \rightarrow 0\right) = \int_0^E \frac{1}{S(E')}\,\mathrm{d}E'. \tag{5.32}$$

It turns out that

$$\text{if} \quad E_2 < E_1 \quad \Rightarrow \quad R(E_2) < R(E_1), \tag{5.33}$$

and we can define

$$R(E_1) = R\left(E_\mathrm{i} = E_1 \rightarrow E_\mathrm{f} = 0\right) = R\left(E_1 \rightarrow 0\right) = \int_0^{E_1} \frac{1}{S(E')}\,\mathrm{d}E', \tag{5.34}$$

$$R(E_2) = R\left(E_\mathrm{i} = E_2 \rightarrow E_\mathrm{f} = 0\right) = R\left(E_2 \rightarrow 0\right) = \int_0^{E_2} \frac{1}{S(E')}\,\mathrm{d}E', \tag{5.35}$$

so that

$$R(E_1) - R(E_2) = \int_0^{E_1} \frac{1}{S(E)}\,\mathrm{d}E_\mathrm{p} - \int_0^{E_2} \frac{1}{S(E)}\,\mathrm{d}E_\mathrm{p} = \int_{E_2}^{E_1} \frac{1}{S(E)}\,\mathrm{d}E_\mathrm{p} = R\left(E_1 \rightarrow E_2\right). \tag{5.36}$$

Is then proved that

$$R(E_1) - R(E_2) = R\left(E_1 \rightarrow E_2\right). \tag{5.37}$$

With Equation (5.37), given a charged particle with initial kinetic energy E_1 entering in a material and given the final kinetic energy E_2 (after coming out from the material) and their associated ranges, $R(E_1)$ and $R(E_2)$, one can compute the thickness $R \equiv R\left(E_1 \rightarrow E_2\right)$ needed so that the thickness of an energy degrader now can be set. The ranges needed for this calculation can be obtained in ESTAR, PSTAR, and ASTAR [Berger et al., 1993] or SRIM (the Stopping and Range of Ions in Matter) [Ziegler et al., 1985].

The energy loss by the individual particle in the slab is of course

$$\Delta E = E_1 - E_2. \tag{5.38}$$

5.3 Monte Carlo simulations of the response functions

The response or nuclear reactions induced in a material (or active region of a detector) by a mono-energetic neutron radiation field is computed by Equation (4.15). For those detectors in which the active region is small in comparison to the volume of the whole detector, considerations explained in Section 4.1 and Section 4.1.3 should be taken into account. Same applies for detector configurations based on neutron moderating materials.

However, before of computing the response function, it is convenient first to introduce

different quantities that characterize materials in general.

Given a material characterized by a mass density, ρ (in units of g cm^{-3}) its atomic density, n_{Targets} (in units of atoms cm^{-3}), is

$$n_{\text{Targets}} = N_{\text{A}} \cdot \frac{\rho}{M_{\text{at.}}} \qquad \text{with units correspondence} \qquad \frac{\text{atoms}}{\text{cm}^3} = \frac{\text{atoms}}{\text{mol}} \cdot \frac{\frac{\text{g}}{\text{cm}^3}}{\frac{\text{g}}{\text{mol}}}. \tag{5.39}$$

Therefore the number of atoms or targets, given a volume in which these targets are found, V_{Targets}, is

$$N_{\text{Targets}} = n_{\text{Targets}} \cdot V_{\text{Targets}}. \tag{5.40}$$

In case we need to express the atomic density in units of atoms cm^{-1} b^{-1} we express

$$n_{\text{Targets}}(\text{atoms cm}^{-1}\ \text{b}^{-1}) = n_{\text{Targets}}(\text{atoms cm}^{-3}) \cdot 10^{-24}. \tag{5.41}$$

MCNP definition of the cells allow us to characterize a MC cell using the mass density ρ (in units of g cm^{-3}) or the atomic density n_{Targets} in units of atoms cm^{-1} b^{-1}.

Now we can write Equation (4.16) as

$$R = n_{\text{Targets}} \cdot V_{\text{Targets}} \cdot \int_E \sigma(E) \cdot \Phi_E^{\text{in}}(E)\text{d}E, \tag{5.42}$$

where we have used Equation (5.40).

The equivalent equation in units to Equation (5.42) is

$$\left(\frac{\text{nuclear reactions}}{\text{sp}}\right) = \left(\frac{\text{atoms}}{\text{cm} \cdot \text{b}}\right) \cdot \left(\text{cm}^3\right) \cdot (\text{b}) \cdot \left(\frac{\text{neutrons}}{\text{cm}^2\ \text{MeV sp}}\right) \cdot (\text{MeV})\,. \tag{5.43}$$

So the response of a detector (*i.e.,* nuclear reactions, for instance) is still not found because the presence of the sp unit.

As by MC, in this section, we are actually computing the response function (not an *absolute* response) we need to compute the response function (in terms of the incident neutron fluence in a detector configuration) as

$$R_{\Phi}(E') = \frac{R(E')}{\Phi(E')}, \tag{5.44}$$

Where $R(E')$ is the response, Equation (5.42), of our thermal neutron detector (in the center of some detector configuration) when the detector configuration is irradiated by mono-energetic neutrons of energy E' and $\Phi(E')$ is the fluence of neutrons reaching the detector configuration.

We can take a great advantage of the unit sp so no more extra MC computations regarding the MC neutron fluence reaching the detector configuration are needed. Indeed, if we iluminate exactly the cross-sectional area of our detector configuration i by a parallel neutron beam of radius r_i, the units $\left[\frac{\text{sp}}{\text{cm}^2}\right]$ actually correspond to the incident neutron fluence over the detector configuration *i.e.,* term $\Phi(E')$ in Equation (5.44).

Therefore, is proved that Equation (5.44) is computed as

$$R_{\Phi,i}(E') = \frac{R_i(E')}{\Phi_i(E')} = \pi r_i^2 \cdot n_{\text{Targets}} \cdot V_{\text{Targets}} \cdot \int_E \sigma(E) \cdot \Phi_E^{\text{in}}(E)\text{d}E, \tag{5.45}$$

with the units equivalent equation

$$\left(\frac{\text{nuclear reactions}}{\left[\frac{\text{sp}}{\text{cm}^2}\right]}\right) = \left(\frac{\text{nuclear reactions}}{\left[\frac{\text{sp}}{\text{cm}^2}\right]}\right) \tag{5.46}$$

$$= \frac{1}{\left[\frac{\text{sp}}{\text{cm}^2}\right]} \cdot \left(\frac{\text{atoms}}{\text{cm} \cdot \text{b}}\right) \cdot \left(\text{cm}^3\right) \cdot (\text{b}) \cdot \left(\frac{\text{neutrons}}{\text{cm}^2\ \text{MeV}}\right) \cdot (\text{MeV})\,. \tag{5.47}$$

5.4 Monte Carlo simulations of the energy distributions of the neutron fluence

As shown in Section 4.6.1 and Section 4.6.2, the MC unit energy distribution of the neutron fluence, $\varphi_E^{\text{MC}}(E)$, is used to compute calibration coefficients from Equations (4.51) and (4.55) *i.e.,*

$$\left[\frac{\int\limits_E R_\Phi(E)\varphi_E(E)\mathrm{d}E}{\int\limits_E Q(E)k_\Phi(E)\varphi_E(E)\mathrm{d}E}\right], \quad \left[\frac{\int\limits_E R_\Phi(E)\varphi_E(E)\mathrm{d}E}{\int\limits_E h^*_\Phi(10,E)\varphi_E(E)\mathrm{d}E}\right]. \tag{5.48}$$

Working in this way means to assume that the energy distribution of the neutron fluence or the evaluated energy distribution of the neutron fluence is $\Phi_E(E) \equiv \Phi_E^{\text{EV}}(E) = \Phi^{\text{Detector}} \cdot \varphi_E^{\text{MC}}(E)$. Where Φ^{Detector} is the total neutron fluence obtained by a radiation detector.

However, from MC simulations we can also compute the total neutron fluence, Φ^{MC}, so that the full MC energy distribution of the neutron fluence would be written as $\Phi_E^{\text{MC}}(E) = \Phi^{\text{MC}} \cdot \varphi_E^{\text{MC}}(E)$.

At this point is important to discuss that although full MC energy distribution of the neutron fluence, $\Phi_E^{\text{MC}}(E) = \Phi^{\text{MC}} \cdot \varphi_E^{\text{MC}}(E)$, could be not reliable (under the simple MC modelling used in this work), this does not necessarily mean that MC unit energy distribution of the neutron fluence, $\varphi_E^{\text{MC}}(E)$, is not reliable at the same degree. This can be reasoned as follows: as explained in Section 5.1, raw full MC energy distribution of the neutron fluence has units of neutron cm^{-2} MeV^{-1} sp^{-1} (sp = MC source particle) which means that it is highly dependant on the MC factor N_{sp} (and therefore, highly dependant on the MC model) used to obtain the MC energy distribution of the neutron fluence in units of neutron cm^{-2} MeV^{-1}. However, MC unit energy distribution of the neutron fluence, $\varphi_E^{\text{MC}}(E) = \frac{\Phi_E^{\text{MC}}(E)}{\Phi^{\text{MC}}}$, has units of MeV^{-1}, which means that it is not directly dependant on the MC factor N_{sp}. In other words, and remembering that unit energy distribution of the neutron fluence can be interpreted as a probability density function (see Section 3.1.1), while $\Phi_E^{\text{MC}}(E)$ is related to the absolute number of neutrons (of energy E) present in the radiation field, $\varphi_E^{\text{MC}}(E)$ is only related with the probability of a neutron (of energy E) to be present in the radiation field.

Another important point of this section is to respect the definition of response function (in terms of fluence). Remember that from the definitions exposed in Section 4.1, the response function (in terms of fluence) is defined for the fluence reaching the boundaries of the radiation detector system without taken into account the influence of the detector system itself over the incident fluence to the device. This means that in the MC computations of

the calibration coefficients one does not have to introduce the materials of the detector.

5.5 Full Monte Carlo neutron dose equivalents

The Full Monte Carlo neutron dose equivalent is the computation of the Equations (3.64) and (3.80). What is done is to obtain, via F4 Tally Card type (see Section 5.1), the energy distribution of the neutron fluence, $\Phi_E(E)$, which will be in units of neutron cm^{-2} sp^{-1} and, in the case of proton radiotherapy computations, the factor N_{sp} is obtained through the F6 Tally Card type as explained in Section 5.1 and Section 5.1.1.

Once this is done, the fluence-to-dose conversion coefficients $Q(E)k_{\Phi}(E)$ (Section 3.1.4.2) and the fluence-to-ambient dose equivalent, $h^*_{\Phi}(10, E)$ (Section 3.1.5) can be properly applied so that, for instance, Equation (3.64) or Equation (3.80) can be used.

5.6 Approximation to avoid double scorings in mixed fields

The problem to discuss in this section is the separation of the dose contributions (computed by MC simulations) of the particles from a mixed radiation field keeping in mind that these MC computations are used along with the equation presented in Chapter 6. I focus our attention in MCNP.

In a mixed radiation field, when scoring quantities as tallies F6 and F4 in a volume we find the problem that we cannot discriminate between the particles coming from outside of the scoring volume (particles crossing the boundary of the scoring volume) and those created inside of the scoring volume. For example, if we do F6:H we are not only going to score the protons coming from the outside but also we will score those protons which are created inside the scoring volume by neutrons. Same would apply in using F4:H.

This is already relevant at time of interpreting the scoring of the doses in a MC simulation but it could be still more important when we want to combine MC data (unit energy distributions of particle fluence) with calibration data of some detector, as we will explore further in Chapter 6. In the equation proposed what is important is which particles (and their energies) are reaching the boundaries of a given detector from the outside. Materials of the detectors must not be introduced in *general* situations (those whose aim is not computing a response function). The scoring region will have the volume that the detector would occupy but with the density and isotopic weight fractions of the material in which is going to be immersed. For the sake of good MC statistics, this volume can be increased as long as the field uniformity approximation holds for each point of the the new volume.

In MCNP it is not allowed to impose importance 0 to *mother* particles in scoring volumes. We consider mother particles neutrons and photons, in the sense that protons and electrons are usually the final charged particles who actually deposit energy in the matter. In the following explanations, when we talk about setting importance = 0, it is only in scoring volumes, not in all the surrounding geometry. MCNP allows to put importance 0 to protons or electrons in scoring volumes, for instance.

One legitimate question is to wonder how one can find the neutron dose if protons are killed in the scoring volume. The strategy is to use cleverly tallies F4 and F6 and to use fluence-to-kerma conversion coefficients for neutral particles. Keep in mind that fluence-

to-kerma conversion coefficients take into account the final energy deposition of neutral particles through charged particles.

Taking into account the previous information we can write

$$\text{IMP N} \neq 0,\ \text{IMP H} = 0 \quad \text{and} \quad \text{F4:N} \ \Rightarrow \ D\,(\text{neutrons}) \tag{5.49}$$

$$\text{IMP N} \neq 0,\ \text{IMP H} \neq 0 \quad \text{and} \quad \text{F4:N} \ \Rightarrow \ D(\ \text{neutrons} + \underbrace{\text{particles} \rightarrow \text{neutrons}}_{\text{inside of the scoring volume}}\ ) \tag{5.50}$$

$$\text{IMP N} \neq 0,\ \text{IMP H} \neq 0 \quad \text{and} \quad \text{F6:H} \ \Rightarrow \ D(\ \text{protons} + \underbrace{\text{particles} \rightarrow \text{protons}}_{\text{inside of the scoring volume}}\ ) \tag{5.51}$$

so that, by substracting Equations (5.50) and (5.49)

$$D(\ \underbrace{\text{particles} \rightarrow \text{neutrons}}_{\text{inside of the scoring volume}}\ ) = D(\ \text{neutrons} + \underbrace{\text{particles} \rightarrow \text{neutrons}}_{\text{inside of the scoring volume}}\ ) - D\,(\text{neutrons})\,. \tag{5.52}$$

In addition, for photons and electrons we can write

$$\text{IMP P} \neq 0,\ \text{IMP E} = 0 \quad \text{and} \quad \text{F4:P} \ \Rightarrow \ D\,(\text{photons}) \tag{5.53}$$

$$\text{IMP P} \neq 0,\ \text{IMP E} \neq 0 \quad \text{and} \quad \text{F4:P} \ \Rightarrow \ D(\ \text{photons} + \underbrace{\text{particles} \rightarrow \text{photons}}_{\text{inside of the scoring volume}}\ ) \tag{5.54}$$

$$\text{IMP P} \neq 0,\ \text{IMP E} \neq 0 \quad \text{and} \quad \text{F6:E} \ \Rightarrow \ D(\ \text{electrons} + \underbrace{\text{particles} \rightarrow \text{electrons}}_{\text{inside of the scoring volume}}\ ) \tag{5.55}$$

so that, by substracting Equations (5.54) and (5.53)

$$D(\ \underbrace{\text{particles} \rightarrow \text{photons}}_{\text{inside of the scoring volume}}\ ) = D(\ \text{photons} + \underbrace{\text{particles} \rightarrow \text{photons}}_{\text{inside of the scoring volume}}\ ) - D\,(\text{photons})\,. \tag{5.56}$$

Therefore, the neutron contribution to the dose from external neutrons regarding the scoring volume, D(neutrons), is computed with Equation (5.49) and the photon contribution to the dose from external photons regarding the scoring volume, D(photons), is computed through Equation (5.53). Keep in mind that in Equations (5.49) and (5.53) we killed the proton and electron transport in the scoring cell, respectively.

To compute the equivalent equations for protons and electrons is not possible to follow the previous methodology by limitations of the code. One suggested way to proceed would be

$$D(\text{protons}) = D(\ \text{protons} + \underbrace{\text{particles} \rightarrow \text{protons}}_{\text{inside of the scoring volume}}\ ) - D(\ \underbrace{\text{particles} \rightarrow \text{protons}}_{\text{inside of the scoring volume}}\ ), \tag{5.57}$$

$$D(\text{electrons}) = D(\ \text{electrons} + \underbrace{\text{particles} \rightarrow \text{electrons}}_{\text{inside of the scoring volume}}\ ) - D(\underbrace{\text{particles} \rightarrow \text{electrons}}_{\text{inside of the scoring volume}}\ ). \tag{5.58}$$

First terms from the right side of Equations (5.57) and (5.58) are known by Equations (5.51) and (5.55), respectively. Regarding the second terms from the right side of Equations (5.57) and (5.58) an approximation could be used, for instance

$$D(\ \underbrace{\text{particles} \rightarrow \text{protons}}_{\text{inside of the scoring volume}}\ ) \propto D(\text{neutrons}) = a \cdot D(\text{neutrons}), \tag{5.59}$$

$$D(\underbrace{\text{particles} \rightarrow \text{electrons}}_{\text{inside of the scoring volume}}\ ) \propto D(\text{photons}) = b \cdot D(\text{photons}). \tag{5.60}$$

In order words, the contribution of the protons generated inside the scoring volume is proportional to the neutrons entering from the boundaries of the scoring volume. Similar interpretation for the case of photons to electrons. a and b would be proportional constants to be set.

A summary of the methodology presented in this section would be

$$D\,(\text{neutrons}) \quad \leftrightarrow \quad \text{IMP N} \neq 0, \text{IMP H} = 0 \quad \text{and} \quad \text{F4:N}. \tag{5.61}$$

$$D\,(\text{photons}) \quad \leftrightarrow \quad \text{IMP P} \neq 0, \text{IMP E} = 0 \quad \text{and} \quad \text{F4:P}. \tag{5.62}$$

$$D(\text{protons}) = \overbrace{D(\ \text{protons} + \underbrace{\text{particles} \rightarrow \text{protons}}_{\text{inside of the scoring volume}}\ )}^{\text{IMP N} \neq 0,\ \text{IMP H} \neq 0 \quad \text{and} \quad \text{F6:H}} - a \cdot D(\text{neutrons}). \tag{5.63}$$

$$D(\text{electrons}) = \overbrace{D(\ \text{electrons} + \underbrace{\text{particles} \rightarrow \text{electrons}}_{\text{inside of the scoring volume}}\ )}^{\text{IMP P} \neq 0,\ \text{IMP E} \neq 0 \quad \text{and} \quad \text{F6:E}} - b \cdot D(\text{photons}). \tag{5.64}$$

In the conditions of this work, we did not have the need of using this approximation. In any case, the effect can result in an overestimation of doses.

5.7 MC geometries and materials used in modeling proton radiotherapy situations

The elements that we are going to describe in this section are

- A model of water tank phantom.
- A model of the anthropomorphic phantom.
- A Range Shifter (RS) and Beam Compensator (BC) as described and used in the IBA proton radiotherapy experiments [Wochnik et al., 2021].
- A Range Modulator System (RMS) and Adaptive Aperture (AA) as described and used in the Mevion proton radiotherapy experiments [Vilches-Freixas et al., 2020].
- Dimensions of the radiotherapy room and wall thicknesses from a facility using the Mevion S250i Hyperscan single-room system.

Water tank phantom

A water tank phantom was introduced in the MC input reproducing the dimensions of the experimental water tank phantom, see Figures 5.1 and 5.2. Relevant details regarding materials composition and geometrical dimensions of the MC model are given in Table 5.2. Figure 5.3 shows that MC model of the water tank phantom.

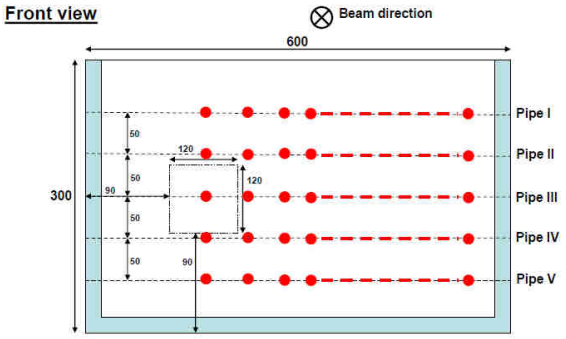

Figure 5.1: Front view of the experimental water tank phantom. From Stolarczyk et al. [2018]

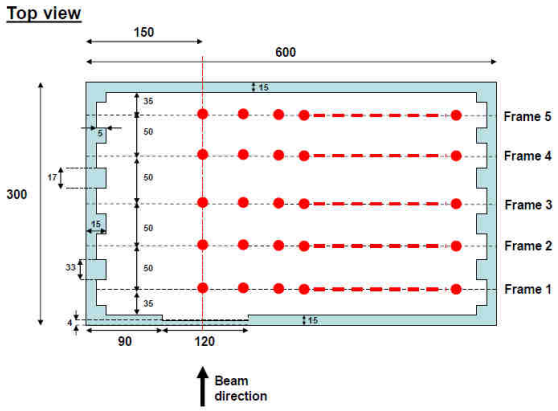

Figure 5.2: Top view of the experimental water tank phantom. From Stolarczyk et al. [2018]

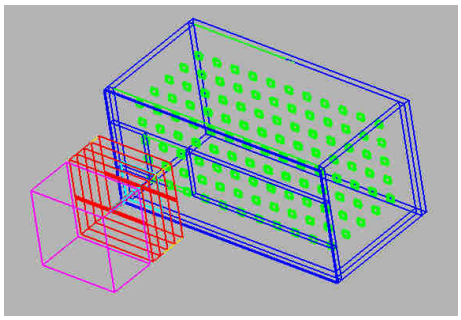

Figure 5.3: 3D picture of the modelled water thank phantom. Elements in pink and red colors actually correspond to the RMS and AA elements that will be described later. See in green the boundaries in which the scoring regions are defined. Notice also the frames and pipes structure.

Table 5.2: Description of the materials and dimensions used in modelling the water tank phantom. The atomic elements used are expressed as a formula in general, when this is not possible, the weight fraction will be given.

Element	Density (g cm^{-3})	Atomic composition	Dimensions	Source
Air surrounding the water tank	0.00120479	C(0.000124) N(0.755267) O(0.231781) Ar(0.012827)	-	[Berger et al., 1993]
Water tank	-	-	30 cm × 30 cm × 60 cm	[Stolarczyk et al., 2018]
Water	0.998207	H_2O	To fill the water tank phantom	[Detwiler et al., 2021]
Walls of the water tank ≡ PMMA ≡ Lucite	1.19	$C_5O_2H_8$	1.5 cm thick and 0.4[a] cm thick	[Detwiler et al., 2021]

[a] Notice the dimensions of the window from which the proton therapeutic beam enters into the water tank phantom. See Figure 5.2.

Anthropomorphic phantom

An anthropomorphic phantom was introduced in the MC input reproducing the dimensions of the experimental anthropomorphic phantom shown in Figure 5.4. Relevant details regarding materials composition and geometrical dimensions of the MC model are given in Table 5.3. See the modelled anthropomorphic phantom in Figures 5.5, 5.6 and 5.7.

Figure 5.4: Pediatric five year old phantom from ATOM: Dosimetry Phantoms [CIRS, 2023].

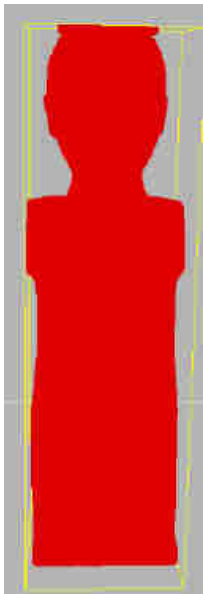

Figure 5.5: MC model of the anthropomorphic phantom. Soft tissue-male and female. See its definition in Table 5.3.

Figure 5.6: MC model of the anthropomorphic phantom. Skeleton-cortical bone. See its definition in Table 5.3. Colourful regions are the scoring regions.

Figure 5.7: MC model of the anthropomorphic phantom. Lung. See its definition in Table 5.3. Colourful regions are the scoring regions.

Table 5.3: Description of the materials and dimensions used in modelling the anthropomorphic phantom. The atomic composition of the different materials is given as weight fraction.

Element	Density (g cm^{-3})	Atomic composition	Dimensions	Source
Air surrounding the water tank	0.00120479	C(0.000124) N(0.755267) O(0.231781) Ar(0.012827)	-	[Berger et al., 1993]
Five year old phantom	-	-	19.3 cm × 18.1 cm × 66.6 cm	-
Soft tissue-male and female	1.00	H(0.102) C(0.143) N(0.034) O(0.708) Na(0.002) P(0.003) S(0.003) Cl(0.003) K(0.003)	-	[ICRU, 1989]
Skeleton-cortical bone	1.92	H(0.034) C(0.155) N(0.042) O(0.435) Na(0.001) Mg(0.002) P(0.103) S(0.003) Ca(0.225)	-	[ICRU, 1989]
Lung	0.26	H(0.103) C(0.105) N(0.031) O(0.749) Na(0.002) P(0.002) S(0.003) Cl(0.003) K(0.002)	-	[ICRU, 1989]

Range Shifter and Beam Compensator

Two types of proton energy degraders were used in this work, namely, a Range Shifter (RS) and a Beam Compensator (BC) (see Figures 5.8 and 5.9) [Wochnik et al., 2021]. These elements were introduced in MC inputs reproducing the experimental dimensions. See the MC modelled elements in Figures 5.10, 5.11, 5.12, 5.13, 5.14 and 5.15. Relevant details regarding materials composition and geometrical dimensions of the MC models are given in Table 5.4.

Figure 5.8: Experimental BC.

Figure 5.9: Experimental BC.

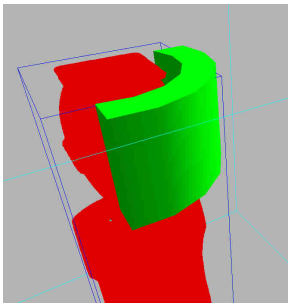

Figure 5.10: MC modeled BC.

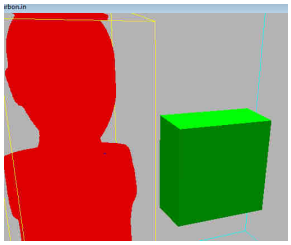

Figure 5.11: MC modelled RS.

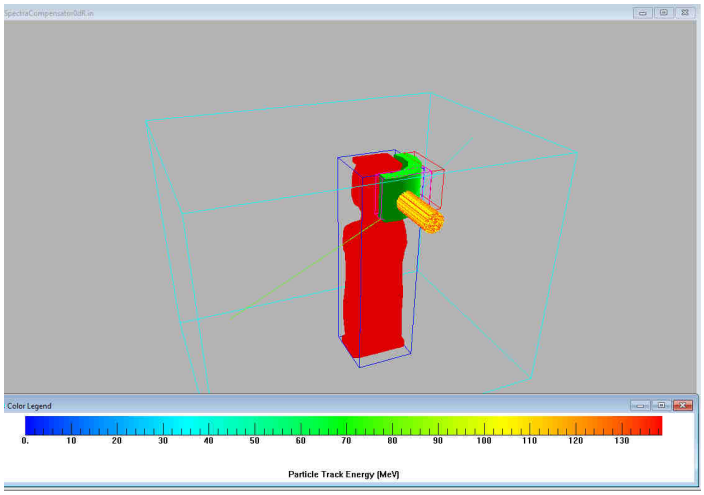

Figure 5.12: BC placed next to the head of the MC anthropomorphic phantom. Proton beam coming from 0°.

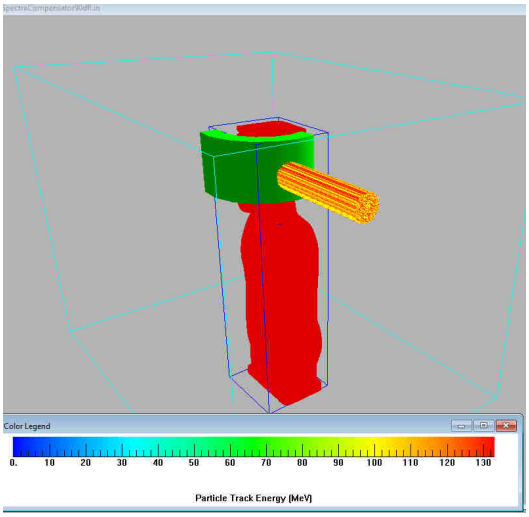

Figure 5.13: BC placed next to the head of the MC anthropomorphic phantom. Proton beam coming from 90°.

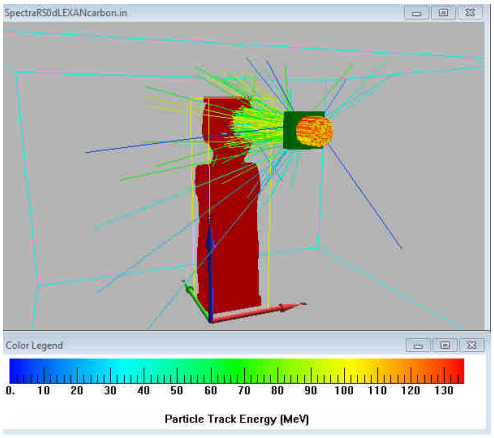

Figure 5.14: RS at 37 cm from MC anthropomorphic phantom isocenter. Proton beam coming from 0°.

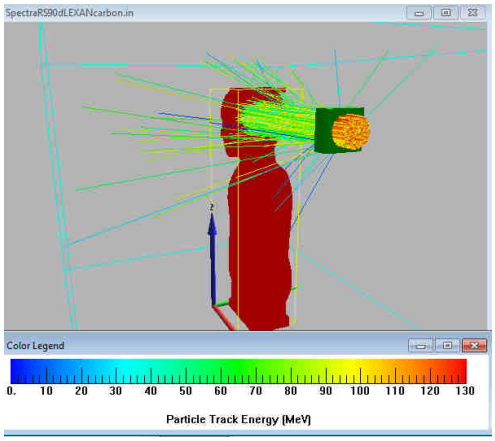

Figure 5.15: RS at 37 cm from MC anthropomorphic phantom isocenter. Proton beam coming from 90°.

Table 5.4: Description of the materials and dimensions used in modelling the RS and BC. The atomic elements used are expressed as a formula.

Element	Density (g cm^{-3})	Atomic composition	Dimensions	Source
Beam compensator made of polylactic acid	1.2	$C_3O_2H_4$	4 cm thick	[Wochnik et al., 2021]
Range shifter made of Lexan ≡ Polycarbonate	1.2	$C_{16}O_3H_{14}$	3.69 cm thick (37 cm distance between MC isocenter and RS)	[Detwiler et al., 2021]

Range Modulator System and Adaptive Aperture

Two particular elements are used in Mevion S250i Hyperscan single-room solution. A Range Modulator System (RMS), which is a proton energy degrader, and an Adaptive Aperture (AA), which is a collimator placed after the RMS. The elements are described in Vilches-Freixas et al. [2020]. A schematic view of Mevion S250i Hyperscan single-room solution is shown in Figure 5.16. MC modelled RMS and AA elements and its effect over a proton beam are shown in Figures 5.17 and 5.18. MC modelled proton radiotherapy situations are shown in Figures 5.19 and 5.20. Relevant details regarding materials composition and geometrical dimensions of the MC models are given in Table 5.5. The geometrical dimensions of AA are given in Vilches-Freixas et al. [2020] but the information about the material is not available. It was assumed that was the material Inconel-600 (see Table 5.5). The approximation described in Section 5.2.1 was used to set the thickness of the RMS.

In general, development of detailed MC models is difficult because manufacturer blueprints are often not readily available, and coding and validation are laborious [Kry et al., 2017].

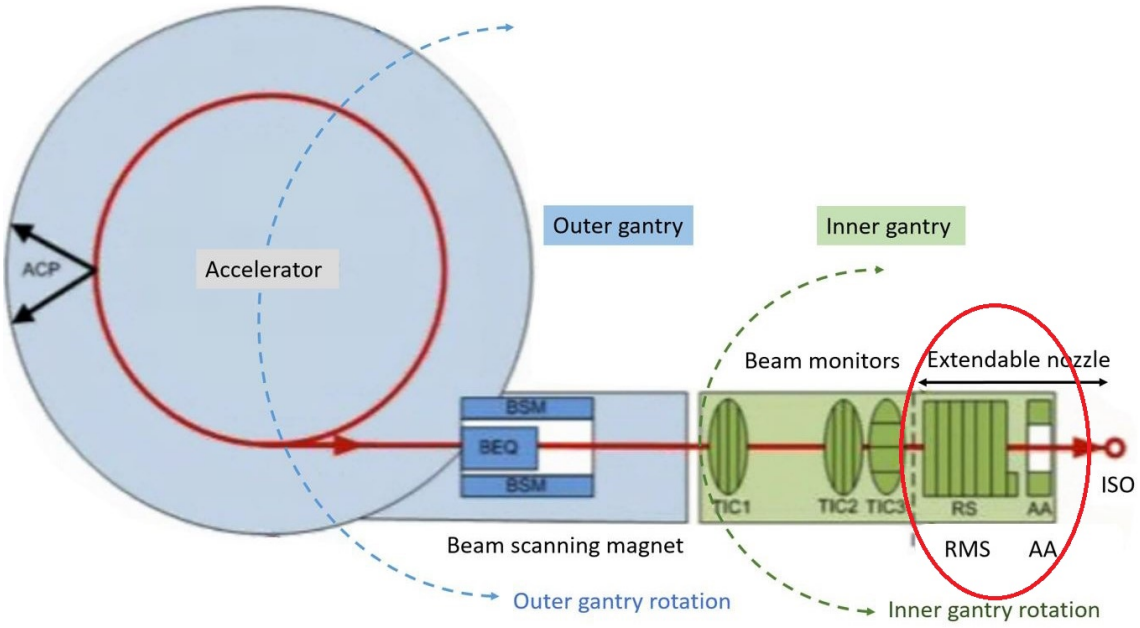

Figure 5.16: Schematic view of Mevion S250i Hyperscan single-room solution. The red circle highlights the RMS (energy degrader) followed by the AA (collimator). From Vilches-Freixas et al. [2020].

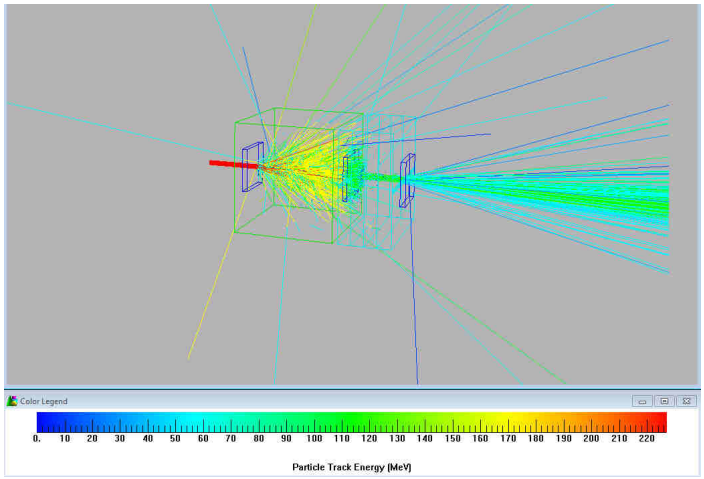

Figure 5.17: Modelling of RMS, AA and proton tracks. See its effects on the proton beam i.e., degradation and collimation of the proton beam. The thickness of the RMS is set according to Table 5.1. The color shown is the kinetic energy of the protons according to the presented scale.

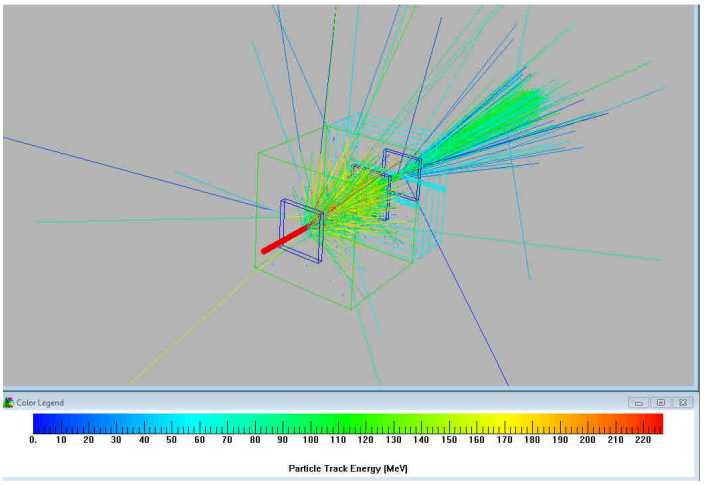

Figure 5.18: Modelling of RMS, AA and proton tracks. See its effects on the proton beam i.e., degradation and collimation of the proton beam. The thickness of the RMS is set according to Table 5.1. The color shown is the kinetic energy of the protons according to the presented scale.

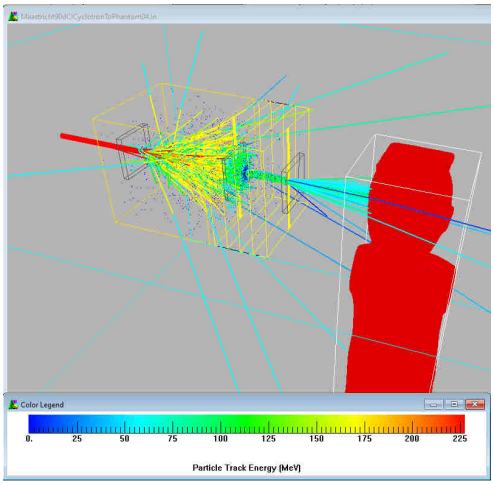

Figure 5.19: Situation in which the RMS and AA elements are used near the anthropomorphic phantom. The distance between the isocenter and the nearer side of the AA is 24 cm. The thickness of the RMS is set according to Table 5.1. Proton beam from 270°.

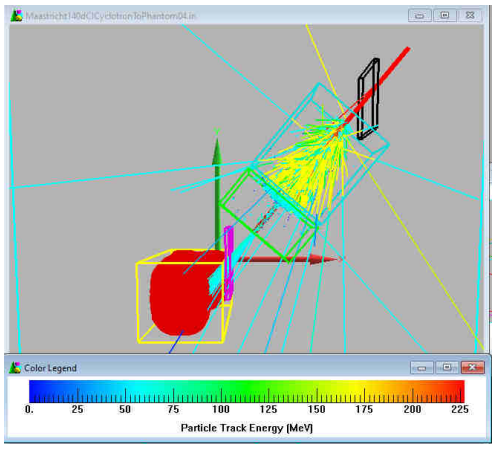

Figure 5.20: Situation in which the RMS and AA elements are used near the anthropomorphic phantom. The distance between the isocenter and the nearer side of the AA is 24 cm. The thickness of the RMS is set according to Table 5.1. Proton beam from 140°.

Table 5.5: Description of the materials and dimensions used in modelling the RMS and AA. The atomic elements used are expressed as a formula in general, when this is not possible, the weight fraction will be given.

Element	Density (g cm^{-3})	Atomic composition	Dimensions	Source
Range modulator system made of Lexan ≡ Polycarbonate	1.2	$C_{16}O_3H_{14}$	According to proton beam and approximation[a]	[Vilches-Freixas et al., 2020]
Adaptive aperture made of Inconel-600[b]	8.47	C(0.00098) Si(0.00325) S(0.0001) Cr(0.155) Mn(0.0065) Fe(0.08) Ni(0.75096) Cu(0.00325)	10 cm thick	∼ [Vilches-Freixas et al., 2020] ∼ [Detwiler et al., 2021]

[a] The thickness of the RMS was set according to the proton beam situation and approximation Section 5.2.1.
[b] Is an approximation.

Dimensions of the radiotherapy room and wall thicknesses from a facility using the Mevion S250i Hyperscan single-room system

In the MC simulations to compute guess energy distributions of the neutron fluence for neutron spectrometry, the walls of the proton radiotherapy room of a facility using the Mevion S250i Hyperscan single-room system were also introduced in the MC input. The thicknesses of the walls are in the range between 224 and 336 cm and they were modelled as concrete, portland ($\rho = 2.3$ g cm^{-3}, with weight fractions H(0.01) C(0.001) O(0.529107) Na(0.016) Mg(0.002) Al(0.033872) Si(0.337021) K(0.013) Ca(0.044) Fe(0.014)) [Detwiler et al., 2021]. See the modelled MC proton radiotherapy room in Figures 5.21, 5.22, 5.23 and 5.24.

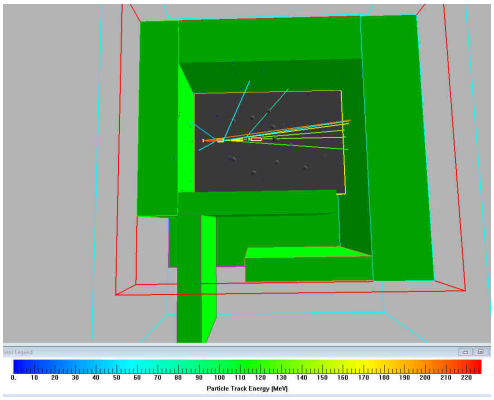

Figure 5.21: A view of the modelled MC proton radiotherapy room of a facility using the Mevion S250i Hyperscan single-room system.

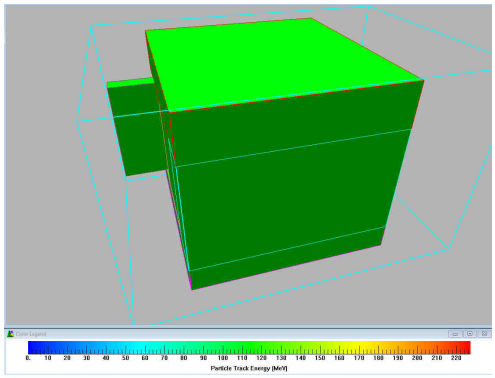

Figure 5.22: A view of the modelled MC proton radiotherapy room of a facility using the Mevion S250i Hyperscan single-room system.

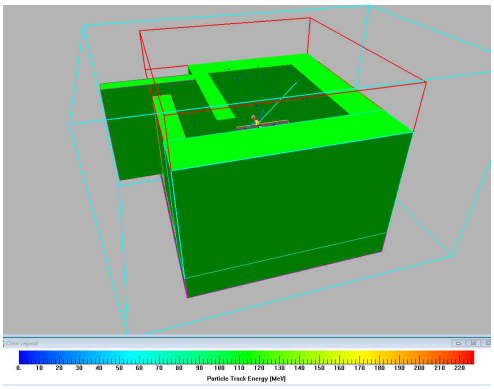

Figure 5.23: A view of the modelled MC proton radiotherapy room of a facility using the Mevion S250i Hyperscan single-room system.

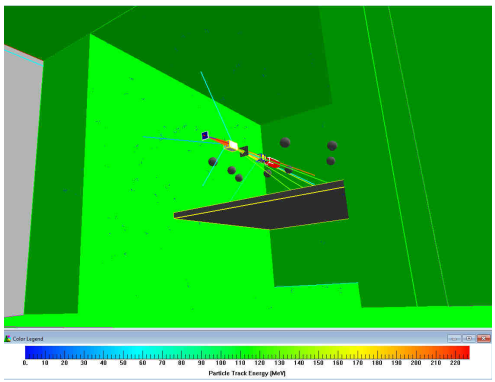

Figure 5.24: A view of the modelled MC proton radiotherapy room of a facility using the Mevion S250i Hyperscan single-room system.

Chapter 6

Proposed equation to characterize mixed radiation fields

The proposed equation intends to provide a mathematical but very practical equation (hereinafter the Radiation Dosimetry Equation (RDE)) in which the total signal in a radiation detector is described by means of the contributions of the energy distributions of the several particles that can appear in a general mixed radiation field.

It is practical in the sense that it relies on the known response functions or calibration coefficients of a detector. It usually makes use of the MC unit energy distributions of the particle fluence , $\varphi_E^{\mathrm{MC}}(E)$, Equation (3.4), or the MC unit energy distribution of the particle absorbed dose, $d_E^{\mathrm{MC}}(E)$, Equation (3.22), for the particles reaching the boundaries of the detector in the experimental and modelled situation.

If neither MC unit quantities ($\varphi_E^{\mathrm{MC}}(E)$ and $d_E^{\mathrm{MC}}(E)$) nor experimental unit energy distribution of the neutron fluence obtained by experimental means, $\varphi_E^{\mathrm{BSS}}(E)$, (for instance, through a Bonner Sphere System) are available, we can still work with the RDE using calibration coefficients obtained to radioactive sources meaning that the response function of the detector is constant and independent of the incident energy.

The RDE simply links the mixed radiation field with the response functions and calibration coefficients so that this link is, precisely, what gives rise to the total signal in the detector. As it will be shown, some experimental methodologies currently employed appear as particular cases of the RDE.

The convention and understanding of the response functions and calibration coefficients in this equation should be taken in the sense explained in Section 4.1. Moreover, in this formalism:

- The RDE relies on response functions or calibration coefficients that have been obtained in terms of experimental primary standards. For instance, the absorbed dose in water, D_{w}, kerma in water, K_{w}, fluence, Φ, etc. Which are quantities guaranteed by the reference/calibration/irradiation facilities. All quantities must be expressed in terms of primary standards. Moreover, detectors usually report results in terms of experimental primary standards. Any use of other quantities that are not standards are a source of uncertainties and complexities during the whole procedure needed to provide a dosimetric (or related to dose) quantity. In case that a transformation of quantities is needed, it must be done at the end of the process.

- According to Figure 3.6 and Section 3.1.4.3, in the RDE we consider that when we talk about neutrons and photons, these are the local neutrons and photons that directly reach the boundary of a radiation detector. There will be also charged particles reaching the radiation detector, these will be essentially understood as produced by non-local neutrons and non-local photons outside the detector. Contribution of charged particles which may be originated inside the detector, due to interaction of the local neutrons and photons, is already introduced in the conventional calibration coefficients or response functions, so that they do not appear in a specific term in the equation. Actually, this simply goes according to the definitions of response funtion and calibration coefficients introduced in Chapter 4.

Let us assume that we have a radiation detector immersed in the situation shown in Figure 3.6. If we denote as R the total signal *stored* by the detector immersed in the mixed radiation field, we can write

$$R = R_{\mathrm{ne}} + R_{\mathrm{ph}} + \sum_i R_{\mathrm{ch},i}, \tag{6.1}$$

where R_{ne} would be the contribution to the signal from local neutrons (neutrons reaching the boundary of the detector), R_{ph} would be the contribution to the signal from local photons (photons reaching the boundary of the detector) and $R_{\mathrm{ch},i}$ would be the contribution of charged particles of type i reaching the boundary of the detector. The concepts of locality and non-locality are shown in Figure 3.6.

Each partial contribution to the total signal *i.e.,* R_{ne}, R_{ph} and $R_{\mathrm{ch},i}$ actually depends on the energy distribution (or LET distribution) of the corresponding particles. This means that we have to expand Equation (6.1), so that

$$\begin{aligned} R &= R_{\mathrm{ne}} + R_{\mathrm{ph}} + \sum_i R_{\mathrm{ch},i} && (6.2)\\ &= \int_E \mathrm{d}R_{\mathrm{ne}}(E) + \int_E \mathrm{d}R_{\mathrm{ph}}(E) + \sum_i \int_L \mathrm{d}R_{\mathrm{ch},i}(L) && (6.3)\\ &= \textstyle\int_E \left[\frac{\mathrm{d}R_{\mathrm{ne}}}{\mathrm{d}\Phi_{\mathrm{ne}}}(E)\right] \mathrm{d}\Phi_{\mathrm{ne}}(E) + \int_E \left[\frac{\mathrm{d}R_{\mathrm{ph}}}{\mathrm{d}\Phi_{\mathrm{ph}}}(E)\right] \mathrm{d}\Phi_{\mathrm{ph}}(E) + \sum_i \int_L \left[\frac{\mathrm{d}R_{\mathrm{ch},i}}{\mathrm{d}D_{\mathrm{ch},i}}(L)\right] \mathrm{d}D_{\mathrm{ch},i}(L). && (6.4) \end{aligned}$$

Where $\mathrm{d}R_{\mathrm{ne}}(E)$ is the contribution of neutrons with energies between E and $E + \mathrm{d}E$ to the total signal R, $\mathrm{d}R_{\mathrm{ph}}(E)$ is the contribution of photons with energies between E and $E + \mathrm{d}E$ to the total signal R and $\mathrm{d}R_{\mathrm{ch},i}(L)$ is the contribution of charged particles of type i with LET between L and $L + \mathrm{d}L$ to the total signal R. The terms $\left[\frac{\mathrm{d}R_{\mathrm{ne}}}{\mathrm{d}\Phi_{\mathrm{ne}}}(E)\right]$, $\left[\frac{\mathrm{d}R_{\mathrm{ph}}}{\mathrm{d}\Phi_{\mathrm{ph}}}(E)\right]$ and $\left[\frac{\mathrm{d}R_{\mathrm{ch},i}}{\mathrm{d}D_{\mathrm{ch},i}}(L)\right]$ are, precisely, the response functions or the calibration coefficients of the radiation detector to neutrons, photons and charged particles. In Equation (6.4), the response functions or the calibration coefficients of the radiation detector to neutrons and photons are given in terms of fluence while the response function or the calibration coefficient of the radiation detector to charged particles of type i is given in terms of absorbed dose (in water, for instance) because these are the variables most commonly employed in the response functions for each type of particle. Including the notation from Equation (4.7) and applying definition Equations (3.4) and (3.22) we can write Equation

(6.4) as

$$R = \Phi_{\mathrm{ne}} \int_E R_{\Phi_{\mathrm{ne}}}(E)\varphi_{E,\mathrm{ne}}(E)\mathrm{d}E + \\ + \ \Phi_{\mathrm{ph}} \int_E R_{\Phi_{\mathrm{ph}}}(E)\varphi_{E,\mathrm{ph}}(E)\mathrm{d}E \ + \ \sum_i D_{\mathrm{ch},i} \int_L R_{D_{\mathrm{ch},i}}(L) d_{L,\mathrm{ch},i}(L)\mathrm{d}L. \quad (6.5)$$

It is important to state that Equation (6.5) will apply to a detector l whose response functions or calibration coefficients will be $R^{(l)}_{\Phi_{\mathrm{ne}}}(E)$, $R^{(l)}_{\Phi_{\mathrm{ph}}}(E)$ and $R^{(l)}_{D_{\mathrm{ch},i}}(L)$, so that Equation (6.5) can be written as

$$\boxed{R^{(l)} = \Phi_{\mathrm{ne}} \int_E R^{(l)}_{\Phi_{\mathrm{ne}}}(E)\varphi_{E,\mathrm{ne}}(E)\mathrm{d}E + \\ + \ \Phi_{\mathrm{ph}} \int_E R^{(l)}_{\Phi_{\mathrm{ph}}}(E)\varphi_{E,\mathrm{ph}}(E)\mathrm{d}E \ + \ \sum_i D_{\mathrm{ch},i} \int_L R^{(l)}_{D_{\mathrm{ch},i}}(L) d_{L,\mathrm{ch},i}(L)\mathrm{d}L.} \quad (6.6)$$

It must, nevertheless, be noticed that terms in the sum of Equation (6.4) may be expressed as a function of any variable in respect to which he corresponding response functions are stated, including absorbed dose, $\mathrm{d}D_i(L)$, fluence, $\mathrm{d}\Phi_i(E)$, ambient dose equivalent, $\mathrm{d}H^*_i(10,E)$, *etc.* As for some detectors used in this work the response function to charged particles is known in terms of fluence, as a function of energy, $R^{(l)}_{\Phi_{\mathrm{ch},i}}(E)$, it is convenient also to write explicitly an equivalent equation to Equation (6.6) when these variables are used

$$\boxed{R^{(l)} = \Phi_{\mathrm{ne}} \int_E R^{(l)}_{\Phi_{\mathrm{ne}}}(E)\varphi_{E,\mathrm{ne}}(E)\mathrm{d}E + \\ + \ \Phi_{\mathrm{ph}} \int_E R^{(l)}_{\Phi_{\mathrm{ph}}}(E)\varphi_{E,\mathrm{ph}}(E)\mathrm{d}E \ + \ \sum_i \Phi_{\mathrm{ch},i} \int_E R^{(l)}_{\Phi_{\mathrm{ch},i}}(E)\varphi_{E,\mathrm{ch},i}(E)\mathrm{d}E.} \quad (6.7)$$

We call Equations (6.6) and (6.7) the Radiation Dosimetry Equation (RDE) in detector l, where:

- $R^{(l)}$ is the experimental measurement or response in detector l in the mixed radiation field under study. In case of PADC based detectors, this is the total track density measured in the detector, in units of tracks cm^{-2}. In the case of active detectors, this is the total number of interacting events counted or the number of nuclear reactions counted in a PHD under a ROI. The exact meaning of $R^{(l)}$ always depends on how exactly is defined the response functions or calibration coefficients ($R^{(l)}_{\Phi_{\mathrm{ne}}}(E)$, $R^{(l)}_{\Phi_{\mathrm{ph}}}(E)$, $R^{(l)}_{D_{\mathrm{ch},i}}(L)$ and $R^{(l)}_{\Phi_{\mathrm{ch},i}}(E)$). We stress here a very important point, the parameters fixed during the whole procedure to finally obtain $R^{(l)}$ and the parameters fixed to find the response functions or calibration coefficients must have the same values. For instance, in ECE procedures, and in particular in UAB, we use the conditions defined by Table 4.8. So in the process of obtaining $R^{(l)}$ as well as $R^{(l)}_{\Phi_{\mathrm{ph}}}(E)$ and $R^{(l)}_{D_{\mathrm{ch},i}}(L)$ the same conditions were used.

- $R^{(l)}_{\Phi_{\mathrm{ne}}}(E)$ is the response function or calibration coefficient of the detector l to neu-

trons, in terms of neutron fluence. $R^{(l)}_{\Phi_{\mathrm{ph}}}(E)$ is the response function or calibration coefficient of the detector l to photons and in terms of photon fluence. $R^{(l)}_{D_{\mathrm{ch},i}}(L)$ is the response function or calibration coefficient of the detector l to charged particles of type i and in terms of absorbed dose (in water, for instance).

- Φ_{ne}, Φ_{ph}, $D_{\mathrm{ch},i}$ and $\Phi_{\mathrm{ch},i}$ are energy or LET integrated quantities. Φ_{ne} is the total neutron fluence in the mixed radiation field situation. Φ_{ph} is the total photon fluence in the mixed radiation field situation. $D_{\mathrm{ch},i}$ is the contribution to the total absorbed dose (in water for instance) by charged particles of type i in the mixed radiation field situation. $\Phi_{\mathrm{ch},i}$ is the total neutron fluence contibution by charged particles of type i in the mixed radiation field situation.

- $\varphi_{E,\mathrm{ne}}(E)$ is the unit energy distribution of the neutron fluence (see Equation (3.4)). $\varphi_{E,\mathrm{ph}}(E)$ is the unit energy distribution of the photon fluence (see Equation (3.4)). $d_{L,\mathrm{ch},i}(L)$ is the unit LET distribution of the absorbed dose (see Equation (3.22)). $\varphi_{E,\mathrm{ch},i}(E)$ is the unit energy distribution of the fluence for charged particles of type i (see Equation (3.4)).

As TLDs need an specific calibration procedure, it is convenient to write Equation (6.6) in a more suitable way for these type of detectors. This equation is obtained by simply dividing (6.4) by the term $\left[\frac{R_{\text{Co-60}}}{D_{\text{Co-60}}}\right]$ defined in Section 4.2 so that

$$\begin{aligned}\frac{R}{\left[\frac{R_{\text{Co-60}}}{D_{\text{Co-60}}}\right]} = &\int_E \frac{\left[\frac{\mathrm{d}R_{\mathrm{ne}}}{\mathrm{d}\Phi_{\mathrm{ne}}}(E)\right]}{\left[\frac{R_{\text{Co-60}}}{D_{\text{Co-60}}}\right]}\mathrm{d}\Phi_{\mathrm{ne}}(E) + \\ &+ \int_E \frac{\left[\frac{\mathrm{d}R_{\mathrm{ph}}}{\mathrm{d}\Phi_{\mathrm{ph}}}(E)\right]}{\left[\frac{R_{\text{Co-60}}}{D_{\text{Co-60}}}\right]}\mathrm{d}\Phi_{\mathrm{ph}}(E) + \sum_i \int_L \frac{\left[\frac{\mathrm{d}R_{\mathrm{ch},i}}{\mathrm{d}D_{\mathrm{ch},i}}(L)\right]}{\left[\frac{R_{\text{Co-60}}}{D_{\text{Co-60}}}\right]}\mathrm{d}D_{\mathrm{ch},i}(L). \end{aligned} \tag{6.8}$$

From the equations in Section 4.2, by Equation (4.21), using a procedure similar to the previous one, we obtain the Radiation Dosimetry Equation for TLDs for a detector l as

$$\boxed{\begin{aligned}\frac{R^{(l)}}{\left[\frac{R_{\text{Co-60}}}{D_{\text{Co-60}}}\right]} = &\Phi_{\mathrm{ne}}\int_E \eta^{(l)}_{\Phi_{\mathrm{ne}}}(E)\varphi_{E,\mathrm{ne}}(E)\mathrm{d}E + \\ &+ \Phi_{\mathrm{ph}}\int_E \eta^{(l)}_{\Phi_{\mathrm{ph}}}(E)\varphi_{E,\mathrm{ph}}(E)\mathrm{d}E + \sum_i D_{\mathrm{ch},i}\int_L \eta^{(l)}_{D_{\mathrm{ch},i}}(L)d_{L,\mathrm{ch},i}(L)\mathrm{d}L. \end{aligned}} \tag{6.9}$$

The term $\frac{R^{(l)}}{\left[\frac{R_{\text{Co-60}}}{D_{\text{Co-60}}}\right]}$ is known as the ^{60}Co gamma equivalent absorbed dose in water.

The meaning of each term from Equations (6.6), (6.7) and (6.9) is essentially the same. But we will repeat here some important comments applied to the TLD case

- $R^{(l)}$ is the experimental measurement or response of the detector in the mixed radiation field under study. In case of TLDs this is the raw luminescence response, which has no sense according to the conventional methodologies applied in TLDs due to the high variability of the parameters involved in the whole procedure. $\frac{R^{(l)}}{\left[\frac{R_{\text{Co-60}}}{D_{\text{Co-60}}}\right]}$ is known as the ^{60}Co gamma equivalent absorbed dose in water. As in the general case, we stress here a very important point, the parameters fixed during the whole

procedure to finally obtain $\frac{R^{(l)}}{\left[\frac{R_{\text{Co-60}}}{D_{\text{Co-60}}}\right]}$ and the parameters fixed to find the response functions, calibration coefficients or relative luminescence efficiencies must be the same.

- $\eta^{(l)}_{\Phi_{\text{ne}}}(E)$ is the response function, calibration coefficient or relative luminescence efficiency of the detector l to neutrons in terms of neutron fluence. $\eta^{(l)}_{\Phi_{\text{ph}}}(E)$ is the response function, calibration coefficient or relative luminescence efficiency of the detector l to photons in terms of photon fluence. $\eta^{(l)}_{D_{\text{ch},i}}(L)$ is the response function, calibration coefficient or relative luminescence efficiency of the detector l to charged particles of type i in terms of absorbed dose (in water, for instance).

- Φ_{ne}, Φ_{ph} and $D_{\text{ch},i}$ are energy or LET integrated quantities. Φ_{ne} is the total neutron fluence in the mixed radiation field situation. Φ_{ph} is the total photon fluence in the mixed radiation field situation. $D_{\text{ch},i}$ is the total absorbed dose (in water for instance) contributed by charged particles of type i in the mixed radiation field situation.

- $\varphi_{E,\text{ne}}(E)$ is the unit energy distribution of the neutron fluence (see Equation (3.4)). $\varphi_{E,\text{ph}}(E)$ is the unit energy distribution of the photon fluence (see Equation (3.4)). $d_{L,\text{ch},i}(L)$ is the unit LET distribution of the absorbed dose (see Equation (3.22)).

A very important point to stress is that in this equation it is understood that all the possible effects produced by the particles once they reach the boundary of the detector are simply taken into account in the response function, calibration coefficient or relative luminescence efficiencies. We do not need to see what is happening inside the detector and to use additional corrections to finally provide a numerical value that will be the dose. Absolutely all the physics and all the effects happening inside the detector are contained in the response function, calibration coefficient or relative luminescence efficiencies. This procedure is already seen in Chapter 4, in particular, when we introduce the response function. The procedure could be considered as a *black box* approach, in the sense that calibration coefficients, response functions and relative luminescence efficiencies are already taking into account all the effects or physics happening inside the boundaries of the detector.

In a *real case*, *i.e.,* when we use the RDEs when we do not know the quantities Φ_{ne}, Φ_{ph} and $D_{\text{ch},i}$, we do measurements with our detectors thus obtaining $R^{(l)}$ and $\frac{R^{(l)}}{\left[\frac{R_{\text{Co-60}}}{D_{\text{Co-60}}}\right]}$. We should have also an idea on how our detectors respond to radiation fields (*i.e.,* we know response functions, calibration coefficients and relative luminescence efficiencies) and we can do MC simulations to know $\varphi_{E,\text{ne}}(E)$, $\varphi_{E,\text{ph}}(E)$ and $d_{L,\text{ch},i}(L)$. So, in a real use of the equation the unknown variables will be Φ_{ne}, Φ_{ph} and $D_{\text{ch},i}$.

In a *test case*, we do measurements with our devices in a calibration or reference facility, *i.e.,* we know the right side of the RDEs. We do measurements with our detectors thus obtaining $R^{(l)}$ and $\frac{R^{(l)}}{\left[\frac{R_{\text{Co-60}}}{D_{\text{Co-60}}}\right]}$ and we compare the right side and the left side from the RDEs.

6.1 Particular cases of the equation

In this section, some common examples found in radiation protection procedures are discussed in order to clarify how Equations (6.6), (6.7) and (6.9) are applied.

6.1.1 Detector sensitive to one type of particle

Let us suppose an ideal radiation detector l that has sensitivity to only one type of particle, for instance to neutrons, this means that $R^{(l)}_{\Phi_{\mathrm{ne}}}(E) \neq 0$ but $R^{(l)}_{\Phi_{\mathrm{ph}}}(E) = 0$ and $R^{(l)}_{D_{\mathrm{ch},i}}(L) = 0$. In this particular case, Equations (6.6) and (6.9) result in

$$R^{(l)} = \Phi_{\mathrm{ne}} \int_E R^{(l)}_{\Phi_{\mathrm{ne}}}(E)\varphi_{E,\mathrm{ne}}(E)\mathrm{d}E. \tag{6.10}$$

$$\frac{R^{(l)}}{\left[\frac{R_{\text{Co-60}}}{D_{\text{Co-60}}}\right]} \equiv D_{\mathrm{w},^{60}\text{Co-eq}} = \Phi_{\mathrm{ne}} \int_E \eta^{(l)}_{\Phi_{\mathrm{ne}}}(E)\varphi_{E,\mathrm{ne}}(E)\mathrm{d}E. \tag{6.11}$$

So that

$$\Phi_{\mathrm{ne}} = \frac{R^{(l)}}{\int_E R^{(l)}_{\Phi_{\mathrm{ne}}}(E)\varphi_{E,\mathrm{ne}}(E)\mathrm{d}E}. \tag{6.12}$$

$$\Phi_{\mathrm{ne}} = \frac{D_{\mathrm{w},^{60}\text{Co-eq}}}{\int_E \eta^{(l)}_{\Phi_{\mathrm{ne}}}(E)\varphi_{E,\mathrm{ne}}(E)\mathrm{d}E}. \tag{6.13}$$

In the particular case that the response function of the radiation detector l is assumed to be a constant or independent of the energy distribution of the particle, let us say $R^{(l)}_{\Phi_{\mathrm{ne}}}(E) = R^{(l)}_{\Phi_{\mathrm{ne}}}(E_0)$ (calibration to a radioactive neutron source such as AmBe), this mathematically means that

$$\Phi_{\mathrm{ne}} = \frac{R^{(l)}}{\int_E R^{(l)}_{\Phi_{\mathrm{ne}}}(E)\varphi_{E,\mathrm{ne}}(E)\mathrm{d}E} \sim \frac{R^{(l)}}{R^{(l)}_{\Phi_{\mathrm{ne}}}(E_0)}. \tag{6.14}$$

$$\Phi_{\mathrm{ne}} = \frac{D_{\mathrm{w},^{60}\text{Co-eq}}}{\int_E \eta^{(l)}_{\Phi_{\mathrm{ne}}}(E)\varphi_{E,\mathrm{ne}}(E)\mathrm{d}E} \sim \frac{D_{\mathrm{w},^{60}\text{Co-eq}}}{\eta^{(l)}_{\Phi_{\mathrm{ne}}}(E_0)}. \tag{6.15}$$

Equations (6.14) and (6.15) are the most common way of determining a physical or dosimetric quantity in general. No Monte Carlo computations of the unit energy distribution of the neutron fluence, $\varphi_{E,\mathrm{ne}}(E)$, are needed.

The specific procedure used in this work to determine neutron dose equivalents in ICRU tissue with the PADC based neutron dosimeter actually uses Equation (6.12). See the equivalence between Equation (6.12) and the procedures described in Section 4.6.1 and Section 4.6.2. On the other hand, see the equivalence between Equations (6.14) and (4.4).

The methodology exposed in Romero-Expósito et al. [2016] can be understood as an approach focusing on Equation (6.12). Given the neutron response functions or rather the calibration coefficients *valid only* in different parts of the energy distribution of the neutron fluence, that is to say, $R^{(l)}_{\Phi_{\mathrm{ne}}}(E = \text{Thermal})$, $R^{(l)}_{\Phi_{\mathrm{ne}}}(E = \text{Epithermal})$, $R^{(l)}_{\Phi_{\mathrm{ne}}}(E = \text{Fast})$ and $R^{(l)}_{\Phi_{\mathrm{ne}}}(E = \text{High energy})$ one can expand Equation (6.12) so that

$$\begin{aligned}
\Phi_{\mathrm{ne}} &= \frac{R^{(l)}}{\int_E R^{(l)}_{\Phi_{\mathrm{ne}}}(E)\varphi_{E,\mathrm{ne}}(E)\mathrm{d}E} \\
&= \frac{R^{(l)}}{\int_0^{E_{\mathrm{Th}}} R^{(l)}_{\Phi_{\mathrm{ne}}}(E)\varphi_{E,\mathrm{ne}}(E)\mathrm{d}E + \int_{E_{\mathrm{Th}}}^{E_{\mathrm{Ep}}} R^{(l)}_{\Phi_{\mathrm{ne}}}(E)\varphi_{E,\mathrm{ne}}(E)\mathrm{d}E + \int_{E_{\mathrm{Ep}}}^{E_{\mathrm{Fa}}} R^{(l)}_{\Phi_{\mathrm{ne}}}(E)\varphi_{E,\mathrm{ne}}(E)\mathrm{d}E + \int_{E_{\mathrm{Fa}}}^{E_{\mathrm{Hi}}} R^{(l)}_{\Phi_{\mathrm{ne}}}(E)\varphi_{E,\mathrm{ne}}(E)\mathrm{d}E}, \\
&= \frac{R^{(l)}}{R^{(l)}_{\Phi_{\mathrm{ne}}}(\mathrm{Th})\int_0^{E_{\mathrm{Th}}} \varphi_{E,\mathrm{ne}}(E)\mathrm{d}E + R^{(l)}_{\Phi_{\mathrm{ne}}}(\mathrm{Ep})\int_{E_{\mathrm{Th}}}^{E_{\mathrm{Ep}}} \varphi_{E,\mathrm{ne}}(E)\mathrm{d}E + R^{(l)}_{\Phi_{\mathrm{ne}}}(\mathrm{Fa})\int_{E_{\mathrm{Ep}}}^{E_{\mathrm{Fa}}} \varphi_{E,\mathrm{ne}}(E)\mathrm{d}E + R^{(l)}_{\Phi_{\mathrm{ne}}}(\mathrm{Hi})\int_{E_{\mathrm{Fa}}}^{E_{\mathrm{Hi}}} \varphi_{E,\mathrm{ne}}(E)\mathrm{d}E}.
\end{aligned} \tag{6.16}$$

Where $R^{(l)}_{\Phi_{\rm ne}}(E = \text{Thermal}) \equiv R^{(l)}_{\Phi_{\rm ne}}(\text{Th})$, $R^{(l)}_{\Phi_{\rm ne}}(E = \text{Epithermal}) \equiv R^{(l)}_{\Phi_{\rm ne}}(\text{Ep})$, $R^{(l)}_{\Phi_{\rm ne}}(E = \text{Fast}) \equiv R^{(l)}_{\Phi_{\rm ne}}(\text{Fa})$ and $R^{(l)}_{\Phi_{\rm ne}}(E = \text{High energy}) \equiv R^{(l)}_{\Phi_{\rm ne}}(\text{Hi})$.

To the author knowledge, many current methodologies employed by radiation protection research groups are compatible with that predicted in this section.

6.1.2 Detector sensitive to two type of particles

Let us suppose a radiation detector l that is sensitive to two types of particles, for instance to neutrons and protons, this means that $R^{(l)}_{\Phi_{\rm ne}}(E), R^{(l)}_{\Phi_{\rm ch,pr}}(E) \neq 0$ but $R^{(l)}_{\Phi_{\rm ph}}(E) = 0$ and $R^{(l)}_{\Phi_{{\rm ch},i\neq{\rm pr}}}(E) = 0$. In this particular case, Equations (6.7) and (6.9) can be written as

$$R^{(l)} = \Phi_{\rm ne}\int_E R^{(l)}_{\Phi_{\rm ne}}(E)\varphi_{E,{\rm ne}}(E){\rm d}E + \Phi_{\rm pr}\int_E R^{(l)}_{\Phi_{\rm pr}}(E)\varphi_{E,{\rm pr}}(E){\rm d}E. \tag{6.17}$$

$$\frac{R^{(l)}}{\left[\frac{R_{\text{Co-60}}}{D_{\text{Co-60}}}\right]} \equiv D_{{\rm w},^{60}\text{Co-eq}} = \Phi_{\rm ne}\int_E \eta^{(l)}_{\Phi_{\rm ne}}(E)\varphi_{E,{\rm ne}}(E){\rm d}E + \Phi_{\rm pr}\int_E \eta^{(l)}_{\Phi_{\rm pr}}(E)\varphi_{E,{\rm pr}}(E){\rm d}E. \tag{6.18}$$

The problem with Equations (6.17) and (6.18) is that, even doing MC simulations to know the unit energy distribution of the neutron and proton fluence ($\varphi_{E,{\rm ne}}(E)$ and $\varphi_{E,{\rm pr}}(E)$, respectively) and even doing measurements with one detector to obtain an experimental measure ($R^{(l)}$ or $\frac{R^{(l)}}{\left[\frac{R_{\text{Co-60}}}{D_{\text{Co-60}}}\right]}$) we have two unknown variables *i.e.,* $\Phi_{\rm ne}$ and $\Phi_{\rm pr}$.

There are two approaches to follow from here

- To employ a second detector with main (or only) sensitive to protons so $\Phi_{\rm pr}$ is known by the procedures of Section 6.1.1, to use it in Equation (6.17) and to isolate $\Phi_{\rm ne}$. This is the preferred method in order to solve the problem. On the other hand, by employing two detectors sensitive to local neutrons and protons, we will have two equations like Equation (6.17). That is to say, for detector 1 ($l = 1$) and detector 2 ($l = 2$) we will have

$$R^{(1)} = \Phi_{\rm ne}\int_E R^{(1)}_{\Phi_{\rm ne}}(E)\varphi_{E,{\rm ne}}(E){\rm d}E + \Phi_{\rm pr}\int_E R^{(1)}_{\Phi_{\rm pr}}(E)\varphi_{E,{\rm pr}}(E){\rm d}E, \tag{6.19}$$

$$R^{(2)} = \Phi_{\rm ne}\int_E R^{(2)}_{\Phi_{\rm ne}}(E)\varphi_{E,{\rm ne}}(E){\rm d}E + \Phi_{\rm pr}\int_E R^{(2)}_{\Phi_{\rm pr}}(E)\varphi_{E,{\rm pr}}(E){\rm d}E. \tag{6.20}$$

  Of course, each kind of detector will have its own response functions, calibration coefficients or relative luminescence efficiencies. Equations (6.19) and (6.20) constitute a equation system that can be solved to find $\Phi_{\rm ne}$ and $\Phi_{\rm pr}$.

- To compute also by MC either the quantity $\Phi_{\rm ne}$ or the quantity $\Phi_{\rm pr}$ according to the *main* sensitivity of the particular radiation detector. If the detector is more sensitive to local neutrons than to protons (remember the meaning of the notions of locality and non-locality in this work) is reasonable to compute by MC $\Phi_{\rm pr}$ and to isolate from Equation (6.17) the quantity $\Phi_{\rm ne}$.

6.2 Additional remarks

When a mixed radiation field is completely known, *i.e.,* we know Φ_{ne}, Φ_{ph} and $D_{\mathrm{ch},i}$ we can apply Equations (3.67) or (3.70) to know the total dose equivalent of a mixed radiation field (see Section 3.1.4.3).

The Radiation Dosimetry Equations (6.6), (6.7) and (6.9) can be applied under *infinite* situations and under different kind of approximations in a way similar to that shown in Section 6.1.1 and Section 6.1.2.

When trying to compute by MC the quantities $\varphi_{E,\mathrm{ne}}(E)$, $\varphi_{E,\mathrm{ph}}(E)$, $\varphi_{E,\mathrm{ch},i}(E)$ and similar, it may be important the double scoring facts exposed in Section 5.6.

When computing the MC quantities the geometry and materials of the facility in which the experimental measurements are carried out should be properly modelled and they should be computed in the location in which the detector is placed when doing the experimental measure.

Equations (6.6), (6.7) and (6.9) were presented in Caballero-Pacheco [2022].

Chapter 7

Applications and results in real neutron fields

In this work, the quantities used which characterize the neutron dose equivalent are:

- The operational quantity, neutron ambient dose equivalent, $H^*_{\mathrm{ne}}(10)$, Equation (4.55), for measurements in air.
- Neutron dose equivalent in ICRU tissue, H_{ne}, Equation (4.51), for measurements in phantom.

This chapter is subdivided into three sections: Section 7.1 summarises the results obtained in the experiments performed in scanning proton radiotherapy facilities, which constitute the mainstream of this Ph.D. Thesis work; Section 7.2 abridges the results from MC calculations of the neutron quality factor, $Q(E)$, in a wide energy range; and finally, Section 7.3 presents the experimental and MC results for other applications both in similar and different neutron energy ranges than in the case of proton radiotherapy. These include the radiation field at specific places of the ALBA synchrotron, at the CERF calibration facility, where a mixed radiation field of photons, electrons, protons, neutrons, pions and muons is found, at ENEA HOTNES source and the contribution to a project to design a device with neutron spectrometric characteristics for soil moisture studies.

7.1 Neutron dose equivalents in particle beam scanning proton radiotherapy

In simple terms, and in the frame of this work, when assessing the performance of a external-beam radiation therapy technique, we should focus in two features:

- How well the therapeutic radiation dose in the tumour is conformed and contained.
- Which out-of-field doses are generated in the process. For these purposes, UAB neutron radiation detectors have been used in order to quantify the neutron out-of-field doses, in particular, in proton radiotherapy.

An introduction about different aspects of proton radiotherapy can be found in Paganetti [2019] while more general reviews about external-beam radiation therapy techniques can be found in Kry et al. [2017] and Xu et al. [2008].

Out-of-field neutron dose equivalents found in proton beam scanning treatments (also known as particle beam scanning (PBS), intensity-modulated proton therapy (IMPT) or spot scanning (SS)) [Paganetti, 2019] performed at proton radiotherapy facilities depend or could depend, a priori, on:

- The beam delivery method used by the facility or the design of the facility itself *i.e.,* the solution provided by companies such as Ion Beam Applications (IBA) [IBA, 2022], Mevion Medical Systems (Mevion) [Mevion, 2022], Varian Medical Systems (Varian) [Varian, 2022], Hitachi [Hitachi, 2022], Sumitomo Heavy Industries (SHI) [SHI, 2022], ProTom [ProTom, 2022], ProNova [ProNova, 2022] and Advanced Oncotherapy [Advanced Oncotherapy, 2022].
- The phantom used as a target of the therapeutic protons (water tank phantom or anthropomorphic phantom).
- The specific parameters used in the treatment plan (energy of the therapeutic protons, size of the scanned volume and absorbed dose rate). See, for instance, Van Hoey et al. [2022].
- The specific measurement point in respect to the isocenter point or reference point in the proton radiotherapy room.

Measurements obtained in the frame of this work correspond to the proton PBS technique.

Nowadays, the cyclotron and the synchrotron are the two typical types of accelerators that are offered by companies and are proven to be reliable machines in clinical facilities. While the first type of accelerators are optimized to provide protons to a fixed energy of 230 or 250 MeV, the second type can deliver protons between 70 MeV and 250 MeV [Paganetti, 2019]. These energy ranges are needed in order to be able to irradiate all possible target volumes in adult patients. Proton ranges of 26–38 cm in tissue (corresponding to proton energies of 200–250 MeV) are required [ICRU, 2007].

Some features, advantages and disadvantages of each type of proton accelerator can be summarised as follows [Paganetti, 2019]:

- In general, neutron production and activation will be higher in cyclotrons as the protons with fixed energy could go through a degrader (element used to reduce the energy of the protons according to the treatment), the energy selection system (to limit the spread of the energy of the protons) and collimators or even additional degraders for treating shallow tumours. A beam extraction efficiency exists, which informs about the protons that are lost in the cyclotron respect to those protons that properly leave the cyclotron structure and are properly directed to the proton line. Extraction efficiencies in cyclotrons should not be less than $60 - 70$ %. As synchrotrons accelerate protons to the desired energy, there is almost no activation generated by beam losses.
- The space required for a proton synchrotron is larger than for a cyclotron, the synchrotron itself has a diameter of $6 - 8$ m and the injection system has a length of $6 - 10$ m. The injection consists of an ion source, one or two linear accelerators

in series and a drift tube linac, as well as and a beam transport system. In general, when superconducting magnet coils are used, the magnet height is 1.5 m with a diameter of 3.5 m so that the total weight is around 100 tons.

These proton accelerators are typically placed in the facilities similar to those shown in Figures 7.1, 7.2, 7.3 and 7.4.

Figure 7.1: IBA single-room solution for PBS proton radiotherapy. A cyclotron is used. Area dimensions of 360 m^2 [IBA, 2022].

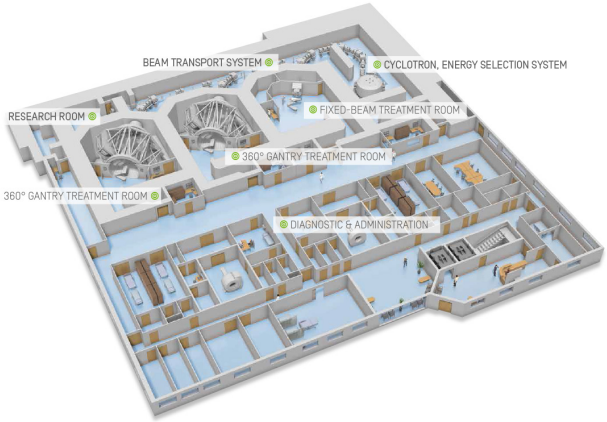

Figure 7.2: IBA multiple-room solution for PBS proton radiotherapy. A cyclotron is used. Area dimensions up to 1800 m^2 [IBA, 2022].

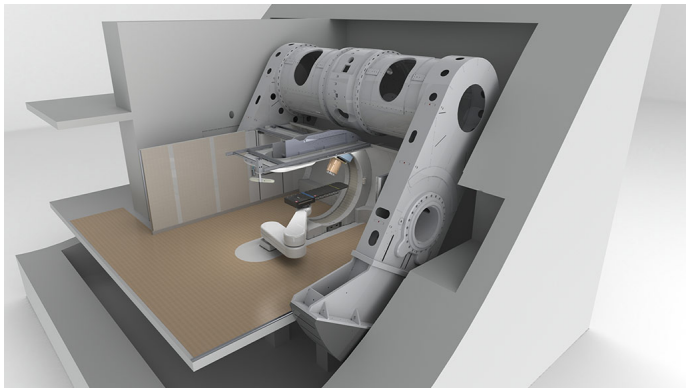

Figure 7.3: Mevion single-room solution for PBS proton radiotherapy. A cyclotron is used. Dimensions of 11.3 m × 9.8 m × 8.5 m [Mevion, 2022].

Figure 7.4: Hitachi single-room solution for PBS proton radiotherapy. A synchrotron is used [Hitachi, 2022].

Tables 7.1 and 7.2 summarise the main parameters characterising the studies where UAB has participated in the EURADOS-WG9 collaboration.

While in Table 7.1 studies related with neutron pasive dosimetry (UAB has contributed with a neutron dosimeter based on PADC, described in Section 4.4.2) are found. In Table 7.2 studies related with active neutron spectrometry or neutron active dosimetry (UAB has contributed in active neutron spectrometry using the active Bonner Sphere System, described in Section 4.5.1) are presented.

In this way, medical physicists can use the results of this work as long as the situation under study matches (or approximately matches) the conditions of the studies shown here.

Table 7.1: Summary of the parameters characterising proton irradiations experiments carried out by EURADOS-WG9 with the participation of UAB in the frame of passive dosimetry.

Article related	Facility type	Proton mean and [most probable] energy (MeV)	Phantom	Size of the field
[Knežević et al., 2017]	IBA multiple-room (C-235 cyclotron)	106 [121] and 120 [131]	AP[b]	Disk 3 cm radius
[Stolarczyk et al., 2018]	IBA multiple-room (C-230 cyclotron)	172[a]	WT[b]	Square 10 × 10 cm^2
[Wochnik et al., 2021]	IBA multiple-room (C-235 cyclotron) + additional energy degrader[c]	[130]	AP	Disk 3 cm radius
[Davídková, 2023]	Mevion S250i Hyperscan single-room	163 [176] & 117 [128] and 93 (see Figures 7.14 and 7.15)	WT & AP	As previous experiments

[a] SOBP was 10 cm in a therapeutic target volume of 10 × 10 × 10 cm^3 with 172 MeV as a maximum proton energy.
[b] AP ≡ anthropomorphic phantom, WT ≡ Water tank phantom.
[c] The additional energy degrader can be a Beam Compensator (BC) or a Range Shifter (RS).

Table 7.2: Summary of the parameters characterising proton irradiations experiments carried out by EURADOS-WG9 with the participation of UAB in the frame of active neutron spectrometry.

Article related	Facility type	Proton most probable energy (MeV)	Phantom	Size of the field
[Farah et al., 2015]	IBA multiple-room (C-230 cyclotron)	172	WT	Square 10 × 10 cm^2
[Mares et al., 2016]	IBA multiple-room (C-235 cyclotron)	144	AP	Disk 2.5 cm radius
[Domingo, 2023]	Mevion S250i Hyperscan single-room	122	AP	Square 5 × 5 cm^2

7.1.1 Neutron passive dosimetry

Two irradiation campaigns were organized by the EURADOS-WG9 collaboration in order to quantify the out-of-field in-phantom doses in two different proton radiotherapy systems. The first irradiation campaign was carried out in a facility that uses a non-compact proton radiotherapy system (or multiple-room solution, see for instance Figure 7.2). In particular, in that facility was used the IBA multiple-room (C-230 cyclotron) solution. The second irradiation campaign was arranged in a proton radiotherapy facility that uses a compact proton radiotherapy system (or single-room solution, see for instance Figure 7.3). Specifically, in that facility was used the Mevion S250i Hyperscan single-room solution.

In the frame of this work, measurements took place in the Mevion S250i Hyperscan single-room system but we will be recalling the already published results obtained in the first irradiation campaign when doing comparisons [Knežević et al., 2017] [Stolarczyk et al., 2018] [Wochnik et al., 2021].

Measurements with UAB neutron dosimeters based on PADC (Section 4.4.2) were done in the same water tank phantom as that described in Stolarczyk et al. [2018] and Bordy et al. [2013]. The water tank phantom has dimensions 30 cm × 30 cm × 60 cm and their walls are, in general, 1.5 cm thick and made of PMMA ($C_5O_2H_8$, $\rho = 1.19$ g cm^{-3}). See geometrical features of the water tank phantom in Figures 7.5 and 7.6.

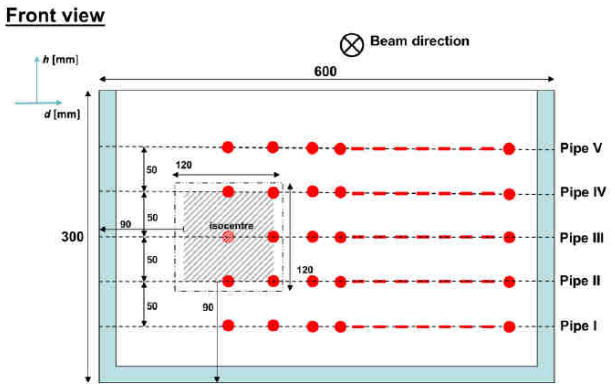

Figure 7.5: Water tank phantom definition and notation. See how pipes are labelled. Front view. From Stolarczyk et al. [2018].

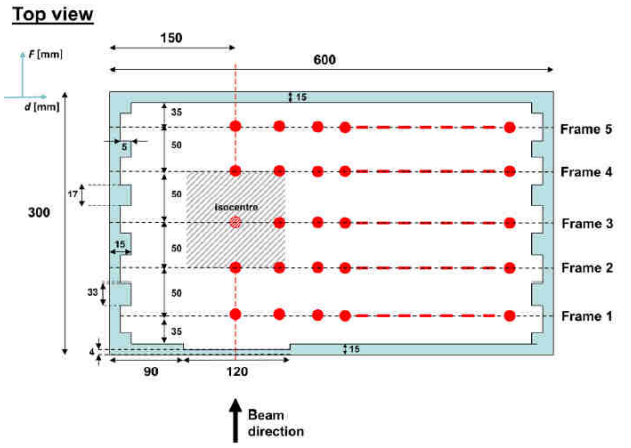

Figure 7.6: Water tank phantom definition and notation. See how frames are labelled. Top view. From Stolarczyk et al. [2018].

Measurements with UAB neutron dosimeters (Section 4.4.2) were also done in the same 5 YO anthropomorphic phantom as the one described in Knežević et al. [2017] and Wochnik et al. [2021]. The 5 YO anthropomorphic phantom is built slice by slice so that dosimeters can be placed inside of each slice. The anthropomorphic phantom is then constituted by 26 slices with a slice thickness of 25 mm so that the anthropomorphic phantom has a height of 65 cm. The anthropomorphic phantom is manufactured by ATOM: Dosimetry Phantoms [CIRS, 2023]. See some views of the anthropomorphic phantom as well as the labelling in their measurement positions in Figures 7.7, 7.8 and 7.9. In addition, see the distances to isocenter for each measurement position, valid only in the experiments regarding the system Mevion S250i Hyperscan single-room, in Table 7.3.

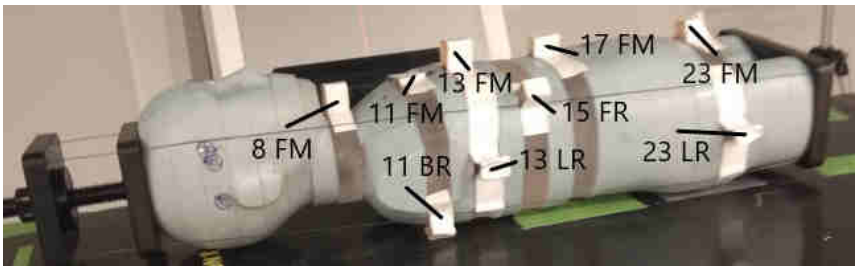

Figure 7.7: General view of the specific points of measurements inside the 5 YO anthropomorphic phantom. Details about the notation in Table 7.3.

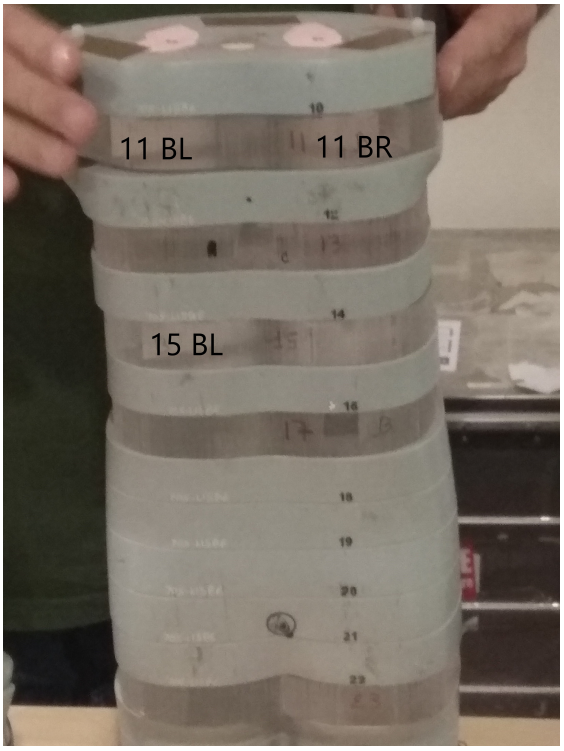

Figure 7.8: Back view of the specific points of measurements inside the 5 YO anthropomorphic phantom. Details about the notation in Table 7.3.

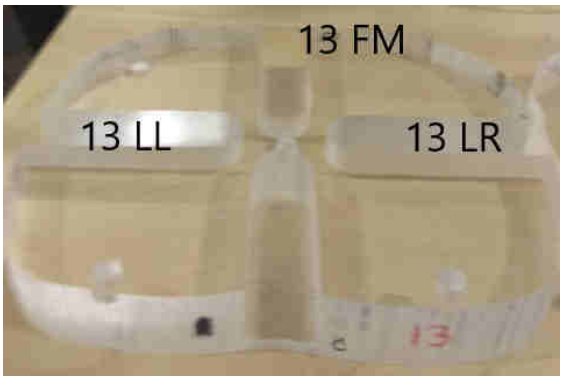

Figure 7.9: View of the specific points of measurements in the slice number 13. Details about the notation in Table 7.3.

Table 7.3: Correspondence between the specific points of measurement inside the 5 YO anthropomorphic phantom and the distance to the isocenter in the proton irradiation experiments regarding the Mevion S250i Hyperscan single-room system.

Slice number	Position	Distance to isocenter (cm)
8	8 FM[a]	12.262
11	11 FM	20.185
11	11 BL[a]	20.107
11	11 BR[a]	20.926
13	13 FM	24.058
13	13 LL[a]	24.778
13	13 LR[a]	24.799
15	15 BL	31.637
15	15 FR	29.483
17	17 FM	34.144
23	23 FM	49.362
23	23 LR	49.409

[a] FM ≡ Front middle, BL ≡ Back left, BR ≡ Back right, LL ≡ Lateral left and LR ≡ Lateral right.

7.1.1.1 Evaluated neutron dose equivalents

In order to compute the neutron dose equivalent in ICRU tissue, H_{ne}, Equation (4.51), with the UAB methodology described in Section 4.6.1, MC simulations to compute the MC unit energy distribution of the neutron fluence, $\varphi_E(E)$, were performed.

Views of the MC models of the water tank phantom and the anthropomorphic phantom as well as the situation of the proton therapeutic beams used in measurements regarding the Mevion S250i Hyperscan single-room system are shown in Figures 7.10, 7.11 and 7.12.

Additional details regarding the MC models can be found in Section 5.7. In the MC models, the distance from the isocenter to the closest face of the collimator (adaptive aperture (AA)) is 24 cm. The modelled proton beam is essentially a dot beam of 0.4472 cm radius. The AA contains a hollow cylinder (*i.e.,* filled with air) with exactly 0.4472 cm radius so that the non-scattered proton beam does not interact with the AA. However, as the energy degrader (range modulator system (RMS)) is located before the AA, the scattered protons will interact with the AA, producing secondary radiation. The thickness of the energy degrader is set according to the strategy explained in Section 5.2. In this work, the employed MC simulations regarding PBS proton radiotherapy are an approximation to the complicated proton beam dynamics involved in PBS proton radiotherapy.

The absorbed doses provided to the water tank phantom were in the range between 20 and 40 Gy (see detailed information in Appendix A). A total absorbed dose of 41 Gy was used in the case of the anthropomorphic phantom, 23 Gy were coming from the proton beam with an angular incidence of 270° and 18 Gy were coming from the proton beam of 140° according to the Figure 7.13.

The energy distribution of the protons incident to the phantoms is specified in Figure 7.14 for the case of the water tank phantom and Figure 7.15 for the case of the anthropomorphic phantom. The field size was a disk of 3 cm radius.

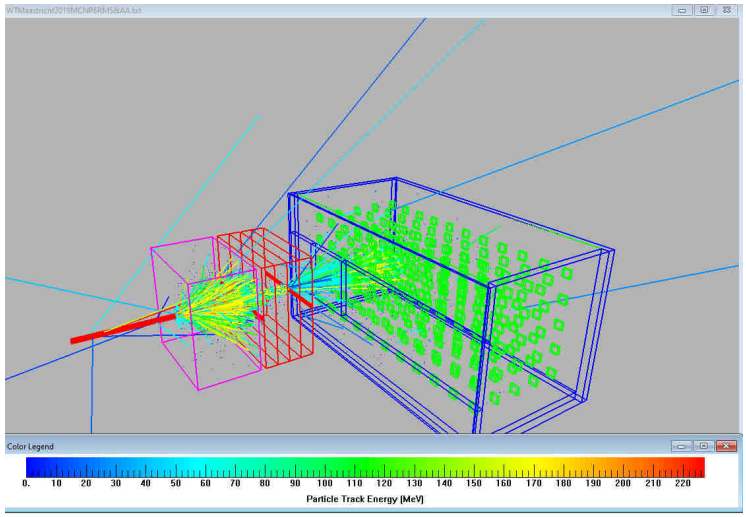

Figure 7.10: MC modelling of the water tank phantom in Mevion S250i Hyperscan single-room. In this figure is shown the modelled range modulation system (RMS) and the modelled adaptive aperture (AA). The distance between the isocenter and the nearer side of the AA is 24 cm. The thickness of the RMS is set according to Table 5.1. Proton tracks and their energy distribution are shown.

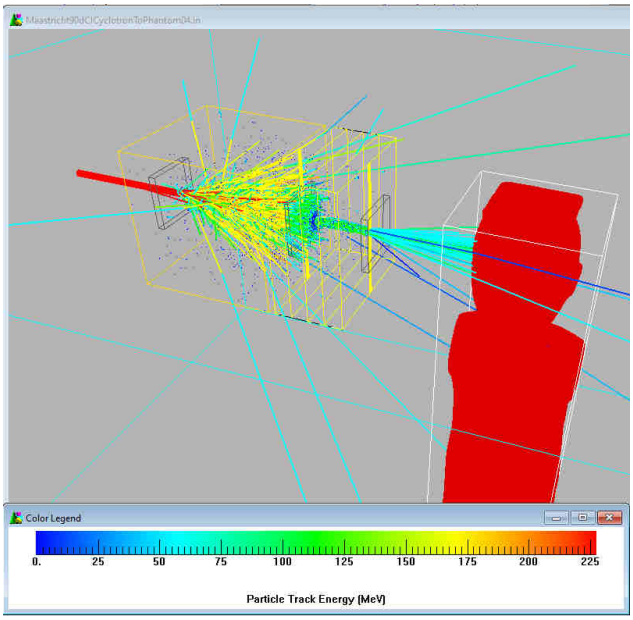

Figure 7.11: MC modelling in Mevion S250i Hyperscan single-room of the situation in which the beam is coming from 270°. In this figure is shown the modelled range modulation system (RMS) and the modelled adaptive aperture (AA). The distance between the isocenter and the nearer side of the AA is 24 cm. The thickness of the RMS is set according to Table 5.1. Proton tracks and their energy distribution are shown.

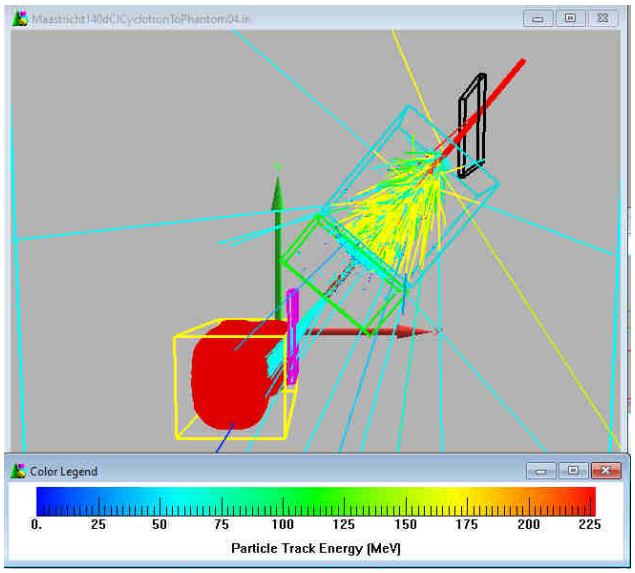

Figure 7.12: MC modelling in in Mevion S250i Hyperscan single-room of the situation in which the beam is coming from 140°. In this figure is shown the modelled range modulation system (RMS) and the modelled adaptive aperture (AA). The distance between the isocenter and the nearer side of the AA is 24 cm. The thickness of the RMS is set according to Table 5.1. Proton tracks and their energy distribution are shown.

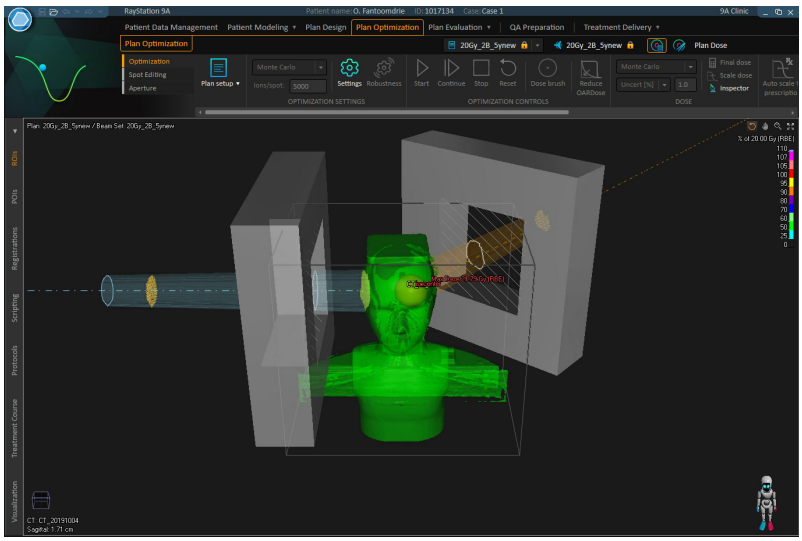

Figure 7.13: Beam directions in measurements regarding the Mevion S250i Hyperscan single-room system. One proton beam was coming from 140° while the other one was coming from 270° (beam coming from the right of the anthropomorphic phantom), producing a total of 41 Gy in the target volume.

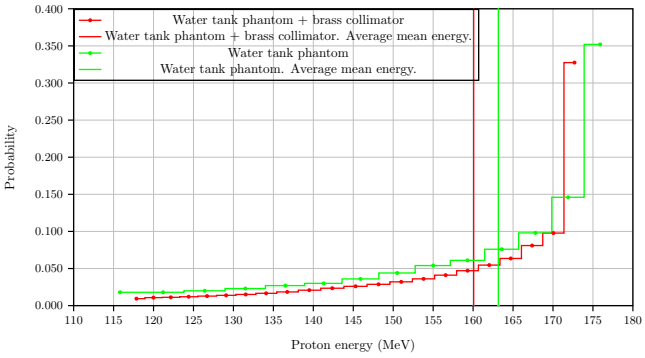

Figure 7.14: Unit energy distributions of the protons used in water tank phantom in IBA multiple-room (C-235 cyclotron) (red line) and in Mevion S250i Hyperscan single-room (green line). Average values for each experiment are identified as vertical lines.

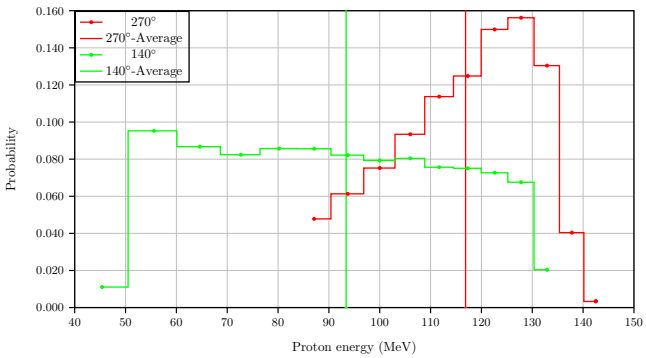

Figure 7.15: Unit energy distributions of the protons used in anthropomorphic phantom in Mevion S250i Hyperscan single-room. Average values for each direction are identified as vertical lines.

The neutron dose equivalent in ICRU tissue, H_{ne}, Equation (4.51), with the UAB methodology described in Section 4.4.2, and per therapeutic Gy (in units of mSv Gy^{-1}) as a function of the lateral distance from isocenter in the conditions described previously is shown in Figure 7.16 in the case of the water tank phantom and shown in Figure 7.17 (in units of μSv Gy^{-1}) in the case of the anthropomorphic phantom.

In the case of the water tank phantom, previous UAB measurements in IBA multiple-room (C-235 cyclotron) system [Stolarczyk et al., 2018] are also shown in Figure 7.16. Let us now focus on the Pipe III located in the Frame 3 in the water tank phantom, that is precisely where the isocenter is placed (see Figures 7.5 and 7.6). Measurement points are perpendicular in respect to the incident direction of the proton beam and they can be located to lateral distances from −11 cm to 40 cm. Measurement points found at lateral distances −10 cm, −5 cm, etc will be labelled as the *symmetric* points in respect to the measurement points 10 cm, 5 cm, etc. In the results shown in Figure 7.16, symmetric points will be labelled with a superscript S.

In the case of the anthropomorphic phantom, previous UAB measurements in IBA multiple-room (C-235 cyclotron) system [Knežević et al., 2017] and UAB measurements also in IBA multiple-room (C-235 cyclotron) system but additionally using two kind of energy degraders (range shifter (RS) and beam compensator (BC)) [Wochnik et al., 2021] are included in Figure 7.17.

Regarding the work of Wochnik et al. [2021], the MC models included properly the RS and BC, as shown in Section 5.7 (see Figures 5.12, 5.13, 5.14 and 5.15).

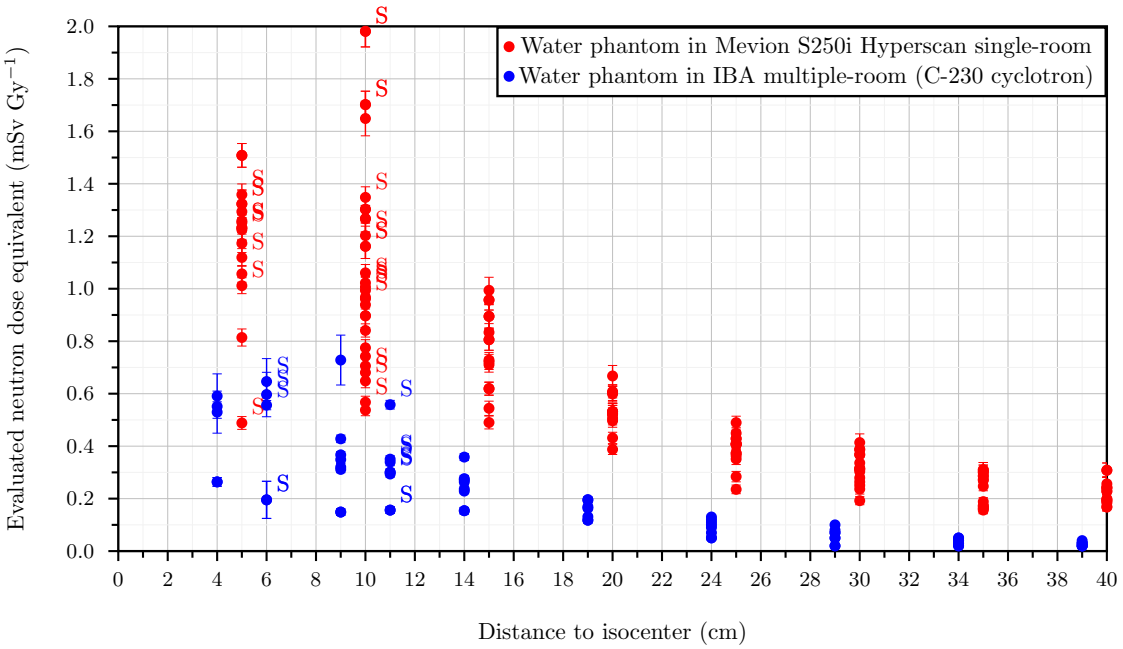

Figure 7.16: Evaluated neutron dose equivalents, Equation (4.51)*, in water tank phantom as a function of the lateral distance from isocenter. Results in IBA multiple-room (C-235 cyclotron) system [Stolarczyk et al., 2018] are shown in blue while results in Mevion S250i Hyperscan single-room system are shown in red. The superscript S means the symmetric point, see text.*

The variability in the neutron dose equivalents shown in Figure 7.16, for instance, in lateral distance to isocenter 15 cm (doses in the range 0.5 to 1 mSv Gy^{-1} are reported) is mainly because information about the exact positioning (*i.e.,* specific Frame and Pipe) in which the measurements are done is not shown in Figure 7.16. The interested reader can see neutron doses in specific locations in Appendix A. For the other hand, representation in Figure 7.16 enable us to see general tendencies.

Neutron doses reported in Figures 7.16 and 7.17 show that neutron doses are higher in Mevion S250i Hyperscan single-room system in comparison to IBA multiple-room (C-235 cyclotron) system, as expected due to the fact that proton accelerator and beam components are nearer to the therapeutic room in the former case than in the later (an idea about this fact can be extracted from the Figures 7.2 and 7.3).

In particular, as already mentioned above, some of the beam components are the energy degrader (in Mevion S250i Hyperscan single-room system is called range modulator system (RMS)) and a collimator (in Mevion S250i Hyperscan single-room system is called the adaptive aperture (AA)). Both elements were included in the MC simulations.

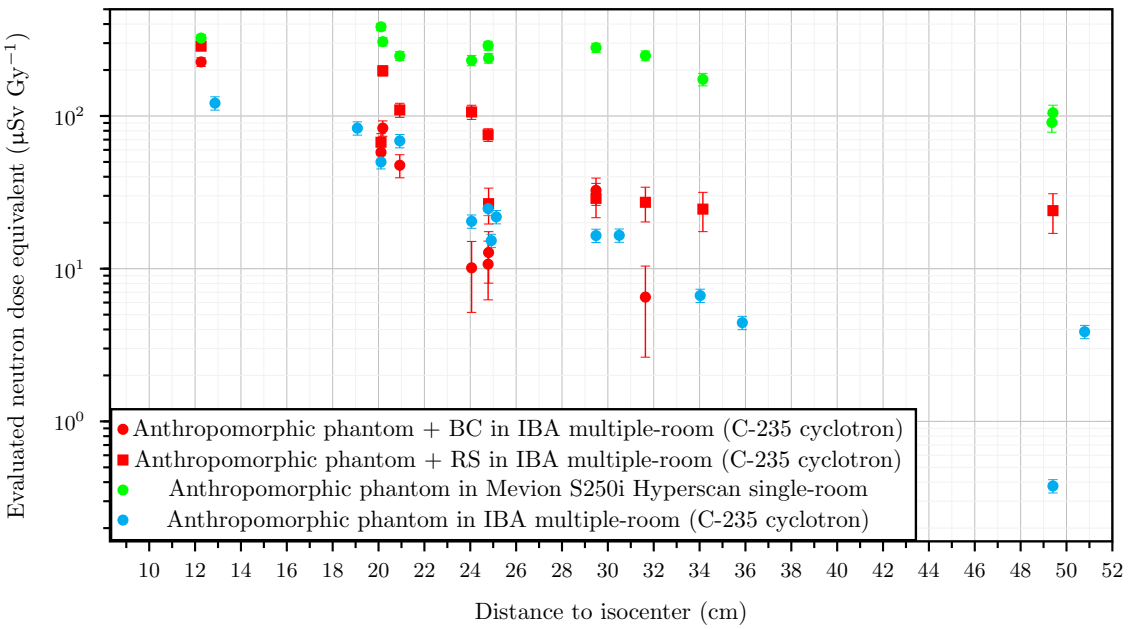

Figure 7.17: Evaluated neutron dose equivalents, Equation (4.51)*, in anthropomorphic phantom as a function of the distance to isocenter. Results in IBA multiple-room (C-235 cyclotron) system are shown in cyan, results in IBA multiple-room (C-235 cyclotron) system when additionally using two kind of energy degraders are shown in red and results in Mevion S250i Hyperscan single-room system are shown in green.*

Results from Figure 7.17 additionally show that neutron differences in the four situations (IBA multiple-room (C-235 cyclotron) system, IBA multiple-room (C-235 cyclotron) system + RS, IBA multiple-room (C-235 cyclotron) system + BC and Mevion S250i Hyperscan single-room system) are more important in increasing the distance to the isocenter.

From Figure 7.17 it is shown for the Mevion S250i Hyperscan single-room system that while neutron dose equivalent is nearly constant and around ~ 300 μSv Gy^{-1} for distances from 12 to 30 cm, it decreases from ~ 100 μSv Gy^{-1} to ~ 20 μSv Gy^{-1} in the same range for the IBA multiple-room (C-235 cyclotron) system. An explanation for this fact could be that the main contribution to the neutron doses in Mevion S250i Hyperscan single-room system is not from the phantom itself, but it is rather due to the mentioned beam components and proton accelerator, so that the phantom can be considered to be uniformly illuminated inside of a sea of neutrons. This is not the interpretation, however, when the main neutron source is the phantom itself, where a clear dependence of the doses as a function of the distance to isocenter is observed. The relative decreasing of neutron dose equivalents in the whole range of distances (from 12 to 50 cm) is 67 % in the case of Mevion S250i Hyperscan single-room system and almost 100 % in the case of IBA multiple-room (C-235 cyclotron) system.

This work proved that in the configuration IBA multiple-room (C-235 cyclotron) system + BC, neutron out-of-field doses found were not significantly increased in respect to the configuration IBA multiple-room (C-235 cyclotron) system alone. This was proved by doing a comparison between the evaluated energy distribution of the neutron fluence ($\Phi_E(E) = \Phi^{\text{CR-39}} \cdot \varphi_E^{\text{MC}}(E)$, see Section 4.6.1) in case of using a RS or in case of using a BC. The comparison was done for specific points of the anthropomorphic phantom and it is shown in Figure 7.18 [Wochnik et al., 2021].

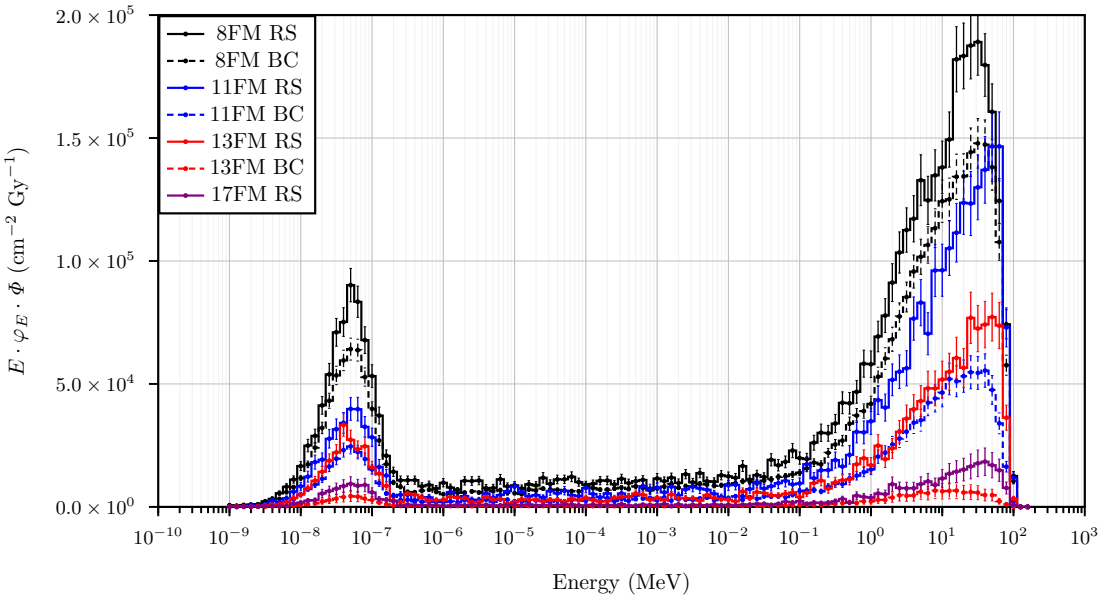

Figure 7.18: Evaluated energy distributions of the neutron fluence using RS (solid) or BC (dashed). From Wochnik et al. [2021].

From the comparison shown in Figure 7.18, it can be concluded that more neutrons were reaching the phantom in case of using the RS instead of using the BC. In this case, this is also translated in neutron dose equivalents that are higher in the case of RS, as shown in Figure 7.17.

7.1.1.2 Comparison of evaluated and full MC neutron dose equivalents

The methodologies used in this work require the MC unit energy distribution of the neutron fluence, $\varphi_E^{\mathrm{MC}}(E)$, not only to compute the full MC neutron dose equivalents, $H_{\mathrm{ne}}^{\mathrm{MC}}$, but it is also needed to quantify the evaluated neutron dose equivalent, H_{ne} ($H_{\mathrm{ne}} \equiv H \equiv H_{\mathrm{ne}}^{\mathrm{EV}}$).

At the same time, when the full MC neutron dose equivalent is used, it is implicitly assumed that the energy distribution of the neutron fluence is $\Phi_E^{\mathrm{MC}}(E) = \Phi^{\mathrm{MC}} \cdot \varphi_E^{\mathrm{MC}}(E)$. Where Φ^{MC} is the total neutron fluence obtained by MC means. On the other hand, when the evaluated neutron dose equivalent is used, it is implicitly assumed that the energy distribution of the neutron fluence is $\Phi_E(E) \equiv \Phi_E^{\mathrm{EV}}(E) = \Phi^{\mathrm{CR\text{-}39}} \cdot \varphi_E^{\mathrm{MC}}(E)$. Where $\Phi^{\mathrm{CR\text{-}39}}$ is obtained by experimental means, as explained in Section 4.6.1.

Comparisons between full MC neutron dose equivalents, $H_{\mathrm{ne}}^{\mathrm{MC}}$, and evaluated neutron dose equivalents, H_{ne}, when using a range shifter or a beam compensator in the IBA multiple-room (C-235 cyclotron) system are shown in Figure 7.19 and numerical data is exposed in Table 7.4.

It can be seen that, in general, there are discrepancies between $H_{\mathrm{ne}}^{\mathrm{MC}}$ and H_{ne}. This is probably due to the lack of complete modelling of the facilities and because development of detailed MC models is difficult since manufacturer blueprints are often not readily available, and coding and validation are laborious [Kry et al., 2017].

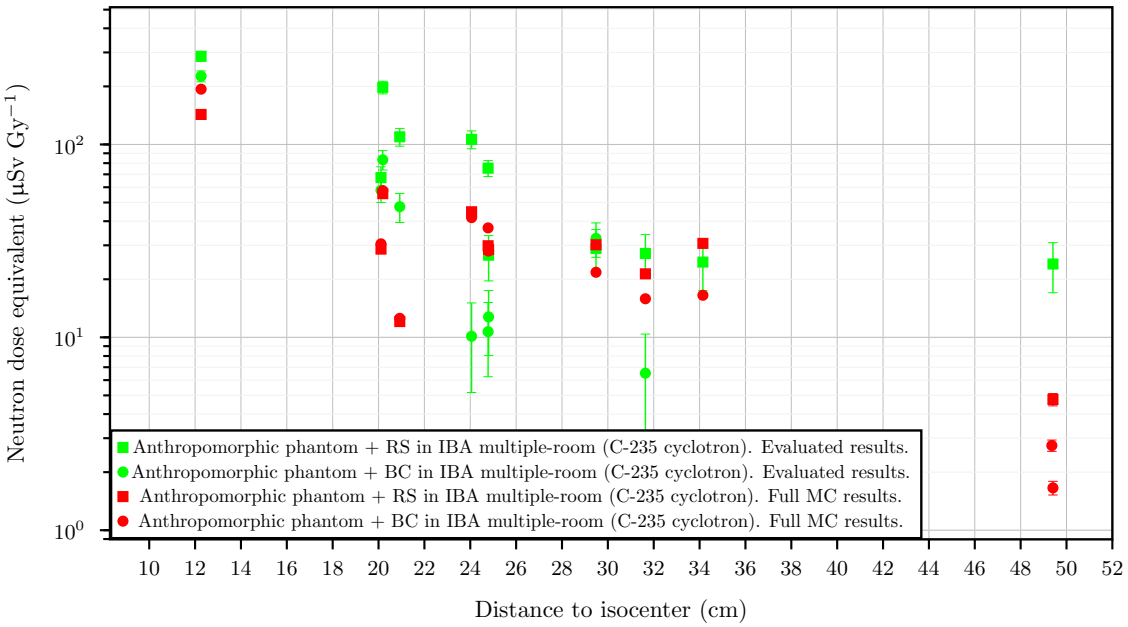

Figure 7.19: Full Monte Carlo neutron dose equivalents, H_{ne}^{MC} (in red) and evaluated neutron dose equivalents, H_{ne} (in green) when using a range shifter or a beam compensator in IBA multiple-room (C-235 cyclotron) system.

Table 7.4: Comparison between Full Monte Carlo neutron dose equivalents, H_{ne}^{MC}, and Evaluated neutron dose equivalents, H_{ne}, when using a range shifter or a beam compensator.

Slice number	Position	Distance to isocenter (cm)	RS_{EV} (μSv Gy^{-1})	BC_{EV} (μSv Gy^{-1})	RS_{MC} (μSv Gy^{-1})	BC_{MC} (μSv Gy^{-1})
8	8 FM[a]	12.262	287 ± 20	226 ± 20	143 ± 1	194 ± 2
11	11 FM	20.185	198 ± 20	83 ± 10	56 ± 1	57.6 ± 0.6
11	11 BL[a]	20.107	67 ± 9	58 ± 8	28.7 ± 0.9	30.5 ± 0.6
11	11 BR[a]	20.926	110 ± 10	48 ± 8	12.1 ± 0.5	12.5 ± 0.3
13	13 FM	24.058	107 ± 10	10 ± 5	44.8 ± 0.9	41.8 ± 0.8
13	13 LL[a]	24.778	75 ± 10	11 ± 4	29.8 ± 0.9	36.9 ± 0.4
13	13 LR[a]	24.799	29 ± 7	13 ± 5	28.5 ± 0.9	28.0 ± 0.6
15	15 BL	31.637	27 ± 7	7 ± 4	21.3 ± 0.6	15.8 ± 0.3
15	15 FR	29.483	29 ± 7	33 ± 7	30.2 ± 0.9	21.7 ± 0.4
17	17 FM	34.144	25 ± 7		30.7 ± 0.9	16.5 ± 0.5
23	23 FM	49.362				2.7 ± 0.2
23	23 LR	49.409	24 ± 7		4.8 ± 0.3	1.7 ± 0.1

[a] FM ≡ Front middle, BL ≡ Back left, BR ≡ Back right, LL ≡ Lateral left and LR ≡ Lateral right

In the case of using the RS, evaluated energy distributions of the neutron fluence *i.e.*, $\Phi_E(E) = \Phi^{\text{CR-39}} \cdot \varphi_E^{\text{MC}}(E)$ are shown in Figure 7.20 while the full MC energy distributions of the neutron fluence *i.e.*, $\Phi_E^{\text{MC}}(E) = \Phi^{\text{MC}} \cdot \varphi_E^{\text{MC}}(E)$ are shown in Figure 7.21 for different points of the anthropomorphic phantom. Labelling inside the anthropomorphic phantom is given in Table 7.3 and the location of the measurement or computation points is given in Figures 7.7 and 7.8.

Similarly, in case of using the BC, evaluated energy distribution of the neutron fluence is shown in Figure 7.22 while the full MC energy distribution of the neutron fluence is shown in Figure 7.23 in the different points of the anthropomorphic phantom.

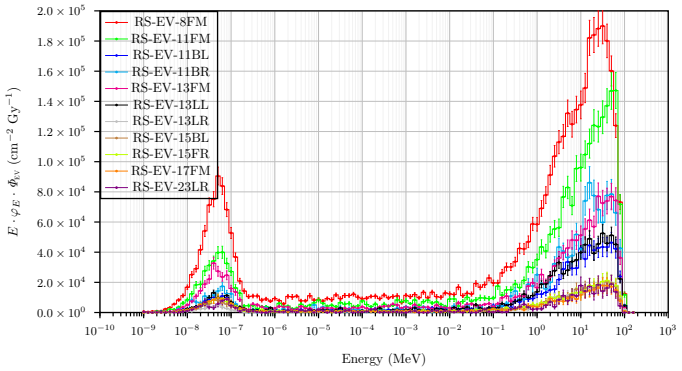

Figure 7.20: Evaluated energy distribution of the neutron fluence for different points of the anthropomorphic phantom when RS is used.

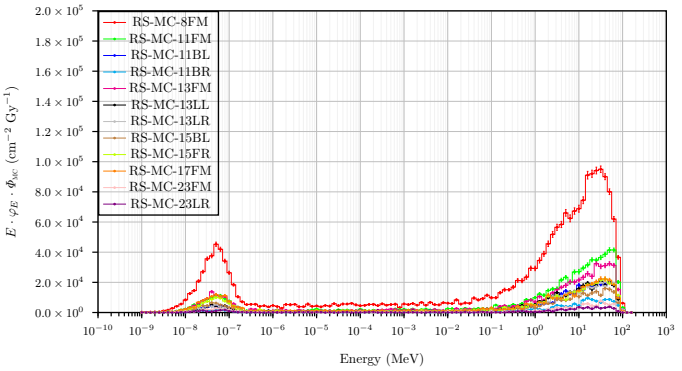

Figure 7.21: Full MC energy distribution of the neutron fluence for different points of the anthropomorphic phantom when RS is used.

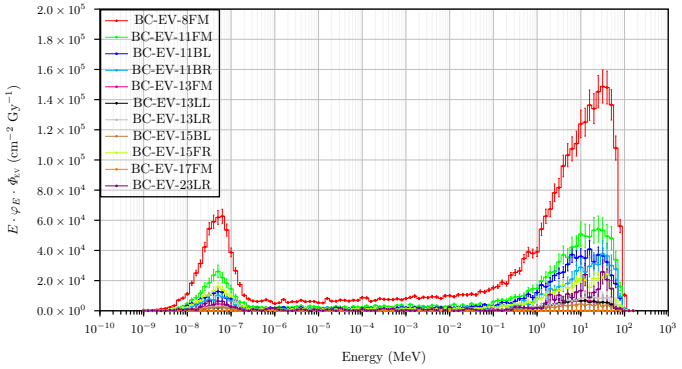

Figure 7.22: Evaluated energy distribution of the neutron fluence for different points of the anthropomorphic phantom when a BC is used.

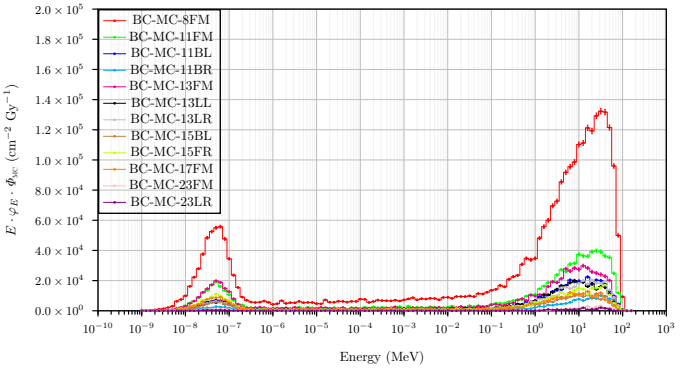

Figure 7.23: Full MC energy distribution of the neutron fluence for different points of the anthropomorphic phantom when a BC is used.

From comparing evaluated results and full MC results (Figures 7.20 and 7.21, and Figures 7.22 and 7.23) one can see the effect of using the total neutron fluence obtained from the CR-39 measurements, $\Phi^{\text{CR-39}}$ (using Equation (4.10)) or using the total neutron fluence from MC simulations, Φ^{MC}. Remind that in this work the unit energy distribution of the neutron fluence, $\varphi_E(E)$, inside of a phantom is always coming from MC simulations ($\varphi_E(E) \equiv \varphi_E^{\text{MC}}(E)$).

Similarly, as just done above, comparisons between full Monte Carlo neutron dose equivalents, $H_{\text{ne}}^{\text{MC}}$, and Evaluated neutron dose equivalents, H_{ne}, in the Mevion S250i Hyperscan single-room system are shown in Figure 7.24 and numerical data is exposed in Table 7.5. Again, it can be concluded that, in general, there are discrepancies between $H_{\text{ne}}^{\text{MC}}$ and H_{ne}.

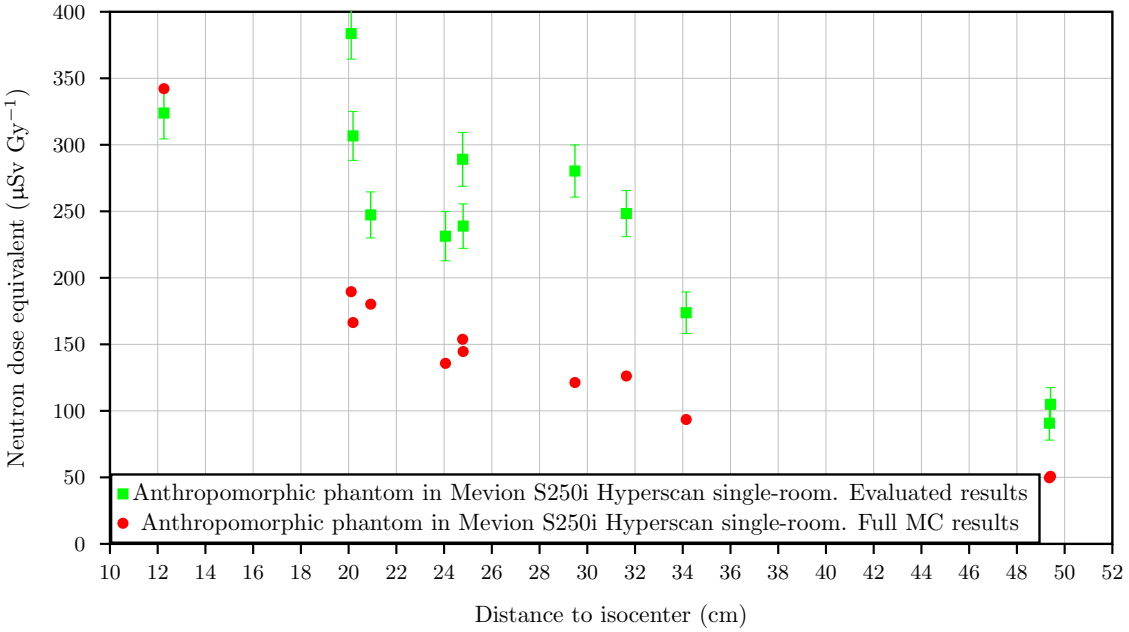

Figure 7.24: Full Monte Carlo neutron dose equivalents, H_{ne}^{MC} (in red) and evaluated neutron dose equivalents, H_{ne} (in green) in Mevion S250i Hyperscan single-room system.

Table 7.5: Comparison between Full Monte Carlo neutron dose equivalents and Evaluated neutron dose equivalents in Mevion S250i Hyperscan single-room system.

Slice number	Position	Distance to isocenter (cm)	H_{EV} (μSv Gy^{-1})	H_{MC} (μSv Gy^{-1})
8	8 FM[a]	12.262	324 ± 20	342
11	11 FM	20.185	307 ± 20	166
11	11 BL[a]	20.107	383 ± 20	189
11	11 BR[a]	20.926	247 ± 20	180
13	13 FM	24.058	231 ± 20	135
13	13 LL[a]	24.778	289 ± 20	153
13	13 LR[a]	24.799	239 ± 20	144
15	15 BL	31.637	248 ± 20	126
15	15 FR	29.483	280 ± 20	121
17	17 FM	34.144	174 ± 20	93
23	23 FM	49.362	91 ± 10	49
23	23 LR	49.409	105 ± 10	50

[a] FM ≡ Front middle, BL ≡ Back left, BR ≡ Back right, LL ≡ Lateral left and LR ≡ Lateral right

For the Mevion S250i Hyperscan single-room system, evaluated energy distribution of the neutron fluence *i.e.*, $\Phi_E(E) = \Phi^{\text{CR-39}} \cdot \varphi_E^{\text{MC}}(E)$, is shown in Figure 7.25 while the full MC energy distribution of the neutron fluence *i.e.*, $\Phi_E^{\text{MC}}(E) = \Phi^{\text{MC}} \cdot \varphi_E^{\text{MC}}(E)$, is shown in Figure 7.26 in different points of the anthropomorphic phantom.

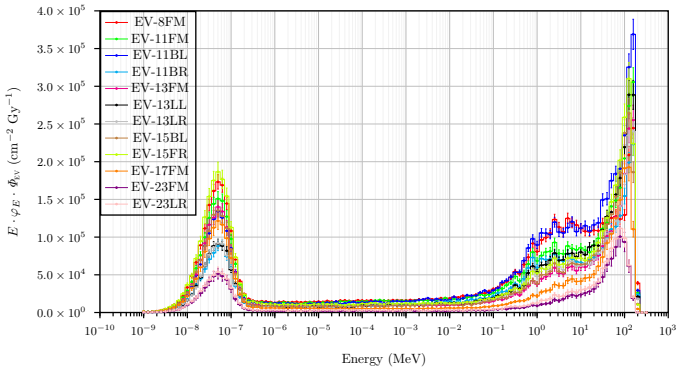

Figure 7.25: Evaluated energy distribution of the neutron fluence for different points of the anthropomorphic phantom in Mevion S250i Hyperscan single-room system.

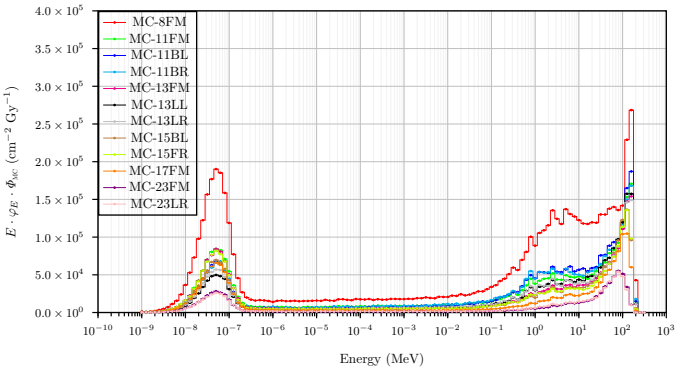

Figure 7.26: Full MC energy distribution of the neutron fluence for different points of the anthropomorphic phantom in Mevion S250i Hyperscan single-room system.

Finally, in Figure 7.27, are shown comparisons between Full Monte Carlo neutron dose equivalents, $H_{\mathrm{ne}}^{\mathrm{MC}}$, and Evaluated neutron dose equivalents, H_{ne}, in the IBA multiple-room (C-235 cyclotron) system (without using any RS or BC). The reference work for the evaluated out-of-field doses in this situation is Knežević et al. [2017]. In this Figure some compatibility between evaluated and full MC results is found, differently from the results presented in Figures 7.19 and 7.24. This may be explained because for this particular facility, a simple MC model is sufficient.

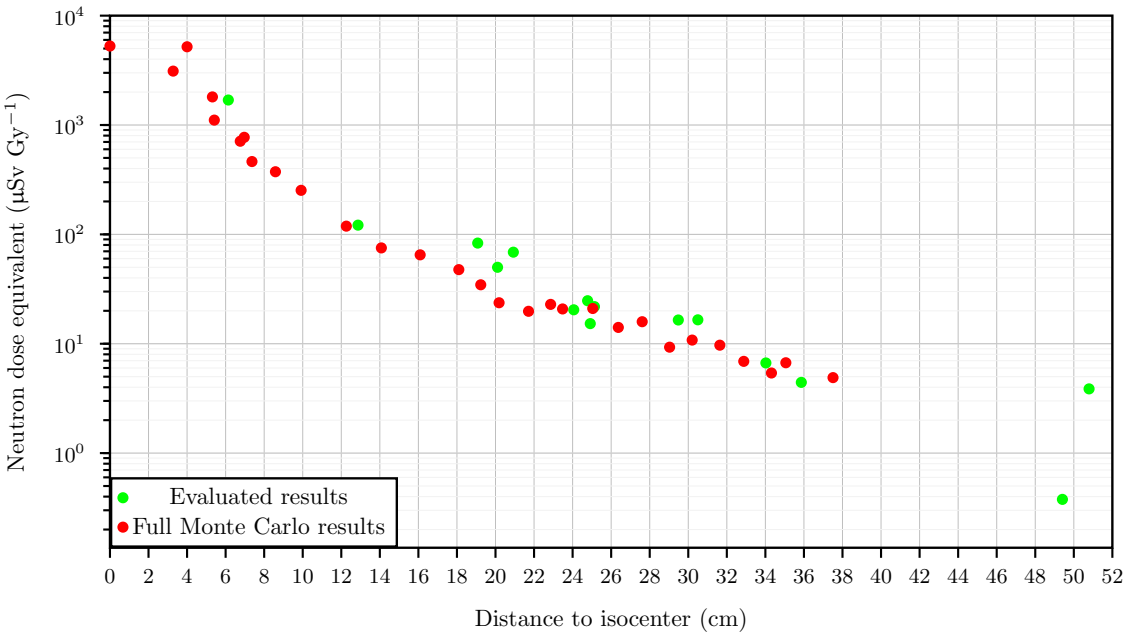

Figure 7.27: Full Monte Carlo neutron dose equivalents, H_{ne}^{MC} (in red) and evaluated neutron dose equivalents, H_{ne} (in green) in the IBA multiple-room (C-235 cyclotron) system (without using any RS or BC).

7.1.2 Neutron active spectrometry

At the same time that EURADOS-WG9 collaboration was arranging proton irradiations to measure out-of-field in-phantom doses with passive dosimetry systems (as explained in Section 7.1.1), proton irradiations were also arranged to study neutron ambient doses in

air, at different points of the irradiation room. The aim was the same as for the passive systems *i.e.,* to compare the neutron production in proton radiotherapy facilities using the IBA multiple-room (C-235 cyclotron) system and the Mevion S250i Hyperscan single-room system. Radiation detectors used to measure the ambient doses were active dosimetry systems and neutron spectrometers. More information about the active dosimetry and spectrometry results can be found in the case of measuring in IBA multiple-room (C-235 cyclotron) system in the work of Mares et al. [2016]. In this section we will focus on the results of the UAB-BSS (whose description is in Section 4.5.1).

In the neutron spectrometry irradiation campaign at the IBA multiple-room (C-235 cyclotron), protons with energies from 100 to 144 MeV and covering a field of a disk of 2.5 cm radius were incident to an anthropomorphic phantom [Mares et al., 2016]. In the neutron spectrometry irradiation campaign at the Mevion S250i Hyperscan single-room system, protons had an energy of 122 MeV an they were covering a square field of 5 × 5 cm^2, in this case they were also incident to the same anthropomorphic phantom. A representation of the situation and measurement points is shown in Figure 7.28 for the measurements done in IBA multiple-room (C-235 cyclotron) system and in Figure 7.29 for the measurements done in Mevion S250i Hyperscan single-room system. Measurements with the UAB-BSS were performed in points 1 and 3 in both cases.

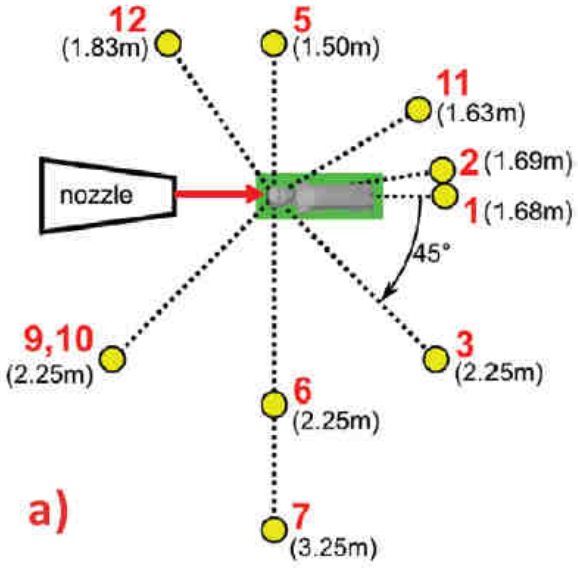

Figure 7.28: Definition and notation of the neutron spectrometry experiment carried out in an environment of the IBA multiple-room (C-235 cyclotron) system. Protons from 100 to 144 MeV were used. The proton field is a disk of 2.5 cm radius (i.e., an area of ∼ 20 cm^2). An anthropomorphic phantom is used [Mares et al., 2016].

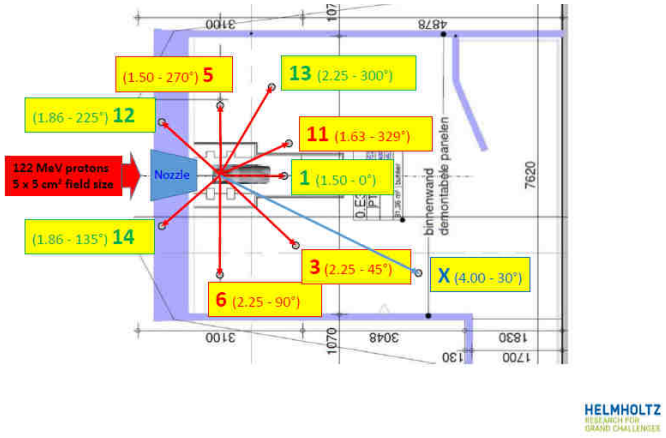

Figure 7.29: Definition and notation of the neutron spectrometry experiment carried out in an environment of the Mevion S250i Hyperscan single-room system. Protons of energy 122 MeV were used. The proton field is a square of 5 × 5 cm^2 (i.e., an area of 25 cm^2). An anthropomorphic phantom is used.

MC simulations were employed to obtain a guess energy distribution of the neutron fluence to be used in the unfolding procedures for spectrometry.

The modelled situation was the map Figure 7.29. The modelling was similar to that already introduced in Section 7.1.1 *i.e.,* in the MC simulations the energy degrader (RMS) and collimator (AA) were included (elements show in Figures 7.10, 7.11 and 7.12) but, in addition, two more neutron producing elements were included as well as realistic walls. Walls are modelled according to the information explained in Section 5.7.

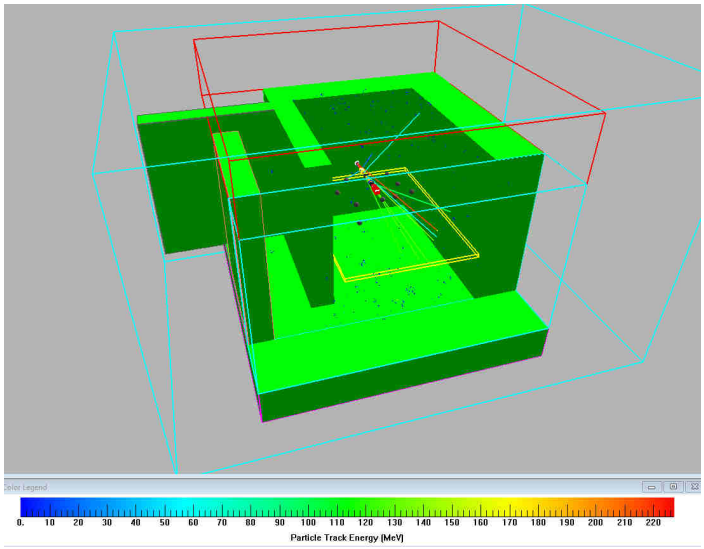

Figure 7.30: A view about the MC modelling of the neutron spectrometry situation defined by Figure 7.29. Gray spheres are scoring volumes representing the points defined in Figure 7.29.

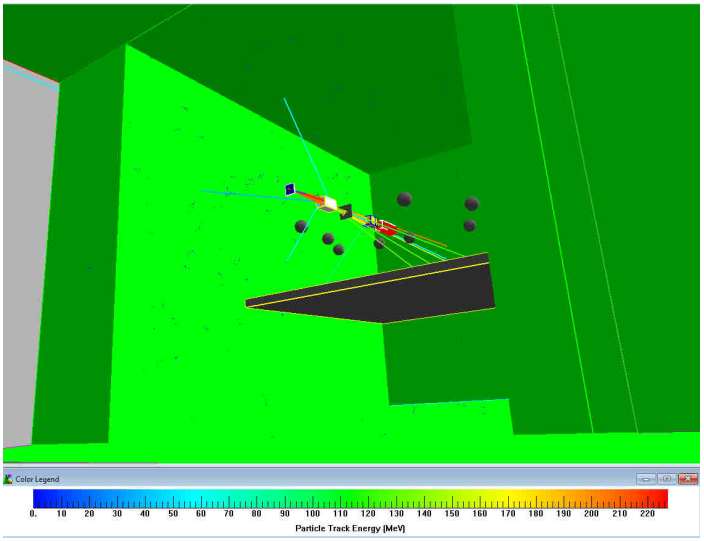

Figure 7.31: Another view about the MC modelling of the neutron spectrometry situation defined by Figure 7.29. Gray spheres are scoring volumes representing the points defined in Figure 7.29.

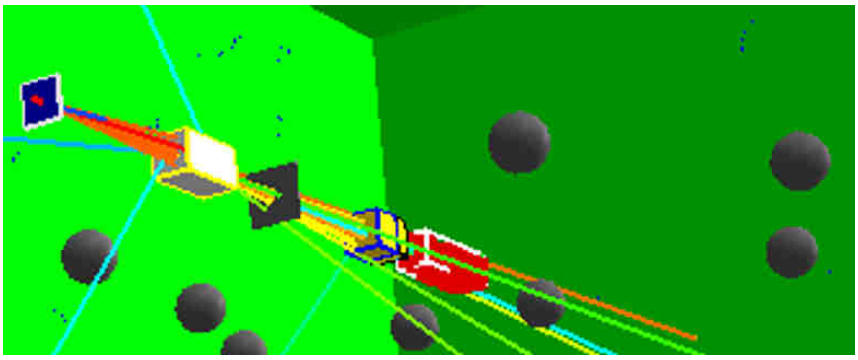

Figure 7.32: From left to right: Cu (3 mm long) element, Fe (40 cm long) element, gray score region in air (is used as a test, not relevant here), the RMS (18.6 cm long in this case) and AA (10 cm long), MC anthropomorphic phantom (67 cm long). The thickness of the RMS is set according to Table 5.1. See text.

Energy distributions of the neutron fluence obtained from BSS-UAB for points P1 and P3 in the case of measuring in the environment of Mevion S250i Hyperscan single-room system (map of Figure 7.29) are shown in Figure 7.33 while integrated neutron fluences and integrated neutron ambient dose equivalents are shown in Table 7.6. Also shown in this Figure 7.33 are the guess energy distribution of the neutron fluence obtained by MC and used in the BSS unfolding procedure.

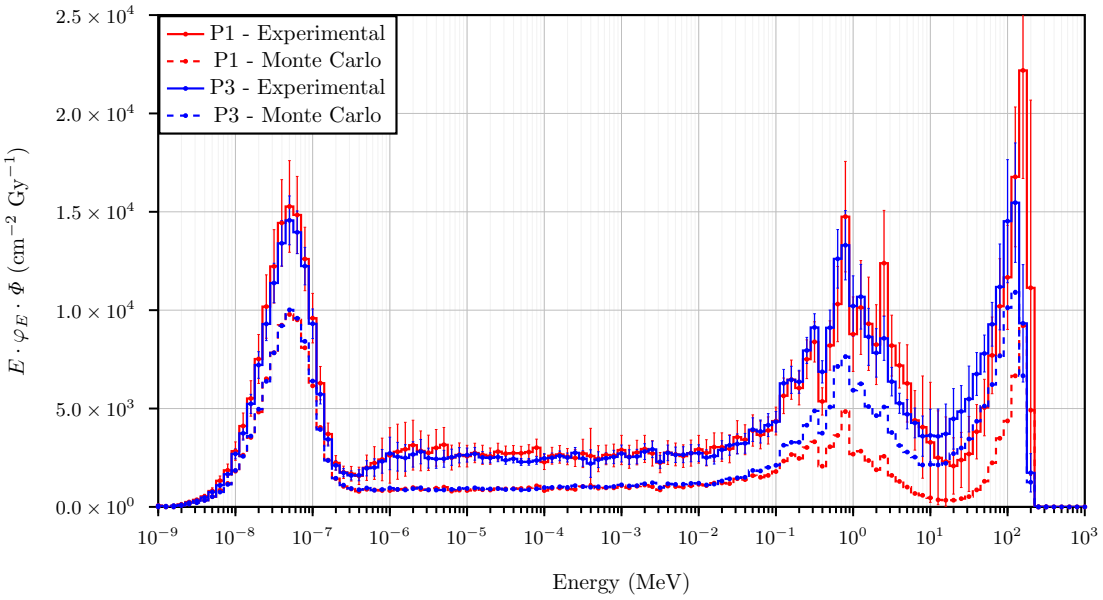

Figure 7.33: Energy distributions of the neutron fluence found by the BSS-UAB in points P1 and P3 in an environment of the Mevion S250i Hyperscan single-room system. See measurements map Figure 7.29.

Table 7.6: Experimental and full Monte Carlo values of the integrated neutron fluence per therapeutic dose, Φ_i, in units of 10^4 cm^{-2} Gy^{-1}, and integrated ambient dose equivalents, $H_i^*(10)$, in units of μSv Gy^{-1}, in the specified energy range i, for the case of Mevion S250i Hyperscan single-room system. The fraction between the integrated quantities and their total quantity are also expressed, in units of %. This Table complements Figure 7.33.

Position - Method	$E < 1$ eV	1 eV $< E <$ 0.1 MeV	0.1 eV $< E <$ 10 MeV	$E >$ 10 MeV	Total
	Φ_{Thermal}	$\Phi_{\text{Epithermal}}$	Φ_{Fast}	$\Phi_{\text{HighEnergy}}$	Φ_{Total}
P1 - Experimental	3.2	3.3	3.6	2.4	12.4 ± 0.5
P3 - Experimental	3.0	3.1	3.5	2.4	11.9 ± 0.3
P1 - Monte Carlo	2.0	1.2	1.1	0.8	5.1
P3 - Monte Carlo	2.0	1.3	1.9	1.6	6.8
	$\frac{\Phi_{\text{Thermal}}}{\Phi_{\text{Total}}} \cdot 100$	$\frac{\Phi_{\text{Epithermal}}}{\Phi_{\text{Total}}} \cdot 100$	$\frac{\Phi_{\text{Fast}}}{\Phi_{\text{Total}}} \cdot 100$	$\frac{\Phi_{\text{HighEnergy}}}{\Phi_{\text{Total}}} \cdot 100$	$\frac{\Phi_{\text{Total}}}{\Phi_{\text{Total}}} \cdot 100$
P1 - Experimental	25.6	26.2	28.9	19.2	100
P3 - Experimental	25.1	25.9	29.4	19.6	100
P1 - Monte Carlo	39.3	23.3	21.2	16.1	100
P3 - Monte Carlo	29.6	18.4	29.0	22.9	100
	$H^*_{\text{Thermal}}(10)$	$H^*_{\text{Epithermal}}(10)$	$H^*_{\text{Fast}}(10)$	$H^*_{\text{HighEnergy}}(10)$	$H^*_{\text{Total}}(10)$
P1 - Experimental	0.4	0.5	12	8	21 ± 1
P3 - Experimental	0.4	0.5	11.7	8.7	21.2 ± 0.7
P1 - Monte Carlo	0.2	0.2	3.4	2.5	6.3
P3 - Monte Carlo	0.2	0.2	6.7	5.7	12.8
	$\frac{H^*_{\text{Thermal}}(10)}{H^*_{\text{Total}}(10)} \cdot 100$	$\frac{H^*_{\text{Epithermal}}(10)}{H^*_{\text{Total}}(10)} \cdot 100$	$\frac{H^*_{\text{Fast}}(10)}{H^*_{\text{Total}}(10)} \cdot 100$	$\frac{H^*_{\text{HighEnergy}}(10)}{H^*_{\text{Total}}(10)} \cdot 100$	$\frac{H^*_{\text{Total}}(10)}{H^*_{\text{Total}}(10)} \cdot 100$
P1 - Experimental	1.8	2.3	58.6	37.3	100
P3 - Experimental	1.7	2.2	55.2	40.9	100
P1 - Monte Carlo	3.7	2.9	54.1	39.2	100
P3 - Monte Carlo	1.8	1.6	52.2	44.4	100

The unfolding procedure, which uses the experimental BSS measurements, results in a final energy distribution of the neutron fluence different from the one used as guess, as

seen in Figure 7.33 and Table 7.6.

During the unfolding procedure it was proved that a good guess for the energy distribution of the neutron fluence is important in order to determine the position and shape of the final energy distribution of the neutron fluence with better detail.

From the energy distributions of Figure 7.33 it is observed that the positioning of the high energy peak (intranuclear cascade neutrons, see Section 2.3.4) depends on the angular positioning of the measurement point with respect to the direction of the proton beam. When the angle between the direction of the proton beam and the measurement point is increased, the high energy neutron peak moves to lower neutron energies. This is also observed from the MC results shown in Figure 7.33. This fact is compatible with differential cross section shown in Figure E.3. The high energy peak is extended up to an energy of 227 MeV which is the fixed proton energy provided by the Mevion S250i Hyperscan single-room system.

Regarding the fast region, the experimental method shows no differences between P1 and P3, while MC shows some difference in P1 and P3. If we suppose that there is a source of fast neutrons coming from the RMS+AA elements and another source of fast neutrons coming from the phantom itself, some difference could be expected in Figure 7.33 as P1 is at 150 cm in respect to the isocenter of the phantom while P3 is at 225 cm in respect to isocenter of phantom. In other words, as P1 is closer to the anthropomorphic phantom in comparison with P3, one could expect more fast neutrons in P1.

On the other hand, keep in mind that although P1 and P3 are in different angular positioning (P1 at 0° and P3 at 45°) we are now studying the fast region, supposed to be emitted isotropically.

As no change is noticed in the fast region from P1 and P3, this indicates that the possible contribution from phantom in this region is negligible in respect to the fast neutrons contributed by the beam components, in particular by RMS+AA. Therefore, it can be considered that both measurement points P1 and P3 are uniformly illuminated by a sea of fast neutrons coming from the beam components and the cyclotron itself.

Regarding the epithermal and thermal part, these neutrons are related to the moderation of fast and high energy neutrons with the materials found in their way to the measurement point. Thermal neutrons are present isotropically in the whole room bouncing constantly with the atoms present in air and walls. The inclusion of walls in MC simulations is required to predict properly the thermal peak.

It is important to keep in mind that each element interacting with the proton beam is a source, in particular, of high energy neutrons and fast neutrons.

Figure 7.34 shows the energy distribution of the neutron fluence obtained in P1 and P3 in the Mevion S250i Hyperscan single-room system (map of Figure 7.29) and in P1 and P3 in the IBA multiple-room (C-235 cyclotron) system (map of Figure 7.28). All energy distributions of Figure 7.34 have been obtained with the UAB-BSS. Integrated quantities are found in Table 7.7.

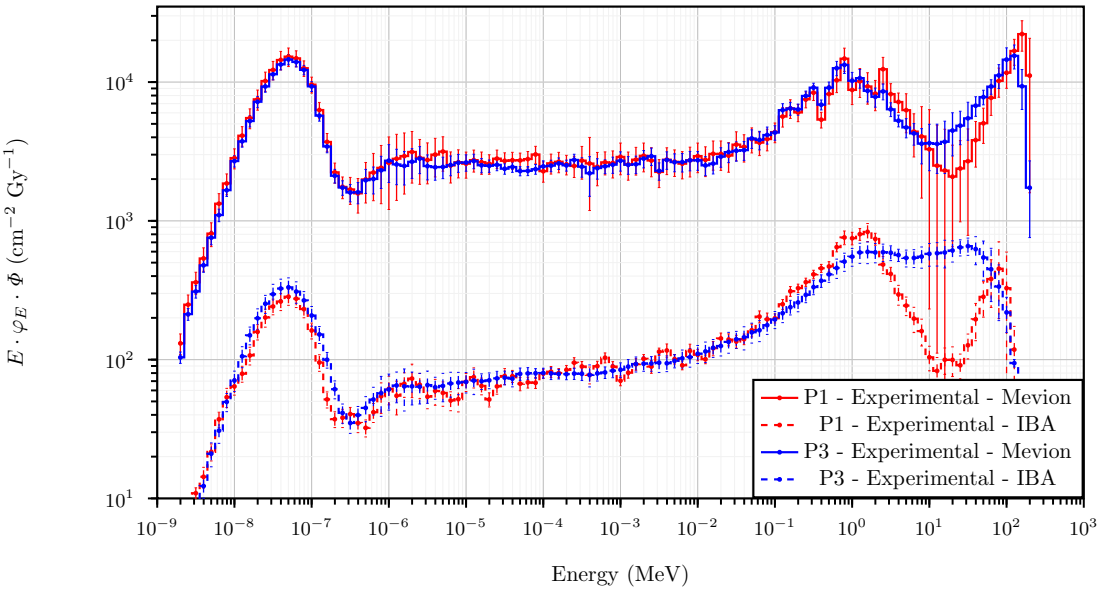

Figure 7.34: Energy distributions of the neutron fluence found by the BSS-UAB in points P1 and P3 in an environment of the Mevion S250i Hyperscan single-room system (see map Figure 7.29) and in points P1 and P3 in an environment of the IBA multiple-room (C-235 cyclotron) system (see map Figure 7.28).

Table 7.7: Experimental and full Monte Carlo values of the integrated neutron fluence per therapeutic dose, Φ_i, in units of 10^4 cm^{-2} Gy^{-1}, and integrated ambient dose equivalents, $H_i^*(10)$, in units of μSv Gy^{-1}, in the specified energy range i. The fraction between the integrated quantities and their total quantity are also expressed, in units of %. This Table complements Figure 7.34.

Position - Method	$E < 1$ eV	1 eV $< E <$ 0.1 MeV	0.1 eV $< E <$ 10 MeV	$E >$ 10 MeV	Total
	Φ_{Thermal}	$\Phi_{\text{Epithermal}}$	Φ_{Fast}	$\Phi_{\text{HighEnergy}}$	Φ_{Total}
P1 - EXP. - Mevion	3.2	3.3	3.6	2.4	12.4 ± 0.5
P3 - EXP. - Mevion	3.0	3.1	3.5	2.4	11.9 ± 0.3
P1 - EXP. - IBA	0.06	0.11	0.21	0.05	0.43 ± 0.02
P3 - EXP. - IBA	0.07	0.10	0.21	0.14	0.52 ± 0.02
	$\frac{\Phi_{\text{Thermal}}}{\Phi_{\text{Total}}} \cdot 100$	$\frac{\Phi_{\text{Epithermal}}}{\Phi_{\text{Total}}} \cdot 100$	$\frac{\Phi_{\text{Fast}}}{\Phi_{\text{Total}}} \cdot 100$	$\frac{\Phi_{\text{HighEnergy}}}{\Phi_{\text{Total}}} \cdot 100$	$\frac{\Phi_{\text{Total}}}{\Phi_{\text{Total}}} \cdot 100$
P1 - EXP. - Mevion	25.6	26.2	28.9	19.2	100
P3 - EXP. - Mevion	25.1	25.9	29.4	19.6	100
P1 - EXP. - IBA	14	24	49	13	100
P3 - EXP. - IBA	14	20	40	26	100
	$H^*_{\text{Thermal}}(10)$	$H^*_{\text{Epithermal}}(10)$	$H^*_{\text{Fast}}(10)$	$H^*_{\text{HighEnergy}}(10)$	$H^*_{\text{Total}}(10)$
P1 - EXP. - Mevion	0.4	0.5	12	8	21 ± 1
P3 - EXP. - Mevion	0.4	0.5	11.7	8.7	21.2 ± 0.7
P1 - EXP. - IBA	0.007	0.02	0.73	0.21	0.97 ± 0.05
P3 - EXP. - IBA	0.009	0.02	0.74	0.64	1.41 ± 0.07
	$\frac{H^*_{\text{Thermal}}(10)}{H^*_{\text{Total}}(10)} \cdot 100$	$\frac{H^*_{\text{Epithermal}}(10)}{H^*_{\text{Total}}(10)} \cdot 100$	$\frac{H^*_{\text{Fast}}(10)}{H^*_{\text{Total}}(10)} \cdot 100$	$\frac{H^*_{\text{HighEnergy}}(10)}{H^*_{\text{Total}}(10)} \cdot 100$	$\frac{H^*_{\text{Total}}(10)}{H^*_{\text{Total}}(10)} \cdot 100$
P1 - EXP. - Mevion	1.8	2.3	58.6	37.3	100
P3 - EXP. - Mevion	1.7	2.2	55.2	40.9	100
P1 - EXP. - IBA	0.7	1.9	75.5	21.9	100
P3 - EXP. - IBA	0.6	1.2	52.7	45.5	100

According to the results shown in Figure 7.34 and Table 7.7, the total neutron fluences are, at least, of the order $\Phi_{\text{MEVION}} \sim 23 \cdot \Phi_{\text{IBA}}$ and total ambient dose equivalents are, at least, of

the order $H^*_{\text{MEVION}}(10) \sim 15 \cdot H^*_{\text{IBA}}(10)$. A more thorough discussion about the relevance and interpretation of these results, compared to photon out-of-field doses in photon treatments is given later (Section 7.1.3).

Regarding the energy distributions in Figure 7.34, as in IBA multiple-room (C-235 cyclotron) system the proton accelerator, energy degrader and remaining beam components are well shielded by facility design, the high energy peaks, as well as their tails are displaced to lower energies in the IBA case in comparison to the Mevion case. While the intranuclear cascade neutrons in Mevion S250i Hyperscan single-room system are generated by a proton beam of 227 MeV (coming from accelerator) interacting with the RMS+AA and also generated by the therapeutic proton beam reaching the phantom ($\sim$ 122 MeV), *i.e.,* there are two sources of intranuclear cascade neutrons. In IBA multiple-room (C-235 cyclotron) system there is only one source of intranuclear cascade neutrons (*i.e.,* the phantom) in which protons of energy $\sim 100 - 144$ MeV are reaching the phantom.

7.1.2.1 Additional Full MC computations

As full MC energy distributions of the neutron fluence were already obtained in P1 and P3 in the case of Mevion S250i Hyperscan single-room system in order to be used as a guess energy distributions in unfolding procedures, it was decided to perform full MC computations in all measurement points shown in the map of Figure 7.29. The results of such MC simulations are displayed in Figure 7.35 and integrated quantities are found in Table 7.8.

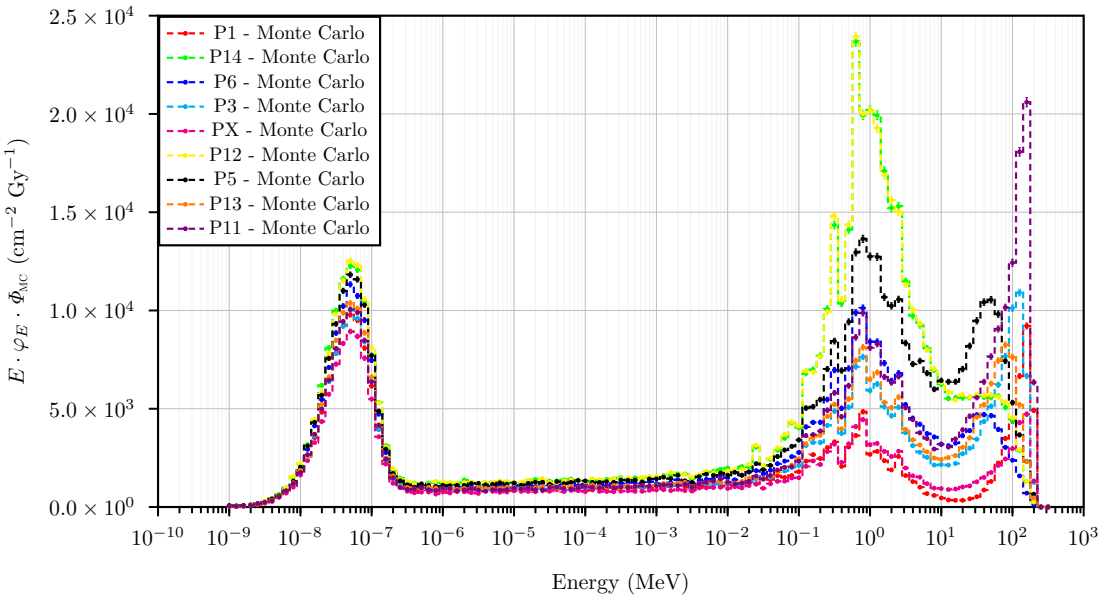

Figure 7.35: Full MC energy distributions of the neutron fluence obtained in measurement points in the case of Mevion S250i Hyperscan single-room system. See map of Figure 7.35 for additional information about the measurement points.

Regarding the energy distributions shown in Figure 7.35, it is observed that the positioning of the high energy peak is, again, depending on the angular positioning of the scoring volume with respect to the direction of the proton beam. As the scoring volume goes from P1 (0°), P11 (31°), P3 (45°), P13 (60°), P5 and P6 (90°) and, P12 and P14 (135°), it is seen that high energy peak positioning moves to lower energies in a way that it dissapears

in P12 and P14, as these points are not in the forward direction in which intranuclear cascade neutrons are emitted. In all cases the high energy region extends up to the energy of the proton accelerator which is 227 MeV, since it is not shielded.

The fast neutron fluence in the scoring volumes is now not simply decreasing when increasing the distance to isocenter as there exist a second source of fast neutrons which is the RMS+AA. This is why P12 and P14 (186 cm in respect to isocenter) have a fast neutron fluence $\sim 5.8 \times 10^4$ cm^{-2} Gy^{-1} and P5 (150 cm in respect to isocenter) has a fast neutron fluence $\sim 3.9 \times 10^4$ cm^{-2} Gy^{-1} even being P5 closer to the phantom and to one of the fast neutron sources. This behaviour in points P12 and P5 is contrary to the tendency shown in the IBA multiple-room (C-235 cyclotron) system (see Mares et al. [2016]).

Table 7.8: Full Monte Carlo values of the integrated neutron fluence per therapeutic dose, Φ_i, in units of 10^4 cm^{-2} Gy^{-1}, and integrated ambient dose equivalents, $H_i^*(10)$, in units of μSv Gy^{-1}, in the specified energy range i, for the case of Mevion S250i Hyperscan single-room system. The fraction between the integrated quantities and their total quantity are also expressed, in units of %. This Table complements Figure 7.35.

Position - Method	$E < 1$ eV	1 eV $< E <$ 0.1 MeV	0.1 eV $< E <$ 10 MeV	$E >$ 10 MeV	Total
	Φ_{Thermal}	$\Phi_{\text{Epithermal}}$	Φ_{Fast}	$\Phi_{\text{HighEnergy}}$	Φ_{Total}
P1 - Monte Carlo	2.0	1.2	1.1	0.8	5.1
P3 - Monte Carlo	2.0	1.3	2.0	1.6	6.8
PX - Monte Carlo	1.8	1.0	1.2	0.6	4.6
P6 - Monte Carlo	2.3	1.5	2.7	1.0	7.5
P14 - Monte Carlo	2.5	1.9	5.8	1.5	11.7
P12 - Monte Carlo	2.6	1.9	5.8	1.5	11.8
P5 - Monte Carlo	2.4	1.7	3.9	2.2	10.2
P13 - Monte Carlo	2.1	1.3	2.1	1.4	7.0
P11 - Monte Carlo	2.1	1.3	2.5	2.6	8.5
	$\frac{\Phi_{\text{Thermal}}}{\Phi_{\text{Total}}} \cdot 100$	$\frac{\Phi_{\text{Epithermal}}}{\Phi_{\text{Total}}} \cdot 100$	$\frac{\Phi_{\text{Fast}}}{\Phi_{\text{Total}}} \cdot 100$	$\frac{\Phi_{\text{HighEnergy}}}{\Phi_{\text{Total}}} \cdot 100$	$\frac{\Phi_{\text{Total}}}{\Phi_{\text{Total}}} \cdot 100$
P1 - Monte Carlo	39.3	23.3	21.2	16.1	100
P3 - Monte Carlo	29.6	18.4	29.0	23.0	100
PX - Monte Carlo	39.2	22.2	25.0	13.6	100
P6 - Monte Carlo	30.4	20.2	36.3	13.1	100
P14 - Monte Carlo	21.7	16.2	49.4	12.7	100
P12 - Monte Carlo	21.6	16.3	49.2	12.9	100
P5 - Monte Carlo	23.6	16.7	38.5	21.3	100
P13 - Monte Carlo	30.2	19.0	30.5	20.2	100
P11 - Monte Carlo	24.1	15.2	29.6	31.1	100
	$H^*_{\text{Thermal}}(10)$	$H^*_{\text{Epithermal}}(10)$	$H^*_{\text{Fast}}(10)$	$H^*_{\text{HighEnergy}}(10)$	$H^*_{\text{Total}}(10)$
P1 - Monte Carlo	0.2	0.2	3.4	2.5	6.3
P3 - Monte Carlo	0.2	0.2	6.7	5.7	12.8
PX - Monte Carlo	0.2	0.2	3.8	2.2	6.4
P6 - Monte Carlo	0.3	0.2	9.3	4.4	14.2
P14 - Monte Carlo	0.3	0.3	20.3	6.6	27.5
P12 - Monte Carlo	0.3	0.3	20.3	6.7	27.7
P5 - Monte Carlo	0.3	0.3	13.7	9.5	23.7
P13 - Monte Carlo	0.2	0.2	7.2	5.6	13.3
P11 - Monte Carlo	0.2	0.2	8.7	9.2	18.3
	$\frac{H^*_{\text{Thermal}}(10)}{H^*_{\text{Total}}(10)} \cdot 100$	$\frac{H^*_{\text{Epithermal}}(10)}{H^*_{\text{Total}}(10)} \cdot 100$	$\frac{H^*_{\text{Fast}}(10)}{H^*_{\text{Total}}(10)} \cdot 100$	$\frac{H^*_{\text{HighEnergy}}(10)}{H^*_{\text{Total}}(10)} \cdot 100$	$\frac{H^*_{\text{Total}}(10)}{H^*_{\text{Total}}(10)} \cdot 100$
P1 - Monte Carlo	3.7	2.9	54.1	39.2	100
P3 - Monte Carlo	1.8	1.6	52.2	44.4	100
PX - Monte Carlo	3.3	2.5	59.4	34.8	100
P6 - Monte Carlo	1.9	1.7	65.4	30.9	100
P14 - Monte Carlo	1.1	1.2	73.8	23.9	100
P12 - Monte Carlo	1.1	1.2	73.5	24.2	100
P5 - Monte Carlo	1.2	1.2	57.8	39.9	100
P13 - Monte Carlo	1.9	1.6	54.5	42.0	100
P11 - Monte Carlo	1.3	1.1	47.3	50.3	100

A very first idea on why energy distributions of neutrons exhibit a high energy peak (intranuclear cascade neutrons) and a fast-evaporation peak can be extracted from a simple analysis of cross sections and their associated differential cross sections. However, it must be clear that radiation transport in matter is complex and is random in nature, a ran-

domness that is governed by the quantum mechanics involved in the radiation transport process and radiation-matter interactions. MC codes include this randomness so that random variables involved in radiation transport must be sampled accordingly as they follow probability density functions. The relevant cross sections involved are presented in Appendix E.

7.1.3 General view of neutron dose equivalents in proton beam scanning

Neutron dose equivalents obtained with the UAB developed neutron dosimeter based on PADC (*i.e.,* results from Figure 7.16 and 7.17) have been summarised in Figure 7.36, in the good understanding that measurement conditions are different (see a summary of some parameters that set the measurement conditions in Table 7.1). The interested reader in taking the neutron dose equivalents per therapeutic Gy must proceed carefully and decide what numerical value of the neutron dose equivalent per Gy represents better his measurement conditions. Neutron dose equivalents per therapeutic Gy (with units of μSv Gy^{-1} or mSv Gy^{-1}) can of course be thought as a therapeutic proton absorbed dose-to-neutron dose equivalent ICRU tissue conversion coefficients.

In Figure 7.36 we have also displayed the results of UAB neutron dosimeter when measuring out-of-field neutron dose equivalents in a water tank phantom or BOMAB-like phantom, when photon radiotherapy treatments have been employed [Di Fulvio et al., 2013]. Additionally, we have included some results of out-of-field neutron dose equivalents obtained in Alderson-Rando phantom when proton beam scanning and photon treatment has been used [Hälg et al., 2014].

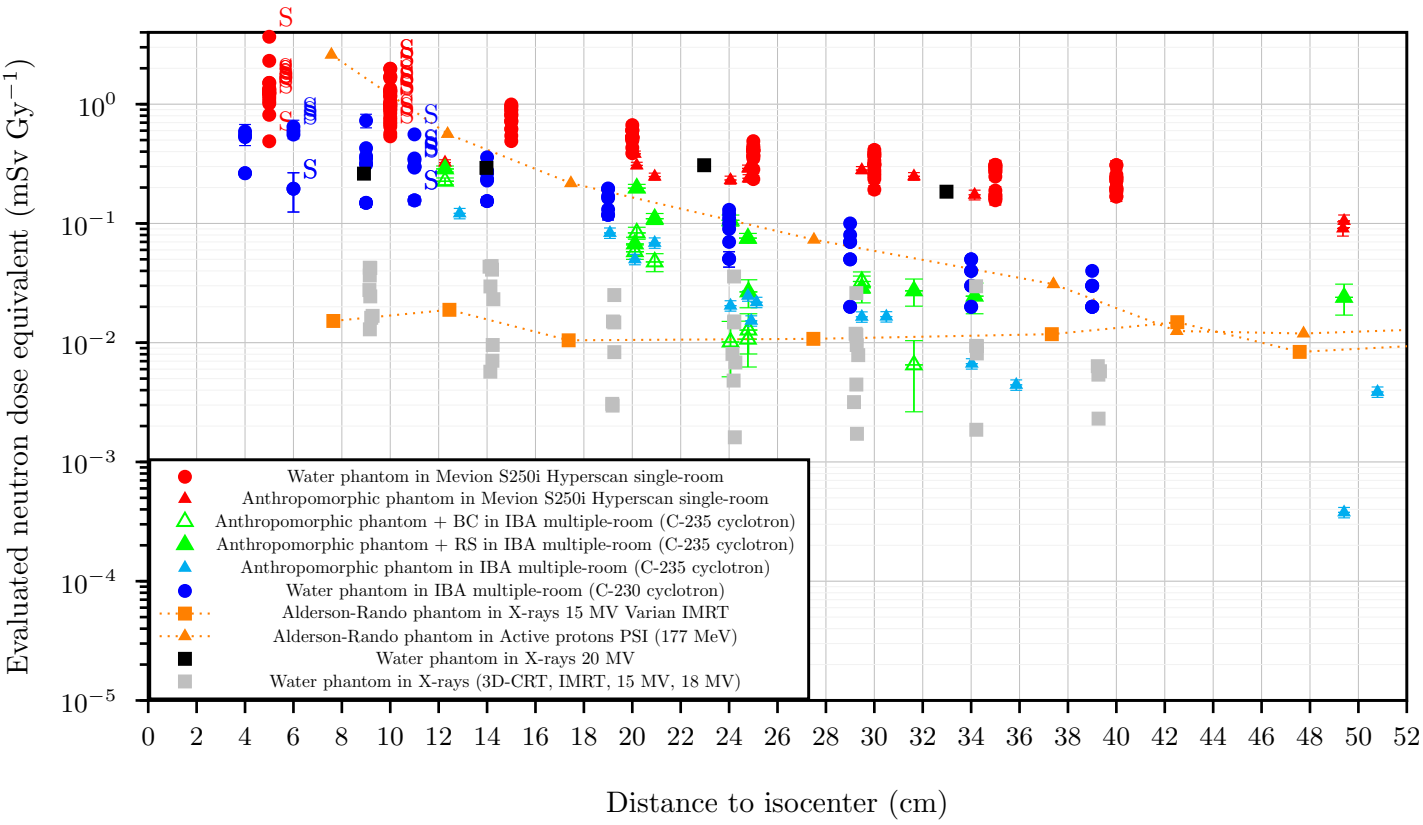

Figure 7.36: Neutron dose equivalents obtained with the UAB neutron dosimeter in proton irradiations specified in Table 7.1. These results are an integration of the results from Figures 7.16 and 7.17. Out-of-field neutron doses obtained with PADC-UAB in photon treatments are also included (black and gray) [Di Fulvio et al., 2013] and results from Hälg et al. [2014] are shown in orange.

In general, neutron dose equivalents are higher in particle beam scanning proton radiotherapy in comparison with treatments using photons in agreement with Hälg et al. [2014] with the exception of the photon treatment using 20 MV X-rays. For one hand, neutron out-of-field doses in photon treatments using 20 MV X-rays are in the same order of magnitude that neutron out-of-field doses from PBS proton radiotherapy (IBA multiple-room (C-235 cyclotron) system) between distances to isocenter from 4 and 18 cm, as already concluded by Stolarczyk et al. [2018]. For the other hand, neutron out-of-field doses using 20 MV X-rays are even higher in comparison to neutron out-of-field doses from PBS proton radiotherapy in the distance to isocenter range from 18 to 34 cm (when comparing with IBA multiple-room (C-235 cyclotron) system).

Assuming that responses from MTS-7 (TLD ^{7}Li enriched) in Figure 7.37 are due to photon out-of-field doses and even assuming that neutron out-of-field doses in photon radiotherapy are negligible (this was already assumed in Knežević et al. [2022]), it is concluded that total out-of-field doses in photon radiotherapy are higher in comparison to proton radiotherapy. Indeed, this is because the photon out-of-field doses in photon treatments are already high (at 14 cm, 10 mGy Gy^{-1}, Figure 7.37) and it turns out that this component is already higher in comparison to neutron plus photon dose of PBS proton radiotherapy (at 14 cm, 1.3 mSv Gy^{-1}, Figure 7.37). Photon out-of-field doses in photon radiotherapy in water tank phantom were measured in work Bordy et al. [2013].

The tendencies shown in neutron and photon out-of-field doses in proton and photon radiotherapy explained above have been already discussed in work Stolarczyk et al. [2018],

Figure 7.37 (for water tank phantom) and in work Knežević et al. [2022], Figures 7.38 and 7.39 (for anthropomorphic phantoms). The observed behaviour is in agreement with work Hälg et al. [2014].

A methodology to deal with responses in mixed radiation fields should be employed to verify the impact of mixed radiation fields in measuring and reporting doses.

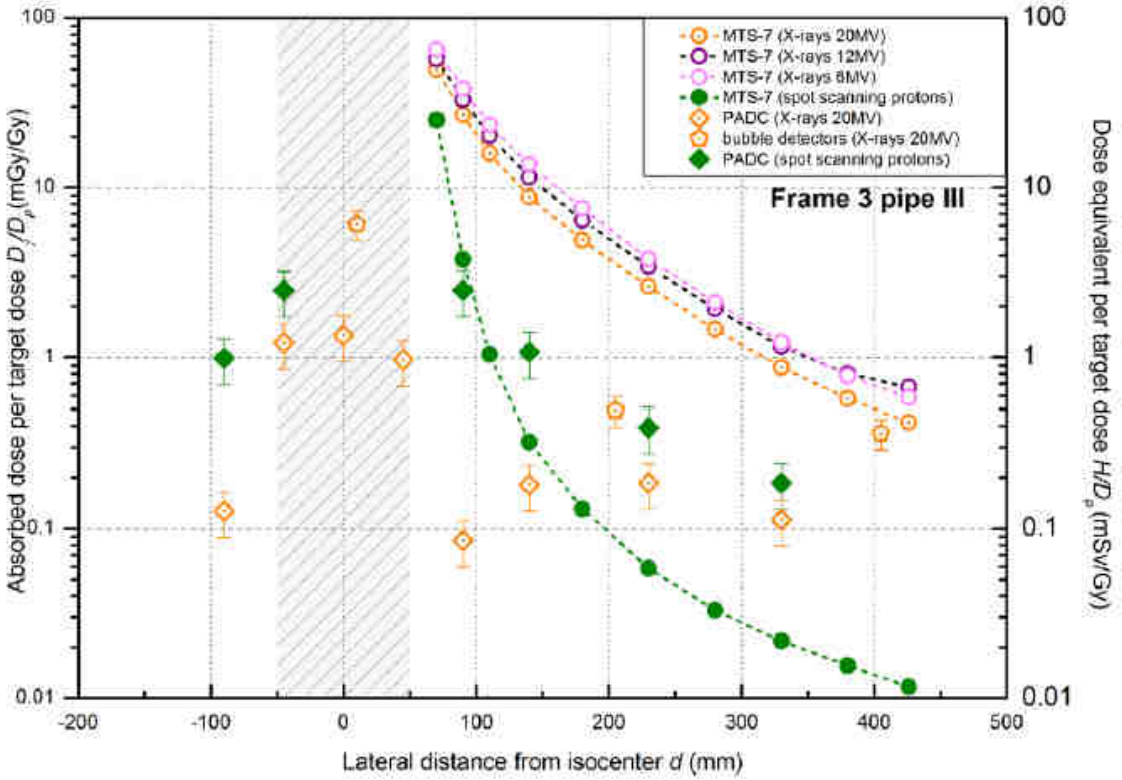

Figure 7.37: Photon and neutron out-of-field doses from photon and PBS proton radiotherapy treatments (also known as IMPT) in the water tank phantom. From Stolarczyk et al. [2018].

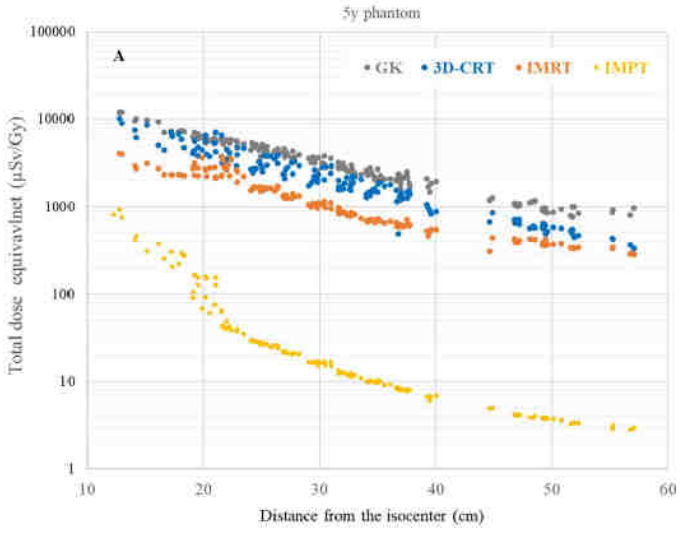

Figure 7.38: Photon and neutron out-of-field doses from photon and PBS proton radiotherapy treatments (also known as IMPT) in the 5 YO anthropomorphic phantom. From Knežević et al. [2022].

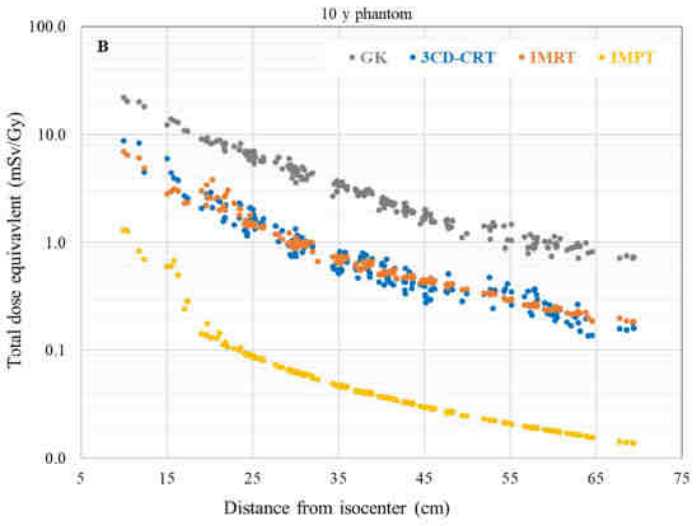

Figure 7.39: Photon and neutron out-of-field doses from photon and PBS proton radiotherapy treatments in the 10 YO anthropomorphic phantom. From Knežević et al. [2022].

7.2 Monte Carlo simulations for $Q(E)$ and $h^*_{\Phi}(10, E)$

When assessing the radiobiological damage induced by neutrons, dose equivalent quantities must be used. In particular, in this work we use the neutron dose equivalent in ICRU tissue, H_{ne}, Equation (4.51), and neutron ambient dose equivalent, $H^*_{\mathrm{ne}}(10)$, Equation (4.55).

When energy distribution of the neutron fluence is known by some means, fluence-to-dose conversion coefficients must be employed, as explained previously. However, neutron quality factors, $Q(E)$, are only known up to neutron energies of 19.5 MeV [Siebert et al., 1995] and there are radiation protection situations in which the energy distribution of the neutron fluence, $\Phi_E(E)$, can be extended to neutron energies beyond 19.5 MeV. Those situations have been found in this work. The situation is different for fluence-to-ambient dose equivalent conversion coefficients for neutrons, $h^*_{\Phi}(10, E)$, as several authors have published numerical values, in particular, Pelliccioni [2000].

From Equation (3.56) one can compute $Q(E)$ by MC simulations. The MC simulations were constituted by an ICRU tissue (see Section 3.1.5) universe with a radius of 200 cm in which an isotropic and mono-energetic neutron source was placed in the middle. The tissue universe must be large enough to stop all secondary charged particles. As $Q(E)$ must be computed for mono-energetic neutrons, in the MC simulations we have only to transport initial neutrons of energy E so that when a neutron has undergone one interaction, it has to be removed from the MC radiation transport process. The approximation taken in this work to deal with that fact is to set an energy cut so that when an initial neutron of energy E (coming from the neutron source) has now an energy $E_{\mathrm{CUT}} = 0.9999 \cdot E$, is removed from the simulation. In this way, secondary charged particles of different types (and their energy deposits) will be always consequence of the initial neutrons of energy E.

MC codes MCNP 6.2 [Werner et al., 2017] and PHITS [Sato et al., 2018] were used to compute $Q(E)$ through the methodology just explained. Additionally, with MCNP we computed $h^*_{\Phi}(10, E)$ with Equation (3.79).

See computed neutron quality factors in Figure 7.40 and fluence-to-ambient dose equivalent conversion coefficients for neutrons in Figure 7.41. Remember the geometrical situation and definition for $h^*_{\Phi}(10, E)$ in Figures 3.9, 3.10 and 3.11.

In the computations of MCNP different combination of nuclear models and degree of recoils were used. The combination of nuclear models used are the ones suggested by the manual of MCNP *i.e.,* combination of Bertini(B)-Dresner(D), Isabel(I)-Dresner, Bertini-ABLA(A), Isabel-ABLA and CEM03.03 nuclear models. INCL nuclear model does not enable the transport of heavy ions and is not included. Degree of recoils are controlled by the 7^{th} entry of instruction PHYS:N and PHYS:H. The entry, in case of neutrons is COILF, and in the case of protons is RECL. When we set values 2, 1.5 and 1.3 for COILF entry, at the same time, we set values 1, 0.5 and 0.3 for RECL entry. Values seen in the legend of Figures 7.40 and 7.41 correspond to RECL entries.

As MCNP does not transport charged particles under 10^{-3} MeV, MCNP results regarding neutron quality factors are only shown from 10^{-3} to 10^{4} MeV.

Thermal effects in the neutron transport are taken into account considering hydrogen bound to polyethylene (poly.10t) as done by Siebert et al. [1995].

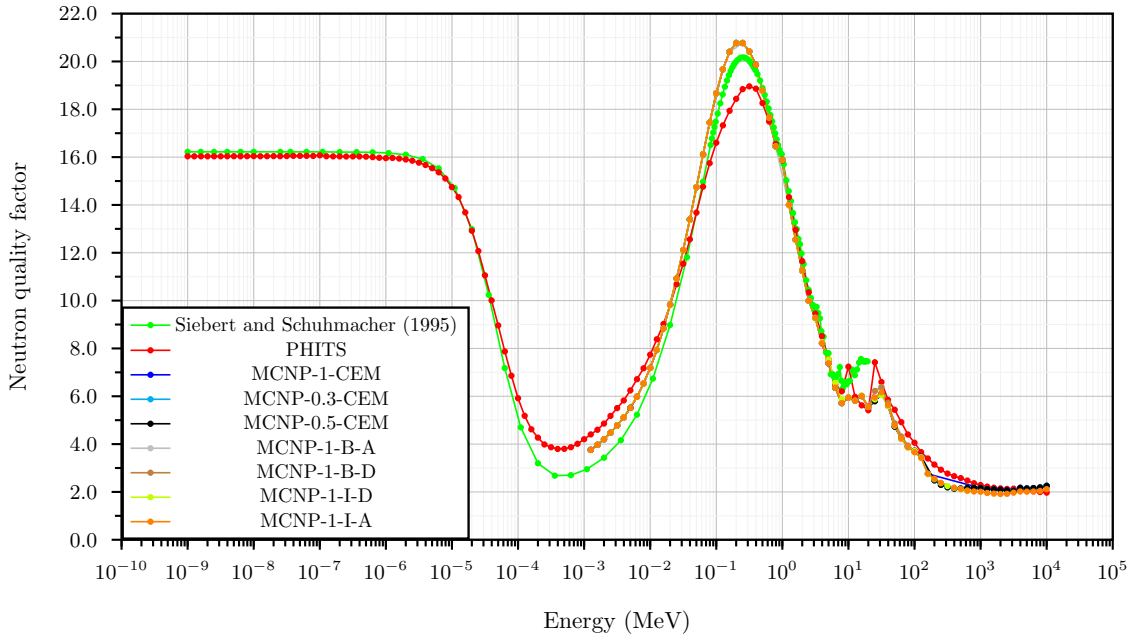

Figure 7.40: Computation of neutron quality factors. The reference Siebert et al. [1995] is shown in green. Computation with PHITS is in red. The rest of colors are computations with MCNP using different combinations of nuclear models and degree of recoils, see text.

According to the results shown in Figures 7.40 and 7.41, general tendencies are well reproduced in comparing with the references. However, computed fluence-to-ambient dose equivalent conversion coefficients for neutrons from 70 MeV can show relative differences up to 100 %.

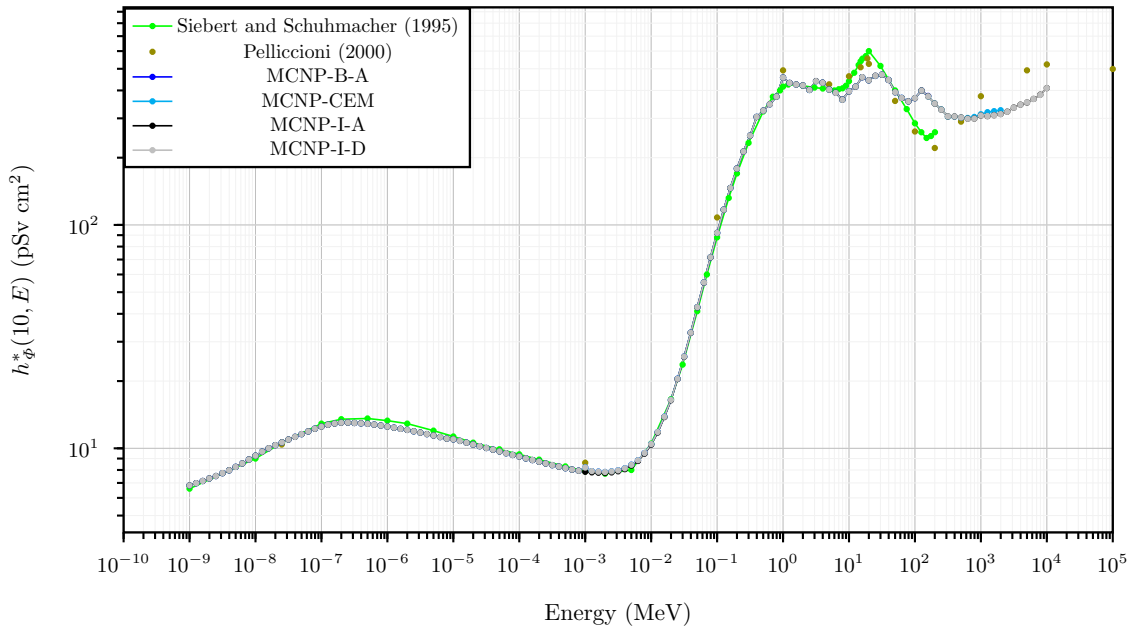

Figure 7.41: Computation of fluence-to-ambient dose equivalent conversion coefficients for neutrons. The references Siebert et al. [1995] and Pelliccioni [2000] are shown in green and khaki. The rest of colors are the computations with MCNP.

Considering the approximations used in our computations, the limitations of cross sections since tabulated tables have a maximum energy of generally 150 MeV, the fact that particle

production cross sections are not always available, considering that nuclear models have to be employed and taking into account that a reference already exists for fluence-to-ambient dose equivalent conversion coefficients for neutrons. No recommendation is done in this work regarding the fluence-to-ambient dose equivalent conversion coefficients for neutrons.

However, as neutron quality factor is, to the knowledge of the author, not explicitly available in the literature, the recommendation of using neutron quality factors in Table 7.9 is done.

Table 7.9: Recommended neutron quality factors from 25 MeV to 10^4 *MeV.*

E (MeV)	$Q(E)$
25.1	7.4216
31.6	6.5966
39.8	5.8470
50.1	5.4361
63.1	4.9186
79.4	4.4024
100.0	4.0567
125.9	3.6657
158.5	3.3991
199.5	3.1424
251.2	2.9285
316.2	2.7678
398.1	2.6579
501.2	2.5767
631.0	2.4744
794.3	2.3630
1000.0	2.2889
1258.9	2.2229
1584.9	2.1770
1995.3	2.1471
2511.9	2.1261
3162.3	2.1372
3981.1	2.0965
5011.9	2.0602
6309.6	2.0265
7943.3	1.9962
10000.0	1.9713

The results shown in Figures 7.40 and 7.41 as well as the methodology employed to obtain them was exposed in Caballero-Pacheco et al. [2022].

7.3 Other applications

7.3.1 Experiments in ALBA synchrotron: Corrections on calibration coefficients

UAB PADC-based neutron dosimeters were used for testing and as complement to the surveillance instruments employed for the continuous dose monitoring in two locations of the ALBA synchrotron facility, both inside and outside bunkers.

The aim of work was to obtain calibration coefficients $\left[\frac{\int_E R_\Phi(E)\varphi_E(E)\mathrm{d}E}{\int_E h^*_\Phi(10,E)\varphi_E(E)\mathrm{d}E}\right]$ in different points at the Spanish synchrotron facility ALBA so that Equation (4.55) can be computed from an experimental measurement using the developed UAB neutron dosimeter based on PADC, R, in units of tracks cm^{-2} (see Section 4.4.2).

In particular, calibration coefficients were obtained in the LINAC area (see Figure 7.42), inside the Tunnel (where boster and storage rings are found and where the boster-to-storage (BTS) transfer is found, see Figure 7.43) and in the Experimental Hall (see Figure 7.43) [García-Fusté et al., 2020].

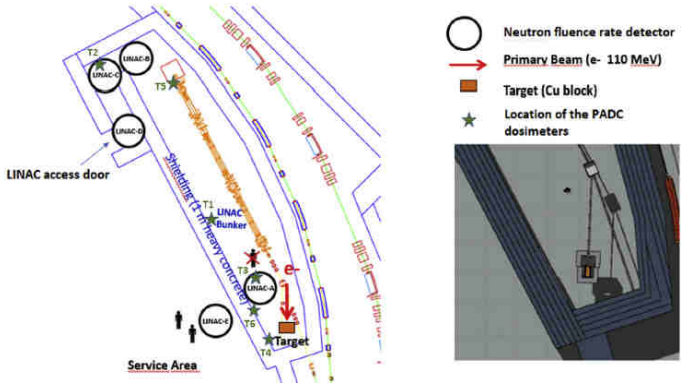

Figure 7.42: Diagram of the LINAC area, with the locations in which the MC FLUKA scoring volumes are created (circular symbols). The inserted figure shows the FLUKA geometry of the situation. From García-Fusté et al. [2020].

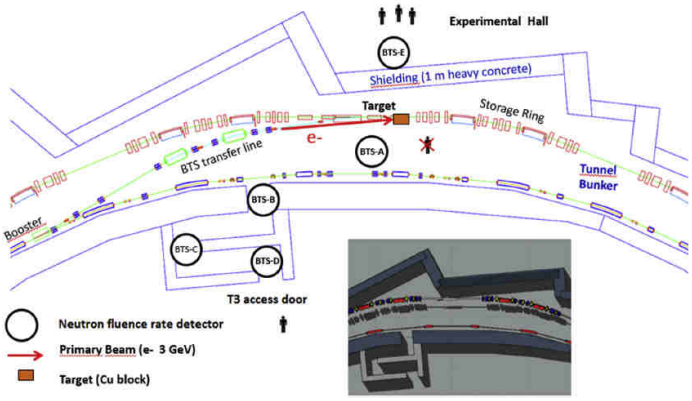

Figure 7.43: Diagram of the BTS area, with the locations in which the MC FLUKA scoring volumes are created (circular symbols). The BSS-UAB was used in BTS-A and BTS-E. The inserted figure shows the FLUKA geometry of the situation. From García-Fusté et al. [2020].

As the calibration coefficient, $\left[\frac{\int_E R_\Phi(E)\varphi_E(E)\mathrm{d}E}{\int_E h^*_\Phi(10,E)\varphi_E(E)\mathrm{d}E}\right]$, can be obtained by computing $\varphi_E(E)$ through MC simulations ($\varphi_E(E) = \varphi_E^{\mathrm{MC}}(E)$) or by measuring $\varphi_E(E)$ with a BSS ($\varphi_E(E) = \varphi_E^{\mathrm{BSS}}(E)$), an option is to do a benchmarking (*i.e.,* to see the goodness of a MC simulation in front of a unit energy distribution provided by a BSS) in some characteristic points and to proceed by MC to compute the unit energy distribution of the neutron fluence in the rest of points where the neutron dosimeter is going to be employed.

Measurements took place in points BTS-A (inside the Tunnel) and BTS-E (outside the Tunnel, in the Experimental Hall) (see Figure 7.43). Active neutron spectrometry with the active BSS-UAB was employed (see Section 4.5.1) obtaining the energy distributions of the neutron fluence, $\Phi_E(E)$, shown in Figure 7.44.

Raw MC energy distribution of the neutron fluence, $\Phi_E^{\mathrm{MC}}(E)$, and MC unit energy distribu-

tions of the neutron fluence, $\varphi_E^{\mathrm{MC}}(E)$, were obtained with FLUKA in 5 points in the LINAC area (see Figure 7.42) and in 5 points in the Tunnel-Experimentall Hall area (see Figure 7.43). In Figures 7.46 and 7.47 presents $\Phi_E^{\mathrm{MC}}(E)$ for the BTS and Linac, respectively. In Figure 7.45 a comparison between the unit energy distribution of the neutron fluence obtained by the active BSS-UAB and the MC unit energy distribution of the neutron fluence is shown.

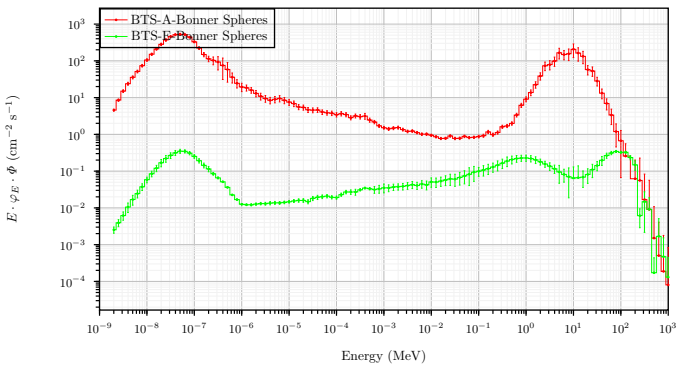

Figure 7.44: Energy distribution of the neutron fluence obtained by BSS-UAB in points BTS-A and BTS-E.

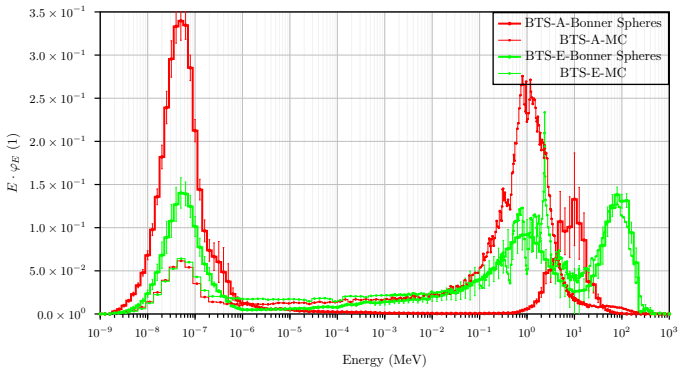

Figure 7.45: Comparison between the unit energy distribution of the neutron fluence obtained by FLUKA simulations (thin lines) and experimentally by BSS-UAB (thick lines) in BTS-A (red line) and BTS-E (green line).

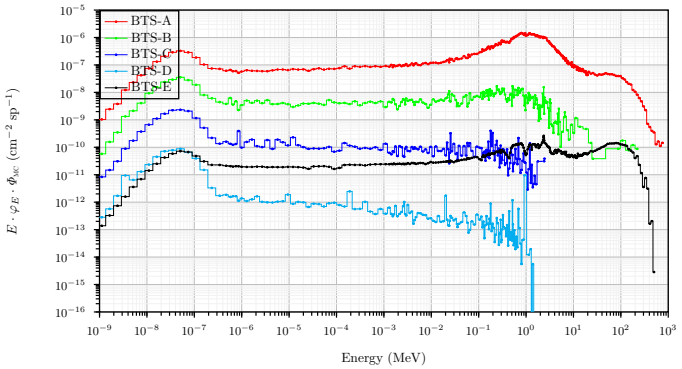

Figure 7.46: Energy distribution of the neutron fluence in five points (BTS A to E) simulated using FLUKA and provided by ALBA staff. Units of cm^{-2} sp^{-1}.

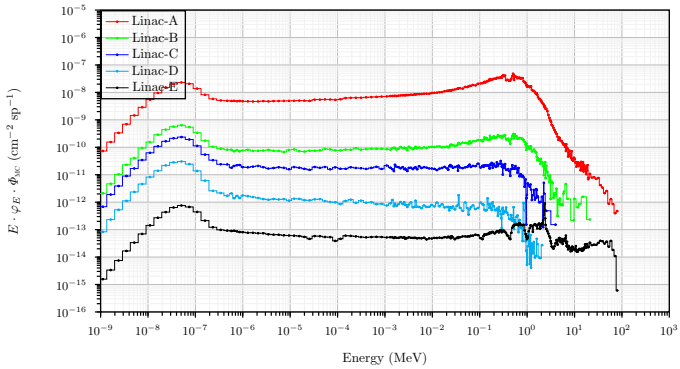

Figure 7.47: Energy distribution of the neutron fluence in five points (LINAC A to E) simulated using FLUKA and provided by ALBA staff. Units of cm^{-2} sp^{-1}.

From comparing $\Phi_E(E)$ and $\Phi_E^{\mathrm{MC}}(E)$, Figure 7.45, we see a good agreement between the two methods in the measurement point located at the Experimental Hall (BTS-E) with the exception of the thermal peak, since prediction from MC is lower in respect to the thermal peak coming from BSS measurements. An explanation compatible with that fact is that MC model does not include all the the geometrical details needed. The agreement is not good in the Tunnel (BTS-A) where even the fast peak positioning is a discrepancy. An explanation compatible with this fact is that the quantity of photons could be so high inside the Tunnel that the pulse height distribution of the ^{3}He proportional counter could be dominated even by pile-up and dead time effects due to photons.

As the benchmarking was considered good enough in the Experimental Hall, it was considered that MC unit energy distribution of the neutron fluence could be valid in the rest of points.

Once the unit energy distribution of the neutron fluence is known by experimental or MC means, the calibration coefficient $\left[\frac{\int_E R_\Phi(E)\varphi_E(E)\mathrm{d}E}{\int_E h^*_\Phi(10,E)\varphi_E(E)\mathrm{d}E}\right]$ can be computed taking the known response function (in terms of fluence) of the UAB neutron dosimeter based on PADC (see Figure 4.27) and taking the fluence-to-ambient dose equivalent conversion coefficient for neutrons (see Figure 3.12). Numerical values of calibration coefficients $\left[\frac{\int_E R_\Phi(E)\varphi_E(E)\mathrm{d}E}{\int_E h^*_\Phi(10,E)\varphi_E(E)\mathrm{d}E}\right]$ are shown in Table 7.10.

Table 7.10: Values of the calibration coefficients for PADC UAB neutron dosimeters to be used in each location characterized by an unit energy distribution of the neutron fluence $\varphi_E(E)$ which can be obtained by experimental or MC means.

Location	$\left[\frac{R}{H^*(10)}\right]_{\mathrm{MC}}$ ($\mathrm{cm^{-2}\ mSv^{-1}}$)	$\left[\frac{R}{H^*(10)}\right]_{\mathrm{EXP}}$ ($\mathrm{cm^{-2}\ mSv^{-1}}$)	$\left[\frac{R}{H^*(10)}\right]_{\mathrm{AmBe}}$ ($\mathrm{cm^{-2}\ mSv^{-1}}$)	$\left[\frac{R}{H^*(10)}\right]_{\mathrm{PADC}}$ ($\mathrm{cm^{-2}\ mSv^{-1}}$)
BTS-A	258 ± 15	219 ± 20		
BTS-B	203 ± 13	-		
BTS-C	79.2 ± 4.7	-		
BTS-D	35.8 ± 2.1	-		
BTS-E	180 ± 11	162 ± 14	307 ± 37	350[a]
LINAC-A	200 ± 12	-		
LINAC-B	177 ± 11	-		
LINAC-C	114.4 ± 6.7	-		
LINAC-D	54.9 ± 2.5	-		
LINAC-E	205 ± 11	-		

[a] Is the numerical value that allow us to consider the UAB passive detector a neutron dosimeter. See Section 4.3 and Domingo et al. [2013].

As the calibration coefficient is dividing the track density obtained by the UAB radiation detector (see Equation (4.55)), this means that if we were going to use calibration coefficients such as (307 ± 37) $\mathrm{cm^{-2}\ mSv^{-1}}$ or 350 $\mathrm{cm^{-2}\ mSv^{-1}}$ instead of the ones from the second or third column of Table 7.10 we would be underestimating the neutron ambient dose equivalent.

7.3.2 Experiments in CERF: Influence of mixed fields in PADC

An irradiation campaign arranged by the EURADOS-WG9 collaboration took place at the CERN-EU high-energy Reference Field (CERF) facility [Mitaroff et al., 2002] [Pozzi et al., 2020] in order to inquire in the topic of a methodology to be used in mixed radiation fields. Measurements with UAB neutron dosimeters (Section 4.4.2) were carried out.

The energy distributions of the particle fluence of different particle types (neutrons, photons, protons, $\mathrm{e^-}$ and $\mathrm{e^+}$, π^- and π^+ and μ) are shown in Figure 7.48. The units of such distributions are $\mathrm{cm^{-2}\ sp^{-1}}$, where sp is, in this case, the number of particles hitting the target copper used to produce, precisely, the secondary radiation shown in Figure 7.48.

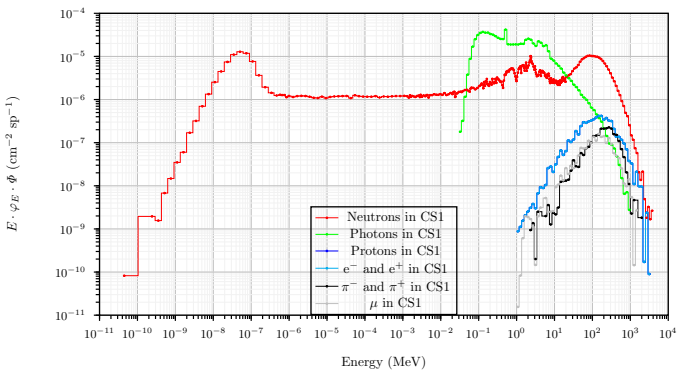

Figure 7.48: Energy distributions of the neutron fluence of different kind of particles found in CERF position CS1. Units of cm^{-2} sp^{-1}. See Pozzi et al. [2020].

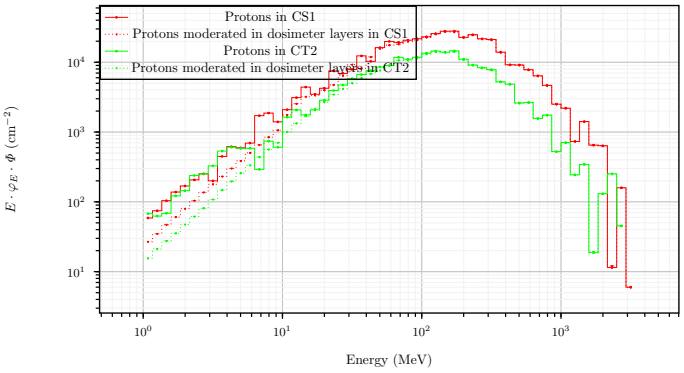

Figure 7.49: Energy distribution of the proton fluence reaching the configuration PADC+Converters (solid) and moderated energy distribution of the proton fluence reaching the PADC alone (dotted) in points CS1 and CT2 of CERF.

The conventional procedure used by UAB to report neutron ambient dose equivalents is to use Equation (4.55) so that R is the track density in units of tracks cm^{-2} and where calibration coefficient $\left[\frac{\int_E R_\Phi(E)\varphi_E(E)\mathrm{d}E}{\int_E h^*_\Phi(10,E)\varphi_E(E)\mathrm{d}E}\right]$ is computed using the unit energy distribution of the neutron fluence derived from CERF, Figure 7.48, response function (in terms of fluence) from Figure 4.27 and fluence-to-ambient dose equivalent conversion coefficients for neutrons from Figure 3.12.

Neutron ambient dose equivalents obtained in points CS1 and CT2 of CERF using the standard methodology explained previously is shown in the third column from Table 7.11. The second column from Table 7.11 shows the reference values reported by CERF in the same conditions of measurement.

Table 7.11: Numerical values of ambient dose equivalent in mSv. Reference values provided by CERF are in column 2. Values of column 2 and 3 are obtained through Equation (4.55).

Location	Reference values $H^*_{\mathrm{CERF}}(10)$ (mSv)	Values obtained with UAB methodology $H^*_{\mathrm{UAB}}(10)$ (mSv)	Values obtained with the proposed methodology $H^*(10)$ (mSv)
CS1	6.6 ± 0.7	8.61 ± 0.65	6.66 ± 0.52
CT2	4.1 ± 0.4	4.75 ± 0.34	4.14 ± 0.31

As CERF is, in particular, a mixed radiation field containing both neutrons and protons (incident to the UAB passive radiation detector) and taking into account that response function to neutrons (in terms of fluence) of the PADC layer + neutron-to-proton converters is Figure 4.27 and response function to protons (in terms of fluence) of the PADC layer alone is Figure 4.20, one can use Equation (6.7) from Chapter 6 so that

$$R^{(\mathrm{PADC+Converters})} = R^{(\mathrm{PADC+Converters})}_{\mathrm{ne}} + \underbrace{R^{(\mathrm{PADC+Converters})}_{\mathrm{pr}}}_{R^{(\mathrm{PADC})}_{\mathrm{pr}}}. \tag{7.1}$$

Where $R^{(\mathrm{PADC+Converters})}$ is the total track density measured and due to the the mixed radiation field reaching the configuration PADC+Converters, $R^{(\mathrm{PADC+Converters})}_{\mathrm{ne}}$ is the track density due to the neutrons reaching the configuration PADC+Converters and $R^{(\mathrm{PADC})}_{\mathrm{pr}}$ is the track density due to the protons reaching the PADC layer. It is important to notice that the response function to protons (in terms of fluence) shown in Figure 4.20 is

only for the PADC layer alone, this means that if there is an energy distribution of the proton fluence hitting the PADC layer + neutron-to-proton converters, one must do a MC simulation to see what is the effect of the neutron-to-proton converters to the external energy distribution of the proton fluence. This was done and the results are shown in Figure 7.49. MC modelling is shown in Figures 7.50 and 7.51.

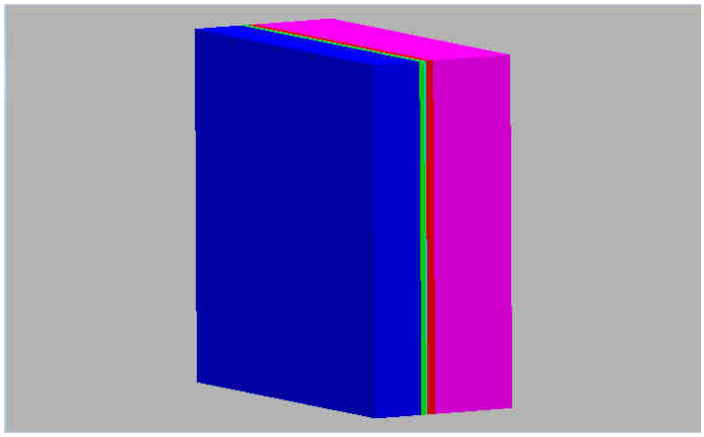

Figure 7.50: MC modelling of the UAB standard neutron dosimeter, see Figure 4.26. The radiation beam comes from the left. From left to right there is 3 mm of polyethylene, 300 µm of Makrofol polycarbonate, 100 µm Nylon type 6 and a scoring region (air) with increased dimensions.

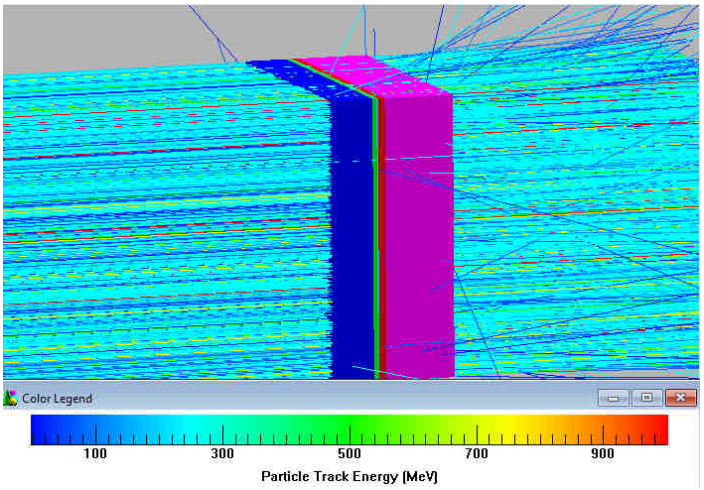

Figure 7.51: MC modelling of the UAB standard neutron dosimeter, see Figure 4.26. The radiation beam comes from the left. From left to right there is 3 mm of polyethylene, 300 µm of Makrofol polycarbonate, 100 µm Nylon type 6 and a scoring region (air) with increased dimensions. Energy distribution of the proton beam is also shown, notice how relevant are 100 to 300 MeV protons, according to Figure 7.48.

Therefore it is clear that the response of the configuration PADC+Converters to the proton field is actually due to the moderated proton field reaching the PADC layer.

Consequently, Equation (7.1), can be written as

$$R^{(\text{PADC+Converters})} = R_{\text{ne}}^{(\text{PADC+Converters})} + \Phi_{\text{pr}}^{(\text{PADC})} \int_E R_{\Phi_{\text{pr}}}^{(\text{PADC})}(E)\varphi_{E,\text{pr}}^{(\text{PADC})}(E)\text{d}E, \tag{7.2}$$

so that the real or actual track density due to neutrons is

$$R_{\text{ne}}^{(\text{PADC+Converters})} = \underbrace{R^{(\text{PADC+Converters})}}_{\text{Experimental measurement}} - \Phi_{\text{pr}}^{(\text{PADC})} \int_E R_{\Phi_{\text{pr}}}^{(\text{PADC})}(E)\varphi_{E,\text{pr}}^{(\text{PADC})}(E)\text{d}E. \tag{7.3}$$

Taking track density from Equation (7.3) and using it in Equation (4.55) results in the ambient dose equivalent labelled as $H^*(10)$ in the fourth column of Table 7.11 reaching a very good agreement with the reference information (second column of Table 7.11).

In PADC based neutron dosimeters, the required LET (in water) to induce tracks is of the order of ~ 5 KeV µm^{-1} [Zhou et al., 2007]. And, as CERF is a mixed radiation field containing other charged particles, is interesting to show the LET in water as a function of the kinetic energy for those charged particles, resulting in Figure 7.52.

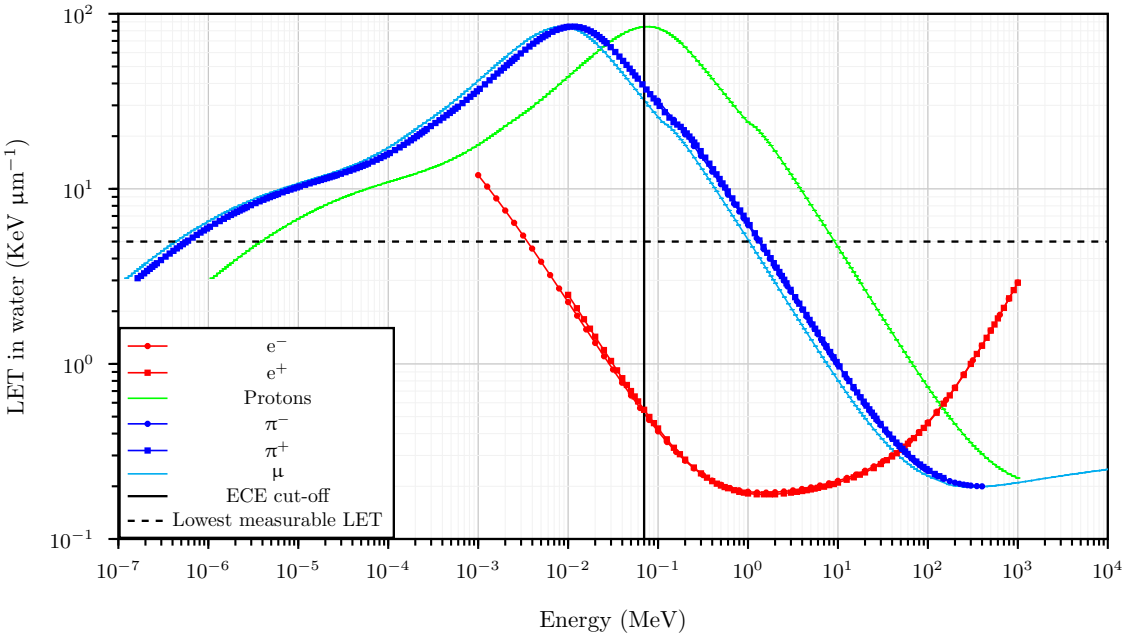

Figure 7.52: LET (in water) as a function of the kinetic energy of the different charged particles that appear in CERF. Horizontal dashed line is the value 5 KeV μm^{-1}, see text. Vertical line corresponds to the minimum proton kinetic energy (∼ 70 KeV) that can be recorded in the UAB PADC based dosimeter, see Fernández et al. [1996].

According to Figure 7.52, at least, μ and π particles with energies from around 70 KeV to $\sim$ 1 MeV could induce tracks in the PADC layer. However, according to Figure 7.48 (the information is scarce anyway) there are 6 orders of magnitude of difference in the lethargy fluence between neutrons, and μ and π of 1 MeV while there are *only* $\sim$ 4 orders of magnitude of difference between neutrons and protons. As 10000 neutrons of 1 MeV will produce 1 track in the PADC layer while 1 proton of 1 MeV will also produce 1 track in the PADC layer, according to the response functions Figures 4.27 and 4.20, it is reasonable to think that protons (the ones not generated by local neutrons by interaction with the converters) have some relevance in contaminating the signal and therefore it is reasonable to think that Equation (7.3) could have some relevance.

7.3.3 Experiments in ENEA Frascati: Passive neutron spectrometry

An irradiation campaign with the passive BSS-UAB (see Section 4.5.2) took place in the HOmogeneous Thermal NEutron Source (HOTNES) design inside the ENEA-Frascati facility [Bedogni et al., 2017].

With an innovative design based on a hollow cavity whose walls are made with polyethylene, HOTNES is capable to provide an homogeneous thermal field by employing an ^{241}Am-B source located at the bottom of the cavity. The effective volume available to irradiate detectors inside the cavity is a cylindrical volume with diameter 30 cm and height 70 cm [Bedogni et al., 2017]. In Figure 7.53 the energy distribution of the neutron fluence in the "reference point $z = 50$ cm" of HOTNES is shown.

Using the procedures described in Section 4.5.2 and Section 4.5.3 is obtained, at the "reference point $z = 50$ cm" (see Bedogni et al. [2017]), the energy distribution of the neutron fluence shown in Figure 7.53 with the numerical data shown in Table 7.12.

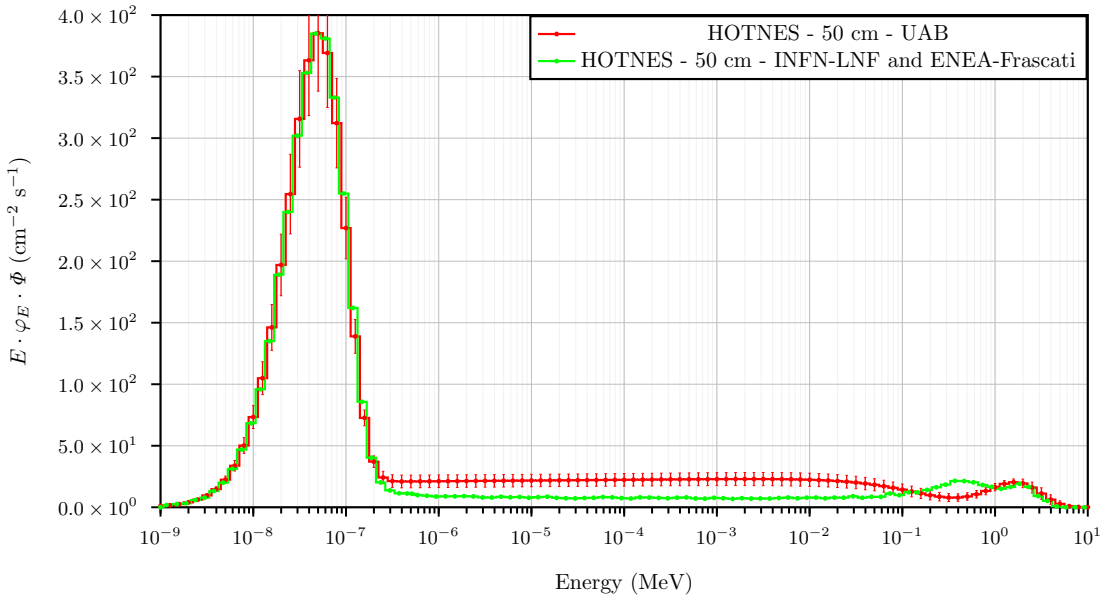

Figure 7.53: Energy distribution of the neutron fluence in HOTNES reference point $z = 50$ cm obtained with the passive BSS-UAB in red. Energy distribution of the neutron fluence in HOTNES reference point $z = 50$ cm obtained in Bedogni et al. [2017] in green.

Table 7.12: Values of the integrated neutron fluence rates, $\dot{\Phi}_i$, in units of cm^{-2} s^{-1}, and integrated ambient dose equivalent rates, $\dot{H}^*_i(10)$, in units of μSv h^{-1}, in the specified energy range i. The fraction between the integrated quantities and their total quantity are also expressed, in units of %.

Institution	$E < 1$ eV	1 eV $< E <$ 0.1 MeV	0.1 eV $< E <$ 10 MeV	Total
	$\dot{\Phi}_{\text{Thermal}}$	$\dot{\Phi}_{\text{Epithermal}}$	$\dot{\Phi}_{\text{Fast}}$	$\dot{\Phi}_{\text{Total}}$
UAB	755	251	50	1056 ± 90
INFN-LNF and ENEA-Frascati	748	92	58	898
	$\frac{\dot{\Phi}_{\text{Thermal}}}{\dot{\Phi}_{\text{Total}}} \cdot 100$	$\frac{\dot{\Phi}_{\text{Epithermal}}}{\dot{\Phi}_{\text{Total}}} \cdot 100$	$\frac{\dot{\Phi}_{\text{Fast}}}{\dot{\Phi}_{\text{Total}}} \cdot 100$	$\frac{\dot{\Phi}_{\text{Total}}}{\dot{\Phi}_{\text{Total}}} \cdot 100$
UAB	71	24	5	100
INFN-LNF and ENEA-Frascati	83	10	7	100
	$\dot{H}^*_{\text{Thermal}}(10)$	$\dot{H}^*_{\text{Epithermal}}(10)$	$\dot{H}^*_{\text{Fast}}(10)$	$\dot{H}^*_{\text{Total}}(10)$
UAB	31	12	59	102 ± 10
INFN-LNF and ENEA-Frascati	31	5	66	102
	$\frac{\dot{H}^*_{\text{Thermal}}(10)}{\dot{H}^*_{\text{Total}}(10)} \cdot 100$	$\frac{\dot{H}^*_{\text{Epithermal}}(10)}{\dot{H}^*_{\text{Total}}(10)} \cdot 100$	$\frac{\dot{H}^*_{\text{Fast}}(10)}{\dot{H}^*_{\text{Total}}(10)} \cdot 100$	$\frac{\dot{H}^*_{\text{Total}}(10)}{\dot{H}^*_{\text{Total}}(10)} \cdot 100$
UAB	31	12	58	100
INFN-LNF and ENEA-Frascati	31	5	65	100

From results shown in Figure 7.53 and Table 7.12 a compatibility among the procedures employed by Bedogni et al. [2017] and the passive BSS-UAB describing the thermal peak is seen. However, there is discrepancy when describing the epithermal and fast region. Work Bedogni et al. [2017] employed MC simulations to provide a guess energy distribution of the neutron fluence for a BSS and, in addition, two more experimental methods were used: a gold foil (bare configuration and Cd configuration) and an active silicon-based thermal neutron detectors (bare configuration and Cd configuration). Taking into account the variety of experimental methods employed as well as the MC support provided in Bedogni et al. [2017], an explanation compatible with the presented results is that uncertainties are

underestimated so that, actually, results are compatible. The only way to clarify further this issue would be the determination of the energy distribution of the neutron fluence with additional detector systems.

7.3.4 Monte Carlo simulations for soil moisture studies

Soil moisture can be quantified through the measurement of neutrons near ground with neutron detectors called cosmic ray neutron sensors (CRNS) [IAEA, 2017] [Schrön et al., 2016] [Köhli et al., 2021] [Joost Iwema, 2017].

Near surface soil moisture (*i.e.,* that in the first meter under the soil) impacts many aspects of human life through its effects on vegetation, surface runoff, aquifer recharge, hill slope stability and land surface interactions with the atmosphere. Soil moisture is important to agriculture, where sufficient water is crucial to support germination and plant growth during critical parts of the growing season. Information on soil water content, determined directly from soil measurements or indirectly from plant health, is used by farmers in water deficient climates to schedule irrigation applications. Soil moisture is a key determinant of yields, through its effects on germination, nutrient availability and plant growth. Where soil moisture has been in prolonged deficit, the result is drought and desertification, with attendant ecological damage [IAEA, 2017].

On the other hand an excess of soil moisture, particularly in the shallow top layers of soil, is a major factor in the occurrence of surface runoff and even catastrophic floods. Furthermore, excess soil moisture is detrimental to plant roots [IAEA, 2017].

Nuclear and related techniques can help develop climate-smart agricultural practices by optimizing water use efficiency. The measurement of soil water content is essential to improve the use of this resource in agriculture. However, most sensors monitor small areas (less than 1 m in radius), hence a large number of sensors are needed to obtain an area averaged representation of soil water content which can be both costly and labor intensive. Wider scale measuring devices are needed as an alternative to the traditional, point approach. The cosmic ray soil neutron sensor (CRNS) is a device that monitors soil water content in a non-invasive, non-hazardous, and continuous way. This recently developed device is used to measure water content in the topsoil over wide areas, covering up to 30 hectares. It fills the gap in measuring soil moisture over large areas for better agricultural water management [IAEA, 2017].

A step in order to design a CRNS is to employ MC simulations to know what is the energy distribution of the neutron fluence near ground and how this energy distribution changes by changing the water content in ground.

It was considered that not so near cosmic neutrons were following the energy distribution provided by EXPACS [Sato, 2015] [EXPACS, 2023], so that ground must be included in the MC simulations in order to score properly the final energy distribution of the neutron fluence in a point near the ground due to the presence of the cosmic neutrons and their interaction with the soil.

MC modelling was really simple, in an universe filled with air there is 50 cm thick ground constituted by the standard ground molecule (63.5 % SiO_2, 15.2 % Al_2O_3 and 21.3 % H_2O, $\rho_{\text{Ground}} = 1.52$ g cm^{-3}). What we call the standard ground molecule is actually the "104 Earth, Typical Western U.S." from Detwiler et al. [2021]. The scoring region was at 170 cm in respect to the ground. The ground as well as the radiation source have a radius of 100 m. See the MC situation in Figures 7.55 and 7.56.

As MCNP needs the density and the isotopic weight fractions, some transformations are needed to go from molecular fractions to isotopic fractions (or isotopic weight fractions). We will work under the approximation that an element is essentially constituted by the most abundant isotope. These transformations are required if we want to study the cases in which the ground water fraction goes from 0 % of H_2O to 100 % H_2O but respecting the presence of the other two molecules (SiO_2 and Al_2O_3). Therefore, the case in which there is 21.3 % H_2O is a particular case and it is what we called the "standard ground".

The weight fraction of SiO_2 in the standard ground molecule is defined as

$$f\left(\frac{\mathrm{SiO_2}}{\mathrm{SiO_2, Al_2O_3, H_2O}}\right) = \frac{M(\mathrm{SiO_2})}{M(\mathrm{SiO_2}) + M(\mathrm{Al_2O_3}) + M(\mathrm{H_2O})} = 0.635, \tag{7.4}$$

where M is the molecular mass. Similarly

$$f\left(\frac{\mathrm{Al_2O_3}}{\mathrm{SiO_2, Al_2O_3, H_2O}}\right) = \frac{M(\mathrm{Al_2O_3})}{M(\mathrm{SiO_2}) + M(\mathrm{Al_2O_3}) + M(\mathrm{H_2O})} = 0.152, \tag{7.5}$$

$$f\left(\frac{\mathrm{H_2O}}{\mathrm{SiO_2, Al_2O_3, H_2O}}\right) = \frac{M(\mathrm{H_2O})}{M(\mathrm{SiO_2}) + M(\mathrm{Al_2O_3}) + M(\mathrm{H_2O})} = 0.213, \tag{7.6}$$

with

$$f\left(\frac{\mathrm{SiO_2}}{\mathrm{SiO_2, Al_2O_3, H_2O}}\right) + f\left(\frac{\mathrm{Al_2O_3}}{\mathrm{SiO_2, Al_2O_3, H_2O}}\right) + f\left(\frac{\mathrm{H_2O}}{\mathrm{SiO_2, Al_2O_3, H_2O}}\right) = 1. \tag{7.7}$$

It is also clear that the fraction of Si in SiO_2 is

$$f\left(\frac{\mathrm{Si}}{\mathrm{SiO_2}}\right) = \frac{M(\mathrm{Si})}{M(\mathrm{SiO_2})} = 0.4665. \tag{7.8}$$

Similarly

$$f\left(\frac{\mathrm{O_2}}{\mathrm{SiO_2}}\right) = \frac{M(\mathrm{O_2})}{M(\mathrm{SiO_2})} = 0.5335. \tag{7.9}$$

For molecules Al_2O_3 and H_2O we would write

$$f\left(\frac{\mathrm{Al_2}}{\mathrm{Al_2O_3}}\right) = \frac{M(\mathrm{Al_2})}{M(\mathrm{Al_2O_3})} = 0.5293, \tag{7.10}$$

$$f\left(\frac{\mathrm{O_3}}{\mathrm{Al_2O_3}}\right) = \frac{M(\mathrm{O_3})}{M(\mathrm{Al_2O_3})} = 0.4707, \tag{7.11}$$

$$f\left(\frac{\mathrm{H_2}}{\mathrm{H_2O}}\right) = \frac{M(\mathrm{H_2})}{M(\mathrm{H_2O})} = 0.1120, \tag{7.12}$$

$$f\left(\frac{\mathrm{O}}{\mathrm{H_2O}}\right) = \frac{M(\mathrm{O})}{M(\mathrm{H_2O})} = 0.8881. \tag{7.13}$$

It is clear that the isotope weight fraction to include in MCNP input would be, for the case of Si

$$f(^{28}\mathrm{Si}) \equiv f(\mathrm{Si}) = f\left(\frac{\mathrm{SiO_2}}{\mathrm{SiO_2, Al_2O_3, H_2O}}\right) \cdot f\left(\frac{\mathrm{Si}}{\mathrm{SiO_2}}\right), \tag{7.14}$$

for the case of Al would be

$$f(^{27}\mathrm{Al}) \equiv f(\mathrm{Al}) = f\left(\frac{\mathrm{Al_2O_3}}{\mathrm{SiO_2, Al_2O_3, H_2O}}\right) \cdot f\left(\frac{\mathrm{Al_2}}{\mathrm{Al_2O_3}}\right), \tag{7.15}$$

for the case of H would be

$$f(^{1}\mathrm{H}) \equiv f(\mathrm{H}) = f\left(\frac{\mathrm{H_2O}}{\mathrm{SiO_2, Al_2O_3, H_2O}}\right) \cdot f\left(\frac{\mathrm{H_2}}{\mathrm{H_2O}}\right), \tag{7.16}$$

and finally for the case of O would be

$$\begin{aligned} f(^{16}\mathrm{O}) \equiv f(\mathrm{O}) = & f\left(\frac{\mathrm{SiO_2}}{\mathrm{SiO_2, Al_2O_3, H_2O}}\right) \cdot f\left(\frac{\mathrm{O_2}}{\mathrm{SiO_2}}\right) + \\ & + f\left(\frac{\mathrm{Al_2O_3}}{\mathrm{SiO_2, Al_2O_3, H_2O}}\right) \cdot f\left(\frac{\mathrm{O_3}}{\mathrm{Al_2O_3}}\right) + \\ & + f\left(\frac{\mathrm{H_2O}}{\mathrm{SiO_2, Al_2O_3, H_2O}}\right) \cdot f\left(\frac{\mathrm{O}}{\mathrm{H_2O}}\right). \end{aligned} \tag{7.17}$$

Numerical values of Equations (7.4), (7.5) and (7.6) are only valid if we consider the soil to be formed by the standard ground molecule. In more or less wet grounds the numerical values of Equations (7.4), (7.5) and (7.6) need to be recalculated. The approximation to find values for $f\left(\frac{\mathrm{SiO_2}}{\mathrm{SiO_2,Al_2O_3,H_2O}}\right)$ and $f\left(\frac{\mathrm{Al_2O_3}}{\mathrm{SiO_2,Al_2O_3,H_2O}}\right)$ is to consider that ratio

$$\frac{f\left(\frac{\mathrm{SiO_2}}{\mathrm{SiO_2,Al_2O_3,H_2O}}\right)}{f\left(\frac{\mathrm{Al_2O_3}}{\mathrm{SiO_2,Al_2O_3,H_2O}}\right)} = 4.1776 \tag{7.18}$$

is a constant when varying the content of water $f\left(\frac{\mathrm{H_2O}}{\mathrm{SiO_2,Al_2O_3,H_2O}}\right)$. Additionally, by using Equation (7.7) we find

$$f\left(\frac{\mathrm{Al_2O_3}}{\mathrm{SiO_2, Al_2O_3, H_2O}}\right) = \frac{1 - f\left(\frac{\mathrm{H_2O}}{\mathrm{SiO_2,Al_2O_3,H_2O}}\right)}{1 + 4.1776}. \tag{7.19}$$

$$f\left(\frac{\mathrm{SiO_2}}{\mathrm{SiO_2, Al_2O_3, H_2O}}\right) = 4.1776 \cdot f\left(\frac{\mathrm{Al_2O_3}}{\mathrm{SiO_2, Al_2O_3, H_2O}}\right). \tag{7.20}$$

When $f\left(\frac{\mathrm{H_2O}}{\mathrm{SiO_2,Al_2O_3,H_2O}}\right)$ ranges from 0 % to 100 %, $f\left(\frac{\mathrm{Al_2O_3}}{\mathrm{SiO_2,Al_2O_3,H_2O}}\right)$ and $f\left(\frac{\mathrm{SiO_2}}{\mathrm{SiO_2,Al_2O_3,H_2O}}\right)$ ranges according to Equations (7.19) and (7.20). Once $f\left(\frac{\mathrm{H_2O}}{\mathrm{SiO_2,Al_2O_3,H_2O}}\right)$, $f\left(\frac{\mathrm{Al_2O_3}}{\mathrm{SiO_2,Al_2O_3,H_2O}}\right)$ and $f\left(\frac{\mathrm{SiO_2}}{\mathrm{SiO_2,Al_2O_3,H_2O}}\right)$ are properly set, Equations (7.14), (7.15), (7.16) and (7.17) can be used to obtain the isotopic weight fractions for MCNP. Take into account that, of course, numerical values of Equations from (7.8) to (7.13) do not change their value.

The initial cosmic neutrons directed to the ground are characterized by an energy distribution of the neutron fluence shown in gray in Figure 7.54 with a total neutron fluence of 6.3956 $\times 10^{-3}$ cm^{-2} s^{-1} [Sato, 2015]. MC normalization factor is found by assuming that the mentioned neutron fluence is directed to the ground perpendicularly. See how the neutron beam is directed to the ground in Figures 7.57 and 7.58.

Figure 7.57 shows that the final neutrons leaving the ground are, in general, isotropic. Of course, these neutrons leaving the ground have been already moderated by the soil.

Figure 7.58 shows those neutron tracks with energies above 0.1 MeV. It is clearly seen that high energy neutrons ($\sim$ orange tracks) have a tendency to go downwards while fast neutrons ($\sim$ yellow tracks) have a tendency to be produced isotropically once the ground is excited by the incoming radiation.

Energy distributions of the neutron fluence computed in the scoring region by varying the quantity of H_2O in the molecule of SiO_2, Al_2O_3 and H_2O are shown in Figure 7.54

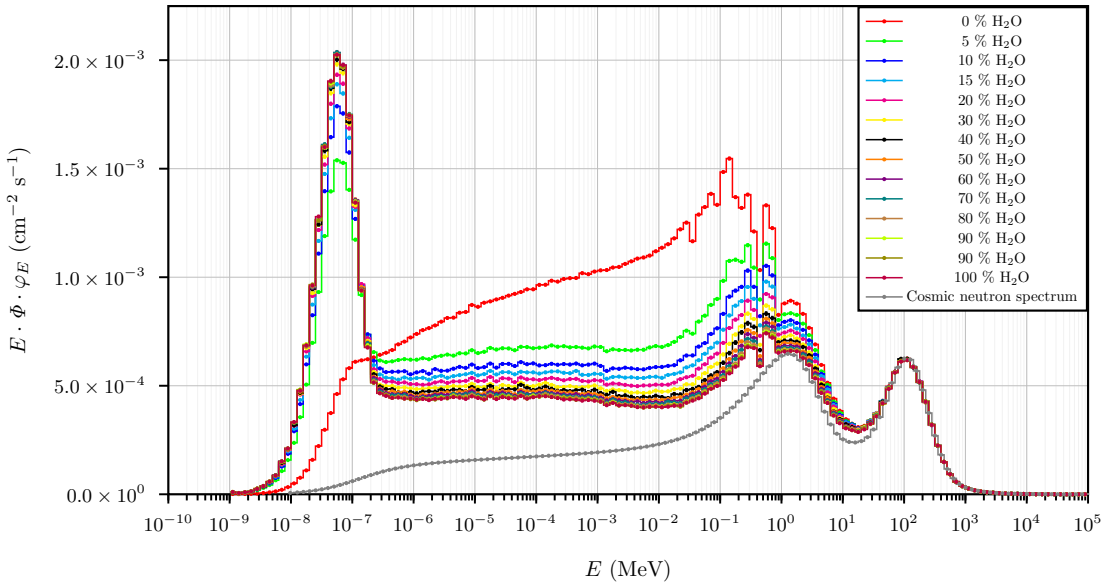

Figure 7.54: Energy distributions of the neutron fluence computed in the scoring region by varying the quantity of H_2O. In gray is shown the initial energy distribution of the neutron fluence directed to the ground.

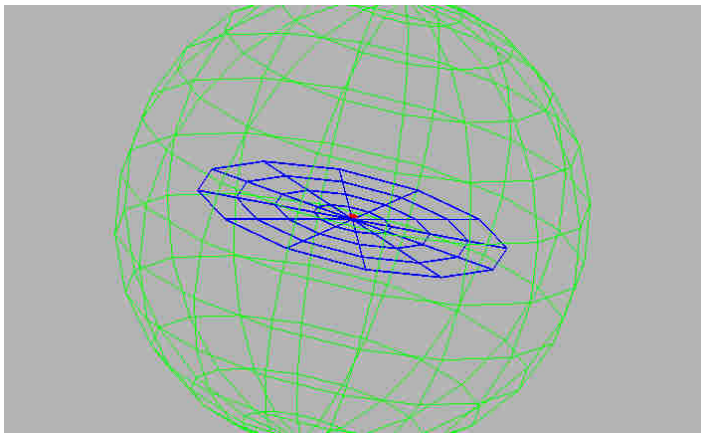

Figure 7.55: General view of the MC universe that is delimited by green lines. Ground is in blue while in red is found the scoring region.

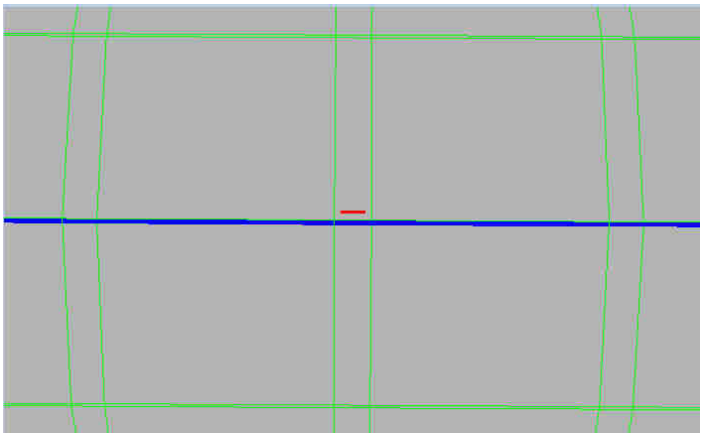

Figure 7.56: Detailed view of the scoring region (in red) MC universe is delimited by green lines. Ground is in blue.

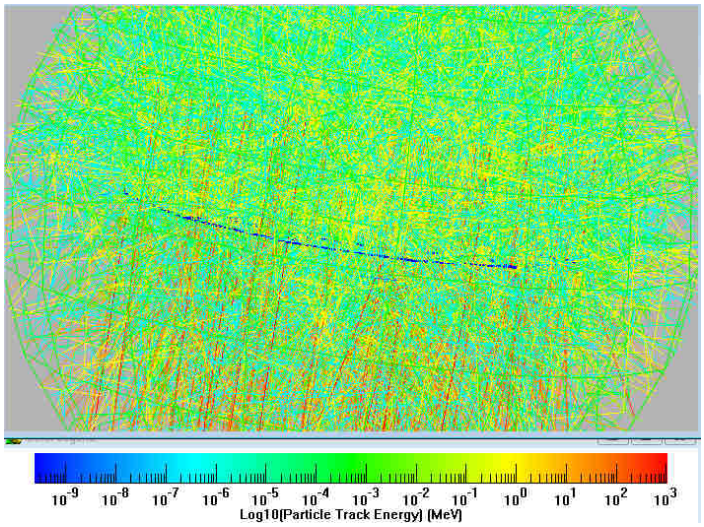

Figure 7.57: MC modelling on how cosmic neutrons reach the soil with the energy distribution indicated. See text for explanation.

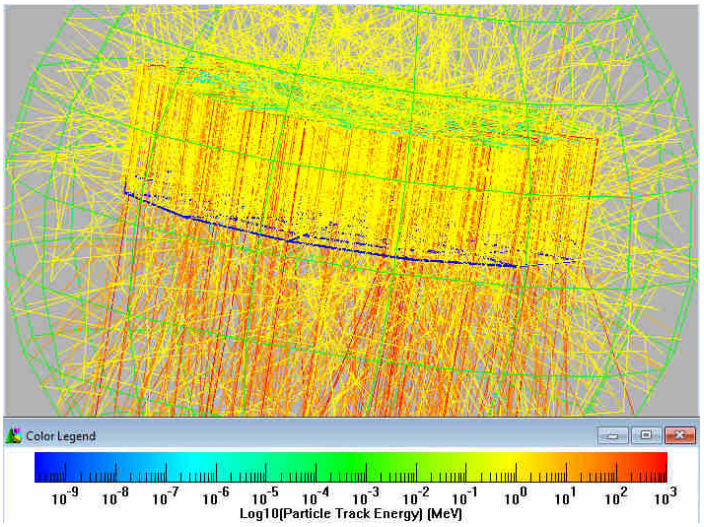

Figure 7.58: MC modelling on how cosmic neutrons reach the soil with the energy distribution indicated. See text for explanation.

The work of Schrön et al. [2016] shows the energy distributions of the neutron fluence as a function of the volumetric water content, θ, which is defined as the volume of water divided by the whole bulk volume [Kranz, 2015] [Weil et al., 2017], as displayed in Figure 7.59.

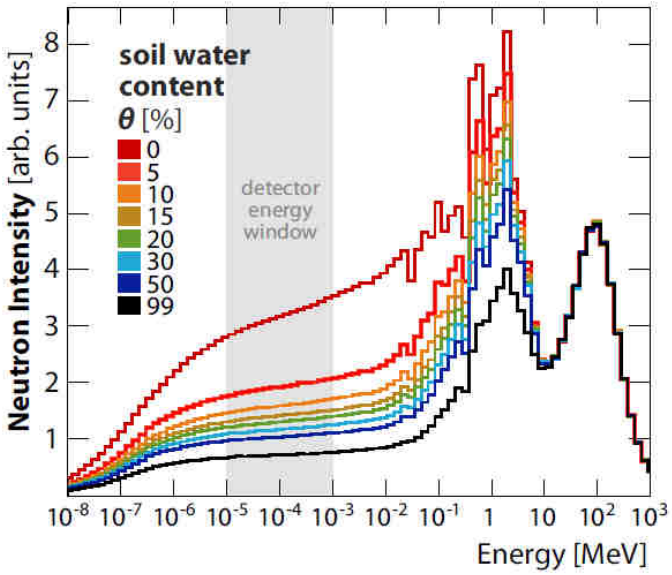

Figure 7.59: Energy distributions of the neutron fluence near ground as a function of the volumetric water content, θ. Thermal neutrons were excluded in those simulations for the sake of computational efficiency. From Schrön et al. [2016].

By comparing the energy distributions from Figures 7.54 and 7.59, and as a first approximation, one could conclude that our results of energy distributions from Figure 7.54 are reasonable.

The physics shown in the energy distributions from Figures 7.54 and 7.59 is understood from the physics explained in Section 2.3.4 and Section 2.4. In summary, intranuclear cascade neutrons are directional (*i.e.*, going downwards in this problem) while evaporation-

fast neutrons are emitted from the ground isotropically so that for more wet grounds, the neutron moderation is higher in a way that epithermal neutrons are different and relevant in the scoring region according to the H_2O percent set in the simulation. In general, the results show that the intensity of natural neutrons is inversely proportional to the amount of water present near the land surface, in agreement with IAEA [2017].

Future steps could include the folding of the energy distributions from Figure 7.54 with the response matrix (in terms of fluence) of hypothesized neutron spectrometers to study if a sample of count rates from the spectrometer (for instance, a similar or adapted system of the conventional Bonner Sphere Systems) have the needed statistical features in order to effectively conclude that a set of count rates correspond indeed to a certain water content of the studied ground.

Chapter 8

Conclusions and perspectives

8.1 Conclusions

The main outputs and conclusions that can be extracted from this work are:

1. Out-of-field neutron dose equivalents per therapeutic Gy are higher in Mevion S250i Hyperscan single-room solution than in IBA multiple-room solutions for similar irradiation conditions.
    - For the water tank phantom, at lateral distances of 10 cm from the isocenter we found $\sim$ 1 mSv Gy^{-1} in Mevion and $\sim$ 0.4 mSv Gy^{-1} in IBA. At lateral distances of 20 cm from the isocenter we found $\sim$ 0.5 mSv Gy^{-1} in Mevion and $\sim$ 0.2 mSv Gy^{-1} in IBA. At lateral distances of 30 cm from the isocenter we found $\sim$ 0.3 mSv Gy^{-1} in Mevion and $\sim$ 0.05 mSv Gy^{-1} in IBA.
    - For anthropomorphic pediatric 5 YO CIRS phantom, at a distance of 12 cm from the isocenter $\sim$ 300 µSv Gy^{-1} in Mevion and $\sim$ 100 µSv Gy^{-1} in IBA were found. At a distance of 20 cm from isocenter $\sim$ 300 µSv Gy^{-1} in Mevion and $\sim$ 70 µSv Gy^{-1} in IBA were found. At a distance of 30 cm from isocenter $\sim$ 300 µSv Gy^{-1} in Mevion and $\sim$ 20 µSv Gy^{-1} in IBA were found. At a distance of 50 cm from isocenter $\sim$ 100 µSv Gy^{-1} in Mevion and $\sim$ 2 µSv Gy^{-1} in IBA were found.
    - For neutron ambient dose equivalents $H^*(10)$ we obtained $\sim$ 20 µSv Gy^{-1} in Mevion and less than $\sim$ 2 µSv Gy^{-1} in IBA at comparable points in the treatment room.
2. In-phantom out-of-field neutron dose equivalents per therapeutic Gy in a proton treatment are higher or in the same order of magnitude in Mevion S250i Hyperscan single-room solution than in in-phantom out-of-field neutron dose equivalent in a photon treatment with 20 MV X-rays.
    - For water tank phantom, photon treatment with 20 MV X-rays produces $\sim$ 0.3 mSv Gy^{-1} while proton treatment in Mevion produces from $\sim$ 1 mSv Gy^{-1} to $\sim$ 0.3 mSv Gy^{-1}.
3. In-phantom out-of-field photon doses are higher in photon treatments than in-phantom out-of-field neutron dose equivalents in the proton treatments studied in this work.

- For water tank phantom, at lateral distance of 16 cm, $\sim$ 10 mGy Gy^{-1} of photon dose (in photon treatments) is obtained while $\sim$ 0.7 mSv Gy^{-1} of neutron dose equivalent is obtained (in proton treatment performed in the Mevion S250i Hyperscan system). At 36 cm, $\sim$ 2 mGy Gy^{-1} of photon dose (in photon treatments) is obtained while $\sim$ 0.2 mSv Gy^{-1} of neutron dose equivalent is obtained (in proton treatment performed in the Mevion S250i Hyperscan system).
- For anthropomorphic pediatric 5 YO CIRS phantom, at a distance of 12 cm from the isocenter is found, $\sim$ 7000 μGy Gy^{-1} of photon dose (in photon treatments) is obtained while $\sim$ 300 μSv Gy^{-1} of neutron dose equivalent is obtained (in proton treatment performed in the Mevion S250i Hyperscan system). At 50 cm, $\sim$ 600 μGy Gy^{-1} of photon dose (in photon treatments) is obtained while $\sim$ 100 μSv Gy^{-1} of neutron dose equivalent is obtained (in proton treatment performed in the Mevion S250i Hyperscan system).

4. If it is assumed that photon out-of-field doses are negligible in respect to neutron out-of-field doses in proton radiotherapy (as proved in a water tank phantom [Stolarczyk et al., 2018], in an IBA environment), then total out-of-field doses in Mevion are lower than total out-of-field doses in photon treatments.

5. Out-of-field neutron dose equivalent conversion coefficients (from therapeutic Gy to out-of-field mSv) are provided in Mevion S250i Hyperscan single-room environment under different parameters and experimental settings. It is the physicist's responsibility to contribute to strategies to minimize the doses as needed and according to ALARA principle.

6. In the conditions of this work, the MC method has not been proved to be capable to provide reliable computations of the full MC neutron dose equivalent and the full MC neutron ambient dose equivalent. In general, a factor of $\sim$ 2 has been found in confronting full MC computations and evaluated results. This is due to the lack of complete modelling of the facility.

7. The MC unit energy distribution of the neutron fluence, $\varphi_E^{\mathrm{MC}}(E)$, is more reliable than the MC energy distribution of the neutron fluence, $\Phi_E^{\mathrm{MC}}(E)$.

8. The MC method is a very important tool to complement experimental work. It has been proven its importance at time of finding the truly (and more detailed) energy distributions of the neutron fluence in neutron spectrometry. In particular, to find the fine structure of the fast and high-energy peak.

9. The approximation taken in this work to model the energy degrader (range modulator system) and collimator (adaptive aperture) is a very good approximation for purposes of providing a MC guess energy distribution to the unfolding code. This is proven by the behaviour of the unfolding code when departing from the MC guess energy distribution to finally provide the experimental energy distributions of the neutron fluence in the neutron spectrometry.

10. The MC method is an essential tool to find energy-response corrections for neutron detectors. UAB *advanced* methodology to provide evaluated neutron dose equivalents depends on MC computations of the unit energy distribution of the neutron fluence. The *advanced* methodology is expected to produce a better assessment on neutron dose equivalents than the *traditional* methodology (to use calibration coefficients obtained in AmBe neutron energy distribution or equivalent) as unit energy distributions of the neutrons found in this work are quite different from the energy distribution of the neutrons found in AmBe or any standard of neutron calibration.

11. A better assessment of the neutron ambient dose equivalent can be performed, using the UAB neutron dosimeter based on PADC, in different points of ALBA synchrotron as calibration coefficients ranging from 36 and 258 cm^{-2} mSv^{-1} are given depending on the specific location to do the measurements and the unit energy distribution of the neutron fluence found in that location.

12. An equation is proposed to deal with mixed radiation fields. The proposed equation simply links the calibration information to all particle types and energies from a given detector (*i.e.,* one should know, if possible, how a detector responds to any particle with any energy) with the probabilities of a given particle of a given energy to reach the boundaries of the detector. In other words, this equation provides mathematical equations that express the fact that each particle type with a specific energy will produce *partial* responses on the detector so that the total interaction of the detector with the whole mixed radiation field will give rise to the total signal in the detector. It is not mandatory to have a complete description on how a dosimeter interacts with each particle type and energy, but in that case, we would be talking about an approximation.

13. The proposed equation is applied to UAB neutron detectors based on PADC. In that situation, neutrons and protons are incident to the PADC-UAB standard configuration (*i.e.,* with neutron converters). Strictly speaking, neutrons and protons have different RBE so they have to be discriminated in a point of space, if possible. Protons produced by the incident neutrons on the PADC-UAB standard configuration are already taken into account in the response function to neutrons. The concepts of *local* and *non-local* particle are introduced to help with the origin of the charged particles. For instance, *local* neutrons are the ones that reach the boundaries of a radiation detector so that when we talk about protons reaching a detector we mean protons created due to *non-local* neutrons. In the application found in this work, we can simply say that part of the *stored* signal of the PADC-UAB is not due to *local* neutrons reaching the detector but rather due to the already *external* protons (not created by the neutrons hitting the PADC-UAB) hitting the detector. In the end, the fact that *external* protons reach the PADC-UAB means that there will be an overestimation of the *local* neutron dose. Anyway, we cannot simply *substract* the proton contribution and forget it, keep in mind that each type of radiation will have different RBE (and depending on the particular energy) so that a total dose equivalent will be produced.

14. The MC method is an essential tool to determine conversion coefficients. Most of the fluence-to-dose quantities conversion coefficients for a given particle in a given situation are found by MC computations. To the knowledge of the author, no neutron quality factors are explicitly shown in energies from 25 MeV to 10^4 MeV. In this work is found that neutron quality factors range from 7.4 to 2 in the energy range defined from 25 MeV to 10^4 MeV.

15. MC simulation work has been done in an area different from the common radiation protection research. It has been found that under a simple MC model is well predicted that the quantity of water present in the soil will influence the energy distribution of the neutrons in a scoring region near ground so it could happen that through the experimental measurement of neutrons near ground, one could deduce the water content of the soil.

8.2 Perspectives

Through the collaboration of UAB with EURADOS it is expected to increase the knowledge on out-of-field neutron dose equivalents in different radiotherapy modalities including photon radiotherapy, proton radiotherapy, ion radiotherapy, neutron capture radiotherapy and flash radiotherapy. The methodologies exposed in this work can be applied in the mentioned radiation modalities.

Through the collaboration of UAB with INFN-LNF and ENEA-Frascati a better description and additional benchmarking of the facility HOTNES is expected. On the other hand, it is also expected to increase the knowledge about neutron detection applied to soil moisture studies. Currently, a spectrometry system based on moderation is under development to see its performance and resolution power when trying to assess the moisture of the soil.

As explained in Section 4.5.1, there exists a characteristic pulse height distribution associated to the nuclear reaction $^{3}He(n,p)^{3}H$ in the UAB Bonner Sphere System. However, in a complicated mixed radiation field with pile-up and dead time effects, this characteristic pulse height distribution could be perturbed, even to the point that spectrometric unfolding could be not possible. In order to establish a limit between the situations in which spectrometry is possible and the complex situation in which is not possible, characterization of the UAB-BSS should be done in complex mixed radiation fields. This situation could be partially studied by MC simulations, taking into account that pile-up and dead time effects could be difficult to model in MC.

As explained in Section 4.5.1, reactions different from $^{3}He(n,p)^{3}H$ could induce some residual response in the active region of the UAB-BSS. Elastic interactions, $^{3}He(n,d)^{2}H$ interactions and photonuclear reactions should be included in the MC simulations of the response function.

A proposed equation to deal with mixed radiation fields was presented in Chapter 6. However, so far, it has only been applied for the UAB PADC neutron dosimeter when it was exposed in the mixed radiation field of CERF facility, as explained in Section 7.3.2. Further experimental work is needed in order to fully understand the applicability of this equation. For achieving this goal, the proposed equation should be applied for as many types of detectors possible and for as many mixed radiation fields possible.

Appendix A

Neutron doses in specific positions of the water phantom in Mevion S250i Hyperscan single-room system

In this appendix, detailed results of evaluated neutron dose equivalents, evaluated energy distributions of the neutron fluence and full MC energy distributions of the neutron fluence inside the water tank phantom when it was irradiated with a PBS proton radiotherapy treatment in the Mevion S250i Hyperscan single-room system are found.

Evaluated information in those points of the water tank phantom in which measurements with PADC-UAB neutron dosimeter were performed is found while full MC energy distributions of the neutron fluence is found in all the defined points (all frames and pipes) of the water tank phantom. See the geometry of the water tank phantom in Figures 7.5 and 7.6.

Therefore, in this appendix, numerical values of Figure 7.16 *i.e.,* detailed information in each frame and pipe are found.

A.1 Evaluated neutron dose equivalents

Color representations of evaluated neutron dose equivalents for each frame of the water tank phantom are found in Figures A.1, A.2, A.3, A.4 and A.5, for frames 1, 2, 3, 4 and 5 respectively.

Numerical values of evaluated neutron dose equivalents for each frame of the water tank phantom are found in Figures A.6, A.7, A.8, A.9 and A.10, for frames 1, 2, 3, 4 and 5 respectively.

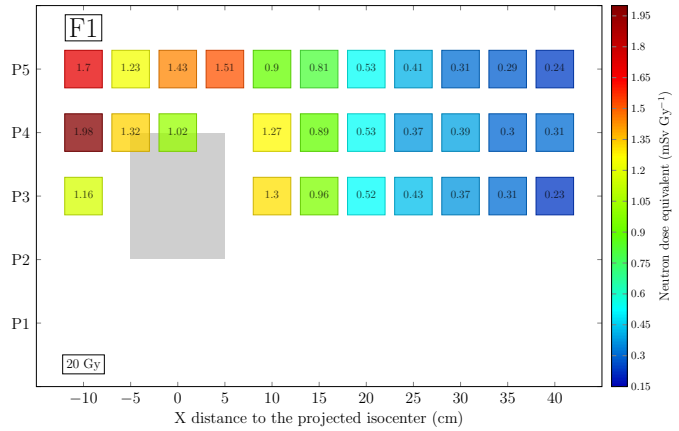

Figure A.1: Color representation of evaluated neutron dose equivalents (mSv Gy^{-1}) in frame 1 of the water tank phantom. Proton therapeutic dose was 20 Gy.

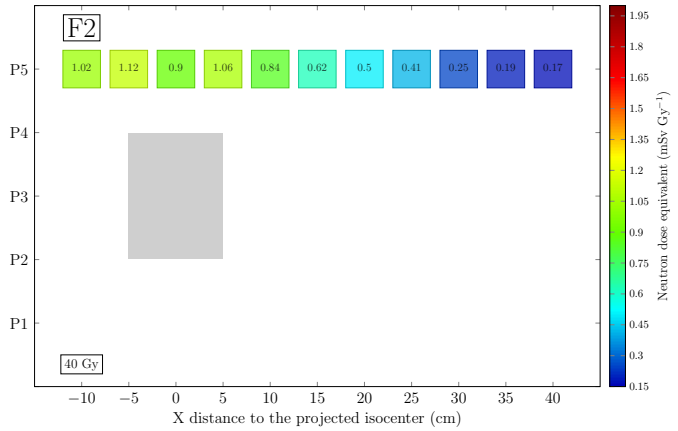

Figure A.2: Color representation of evaluated neutron dose equivalents (mSv Gy^{-1}) in frame 2 of the water tank phantom. Proton therapeutic dose was 40 Gy.

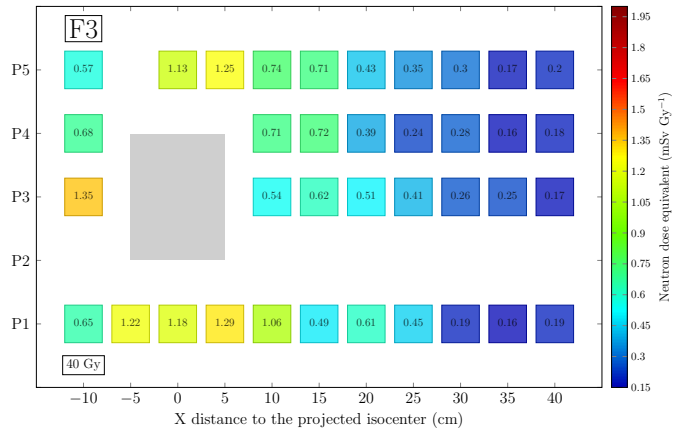

Figure A.3: Color representation of evaluated neutron dose equivalents (mSv Gy^{-1}) in frame 3 of the water tank phantom. Proton therapeutic dose was 40 Gy.

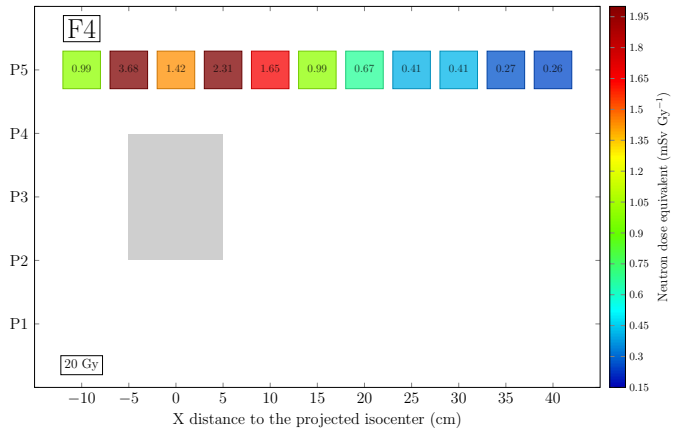

Figure A.4: Color representation of evaluated neutron dose equivalents (mSv Gy^{-1}) in frame 4 of the water tank phantom. Proton therapeutic dose was 20 Gy.

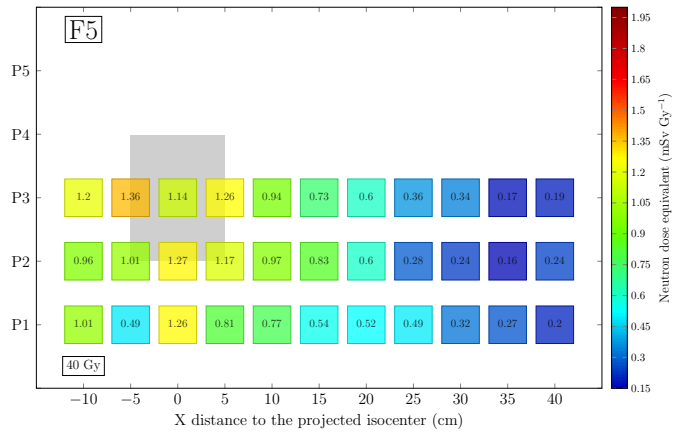

Figure A.5: Color representation of evaluated neutron dose equivalents (mSv Gy^{-1}) in frame 5 of the water tank phantom. Proton therapeutic dose was 40 Gy.

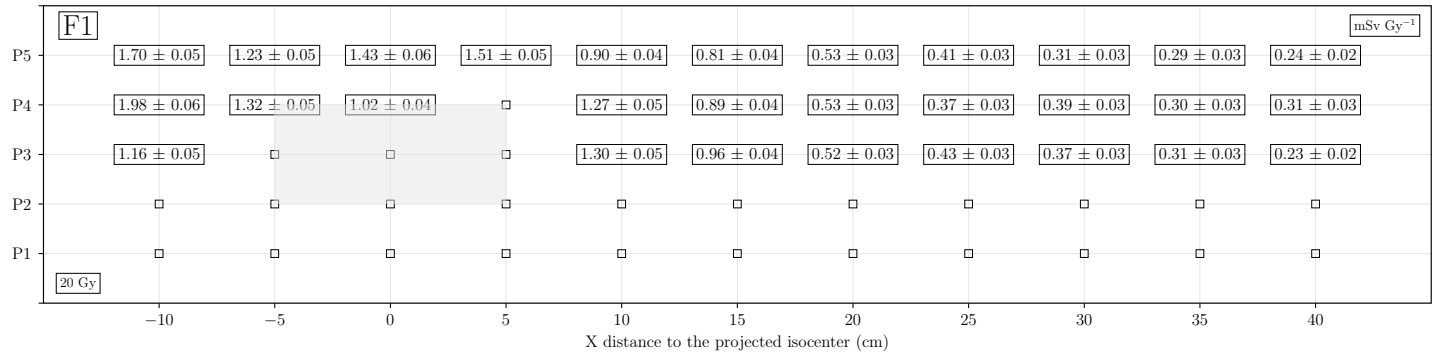

Figure A.6: Numerical values of evaluated neutron dose equivalents (mSv Gy^{-1}) in frame 1 of the water tank phantom. Proton therapeutic dose was 20 Gy. Proton field or its projection is shown in gray.

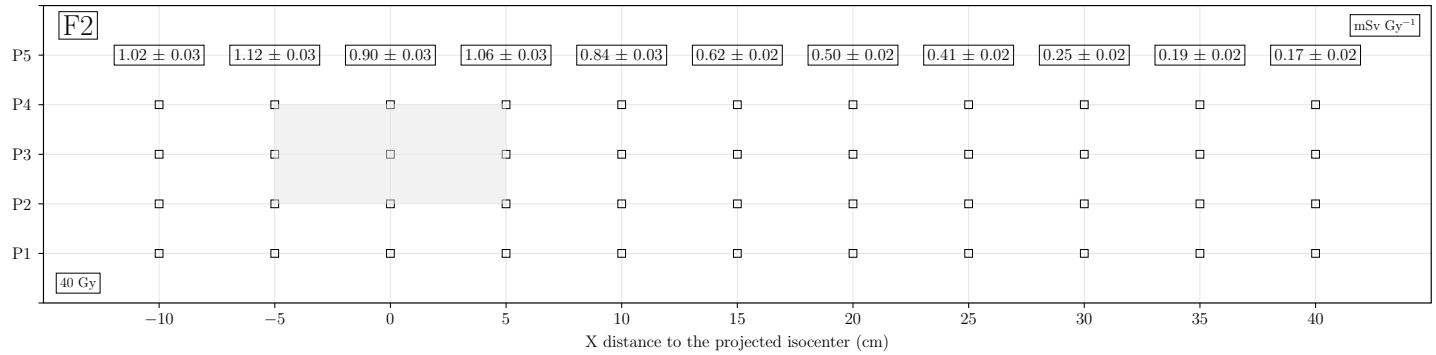

Figure A.7: Numerical values of evaluated neutron dose equivalents (mSv Gy^{-1}) in frame 2 of the water tank phantom. Proton therapeutic dose was 40 Gy. Proton field or its projection is shown in gray.

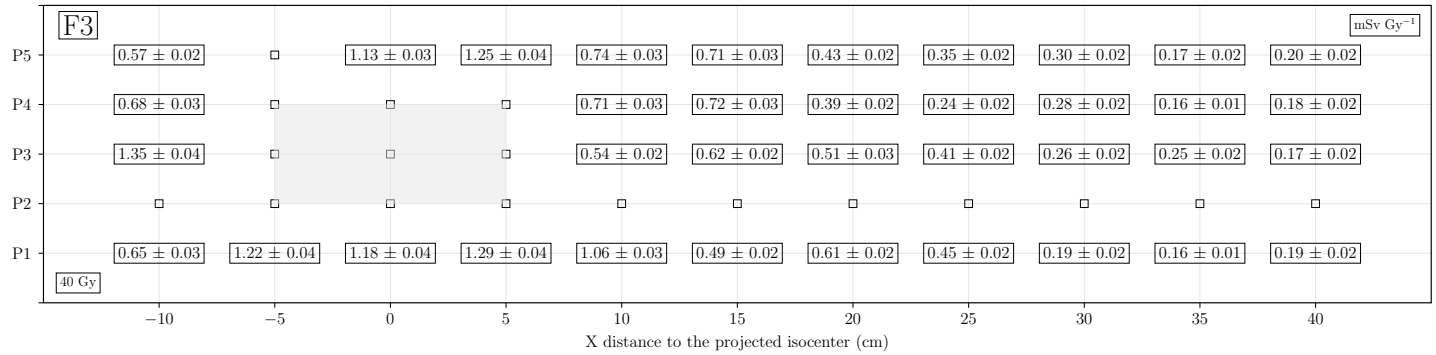

Figure A.8: Numerical values of evaluated neutron dose equivalents (mSv Gy^{-1}) in frame 3 of the water tank phantom. Proton therapeutic dose was 40 Gy. Proton field or its projection is shown in gray.

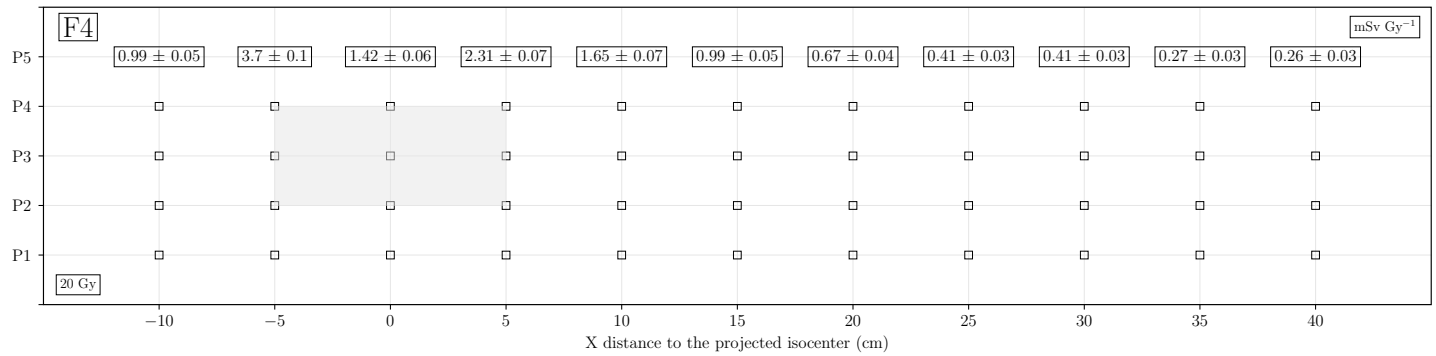

Figure A.9: Numerical values of evaluated neutron dose equivalents (mSv Gy^{-1}) in frame 4 of the water tank phantom. Proton therapeutic dose was 20 Gy. Proton field or its projection is shown in gray.

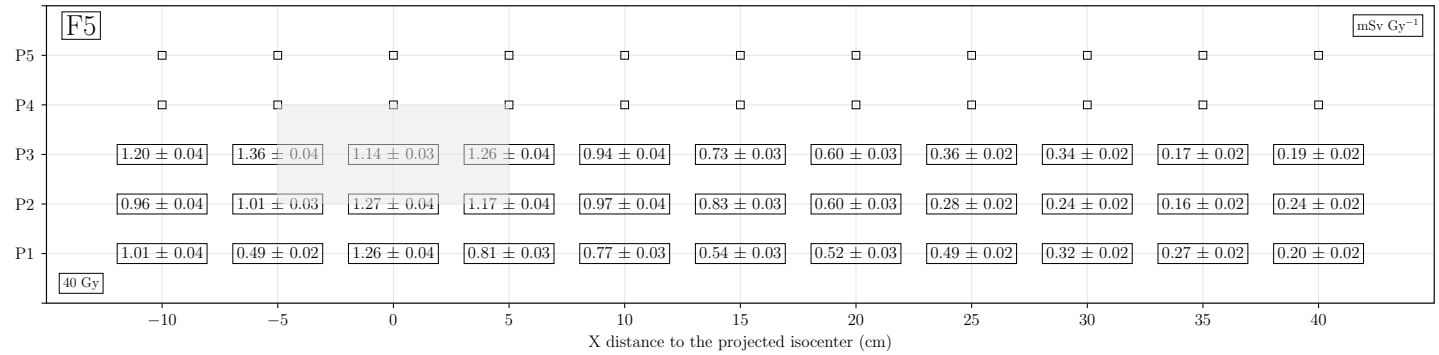

Figure A.10: Numerical values of evaluated neutron dose equivalents (mSv Gy^{-1}) in frame 5 of the water tank phantom. Proton therapeutic dose was 40 Gy. Proton field or its projection is shown in gray.

A.2 Full MC energy distributions of the neutron fluence

We now show the full MC energy distributions of the neutron fluence, $\Phi_E^{\mathrm{MC}}(E) = \Phi^{\mathrm{MC}} \cdot \varphi_E^{\mathrm{MC}}(E)$, in all the points of the water tank phantom.

See the correspondences of the MC cells and exact positioning in the water tank phantom in Figures A.11, A.17, A.23, A.29 and A.35, for frames 1, 2, 3, 4 and 5, respectively.

Full MC energy distributions of the neutron fluence are shown in A.12 (frame 1 - pipe 5), A.13 (frame 1 - pipe 4), A.14 (frame 1 - pipe 3), A.15 (frame 1 - pipe 2), A.16 (frame 1 - pipe 1), A.18 (frame 2 - pipe 5), A.19 (frame 2 - pipe 4), A.20 (frame 2 - pipe 3), A.21 (frame 2 - pipe 2), A.22 (frame 2 - pipe 1), A.24 (frame 3 - pipe 5), A.25 (frame 3 - pipe 4), A.26 (frame 3 - pipe 3), A.27 (frame 3 - pipe 2), A.28 (frame 3 - pipe 1), A.30 (frame 4 - pipe 5), A.31 (frame 4 - pipe 4), A.32 (frame 4 - pipe 3), A.33 (frame 4 - pipe 2), A.34 (frame 4 - pipe 1), A.36 (frame 5 - pipe 5), A.37 (frame 5 - pipe 4), A.38 (frame 5 - pipe 3), A.39 (frame 5 - pipe 2), A.40 (frame 5 - pipe 1).

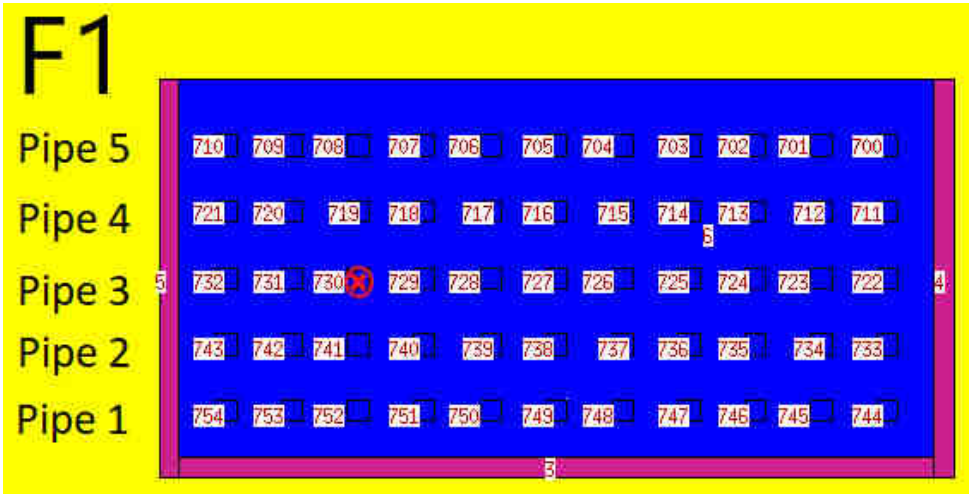

Figure A.11: MC cells and exact positioning labels for frame 1.

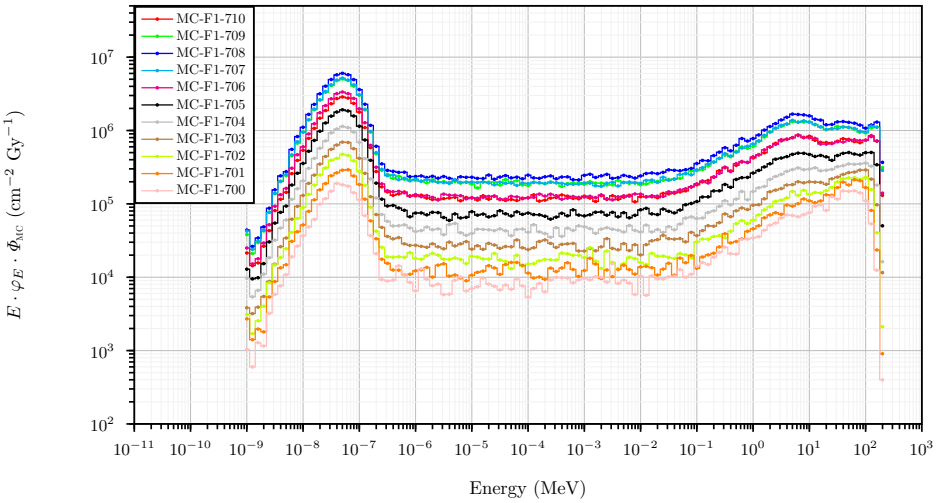

Figure A.12: Full MC energy distributions of the neutron fluence in frame 1 - pipe 5 positions inside the water tank phantom.

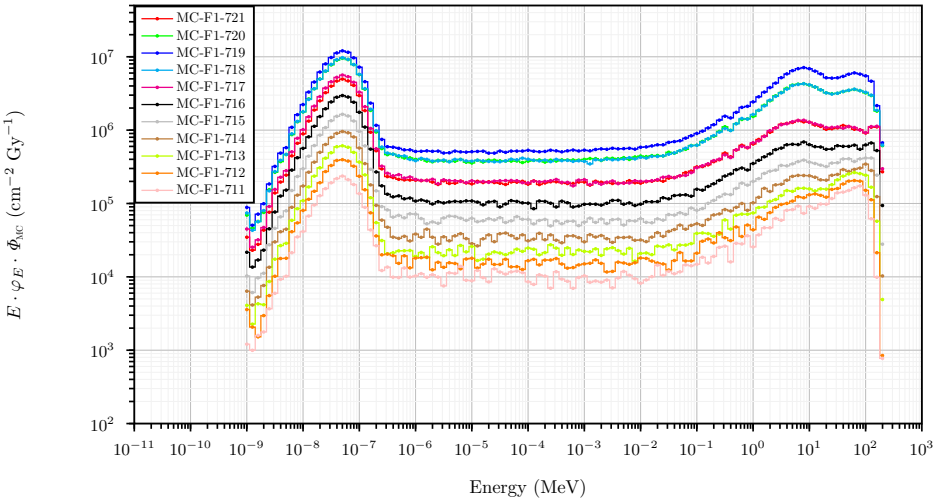

Figure A.13: Full MC energy distributions of the neutron fluence in frame 1 - pipe 4 positions inside the water tank phantom.

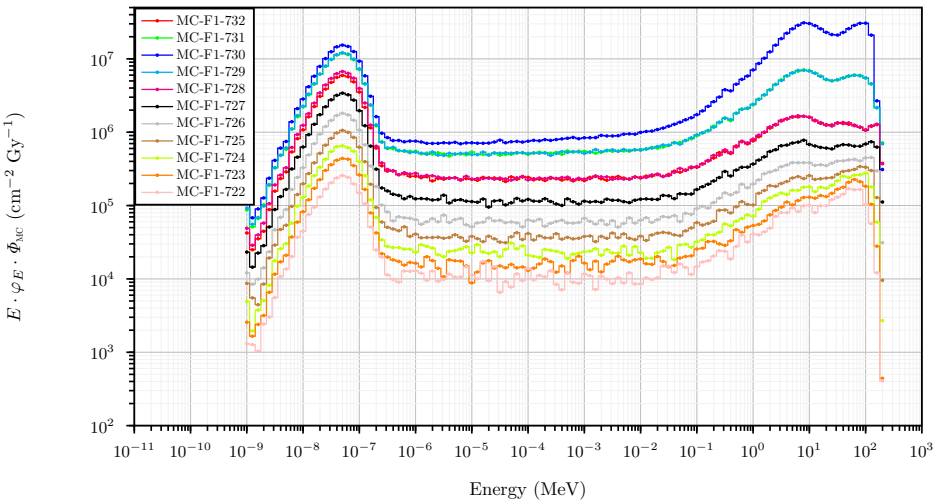

Figure A.14: Full MC energy distributions of the neutron fluence in frame 1 - pipe 3 positions inside the water tank phantom.

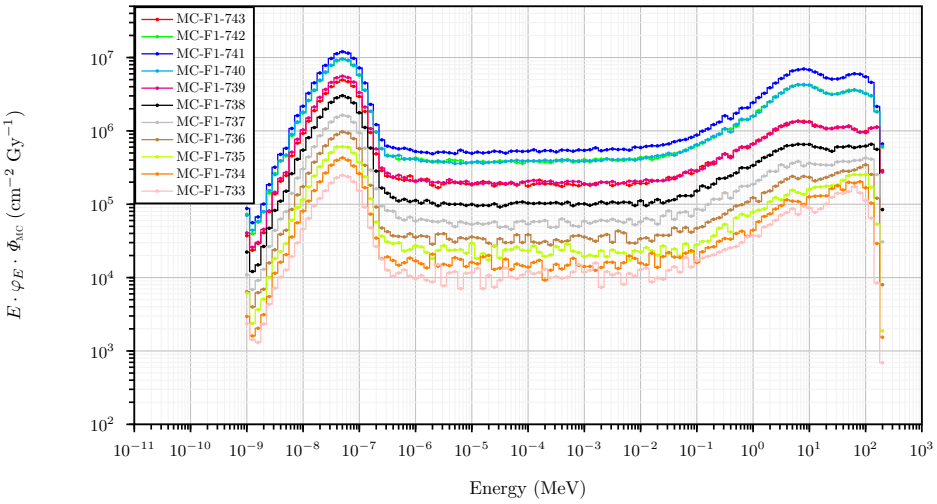

Figure A.15: Full MC energy distributions of the neutron fluence in frame 1 - pipe 2 positions inside the water tank phantom.

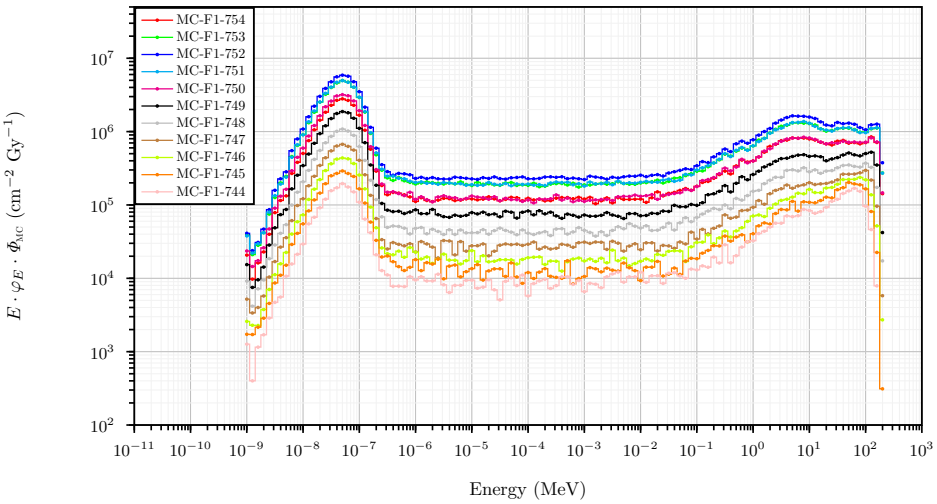

Figure A.16: Full MC energy distributions of the neutron fluence in frame 1 - pipe 1 positions inside the water tank phantom.

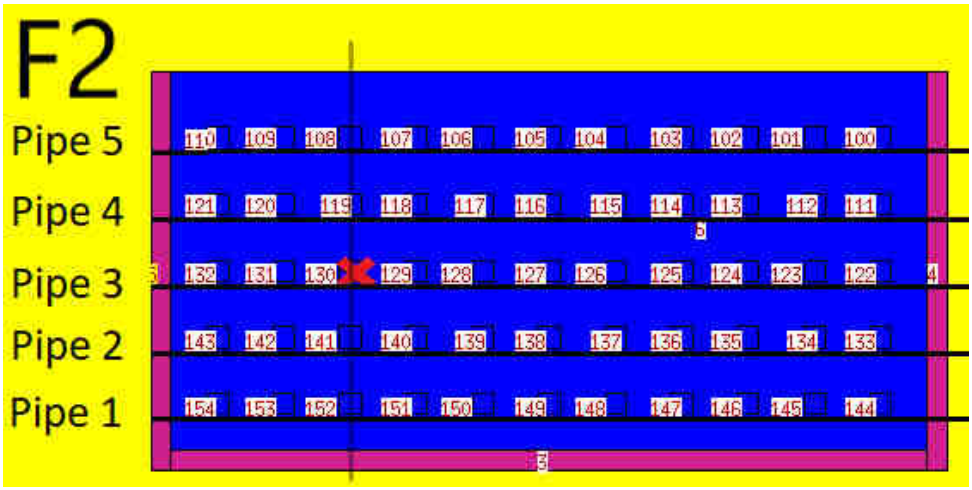

Figure A.17: MC cells and exact positioning labels for frame 2.

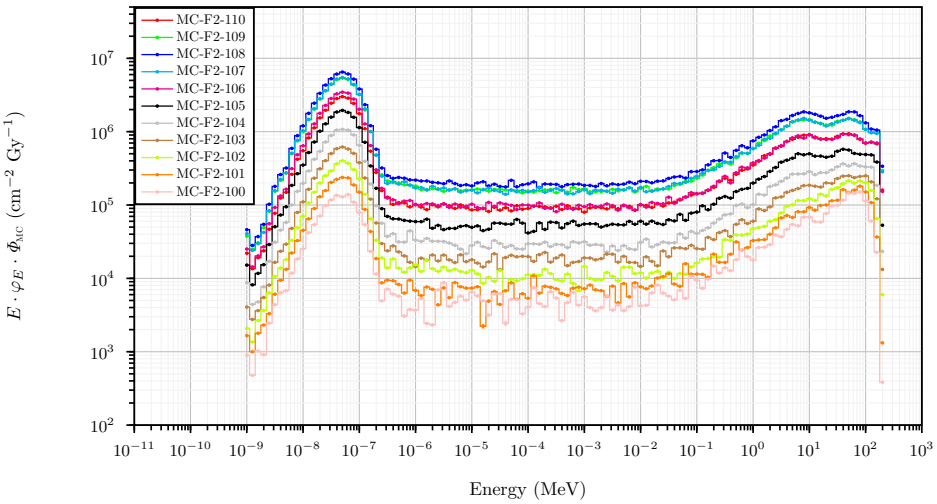

Figure A.18: Full MC energy distributions of the neutron fluence in frame 2 - pipe 5 positions inside the water tank phantom.

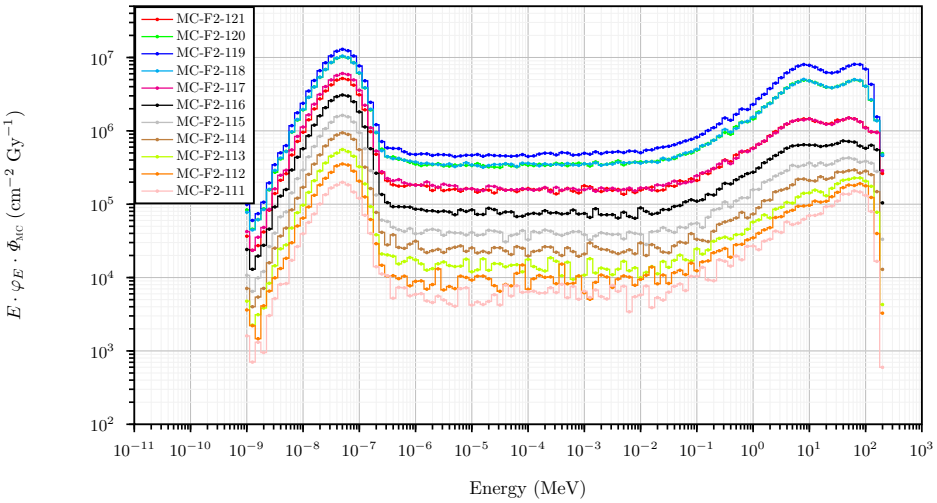

Figure A.19: Full MC energy distributions of the neutron fluence in frame 2 - pipe 4 positions inside the water tank phantom.

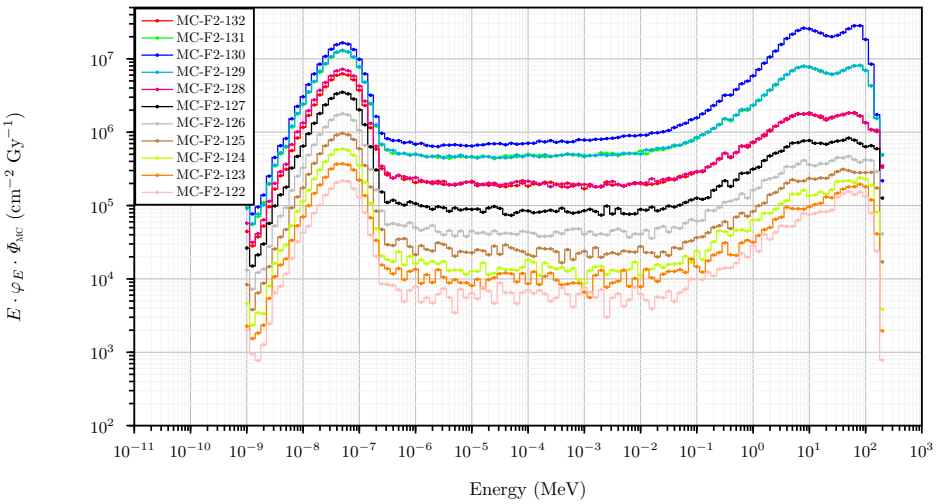

Figure A.20: Full MC energy distributions of the neutron fluence in frame 2 - pipe 3 positions inside the water tank phantom.

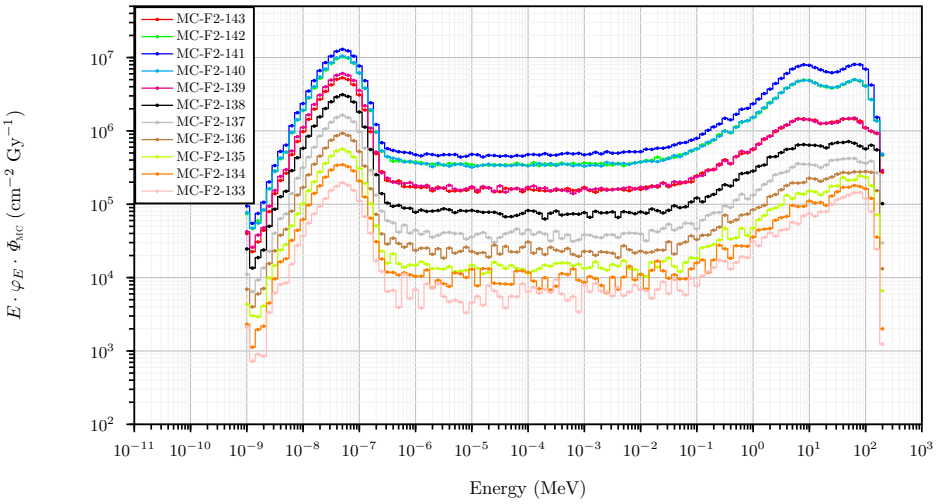

Figure A.21: Full MC energy distributions of the neutron fluence in frame 2 - pipe 2 positions inside the water tank phantom.

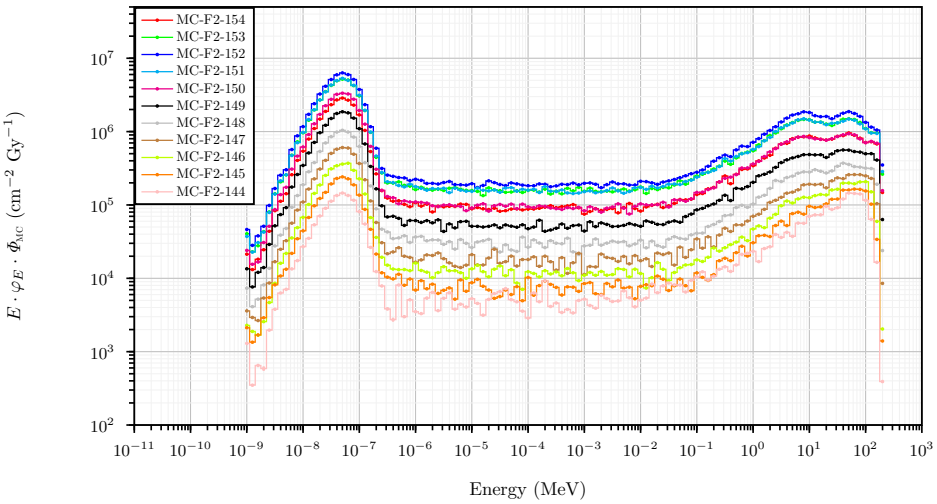

Figure A.22: Full MC energy distributions of the neutron fluence in frame 2 - pipe 1 positions inside the water tank phantom.

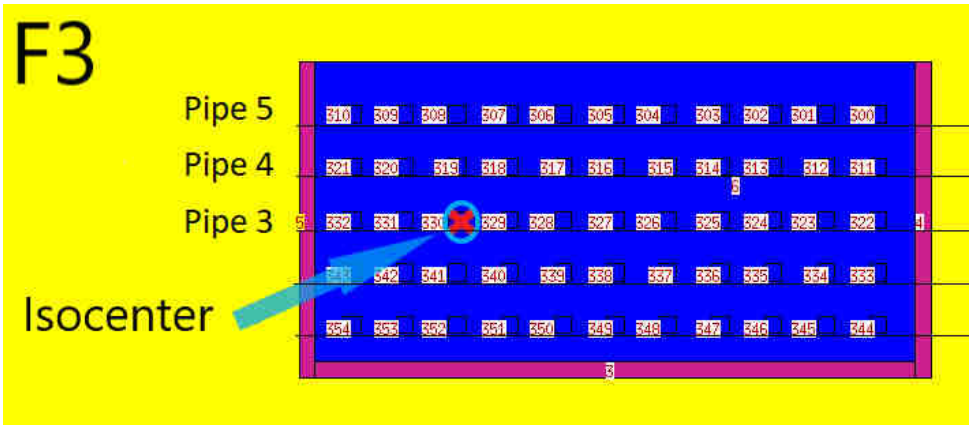

Figure A.23: MC cells and exact positioning labels for frame 3.

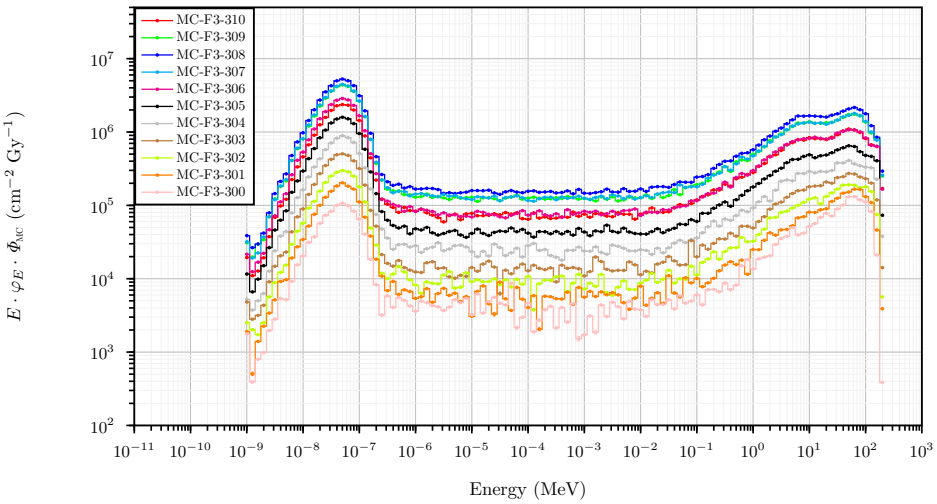

Figure A.24: Full MC energy distributions of the neutron fluence in frame 3 - pipe 5 positions inside the water tank phantom.

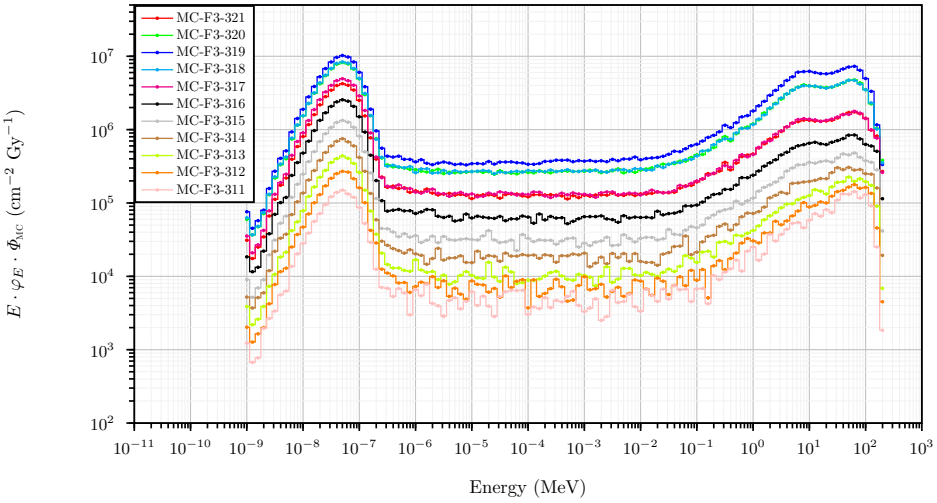

Figure A.25: Full MC energy distributions of the neutron fluence in frame 3 - pipe 4 positions inside the water tank phantom.

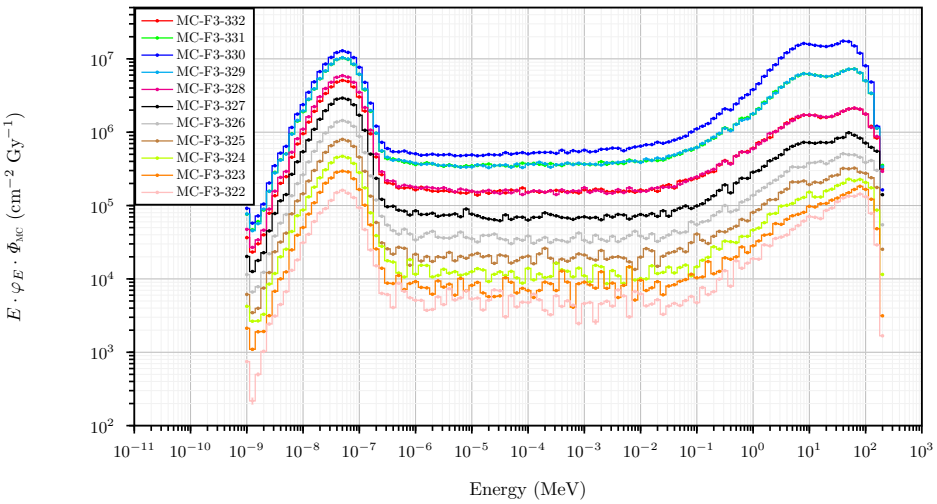

Figure A.26: Full MC energy distributions of the neutron fluence in frame 3 - pipe 3 positions inside the water tank phantom.

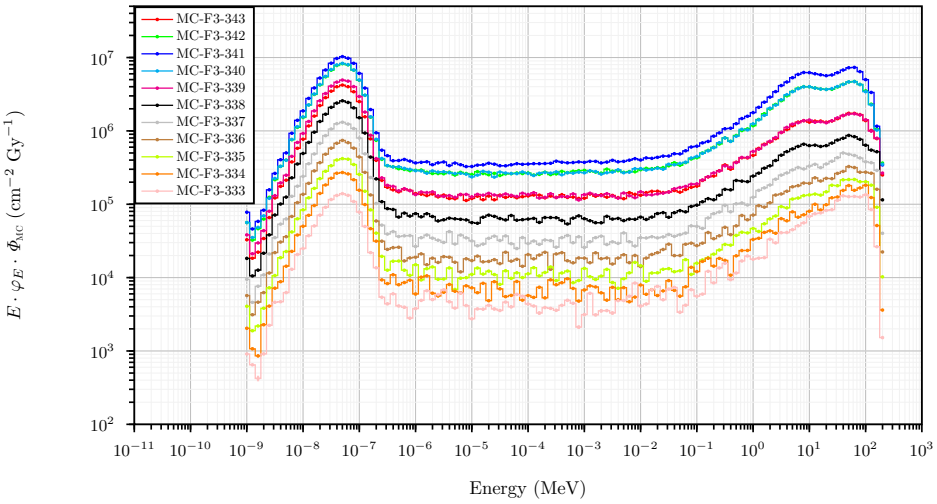

Figure A.27: Full MC energy distributions of the neutron fluence in frame 3 - pipe 2 positions inside the water tank phantom.

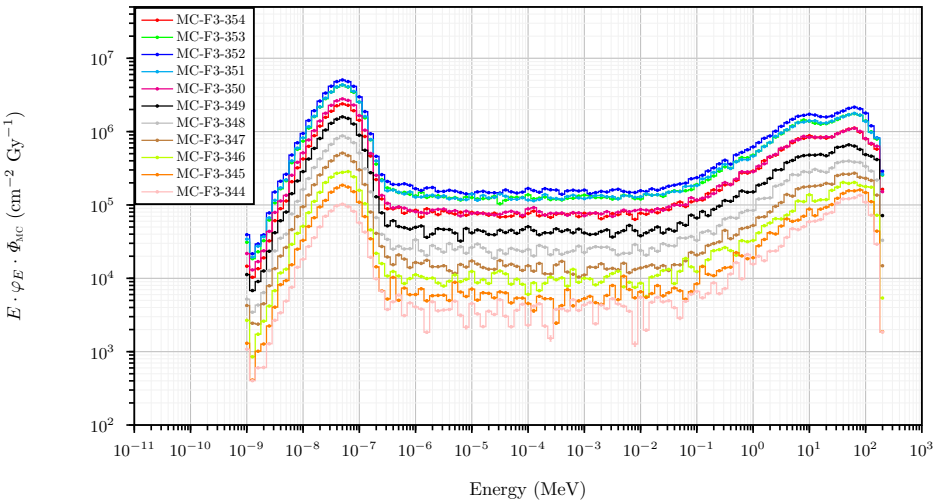

Figure A.28: Full MC energy distributions of the neutron fluence in frame 3 - pipe 1 positions inside the water tank phantom.

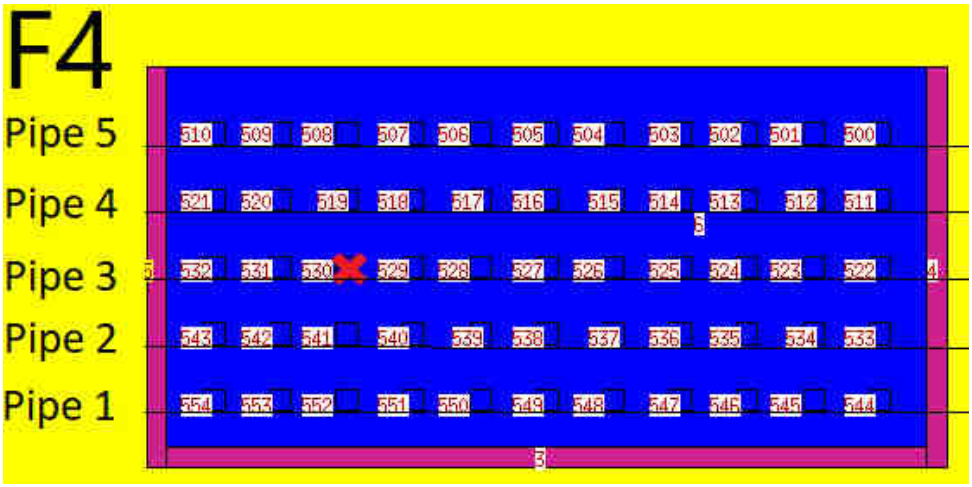

Figure A.29: MC cells and exact positioning labels for frame 4.

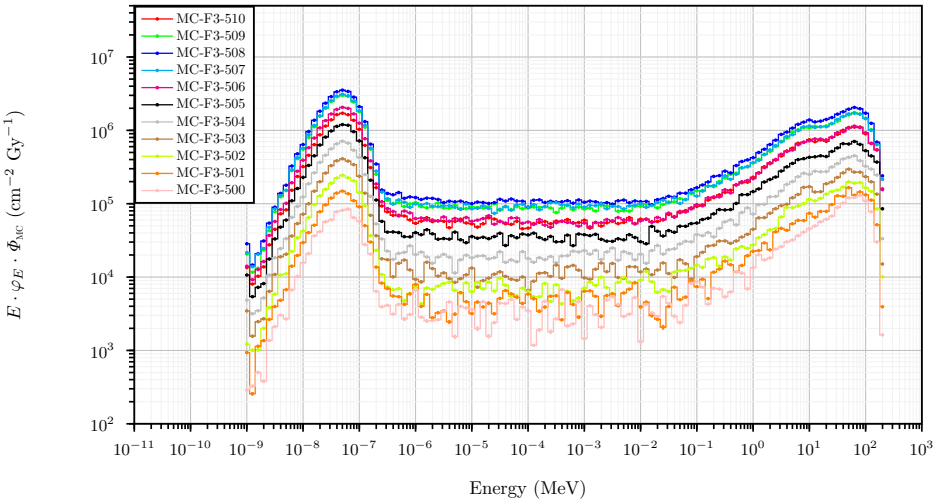

Figure A.30: Full MC energy distributions of the neutron fluence in frame 4 - pipe 5 positions inside the water tank phantom.

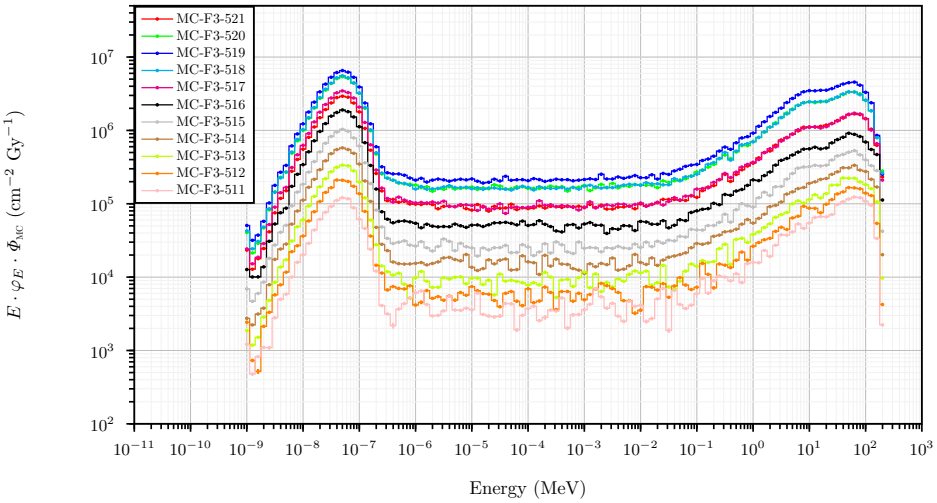

Figure A.31: Full MC energy distributions of the neutron fluence in frame 4 - pipe 4 positions inside the water tank phantom.

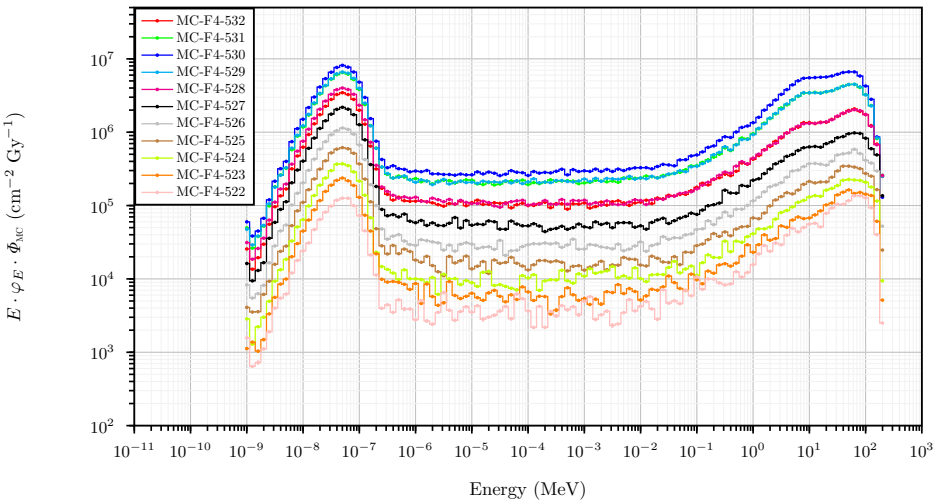

Figure A.32: Full MC energy distributions of the neutron fluence in frame 4 - pipe 3 positions inside the water tank phantom.

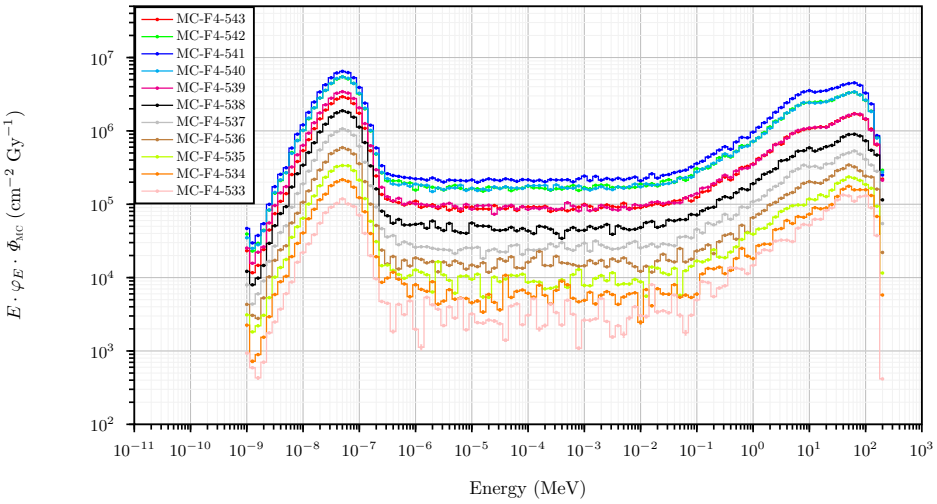

Figure A.33: Full MC energy distributions of the neutron fluence in frame 4 - pipe 2 positions inside the water tank phantom.

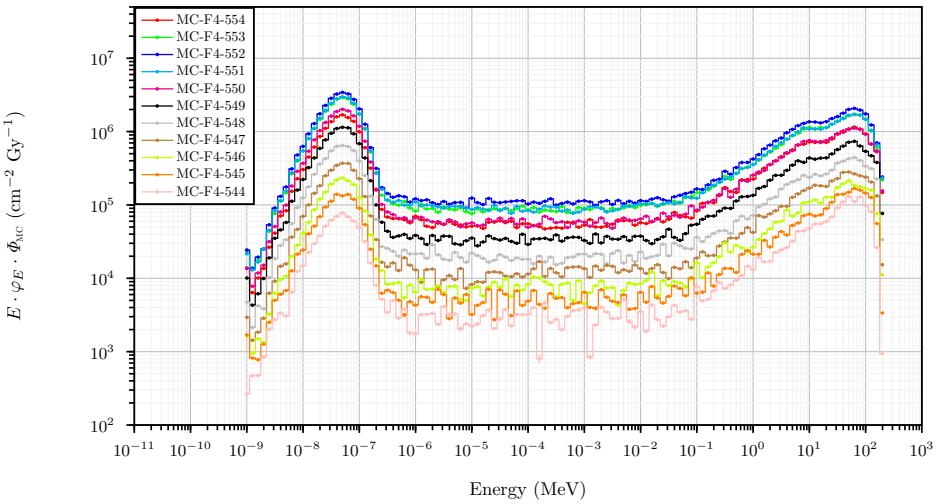

Figure A.34: Full MC energy distributions of the neutron fluence in frame 4 - pipe 1 positions inside the water tank phantom.

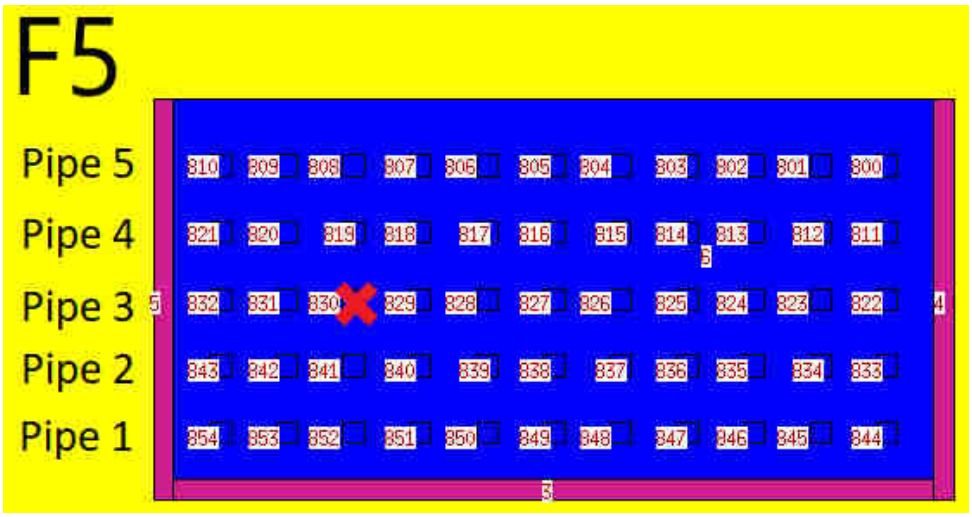

Figure A.35: MC cells and exact positioning labels for frame 5.

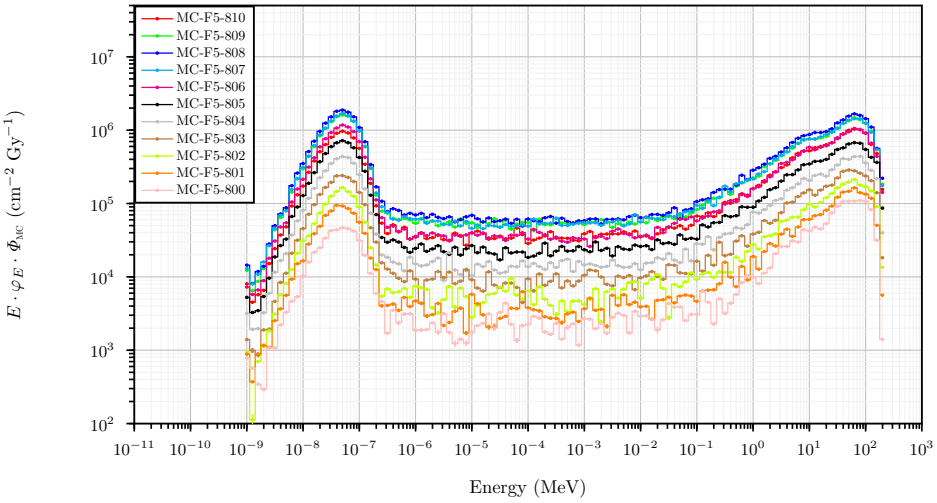

Figure A.36: Full MC energy distributions of the neutron fluence in frame 5 - pipe 5 positions inside the water tank phantom.

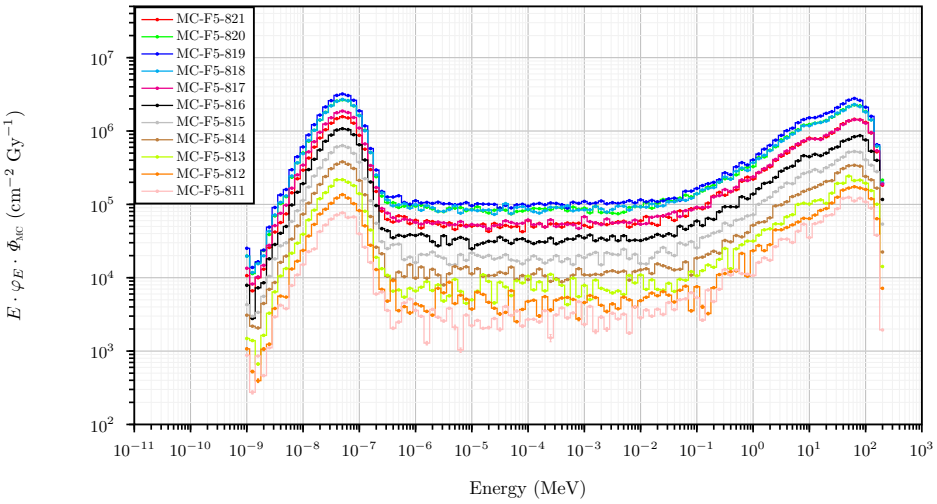

Figure A.37: Full MC energy distributions of the neutron fluence in frame 5 - pipe 4 positions inside the water tank phantom.

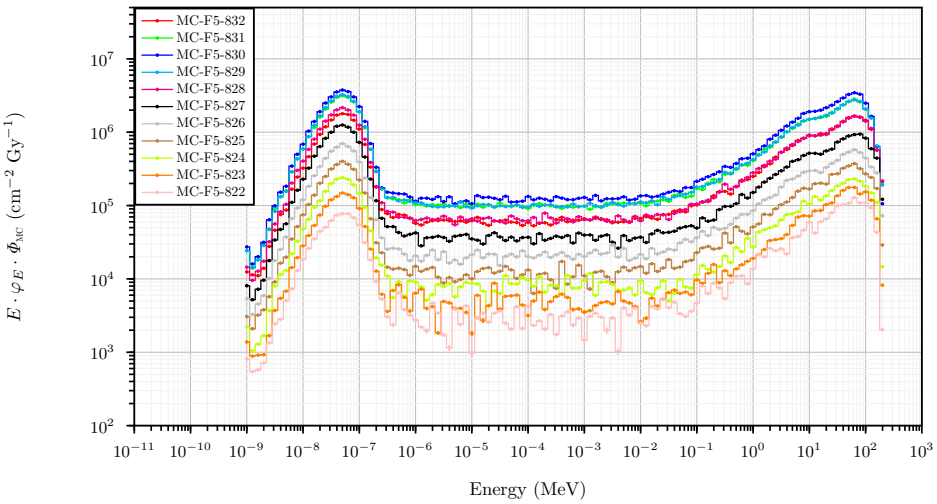

Figure A.38: Full MC energy distributions of the neutron fluence in frame 5 - pipe 3 positions inside the water tank phantom.

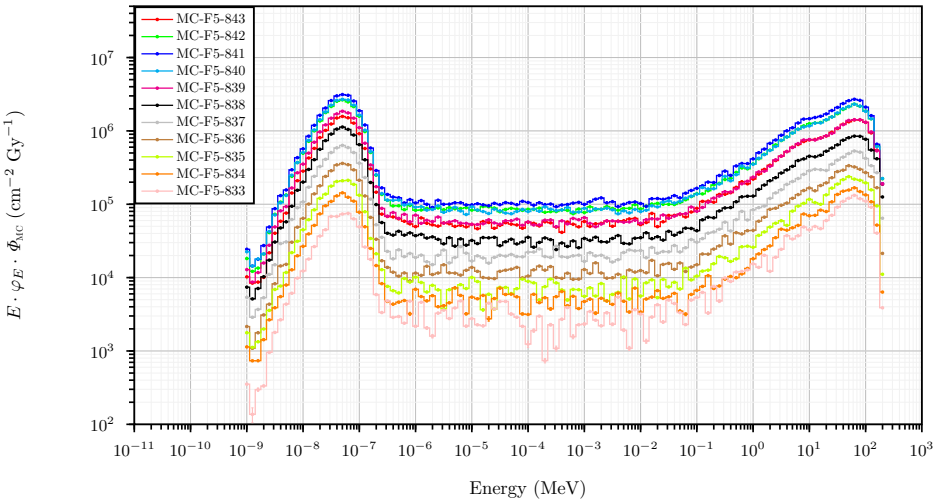

Figure A.39: Full MC energy distributions of the neutron fluence in frame 5 - pipe 2 positions inside the water tank phantom.

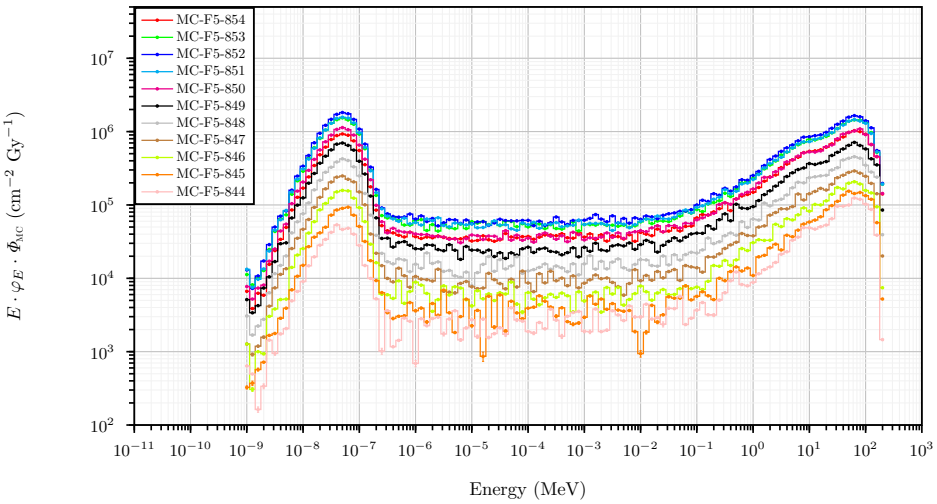

Figure A.40: Full MC energy distributions of the neutron fluence in frame 5 - pipe 1 positions inside the water tank phantom.

A.3 Evaluated energy distributions of the neutron fluence

As explained in Section 4.6.1 and further discussed in Section 7.1.1.2, the *evaluated* quantities, and in particular, the evaluated neutron dose equivalent inside of a phantom, requires the knowledge by MC of the unit energy distribution of the neutron fluence as explicitly shown in Equation (4.51).

In other words, evaluated neutron dose equivalents shown in Figure 7.16 mean that the evaluated energy distributions of the neutron fluence, $\Phi_E(E) \equiv \Phi_E^{\text{EV}}(E) = \Phi^{\text{CR-39}} \cdot \varphi_E^{\text{MC}}(E)$, are assumed to be the ones shown in Figures A.42 (frame 1 - pipe 5), A.43 (frame 1 - pipe 4) and A.44 (frame 1 - pipe 3) for frame 1 (see the correspondence of the MC cells and exact positioning in the water tank phantom in Figure A.41). In Figure A.46 is shown the evaluated energy distribution of the neutron fluence for frame 2 - pipe 5 where the correspondence for this frame is in Figure A.45. The evaluated energy distributions for the rest of points are shown in Figures A.48 (frame 3 - pipe 5), A.49 (frame 3 - pipe 4), A.50 (frame 3 - pipe 3), A.51 (frame 3 - pipe 1), A.53 (frame 4 - pipe 5), A.55 (frame 5 - pipe 3), A.56 (frame 5 - pipe 2) and A.57 (frame 5 - pipe 1). See the correspondences of the MC cells and exact positionings in the water tank phantom in Figures A.47, A.52 and A.54 for frames 3, 4 and 5, respectively.

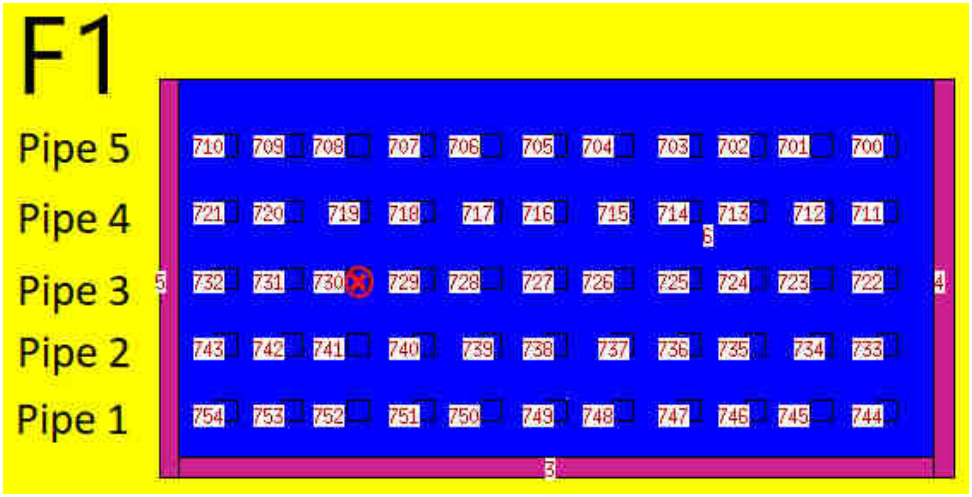

Figure A.41: MC cells and exact positioning labels for frame 1.

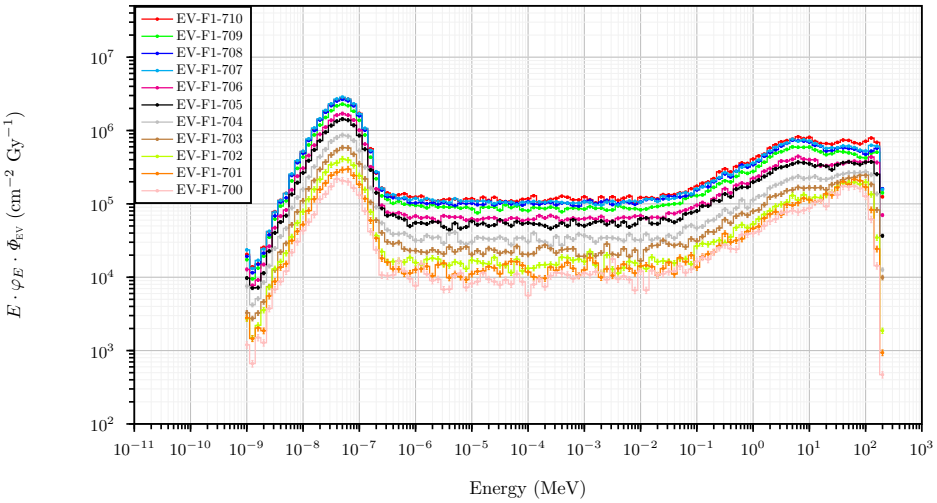

Figure A.42: Evaluated energy distributions of the neutron fluence in frame 1 - pipe 5 positions inside the water tank phantom.

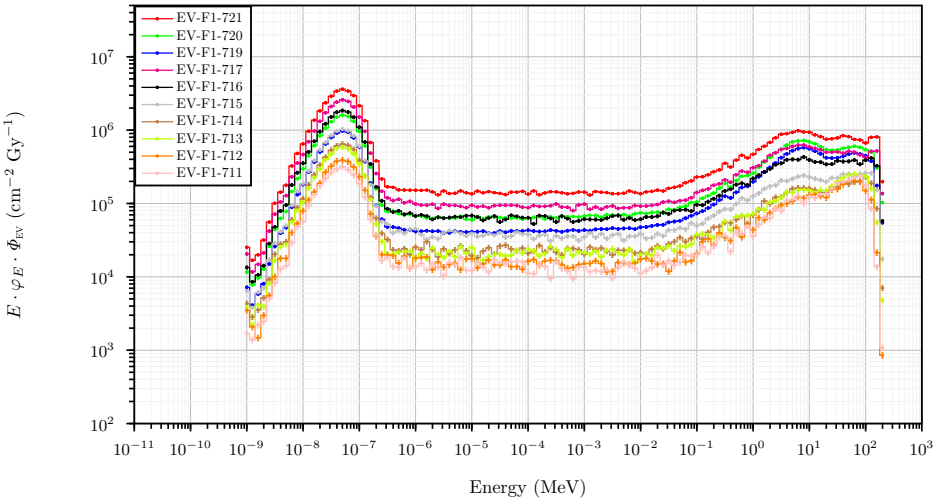

Figure A.43: Evaluated energy distributions of the neutron fluence in frame 1 - pipe 4 positions inside the water tank phantom.

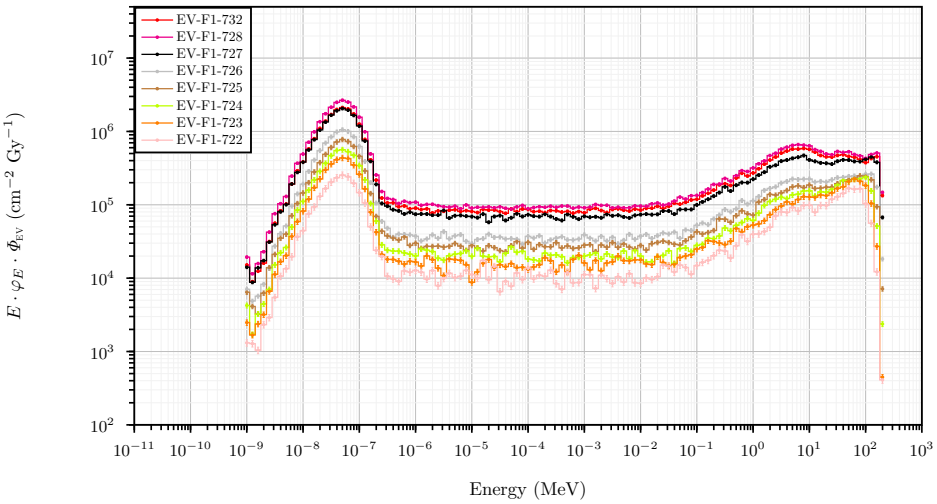

Figure A.44: Evaluated energy distributions of the neutron fluence in frame 1 - pipe 3 positions inside the water tank phantom.

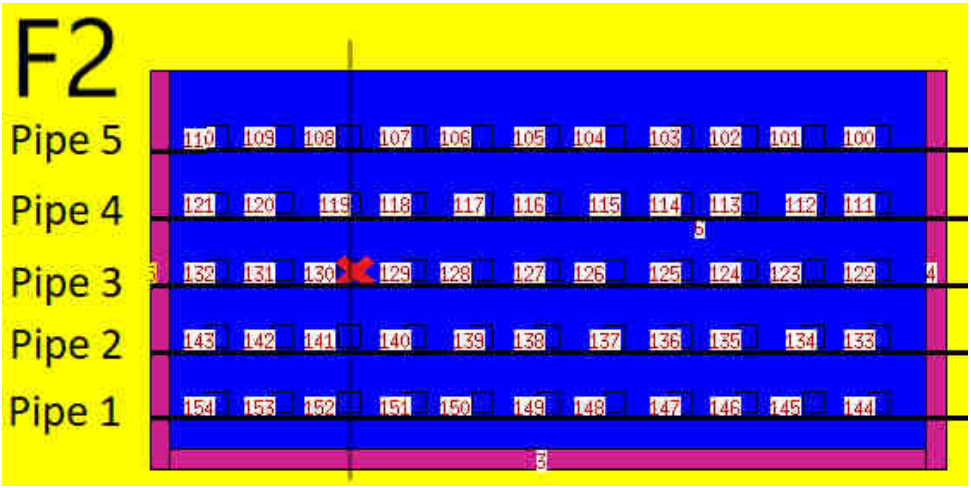

Figure A.45: MC cells and exact positioning labels for frame 2.

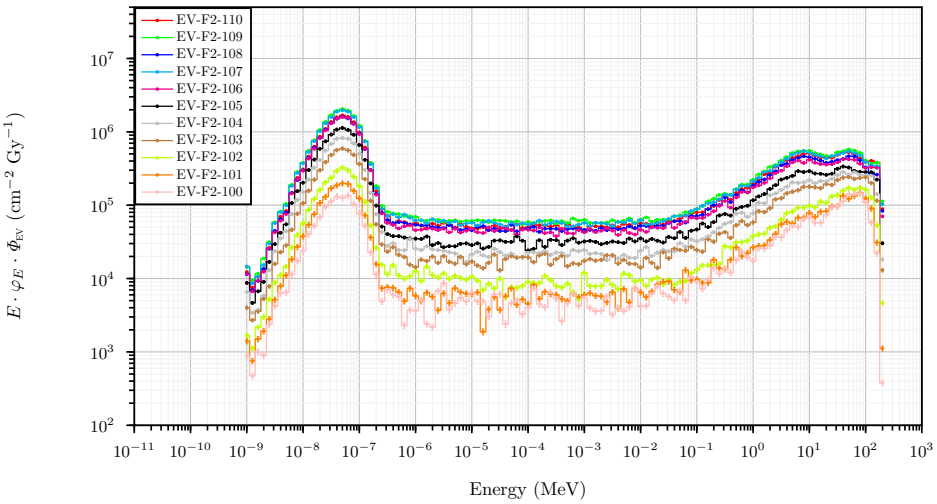

Figure A.46: Evaluated energy distributions of the neutron fluence in frame 2 - pipe 1 positions inside the water tank phantom.

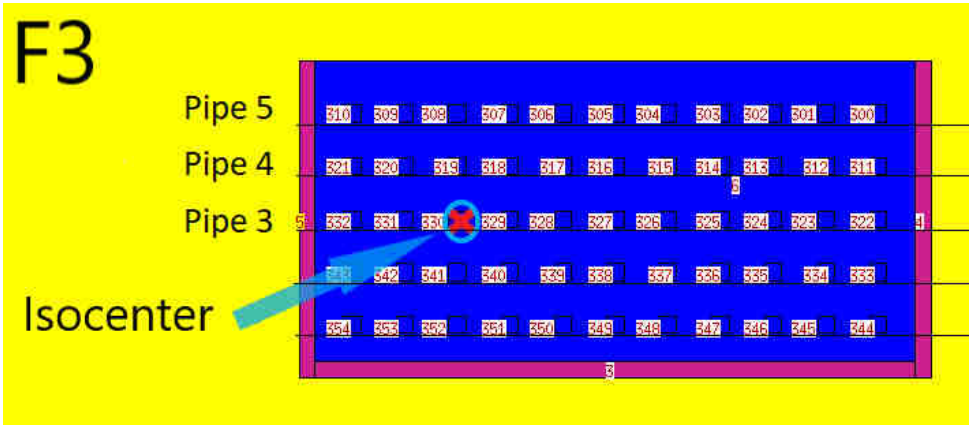

Figure A.47: MC cells and exact positioning labels for frame 3.

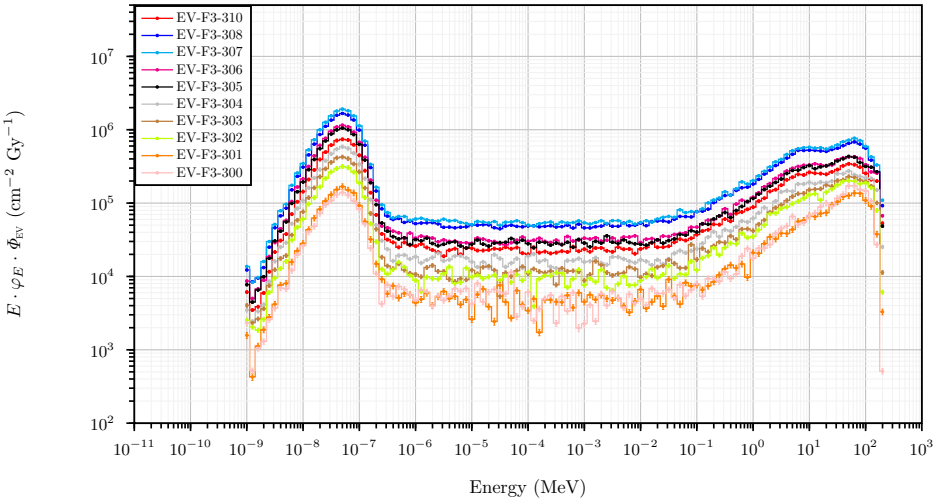

Figure A.48: Evaluated energy distributions of the neutron fluence in frame 3 - pipe 5 positions inside the water tank phantom.

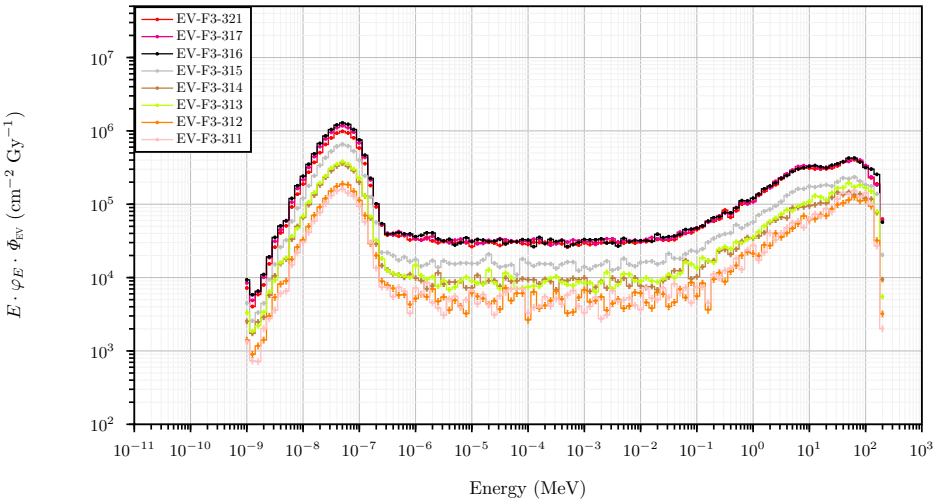

Figure A.49: Evaluated energy distributions of the neutron fluence in frame 3 - pipe 2 positions inside the water tank phantom.

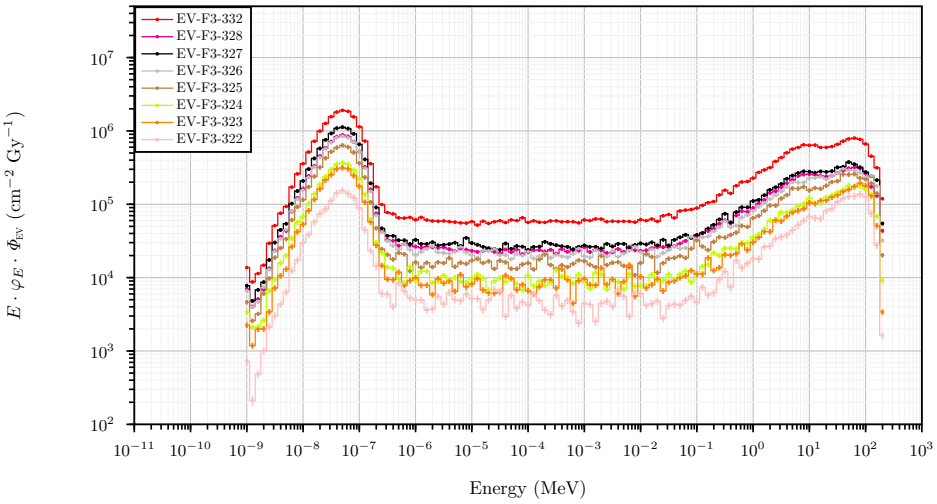

Figure A.50: Evaluated energy distributions of the neutron fluence in frame 3 - pipe 3 positions inside the water tank phantom.

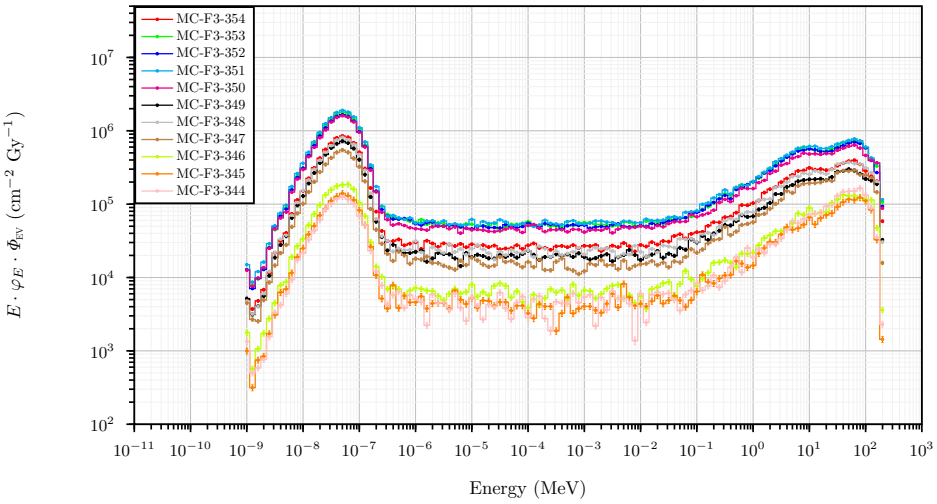

Figure A.51: Evaluated energy distributions of the neutron fluence in frame 3 - pipe 1 positions inside the water tank phantom.

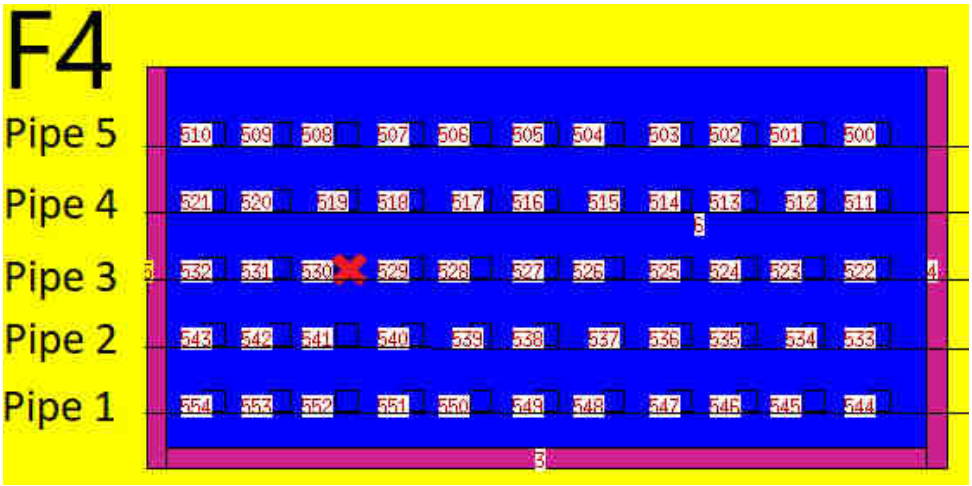

Figure A.52: MC cells and exact positioning labels for frame 4.

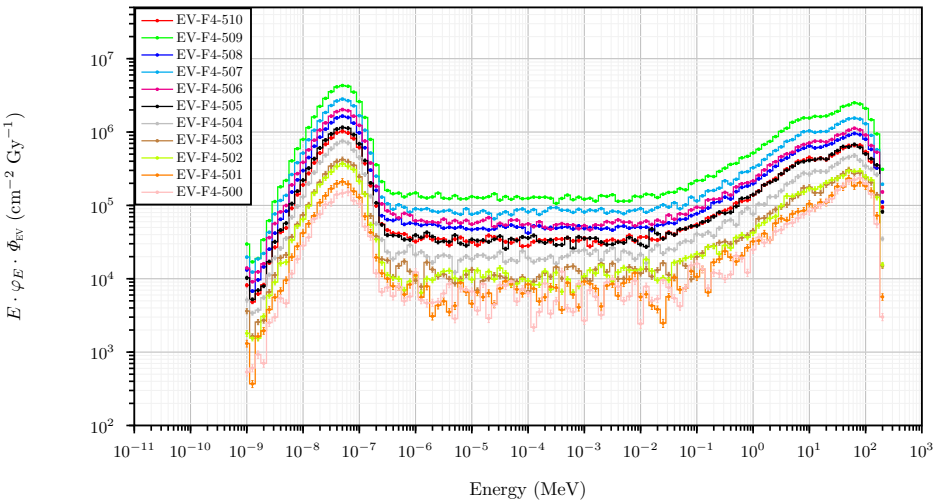

Figure A.53: Evaluated energy distributions of the neutron fluence in frame 4 - pipe 5 positions inside the water tank phantom.

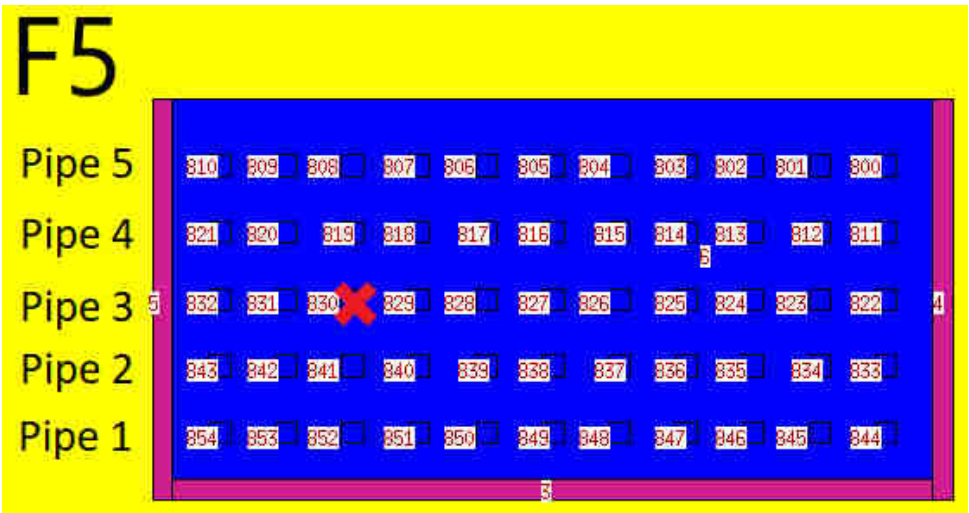

Figure A.54: MC cells and exact positioning labels for frame 5.

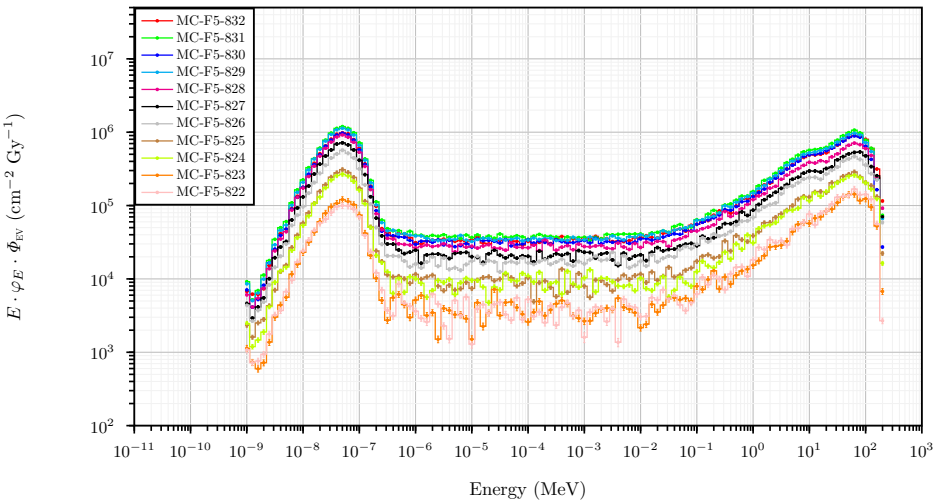

Figure A.55: Evaluated energy distributions of the neutron fluence in frame 5 - pipe 3 positions inside the water tank phantom.

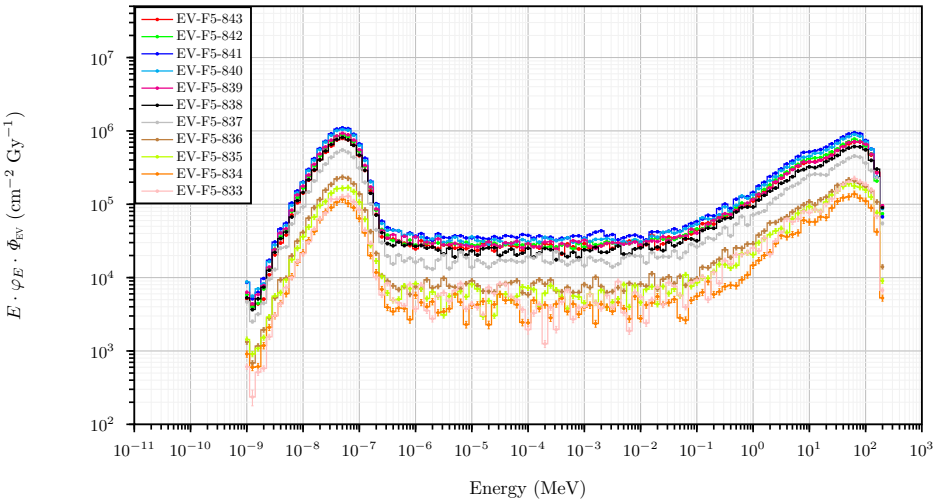

Figure A.56: Evaluated energy distributions of the neutron fluence in frame 5 - pipe 2 positions inside the water tank phantom.

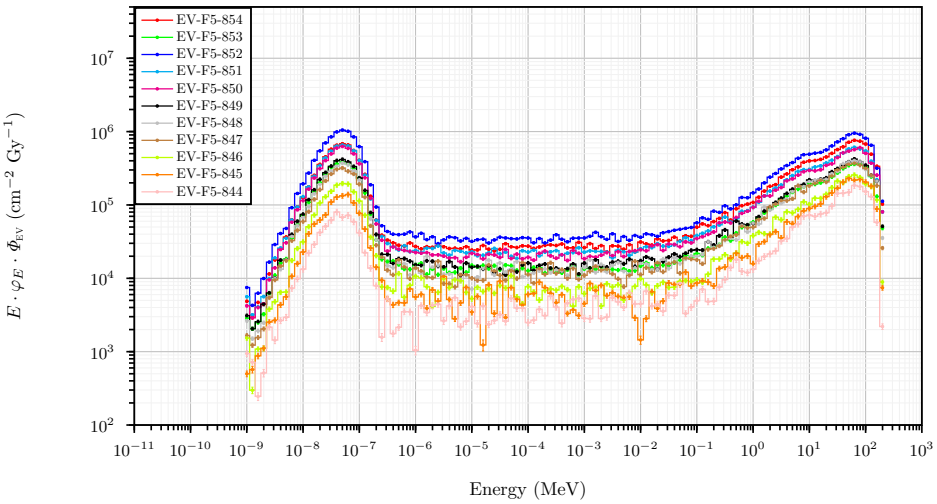

Figure A.57: Evaluated energy distributions of the neutron fluence in frame 5 - pipe 1 positions inside the water tank phantom.

Appendix B

Images of CR-39: track densities and neutron dose equivalents

In this appendix we present some images of our CR-39 layers after the ECE procedure is finished. The CR-39 layers are used in our neutron passive dosimeter described in Section 4.4.2.

In particular, now we will specify the track density, R, which is the response of this radiation detector, in units of tracks cm^{-2} *i.e.,* tracks counted in a surface of the CR-39 later (this surface is usually 4 mm $\times$ 4 mm) and we also specify the neutron dose equivalent, H, from Equation (4.51) (see Section 4.6.1) in units of mSv.

Is important to keep in mind that, more/less track density does not necessarily mean more/less neutron dose equivalent when comparing two points. Equation (4.51) is very clear in this regard. The relationship between the experimental response of the radiation detector R and the neutron dose equivalent H can be complicated due to the dependencies of the calibration coefficient, $\left[\frac{\int_E R_\Phi(E)\varphi_E(E)\mathrm{d}E}{\int_E Q(E)k_\Phi(E)\varphi_E(E)\mathrm{d}E}\right]$, that is not necessarily constant when we compare neutron dose equivalents in two different points.

For instance, according to the response funtion of the UAB passive neutron dosimeter (Figure 4.27) the response function for neutrons of 100 MeV is one order of magnitude lower in respect to fast neutrons while the fluence-to-dose conversion coefficients are also different (see Figure 3.12) so that the calibration coefficient is different if we measure in a neutron field dominated by fast neutrons or if we measure in a neutron field dominated by a high energy component. In the extreme case that a radiation detector has a low sensitivity to a particle in energy regions in which the biological damage is enhanced, the calibration coefficient would be very small. In case that the calibration coefficient is constant (or can be considered constant), it is true that more/less track density means more/less neutron dose equivalent.

According to the experience of the author, the calibration coefficient $\left[\frac{\int_E R_\Phi(E)\varphi_E(E)\mathrm{d}E}{\int_E Q(E)k_\Phi(E)\varphi_E(E)\mathrm{d}E}\right]$ can range between values of around 150 to 350 cm^{-2} mSv^{-1} (in proton radiotherapy out-of-field neutron doses) so a difference of more than 2 could found in neutron dose equivalents by using one calibration coefficient or another. It is clear that any scientific work should include what calibration coefficient has been used and, if needed, to specify both, the

track density and the calibration coefficient employed to finally provide a neutron dose equivalent.

All the images shown in this appendix correspond to images of neutron dosimeters placed in proton radiotherapy situations (in-phantom out-of-field doses) and although it is true that the unit energy distribution of the neutron fluence, $\varphi_E(E)$, is different enough so that $\left[\frac{\int_E R_\Phi(E)\varphi_E(E)\mathrm{d}E}{\int_E Q(E)k_\Phi(E)\varphi_E(E)\mathrm{d}E}\right]$ can be different enough, what is true is that we are not comparing extremely different unit energy distributions of the neutron fluence (none of the comparing points have, for instance, a very thermalized neutron field or an AmBe neutron field). In consequence, we will see that in this case is true that more/less track density means more/less neutron dose equivalent.

In Figures from B.1 to B.11 are shown figures and values of track densities and associated neutron dose equivalents ranging from 45 mSv to 1 mSv.

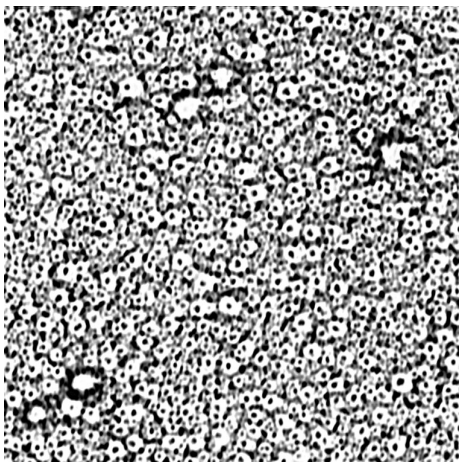

Figure B.1: R = 7305 tracks cm^{-2}. H = 45 mSv. CR-39 labelled as 1309. The image has dimensions 4 mm × 4 mm.

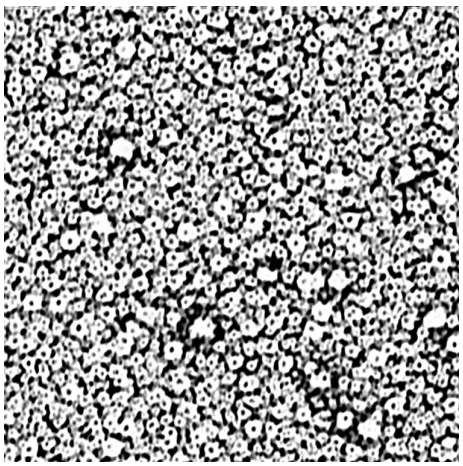

Figure B.2: R = 6324 tracks cm^{-2}. H = 36 mSv. CR-39 labelled as 1290. The image has dimensions 4 mm × 4 mm.

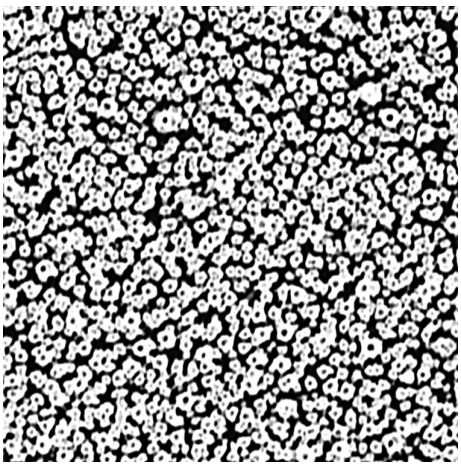

Figure B.3: R = 4093 tracks cm^{-2}. H = 26 mSv. CR-39 labelled as 1228. The image has dimensions 4 mm × 4 mm.

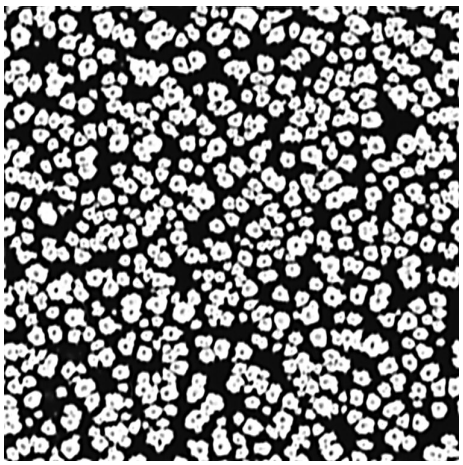

Figure B.4: R = 3105 tracks cm^{-2}. H = 20 mSv. CR-39 labelled as 1324. The image has dimensions 4 mm × 4 mm.

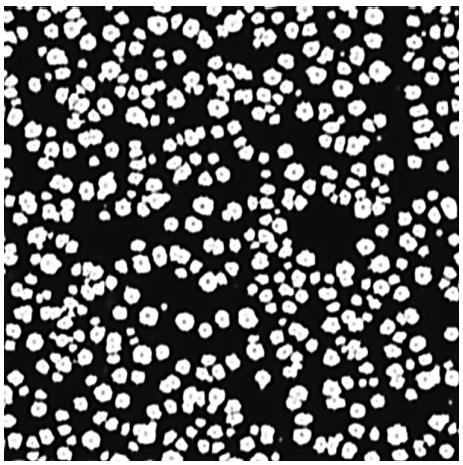

Figure B.5: R = 2249 tracks cm^{-2}. H = 16 mSv. CR-39 labelled as 1313. The image has dimensions 4 mm × 4 mm.

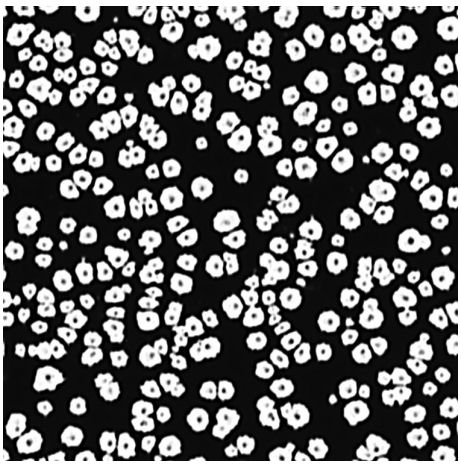

Figure B.6: R = 1461 tracks cm^{-2}. H = 10 mSv. CR-39 labelled as 1345. The image has dimensions 4 mm × 4 mm.

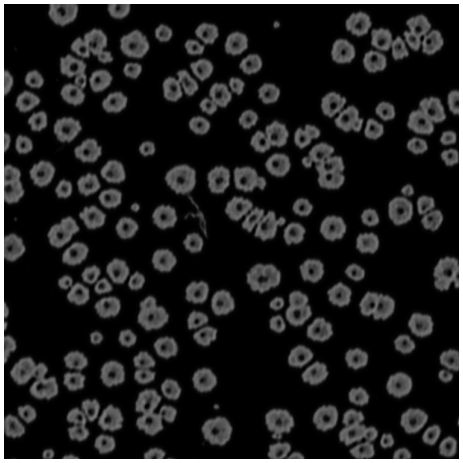

Figure B.7: $R = 799$ tracks cm^{-2}. $H =$ 7 mSv. CR-39 labelled as 1334. The image has dimensions 4 mm × 4 mm.

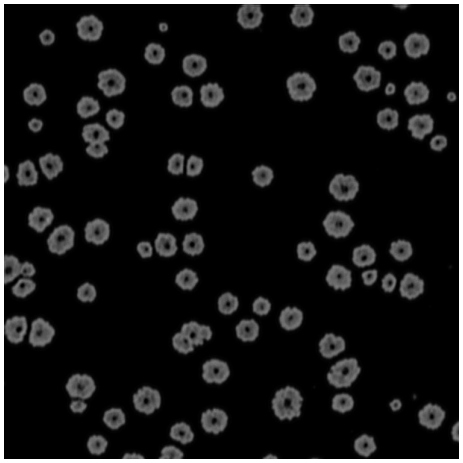

Figure B.8: $R = 411$ tracks cm^{-2}. $H =$ 4 mSv. CR-39 labelled as 1351. The image has dimensions 4 mm × 4 mm.

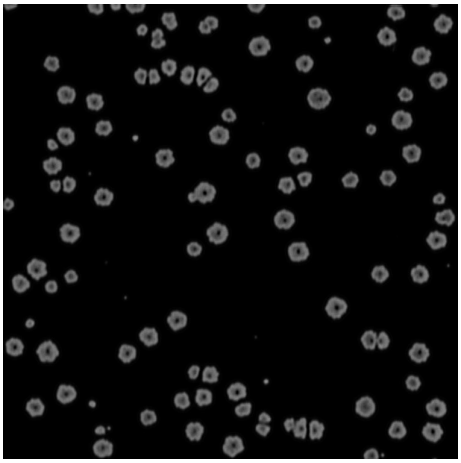

Figure B.9: $R = 545$ tracks cm^{-2}. $H =$ 3 mSv. CR-39 labelled as 1174. The image has dimensions 4 mm × 4 mm.

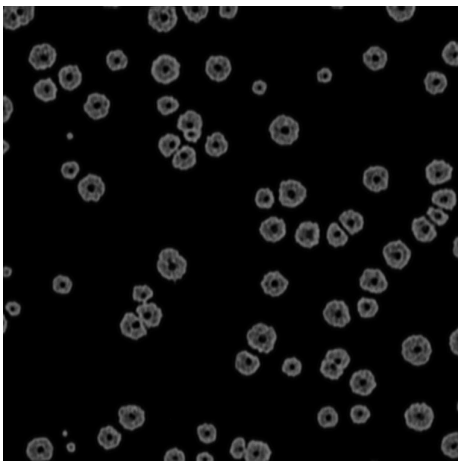

Figure B.10: $R = 336$ tracks cm^{-2}. $H = 2$ mSv. CR-39 labelled as 1149. The image has dimensions 4 mm × 4 mm.

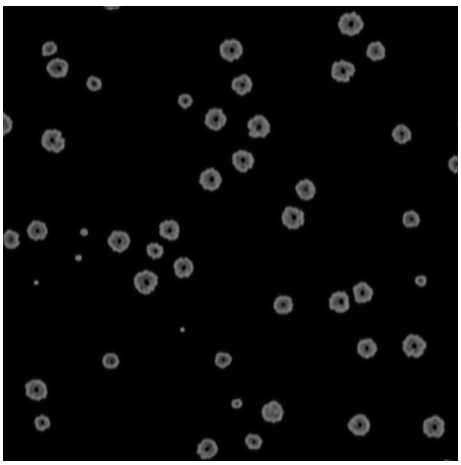

Figure B.11: $R = 186$ tracks cm^{-2}. $H = 1$ mSv. CR-39 labelled as 1146. The image has dimensions 4 mm × 4 mm.

B.1 Background track densities in IBA multiple-room (C-230 cyclotron) campaign

The track density of the background in the irradiation campaign in IBA multiple-room (C-230 cyclotron) is

$$\bar{R}_{\mathrm{B}} = 120 \pm 20 \text{ tracks cm}^{-2}. \tag{B.1}$$

So that the *detection limit* or critical level, $L_{\mathrm{C}} = 2.33 \cdot \sigma_{R_{\mathrm{B}}}$ [Knoll, 2010] is

$$L_{\mathrm{C}} = 50 \text{ tracks cm}^{-2}. \tag{B.2}$$

This means that a dosimeter exhibiting a net track density $R = R' - \bar{R}_{\mathrm{B}} > L_{\mathrm{C}}$ is over the detection limit and the possibility that there is a *false-positive* (*i.e.,* measurement of radiation when actually there is no a radiation source besides background) is less than a 5 %. The track density of the background, Equation (B.1), is computed with the neutron

dosimeters whose CR-39 images are Figures from B.12 to B.18.

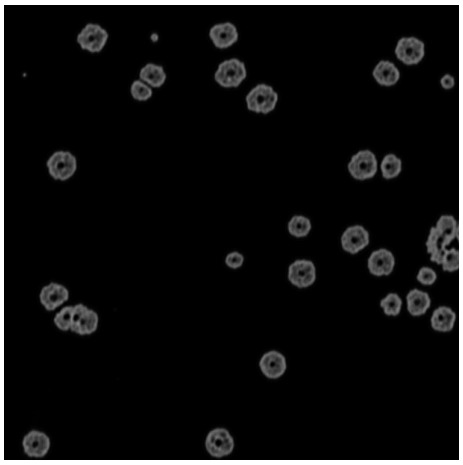

Figure B.12: A background CR-39. The image has dimensions 4 mm × 4 mm.

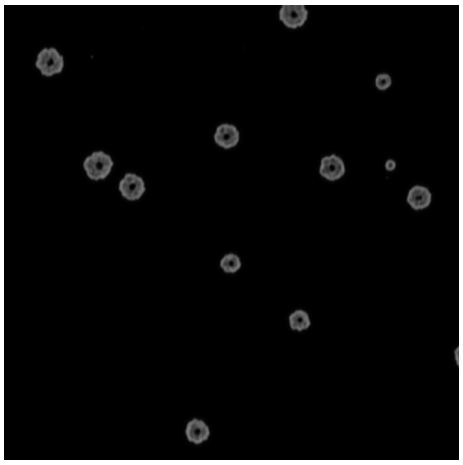

Figure B.13: A background CR-39. The image has dimensions 4 mm × 4 mm.

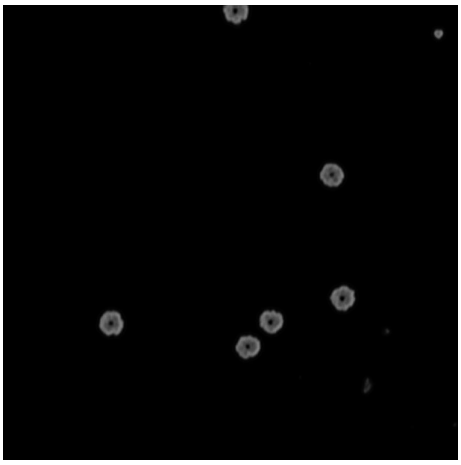

Figure B.14: A background CR-39. The image has dimensions 4 mm × 4 mm.

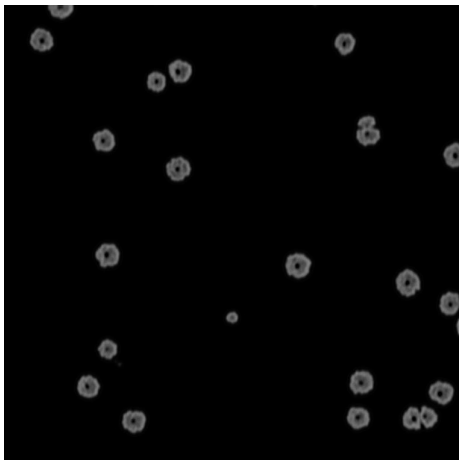

Figure B.15: A background CR-39. The image has dimensions 4 mm × 4 mm.

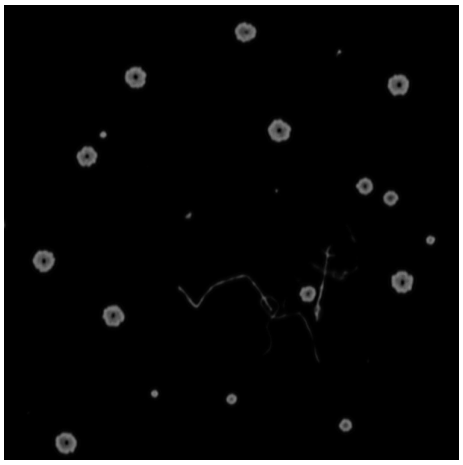

Figure B.16: A background CR-39. The image has dimensions 4 mm × 4 mm.

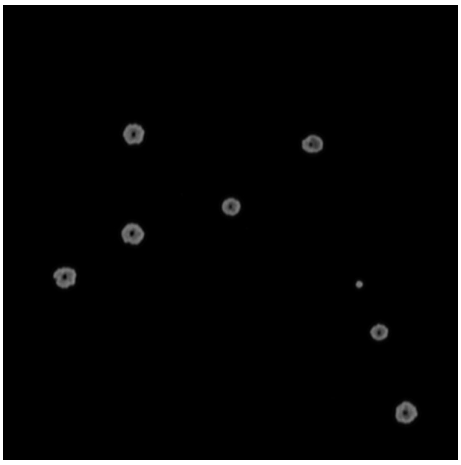

Figure B.17: A background CR-39. The image has dimensions 4 mm × 4 mm.

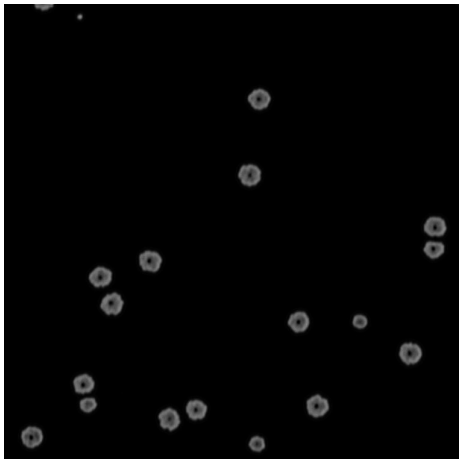

Figure B.18: A background CR-39. The image has dimensions 4 mm × 4 mm.

B.2 Background track densities in Mevion S250i Hyperscan single-room campaign

The track density of the background in the irradiation campaign in Mevion S250i Hyperscan single-room is

$$\bar{R}_{\mathrm{B}} = 86 \pm 6 \text{ tracks cm}^{-2}. \tag{B.3}$$

So that the detection limit is

$$L_{\mathrm{C}} = 14 \text{ tracks cm}^{-2}. \tag{B.4}$$

The track density of the background, Equation (B.3), is computed with the neutron dosimeters whose CR-39 images are Figures from B.19 to B.24.

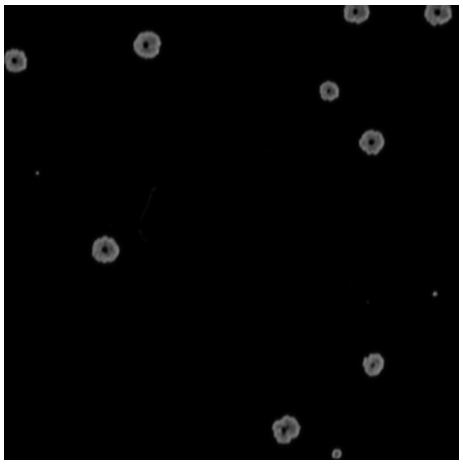

Figure B.19: A background CR-39. The image has dimensions 4 mm × 4 mm.

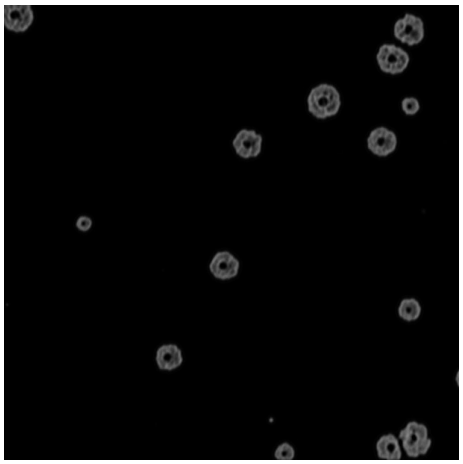

Figure B.20: A background CR-39. The image has dimensions 4 mm × 4 mm.

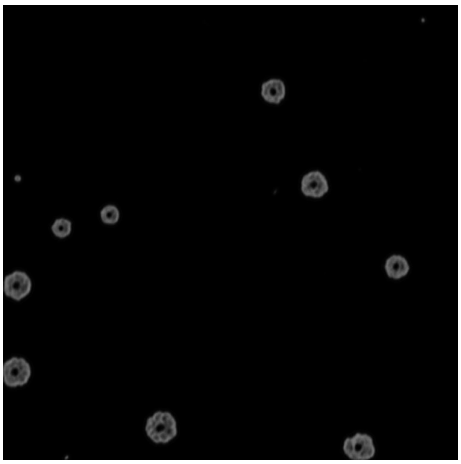

Figure B.21: A background CR-39. The image has dimensions 4 mm × 4 mm.

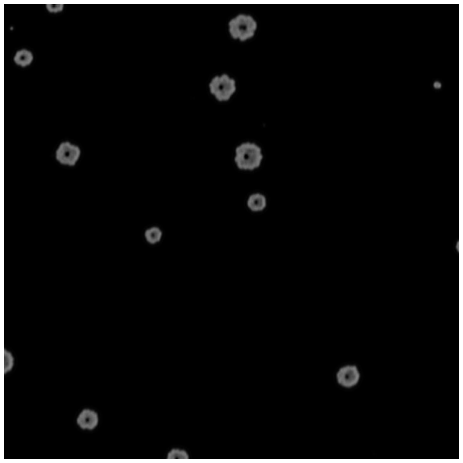

Figure B.22: A background CR-39. The image has dimensions 4 mm × 4 mm.

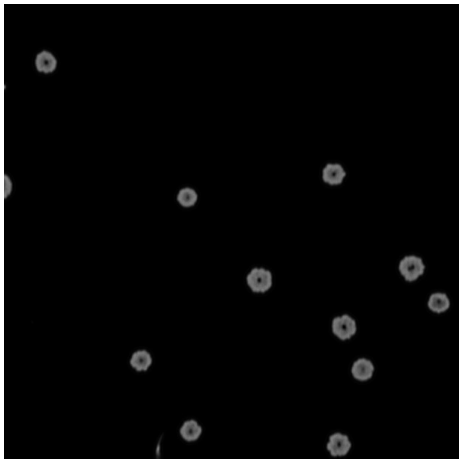

Figure B.23: A background CR-39. The image has dimensions 4 mm × 4 mm.

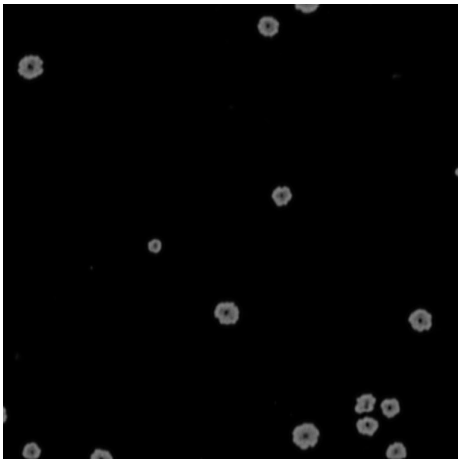

Figure B.24: A background CR-39. The image has dimensions 4 mm × 4 mm.

Appendix C

Lethargy representation of the energy distribution of a quantity

The energy distributions of the neutron fluence found in this work can extend from 10^{-9} MeV to 10^{3} MeV *i.e.,* a total of 12 decades. As the main topics of this work are related to radiation protection and fluence-to-dose quantities as well as the neutron quality factor depend strongly on each energy decade (see Figure 3.5), we are forced to have information about the neutron fluence in each energy decade.

The only possible way to visually have an idea about the relevance of an energy distribution of the neutron fluence extended over 12 decades is to use plots whose X $\equiv E$ axis is in log scale. This has consequences, if we try to represent $\Phi_E(E) = \frac{\mathrm{d}\Phi(E)}{\mathrm{d}E}$ as a function of E (this E would be the central value of an energy bin defined by $\mathrm{d}E \sim \Delta E = E_{i+1} - E_i$) in a log scale, as ΔE is not a constant in a log X axis ($\underbrace{10^{-8} - 10^{-9}}_{1 \text{ decade}} \neq \underbrace{10^{1} - 10^{0}}_{1 \text{ decade}}$) and $\Phi_E(E)$ directly depends on the $\mathrm{d}E$ since $\Phi_E(E) = \frac{\mathrm{d}\Phi(E)}{\mathrm{d}E}$, we simply can not understand the energy distribution of the neutron fluence in that representation because in that plot we can not know if $\Phi_E(E)$ is big or small as a consequence of the fluence of neutrons found in that energy bin $\mathrm{d}\Phi(E)$ or if it is rather a consequence of the $\mathrm{d}E$ itself. In a log X axis, when a first pair of points (P_1 and P_2) and a second pair of points (P_3 and P_4) have the same visual internal distance in each pair (when we see them in a plot) what they actually have is the same log internal distance.

Therefore, if we are forced to use the log X axis, what we have to plot is not $\Phi_E(E) = \frac{\mathrm{d}\Phi(E)}{\mathrm{d}E}$ is rather its lethargy $\tilde{\Phi}_E(E) = \frac{\mathrm{d}\Phi(E)}{\mathrm{d}\log E} = E \cdot \frac{\mathrm{d}\Phi(E)}{\mathrm{d}E} \sim \frac{\mathrm{d}\Phi(E)}{\log E_{i+1} - \log E_i}$. Indeed, $\mathrm{d}\log E \sim \log E_{i+1} - \log E_i$ is a constant when we run through the X axis, as seen before, $\underbrace{10^{-8} - 10^{-9}}_{1 \text{ decade}} \neq \underbrace{10^{1} - 10^{0}}_{1 \text{ decade}}$ but $\underbrace{\log 10^{-8} - \log 10^{-9}}_{1 \text{ decade}} = \underbrace{\log 10^{1} - \log 10^{0}}_{1 \text{ decade}} = 1$. Now if we represent $\tilde{\Phi}_E(E) = \frac{\mathrm{d}\Phi(E)}{\mathrm{d}\log E} = E \cdot \Phi_E(E) = E \cdot \frac{\mathrm{d}\Phi(E)}{\mathrm{d}E}$ as a function of E in log scale, as $\mathrm{d}\log E$ is a constant (as a difference with $\mathrm{d}E$) when we run through the log X or log E axis, we can now be sure that if $\tilde{\Phi}_E(E)$ has a low value it is actually because $\mathrm{d}\Phi(E)$ is really low in the energy bin defined by $\mathrm{d}\log E \sim \log E_{i+1} - \log E_i$.

Usually we are used to do integrals by eye when we analyse a plot in linear X scale (area under a curve). Remember that in linear plots $\mathrm{d}x \sim \Delta x$ is constant throughout the X axis, this is not true in log X scale. This is specially tricky because in log X scale, visually two points at the same distance (for instance, the visual distance between 10^{-9} and 10^{-8} and

the visual distance between 10^0 and 10^1 is the same, however $\underbrace{10^{-8}-10^{-9}}_{1\text{ decade}} \neq \underbrace{10^{1}-10^{0}}_{1\text{ decade}}$). Therefore, the meaning of two equal visual distances in a log X scale is that the log distance between the points is constant $\underbrace{\log 10^{-8}-\log 10^{-9}}_{1\text{ decade}} = \underbrace{\log 10^{1}-\log 10^{0}}_{1\text{ decade}} = 1$. This means that when we do a visual integral over the log X axis, we are actually doing the integrals of the Y quantity over $\mathrm{d}\log x$ rather than in $\mathrm{d}x$ (this would be the case if X axis was in linear scale).

$$A_{E_1<E<E_2} = \int_{E_1}^{E_2} \tilde{\Phi}_E(E)\cdot \mathrm{d}(\log E) \tag{C.1}$$

$$= \int_{E_1}^{E_2} E\cdot \Phi_E(E)\cdot \mathrm{d}(\log E) \tag{C.2}$$

$$= \int_{E_1}^{E_2} E\cdot \Phi_E(E)\cdot \frac{\mathrm{d}E}{E} \tag{C.3}$$

$$= \int_{E_1}^{E_2} \Phi_E(E)\cdot \mathrm{d}E \tag{C.4}$$

$$= \int_{E_1}^{E_2} \mathrm{d}\,\Phi(E) = \Phi_{E_1<E<E_2}. \tag{C.5}$$

In summary,

$$\overbrace{A_{E_1<E<E_2}}^{\text{Visual integration (area under curve)}} = \underbrace{\int_{E_1}^{E_2} \tilde{\Phi}_E(E)\cdot \mathrm{d}(\log E)}_{\text{Visual integration (area under curve)}} = \Phi_{E_1<E<E_2}. \tag{C.6}$$

Is then proved that,

$$\overbrace{A_{E_1<E<E_2}}^{\text{Visual integration (area under curve)}} = \underbrace{A_{E_3<E<E_4}}_{\text{Visual integration (area under curve)}} \quad\leftrightarrow\quad \Phi_{E_1<E<E_2} = \Phi_{E_3<E<E_4}, \tag{C.7}$$

Which means that **same visual areas** in a lethargy plot have the **same integrated fluences**. The individual numerical values of each of the two areas or integrated fluences can be numerically found by any of the Equations between (C.1) and (C.5).

At time of choosing an energy binning, one important question is what is the log distance that we want to set for our energy binnings (width of the energy bin). This set the equation for the energy bin log width, Δ, as

$$\Delta_i = \log E_{i+1} - \log E_i \leftrightarrow E_{i+1} = E_i\cdot 10^{\Delta_i}. \tag{C.8}$$

In case we want to set a constant log binning or equi-log binning the Equation (C.8) is simply

$$\Delta = \text{constant} = \log E_{i+1} - \log E_i \leftrightarrow E_{i+1} = E_i\cdot 10^{\Delta}. \tag{C.9}$$

Given an energy bin defined by E_i and E_{i+1} we can find what would be the E value that leaves the same log distance between E_i and E, and E and E_{i+1}, this is translated mathematically as

$$\log E - \log E_i = \log E_{i+1} - \log E \leftrightarrow E = \sqrt{E_i \cdot E_{i+1}}. \tag{C.10}$$

Actually, if the log distance between E_i and E_{i+1} is Δ then Equation (C.10) is

$$\log E - \log E_i = \log E_{i+1} - \log E = \frac{\Delta}{2} \leftrightarrow E = E_i \cdot 10^{\frac{\Delta}{2}}. \tag{C.11}$$

Which has the same form as Equation (C.8) understanding that central energy values break each energy binning in two.

Appendix D

Experimental validation of the MC response functions

Each detector configuration i must be simulated in order to obtain the response function and after that, each response function, $R_{\Phi,i}(E)$, must be validated in all reference fields possibles to obtain the calibration factors, f_i.

The calibration factor for a specific detector configuration, f_i, is defined as the ratio between the experimental response, R_i^{EXP}, and the reference response, R_i^{REF}, when the detector configuration is placed in a known reference field with energy distribution of the neutron fluence $\Phi_E^{\mathrm{REF}}(E) = \Phi^{\mathrm{REF}} \cdot \varphi_E^{\mathrm{REF}}(E)$. Therefore, the calibration factor, f_i, can be written as:

$$f_i = \frac{R_i^{\mathrm{EXP}}}{R_i^{\mathrm{CALC}}} = \frac{R_i^{\mathrm{EXP}}}{\Phi^{\mathrm{REF}} \int_E R_{\Phi,i}(E)\varphi_E^{\mathrm{REF}}(E)\mathrm{d}E} = \frac{\Phi_i^{\mathrm{EXP}}}{\Phi_i^{\mathrm{REF}}}. \tag{D.1}$$

The general calibration factor, f, is then obtained as a weighted mean [Bevington et al., 2003] where the weights are $\left[\frac{1}{\sigma_{f_i}^2}\right]$ so that:

$$f = \frac{1}{\sum_j \left[\frac{1}{\sigma_{f_j}^2}\right]} \sum_i \left[\frac{1}{\sigma_{f_i}^2}\right] \cdot f_i. \tag{D.2}$$

Equation (D.1) can be seen as a way to quantify how accurate are MC simulations for the computation of the response function. Of course, all quantities involved in Equation (D.1) have uncertainties and all of them could contribute to the fact that $f_i \neq 1$. However, the fact that the ideal situation is not achieved ($f_i = 1$) is probably because the MC simulations are not capable of computing perfectly the response function. This could be because the internal structure of the detector is not perfectly known and therefore, it is not perfectly modelled in the MC simulations or it could be also due to the fact that physics in the MC code is subjected to uncertainties or nuclear models.

It is clear that the true response of the detector configuration in the reference situation is the experimental response or experimental measurement, R_i^{EXP}. When the detector system is going to be employed in a unknown energy distribution of the neutron fluence, $\Phi_E(E) = \Phi \cdot \varphi_E(E)$, the fact explained in the previous paragraph will remain (accuracy of the response function) and must be taken into account and included in the whole unfolding procedure. Assuming that we are in front of a linear phenomenon and assuming that f is

the best factor, in general, to take into account the previous facts, Equation D.1 can be also written as:

$$f = \frac{R_i^{\mathrm{EXP}}}{R_i^{\mathrm{BEST}}} = \frac{R_i^{\mathrm{EXP}}}{\Phi_i^{\mathrm{BEST}} \int_E R_{\Phi,i}(E)\varphi_E^{\mathrm{BEST}}(E)\mathrm{d}E} = \frac{\Phi_i^{\mathrm{EXP}}}{\Phi_i^{\mathrm{BEST}}}. \tag{D.3}$$

Where R_i^{EXP} is the experimental response or measurement of the detector configuration i, $\varphi_E^{\mathrm{BEST}}(E)$ is the best unit energy distribution of the neutron fluence found by the unfolding procedure (see Bedogni et al. [2007] and Bedogni [2006]) and Φ_i^{EXP} will be the truly neutron fluence found by the detector configuration i through the Equation (D.4), as f is found in the experimental validation of the response functions. Indeed, we can isolate Φ_i^{EXP} from (D.3) so that:

$$\Phi_i^{\mathrm{EXP}} = f \cdot \Phi_i^{\mathrm{BEST}}. \tag{D.4}$$

The factors f used in the Bonner Sphere Systems presented in this work (Section 4.5.1 and Section 4.5.2) are the ones shown in Table D.1.

Table D.1: Factors f used in the BSSs of this work.

BSS	f
Active BSS with ^{3}He	0.9143
Passive BSS with gold foil	0.988

Appendix E

Neutron cross sections

In Figure E.1 the cross section to produce neutrons via protons in HCNO materials (tissue and detectors) is shown while Figure E.2 shows the cross section to produce neutrons via protons in beam components of proton radiotherapy delivery systems.

Figures E.3, E.5, E.6 and E.7 present the differential cross sections to produce energy distributions of outgoing neutrons via incidence of protons in tissue or detector materials. These differential cross sections could be related to the measured energy distributions of the neutron fluence.

In Figures E.8, E.9, E.10 and E.11 the differential cross sections to produce energy distributions of outgoing neutrons via incidence of protons in beam components are found. These differential cross sections could be also related to the measured energy distributions of the neutron fluence.

From the displayed differential cross sections, one can observe that maxima are obtained in generating neutrons around 1 MeV and sometimes these maxima are independent of the exit angle in which the energy distributions (from the differential cross sections) are measured. The fact that maxima are located around 1 MeV justify the existence of the fast-evaporation peaks and the fact that the measured differential cross sections can show angular independence in respect to the maximum justify that the emission of fast-evaporation neutrons is quite isotropic.

Some differential cross sections (for ^{12}C, Figure E.3 and for ^{16}O, Figure E.5) show an increased probability to the emission of more energetic neutrons in forward directions than in not so forward directions. These facts justify the energy and directionality of the measured intranuclear cascade neutrons.

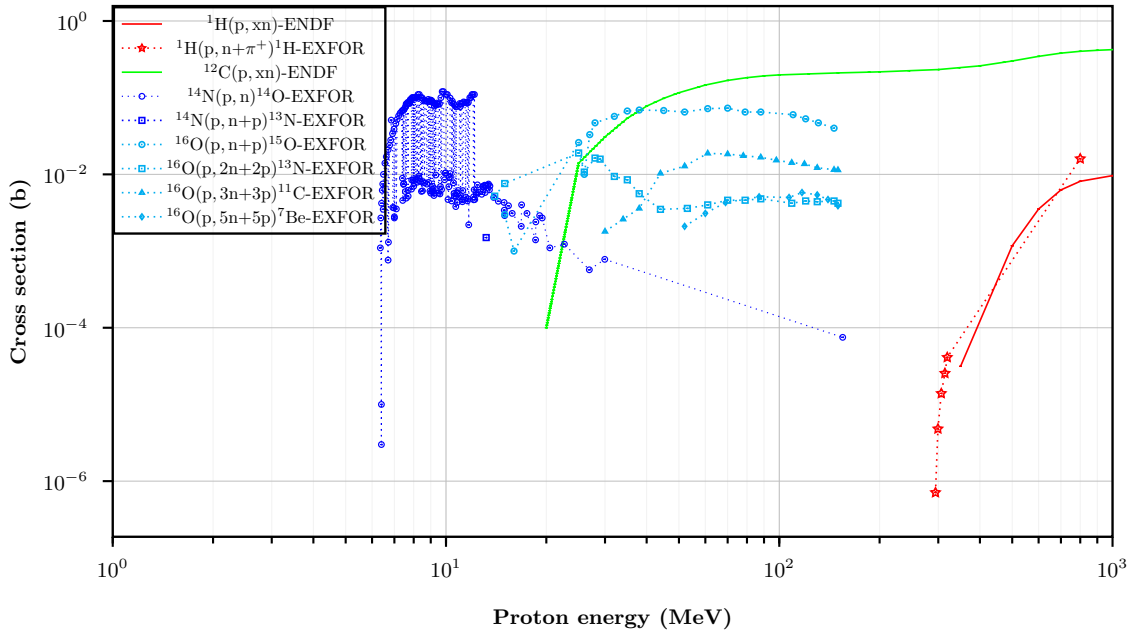

Figure E.1: Cross sections to produce neutrons through incident protons for HCNO materials. From EXFOR [2022] and ENDF [2022].

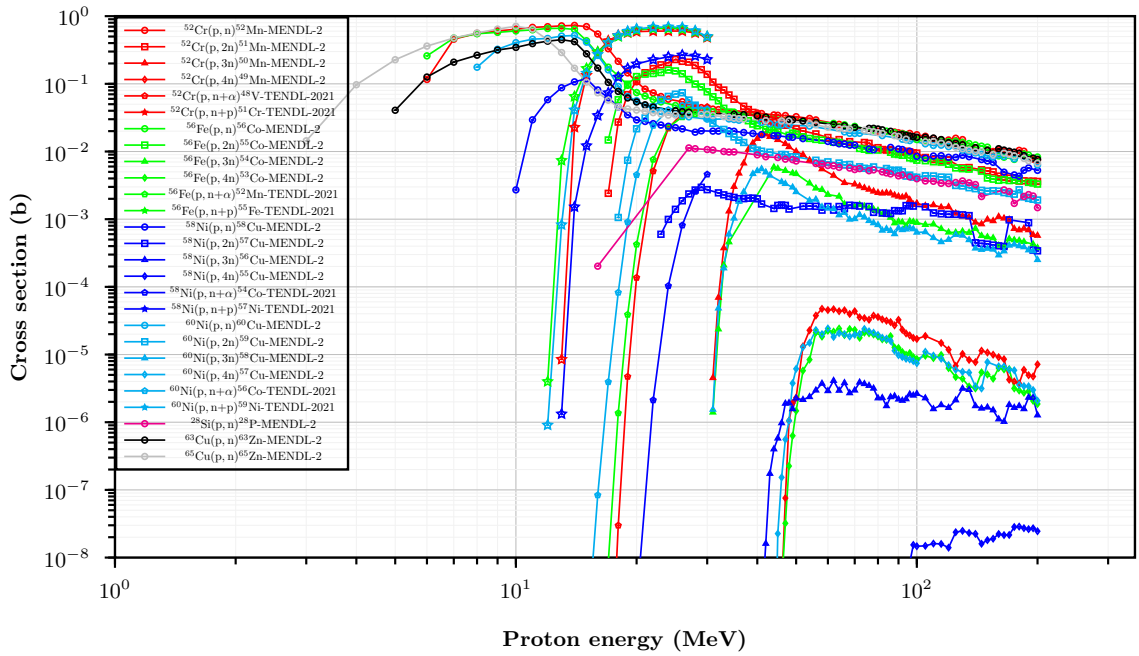

Figure E.2: Cross sections to produce neutrons through incident protons for materials involved in beam components of proton radiotherapy (isotopes from Cr, Fe, Ni, Si, Cu). From EXFOR [2022] and ENDF [2022].

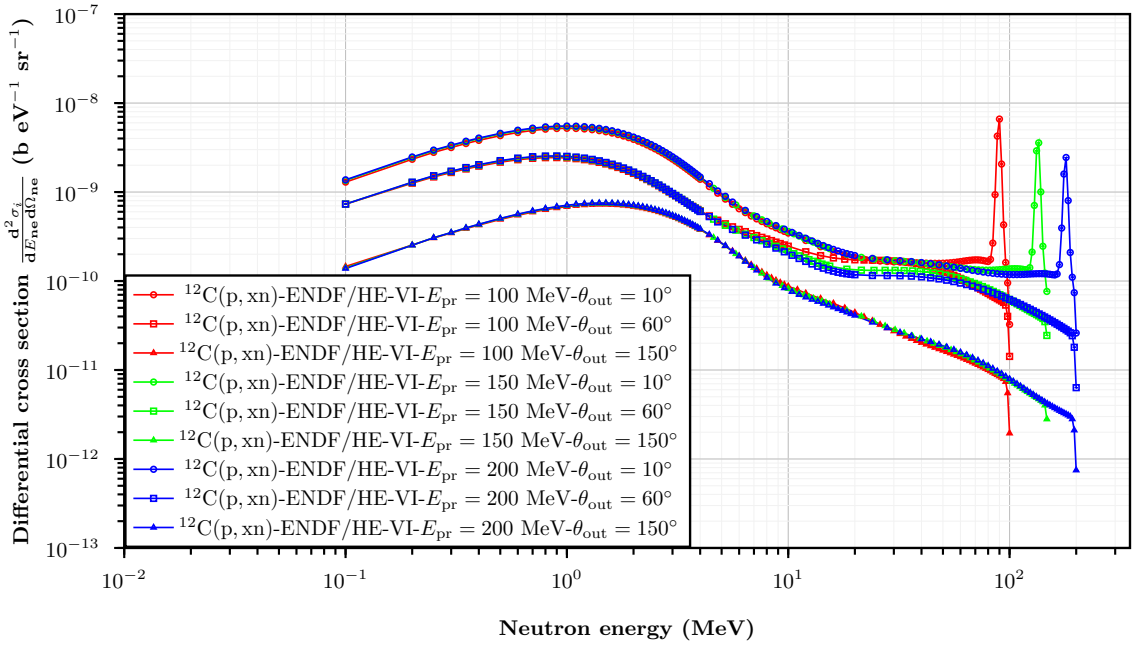

Figure E.3: Differential cross sections to produce energy distributions of neutrons through incident protons in ^{12}C. From EXFOR [2022] and ENDF [2022].

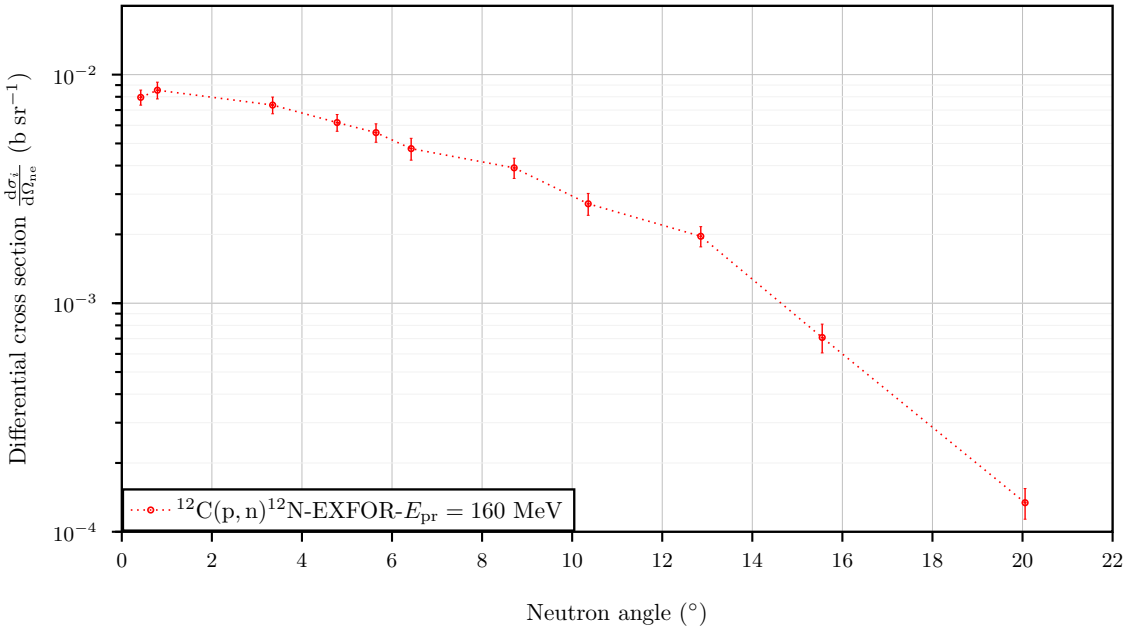

Figure E.4: Angular distribution of neutrons generated by protons incident on ^{12}C. Data taken from EXFOR [2022] and ENDF [2022].

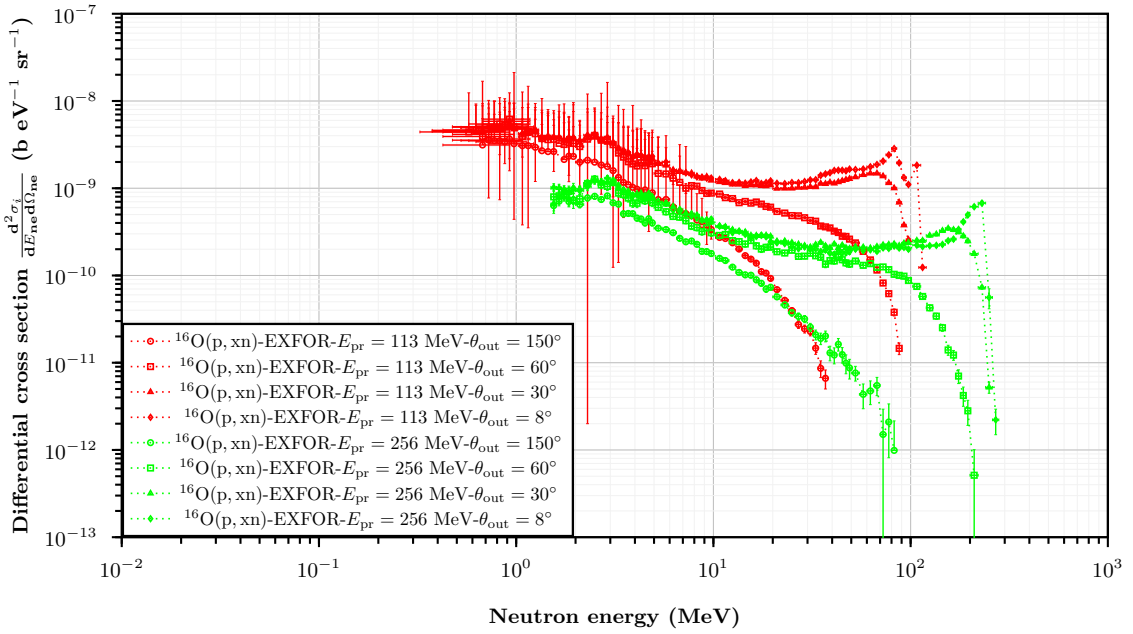

Figure E.5: Differential cross sections to produce energy distributions of neutrons through incident protons in ^{16}O. From EXFOR [2022] and ENDF [2022].

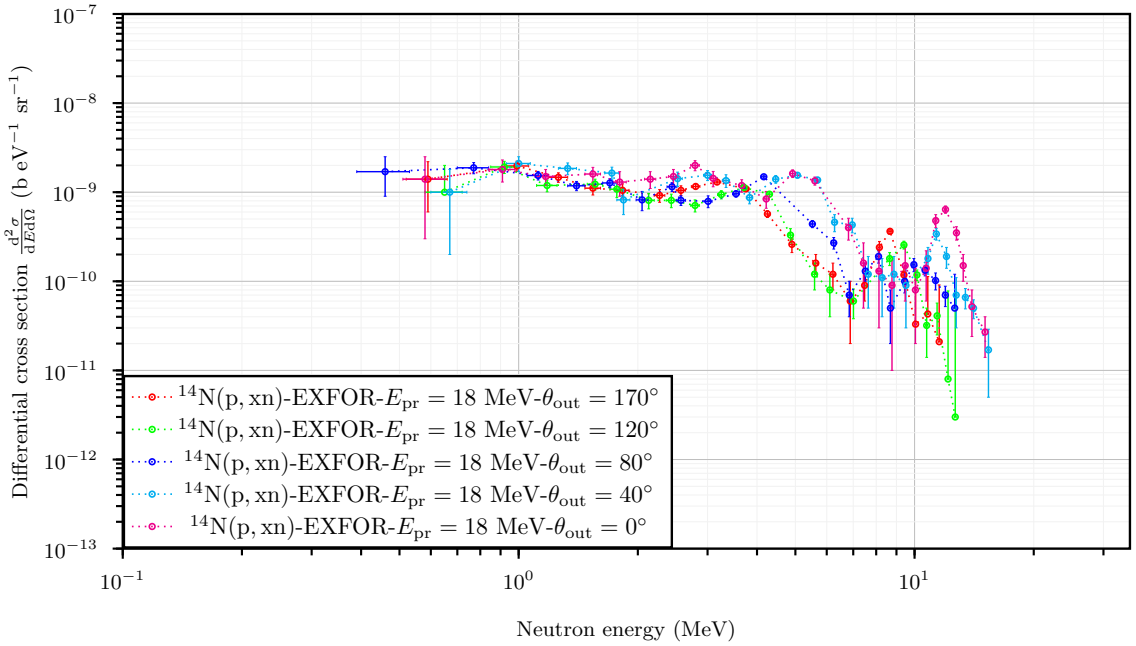

Figure E.6: Differential cross sections to produce energy distributions of neutrons through incident protons in N. From EXFOR [2022] and ENDF [2022].

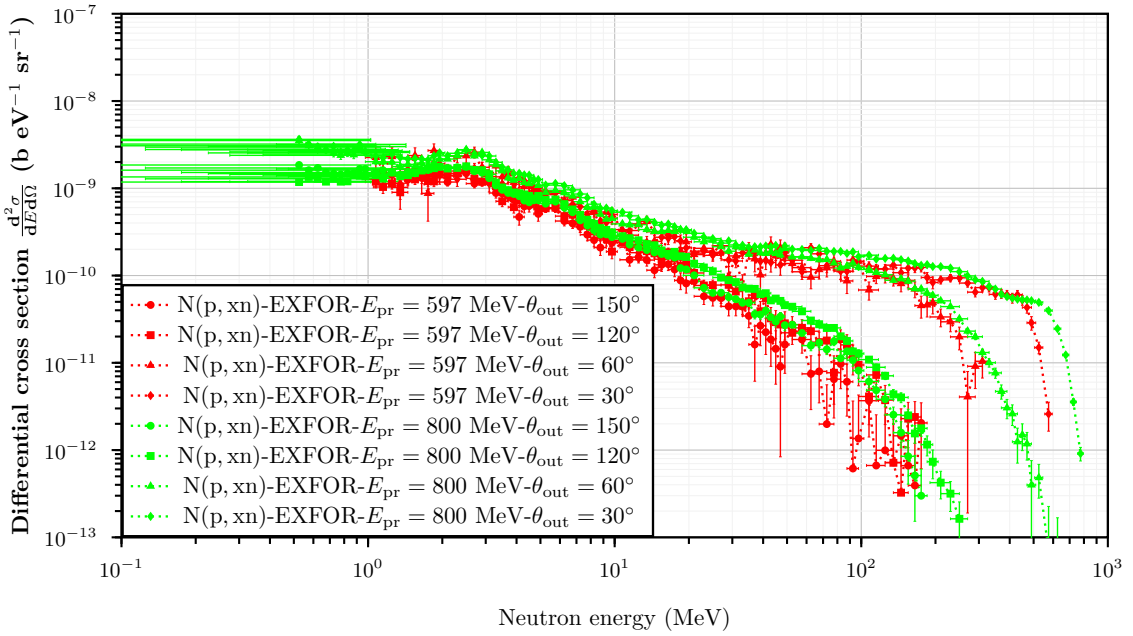

Figure E.7: Differential cross sections to produce energy distributions of neutrons through incident protons in N. From EXFOR [2022] and ENDF [2022].

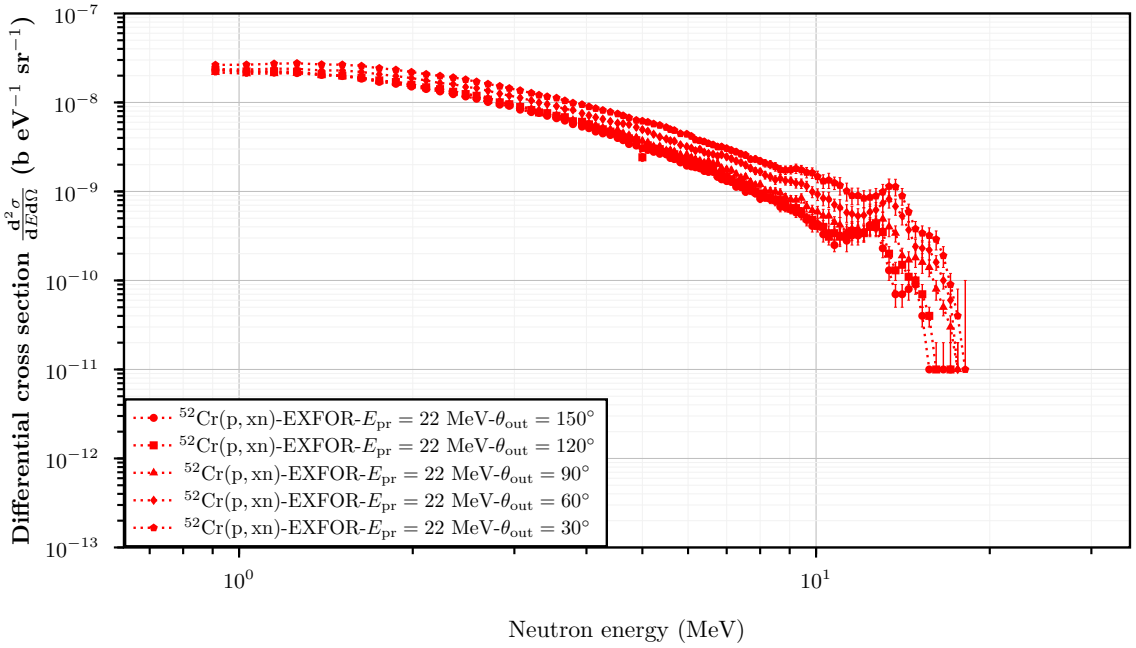

Figure E.8: Differential cross sections to produce energy distributions of neutrons through incident protons in ^{52}Cr. From EXFOR [2022] and ENDF [2022].

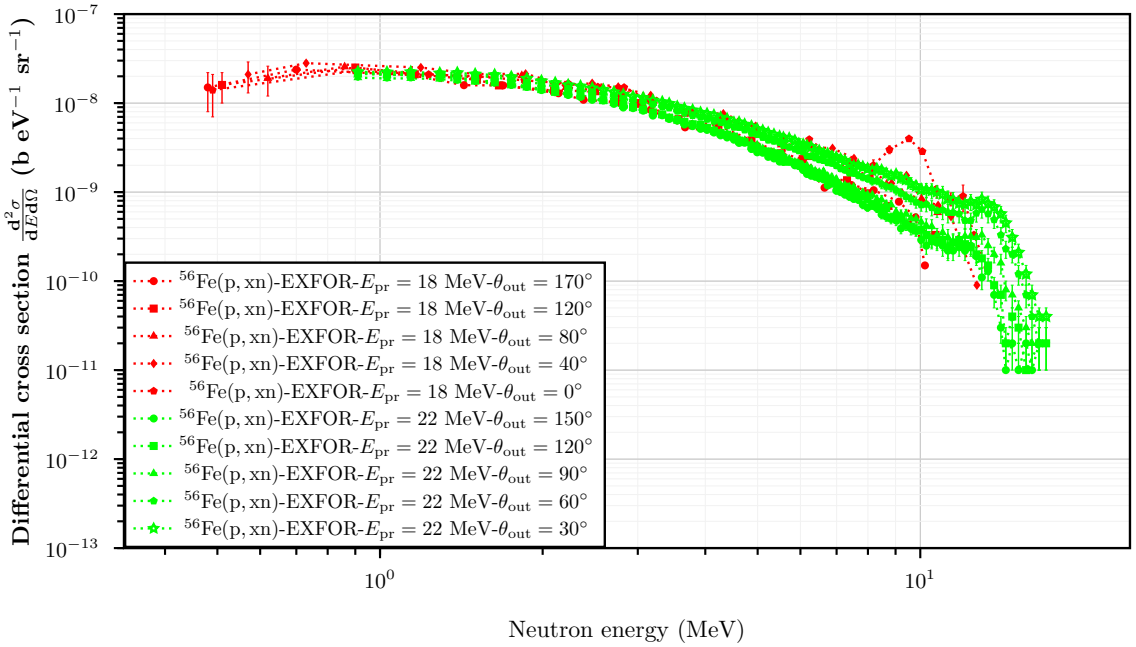

Figure E.9: Differential cross sections to produce energy distributions of neutrons through incident protons in ^{56}Fe. From EXFOR [2022] and ENDF [2022].

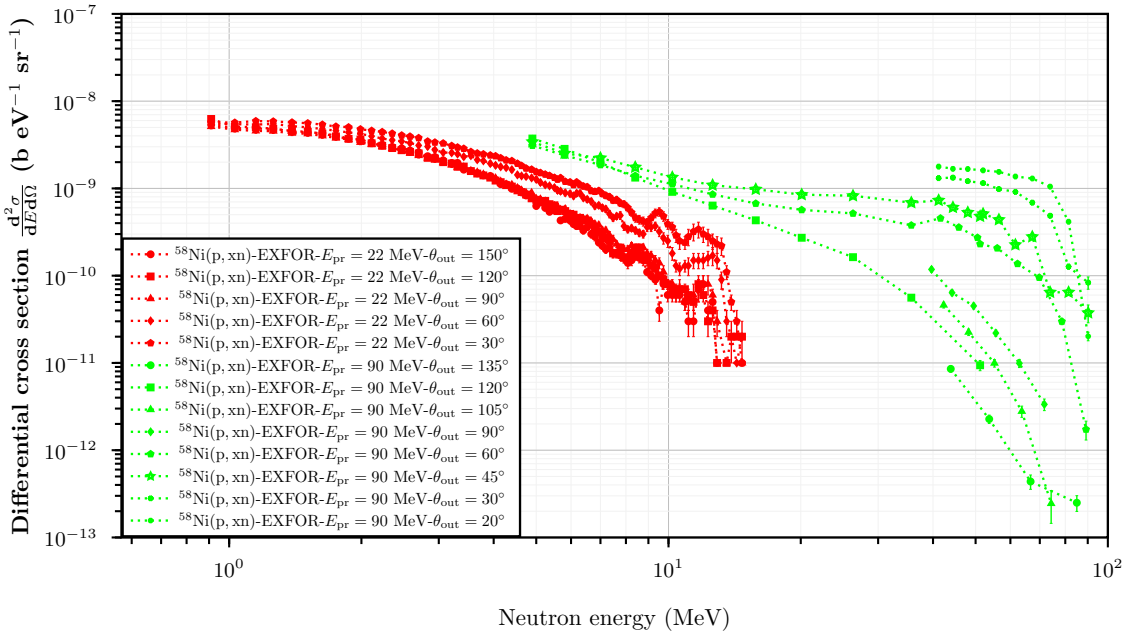

Figure E.10: Differential cross sections to produce energy distributions of neutrons through incident protons in ^{58}Ni. From EXFOR [2022] and ENDF [2022].

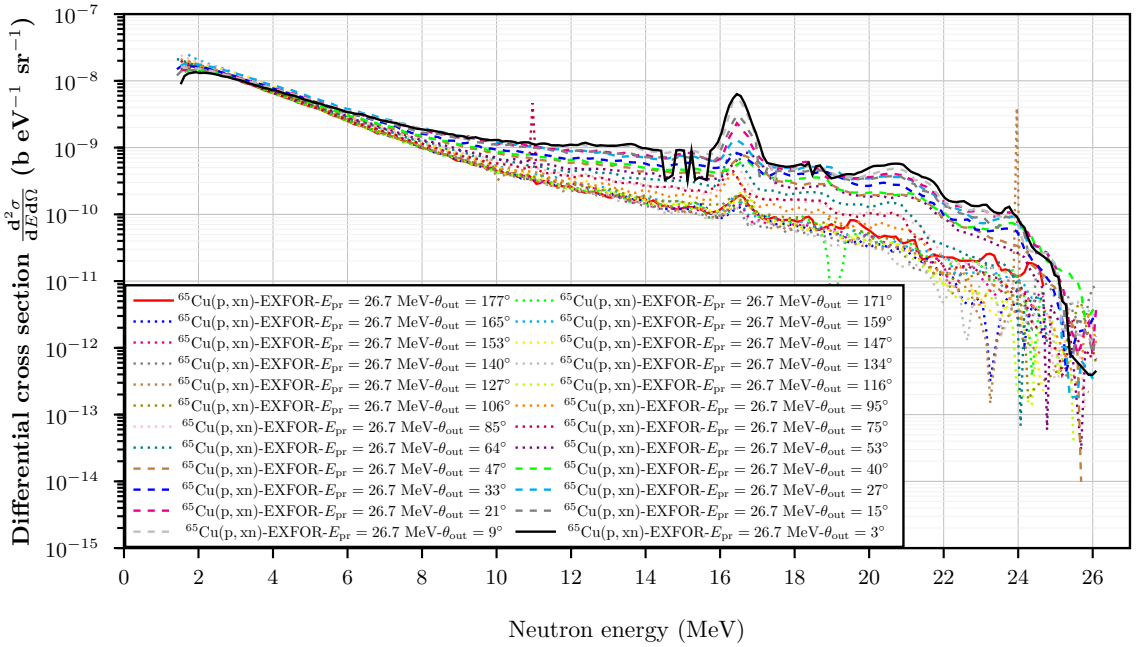

Figure E.11: Differential cross sections to produce energy distributions of neutrons through incident protons in ^{65}Cu. From EXFOR [2022] and ENDF [2022].

Bibliography

Advanced Oncotherapy (2022). "Proton radiotherapy solutions by Advanced Oncotherapy". URL: http://www.avoplc.com/en-gb/Technology/Overview-of-the-LIGHT-System.

Alsmiller, G. R., Gabriel, A. T., and Guthrie, P. M. (1970). "The Energy Distribution of Photoneutrons Produced by 150-MeV Electrons in Thick Beryllium and Tantalum Targets". Nuclear Science and Engineering 40, pp. 365–374. DOI: 10.13182/NSE70-A20187.

Amgarou, K., Lacoste, V., Muller, H., and Fernández, F. (2007). "Set-up of a passive Bonner sphere system for neutron spectrometry at mixed fields with predominant photon component based on activation detector". Radiation Protection Dosimetry 126, pp. 337–341. DOI: 10.1093/rpd/ncm070.

Amgarou, K., Domingo, C., Bouassoule, T., and Fernández, F. (2009). "Monte Carlo simulation of the NaI(Tl) detector response to measure gold activated foils". Nuclear Instruments and Methods in Physics Research B 267, pp. 2944–2951. DOI: 10.1016/j.nimb.2009.06.087.

Amgarou, K. and Lacoste, V. (2010). "Response matrix evaluations of a passive Bonner sphere system used for neutron spectrometry at pulsed, intense and complex mixed fields". Journal of Instrumentation 5, P09002. DOI: 10.1088/1748-0221/5/09/P09002.

Amgarou, K., Bedogni, R., Domingo, C., Esposito, A., Gentile, A., Carinci, G., and Russo, S. (2011). "Measurement of the neutron fields produced by a 62MeV proton beam on a PMMA phantom using extended range Bonner sphere spectrometers". Nuclear Instruments and Methods in Physics Research Section A: Accelerators, Spectrometers, Detectors and Associated Equipment 654, pp. 399–405. DOI: https://doi.org/10.1016/j.nima.2011.07.027.

Al-Najjar, R. A. S., Bull, K. R., and Durrani, A. S. (1979). "Electrochemical etching of CR-39 plastic: applications to radiation dosimetry". Nucl. Tracks 3, pp. 169–183. DOI: 10.1016/0191-278X(79)90014-3.

Armstrong, A. T., Hogg, R. W., Lewis, M. G., Robertson, W. A., Brookes, R. G., Clough, S. A., Freeland, H. J., Galbraith, W., King, F. A., Rawlinson, R. W., Tait, S. R. N., Thompson, C. J., and Tolfree, L. W. D. (1972). "The total photon deuteron hadronic cross section in the energy range 0.265-4.215 GeV". Nuclear Physics B41, pp. 445–473. DOI: 10.1016/0550-3213(72)90403-8.

Bacon, E. G. (1966). *X-ray and neutron diffraction*. Edition 1. Pergamon Press.

Bakali, M. (2001). "ESPECTROMETRÍA NEUTRÓNICA EN LAS CENTRALES NUCLEARES MEDIANTE UN SISTEMA DE ESFERAS BONNER". PhD Thesis. URL$_1$: https://www.educacion.gob.es/teseo/mostrarRef.do?ref=253248, URL$_2$: https://www.tdx.cat/handle/10803/3345#page=1 and URL$_3$: https://dialnet.unirioja.es/servlet/tesis?codigo=4792.

Baldin, A. M., Goldanskii, V. I., and Rozenthal, I. L. (1961). *Kinematics of nuclear reactions*. Edition 1. Pergamon Press.

Baumgartner, V. W. and Brackenbush, W. L. (1966). "Neutron dosimetry using the fission fragment damage principle". Dosimetry Technology Section. Environmental Health and Engineering Department. Pacific Northwest Laboratory. BNWL-332. UC-41. Health and Safety. DOI: 10.2172/4444236.

Bedogni, R. (2006). "NEUTRON SPECTROMETRY AND DOSIMETRY FOR RADIATION PROTECTION AROUND A HIGH ENERGY ELECTRON/POSITRON COLLIDER". PhD Thesis. URL$_1$: https://www.educacion.gob.es/teseo/mostrarRef.do?ref=399402, URL$_2$: https://www.tdx.cat/handle/10803/3380#page=1 and URL$_3$: https://dialnet.unirioja.es/servlet/tesis?codigo=5693.

Bedogni, R., Domingo, C., Esposito, A., and Fernández, F (2007). "FRUIT: An operational tool for multisphere neutron spectrometry in workplaces". Nuclear Instruments and Methods in Physics Research Section A: Accelerators, Spectrometers, Detectors and Associated Equipment 580, pp. 1301–1309. DOI: https://doi.org/10.1016/j.nima.2007.07.033.

Bedogni, R., Bortot, D., Pola, A., Introini, M.V., Lorenzoli, M., Gómez-Ros, J.M., Sacco, D., Esposito, A., Gentile, A., Buonomo, B., Palomba, M., and Grossi, A. (2015). "Experimental characterization of semiconductor-based thermal neutron detectors". Nuclear Instruments and Methods in Physics Research Section A: Accelerators, Spectrometers, Detectors and Associated Equipment 780, pp. 51–54. DOI: https://doi.org/10.1016/j.nima.2015.01.058.

Bedogni, R., Sperduti, A., Pietropaolo, A., Pillon, M., Pola, A., and Gómez-Ros, J.M. (2017). "Experimental characterization of HOTNES: A new thermal neutron facility with large homogeneity area". Nuclear Instruments and Methods in Physics Research Section A: Accelerators, Spectrometers, Detectors and Associated Equipment 843, pp. 18–21. DOI: https://doi.org/10.1016/j.nima.2016.10.056.

Benton, V. E., Oswald, A. R., and Frank, L. A (1981). "Proton-recoil neutron dosimeter for personnel monitoring". Health Physics 40, pp. 801–809. DOI: 10.1097/00004032-198106000-00002.

Berger, M.J., Hubbell, J.H., Seltzer, S.M., Chang, J., Coursey, J.S., Sukumar, R., Zucker, D.S., and Olsen, K. (2022). "XCOM: Photon Cross Sections Database". URL: https://www.nist.gov/pml/xcom-photon-cross-sections-database.

BERTHOLD (2023). "BERTHOLD". URL: https://www.berthold.com/en/radiation-protection/products/dose-and-dose-rate/neutron-dose-rate-probe-lb-6411/.

Berger, J. M. and Seltzer, M. (1964). "Tables of energy losses and ranges of electrons and positrons". Reviews of Modern Physics. NASA SP-3012. URL: https://ntrs.nasa.gov/citations/19650002905.

Berger, M. J., Coursey, J. S., Zucker, M. A., and Chang, J (1993). "ESTAR, PSTAR and ASTAR: Computer Programs for Calculating Stopping-Power and Range Tables for Electrons, Protons and Helium Ions". National Institute of Standards and Technology. URL: http://physics.nist.gov/Star.

Bevington, P. R. and Robinson, D. K. (2003). *Data reduction and error analysis for the physical sciences*. Edition 3. McGraw-Hill.

Birks, J. B. (1964). *The theory and practice of scintillation counting*. Edition 1. Pergammon press.

Bolzonella, M., Caresana, M., Ferrarini, M., and Babut, R. (2021). "Characterization of a novel passive personal fast neutron dosimeter based on a CR-39 track detector in monochromatic neutron fields via Monte Carlo simulations and experiments". Radiation Measurements 146, p. 106627. DOI: https://doi.org/10.1016/j.radmeas.2021.106627.

Bordy, J.M., Bessieres, I., d'Agostino, E., Domingo, C., d'Errico, F., di Fulvio, A., Knežević, Ž., Miljanić, S., Olko, P., Ostrowsky, A., Poumarede, B., Sorel, S., Stolarczyk, L., and Vermesse, D. (2013). "Radiotherapy out-of-field dosimetry: Experimental and computational results for photons in a water tank". Radiation Measurements 57, pp. 29–34. DOI: https://doi.org/10.1016/j.radmeas.2013.06.010.

Bouassoule, F., Fernández, F., Tomás, M., Bakali, M., Castelo, J., Carmena, P., and Lara, L (2001). "Monte Carlo calculations and experimental calibrations of Bonner sphere systems with a new cylindrical helium-3 proportional counter". Radiation Measurements 34. Proceedings of the 20th International Conference on Nuclear Track s in Solids, pp. 199–202. DOI: https://doi.org/10.1016/S1350-4487(01)00151-2.

Bouassoule, T, Fernández, F., Martín, M., and Tomás, M. (1999). "A dosemeter based on nuclear etched track detectors for thermal, fast and high energy neutrons with flat response". Radiation Protection Dosimetry 85, pp. 39–43. DOI: 10.1093/oxfordjournals.rpd.a032879.

Boytsov, A. A. and Starostov, B. I. (1984). "High precision prompt neutron spectrum measurement from Cf-252 spontaneous fission in the energy range 0.01 - 3 MeV". Proc.Conf.Neutron Physics, Kiev 2. URL$_1$: https://www-nds.iaea.org/exfor/servlet/X4sShowPubl?File=C,83KIEV,2,298,1983, URL$_2$: https://www-nds.iaea.org/exfor/servlet/X4sGetSubent?reqx=5961&subID=40874002, p. 298.

Bransden, B. H. and Joachain, C. J. (2000). *Quantum Mechanics*. Edition 2. Pearson.

Bramblett, Richard L., Ewing, Ronald I., and Bonner, T.W. (1960). "A new type of neutron spectrometer". Nuclear Instruments and Methods 9, pp. 1–12. DOI: https://doi.org/10.1016/0029-554X(60)90043-4.

Brand, J. Van der and Witt Huberts, P. de (1996). "Inside the neutron". Physics World 9, p. 35. DOI: 10.1088/2058-7058/9/2/27.

Brown, D.A. et al. (2018). "ENDF/B-VIII.0: The 8th Major Release of the Nuclear Reaction Data Library with CIELO-project Cross Sections, New Standards and Thermal Scattering Data". Nuclear Data Sheets 148, pp. 1–142. DOI: https://doi.org/10.1016/j.nds.2018.02.001.

Burgkhardt, B., Fieg, G., Klett, A., Plewnia, A., and Siebert, B.R.L. (1997). "The Neutron Fluence and H*(10) Response of the New LB 6411 REM Counter". Radiation Protection Dosimetry 70, pp. 361–364. DOI: 10.1093/oxfordjournals.rpd.a031977.

Burneni, Joseph L. (1997). "The History of CR-39". URL: https://web.archive.org/web/20090613034959/http://corporateportal.ppg.com/NA/chemicals/Optical/CR39/cr39History.htm.

Cartwright, G. B and Shirk, K. E. (1978). "A nuclear-track-recording polymer of unique sensitivity and resolution". Nuclear Instruments and Methods 153, pp. 457–460. DOI: 10.1016/0029-554X(78)90989-8.

Cassou, M. R. and Benton, V. E. (1978). "Properties and applications of CR-39 ppolymeric nuclear track detector". Nuclear Track Detection 2, pp. 173–179. DOI: 10.1016/0145-224X(78)90021-2.

Caswell, R. S., Coyne, J. J., and Randolph, M. L (1980). "Kerma Factors for Neutron Energies Below 30 MeV". Radiat. Res. 83, pp. 217–254. DOI: 10.2307/3575276.

Chadwick, B. M., Young, G. P., MacFarlane, E. R., White, C. M., and Little, C. R (2003). "Photonuclear Physics in Radiation Transport-I: Cross Sections and Spectra". Nuclear Science and Engineering 144, pp. 157–173. DOI: 10.13182/NSE144-157.

Chang, R. and Goldsby, K. A. (2017). *Chemistry*. Edition 12. McGRAW-HILL.

Chadwick, J. (1932). "Possible Existence of a Neutron." Nature 129, p. 312. DOI: 10.1038/129312a0.

Chadwick, B. M. and Young, G. P. (1994). "Photonuclear Reactions in the GNASH Code: Benchmarking Model Calculations for Reactions on Lead up to 140 MeV". Lawrence Livermore National Laboratory. UCRL-ID-118721. DOI: 10.2172/46728.

Chartier, J.L., Kurkdjian, J., Paul, D., Itie, C., Audoin, G., Pelcot, G., and Posny, F. (1995). "Progress on Calibration Procedures with Realistic Neutron Spectra". Radiation Protection Dosimetry 61, pp. 57–61. DOI: 10.1093/oxfordjournals.rpd.a082754.

Chadwick, M. B., Barschall, H. H., Caswell, R. S., DeLuca, P. M., Hale, G. M., Jones, D. T. L., MacFarlane, R. E., Meulders, J. P., Schuhmacher, H., Schrewe, U. J., Wambersie, A., and Young, P. G (1999). "A consistent set of neutron kerma coefficients from thermal to 150 MeV for biologically important materials". Med. Phys. 26, pp. 974–991. DOI: 10.1118/1.598601.

CIRS (2023). "Sun Nuclear & CIRS: Computerized Imaging Reference Systems". 900 Asbury Ave Norfolk, VA 23513 USA. URL$_1$: https://www.cirsinc.com/ and URL$_2$: https://www.cirsinc.com/products/radiation-therapy/atom-phantom-family/.

Caballero-Pacheco, M. Á., Gómez-Ros, J. M., and Domingo, C (2022). "Methodology to obtain quality factors for neutrons beyond 19.5 MeV using standard Monte Carlo codes". International Conference on Individual Monitoring of Ionising Radiation (IM2022) and Neutron and Ion Dosimetry Symposium (NEUDOS-14). Poster. April 25th - 29th, 2022 Kraków, Poland. URL$_1$: https://imneudos.jordan.pl/upload/Neudos/5.05.2022_IM2022_NEUDOS14_BOOK-OF-ABSTRACTS_FIN-(1).pdf and Reference P1-50 URL$_2$: https://imneudos.jordan.pl/upload/Neudos/5.05.2022_IM_NEUDOS_Programme_FIN.pdf.

Caballero-Pacheco, M.Á. (2022). "Methodology for dose equivalent assessment in mixed radiation fields combining measurements from different types of detectors". International Conference on Individual Monitoring of Ionising Radiation (IM2022) and Neutron and Ion Dosimetry Symposium (NEUDOS-14). Poster. April 25th - 29th, 2022 Kraków, Poland. URL$_1$: https://imneudos.jordan.pl/upload/Neudos/5.05.2022_IM2022_NEUDOS14_BOOK-OF-ABSTRACTS_FIN-(1).pdf and Reference P2-42 URL$_2$: https://imneudos.jordan.pl/upload/Neudos/5.05.2022_IM_NEUDOS_Programme_FIN.pdf.

Cross, G. W., Arneja, A., and Ing, H. (1986). "The response of electrochemically-etched CR-39 to protons of 10 KeV to 3 MeV". Nuclear Tracks 12, pp. 649–652. DOI: 10.1016/1359-0189(86)90671-0.

Cross, G. W., Arneja, A., and Kim, L. J. (1987). "The neutron energy and angular response of electrochemically etched CR-39 dosemeters". Radiation Protection Dosimetry 20, pp. 49–55. DOI: 10.1093/oxfordjournals.rpd.a080003.

Davídková, M. et al (2023). "Passive dosimetry in Mevion S250i Hyperscan single-room environment. Paper under preparation."

De, Sukanya, Mishra, G., Thomas, R. G., Kumar, Ajay, Mitra, A., and Nayak, B. K. (2020). "Measurement of prompt fission neutron and gamma spectra in the fast neutron induced fission of ^{232}Th". The European Physical Journal A 56, p. 116. DOI: 10.1140/epja/s10050-020-00127-7.

Detwiler, R.S., McConn, R.J., Grimes, T.F., Upton, S.A., and Engel, E.J. (2021). "Compendium of Material Composition Data for Radiation Transport Modeling". Richland, WA: Pacific Northwest National Laboratory. URL$_1$: https://www.pnnl.gov/publications/compendium-material-composition-data-radiation-transport-modeling-1 and URL$_2$: https://www.pnnl.gov/main/publications/external/technical_reports/PNNL-15870Rev2.pdf and URL$_3$: https://www.pnnl.gov/main/publications/external/technical_reports/PNNL-15870Rev1.pdf.

Di Fulvio, Angela, Tana, Luigi, Caresana, Marco, D'Agostino, Emiliano, de San Pedro, Marc, Domingo, Carles, and d'Errico, Francesco (2013). "Clinical simulations of prostate radiotherapy using BOMAB-like phantoms: Results for neutrons". Radiation Measurements 57, pp. 48–61. DOI: https://doi.org/10.1016/j.radmeas.2013.06.012.

Domingo C. García-Fusté, J. M., Amgarou, K., Morales, E, and Castelo, J. (2009). "Measurements in quasi-monoenergetic neutron beams at the EC-IRMM Van der Graaf accelerator for calibration of the UAB PADC based neutron dosimeter". Radiation Measurements 44, pp. 981–984. DOI: 10.1016/j.radmeas.2009.10.093.

Domingo, C., San-Pedro, M. de, García-Fusté, J. M., Romero, T. M., Amgarou, K, and Fernández, F. (2013). "Estimation of the response function of a PADC based neutron dosimeter in terms of fluence and ($H_p(10)$)". Radiation Measurements 50, pp. 82–86. DOI: 10.1016/j.radmeas.2012.02.016.

Domingo, C. et al (2023). "Neutron spectrometry in Mevion S250i Hyperscan single-room environment. Paper under preparation."

Dowdell, S.J. (2011). "Pencil beam scanning proton therapy: the significance of secondary particles". PhD Thesis. URL: https://ro.uow.edu.au/theses/3275/.

Durrani, S. A. and Al-Najjar, R. A. S. (1980). "Electrochemical etching studies of the CR-39 plastic." Nuclear Instruments and Methods 173, pp. 97–102. DOI: 10.1016/0029-554X(80)90572-8.

Durrani, S. A. and Bull, R. K. (1987). *Solid State Nuclear Track Detection: Principles, Methods and Applications*. Edition 1. Pergamon press.

ENDF (2022). "Evaluated Nuclear Data File (ENDF)". URL: https://www-nds.iaea.org/exfor/endf.htm.

EREMIN, N. V., PASKHALOV, A. A., MARKOCHEV, S. S., TSVETKOV, E. A., MANDAGLIO, G., MANGANARO, M., FAZIO, G., GIARDINA, G., and ROMANIUK, M. V. (2010). "NEW EXPERIMENTAL METHOD OF INVESTIGATION THE RARE NUCLEAR TRANSFORMATIONS ACCOMPANYING ATOMIC PROCESSES: BREMSSTRAHLUNG EMISSION IN SPONTANEOUS FISSION OF 252Cf". International Journal of Modern Physics E 19, pp. 1183–1188. DOI: 10.1142/S0218301310015655.

European Commission, Directorate-General for Energy and Transport, Ambrosi, P., Garcia-Alves, J., and Bartlett, D. (2009). "Technical recommendations for monitoring individuals occupationally exposed to external radiation. Radiation protection no. 160." Publications Office. DOI: 10.2768/19817.

Eurisys (1999). "Compteur ^{3}He. Technical report, Eurisys. Z.I. La vallée du Parc. 37600 Loches, France."

EXFOR (2022). "Experimental Nuclear Reaction Data (EXFOR)". URL: https://www-nds.iaea.org/exfor/.

EXPACS (2023). "EXPACS: EXcel-based Program for calculating Atmospheric Cosmic-ray Spectrum". URL: https://phits.jaea.go.jp/expacs/.

Farah, J., Mares, V., Romero-Expósito, M., Trinkl, S., Domingo, C., Dufek, V., Klodowska, M., Kubancak, J., Knežević, Ž., Liszka, M., Majer, M., Miljanić, S., Ploc, O., Schinner, K., Stolarczyk, L., Trompier, F., Wielunski, M., Olko, P., and Harrison, R. M. (2015). "Measurement of stray radiation within a scanning proton therapy facility: EURADOS WG9 intercomparison exercise of active dosimetry systems". Medical Physics 42.5, pp. 2572–2584. DOI: https://doi.org/10.1118/1.4916667.

Fernández, F., Bouassoule, T., Amgarou, K., Domingo, C., Garcia, M. J., Lacoste, V., Gressier, V., and Muller, H. (2007). "Monte Carlo calculations and validation of a gold foil-based Bonner sphere system". Radiation Protection Dosimetry 126, pp. 366–370. DOI: 10.1093/rpd/ncm076.

Fernández, F., Baixeras, C., Zamani, M., López, D., Jokic, S., Debeauvais, M., and Ralarosy, J. (1988). "CR-39 registration efficiency of protons using electrochemical etching". Radiation Protection Dosimetry 23, pp. 175–178. DOI: 10.1093/oxfordjournals.rpd.a080154.

Fernández, F., Domingo, C., Baixeras, C., Luguera, E., Zamani, M., and Debeauvais, M. (1991). "Fast neutron dosimetry with CR-39 using electrochemical etching". Nuclear Tracks and Radiation Measurements 19, pp. 467–470. DOI: 10.1016/1359-0189(91)90246-E.

Fernández, F., Domingo, C., Luguera, E., and Baixeras, C. (1992). "Experimental and theorical determination of the fast neutron response using CR-39 plastic detectors and polyethylene". Radiation Protection Dosimetry 44, pp. 337–340. DOI: 10.1093/rpd/44.1-4.337.

Fernández, F., Bouassoule, T, Domingo, C., Luguera, E., and Baixeras, C. (1996). "Response of a CR-39 fast neutron dosemeter with a polyethylene converter improved with makrofol". Radiation Protection Dosimetry 66, pp. 343–347. DOI: 10.1093/oxfordjournals.rpd.a031750.

Filges, D. and Goldenbaum, F. (2009). *Handbook of Spallation Research: Theory, Experiments and Applications*. Edition 1. WILEY-VCH Verlag GmbH & Co. KGaA.

Fleischer, L. R., Price, B. P., and Walker, M. R. (1964). "Track Registration in Various Solid-State Nuclear Track Detectors". Physical Review 133, A1443–A1449. DOI: 10.1103/PhysRev.133.A1443.

Fleischer, L. R., Price, B. P., and Walker, M. R. (1965). "Ion Explosion Spike Mechanism for Formation of Charged-Particle Tracks in Solids". Journal of applied physics 36, pp. 3645–3652. DOI: 10.1063/1.1703059.

Fleischer, L. R., Price, B. P., and Walker, M. R. (1967). "Criterion for Registration in Dielectric Track Detectors". Physical Review 156, pp. 353–355. DOI: 10.1103/PhysRev.156.353.

Fleischer, R. L., Price, B., and Walker, M. R. (1975). *Nuclear tracks in solids: Principles and Applications*. University of California press.

Gabriel, A. T. and Alsmiller, G. R. (1958). "Photonuclear Disintegration at High Energyes (< 350 MeV)". Physical Review 110, pp. 941–953. DOI: 10.1103/PhysRev.110.941.

Gammage, B. R. and Chowdhury, A (1982). "Partial optimization of electrochemical-ething parameters for highly sensitive CR-39 fast neutron dosimeters". Health Physics 43, pp. 225–229. DOI: 10.1097/00004032-198208000-00004.

García, J. M., Amgarou, K., Domingo, C., and Fernández, F. (2005). "Neutron response study of two CR-39 personal dosemeters with air and nylon converters". Radiation Measurements 40, pp. 607–611. DOI: 10.1016/j.radmeas.2005.04.017.

García-Fusté, M. J. (2010). "NEUTRON SPECTROMETRY IN COMPLEX N-G FIELDS: APPLICATION TO LINAC AND PET FACILITIES". PhD Thesis. URL$_1$: https://www.educacion.gob.es/teseo/mostrarRef.do?ref=885909, URL$_2$: https://www.tdx.cat/handle/10803/3427#page=1 and URL$_3$: https://dialnet.unirioja.es/servlet/tesis?codigo=87659.

García-Fusté, M.J., Devienne, A., M., Romero-Expósito., Caballero-Pacheco, M.A., and Domingo, C (2020). "Calibration of neutron dosimeters for radiation protection use at the ALBA synchrotron experimental hall". Radiation Physics and Chemistry 171, p. 108749. DOI: https://doi.org/10.1016/j.radphyschem.2020.108749.

Gomaa, M. A. and Kasim, A. S. (1980). "Neutron personnel dosimetry using a CR-39 carbonate plastic detector". Nuclear Instruments and Methods 176, pp. 579–582. DOI: 10.1016/0029-554X(80)90390-0.

GoodFellow (2023). "GoodFellow". URL: https://www.goodfellow.com/de/en-gb.

Green, T. P., Ramli, G. A., Hashemi-Nazhad, R. S., Al-Najar, R. A. S., Ooi, M. C., Abu-Jarad, F., Bull, K. R., and Durrani, A. S. (1982). "On the optimisation of etching conditions for CR-39 and other plastic track detectors." Solid State Nuclear Track Detectors - Proceedings of the 11th International Conference Bristol, 7-12, September 1981., pp. 179–182. DOI: 10.1016/B978-0-08-026509-4.50042-8.

Griffith, V. R., Hankins, E. D., Gammage, B. R., Tommasino, L, and Wheeler, V. R. (1979). "Recent developments in personnel neutron dosimeters - A review". Health Physics 36, pp. 235–260. DOI: 10.1097/00004032-197903000-00002.

Guo, S., C., Bao-Liu, and Durrani, A. S. (2020). "Chapter 3 - Solid-state nuclear track detectors". Handbook of Radioactivity Analysis 1, pp. 307–407. DOI: 10.1016/B978-0-12-814397-1.00003-0.

Górski, Z. A., Grümmer, F., and Goeke, K (1992). "Nucleon electric form factors and quark sea polarization in the Nambu-Jona-Lasinio model". Physics Letters B 278, pp. 24–28. DOI: 10.1016/0370-2693(92)90705-9.

Halpern, O. and Johnson, H. M. (1938). "On the magnetic scattering of neutrons". Physical Review 55, pp. 898–923. DOI: 10.1103/PhysRev.55.898.

Hankins, E. D., Homann, G. S., and Davis, M. J (1986). "Personnel neutron dosimetry using hot, low-frequency electrochemical etching". Nuclear Tracks 12, pp. 641–644. DOI: 10.1016/1359-0189(86)90669-2.

Higgins, P. D., Attix, F. H., Hubbell, J. H., Seltzer, S. M., Berger, M. J., and Sibata, C. H. (1992). "Mass Energy-Transfer and Mass Energy-Absorption Coefficients, Including In-Flight Positron Annihilation for Photon Energies 1 KeV to 100 MeV". National Institute of Standards. NISTIR 4812. URL: https://nvlpubs.nist.gov/nistpubs/Legacy/IR/nistir4812.pdf.

Hitachi (2022). "Proton radiotherapy solutions by Hitachi". URL: https://www.hitachi.com/businesses/healthcare/products-support/pbt/probeat/solution/index.html.

Hashemi-Nezhad, R. S., Green, F. P., Durrani, A. S., and Bull, K. R. (1982). "Effect of etching conditions on the bulk-etch rate and track-etching response of CA80-15 cellulose nitrate". Nuclear Instruments and Methods 200, pp. 525–531. DOI: 10.1016/0167-5087(82)90480-X.

Hälg, R A, Besserer, J, Boschung, M, Mayer, S, Lomax, A J, and Schneider, U (2014). "Measurements of the neutron dose equivalent for various radiation qualities, treatment machines and delivery techniques in radiation therapy". Physics in Medicine & Biology 59, p. 2457. DOI: 10.1088/0031-9155/59/10/2457.

IAEA (2017). *Cosmic Ray Neutron Sensing: Use, Calibration and Validation for Soil Moisture Estimation*. TECDOC Series 1809. URL: https://www.iaea.org/publications/11097/cosmic-ray-neutron-sensing-use-calibration-and-validation-for-soil-moisture-estimation.

IAEA (2018). *Radiation Protection of the Public and the Environment*. URL: https://www.iaea.org/publications/11183/radiation-protection-of-the-public-and-the-environment.

IAEA (2020). *Modern Neutron Detection*. TECDOC Series 1935. URL: https://www.iaea.org/publications/14690/modern-neutron-detection.

IAEA (2021). *Compact Accelerator Based Neutron Sources*. TECDOC Series 1981. Vienna. ISBN: 978-92-0-127022-1. URL: https://www.iaea.org/publications/14948/compact-accelerator-based-neutron-sources.

IBA (2022). "Proton radiotherapy solutions by IBA". URL: https://www.iba-worldwide.com/pt/proton-therapy/proton-therapy-solutions/.

ICRP (2003). "Relative Biological Effectiveness (RBE), Quality Factor (Q), and Radiation Weighting Factor (w_R). ICRP Publication 92." Annals of the ICRP. URL: https://www.icrp.org/publication.asp?id=ICRP%20Publication%2092.

ICRP (2007a). "1977 Recommendations of the International Commission on Radiological Protection. ICRP Publication 26." Annals of the ICRP. URL: https://www.icrp.org/publication.asp?id=icrp%20publication%2026.

ICRP (2007b). "2007 Recommendations of the International Commission on Radiological Protection. ICRP Publication 103." Annals of the ICRP. URL: https://www.icrp.org/publication.asp?id=ICRP%20Publication%20103.

ICRU (2007). "Prescribing, Recording, and Reporting Proton-Beam Therapy, ICRU Report 78." International Commission on Radiation Units and Measurements. URL: https://journals.sagepub.com/toc/crua/7/2.

ICRP (2010). "Conversion Coefficients for Radiological Protection Quantities for External Radiation Exposures. ICRP Publication 116." Annals of the ICRP. URL: https://www.icrp.org/publication.asp?id=icrp%20publication%20116.

ICRU (2011). "Fundamental quantities and units for ionizing radiation (Revised), ICRU Report 85." International Commission on Radiation Units and Measurements. URL: https://www.icru.org/report/fundamental-quantities-and-units-for-ionizing-radiation-icru-report-85a-revised/.

ICRU (1983). "Microdosimetry, ICRU Report 36." International Commission on Radiation Units and Measurements. URL: https://journals.sagepub.com/toc/crub/os-19/1.

ICRU (1984). "Stopping Powers for Electrons and Positrons, ICRU Report 37." International Commission on Radiation Units and Measurements. URL: https://journals.sagepub.com/toc/crub/os-19/2.

ICRU (1986). "The Quality Factor in Radiation Protection, ICRU Report 40." International Commission on Radiation Units and Measurements. URL: https://www.icru.org/report/the-quality-factor-in-radiation-protection-report-40/.

ICRU (1989). "Tissue Substitutes in Radiation Dosimetry and Measurement, ICRU Report 44." International Commission on Radiation Units and Measurements. URL: https://www.icru.org/report/tissue-substitutes-in-radiation-dosimetry-and-measurement-report-44/.

ICRP (1991). "1990 Recommendations of the International Commission on Radiological Protection. ICRP Publication 60." Annals of the ICRP. URL: https://www.icrp.org/publication.asp?id=icrp%20publication%2060.

ICRU (1992). "Measurement of Dose Equivalents from External Photon and Electron Radiations, ICRU Report 47." International Commission on Radiation Units and Measurements. URL: https://www.icru.org/report/measurement-of-dose-equivalents-from-external-photon-and-electron-radiations-report-47/.

ICRU (1993). "Stopping Powers and Ranges for Protons and Alpha Particles, ICRU Report 49." International Commission on Radiation Units and Measurements. URL: https://www.icru.org/report/stopping-power-and-ranges-for-protons-and-alpha-particles-report-49/.

ICRU (1998). "Conversion Coefficients for use in Radiological Protection Against External Radiation, ICRU Report 57." International Commission on Radiation Units and Measurements. URL: https://www.icru.org/report/conversion-coefficients-for-use-in-radiological-protection-against-external-radiation-report-57/.

International Atomic Energy Agency (1979). *Radiological Safety Aspects of the Operation of Electron Linear Accelerators*. Technical Reports Series 188. Vienna. ISBN: 92-0-125179-3. URL: https://www.iaea.org/publications/1289/radiological-safety-aspects-of-the-operation-of-electron-linear-accelerators.

ISO-8529-2:2000 (2000). "Reference neutron radiations — Part 2: Calibration fundamentals of radiation protection devices related to the basic quantities characterizing the radiation field. ISO 8529-2:2000." International Organization for Standardization. URL: https://www.iso.org/standard/25667.html.

ISO-8529-1:2021 (2021). "Neutron reference radiations fields — Part 1: Characteristics and methods of production. ISO-8529-1:2021." International Organization for Standardization. URL: https://www.iso.org/standard/80060.html.

ISO-8529-3:1998 (1998). "Reference neutron radiations — Part 3: Calibration of area and personal dosimeters and determination of response as a function of energy and angle of incidence. ISO-8529-3." International Organization for Standardization. URL: https://www.iso.org/standard/25668.html.

Jadrníčková, Iva and Spurný, František (2008). "To the spectrometry of linear energy transfer in charged particle beams by means of track-etch detectors". Radiation Measurements 43, S191–S194. DOI: https://doi.org/10.1016/j.radmeas.2008.04.010.

Joiner, M. and Kogel, A. van der (2009). *Basic Clinical Radiobiology*. Edition 4. Edward Arnold.

Jones, W. L. and Terwilliger, M. K. (1953). "Photoneutron Production Excitation Functions to 320 MeV". Physical Review 91, pp. 699–707. DOI: 10.1103/PhysRev.91.699.

Joost Iwema (2017). "Opportunities and limitations of the cosmic-ray neutron soil moisture sensor under humid conditions". PhD Thesis. URL: https://indico.ictp.it/event/9562/session/5/contribution/24/material/slides/1.pdf.

Kashual, N. N., Winhold, J. E., Yergin, F. P., Medicus, A. H., and Auguston, H. R. (1968). "Fast-Photoneutron Spectra due to 55-85 MeV Photons". Physical Review 175, pp. 1330–1336. DOI: 10.1103/PhysRev.175.1330.

Kellerer, M. A., Hahn, K., and Rossi, H. H. (1992). "Intermediate Dosimetric Quantities". Radiation Research 130, pp. 15–25. DOI: 10.2307/3578474.

Kishida, N., Murata, T., Asami, T., Kosako, K., Maki, K., Harada, H., Lee, O. Y., Chang, J., Chiba, S., and Fukahori, T. (2005). "JENDL Photonuclear Data File". AIP Conference Proceedings 769, pp. 199–202. DOI: 10.1063/1.1944989.

Kittel, C. (2005). *Introduction to Solid State Physics*. Edition 8. John Wiley & Sons, Inc.

Knežević, Ž., Ambrozova, I., Domingo, C., De Saint-Hubert, M., Majer, M., Martínez-Rovira, I., Miljanić, S., Mojżeszek, N., Porwoł, P., Ploc, O., Romero-Expósito, M., Stolarczyk, L., Trinkl, S., Harrison, R. M., and Olko, P. (2017). "COMPARISON OF RESPONSE OF PASSIVE DOSIMETRY SYSTEMS IN SCANNING PROTON RADIOTHERAPY—A STUDY USING PAEDIATRIC ANTHROPOMORPHIC PHANTOMS". Radiation Protection Dosimetry 180.1-4, pp. 256–260. DOI: 10.1093/rpd/ncx254.

Knežević, Željka, Stolarczyk, Liliana, Ambrožová, Iva, Caballero-Pacheco, Miguel Á., Davídková, Marie, De Saint-Hubert, Marijke, Domingo, Carles, Jeleń, Kinga, Kopeć, Renata, Krzempek, Dawid, Majer, Marija, Miljanić, Saveta, Mojżeszek, Natalia, Romero-Expósito, Maite, Martínez-Rovira, Immaculada, Harrison, Roger M., and Olko, Paweł (2022). "Out-of-Field Doses Produced by a Proton Scanning Beam Inside Pediatric Anthropomorphic Phantoms and Their Comparison With Different Photon Modalities". Frontiers in Oncology 12. DOI: 10.3389/fonc.2022.904563.

Knoll, F. G. (2010). *Radiation detection and measurement*. Edition 4. Wiley.

Koch, W. H. and Motz, W. J (1959). "Bremsstrahlung cross-section formulas and related data". Reviews of Modern Physics 31, pp. 920–956. DOI: 10.1103/RevModPhys.31.920.

Kranz, W. L. (2015). "Irrigation and Nitrogen Management User Education/Certification Program. Section C: Soil characteristics that influence nitrogen and water management". Institute of Agriculture and Natural Resources at the University of Nebraska–Lincoln. URL_1: https://water.unl.edu/documents/Section%20C.pdf and URL_2: https://extensionpublications.unl.edu/assets/pdf/ec2008.pdf.

Krane, K. S. (1987). *Introductory Nuclear Physics*. Edition 1. John Wiley & Sons.

Kry, Stephen F., Bednarz, Bryan, Howell, Rebecca M., Dauer, Larry, Followill, David, Klein, Eric, Paganetti, Harald, Wang, Brian, Wuu, Cheng-Shie, and George Xu, X. (2017). "AAPM TG 158: Measurement and calculation of doses outside the treated volume from external-beam radiation therapy". Medical Physics 44, e391–e429. DOI: https://doi.org/10.1002/mp.12462.

Köhli, Markus, Weimar, Jannis, Schrön, Martin, Baatz, Roland, and Schmidt, Ulrich (2021). "Soil Moisture and Air Humidity Dependence of the Above-Ground Cosmic-Ray Neutron Intensity". Frontiers in Water 2. DOI: 10.3389/frwa.2020.544847.

Lacoste, V., Gressier, V., Muller, H., and Lebreton, L. (2004a). "Characterisation of the IRSN graphite moderated Americium–Beryllium neutron field". Radiation Protection Dosimetry 110, pp. 135–139. DOI: 10.1093/rpd/nch188.

Lacoste, V., Gressier, V., Pochat, J.-L., Fernández, F., Bakali, M., and Bouassoule, T. (2004b). "Characterization of Bonner sphere systems at monoenergetic and thermal neutron fields". Radiation Protection Dosimetry 110, pp. 529–532. DOI: 10.1093/rpd/nch279.

Lajtai, A., Kecskeméti, J., Sáfár, J., Dyachenko, P. P., and Piksaikin, V. M. (1985). "Prompt neutron spectra for energy range 30 KeV - 4 MeV from fission of $_{233}$U induced by thermal neutrons". URL: https://www-nds.iaea.org/exfor/servlet/X4sShowPubl?File=R,IAEA-335,312,1985.

Lajtai, A., Dyachenko, P.P., Kononov, V.N., and Seregina, E.A. (1990). "Low-energy neutron spectrometer and its application for 252Cf neutron spectrum measurements". Nuclear Instruments and Methods in Physics Research Section A: Accelerators, Spectrometers, Detectors and Associated Equipment 293, pp. 555–561. DOI: https://doi.org/10.1016/0168-9002(90)90323-X.

Leuthold, G., Mares, V., and Schraube, H. (1992). "Calculation of the neutron ambient dose equivalent on the basis of the ICRP revised quality factors". Radiat. Prot. Dosim. 40, pp. 77–84. DOI: 10.1093/oxfordjournals.rpd.a081194.

Levinger, S. J. (1951). "The High Energy Nuclear Photoeffect". Physical Review 84, pp. 43–51. DOI: 10.1103/PhysRev.84.43.

Lounis-Mokrani, Z., Fromm, M., Barillon, R., Chambaudet, A., and Allab, M (2003). "Characterization of chemical and optical modifications induced by 22.5 MeV proton beams in CR-39 detectors". Radiation Measurements 36, pp. 615–620. DOI: 10.1016/S1350-4487(03)00211-7.

Luke, S. J., Gossett, C. A., and Vandenbosch, R. (1991). "Search for high energy γ rays from the spontaneous fission of ^{252}Cf". Phys. Rev. C 44, pp. 1548–1554. DOI: 10.1103/PhysRevC.44.1548.

Lynn, W. J. (2012). *Magnetic Neutron Scattering*. Wiley Online Library. DOI: 10.1002/0471266965.com101.pub2. URL: https://tsapps.nist.gov/publication/get_pdf.cfm?pub_id=908109.

Mares, V., Romero-Expósito, M., Farah, J., Trinkl, S., Domingo, D., Dommert, M., Stolarczyk, L., Van Ryckeghem, L, Wielunski, M., Olko, P., and Harrison, R. M. (2016). "A comprehensive spectrometry study of a stray neutron radiation field in scanning proton therapy". Physics in Medicine & Biology 61.11, p. 4127. DOI: 10.1088/0031-9155/61/11/4127.

McKeever, S. W. S. (1983). *Thermoluminescence of solids*. Edition 1. Cambridge university press.

Mevion (2022). "Proton radiotherapy solutions by Mevion". URL: https://www.mevion.com/products.

Mitaroff, A. and Silari, M. (2002). "The CERN-EU High-energy Reference Field (CERF) Facility for Dosimetry at Commercial Flight Altitudes and in Space". Radiation Protection Dosimetry 102, pp. 7–22. DOI: 10.1093/oxfordjournals.rpd.a006075.

Morejon, L., Fedynitch, A., Boncioli, D., Biehl, D., and Winter, W. (2019). "Improved photomeson model for interactions of cosmic ray nuclei". Journal of Cosmology and Astroparticle Physics 2019. DOI: 10.1088/1475-7516/2019/11/007.

Muller, H., Fernández, F., Van Ryckeghem, L., Alexandre, L., Bouassoule, T., Pochat, J. L., and Tomas, M (2002). "Monte Carlo calculations and experimental results of Bonner spheres systems with a new cylindrical Helium-3 proportional counter". Nuclear Instruments and Methods in Physics Research Section A: Accelerators, Spectrometers,

Detectors and Associated Equipment 476, pp. 411–415. DOI: https://doi.org/10.1016/S0168-9002(01)01480-2.

Naik, H., Dange, P. S., Jang, W., and Singh, J. R. (2021). "Post-Neutron Mass Yield Distributions in the Spontaneous Fission of ^{252}Cf". Nuclear Science and Engineering 195, pp. 717–740. DOI: 10.1080/00295639.2020.1866389.

NCRP (2003). "Radiation Protection for Particle Accelerator Facilities. NCRP report 144." National Council on Radiation Protection and Measurements. Bethesda, MD 20814-3095. URL: https://ncrponline.org/shop/reports/report-no-144-radiation-protection-for-particle-accelerator-facilities-2003/.

Nefedov, V. N., Starostov, B. I., and Boytsov, A. A. (1984). "High precision spectra measurements for neutrons arising from the fission of Cf-252, U-233, U-235, Pu-239 in the energy range 0.04 - 5 MeV". Proc.Conf.Neutron Physics, Kiev 2. URL$_1$: https://www-nds.iaea.org/exfor/servlet/X4sShowPubl?File=C,83KIEV,2,285,1983, URL$_2$: https://www-nds.iaea.org/exfor/servlet/X4sGetSubent?reqx=5961&subID=40871005 and URL$_3$: https://www.nndc.bnl.gov/nsr/nsrlink.jsp?1984NEZT, p. 285.

Oberstedt, A., Billnert, R., Hambsch, F.-J., and Oberstedt, S. (2015). "Impact of low-energy photons on the characteristics of prompt fission γ-ray spectra". Phys. Rev. C 92, p. 014618. DOI: 10.1103/PhysRevC.92.014618.

Paganetti, H. (2014). "Relative biological effectiveness (RBE) values for proton beam therapy. Variations as a function of biological endpoint, dose, and linear energy transfer." Physics in Medicine & Biology 59, R419–R472. DOI: 10.1088/0031-9155/59/22/R419.

Paganetti, H. (2019). *Proton Therapy Physics*. Edition 2. CRC Taylor and Francis group.

Pandit, Deepak, Mukhopadhyay, S., Bhattacharya, Srijit, Pal, Surajit, De, A., and Banerjee, S.R. (2010). "Coherent bremsstrahlung and GDR width from 252Cf cold fission". Physics Letters B 690, pp. 473–476. DOI: https://doi.org/10.1016/j.physletb.2010.05.079.

Pandit, Deepak, Mondal, Debasish, Ghosh, T.K., Mukhopadhyay, S., Pal, Surajit, Sen, A., Saha, A.K., Jha, V.N., Saha, Satyajit, Bhattacharya, C., and Mohanty, A.K. (2021). "Search for coherent bremsstrahlung from spontaneous fission at 555 meter deep underground laboratory". Physics Letters B 823, p. 136760. DOI: https://doi.org/10.1016/j.physletb.2021.136760.

Pelliccioni, M. (2000). "Overview of Fluence-to-Effective dose and Fluence-to-Ambient Dose Equivalent Conversion Coefficients for high energy radiation calculated using the FLUKA code". Radiat. Prot. Dosim. 88, pp. 279–297. DOI: 10.1093/oxfordjournals.rpd.a033046.

Pelowitz, D.B. (2011). "MCNPX Users Manual Version 2.7.0". LA-CP-11-00438. URL: https://mcnp.lanl.gov/manual.html.

Ploeg, H. van der, Postma, R., Bacelar, J. C., Berg, T. van den, Iacob, V., Jongman, J., and Woude, A. van der (1992). "Large gamma anisotropy observed in the ^{252}Cf spontaneous-fission process". Phys. Rev. Lett. 68 (21), pp. 3145–3147. DOI: 10.1103/PhysRevLett.68.3145.

Pozzi, F. and Silari, M. (2020). "The CERN-EU high-energy Reference Field (CERF) facility: New FLUKA reference values of spectral fluences, present and newly proposed operational quantities". Nuclear Instruments and Methods in Physics Research Section A: Accelerators, Spectrometers, Detectors and Associated Equipment 979, p. 164477. DOI: https://doi.org/10.1016/j.nima.2020.164477.

Price, G. A (1954). "Energy Spectra and Angular Distributions of Photoneutrons from Heavy Nuclei". Physical Review 93, pp. 1279–1285. DOI: 10.1103/PhysRev.93.1279.

ProNova (2022). "Proton radiotherapy solutions by ProNova". URL: https://provisionhealthcare.com/about-us/innovative-solutions/proton-therapy-system/.

ProTom (2022). "Proton radiotherapy solutions by ProTom". URL: https://www.protominternational.com/about-radiance-330/.

Pynn, R. (n.d.). "Lecture 1: Introduction & neutron scattering theory". Los Alamos National Laboratory (). URL: https://www.ncnr.nist.gov/summerschool/ss14/pdf/Lecture_1_Theory.pdf.

Qi, L., Lebois, M., Wilson, J. N., Chatillon, A., Courtin, S., Fruet, G., Georgiev, G., Jenkins, D. G., Laurent, B., Le Meur, L., Maj, A., Marini, P., Matea, I., Morris, L., Nanal, V., Napiorkowski, P., Oberstedt, A., Oberstedt, S., Schmitt, C., Serot, O., Stanoiu, M., and Wasilewska, B. (2018). "Statistical study of the prompt-fission γ-ray spectrum for ^{238}U(n, f) in the fast-neutron region". Phys. Rev. C 98, p. 014612. DOI: 10.1103/PhysRevC.98.014612.

Rachen, P. J (1996). "Interaction Processes and Statistical Properties of the Propagation of Cosmic Rays in Photon Backgrounds". PhD Thesis. DOI: 10.5281/zenodo.3242300.

Romero-Expósito, M., Domingo, C., Sánchez-Doblado, F., Ortega-Gelabert, O., and Gallego, S. (2016). "Experimental evaluation of neutron dose in radiotherapy patients: Which dose?" Medical Physics 43, pp. 360–367. DOI: https://doi.org/10.1118/1.4938578.

Reedy, R.C. and Frankle, S.C. (2002). "PROMPT GAMMA RAYS FROM RADIATIVE CAPTURE OF THERMAL NEUTRONS BY ELEMENTS FROM HYDROGEN THROUGH ZINC". Atomic Data and Nuclear Data Tables 80, pp. 1–34. DOI: https://doi.org/10.1006/adnd.2001.0870.

Reinhardt, C. G. and Whitehead, D. W. (1962). "Angular distribution of fast photoneutrons". Nuclear Physics 30, pp. 201–214. DOI: 10.1016/0029-5582(62)90044-5.

Sato, Tatsuhiko (2015). "Analytical Model for Estimating Terrestrial Cosmic Ray Fluxes Nearly Anytime and Anywhere in the World: Extension of PARMA/EXPACS". PLOS ONE 10, pp. 1–33. DOI: 10.1371/journal.pone.0144679.

Sato, Tatsuhiko, Iwamoto, Yosuke, Hashimoto, Shintaro, Ogawa, Tatsuhiko, Furuta, Takuya, Abe, Shin ichiro, Kai, Takeshi, Tsai, Pi-En, Matsuda, Norihiro, Iwase, Hiroshi, Shigyo, Nobuhiro, Sihver, Lembit, and Niita, Koji (2018). "Features of Particle and Heavy Ion Transport code System (PHITS) version 3.02". Journal of Nuclear Science and Technology 55.6, pp. 684–690. DOI: 10.1080/00223131.2017.1419890.

Schneider, C. A., Rasband, W. S., and Eliceiri, K. W. (2012). "NIH Image to ImageJ: 25 years of image analysis". Nature Methods 9, pp. 671–675. DOI: 10.1038/nmeth.2089.

Schrön, M., Zacharias, S., Köhli, M., Weimar, J., and Dietrich, P. (2016). "Monitoring Environmental Water with Ground Albedo Neutrons from Cosmic Rays". The 34th International Cosmic Ray Conference (ICRC2015) - Cosmic Ray Physics: Methods, Techniques and Instrumentation 236. DOI: https://doi.org/10.22323/1.236.0231.

Sagrado García, I. C., Lecolley, J. F., Lecolley, F. R., Blideanu, V., Ban, G., Fontbonne, J. M., Itis, G., Lecouey, J. L., Lefort, T., Marie, N., Steckmeyer, J. C., Le Brun, C., Blomgren, J., Johansson, C., Klug, J., Orhn, A., Mermod, P., Olsson, N., Pomp, S., Osterlund, M., Tippawan, U., Prokofiev, A. V., Nadel-Turonski, P., Fallot, M., Foucher, Y., Guertin, A., Haddad, F., and Vatre, M. (2011). "Neutron production in neutron-induced reactions at 96 MeV on ^{56}Fe and ^{208}Pb". Phys. Rev. C 84, p. 044619. DOI: 10.1103/PhysRevC.84.044619.

SHI (2022). "Proton radiotherapy solutions by SHI". URL: https://www.shi.co.jp/industrial/en/product/medical/proton-therapy/proton-therapy-system.html.

Shin, M. Y., Rawlins, A. J., Buss, W., and Evwaraye, O. A. (1970). "Photoneutron angular distributions from the ^{2}H(γ, n)H reaction". Nuclear Physics 154, pp. 482–496. DOI: 10.1016/0375-9474(70)90120-X.

Siebert, B. R. L. and Schuhmacher, H (1995). "Quality factors, ambient and personal dose equivalent for neutrons, based on the new ICRU stopping power data for protons and alpha particles". Radiat. Prot. Dosim. 3, pp. 177–183. DOI: 10.1093/oxfordjournals.rpd.a082612.

Silk, E. C. H., Barnes, R. S., and Harwell, A. E. R. E. (1959). "Examination of Fission Fragment Tracks with an Electron Microscope". Philosophical Magazine 4:44, pp. 970–972. DOI: 10.1080/14786435908238273.

Simakov, S.P., Devkin, B.V., Kobozev, M.G., Lunev, V.P., Lychagin, A.A., Talalaev, V.A., Titarenko, N.N., Zeleneckij, A.B., and Zhuravlev, B.V. (1990). "Differential neutron emission and inelastic cross section from ^{208}Pb and ^{209}Bi and 14.1 MeV incident energy". International Atomic Energy Agency, Vienna (Austria). International Nuclear Data Committee. URL$_1$: https://inis.iaea.org/search/search.aspx?orig_q=RN:21089270 and URL$_2$: https://inis.iaea.org/collection/NCLCollectionStore/_Public/21/089/21089270.pdf?r=1.

Smith, A. B., Fields, P. R., and Friedman, A. M. (1956). "Prompt Gamma Rays Accompanying the Spontaneous Fission of Cf^{252}". Phys. Rev. 104, pp. 699–702. DOI: 10.1103/PhysRev.104.699.

Sohrabi, M. (1981). "Electrochemical etching of fast-neutron-induced recoil tracks: The effects of field strength and frequency." Nuclear Tracks 4, pp. 131–140. DOI: 10.1016/0191-278X(80)90003-7.

Somogyi, G. (1977). "Processing of plastic track detectors." Nuclear Track Detection 1, pp. 3–18. DOI: 10.1016/0145-224X(77)90018-7.

San Pedro Pérez, M. de (2011). "Millora del sistema de revelat, lectura i comptatge en dosimetría neutrònica basat en detector plàstic CR-39 i estudi de la seva resposta". Bachelor Final Project.

Starostov, B. I., Nefedov, V. N., and Boytsov, A. A. (1984). "High precision prompt neutrons spectra measurement for neutrons from Cf-252, U-233, U-235, Pu-239 fission in the energy range 2. - 11. MeV". Proc.Conf.Neutron Physics, Kiev 2. URL$_1$: https:

//www-nds.iaea.org/exfor/servlet/X4sShowPubl?File=C,83KIEV,2,290,1983, URL$_2$: https://www-nds.iaea.org/exfor/servlet/X4sGetSubent?reqx=5961&subID=40872002 and URL$_3$: https://www.nndc.bnl.gov/nsr/nsrlink.jsp?1984STZR, p. 290.

Stolarczyk, L., Trinkl, S., Romero-Expósito, M., Mojżeszek, N., Ambrozova, I, Domingo, C., Davídková, M., Farah, J., Kłodowska, M., Knežević, Ž., Liszka, M., Majer, M., Miljanić, S., Ploc, O., Schwarz, M., Harrison, R. M., and Olko, P. (2018). "Dose distribution of secondary radiation in a water phantom for a proton pencil beam—EURADOS WG9 intercomparison exercise". Physics in Medicine & Biology 63.8, p. 085017. DOI: 10.1088/1361-6560/aab469.

Status of Fast Reactor Research and Technology Development (2013). TECDOC Series 1691. Vienna: International Atomic Energy Agency. URL: https://www.iaea.org/publications/8667/status-of-fast-reactor-research-and-technology-development.

Terranova, M. L., Kezerashvili, G. Ya., Milov, A. M., Mishnev, S. I., Muchnoi, N. Yu., Naumenkov, A. I., Protopopov, I. Ya., Simonov, E. A., Shatilov, D. N., Tavares, O. A. P., Paiva, E. De., and Moreira, E. L. (1998). "Photofission cross section and fissility of pre-actinide and intermediate-mass nuclei by 120 and 145 MeV Compton backscattered photons". Journal of Physics G: Nuclear and Particle Physics 24, pp. 205–216. DOI: 10.1088/0954-3899/24/1/023.

Tipler, A. P. and Mosca, G. (2008). *Physics for scientists and engineers*. Edition 6. W. H. Freeman and Company.

Tommasino, L. (1970). "Electrochemical etching of damaged track detectors by H. V. pulse and sinusoidal waveform". Internal Rept. Lab. Dosimetria e Standardizzazione. CNEN Casaccia, Rome.

Tommasino, L. and Armellini, C. (1973). "A new etching technique for damage track detectors". Radiation Effects 20, pp. 253–255. DOI: 10.1080/00337577308232292.

Tommasino, L., Zapparoli, G., Spiezia, P., Griffith, V. R., and Espinosa, G. (1984). "Different etching processes of damage track detectors for personnel neutron dosimetry". Nuclear Tracks and Radiation Measurements 8, pp. 335–339. DOI: 10.1016/0735-245X(84)90116-9.

Turner, E. J. (2007). *Atoms, Radiation and Radiation Protection*. Edition 3. Wiley.

United States Nuclear Regulatory Comission (2023). "U.S. Nuclear Regulatory Commission Regulations: Title 10, Code of Federal Regulations". URL$_1$: https://www.nrc.gov/reading-rm/doc-collections/cfr/index.html and URL$_2$: https://www.nrc.gov/reading-rm/doc-collections/cfr/part020/part020-1004.html.

Varian (2022). "Proton radiotherapy solutions by Varian". URL: https://www.varian.com/products/proton-therapy/treatment-delivery/probeam.

Vilches-Freixas, G., Unipan, M., Rinaldi, I., Martens, J., Roijen, E., Almeida, I. P., Decabooter, E., and Bosmans, G (2020). "Beam commissioning of the first compact proton therapy system with spot scanning and dynamic field collimation". The British Journal of Radiology 93.1107, p. 20190598. DOI: 10.1259/bjr.20190598.

Van Hoey, O., Stolarczyk, L., Lillhök, J., Eliasson, L., Mojzeszek, N., Liszka, M., Alkhiat, A., Mares, V., Trompier, F., Trinkl, S., Martínez-Rovira, I., Romero-Expósito, M., Domingo, C., Ploc, O., Harrison, R., and Olko, P. (2022). "Simulation and experimental verification of ambient neutron doses in a pencil beam scanning proton therapy room as a function of treatment plan parameters". Frontiers in Oncology 12, pp. 1–33. DOI: 10.3389/fonc.2022.903537.

Vorobyev, A. S. and Shcherbakov, O. A. (2011). "Integral prompt neutron spectrum for fission of $_{235}$U by thermal neutrons". URL: https://nds.iaea.org/publications/indc/indc-ccp-0455.pdf.

Walker, M. R., Price, B. P., and Fleischer, L. R. (1963). "A versatile, disposable dosimeter for slow and fast neutrons". Applied Physics Letters 3, pp. 28–29. DOI: 10.1063/1.1753861.

Weil, R. R. and Brady, N. C. (2017). *The Nature and Properties of Soils*. Edition 15. Pearson Education Limited.

Werner, Christopher John, Armstrong, Jerawan Chudoung, Brown, Forrest Brooks, Bull, Jeffrey S., Casswell, Laura, Cox, Lawrence James, Dixon, David A., Forster III, Robert Arthur, Goorley, John Timothy, Hughes III, Henry Grady, Favorite, Jeffrey A., Martz, Roger Lee, Mashnik, Stepan Georgievich, Rising, Michael Evan, Solomon Jr., Clell Jeffrey, Sood, Avneet, Sweezy, Jeremy Ed, Zukaitis, Anthony J., Anderson, Casey Alan, Elson, Jay Samuel, Durkee Jr., Joe W., Johns, Russell Craig, McKinney, Gregg Walter, McMath, Garrett Earl, Hendricks, John S., Pelowitz, Denise B., Prael, Richard Edward, Booth, Thomas Edward, James, Michael R., Fensin, Michael Lorne, Wilcox, Trevor A., and Kiedrowski, Brian Christopher (2017). "MCNP User's Manual Code Version 6.2". LA-UR-17-29981. URL$_1$: http://permalink.lanl.gov/object/tr?what=info:lanl-repo/lareport/LA-UR-17-29981 and URL$_2$: https://mcnp.lanl.gov/manual.html.

Whitehead, C., McMurray, R. W., Aitken, J. M., Middlemas, N., and Collie, H. C. (1958). "Ejection of Photoprotons from Light Elements by 45-110 MeV Bremsstrahlung". Physical Review 110, pp. 941–953. DOI: 10.1103/PhysRev.110.941.

Wochnik, A., Stolarczyk, L., Ambrozová, I., Davídková, M., De Saint-Hubert, M., Domanski, S., Domingo, C., Knezevic, Z., Kopec, R., Kuc, M., Majer, M., Mojzeszek, N., Mares, V., Martínez-Rovira, I., Caballero-Pacheco, M.Á., Pyszka, E., Swakon, J., Trinkl, S., Tisi, M., Harrison, R., and Olko, P. (2021). "Out-of-field doses for scanning proton radiotherapy of shallowly located paediatric tumours-a comparison of range shifter and 3D printed compensator". Phys. Med. Biol. 66. DOI: 10.1088/1361-6560/abcb1f.

Xu, X George, Bednarz, Bryan, and Paganetti, Harald (2008). "A review of dosimetry studies on external-beam radiation treatment with respect to second cancer induction". Physics in Medicine & Biology 53, R193. DOI: 10.1088/0031-9155/53/13/R01.

Young, D. A. (1958). "Etching of radiation damage in lithium fluoride". Nature 66.4632, pp. 375–377. DOI: 10.1038/182375a0.

Zaliznyak, O. I. and Tranquada, M. J. (2015). *Neutron Scattering and its application to strongly correlated systems*. Vol. 180. Springer Series in Solid-State Sciences, pp. 205–235. DOI: 10.1007/978-3-662-44133-6_7.

Zhou, D., Semones, E., Weyland, M., and Benton, E.R. (2007). "LET calibration for CR-39 detectors in different oxygen environments". Radiation Measurements 42.9, pp. 1499–1506. DOI: https://doi.org/10.1016/j.radmeas.2007.08.001.

Ziegler, J. F., Biersack, J. P., and Haggmark, L (1985). "SRIM - The Stopping and Range of Ions in Solids". URL: http://www.srim.org/.